

Sheffield Hallam University

Deoxidation mechanisms in liquid steel.

KAY, Helen.

Available from the Sheffield Hallam University Research Archive (SHURA) at:

<http://shura.shu.ac.uk/19899/>

A Sheffield Hallam University thesis

This thesis is protected by copyright which belongs to the author.

The content must not be changed in any way or sold commercially in any format or medium without the formal permission of the author.

When referring to this work, full bibliographic details including the author, title, awarding institution and date of the thesis must be given.

Please visit <http://shura.shu.ac.uk/19899/> and <http://shura.shu.ac.uk/information.html> for further details about copyright and re-use permissions.

SHEFFIELD HALLAM UNIVERSITY
CITY COLLEGE SHEFFIELD
SHEFFIELD S1 1WB

101 522 975 1



Bm 367333

Sheffield Hallam University

REFERENCE ONLY

ProQuest Number: 10697205

All rights reserved

INFORMATION TO ALL USERS

The quality of this reproduction is dependent upon the quality of the copy submitted.

In the unlikely event that the author did not send a complete manuscript and there are missing pages, these will be noted. Also, if material had to be removed, a note will indicate the deletion.



ProQuest 10697205

Published by ProQuest LLC (2017). Copyright of the Dissertation is held by the Author.

All rights reserved.

This work is protected against unauthorized copying under Title 17, United States Code
Microform Edition © ProQuest LLC.

ProQuest LLC.
789 East Eisenhower Parkway
P.O. Box 1346
Ann Arbor, MI 48106 – 1346

Deoxidation Mechanisms in Liquid Steel

by

Helen Kay BSc

A thesis submitted to Sheffield Hallam University in partial
fulfilment of the requirements for the degree of
Doctor of Philosophy

Sponsoring Establishment: Sheffield Hallam University

Collaborating Establishment: British Steel

April 1996

Preface

The work presented in this thesis was carried out during the period October 1987 to March 1996 in the School of Engineering, Sheffield Hallam University.

The work described in this thesis is, to the best of my knowledge, original except where reference has been made to others, and no part of it has been submitted for an award at any college or University.

During the period of this work regular meetings were held to discuss progress and the following conference was attended:

The Control of Oxygen during Steelmaking and the Production of Ultra Clean Steel. 5-6 April 1989, Institute of Metals, London.

In addition the author attended the following units from the part-time MSc in Metallurgical Process Management at Sheffield Hallam University:

Process Metallurgy - Transport Phenomena

Slag Chemistry

Deoxidation Mechanisms in Liquid Steel

by
Helen Kay

Abstract

Quantitative chemical and scanning electron microscopical techniques have been employed to investigate the deoxidation kinetics and changes in oxidation product morphology in low carbon steel melts. The techniques have been used to study the deoxidation processes associated with aluminium, titanium, silicon, zirconium and a calcium-aluminium alloy.

After the addition of the deoxidant, the total oxygen concentrations of all melts rapidly decreased corresponding with a decrease in the size and number of inclusions observed. This continued to a plateau level of total oxygen concentration and mean inclusion diameter.

Samples removed from the melts prior to deoxidation were found to contain globular MnO-FeO inclusions.

It was discovered that the morphological sequence for single element deoxidants involved a progressive evolution from liquid globular to solid spherical inclusions followed by polyhedral, dendritic and coralline morphologies. Finally, sintered agglomerates were formed when inclusion clusters collapsed. The extent to which the oxidation products went down the sequence depended on: the dissolution characteristics of the deoxidant; the thermodynamic affinity of the deoxidant for oxygen in the melt; the inclusion/melt interfacial energy characteristics; the refractoriness of the oxidation products and intermediate compounds; and the degree of turbulence experienced by the melt. Explanations have been postulated which elucidate the behaviour of the different deoxidants, as not all displayed the whole morphological sequence. Silicon deoxidation produced spherical silicates, whereas the zirconia inclusions were either spherical or dendritic and the titanium oxidation products had spherical or polyhedral morphologies. Aluminium exhibited all morphologies in the sequence.

Deoxidation with the calcium-aluminium alloy was found to have preceded by a two stage process. The initial stage was dominated by the formation of aluminium rich solid oxides followed by the progressive reduction by calcium, resulting in an adhesive liquid calcium-aluminate surface coating.

The role of refractory crucible as a collecting surface for the capture and removal of deoxidation products from the melt was investigated, which confirmed that the inclusions were generally incorporated into the low melting point matrix phases. Turbulence also increased the probability that emergence would take place at these capture sites.

Acknowledgements

I would like to thank my supervisors, Dr R Acheson and Dr R Jackson for their extremely helpful discussions, guidance and patience throughout the supervision of this work. I would like to thank my industrial supervisor, Mr M Heesom, for his encouragement and discussions during the early stages of this work.

I would also like to express my thanks to colleagues for useful discussions, especially Prof. A D W Hills and Prof. F B Pickering, and to the members of technical staff of both the School of Engineering and Materials Research Institute who contributed in various ways during the course of this work. Particular thanks go to Mr John Bradshaw, Mr Tony Earnshaw, Mr Derek Latimer, Dr Brian Lewis and Mr Paul Slingsby.

Contents

	Page No
Contents	i
Symbols	v
Chapter 1 Introduction	1
Chapter 2 Literature Review	4
2.1 Introduction	5
2.2 Deoxidant Elements & Alloys	6
2.3 Thermodynamics of Steel Deoxidation	7
2.4 Kinetics of Deoxidation	11
2.4.1 Solution of Deoxidant	11
2.4.2 Nucleation of Deoxidation Products	12
2.4.3 Particle Growth Mechanisms	18
2.4.4 Removal of Deoxidation Products from Steel Melts	29
2.5 The Effect of Surface Active Elements on the Surface Properties of Inclusions	37
2.6 The Effect of the Crucible Material on the rate of Deoxidation	39
2.7 Aluminium Deoxidation	41
2.7.1 Spherical Alumina Morphologies	43
2.7.2 Dendritic & Associated Alumina Morphologies	46
2.7.3 Dendritic Growth Theories	47
2.7.4 Observations & Mechanisms of Alumina Dendritic Growth	50
2.7.5 Polyhedral Alumina Morphologies	53
2.7.6 Polyhedral Growth Theories	53
2.7.7 Polyhedral Alumina Observations	54
2.7.8 The Effect of Surface Active Elements on Polyhedral Growth	54
2.8 Calcium Deoxidation	55

2.9	Silicon Deoxidation	57
2.10	Titanium Deoxidation	59
2.11	Zirconium Deoxidation	59
Chapter 3	Apparatus & Experimental Procedure	61
3.1	Introduction	62
3.2	Melting Equipment	63
	3.2.1 High Frequency Furnace	63
	3.2.2 Vertical Tube Furnace	64
3.3	Experimental Procedures	66
	3.3.1 Induction Furnace Heating Procedure	66
	3.3.2 Vertical Tube Heating Procedure	66
	3.3.3 Deoxidation Technique	67
	3.3.4 Sampling Technique	67
3.4	Bulk chemical Analysis Techniques	68
	3.4.1 Spark Emission Spectroscopy	68
	3.4.2 Inductively Coupled Plasma-Emission Spectroscopy	69
	3.4.3 Leco Oxygen Analysis	70
3.5	Scanning Electron Microscopy	71
	3.5.1 Scanning Electron Microscopy	71
	3.5.2 Sample Preparation	73
	3.5.3 Particle Size Analysis	75
	3.5.4 Energy Dispersive X-ray Analysis	76
	3.5.5 X-ray Elemental Mapping	79
3.6	Optical Microscopy	80
Chapter 4	Experimental Results	81
4.1	Introduction	82

4.2	Aluminium Deoxidised Melts	
	4.2.1 The Aluminium Vertical Tube Furnace Melt	82
	4.2.2 The Aluminium High Frequency Melt	88
4.3	Titanium Deoxidised Melts	91
	4.3.1 The Titanium Vertical Tube Furnace Melt	91
	4.3.2 The Titanium High Frequency Melt	95
4.4	Silicon Deoxidised Melts	98
	4.4.1 The Silicon Vertical Tube Furnace Melt	98
	4.4.2 The Silicon High Frequency Melt	101
4.5	Calcium-Aluminium Deoxidised Melts	103
	4.5.1 The Calcium-Aluminium Vertical Tube Furnace Melt	103
	4.5.2 The Calcium-Aluminium High Frequency Melt	104
4.6	Zirconium Deoxidised Melts	106
	4.6.1 The Zirconium Vertical Tube Furnace Melt	106
	4.6.2 The Zirconium High Frequency Melt	107
4.7	Crucible-Melt Interactions	108
	4.7.1 The Original Crucible Material	108
	4.7.2 The Crucible Interface in Contact with Undeoxidised Steel	109
	4.7.3 The Crucible Interface in Contact with the Aluminium deoxidised Steel	109
	4.7.4 The Crucible Interface in Contact with the Titanium deoxidised Steel	110
	4.7.5 The Crucible Interface in Contact with the Silicon deoxidised Steel	111
	4.7.6 The Crucible Interface in Contact with the Calcium-Aluminium deoxidised Steel	111
	4.7.7 The Crucible Interface in Contact with the Zirconium deoxidised Steel	112
Chapter 5	Discussion	113
5.1	Experimental Procedures	114
	5.1.1 Melting Equipment and Procedures	114

5.1.2	Metallography	115
5.1.3	Energy Dispersive X-ray analysis	116
5.2	Steel Melt Prior to Deoxidation	116
5.3	Aluminium Deoxidised Melts	117
5.4	Titanium Deoxidised Melts	127
5.5	Zirconium Deoxidised Melts	132
5.6	Silicon Deoxidised Melts	135
5.7	Calcium-Aluminium Deoxidised Melts	138
5.8	General Model for Deoxidation	143
5.9	The Crucible Melt Interface	151
5.9.1	The Undeoxidised Melts	151
5.9.2	Silicon Deoxidised Melts	152
5.9.3	Calcium-Aluminium Deoxidised Melts	153
5.9.4	Aluminium Deoxidised Melts	153
5.9.5	Titanium Deoxidised Melts	154
5.9.6	Zirconium Deoxidised Melts	154

Chapter 6	Conclusions	155
------------------	--------------------	------------

References

Tables

Figures

Plates

Symbols

a	activity at equilibrium
a'	actual activity
h	Planks Constant
h	Henrian activity
g	acceleration due to gravity, 9.81 m.s^{-1}
k	Boltzmanns Constant
n^*	number of critical sized nuclei per unit volume
n_v	number of atoms per unit volume
r	radius
r^*	critical radius of the embryonic nucleus
r_i	radius of the growing inclusion
r_o	radius of the diffusion volume
t	time
y	Henrian activity coefficient
A, A'	Frequency factors
B	Frequency factor
C_i	oxygen concentration in the inclusion
C_{im}	oxygen concentration in equilibrium with the deoxidation product
C_m	time dependent mean oxygen concentration in solution
C_o	initial uniform concentration of oxygen in the liquid steel
D	diffusion coefficient
F_b	buoyancy force
F_b	drag force
ΔG	chemical free energy change, J.mol^{-1}
$\Delta G''$	surface free energy change, J.m^{-2}
ΔG^*	activation energy for the formation of an inclusion nucleus

ΔG_D	activation energy for diffusion across the melt/nucleus interface
I	rate of nucleation
K	equilibrium constant
K'	reaction quotient at actual steelmaking conditions
K_S	equilibrium solubility product
K'_S	actual solubility product in the supersaturated solution
M	molecular mass, g.mol ⁻¹
R	gas constant, 8.314 J.mol ⁻¹ .K ⁻¹
S	supersaturation ratio
T	temperature
V	molar volume
Z	number of inclusions

Greek

β	coefficient of sliding friction
η	viscosity
θ	contact angle
ρ	density
σ_{im}	interfacial energy
σ_i	surface energy of the inclusion
σ_m	surface energy of the melt
τ	film thickness
v	velocity
ω	emergence coefficient
ξ	Stokes constant

1 INTRODUCTION

The process of steelmaking inevitably results in the presence of oxygen in the melt and to ensure internal integrity after solidification, steel is chemically deoxidised whilst still liquid. Deoxidation is the removal of dissolved oxygen from solution to form a fine dispersion of oxide particles. If the particles remain trapped in the solid steel they may have an adverse effect on the mechanical properties of the steel. Current trends in manufacture have been aimed at achieving ever lower residual oxygen concentrations to improve the ductility of steels used in adverse environments. Many studies have been carried out on the thermodynamics of deoxidation, and the effect of inclusions on the structure and properties of steel. However, there is still a need for a basic understanding of the effects of inclusion morphology on the kinetics of their removal from the melt.

The work described in this thesis was undertaken to develop a greater understanding of the mechanisms which influence the kinetics of oxygen removal in deoxidised steel melts. A comparative study was made using a range of deoxidants, which display a relatively high chemical affinity for oxygen but exhibit distinct physical properties and different interaction characteristics in oxygen containing melts. The deoxidants considered included aluminium, silicon, titanium, zirconium and a calcium-aluminium alloy. A detailed study has been made of the relationship between the morphological characteristics and the kinetics of removal of deoxidation products from melts produced under a variety of conditions. The overall objective of the work has been to establish a generalised mechanistic model for the formation and evolution of oxide particles within a steel melt and the implication this has for the kinetics of the deoxidation process. A better understanding of such processes would contribute to the development of

Chapter 2

Literature Review

2.1 INTRODUCTION

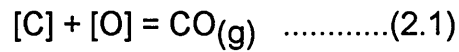
As a result of the chemistry of the processes involved, all modern commercial steelmaking practices produce steel containing oxide inclusions of some kind, at least in small quantities¹. The number of oxide inclusions present in every tonne of commercially produced steel is of the order of magnitude of 10^{12} - 10^{15} inclusions². These oxide inclusions have a profound effect on the physical and mechanical properties of the steel, depending on their size, shape, composition and distribution in the steel.

Many inclusion types are regarded as deleterious to the properties of the solid steel. Some oxide inclusions (e.g. alumina and some calcium aluminate inclusions) are particularly detrimental for the fatigue properties of steel, the tensile strength and the ductility of steel is also known to decrease with increase in the number of alumina inclusions³. The machinability of steel has been linked with the high temperature hardness of the inclusion phases contained within the steel, with abrasion being the most probable wear mechanism affecting the machine tools. However, not all oxide inclusions are harmful. Silica, calcium aluminate and calcium alumino-silicate inclusions have all been shown under certain circumstances to be beneficial to the machining properties of steel⁴.

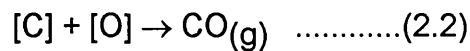
The steel-maker must ensure that the steelmaking practice results in the optimum inclusion composition and content with respect to the particular property requirements of the steel user. Accordingly it is important to understand the mechanisms of inclusion formation and removal from the steel melt.

Oxide inclusions arise because of the need to deoxidise steel. Elemental

oxygen is soluble in liquid iron to above 0.2 mass% at normal steel refining temperatures⁵, Figure 2.1. During active refining an excess of oxygen is maintained in the molten steel. If the supply of oxygen is then discontinued, the carbon- oxygen reaction goes towards equilibrium,



However, with falling temperature the equilibrium constant increases causing the reaction to go to the right with falling temperature,



As oxygen is virtually insoluble in solid iron, the rejection of the oxygen to the remaining liquid during freezing causes the continuation of reaction (2)¹.

In order to prevent the formation of carbon monoxide during cooling, resulting in the formation of blowholes, elements or alloys are added to the melt. These react with the dissolved oxygen producing either liquid or solid compounds, which by necessity are more stable than carbon monoxide.

2.2 DEOXIDANT ELEMENTS AND ALLOYS

A deoxidant should have a high affinity for oxygen and should be soluble in steel, so that a low equilibrium oxygen content may be obtained. The products should be insoluble in liquid steel and separate rapidly, while the residual deoxidants and deoxidation products should not be detrimental to the steel properties⁶.

Various elements can be used as deoxidants, these include: chromium,

silicon, manganese and vanadium which have moderate deoxidising capabilities^{7→10}; zirconium, titanium and aluminium which have strong affinities for oxygen^{11→13}. Calcium and magnesium are strong deoxidants but only have a limited solubility in liquid steel¹⁴. Rare earth elements whilst having a strong affinity for oxygen are relatively expensive, which often precludes their use as the sole deoxidant^{1,13,15}.

If all the deoxidation requirements cannot be fulfilled by any single element, improved performance of some deoxidisers may be achieved by using them in combination with other elements. For example, silicon with manganese produces a lower oxygen content than that achieved by silicon alone¹⁶. Commercial steels invariably contain specified quantities of manganese and other elements which have some deoxidising power. Their presence may significantly modify the performance of a stronger deoxidiser. The majority of deoxidation practices make use of two or more deoxidising elements added either in specified succession or as proprietary alloys^{6,14,17→25}. Consequently, the reactions of single, dual and complex deoxidants are important in steelmaking and foundry practice.

2.3 THERMODYNAMICS OF STEEL DEOXIDATION

The deoxidation of steel by a reactive element in solution [M] may be represented by a generalised relation of the form



for which the equilibrium constant, K, at a given temperature, is given by

$$K = \left(\frac{a_{(M_xO_y)}}{a_{[M]}^x \cdot a_{[O]}^y} \right) \quad (2.4)$$

where $a_{[M]}$ and $a_{[O]}$ represent the activities of the deoxidant and the oxygen in solution in the liquid steel at equilibrium.

The free energy change accompanying the formation of the deoxidation product M_xO_y is given by

$$\Delta G = -RT \ln K \quad (2.5)$$

where R is the gas constant and T the absolute temperature.

For actual steel making conditions equilibrium may not be achieved in which case it is possible to define a reaction quotient, K' , given by

$$K' = \left(\frac{a'_{(M_xO_y)}}{a'_{[M]}^x \cdot a'_{[O]}^y} \right) \quad (2.6)$$

where $a'_{[M]}$ and $a'_{[O]}$ are the actual activities of the deoxidant and oxygen in the steel bath.

The supersaturation ratio in the melt is given by

$$S = \frac{K}{K'} \quad (2.7)$$

Simple deoxidation products are assumed to have essentially stoichiometric compositions, (i.e. the deoxidant reacts with oxygen to form a pure oxide

product), and the activity of the deoxidation product is assumed to be unity. However, deoxidation by more than one element may result in the formation of complex oxides exhibiting a degree of solid solubility and consequently the activity of the deoxidation product will be less than one.

For reaction (2.3) it is possible to define a solubility product, K_s , for the deoxidation product in liquid iron alloys:

$$K_s = \left(\frac{a_{[M]}^x \cdot a_{[O]}^y}{a_{(M_xO_y)}} \right) \quad (2.8)$$

Since the concentrations of deoxidants in steel are usually quite low, they can be assumed to be dilute solution, in which case the activities of the solutes may be defined in terms of Henrian activities. For concentrations given in mass% M and mass% O the Henrian activities of [M] and [O] may be defined as

$$h_M = y_M \cdot \text{mass\% M} \quad (2.9)$$

$$h_O = y_O \cdot \text{mass\% O} \quad (2.10)$$

where y_M and y_O are the Henrian activity coefficients of the deoxidant and oxygen respectively.

By adopting Henrian activities for [M] and [O] and assuming that the activity of the deoxidation product is unity, the solubility product, K_s , for reaction (2.3) becomes

$$K_s = [\text{mass\% M}]^x \cdot [\text{mass\% O}]^y \cdot y_M^x \cdot y_O^y \quad (2.11)$$

where y_M and y_O approach 1 as mass% M \rightarrow 0.

Values of the solubility product, K_s , as a function of temperature are available in the literature for most deoxidants, examples of which are given in Table 2.17,13,26,27,28.

Data, determined by Turkdogan^{29,30} and other investigators^{7,11,31}, in which oxygen and the deoxidant in solution were in equilibrium with the pure deoxidation product at one atmosphere pressure and 1600°C is shown in Figure 2.2, demonstrating relative deoxidising power of various elements.

For deoxidation with some elements such as Al and Ti the solubility of oxygen initially decreases with increasing content of the deoxidiser as shown in Figure 2.2. Further increase in the concentration of the deoxidant brings about an increase in the oxygen solubility. The minimum oxygen solubility in equilibrium with the deoxidation product is caused by changes in the activity coefficients y_M and y_O with mass% M. As the concentration of the deoxidant element increases, so does the activity and the activity coefficient of oxygen decreases. The result is that a minimum may occur in the solubility of oxygen. The general trend is that the minimum oxygen content attainable decreases as the stability of the deoxidation product increases and the alloy content at which the minimum occurs decreases with increasing stability of the oxide.

2.4 KINETICS OF DEOXIDATION

The deoxidation process has been subdivided into four stages³²:-

- (a) solution of the deoxidant;
- (b) nucleation of the deoxidation product;
- (c) growth of deoxidation product;
- (d) elimination of deoxidation products from the melt.

In practice these stages overlap and there are other phenomena, e.g. reoxidation, which can occur simultaneously. The four stages are considered separately in the following sections to assess their individual effect upon deoxidation kinetics.

2.4.1 SOLUTION OF DEOXIDANT

Deoxidation reactions do not reach equilibrium immediately after the addition of a deoxidant. A period of time is required to obtain complete mixing throughout the volume of the steel to which it is added. Initially, in the process of solution of the deoxidant, there are certain volume elements of the melt which contain higher concentrations of deoxidiser than others and some volume elements which retain much of their original oxygen content. The homogenisation of the deoxidant consists of the subdivision and ultimate distribution of these liquid segregates through a process of shear due to turbulence and elimination of the concentration gradients by diffusion³³.

Levin³⁴ has shown that the addition of a deoxidant element even below its bulk equilibrium concentration causes precipitation of oxides due to the local equilibrium concentration being exceeded as it progressively dissolves. The formation of a layer rich in fine oxide particles has been suggested³³ as

holding back the diffusion of the deoxidant, which may delay the overall time for homogenisation of the melt with respect to the deoxidant. This links in with observations³⁵ that the method of introducing the deoxidant to the steel influences the kinetics of deoxidation, as an even distribution of the deoxidant is obtained much more quickly for an aluminium addition in the liquid state compared with one in the solid state. Some workers³⁶ have suggested^{ed} that the deoxidant is dispersed throughout the melt as an emulsion of fine droplets, rather than dissolution being responsible for its dispersion throughout the melt.

Also on a macroscopic scale, a certain heterogeneity of alloying elements is always observed; on a microscopic scale, it can be much greater. It has been shown that various calcium alloys contain a number of phases, which have different melting points. Consequently, the phases dissolve at different rates, which upon addition to steel may result in several different localised reactions²⁵ and hence heterogeneity of the deoxidant is even more likely. Therefore it appears that both the solution and homogeneous distribution of the deoxidant is not instantaneous and is liable to cause delay in the overall deoxidation process. However, this stage is not considered the most decisive factor for the success of the overall deoxidation process³².

2.4.2 NUCLEATION OF DEOXIDATION PRODUCTS

When the deoxidant is added to the melt, in simple deoxidation, it is assumed that the deoxidant and oxygen react to form a pure product. Nucleation of the deoxidation product occurs^{32,37} either by :

- (a) homogeneous nucleation without the assistance of any pre-existing nucleation sites, or;
- (b) heterogeneous nucleation on pre-existing particles distributed

throughout the melt or the crucible wall, etc.

From the classical theory^{38,39}, the net free energy change for the homogeneous nucleation of a small spherical deoxidation product of radius, r , is given by :

$$\Delta G_r = 4\pi r^2 \sigma_{im} - 4/3\pi r^3 \frac{\Delta G}{V} \quad (2.12)$$

where σ_{im} is the interfacial tension between molten iron and the deoxidation product, V is the molar volume of the deoxidation product, and ΔG_r is the chemical free energy change accompanying the formation of the deoxidation product:

$$\Delta G = -RT \ln \frac{(h_M^x \cdot h_O^y)_{act}}{(h_M^x \cdot h_O^y)_{equ}} \quad (2.13)$$

$$= -RT \ln \left(\frac{K_s'}{K_s} \right) \quad (2.14)$$

where K_s is the equilibrium solubility product, K_s' is the corresponding product for the actual components in the supersaturated solution.

When r is small the interfacial energy term predominates and the embryonic nucleus tends to dissolve. Above a critical radius, r^* , the embryonic nucleus becomes stable and continues to grow. The critical radius, r^* , is given by

$$r^* = \left(\frac{2\sigma_{im} V}{\Delta G} \right) \quad (2.15)$$

The activation energy necessary to form this nucleus is

$$\Delta G^* = \left(\frac{16\pi\sigma_{im}^3 V^2}{3(\Delta G)^2} \right) \quad (2.16)$$

This represents the thermodynamic barrier to the formation of the deoxidation product.

The embryonic nucleus is assumed to grow or shrink by the addition or removal of single atoms or molecules. There will be an activation energy, ΔG_D , for an atom or a molecule to diffuse across the metal-nucleus interface, (the kinetic barrier).

Under steady state conditions the number of critical sized nuclei per unit volume is given by:-

$$n^* = n_v \exp \left(\frac{-\Delta G^*}{kT} \right) \quad (2.17)$$

where n_v is the number of atoms per unit volume of liquid and k is Boltzmann's constant.

The rate of nucleation, I , is proportional to n^* and to the number of atoms crossing the metal-nucleus interface per second, (i.e. proportional to the probability that an atom or molecule will cross the barrier). So

$$I = A' \exp \left(\frac{-\Delta G^* + \Delta G_D}{kT} \right) \quad (2.18)$$

where A' is a frequency factor and to a good approximation

$$A' = \left(\frac{n_v kT}{h} \right) \quad (2.19)$$

where h is Planks constant.

Turnbull and Fisher⁴⁰ defined a second frequency factor, A,

$$A = A' \exp \left(\frac{\Delta G_D}{kT} \right) \quad (2.20)$$

So

$$I = A \exp \left(\frac{-\Delta G^*}{kT} \right) \quad (2.21)$$

Values for the frequency factor, A, have been estimated³⁸ as: Al₂O₃, 10²⁶; FeO.Al₂O₃, 10²⁵; SiO₂, 10²⁸; FeO, 10³⁰.

Thus the interfacial tension, σ_{im} , at the melt/nucleus boundary is a major component of the free energy change required to form a stable nucleus. The higher the interfacial tension of the deoxidation product the more difficult the possibility of inclusion formation in the melt⁴². For oxides in molten steel the interfacial tension at the oxide/molten steel boundary is about 1.0 J.m⁻² ⁴¹, but as shown in Table 2.2 in some cases it may be greater. However, there are few measurements of interfacial tensions between deoxidation products and liquid iron.

The supersaturation required to overcome the barrier imposed by the interfacial tension, σ_{im} ,⁴¹ may be obtained from

$$-RT \ 2.303 \log \left(\frac{K_s'}{K_s} \right) = -2.7 V \left(\frac{\sigma_{im}^3}{kT \log A} \right)^{1/2} \quad (2.22)$$

The amount of 'supersaturation' necessary before inclusions will nucleate

homogeneously can be measured. Sigworth and Elliott⁹ used the following cell :-



to add oxygen electrolytically to iron-silicon melts containing up to 1% Si. They determined the change in oxygen potential as the oxygen reacted with the silicon and related the supersaturation necessary to produce homogeneous nucleation to the concentration polarisation of the cell. From these experiments they estimated that the 'supersaturation ratio'

$$S = \frac{K_s'}{K_s} = \frac{a'_{[\text{Si}]} \cdot a'_{[\text{O}]}^2}{a_{[\text{Si}]} \cdot a_{[\text{O}]}^2}$$

was of the order of 80 when homogeneous nucleation occurred. This indicates that

$$\frac{a'_{[\text{O}]}^2}{a_{[\text{O}]}^2} = 9$$

Alumina has a higher interfacial tension value, σ_{im} , than SiO_2 , Table 2.2, and consequently is more difficult to nucleate homogeneously. This is reflected in the very high supersaturation ratio⁴³

$$\frac{a'_{[\text{Al}]}^2 \cdot a'_{[\text{O}]}^3}{a_{[\text{Al}]}^2 \cdot a_{[\text{O}]}^3} = 3 \times 10^6$$

which gives a ratio of $\frac{a'_{[\text{O}]}^3}{a_{[\text{O}]}^3}$ of about 145 for aluminium deoxidation⁴⁴. Other

examples of the supersaturation ratios necessary for homogeneous nucleation are given in Table 2.3^{37,43,45→47}.

After the addition of the deoxidant certain regions of the melt may be locally

sufficiently rich in deoxidant for homogeneous nucleation of the deoxidation product to occur²⁹. But the fact that homogeneous nucleation may be possible for strong deoxidants does not imply that all deoxidation products will be nucleated homogeneously. Heterogeneous nucleation is more likely to occur because of the high energy barrier which must be overcome for homogeneous nucleation and because of the high probability of the presence of particles in the melt which can act as a substrate for the formation of the deoxidation product, as can the inner surface of the crucible wall^{37,48→51}.

For the formation of a spherical cap of liquid second phase precipitate on a planar substrate the supersaturation must overcome the critical free energy barrier, ΔG^*_{het} ⁵² given by

$$\Delta G^*_{het} = \Delta G^*_{hom} \cdot f(\theta) \quad (2.23)$$

where θ is the contact angle between the deoxidation product and the substrate, and

$$f(\theta) = \frac{1}{4} (2 + \cos\theta) (1 - \cos\theta)^2 \quad (2.24)$$

The rate of heterogeneous nucleation per unit area of surface is given by⁵³

$$I_{het} = B f(\theta) \cdot 0.167 \cdot \exp \left(\frac{-\Delta G^*_{het}}{kT} \right) \quad (2.25)$$

where B is a frequency factor. The supersaturation required for heterogeneous nucleation is always less than for homogeneous nucleation³².

The possibility of homogeneous nucleation of oxides with low interfacial tensions followed by heterogeneous growth of other less easily nucleated oxides on the substrate provided, has been suggested^{54,55} as a mechanism by which such inclusions are nucleated.

2.4.3 PARTICLE GROWTH MECHANISMS

The homogeneous and heterogeneous nucleation of deoxidation products ceases as soon as the concentration of the deoxidant in the melt falls below the necessary degree of supersaturation³². Four main growth processes have been used to describe the subsequent growth of the nuclei to inclusion size:-

- (a) Brownian Motion
- (b) Ostwald Ripening
- (c) Diffusion
- (d) Collisions

2.4.3.1 BROWNIAN MOTION

Brownian motion is the random movement observed among microscopic particles suspended in a fluid medium. The movement is understood to be due to the thermal agitation of the suspended medium. The expression for the decrease in the number of particles, Z , in a fluid resulting from collisions due to Brownian motion after time, t , is given by

$$Z \approx \frac{3\eta}{8kTt} \quad (2.26)$$

where k is the Boltzmann's Constant and η is the viscosity of the fluid.

In the case of inclusions in steel, it would take approximately three hours for the number of inclusions, Z, to be reduced to about 10^7 particles.cm⁻³, when the particle size is in the micron size range⁵⁶. The growth of inclusions resulting from Brownian Motion is thus insignificant under deoxidation conditions^{29,32}.

2.4.3.2 OSTWALD RIPENING

When dispersed particles of a second phase exist in a solution, there is a tendency for smaller particles to dissolve and larger ones to grow, by the transfer of solute through the solvent from particle to particle. This phenomenon is known as diffusion coalescence or Ostwald Ripening. The driving force is derived from the consequent reduction in the total interfacial energy^{57,58}.

The process has been analysed⁵⁹ in terms of the resultant diffusion flow from the smaller to the larger particles. The rate of change in size of an individual particle due to this effect is given by

$$\frac{dr}{dt} = DS \frac{2M\sigma_{im}}{RT\rho^2r_i} \left(\frac{1}{\bar{r}} - \frac{1}{r_i} \right) \quad (2.27)$$

where D is the diffusion coefficient of the solute in the liquid, S is the true solubility of the solute, ρ is the density of the solid of molecular mass M, σ_{im} is the interfacial tension, r_i is the particle radius and \bar{r} is the mean particle radius.

It has been estimated⁵⁸ that it would take approximately half an hour for the average inclusion to grow from the critical nuclei dimension to 2.5 μ m, or e.g.

from 2.5 to 3.0 μm . Thus diffusion coalescence is a slow process which has a limited effect on inclusions observed in the first minutes after deoxidation. However, it may have a contribution to growth over long periods of time^{29,58,60}.

2.4.3.3 DIFFUSION

The transition from a nucleus to an inclusion may be explained by the diffusion of solutes in the liquid steel to the oxide nuclei. Turkdogan⁶¹ suggested that if at the time of addition of the deoxidant, the resultant nuclei are assumed to be uniformly distributed in the melt, e.g. Z particles. cm^{-3} of melt, each particle would form the centre of a diffusion volume, with these forming a closed packed array of equal sized diffusion volumes. If it was further assumed that there was local equilibrium at the surface of the growing oxide inclusion in the melt and pseudo-steady-state conditions prevailed in each diffusion volume, then the simplified form of the diffusion equation derived by Ham⁶² could be used to describe the diffusion process:-

$$\frac{Dt}{r_o^2} \left(\frac{C_o - C_{im}}{C_i} \right)^{1/3} = \frac{1}{6} \ln \frac{u^2 + u + 1}{(u-1)^2} - \frac{1}{\sqrt{3}} \tan^{-1} \frac{2u+1}{\sqrt{3}} + \frac{1}{\sqrt{3}} \tan^{-1} \frac{1}{\sqrt{3}} \quad (2.28)$$

where $u = \left(\frac{C_o - C_m}{C_o - C_{im}} \right)^{1/3}$, C_o is the initial uniform oxygen concentration in the liquid steel, C_{im} is the oxygen concentration in equilibrium with the deoxidation product, C_m is the time dependent mean oxygen concentration in solution, C_i is the oxygen concentration in the inclusion, r_o is the radius of the diffusion volume ($\approx 0.62 Z^{-1/3}$) and D is the diffusivity of oxygen.

From the value of C_m and known initial conditions, the radius of the growing inclusions, r_i , at time, t , may be calculated from

$$r_i = r_o \left(\frac{C_o - C_m}{C_i} \right)^{1/3} \quad (2.29)$$

It was concluded⁶¹ that the greater the number of nuclei, the shorter the time necessary for completion of diffusion-controlled deoxidation reactions. By taking D as $10^4 \text{ cm}^2\text{s}^{-1}$ and Z as $10^5 \text{ particles.cm}^{-3}$, with an oxygen concentration of 0.05 mass%, the diffusion controlled deoxidation reaction is essentially complete in about 10 seconds. If, however, a small number of nuclei, $Z=10^3 \text{ particles.cm}^{-3}$, are present then the diffusion-controlled deoxidation reaction required 6-7 minutes to complete growth.

In steelmaking practice the number of nuclei formed is believed to be high, Z being between 10^7 and 10^8 particles per cm^3 ⁵⁵. Thus diffusion controlled growth is essentially complete in a few seconds, consequently it has been suggested^{29,32,63,64} that inclusions grow by diffusion and the rate limiting step in the growth from nucleus size to inclusion size is not the precipitation reaction, but the homogenisation of the deoxidant in the melt.

2.4.3.4 GROWTH BY INTERPARTICLE COLLISIONS

The diameter of oxide inclusions at the completion of growth by diffusion in silicon treated melts has been found to be about $2\text{-}4\mu\text{m}$ and for alumina inclusions in Al treated melts it has been found to be distributed about a peak of $3\text{-}4\mu\text{m}$ ^{32,63,65}. Further substantial growth can only continue by means of collisions followed by coalescence/agglomeration.

A number of possible collision mechanisms have been suggested for the subsequent growth of the inclusions^{58,60,66,67}:-

- (a) 'Stokes' Collisions',
- (b) 'Velocity Gradient Collisions',
- (c) 'Eddy Induced Collisions'.

(a) 'STOKES' COLLISIONS'

This is a mechanism of growth by which particles collide by means of their differential upward float-out velocity. Inclusions in a steel bath tend to rise relative to the melt, since they usually have a lower density. The velocity of rise, of a solid inclusion in a stagnant melt of molten steel, v , is determined by equating the gravitational and the drag forces and is given by^{58,68}

$$v = \frac{2r^2}{9\eta}(\rho_m - \rho_i)g = \xi r^2 \quad (2.30)$$

where g is the acceleration due to gravity, ρ_i is the density of spherical inclusions, ρ_m is the density of liquid iron, η is the viscosity of liquid iron, and ξ is the Stokes' Constant.

This is valid for the creeping flow (Stokes' Law) regime, where the particle motion through the fluid is laminar, ie up to a radius of about 50 μ m. Typical deoxidation products in liquid steel are smaller than this. Collisions arise whenever large particles rising through the melt at a higher relative velocity hit smaller particles in their way, which are moving at a slower relative velocity⁵⁸. Miyashita et al.⁶⁶ concluded that the rising velocity of silica inclusions in a tranquil iron bath is in agreement with Stokes' Law.

(b) GROWTH BY 'VELOCITY GRADIENT COLLISIONS'

It has been suggested⁶⁰ that the motion of inclusions in liquid steel is not simply governed by differential upward floating velocities, ie Stokes' Law, but is due more to the melt being stirred⁶⁶. For an average fluid velocity of, v (cm.s^{-1}), the resistance to motion (drag) experienced by the inclusion is given by:-

$$F_g = 6\pi\eta r_i v \quad (2.31)$$

and the buoyancy force experienced by the inclusion is given by;

$$F_b = \frac{4}{3}\pi r_i^3 (\rho_m - \rho_i)g \quad (2.32)$$

Calculations have shown that for an inclusion 20 μm in diameter, a fluid velocity of 0.015 cm.s^{-1} is sufficient to make the drag force, F_g , greater than the buoyancy force, F_b , by an order of magnitude. Such velocities are quite feasible with natural convection. Natural convection is inevitable in liquid steel if a temperature gradient of 0.1 $^\circ\text{C.cm}^{-1}$ is present in the melt⁶⁰. The free convection results in the stirring of the liquid metal and the inclusions are entrained in the flowing fluid. Inclusions no longer move vertically in accordance with Stokes' Law, but are carried along in currents in the liquid metal. Consequently, the motion of small inclusions are governed more by fluid velocity than by buoyancy. Thus growth by velocity gradient collisions is the dominant mechanism controlling the growth of inclusions in non-quiescent melts^{58,60}.

(c) 'EDDY INDUCED COLLISIONS'

Hills and Pickering⁶⁷ have proposed a mechanism for the growth of deoxidation products, by concentration and collision of inclusions within local

eddies present in the melt. Such eddies are inevitable due to local velocity, temperature and density differences.

Within each eddy the inclusions will experience a centripetal force, because the density of the inclusions is generally about half that of the molten steel. The inclusions are accelerated towards the centre of the eddy, increasing the local volume fraction of the inclusions locally. This decreases the interparticle spacing of the inclusions, thereby increasing the probability of the inclusions colliding. The inclusions are subsequently eliminated by flotation according to Stokes' Law and the bulk motion of the fluid.

It was further suggested that the eddy induced collisions and forces might be the cause of the collapse and sintering of alumina dendrites to form sintered agglomerates.

2.4.3.5 GROWTH OF LIQUID INCLUSIONS

Once an inclusion has collided with another inclusion, the inclusions either coalesce or agglomerate depending on their physical state at the time of collision. In order for the collision to result in a successful coalescence or agglomeration a period of time must elapse and a number of criteria must be satisfied⁶⁰. These depend on the interfacial phenomena and the viscosity of the metal.

The successful growth of liquid inclusions, following a collision brought about by the effect of buoyancy or the influence of velocity gradients involves two main steps^{69,70}:

- (a) Flocculation;
- (b) Coalescence.

The flocculation step can be divided into two stages, the first stage involves the thinning of the metal film which still prevents the contact of the two inclusions even after a collision has taken place. Provided there are no repulsive forces due to electrical double layers, when inclusions approach each other, drainage is controlled by the metal viscosity. Estimates of the duration of the drainage stage suggest that drainage is very fast for small inclusions, but slows as the size of the inclusion increases⁷⁰. Any increase in the apparent viscosity of the liquid steel, e.g. due to the precipitation of tiny iron crystals, would increase the drainage time.

If electrical double layers are present at the interface of the two inclusions, they can exert repulsive forces on each other and drastically slow the film thinning stage. In metal-oxide systems this double layer phenomena could possibly arise in the presence of oxygen and sulphur which are very surface active.^{70,71}

In the second stage of flocculation, film rupture occurs as a consequence of hydrodynamic instabilities arising from perturbations resulting from differences in the forces acting upon an element of liquid in the thin metal film and in the bulk fluid. Such forces are caused by London-Van de Waals interactions between the surrounding molecules of the liquid and with those of the inclusion. If the perturbation grows it leads to the rupture of the film⁷². Estimates from model studies of steel films with clean surfaces infer very short times of rupture, less than 10 seconds for 0.01 μm thick films. Minute quantities of surface active pollutants, e.g. oxygen and sulphur, may have a strong damping effect on the waves at the surface and may increase the rupture time by several orders of magnitude^{70,72}.

Thus, when two inclusions approach each other up to a certain distance, d , the drainage step will begin. If the inclusions do not stay at a distance, d , for more than a time, t , the flocculation step will not have been completed and the inclusions will not coalesce. However, the time, t , is reported to be very small^{69,70}. Any retarding mechanisms would be linked to dissolved oxygen and sulphur in the vicinity of the interfaces and may be operative in both drainage and rupture of the metal film⁷⁰.

After flocculation steps have been completed, the two liquid inclusions can coalesce into a single larger inclusion by deformation caused by mutual mass flow⁶⁹.

2.4.3.6 GROWTH OF SOLID INCLUSIONS

Inclusions which are solid at steelmaking temperatures cannot coalesce as liquid inclusions do. Such inclusions have a size range of 1-3 μm , which remains constant after the diffusion processes have been completed⁵⁸.

These tend to form clusters of inclusions, which sinter together at the points of contact.

In the case of small inclusions the various steps of film drainage and film rupture are similar whether they are solid or liquid⁷⁰. However, some solid inclusions have greater tendency towards cluster formation than others. If the contact angle, θ , between the solid oxide and the liquid steel exceeds 90° , cluster formation is feasible. The higher the contact angle the greater the tendency for cluster formation⁷⁰.

Once primary contact between two particles has taken place due to collision,

another process is required to maintain contact between the two inclusions, since if fluid flow in the bath is sufficient to establish primary contact, it is sufficient to separate the particles. The mechanism involved is believed to be the retreat of the metal from the space between the inclusions, which still exists when the inclusions have collided. The retreat of the liquid metal, starting from the points of contact of the two solid inclusions, can be spontaneous only when the contact angle, θ , exceeds 90° . It is suggested^{73,74} that a convex meniscus is formed when the contact angle, θ , is greater than 90° , whilst a concave meniscus is formed when the contact angle, θ , is less than 90° . The analogy of two plane lamellae which are parallel to each other and partially immersed in a liquid may be used to explain the meniscus phenomena⁷⁴. When the contact angle, θ , between the liquid and the lamellae exceeds 90° , a convex meniscus exists between the two lamellae as they approach one another. The meniscus is lowered and the metal tends to be removed from the space between the lamellae. When the contact angle, θ , is less than 90° , a concave meniscus exists between the two lamellae. In this case capillary rise will occur as the lamellae approach one another and as a result the space between the lamellae will be increasingly filled with liquid. This reasoning can be applied to any shaped inclusions which possess small elements of essentially plane surface. When an inclusion has a contact angle, θ , greater than 90° , a successful collision between two inclusions results in the formation of a metal-vacuum meniscus between the two inclusions, which enables a stable contact to take place. When an inclusion has a contact angle, θ , less than 90° , metal forces itself between the contact points, resulting from the initial collision, forcing the two inclusions apart⁷⁴, Figure 2.3.

From the thermodynamic point of view the retreat of the metal from the space

between the two inclusions causes the formation of two inclusion-vacuum surfaces and the removal of two metal-inclusion surfaces. The energy change accompanying this, $\Delta G''$, is given by:-

$$\Delta G'' = 2(\sigma_i - \sigma_{im}) \quad (2.33)$$

where σ_i is the surface tension of the inclusion and σ_{im} is the interfacial tension between the inclusion and the liquid iron, per unit surface of each inclusion.

The energy required to separate the inclusions is equal to;

$$\Delta G'' = 2\sigma_m \cos\theta \quad (2.34)$$

where σ_m is the surface free energy of the liquid iron.

Thus the retreat of the liquid film only becomes spontaneous when $\Delta G < 0$. The necessary condition for this is that $\theta > 90^\circ$. Cluster formation is consequently dependent on the contact angle, θ , between the liquid steel and the solid oxide. With solid oxides with contact angles less than 90° , primary contact between inclusions is possible, but, the contacts would not be stable. Solid oxides with contact angles greater than 90° will, after the establishment of contact points form stable contacts. As the contact angle, θ , increases above 90° , there is a corresponding increase in the probability of forming stable agglomerates. Contact angles for various oxides in contact with molten iron are given in Table 2.4. Solid oxides with high contact angles have a tendency to form very large clusters up to 5mm^{76,77}.

Once a stable contact between inclusions has taken place, agglomeration of the inclusions can take place by means of sintering. Sintering is essentially a process in which several particles in contact with one another agglomerate when heated to a suitable temperature. The agglomeration is usually accompanied by a decrease in the porosity of the particles and consequently an increase in the bulk density of the mass. At the same time the surface area decreases, so that the surface free energy and hence the total free energy of the system decreases. This reduction in energy provides the driving force for growth. The growth probably occurs both by volume diffusion and by dissolution and re-precipitation of the oxide. Thus, as the sintering process proceeds, 'necks' grow between the adjacent particles as well as densification of the particles^{77,78}.

2.4.4 REMOVAL OF DEOXIDATION PRODUCTS FROM STEEL MELTS.

Inclusions are eventually eliminated from the melt when they reach the surface of the melt or stick to the refractory walls of the containing vessel. The inclusions are brought there by the process of fluid flow. There are many factors which influence the rate of removal of inclusions from the melt, for example, the inclusion size, the density difference between the inclusion phase and the metal, the viscosity of the metal and the size of the system^{17,79,80}. However, stirring has perhaps the most significant effect on the removal rate^{17,66,74,81,82}. Under industrial conditions metal stirring is achieved in a number of ways; by mechanical action, by using an electromagnetic field, and by the injection of an inert gas⁸³. Numerous workers^{17,49,50,51,58,60,63,66,79→82,84} have studied the factors influencing the removal rate, and some have developed mathematical models for the removal of inclusions from the melt^{58,60,79,81,84}.

2.4.4.1 REMOVAL OF DEOXIDATION PRODUCTS FROM STIRRED

MELTS

Several models for the removal of deoxidation products from stirred iron melts have been proposed^{58,60,79,81}.

Miyashita et al.⁶⁶ showed that the separation rate of inclusions in an agitated melt was generally larger than in a quiescent melt, concluding that Stokes' Law was not appropriate to describe the removal of deoxidation products from liquid steel under such circumstances.

Lindborg and Torsell⁵⁸ made a quantitative, statistical analysis of the growth and separation of inclusions based on a collision theory. They postulated that an interparticle collision would result in the instantaneous coalescence of the particles into one large particle, which in turn collides with other particles until separation takes place at the top surface of the melt. It was suggested that stirring the melt has two effects on deoxidation:-

- (i) the homogenisation of the melt with respect to the deoxidant and,
- (ii) increasing the number of interparticle collisions.

There are however, inconsistencies in their proposed growth mechanisms, when compared with other experimental observations⁸². Their calculations suggested that the rate of gradient collisions was less than the rate of Stokes' collisions. The major weakness in Lindborg and Torsell's⁵⁸ model was that the trajectory of the moving particle was assumed not to be affected by an approaching particle, and that every collision resulted in coalescence.

Three possible mechanisms for the removal of oxygen in deoxidised,

induction stirred steel, melts were postulated by Lindskog and Sandberg⁴⁹;

(a) the deoxidation products were nucleated directly on the surface of the crucible;

(b) the inclusions rose to the surface of the melt with a velocity given by Stokes' Law;

(c) the inclusions were adsorbed on the inner surface of the crucible wall due to the fluid flow within the system.

Total oxygen and dissolved oxygen measurements indicated that some deoxidation products were formed in the melt. If all the deoxidation products had been nucleated directly on the crucible wall the total oxygen content of the melt would equal the dissolved oxygen content of the melt, which was shown not to be the case, Figure 2.4. It was proposed that during the initial precipitation period, direct nucleation of the deoxidation products on the crucible wall, flotation according to Stokes' Law and adsorption on the inner surface of the crucible could all be active in the removal of the deoxidation products. However, after precipitation had ceased, direct nucleation onto the crucible wall could no longer occur and deoxidation products could only be removed by flotation due to Stokes' Law or by adsorption onto the crucible wall.

Further evidence of the importance of inclusion adsorption onto crucible walls has been presented by Nakanishi et al.⁸⁵, who detected an adsorbed layer of Al_2O_3 in the inner surfaces of SiO_2 and CaO crucibles after the deoxidation of liquid iron with aluminium in a high frequency induction furnace.

Results obtained by deoxidising induction melted steel with radioactive ^{31}Si indicated that 60% of the oxygen removed from the melt, after precipitation ceased, was removed by adsorption onto the crucible wall. The SiO_2 particles were adsorbed preferentially onto the upper part of the side wall just below the slag line and the centre part of the bottom of the crucible. Other experiments have shown^{49,85} that Al_2O_3 deoxidation products can also be absorbed in high concentrations in the centre part of the bottom floor and the upper part of the side wall of the crucibles. The high concentrations coincide with the points where the stream of liquid metal is thought to encounter the crucible at right angles in an induction stirred melt, Figure 2.5.

Linder⁷⁹ considered the hypothetical behaviour of small spherical particles in a turbulent metallic melt for situations similar to those for the deoxidation of steel in stirred systems. It was stated that the most important mechanisms to achieve relative movement of two particles in a turbulent melt are associated with the rise of the particles due to the gravitational force and with turbulent velocity gradients. Differentiations were made between three possible situations when collisions could take place.

1. The rise velocity due to the gravitational force is small compared with the relative movements due to the velocity gradients in the melt. In this case the main collision mechanism is gradient collision.
2. The rise velocity due to gravitational forces is greater than the relative movement due to velocity gradients in the melt, in this case the particles can be considered as rising in a quiet viscous fluid. If a large particle approaches a smaller particle, Figure 2.6, at first it would appear that a collision would take place if the distance between the smaller particle and

the central axis of the large particle is smaller than $L' + L''$, but as the two particles come closer, the smaller particle will be pressed aside by the flow around the larger particle. Only particles coming from a distance $L_C < L' + L''$ will collide, where L' and L'' are the radii of the small and large particles respectively and L_C is the critical distance for a collision.

Linder⁷⁹ suggested that the possibility for a collision by this mechanism for two deoxidation products is quite limited and "Stokes' Collisions" could probably be neglected when discussing the removal of deoxidation products.

3. The velocity rise due to gravitational forces and the velocity due to velocity gradients are of the same order of magnitude, there might be a mutual interaction effect such that the number of collisions are not just a sum of (1) and (2) considered separately.

The method presented by Linder⁷⁹ to predict the behaviour of the small fluid spherical particles in a stirred metallic melt gave some indication of the parameters which when varied might affect a change in the rate of a deoxidation operation, i.e. the amount of stirring, the mean flow velocity, the size and shape of the system, the density difference between the deoxidation product and the liquid steel, and the viscosity of the liquid steel. However, much of the Linders' work was based on the use of hydrodynamic parameters for which values are generally not known, and to overcome this, many of the hydrodynamic parameters were estimated.

Engh and Lindskog⁸¹ produced a fluid mechanical model for inclusion removal, where the separation rate of inclusions was given as a function of the stirring power. The model was based on the eddy diffusivity concept,

which was used to calculate the rate of removal of inclusions to the walls. However, the values tended to give too high removal rates, which may have been due to the fact that not all inclusions which contact the walls of the containing vessel will adhere to it.

2.4.4.2 REMOVAL FROM MELTS STIRRED BY NATURAL CONVECTION

It is generally considered^{58,60,66,81,82} that the rate of removal of liquid deoxidation products is slower under conditions of natural convection, than with stirred melts.

Miyashita et al⁶⁶ investigated the rate of removal of primary deoxidation products from a quiescent iron melt and reported that experimentally the results lay between values calculated for Stokes' Law and values calculated from the following equation for the case where slip occurring at the particle/liquid interface was used to express the rising velocity of the particles:-

$$v = \frac{2gr_i^2(\rho_m - \rho_i)}{9\eta} \cdot \frac{3\eta + \beta r_i}{2\eta + \beta r_i} \quad (2.35)$$

where β is the coefficient of sliding friction. This gave a velocity 1.5 times as large as that calculated by Stokes' Law. They concluded that the rising velocity of deoxidation products in a quiescent iron melt is almost identical with that calculated by Stokes' Law.

Analysis of the size distribution⁶⁰ of inclusions in samples taken from different depths in a melt after various time intervals indicated the presence

of some large inclusions which could not be accounted for by Stokes' Law. It was calculated that under their experimental conditions, the removal of inclusions less than 20 μ m in diameter would be governed more by fluid velocity than by buoyancy. A model was proposed whereby large inclusions grew by a process of collision and coalescence, and moved along with currents in the liquid melt rather than vertically due to Stokes' Law. When inclusions were brought near to the liquid metal-slag or liquid metal-refractory interface a process of assimilation could take place. As the inclusions approach the boundary phase an interfacial film of steel is created which eventually ruptures allowing the inclusion to become assimilated into the slag/refractory phase. However, only a fraction of the inclusions are assimilated, the remaining inclusion^s_A being returned to the bulk of the melt where some may again collide, coalesce and are brought once more near to a boundary phase.

A mathematical model⁶⁰ was produced which was said to quantitatively explain the presence of some large inclusions (>15 μ m diameter), even after 60 minutes. The model predicted that the diameter of the largest inclusions in the melt decreased with time, but at a much slower rate than that given by Stokes' Law. The model gave credence to the evolving concept that inclusion motion in stirred liquid steel is not according to Stokes' Law but due to velocity gradients in the liquid steel, and that inclusions travel at a velocity faster than that postulated by Stokes' Law.

2.4.4.3 THE EMERGENCE OF INCLUSIONS FROM THE MELT.

Inclusions are removed from the melt when they are brought to the top surface of the melt or into contact with the walls of the containing vessel. When inclusions come close to a collecting surface they are offered only a

short period to emerge from the melt before they are returned to the bulk of the melt by the motion of the fluid.

(a) Liquid Inclusions.

The process of emergence of liquid inclusions involves three main steps ⁷⁰, Figure 2.7. The preliminary approach to the interface under the influence of buoyancy or due to the bulk motion of the fluid is followed by the thinning of the metal film still preventing contact with the boundary phase, (slag, gas or refractory). The subsequent drainage of the metal film is controlled by metal viscosity when no repulsive forces are present (ie. electrical double layers) ⁷¹. The time required for a film thicknesses τ_0 to be reduced to a thickness τ can be estimated⁷⁰ from

$$t = \frac{2}{\omega} \cdot \frac{(\rho_m - \rho_i) \cdot g}{\sigma_{im}} \cdot r_i^5 \cdot \eta \cdot \left[\frac{1}{\tau^2} - \frac{1}{\tau_0^2} \right] \quad (2.36)$$

where ρ_m and ρ_i are the densities of the metal and the inclusion, g is the acceleration due to gravity, r_i is the radius of the inclusion, η is the viscosity of the metal, σ_{im} is the interfacial tension between the metal and the inclusion, ω is the coefficient which is equal to about 2 for the emergence at a solid interface or contact with another inclusion, or 0.5 for the emergence at the slag interface. The drainage step is very fast for small inclusions, but it becomes slower as the particle size increases.

Finally, film rupture occurs as a result of hydrodynamic instabilities similar to those experienced during agglomeration⁷². The film rupture stage is very rapid, 10^{-3} seconds has been estimated as the time for the rupture of a $0.01\mu\text{m}$ thick film. However, this can be retarded by surface active elements

which damp down the instabilities thought to initiate the rupture⁷⁰.

(b) Solid Inclusions.

The contact angle, θ , between liquid metal and solid oxide, as well as determining the likelihood of inclusion cluster formation⁷³, also allows the evaluation of the stable position of an inclusion during emergence⁷⁰.

For a sphere of a few microns in diameter resting at a steel/gas or steel/slag interface the surface forces are predominant over buoyancy forces and the stable position is such that the angle is almost equal to θ , Figure 2.8A. For more complex inclusion shapes, such as dendrites or clusters, the contact angle is even more critical, as small variations in θ , may result in the stable position at the interface being before or beyond a neck, Figure 2.8B.

Relatively small variations can lead to substantial variations in the emerged fraction. If the emerged fraction of a cluster is too small the cluster could be torn away from the interface and drawn back into the bulk of the melt by strong eddies.

The various steps of film drainage and film rupture are reasonably similar, Figure 2.7, for solid and liquid inclusions in the case of small inclusions.

Once contact is established with the boundary phase the mechanical strength of the assemblage is dependent upon sintering. If this is not achieved quickly enough the inclusion may be re-entrained.

2.5 THE EFFECT OF SURFACE ACTIVE ELEMENTS ON THE SURFACE PROPERTIES OF INCLUSIONS.

Some elements in solution in the liquid steel have the effect of altering the surface properties of the system^{86,87}. Group VI elements are surface active

agents and their surface activity increases in the order of oxygen, sulphur, selenium and tellurium. It has been demonstrated that the contact angle, θ , between liquid iron and alumina decreases with increase in the oxygen content and increases with the addition the of Se and Te, whilst sulphur scarcely affects the contact angle^{73,86,88}, Figure 2.9. The surface tension between molten iron and alumina decreases with increased content of Group VI elements in the melt^{6,86,89}, Figure 2.10. The surface tension of the liquid iron is lowered most markedly by the Group VI elements O, S, Se, and Te, but also to a lesser extent by Sn, Sb, N and As^{86,88}. Thus surface active elements affect the propensity of inclusions to form agglomerates and to be eliminated from the melt by altering their surface properties.

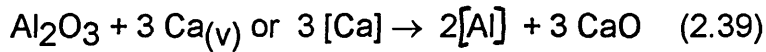
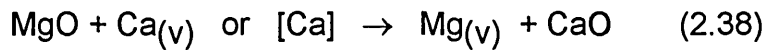
It has also been proposed^{71,73} that the behaviour of oxygen and sulphur at the interface between an inclusions and the liquid metal causes an electrical double layer. The metal/inclusion interface is composed of an anionic outer layer and an cationic inner layer, causing repulsion forces when two such interfaces are brought into contact.

The most spectacular effect of surface active elements is the emergence of alumina inclusions from Te containing steels, in this case angle θ is so large, Figure 2.11, that stable position of the inclusions is a complete or almost complete emergence⁷⁰. The alumina dendrites and clusters float out of the slag-free metal interface, each cluster probably pushing the preceding cluster. An alumina powder-like product, mostly not adhering to the metal, is recovered at the surface after cooling.

2.6 THE EFFECT OF THE CRUCIBLE MATERIAL ON THE RATE OF DEOXIDATION.

The composition of the crucible material has been shown to have an effect upon the rate of removal of oxygen from deoxidised steel melts^{49,66,85,90}. The changes in the oxygen content of liquid iron deoxidised with 0.5 mass% aluminium in a high frequency furnace for different crucible compositions at 1600°C are shown in Figures 2.12 and 2.13. The changes in oxygen content of liquid iron deoxidised with 0.5 mass% silicon in a high frequency furnace using SiO₂, Al₂O₃, MgO and CaO crucibles at 1600°C are shown in Figure 2.14⁹⁰. It has been suggested⁶⁹ that the separation rate of deoxidation products is regulated by the adsorption rate of products to the crucible wall and the rate largely depends on the composition of the crucible material. Saxena⁹¹ suggested that crucible materials which have a strong chemical affinity for primary deoxidation products show high rates of inclusion adsorption, whilst those with a weak affinity were not so effective. **Contrary to this**, Patsiogiannis⁹² indicated that the separation of inclusions by adherence to the refractory wall did not seem to play a major role in inclusion removal.

Otarani¹⁴ considered the effect of the strong affinity of Ca to oxygen on the type of crucible material used, in influencing the rate and total degree of deoxidation. The decrease of oxygen content in absolute values as a function of the time after the addition of the calcium are shown in Figure 2.15. The final oxygen content was lowest for the Al₂O₃ crucible, somewhat higher for CaO, while for MgO only a relatively small reduction in oxygen could be realised. Considering the stabilities of the oxides, the Standard Gibbs Free energies of formation at 1600°C are -705, -720, and -840 kJ.mol⁻¹ for MgO, Al₂O₃ and CaO respectively. It follows that for the reactions:



it can be assumed the the first two reactions will proceed to the right. For Al_2O_3 crucibles, $[\text{Al}]$ will enter the melt, combine with $[\text{O}]$ according to the third reaction and thus contribute to the total deoxidation. On the other hand, in the case of the MgO crucibles the Magnesium produced by the first reaction will also enter the melt, however in the form of Magnesium vapour. The vapour pressure of Magnesium at 1600°C is 19 atm., thus the high vapour pressure combined with the low solubility of magnesium in molten iron prevents the deoxidation reaction:



from proceeding. Thus part of the calcium is lost to the reaction with the crucible material, while the release of the Mg vapour can not contribute to the deoxidation process. It was shown that in the case of the Al_2O_3 crucibles there was an initial $[\text{Al}]$ concentration of 0.001%. Within 10 seconds after the addition of the calcium, the $[\text{Al}]$ content had increased to 0.036%, indicating the strong attack of the calcium on the crucible material. The subsequent decrease in the $[\text{Al}]$ content of the melt can be explained by the progressing deoxidation reaction (2.40), which removes the soluble aluminium from the melt. The melt contained in the MgO crucible showed only a small increase in the $[\text{Mg}]$ content due to the high vapour pressure and the low solubility of the magnesium released by reaction (2.38).

2.7 ALUMINIUM DEOXIDATION.

There have been a number of investigations into the deoxidation of iron-oxygen melts by aluminium^{11,12,45,49,76}. Sloman and Evans⁷⁶ conducted the first extensive investigation into the effects of deoxidation by aluminium in iron-oxygen melts. It was concluded that aluminium additions in stoichiometric excess of the oxygen content produced alumina inclusions, whilst additions of less than the stoichiometric proportions gave rise to mixed oxide phases containing hercynite, their constitution depending on the aluminium to oxygen ratio.

A number of workers^{12,93} have suggested that spinel phases may form rather than alumina, even under conditions where alumina would be a stable phase. Watanabe et al.⁹⁴ investigated the deoxidation of iron by aluminium and identified the phases produced using X-ray photoelectron spectroscopy. The oxides produced during the rapid cooling and solidification were identified as FeAl_2O_4 , γ -, κ -, θ -, and α - Al_2O_3 , and it has been suggested that they are produced in that order. It was postulated that a nucleus consisting of iron, aluminium and oxygen is formed in the molten iron, which grows until the chemical composition reaches that of FeAl_2O_4 . If there is an excess of aluminium relative to oxygen at the crystal interface, the aluminium will displace some or all of the iron from the hercynite. As the reaction continues the amount of iron remaining in the oxide becomes smaller, and the chemical composition of the oxide eventually reaches that of γ -alumina. The γ -alumina formed by this mechanism may retain the characteristic spinel structure of hercynite from which it is derived. The γ -alumina may transform to α -alumina via the intermediate κ - and θ -forms. The mechanism is shown schematically in Figure 2.16. Adachi⁹⁵ indicated that γ -alumina formed when a small 'lump' of aluminium was added to an iron melt, whereas when a 'platelet' of

aluminium was added to an iron melt chiefly θ - and possibly γ - and κ - alumina were observed. Considering Watanabe⁹⁴ and Adachi's⁹⁵ work it would be reasonable to assume that γ -alumina forms at low levels of supersaturation with respect to aluminium. As the aluminium content of the melt progressively increases during the dissolution of the deoxidant κ -, θ - and α - alumina are formed.

Vorob'ev and Levin⁹⁶ have postulated that the formation of complex liquid FeO-Al₂O₃ nuclei is due to a reduction in the interfacial energy caused by a chemical reaction between FeO and Al₂O₃. The composition of such nuclei being determined by the oxygen content of the melt prior to deoxidation, Figure 2.17. Areas A-E represent the regions of stability of various oxide nuclei compositions. Area A represents the unsaturated region of the melt, where the formation of the inclusions cannot occur. In Area B the supersaturation is insufficient for the formation of stable nuclei. Area C is the supersaturated region where only liquid oxides can nucleate. Area D is the region where liquid mixed oxides and pure alumina nucleate. And finally, Area E is the region where alumina nuclei can precipitate.

According to Vorob'ev⁹⁶, on the addition of the deoxidant the initial state of the melt is in Area A. As the concentration of the aluminium increases the melt becomes sufficient for oxide phases to separate. Sufficiently high concentrations of oxygen (0.05%) results in liquid mixed oxides forming in Area C, if the oxygen concentration is less than 0.01% before deoxidation, the oxide phase will separate in the form of alumina, Area E.

Thus the composition of aluminium deoxidation products depend not only on the supersaturation with respect to the solubility product but also on the

oxygen concentration of the liquid metal before the aluminium addition.

The scanning electron microscope has enabled the morphology of aluminium deoxidation products to be studied in detail^{77,97→103}. There is evidence^{100→103} that a number of different morphological types coexist in aluminium deoxidised melts, however, little systematic work concerning the mechanisms of formation of the different alumina morphologies has been undertaken with the exception of Robinson et al.¹⁰⁰. And much confusion is evident in the nomenclature used to define the different morphological types present.

2.7.1 SPHERICAL ALUMINA MORPHOLOGIES.

Straube et al.⁵⁵ reported the presence of alumina inclusions which exhibited a spherical glassy morphology. The inclusions were described as having an almost perfect spherical habit, resembling small glassy silicate inclusions rather than crystalline alumina inclusions. The analysis of this type of inclusion indicated that they were almost pure alumina. However, Braun et al.⁷⁷ identified a few spherical particles with a similar morphology which were either silica or iron-alumino-silicates, but, they were only observed in aluminium deoxidised steel samples taken one second after deoxidation. Many works^{55,104}, consider that these inclusions must have been liquid in order to develop their spherical morphology.

The possibility of homogeneous nucleation of oxides with low interfacial energies followed by heterogeneous growth of other less easily nucleated oxides on the substrate provided, has been suggested⁵⁵ as a mechanism of formation of these spherical inclusion morphologies. The interfacial tension is the major component of the free energy change required to form a stable

nucleus in the melt. FeO and FeO-Al₂O₃ exhibit lower interfacial tensions than Al₂O₃, Table 2.2, and consequently will be more easily nucleated. Therefore, liquid mixed oxides and hercynite can form in preference to alumina¹⁰⁵.

The change in composition of inclusions in an iron- manganese melt deoxidised with aluminium was studied by Straube et al.⁵⁵, by taking suction samples directly from the melt at various intervals after making the aluminium addition. These workers found that the primary deoxidation products underwent a marked change in composition during the course of their formation. Very small FeO-MnO inclusions containing small quantities of Al₂O₃ were observed within one second of the aluminium addition. Within a few seconds the aluminium content of the melt increased until a hercynite based spinel phase was precipitated, Figure 2.18. Pure hercynite is a solid at normal steel making temperatures, however, in the presence of manganese the phase has a lower melting point, Figure 2.19. With a further increase in time the inclusions developed a two phase structure, comprising of a spinel core and an alumina outer layer.

It has been reported¹⁰⁵ that hercynite particles inserted into iron-aluminium melts were reduced by the aluminium to a depth of 15 µm, indicating that small spinel inclusions could be completely reduced to alumina. It has been suggested^{33,54} that an Al₂O₃ layer is formed on the surface of the aluminium immediately after its addition to the melt. An alumina layer may also be present on the surface of the aluminium even before the addition of the deoxidant to the melt. This layer has the effect of retarding the solution of the deoxidant. However, convection and stirring effects result in the rapid distribution of the Al₂O₃ particles throughout the melt.

In regions of sufficient supersaturation, FeO-MnO precipitates heterogeneously on the Al_2O_3 particles, the Al_2O_3 then dissolves in the mangano-wustite to form a fully molten oxide. This liquid oxide inclusion then acts as a substrate for the heterogeneous nucleation of Al_2O_3 . Inclusions containing a core of ZrO_2 surrounded by mangano-wustite have also been observed after deoxidation with zirconium, suggesting that zirconia is formed initially and FeO-MnO nucleates heterogeneously on the substrate provided by the zirconia particles¹⁰⁸.

Thus small almost pure alumina particles may be formed by the direct reduction of liquid mixed oxides. Alternatively, heterogeneous nucleation of liquid mixed oxides may occur on a substrate provided by alumina particles present in the melt immediately after the addition of the deoxidant. Subsequently, the liquid oxides would be rapidly reduced by the aluminium in solution. The completeness of the reduction being dependent on the size of the liquid oxide inclusions¹⁰⁹.

Waudby and Salter¹⁰⁴ suggested that any such reaction would rapidly produce a solid rim structure, further reaction resulting in the internal precipitation of iron globules. However, the small spherical inclusions are characterised by their glassy appearance and apparent absence of enclosed metal.

Venkatadri¹¹⁰ proposed that the alumina coating over the spinel core is not pervious but, discontinuous. Whenever a discontinuity is present, the spinel core is exposed and reduced by the aluminium dissolved in the steel.

An alternative explanation¹⁰⁹ for the formation of spherical morphologies may involve the local temperature rise caused by the liberation of the enthalpy of formation of alumina. This could locally raise the temperature sufficiently for the alumina to be momentarily liquefied, so that the inclusions form in a fluid or viscous state. However, it has been shown by a simple heat balance¹⁰⁴, that the temperature rise is only in the order of 45°C.

2.7.2 DENDRITIC AND ASSOCIATED ALUMINA MORPHOLOGIES.

Dendritic growth forms have been divided into four main types which represent progressive changes in morphology. These are influenced by changes in the physico-chemical conditions within the melt and interaction with other inclusion types. The growth forms are as follows:

a) Dendrites; these are single crystals of alumina¹⁰⁰ which have clearly discernible dendrite stems⁷⁷. They consist of dendrite stems spreading out more or less radially, from a central point of origin. Branches grow out from the dendrite stems and in some cases secondary branches grow in a similar manner from the primary branches. Dendrites have been further subdivided^{101,102}, according to their size, development and two- or three-dimensional nature.

b) Coralline alumina; this is a branched irregular/globular shaped form of dendritic alumina^{100→103,112}, which consists of a single crystal of alumina¹⁰³.

c) Sintered polycrystalline aggregates; these are large particles, (5-20µm in diameter)¹⁰², with a polycrystalline structure. They are mainly composed of dendritic or coralline alumina^{100,101}, but may also contain non-dendritic

morphologies¹⁰¹.

d) Small globular particles; these are small globular/spherical inclusions, generally 1-2 μm in diameter⁷⁷.

e) Finger shaped dendrites, (c. 10 μm across), star shaped inclusions with finger like stems growing from a central point¹¹².

2.7.3 DENDRITIC GROWTH THEORIES

When a crystal nucleates in a solution the supersaturation is normally much higher than that at which subsequent growth occurs. The initial growth of spontaneously nucleated crystals in supersaturated solutions tends to be highly dendritic. The dendrites grow along fast growth directions, and this growth rapidly reduces the supersaturation¹¹³. A dendrite consists of a primary stem onto which branches grow, and secondary branches appear on the primary branches. This may occur in one plane or three dimensionally. Dendrites are normally single crystals and the branches follow definite crystallographic directions¹¹⁴.

It has been suggested¹¹⁵ that the reason for dendritic growth is the necessity to dissipate the heat of fusion generated at the solid-liquid front during rapid crystallisation from the melt. An effective method to remove the heat more rapidly than at a flat interface is to increase the interfacial area, which is accomplished by branching. As the surface area increases so does the surface energy, consequently surfaces with the lowest energy grow, which is the reason for the orientation relationships among stems and branches.

The branches are often spaced out at regular intervals and the opposite

sides of the dendrites exhibit remarkable symmetry. The spacing of branches may be due to variations in the supersaturation in the neighbouring solution so that a further branch cannot form until a point some distance along the main stem where sufficient supersaturation is encountered¹¹⁴. Thus the branches would then appear at regular intervals along the main stem by repetition of this process. This would indicate that the primary cause of dendritic growth is high supersaturation with diffusional fields having a secondary effect.

However, Saratovkin¹¹⁶ suggested that the lack of dendritic growth in pure metals in spite of the temperature effect, suggested that accumulations of impurities around the growing crystals are needed for dendrites to form. The dendrites grow because the solvent molecules do not have time to leave the surface of the crystal by convection or diffusion. And the crystal rapidly grows avoiding areas of the solution already depleted in solute.

The mechanism of dendrite formation proposed¹¹⁶ is as follows: an edge where two adjacent faces AB and BC meet is considered, Figure 2.20. The faces grow at rates V_A and V_C , and after a time, t , they occupy a position A_1O and OC_1 , respectively. The solvent around A_1 and B_1 will become depleted in solute, given $AA_1 = BB_1$. However, at D_1 there will be less solute depleted solvent, since $DD_1 < BB_1$, and the solute depleted solvent is displaced as soon as the edge reaches D. Hence the solute depleted solvent in OB_1 will be less than over the rest of the face, the more so the nearer to O. OB_1 will be less hindered in growth than the rest of the face. Eventually, the solute depleted solvent accumulates to such an extent that growth virtually ceases, but, growth can still continue over OB_1 . Growth soon ceases at points further away from O than the distance OB_1 , whilst

growth at O continues as before. Thereby a stem growing in direction BF is produced, Figure 2.21.

The mechanisms of stem formation are fairly complicated, the concentration of the solute depleted solvent over OB_1 varies from point to point, the maximum being at B_1 . The solute is thus most readily deposited about point OB_1 . The faces are thus built up from layers starting from the point, Figure 2.22. The lengths of the growing layers are determined by the distance OB_1 , whilst the thickness depends, primarily on the crystallisation rate. The layers may trap sublayers of 'impurities' parallel to the growing faces.

The layer of solute depleted solvent may permit growth normal to the stem axis. Growth of side branches occur from projections on the primary stem, Figure 2.23, the projections are covered with crystallographic faces normal to those on the primary stem. The projection gives rise to a branch the thickness of which will be small compared with that of the main needle, given that the solvent will be depleted in solute. However, the projection may eventually penetrate into regions of the melt where the solute content is greater, and layers similar to those on the primary stem will then be produced. In this way branches are produced which are the same thickness as the primary stem, but are attached to the stem by a very thin neck.

The crystal subsequently grows via these stems on which primary, secondary and even tertiary branches also form, thereby taking on the characteristic form known as 'Dendritic'.

Saratovkin¹¹⁶ suggested that the lines surrounding the dendrite, Figures 2.20 and 2.21, also correspond to the temperature around the crystal

and hence the degree of supercooling. It was considered that the temperature effect alone may be responsible for dendrites forming during the crystallisation of rapidly cooled pure substances, but, the main effect in solutions is the accumulation of impurities around the growing crystal.

2.7.4 OBSERVATIONS AND MECHANISMS OF ALUMINA DENDRITIC GROWTH.

Dendritic alumina has been observed in melts with various initial oxygen contents and deoxidant additions^{100,103}, and different stirring conditions^{102,103}. The major criteria for the formation of dendritic alumina in steel melts are conditions of high supersaturation¹⁰⁰, with further development dependent upon the prevailing oxygen content and the degree of stirring experienced by the melt^{102,103}.

Robinson et al.¹⁰⁰ suggested that high supersaturation resulted in direct precipitation of dendritic alumina. Highly branched, well developed dendritic alumina occurred at high oxygen and aluminium concentrations, whilst at lower oxygen concentrations growth was less well developed, with the dendrite arms tending to spheroidise. At low oxygen contents the growth became almost completely spheroidal. The variations in dendrite morphology was attributed to both local variations in oxygen content and the reduction in the oxygen content of the melt as deoxidation progressed^{100,117}. Each dendrite was confirmed as being a single alumina crystal, and some crystals showed evidence of growth faults in some dendrite arms¹⁰⁰.

Observations¹⁰² indicated that the coralline morphology formed at low oxygen contents (>0.019%), and consisted of a single alumina crystal. This morphology corresponded to the spheroidised dendrite form described by

Robinson¹⁰⁰, which was observed at low (c. 0.03%) oxygen concentrations. Ooi¹⁰² interpreted this morphology as dendrite stems or branches changing from dendritic to spherulitic alumina.

Several mechanisms for the formation of small globular morphologies from pre-existing dendrite morphologies have been suggested^{77,117}. Martin¹¹⁷ suggested that as the growth of dendrite stems proceeds the surrounding liquid iron will be depleted in oxygen. Projections on the dendrite stems gave rise to branches, the initial thickness of which were small compared with the main stem, since the liquid iron would have been depleted with respect to oxygen. As the branches grow they penetrate into regions containing higher oxygen concentrations and the growth would correspond to that of the main stem since conditions would have been similar. Hence, branches of similar thickness to that of the main stem are attached to the main dendrite stem by very thin necks.

As the branches grow into the liquid iron, the oxygen content continuously falls, and will be very low in the vicinity of the dendrite stem. With the decrease in oxygen content of the melt the interfacial energy between alumina and liquid iron increases⁸⁷. In order to reduce this increased interfacial energy the alumina will tend to reduce its surface area and consequently the tips of the dendrite branches begin to spheroidise. Growth faults in the dendrite branches cause local weaknesses in the branches and spheroidisation will be initiated at these points¹¹⁷.

The possibility of dendrite branches melting-off due to the local heating of the liquid iron caused by the heat of formation of alumina can not be explained. It has been shown thermodynamically that the temperature rise due to the

formation of alumina is only at maximum 30- 50°C¹⁰⁴.

However, Braun⁷⁷ made calculations describing the coarsening and break-up of cylindrical rods into spheres due to the remelting of dendrite stems and branches by curvature induced freezing point depression. And, although the magnitude of the increase in solubility is small, it was suggested that the dissolution process due to curvature could be still operative.

Robinson¹⁰⁰ suggested that the formation of dendrites and spherical sintered alumina agglomerates were part of the same dynamic process activated largely by the change in surface energy at the alumina/melt interface as deoxidation progressed and oxygen is removed from solution in the liquid metal. The initial dendritic growth causes a reduction in the oxygen content of the melt, which results in an increase in interfacial energy. Consequently, the surface/volume ratio of the inclusions decreases in order to minimise the surface energy, resulting in spheroidisation of the dendrite stems and branches. As spheroidisation progresses partially or completely spheroidised dendrite stems and branches contact each other and the liquid metal withdraws from the points of contact due to the high surface energy. The retraction of the meniscus causes radial forces to develop between the touching particles and the particles begin to sinter. Many sinter points develop between the collapsing and spheroidising dendrites, eventually resulting in spherical sintered polycrystalline aggregates.

The collapse of the dendrites and the formation of sintered aggregates was supported by the presence of iron trapped between the sintered alumina crystals. Large central metal-filled cavities were observed in the sintered aggregates, which were invariably connected to the outer surface of

particles. It was suggested that this cavity was a vent through which the metal entrapped between the collapsing dendrites was expelled as sintering progressed. The internal surfaces of the porosity indicated the polycrystalline nature of the sintered aggregates as did the partial spheroidisation and sintering of the remnant dendrite stems and branches protruding into the cavity.

2.7.5 POLYHEDRAL ALUMINA MORPHOLOGIES

Polyhedral morphologies are essentially those inclusions which exhibit faceted surfaces. Braun⁷⁷ defined two types of polyhedral inclusions; faceted inclusions which had well formed facet planes and were three dimensional in nature; and plate-like inclusions which had well formed facet planes, but, were more two dimensional. Ooi¹⁰² also described two types of polyhedral inclusions, angular and octahedral inclusions.

2.7.6 POLYHEDRAL GROWTH THEORIES

Polyhedral crystals form from 'dilute' solution and are the growth forms of 'real' crystals, which are formed, with clearly developed faces. The polyhedra grow as suitable molecules are brought to the crystal face by convection¹¹⁶. The diffusion of molecules is facilitated by convection gradients at the crystal/solution interface. The molecules are absorbed on the crystal face and are subsequently incorporated into the lattice structure. The crystal lattice grows by the addition of molecules at a point (A), where the binding energy is greatest, Figure 2.24. Thereby, layers of molecules form across the face of the growing crystal in what is referred to as 'the repeatable step'¹¹⁴. The polyhedra is therefore composed of growth pyramids of its faces resulting from these layers of adsorbed molecules¹¹⁶, Figure 2.25.

2.7.7 OBSERVATIONS OF POLYHEDRAL ALUMINA MORPHOLOGIES.

It was observed⁷⁷ that polyhedral inclusions were more frequent in melts with low initial oxygen contents and their frequency decreased with increase in initial oxygen content. They were also the dominant morphological type in stirred melts and as the stirring increased they became more prevalent. However, no mechanism has been put forward as to their mode of formation, other than the vague suggestion that they were formed by 'short term' diffusional growth¹⁰¹.

2.7.8 THE EFFECT OF SURFACE ACTIVE SUBSTANCES ON POLYHEDRAL GROWTH.

Surface active elements may effect crystallisation as they tend to accumulate at the crystal-solution interface, i.e. on the crystal surface, resulting in a material change in the growth rate of the various crystal faces. Wulff's law states that the growth rate of a crystal face is proportional to its surface tension. Surface active elements adsorbed on interfaces reduce the surface tension. This reduction in surface tension varies with the face, consequently, the growth rates of the faces are affected unequally.

As well as having an external surface effect changing the surface tension at the faces of the growing crystal, surface active elements may also interact chemically changing the crystal habit. Thus, surface active elements can alter the ratio of the growth rates of faces, inevitably altering the crystal habit, as consequence faces previously absent will appear and visa versa¹¹⁵.

2.8 CALCIUM DEOXIDATION.

Calcium has a high affinity for oxygen but its use at steelmaking temperatures presents several problems. Elemental calcium has a very low solubility in liquid steels¹¹⁸ (0.032% at 1607°C), the calcium vapour pressure at 1600°C of 1.6 atm. results in rapid loss by vaporisation of pure metal additions and the low density of calcium metal and alloys leads to rapid float-out of the additions. However, the use of calcium alloys after prior deoxidation with aluminium, because calcium has a higher affinity for oxygen than aluminium, has been shown to improve cleanness and modify inclusion composition to such an extent that the mechanical properties are enhanced.

On the addition of a lump of calcium bearing deoxidant, it will begin to dissolve causing the thin boundary layer of the steel immediately in contact with the alloy to become rapidly saturated with calcium, (due to its limited solubility). Any further dissolution will thus be prevented until the calcium in the boundary layer has had time to diffuse away into the bulk of the melt. The diffusion would probably be relatively slow due to the comparatively large size of the calcium atom. Consequently most of the calcium contained in the addition would be expected to boil-off into the atmosphere. Thus only a tiny fraction of the total calcium added may actually be retained in the steel¹¹⁹. As a result of this approach calcium was alloyed with elements which reduce the activity and the vapour pressure of the calcium.

Results show that calcium is much more effective as an inclusion modifier after prior deoxidation than it is a primary deoxidiser.

A mechanism for the modification of alumina deoxidation products by calcium has been proposed by Hilty and Popp¹¹⁹, developed from the earlier work of

Hilty and Crafts¹²⁰. The fluxing effect of CaO on Al₂O₃ are shown in Figure 2.27, a relatively small amount of CaO substantially lowers the melting point of Al₂O₃. The influence of the CaO on Al₂O₃ should cause a major shift in the position of the metal/oxide eutectic. As calcium has a larger affinity for the oxygen than aluminium, an expansion of the liquid metal-liquid oxide solubility gap should also be expected. If the initial precipitation of the oxide occurs as a liquid rounded inclusions are formed.

Pickering¹²¹ extended the calcium dissolution theory of Hilty and Popp¹¹⁹, suggesting the Al and Ca, added together, may cause calcium aluminate films to be formed around the dissolving deoxidant. Having a relatively low melting point such films would then collapse allowing the calcium-aluminium to again diffuse into the steel. It was further proposed¹²¹ that alternatively, if the calcium and aluminium were added separately, solid films of CaO and Al₂O₃ could form around the calcium and aluminium rich areas respectively and retard the diffusion of the deoxidising species. It was also suggested that a more reproducible utilisation of calcium may be achieved by the addition of the calcium bearing deoxidants only after prior aluminium deoxidation. In this way the calcium could then modify alumina inclusions, causing the aggregates to be replaced by calcium aluminates. Some CaO may also be precipitated, probably on the surface of the alumina particles. Since both of these oxides are solid at steel making temperatures any reaction taking place to form calcium aluminates would be slow. The fact that calcium aluminates themselves have low melting points could, however, lead to the formation of a liquid layer on the surface of the alumina particles which could then act as a "sink" dissolving both the CaO and Al₂O₃. Such a mechanism could help to explain the relatively rapid modification of Al₂O₃ to calcium aluminates.

The other major draw back of the use of calcium in steelmaking in addition to the low solubility, low boiling point and high vapour pressure is its often violent reaction with the melt. In general, the more dilute the addition the less violent the reaction. There appears to be an optimum calcium content of the alloy of 20%¹²², above which no further improvement in performance can be achieved and similarly there is a maximum useful quantity of addition of between 1-2% of the alloy according to various authors. The rate deoxidation and floating velocities of the deoxidation products from calcium treatment is subject to considerable controversy. Some authors have concluded that calcium bearing deoxidation products float out of the melt more rapidly compared with conventional aluminium deoxidation products^{123,124}, whereas Asono and Nakano¹²⁵ forwarded the opposite view, stating that alumina clusters produced during aluminium deoxidation float-out quicker than globular inclusions formed during calcium deoxidation.

2.9 SILICON DEOXIDATION

Silicon is a moderate deoxidant, Figure 2.4, it is a much more effective deoxidiser than manganese and is often used in combination with that element¹²⁶. Silicon in the form of ferrosilicon and silicomanganese, is often employed to deoxidise melts which are to be used in the production of steels requiring good surface finishes, manganese and silicon being employed in combination because of their synergistic effect on the deoxidation process¹⁶. There have been a number of investigations on the deoxidation of iron with silicon^{9,16,27,127,128,129}. If pure iron is deoxidised with silicon the deoxidation products are either iron silicates, which are liquid at the melting point of iron, or solid SiO₂. In silicon killed steels a variety of Fe-Mn-silicates are formed during deoxidation, the composition largely depending on the Si:Mn ratio¹³⁰. At low silicon levels inclusions consisting of

mangano-wustite in a eutectic matrix are formed. At higher silicon levels these pass into the olivine region of the phase system, Figure 2.27, and occasional single phased inclusions of either fayalite ($2\text{FeO}\cdot\text{SiO}_2$), tephronite ($2\text{MnO}\cdot\text{SiO}_2$) or rhodonite ($\text{MnO}\cdot\text{SiO}_2$) have been observed^{126,133}. At even higher silicon levels the deoxidation products are usually glassy, having compositions within the miscibility gap which extends across the ternary system. Under certain circumstances during deoxidation with silicon the inclusions can develop a 'raspberry' or 'rosette' morphology^{41,127,128,129}. Turpin and Elliott⁴¹ proposed that liquid iron oxide is the nucleating phase, the particle grows by the addition of an oxide phase in which the ratio of SiO_2/FeO may increase to saturation with SiO_2 . When saturation is reached, either particles of silica nucleate heterogeneously at isolated spots on the surface and grow as separate particles, or, alternatively, saturation results in continued growth, but in a new mode, from selected points on the periphery of the original FeO particle. Whereas, Zapffe and Simms¹²⁹ explained the morphology as having resulted from a coalescence phenomenon. These rosettes have been reported as being composed of a highly siliceous glass.

The more general occurrence of silica is as a highly siliceous, very transparent spherical particle. Gatellier and Olette⁶⁵ indicated that the supersaturation in silicon deoxidised melts was insufficient for homogeneous nucleation, with the only explanation for the precipitation of the silicon oxides being heterogeneous nucleation. It has also been reported¹³³ that the near spherical shape of some silica inclusions is due to the reduction of a spherical liquid silicate inclusion.

Dendritic silica inclusions have been observed^{134,135} and classified roughly

into two types: those existing in the interdendritic region of the matrix, and those which had grown from spherical primary inclusions. It was suggested that the former were formed by a suitable gradient of supersaturation in the interdendritic liquid. Whilst, the latter were formed by a suitable gradient of supersaturation around the primary inclusion. They concluded that the dendrites did not grow from the crystallographic growth directions of the inclusion but formed by a suitable gradient of sufficient supersaturation during cooling.

2.10 TITANIUM DEOXIDATION

The uses of titanium and its effect on steel and cast iron have been extensively reviewed by Comstock¹³⁶. Titanium is one of the strongest deoxidisers commonly used in steelmaking and is known^{11,137} to significantly reduce the solubility of oxygen in liquid iron. The data for the deoxidation equilibria in Fe-Ti-O melts at 1600°C are presented in Figure 2.4.

Investigations have been carried out^{138,139,140,141} to study the deoxidation mechanisms of iron by titanium. A series of different titanium-iron-oxygen compounds have been identified microscopically¹⁴² and by X-ray diffraction techniques^{138,140}, and have been reviewed by Kiessling and Lange¹⁴³. It has been reported¹³⁸ that FeO.Ti₂O₃ is formed in iron melts when the titanium concentration is low. Ti₃O₅ is the deoxidation product in melts containing up to 0.2% Titanium, whilst between 0.2% and 2.0% Ti α -Ti₂O₃ is observed, above 2.0% titanium, TiO is the deoxidation product^{138,140}.

2.11 ZIRCONIUM DEOXIDATION

Generally, zirconium additions to iron and steel are made in the form of zirconium alloys; these include iron-silicon-zirconium and silicon-zirconium.

It is also a component in some alloys containing Ca, Al, Mn, Cr, Ti and B. The use of zirconium as an addition to steel is associated with its strong chemical affinity for oxygen, nitrogen, carbon and sulphur, with its largest use being as a deoxidant¹⁴⁴.

The equilibrium value for the deoxidation product is illustrated in Figure 2.2, it has been suggested that zirconium will lower the activity and solubility of oxygen in liquid iron in much the same way as aluminium¹⁴⁵.

Bogdandy et al.⁴⁵ indicated that there was a strong inhibition to the nucleation of zirconium oxide. In a steady bath it was suggested that zirconium oxide precipitates in layers which follow one another chronologically and spatially. The inclusions only formed in places where the supersaturation was high. Large dendrites were formed up to 100 μ m in length.

Chapter 3

Apparatus & Experimental Procedures.

3.1 INTRODUCTION

A series of low carbon steel charges contained in magnesia crucibles were melted in either a high frequency furnace or a pyrox vertical tube furnace. When a stable temperature of 1600°C was achieved^d_Λ the melts were deoxidised with a number of deoxidants including aluminium, titanium, silicon, a calcium-aluminium alloy and zirconium. Prior to and at intervals after the addition of the deoxidant, samples were removed from the melt by sucking the liquid steel into quartz sample tubes.

The chemical composition of the original steel charge and the solidified steel remaining in the crucibles after the experiments had been terminated were analysed using spark emission and inductively coupled plasma emission spectroscopy.

The deoxidised steel samples were analysed using a Leco oxygen analyser to ascertain their total oxygen content. Sections of the samples were examined both optically and in a scanning electron microscope using quantitative energy dispersive X-ray analysis to determine the chemical composition of the deoxidation products contained within the samples. Particle size analysis was also carried out to establish the size distribution of the deoxidation products.

Samples of the crucible which had been in contact with the liquid steel were examined in a scanning electron microscope using quantitative energy dispersive X-ray analysis to evaluate the chemical composition of the phases present. X-ray elemental mapping was also used to show the relative distribution of the elements present.

Details of the equipment used and the procedures adopted are described in the subsequent sections.

3.2 MELTING EQUIPMENT.

3.2.1 HIGH FREQUENCY FURNACE.

The induction furnace for the induction melting experiments, employed a 15 kVA, 350-450 kc/s Electroheating power source, the output being varied by the operator using a hand wheel located on the front panel of the unit. As there was no output current meter on the unit, the power setting was gauged from the position of the hand wheel pointer which covered a circular scale marked 0-75. A meter giving the anode current to the valve oscillator was another indication of the power being supplied to the coil.

Water cooled, flexible, high frequency leads from the generator were connected by brass couplings to a copper induction coil. The induction coil was made from 12 mm external diameter bright annealed copper tubing, and covered with a close fitting insulating sheath of vida flex. The coil had seven turns in total, the diameter of each turn being 9cm.

The melting assembly used is illustrated in Figure 3.1 and briefly comprises of an alumina refractory brick placed at the base of the induction coil, to act as a support for the crucible. The coil was lined with kaopaper and an alumina (Al-sint) protection tube placed in the centre. The area between the kaopaper and the protection tube was tightly packed with coarse, granular magnesia (Thermag). A coarse grained, spinel bonded magnesia crucible containing a cylindrical charge of low carbon steel weighing approximately 500g was placed in the alumina protection tube. The composition of the refractory materials are given in Table 3.1(a).

The protection tube had two functions:

1. it acted as a protective barrier if the magnesia crucible failed during the experiment; and
2. enabled an inert atmosphere to be maintained above the melt to prevent reoxidation of the melt by atmospheric oxygen.

The top of the protection tube was fitted with a porous alumina refractory plug. The plug had two openings; one held a 3mm external diameter alumina tube providing an inlet for the argon gas shroud, the composition of the argon is given in Table 3.1 (b). The second was used to gain access to the melt in order to take both the temperature of the melt and samples during the experiments.

Temperature measurements in the high frequency furnace were made with the aid of a Pt/Pt13%Rh thermocouple, protected by a 5mm external diameter silica sheath. The temperature was read from a chart recorder with the appropriate compensations being made.

3.2.2 VERTICAL TUBE FURNACE.

A Carbolite vertical tube furnace with Pyrox elements was used to melt steel samples under conditions of natural convection. The furnace consisted of an 855mm long, 440mm external diameter insulated case containing a central alumina (Al-sint) work tube, the composition of which is given in Table 3.1(a), (1000mm long and 75mm external diameter). Arranged around the work tube were eight Pyrox 2000 heating elements, the main constituent of the Pyrox element was lanthanum chromite. The furnace required a 240 volt single phase power supply and had a maximum power output of 7kW. The maximum working temperature in the vertical position was 1800°C. The

furnace controls were housed in a separate control cabinet which included an ammeter and a Eurotherm type 017 P1D 3 term controller with an integral temperature indicator.

A temperature profile of the furnace was determined using a chromel alumel thermocouple with the furnace temperature set at 1000°C, Figure 3.2. The temperature sensor subsequently used was a Pt30%Rh/Pt6%Rh thermocouple which was placed adjacent to the Pyrox elements in the hot zone of the furnace. This acted as the control thermocouple as well as the furnace temperature monitor. The control temperature was in good agreement with the monitoring thermocouple at 1000°C within the accuracy of the thermocouples. The temperature was read from a continuous digital display on the control cabinet.

At the base of the Pyrox Vertical Tube Furnace was a water cooled aluminium plate on top of which the alumina (Al-sint) work tube was mounted, as illustrated in Figure 3.3. An aluminium spigot was screwed into the plate, this acted as a location point for a second 50mm external diameter and 50cm long alumina (Al-sint) tube. This functioned as a support and ensured that the crucible was located in the hot zone of the furnace. Argon gas, used to create the inert atmosphere during melting, entered the assembly through the aluminium spigot.

A coarse grained, spinel bonded, magnesia crucible of identical composition to the crucibles used in the high frequency experiments, was contained within a 65mm external diameter alumina protection tube. The protection tube was sealed at the base with sodium silicate bonded granular magnesia and rested on the top of the support tube. The main alumina work tube was

extended using a second slightly smaller diameter alumina tube, the junction between the two tubes was sealed with a kaopaper gasket. The extension was sealed with a water cooled aluminium end assembly. This contained one orifice with a stopper which could be removed to enable samples to be taken during the experiment and two outlets which allowed the argon gas to flow from the assembly.

3.3. EXPERIMENTAL PROCEDURES.

3.3.1 INDUCTION FURNACE HEATING PROCEDURE.

The high frequency furnace equipment was assembled and allowed to dry over night. The steel charge was placed in the crucible and the power switched on. To prevent the preformed crucible from cracking the current was increased gradually up to a maximum of 2.6A. The furnace took approximately one hour to reach the experimental temperature of 1600°C. During the entire experiment an argon shroud was maintained over the melt with a flow rate of 1 litre per minute. Once sampling was complete the power was switched off and the furnace allowed to cool to room temperature.

3.3.2 PYROX VERTICAL TUBE FURNACE HEATING PROCEDURE

The pyrox vertical tube furnace equipment was assembled and the crucible containing the steel charge carefully lowered into the protection tube. The water cooled end assembly was secured in position at the top of the work tube and the water supply switched on. The argon was supplied at a rate of one litre per minute through the aluminium spigot at the base of the assembly. The furnace was heated over night according to the heating schedule given in Table 3.2. It took 16 hours to reach the experimental temperature which was maintained for one and a half hours during which the deoxidation and subsequent sampling took place. The furnace was

subsequently cooled to room temperature over a period of eight hours.

3.3.3 DEOXIDATION TECHNIQUE

When a stable temperature of 1600°C had been achieved the deoxidant was introduced into the liquid steel. For safety reasons the power was switched off during this procedure when using the induction furnace, but this was not necessary for the vertical tube furnace melts. For rapid homogenisation within the liquid steel, every effort was made to ensure that the deoxidant was introduced into the centre of the melt. This was achieved by winding or wrapping the quantity of deoxidant required around the base of a quartz tube and 'spearing' it into the melt. Experiments were carried out using aluminium, titanium, silicon, zirconium and a calcium-aluminium alloy as deoxidants, Table 3.3, in each case 0.6 mole% was used, this ensured that excess deoxidant was present in the melt and corresponded to the quantities used by previous works⁸⁰.

3.3.4 SAMPLING TECHNIQUE.

Samples were taken by sucking liquid into 3mm internal diameter quartz tubes, 1000mm long tubes were required for melts in the Pyrox vertical tube furnace and 300mm long tubes for the high frequency furnace melts. A rubber bulb was attached to one end of the sample tube, which when squeezed provided sufficient suction to draw liquid metal some 100-150mm up the bore of the tube where it rapidly solidified. The quartz tubes were flushed with argon gas, Figure 3.4, before use in order that oxygen should not be introduced into the melt during sampling. After the metal had been sucked into the sample tube, the tube was removed from the melt and quenched into a bath of cold water.

An initial sample was taken just prior to the addition of the deoxidant to the melt. Immediately after deoxidation, samples were taken as frequently as was practically possible. Between 3 and 7.5 minutes after deoxidation the sampling interval was increased to between 30 and 60 seconds; after this period the sampling interval was further increased to 150 seconds until approximately 20 minutes after deoxidation when the experiment was terminated. The furnace was switched off and allowed to cool to room temperature.

Chemical analysis, and optical and scanning electron microscopical examinations were carried out on the steel samples removed from the melt in the quartz tubes. The initial steel charge and the solidified steel remaining in the crucible at the end of the experiment were analysed. The interface between the crucible and the solidified melt was also chemically and microscopically analysed.

3.4 BULK CHEMICAL ANALYSIS TECHNIQUES.

3.4.1 SPARK EMISSION SPECTROSCOPY.

The original steel charge and the solidified steel remaining in the crucibles after the experiments had been terminated were analysed to determine the concentrations of the following elements:

C; Mn; Si; S; P; Ni; Cr; Mo; Cu; V; Sn; Ti; Al.

This was achieved by Spark Emission Spectroscopy using a Direct Reading Applied Research Laboratories 29500 Spectrometer. Each of the steel samples was prepared by sectioning through the sample and finishing the surface until it was smooth. The samples were then mounted onto the instrument and a spark was initiated between the sample and the silver

counter-electrode. The spark caused high temperatures to be experienced at the sample surface resulting in atomisation of the sample and excitation of the atoms to higher electronic states. The lifetime of the excited atom is brief and as it returns to the ground state photon radiation is emitted. The light is characteristic in the wave lengths of the elements from which it was emitted, the light intensity being proportional to the concentration of the elements. The wavelengths were analysed by the Direct Reading Spectrometer and the output from each of the element channel recorded and converted into mass percentages of each element using suitably prepared calibration graphs.

3.4.2 INDUCTIVELY COUPLED PLASMA-EMISSION SPECTROSCOPY.

Since the Direct Reading Spectrometer did not contain channels for Magnesium or Zirconium, the concentrations of these elements were determined by Inductively Coupled Plasma-Emission Spectroscopy (ICP-ES) using a Thermo-Jarrel Ash ICPA 9000 instrument.

Drillings were taken from each of the steel samples and a suitable mass was digested in acid (hydrochloric and nitric), and the resultant solutions diluted to a known volume. The solutions were pumped at 1 millilitre per minute into a nebuliser, which generated an aerosol, this was swept into the device by a stream of argon gas. The plasma was induced and sustained by radio frequency energy (27.1 MHz), which generated high temperatures (6-10,000 K). As the aerosol passed into the device, atomisation and ionisation of the elements present occurred. The resulting excitation causes electronic transitions, and on returning to the ground state the atoms emit a photon of radiation. The light emitted is proportional in concentration to the element causing the emission. This light was analysed by the spectrometer and the data acquired by a micro-computer running on dedicated software,

concentration values were calculated using calibration data gained by the use of appropriate standards and the concentrations of magnesium and zirconium were obtained as mass percentages.

3.4.3 LECO OXYGEN ANALYSIS.

The determination of the total oxygen content of the steel samples was carried out at the Swinden Laboratories of British Steel, using a Leco Oxygen Analyser. The Leco Oxygen Analyser consists of an inert gas purification unit, a high frequency induction furnace with a reaction tube and an analyser¹⁴⁶.

The steel sample to be tested weighing approximately 1.0 g was dropped into a heated graphite crucible, where the oxides are reduced in the presence of an excess of carbon. The resulting carbon monoxide, containing all the oxygen in the sample, is then swept through the rest of the device by an inert gas flow. Along with the carbon monoxide, hydrogen and nitrogen are also evolved. All three gases are passed over an oxidising agent, where the carbon monoxide is converted to carbon dioxide and then transported into a collection device. After a preset time the gases are released from the trap and carried by the inert gas into a selective chemical filtering tube. This filter separates the carbon dioxide from the other gases. All the gases in turn pass into a thermal conductivity cell where the change in resistance due to the thermal conductivity of the carbon dioxide alone is read as 'counts' on an integrator clock set to start at the precise time when the carbon dioxide is passing through. These counts are then related to the percentage oxygen on a graph prepared by taking samples of known oxygen content through the analysis process.

3.5 SCANNING ELECTRON MICROSCOPY.

3.5.1 SCANNING ELECTRON MICROSCOPY.

In the examination of the deoxidised steel and crucible samples, two instruments were used: the Jeol JXA 840A and the Philips PSEM 500 Scanning Electron Microscopes. The latter was primarily used for the energy dispersive X-ray analysis and morphological examinations, whilst the former was used for particle size analysis, X-ray elemental mapping and some morphological examinations.

The advantages of the SEM over optical microscopy include the superior resolution and magnification available to the SEM which is particularly valuable when examining the three dimensional morphology of deoxidation products in the deep etched steel samples. Secondly, since both machines were equipped with EDX facilities the identification of a range of elements both quantitatively and qualitatively was available. Relatively accurate particle size analysis of the steel samples was achieved using the high magnifications. However, particle size analysis using the SEM is time consuming and a smaller area of the sample was analysed compared with the area which would be analysed with an optical system.

For particle size analysis a backscattered electron image was employed. A backscattered electron is an elastically scattered electron formed when a beam electron passes close to a positively charged atomic nucleus, to which it is attracted. This results in the electron changing direction, with hardly any (<1eV) loss of energy. The angle through which it is deflected (the scatter angle), depends on how much energy it has and how close it passes to the nucleus. This varies from almost zero to 180 degrees, so the electron may be hardly affected at all, or may end up travelling back in the same direction

from which it came. Elastic scattering is more likely to occur in phases composed of high atomic number elements and when low accelerating voltage beams are used. Consequently, phases composed of elements with high atomic numbers emit more backscattered electrons and appear light on a backscattered electron image. Whilst, phases composed of low atomic mass elements appear dark on a backscattered electron images. Therefore, with flat 'polished' specimens showing little topographic detail, the backscattered image provides very detailed 'atomic number contrast', enabling different phases to be more readily distinguished.

To determine the three dimensional morphology of the deoxidation products in the deep etched steel samples a secondary electron image was used. Secondary electrons are produced when incident primary electrons knock out loosely bound conduction electrons from the sample surface. These weak electrons are released within about 10nm of the sample surface.

The resolution of the SEM images produced are limited by the diameter of the incident electron beam ('spot size'), the smaller the spot size the sharper the image. However, whilst providing high resolutions small spot sizes produce 'noisy' images. At high acceleration voltages the resolution is good, but the image tends to lack contrast and can result in charge building up in the specimen, this is especially important when examining phases containing low atomic mass elements. Consequently, a compromise has to be made between spot size (resolution) and acceleration voltage (contrast).

3.5.2 SAMPLE PREPARATION.

3.5.2.(A) PREPARATION OF DEOXIDISED STEEL SAMPLES.

The chilled, steel samples were removed from the quartz tubes by breaking the quartz surrounding the metal with a hammer. The samples were then transversely sectioned into shorter lengths, approximately 8cm being required for oxygen analysis. Smaller transverse sections, about 5mm long, were mounted in electrically conducting bakelite using a hot mounting press. The conducting bakelite was used to avoid any charge build-up during examination in the electron microscope. The mounted specimens were prepared by wet grinding using a series of grades of grinding paper from 240 to 600 mesh. The final polishing was carried out on pads impregnated with Hyprez diamond lapping compound, from 6 to 1 μ m.

It was necessary to ensure that all the scratches were removed from the specimen surface, during the final polish using the diamond impregnated pads. However, topographical contrast resulting from variations in hardness of the specimen constituents had to be minimised to ensure accuracy in the subsequent assessments. This was achieved by avoiding prolonged polishing thereby preventing bevelling of the isolated harder phases, this was especially important for particle size analysis. The polished samples were then carbon coated using an Edwards E306A carbon coater, this provided a conducting layer on the sample surface so the incident electron beam would penetrate the sample rather than being deflected.

For the morphological examination of the deoxidation products the polished and mounted samples were deeply etched for 6 to 7 minutes in a solution of 5% bromine in water free methanol. After carefully washing in methanol the samples were dried and immediately coated with platinum, using a Polaron

SEM coating unit E5100, in order to render the surface of the deoxidation products conducting.

3.5.2.(B) PREPARATION OF CRUCIBLE SAMPLES.

Crucible-melt interface samples were sectioned from the crucibles containing the remaining steel charges after solidification and cooling to room temperature. This was achieved using a Metaserv C1600 automatic cut-off machine incorporating a silicon carbide abrasive wheel. After drying overnight in an oven at 120°C, the specimens were mounted and vacuum impregnated in Struers Epofix resin contained in 30mm diameter plastic moulds to maintain the integrity of the interface and refractory crucible material.

The mounted specimens were prepared for microscopical examination by wet grinding using 120, 240 and 320 grit silicon carbide papers. Subsequent polishing was carried out on a 6µm Kemet ceramic wheel, followed by 6, 3 and 1µm Hyprez PSU adhesive polishing pads impregnated with Hyprez diamond lapping compound and finally a 1µm velvet cloth impregnated with Hyprez diamond lapping compound.

The polished samples were then carbon coated using a Edwards E306A carbon coater. A small amount of Agar Scientific Ltd, quick drying silver paint was placed on one edge of the mounted sample and dragged down the side of the sample mount to make a contact between the refractory sample and the copper SEM sample holder, in order that any charge build-up during analysis could be dissipated.

3.5.3 PARTICLE SIZE ANALYSIS

A Link Systems image analysis package, Digiscan, was used in conjunction with the JEOL JXA 840A Scanning Electron Microscope for the particle size analysis. Digiscan was used to classify the features observed according to their cross sectional area and diameter.

Because of the relatively small size of the deoxidation product particles, the SEM was initially focused using a secondary electron image. The typical magnification used was X2000, with an acceleration voltage of 15kV. Once the secondary electron image was focused, the SEM was switched to the backscattered electron image. The image was acquired by Digiscan, the contrast and brightness optimised and displayed on a VDU. The grey level of the deoxidation product was 'thresholded' so when a phase of the same intensity was subsequently encountered by the detector, the area it occupied could be measured and hence the volume fraction of the particles within the sample determined.

The particle size analysis involved examining 30 fields of view on each sample, each field being $40.6\mu\text{m}^2$. The minimum particle size detected was 6 grid points, corresponding to a particle with a diameter of between 0.08 and $0.16\mu\text{m}$, to prevent 'image noise' being registered as features. Each particle was sampled 20 times and averaged to minimise the effect of noise.

The particle size was quantified by obtaining the area of the feature directly from the detection programme. The area is the ratio of the total number of grid units occupied by the particle to the total number of grid units covering the whole field of view, multiplied by area of the field (μm^2). The programme calculates the mean diameter from the total area of each feature, by

assuming the area of the feature is a circle. The programme cannot distinguish between an individual inclusion and a number of inclusions sintered together, it treats both as a single feature. The volume fraction of the inclusions was calculated assuming the features represented a distribution of non-uniformly sized spheres¹⁴⁷.

3.5.4 ENERGY DISPERSIVE X-RAY ANALYSIS

The chemical constitution of individual inclusions and phases in the crucibles used in the deoxidation experiments were determined using a Philips PSEM 500 Electron Microscope incorporating a Link 860 Energy Dispersive X-ray Analyser, EDX.

The EDX analyser directs an electron beam at a specimen. When the electrons strike the specimen, an X-ray spectrum characteristic of the atoms present is produced. Two parameters can be determined from the X-ray spectrum emitted by the specimen:-

1. comparing the specimen spectrum with spectra of individual elements enables the elements present in the specimen to be defined; and
2. the intensity of characteristic X-ray peaks indicates the quantity of the element present, i.e. the concentration.

Most elements produce several strong characteristic X-ray lines. Generally, the most intense lines are designated the K-alpha lines, consisting of the K-alpha 1 and K-alpha 2 lines. These are often so close together that they can not be distinguished from one another. Consequently the K-alpha 'doublet' is most frequently used for analysis. Exceptions arise when analysing elements of high atomic mass with low acceleration voltages, as the energy may not be sufficient to excite any K lines. In these instances the

'L series of lines' may be used. Generally elements have at least one strong X-ray line with an energy less than 10 keV, Table 3.4, and hence there should be no difficulty in analysing for most elements, provided the phase volume being analysed is large enough.

The scale on which micro-analysis can be carried out is limited by the 'Interaction Volume' which is the volume of the specimen penetrated by the electrons and from which X-rays are emitted¹⁴⁸.

The primary electron beam hitting the solid specimen is scattered throughout a pear-shaped region, as illustrated in Figure 3.5, before the electrons have lost so much of their energy that they can no longer excite X-rays. The depth to which the electron beam penetrates into the sample is known as the spatial resolution. The spatial resolution is defined by the following relationship:-

$$d = 0.077 \left(\frac{E_o^{3/2} - E_c^{3/2}}{\rho} \right) \quad (3.1)$$

where:- d = the penetration depth (μm)

E_o = the acceleration voltage (keV)

E_c = the critical excitation energy of the element (keV)

ρ = the density of the solid (g.cm^{-3})

The depths of penetration of electron beams into various solid specimens over range of acceleration voltages are given in Figure 3.6. It can be clearly seen that at high acceleration voltages, the electron beam is able to pass through a small particle composed of low atomic number elements. Thus the resulting particle analysis would be 'contaminated' by the X-rays generated

from the surrounding matrix material. Therefore, depending on the size and the suspected chemical composition of the inclusion, the acceleration voltage used in quantitative micro-analysis needed to be selected with care.

If an acceleration voltage of say 25 keV had been used to analyse a small (< 1µm diameter) alumina inclusions in an iron matrix the electron beam would have penetrated through the inclusions and excited the surrounding matrix material, Figure 3.7. Thus the analysis results may exhibit the presence of iron which may not have originated from the inclusion.

Consequently, it was considered prudent to select an acceleration voltage higher than the critical excitation voltage of manganese (6.45 keV) and iron (7.11 keV), given that some deoxidation products can form by heterogeneous nucleation on a 'liquid Mn-Fe-O' substrate⁵⁵. To detect the presence of iron and manganese an acceleration voltage of at least 8 keV was required. An acceleration voltage of 12 keV was selected for the analysis of the deoxidation products in the steel samples. This gave a spatial resolution of approximately 0.77µm for aluminium in alumina and 0.55µm for titanium in titania, thus in most cases the beam would not penetrate into the matrix material. During analysis the diameter of each inclusion was carefully noted to determine whether any high iron concentrations represented possible contamination by matrix material. If the iron was associated with relatively high manganese concentrations the analysis was considered to reflect the composition of the inclusion. If manganese was absent, the iron was considered to represent iron from the surrounding matrix material.

The Philips PSEM 500 Electron Microscope incorporating a Link 860 EDX

Analyser was standardised using acceleration voltages of both 12 and 25 keV. Standard spectra were obtained from specially prepared and mounted samples of known chemical composition, normally 100% pure elements, although some compounds were used. The spectra were collected for 100 seconds with the spot size being adjusted to maximise the number of counts whilst maintaining the optimum dead time. The information was processed and stored on disc, subsequently the spectra were compared with spectra collected from the analysis of the inclusions, thereby ensuring that the analysed results had a maximum error of $\pm 0.5\%$.

3.5.5 X-RAY ELEMENTAL MAPPING

The elemental distribution at the crucible-melt interface was mapped using a JEOL JXA 840A Scanning Electron Microscope and a Link An 10000 Energy Dispersive X-ray Analyser. Initially a standard spectrum of the full area of interest was obtained by the normal EDX analysis method. The spectrum was subsequently processed by digitally highlighting the K- alpha spectrum lines of the elements under consideration. This information was stored and used as a reference during the subsequent X-ray mapping.

The Acquired Digital Mapping Programme (ADM) was used for data acquisition. The elemental maps were generated from X-ray signals obtained via the EDX detector. The detector analysed 128 X 128 grid points in each area mapped. The information from each grid point was related to the reference spectra and if a corresponding K-alpha spectrum line was detected the presence was registered on the relevant element map.

A Digital Image Processing and Display Programme (DIGIPAD) enabled the elemental maps of the various elements to be processed and viewed. The

processing of the image allowed any background information detected during analysis to be subtracted from the elemental maps. The elemental maps were then formatted and annotated, as required, and photographed.

Scanning Electron micrographs of each area mapped were taken, in order that the morphology and the atomic contrast of the specimens could be compared with the elemental maps.

3.6 OPTICAL MICROSCOPY

The steel samples were mounted and prepared for optical examination by the usual metallographic methods. The samples were ground on 240, 400 and 600 grit wet carborundum paper. The final polishing was carried out on pads impregnated with 6 μ m and 1 μ m Hyprez diamond lapping compound.

Optical examination of selected samples was performed in the unetched condition using a Zeiss Photomicroscope II, which incorporated polarising equipment and a rotary stage.

Chapter 4

Experimental Results

4.1 INTRODUCTION

The results relating to the deoxidation of melts with aluminium, titanium, silicon, calcium-aluminium and zirconium are presented in each of the following sections. The melting techniques are reviewed separately for each deoxidant. The results relating to the interactions taking place at the interface between the deoxidised melts and the crucible are presented in the last section.

4.2 ALUMINIUM DEOXIDISED MELTS.

4.2.1 THE ALUMINIUM VERTICAL TUBE FURNACE MELT

Melt AVT was melted in the vertical tube furnace and deoxidised with a 0.3 mass% aluminium addition when a stable temperature of 1600°C was achieved. The bulk composition of the steel prior to and after melting are given in Tables 4.1.

The total oxygen analysis data, from the samples taken before and at time intervals after the addition of the deoxidant, are given in Table 4.2, and graphically represented in Figure 4.1(a) and 4.1(b). These indicate an initial rapid decrease in the oxygen content of the melt, from a pre-deoxidation concentration of 0.0415 mass%. A stable oxygen content was achieved approximately 200 seconds after deoxidation. The residual oxygen content of the melt was approximately 0.005 mass%.

The number of inclusions measured in each sample are shown in Figure 4.2. These data show a rapid decrease in the number of inclusions measured in the initial 100 seconds after the addition of the deoxidant. The volume fraction of the inclusions measured in each sample is given in Figure 4.3. This information indicates that between 12 and 22 seconds after deoxidation

there was an increase in the inclusion volume fraction. The volume fraction then declined rapidly until approximately 100 seconds after deoxidation, subsequently there was a slower rate of decline.

The size distribution of the inclusions measured in each sample are given in Figures 4.4(a) to 4.4(k). Figure 4.4(a) indicates that the majority of the inclusions measured in the sample, taken 12 seconds after deoxidation were less than $1\mu\text{m}$ in diameter. Table 4.3 shows that the inclusions ranged in size from 0.3 to $1.5\mu\text{m}$ in diameter, with a mean diameter of $0.6\mu\text{m}$. The distribution of inclusion diameter in the sample taken 22 seconds after deoxidation indicates that the bulk of the inclusions were less than $1.5\mu\text{m}$ in diameter, however a small number of larger inclusions were also encountered around $4\mu\text{m}$ in diameter, Figure 4.4(b). Table 4.3 reveals that whilst the mean minimum band diameter remained similar to that observed in the sample taken 12 seconds after deoxidation the mean maximum band diameter had increased to $3.7\mu\text{m}$, and consequently the mean inclusion diameter increased to $0.97\mu\text{m}$. The size ranges of the inclusion diameters are summarised in Table 4.3 and the mean, mean minimum band and mean maximum band diameters are plotted against the time after the addition of the deoxidant in figure 4.5.

After the initial increase in size range from the sample taken 12 seconds to that taken 22 seconds after deoxidation, there is a suggestion of a general decrease in the size range. The mean minimum band diameter remains constant at approximately $0.3\mu\text{m}$ but the mean maximum band diameter decreases. However, the mean inclusion diameter continues to increase with a maximum mean diameter being observed in the sample taken 113 seconds after deoxidation. Thereafter there is a gradual decline in the mean diameter

with the smallest size range and mean diameter of $0.8\mu\text{m}$ being observed in the sample taken 240 seconds after deoxidation. Figures 4.4(c) to 4.4(k) illustrate the general shift in the size distributions of the inclusions.

Selected samples were prepared for microscopical examination and deeply etched so that the morphology of the inclusion contained in the samples could be studied using a scanning electron microscope. The sample taken prior to deoxidation contained an interdendritic distribution of spherical inclusions, Plate 4.1. Electron microprobe analysis revealed that these inclusions were principally composed of FeO, with approximately 8.50 mass% MnO and 3.50 mass% Al_2O_3 . They ranged in size from 0.5 to $1.0\mu\text{m}$ in diameter.

After the addition of the deoxidant, inclusions with different morphologies were observed in the samples. In the sample taken 12 seconds after the addition of the deoxidant, an interdendritic distribution of spherical inclusions, with a size range from 0.5 to $1.0\mu\text{m}$, was observed towards the edge of the sample. Slightly larger spherical inclusions, with a particle size range from 1.0 to $2.0\mu\text{m}$, were observed randomly distributed throughout the sample, Plate 4.2. Spherical inclusions were also seen incorporated into large inclusion clusters, Plate 4.3. Whilst the majority of these inclusions were similar in size to the randomly distributed spherical inclusions, i.e. 1.0 - $2.0\mu\text{m}$, spherical inclusions up to $4\mu\text{m}$ were also periodically observed.

The 12 second sample also contained numerous dendritic inclusions. These varied from large well developed dendrites exhibiting stems and primary, secondary and even tertiary branching, Plate 4.3, to relatively underdeveloped dendrites exhibiting stems and spheroidising primary

branches, Plate 4.4. The stems of well developed dendrites were typically about $1\mu\text{m}$ in cross-section, as were the dendrite branches. However, the points of contact between the stems and the primary branches, and similarly the primary branches and secondary branches, were only about $0.5\mu\text{m}$ in cross-section, Plate 4.3 and 4.4. Associated with the less well-developed dendrite morphologies were globular coralline morphologies. These coralline morphologies appeared to originate from the ends of dendrite stems, as a continuation of the dendritic structure, Plate 4.4. The large surface area of the dendritic and coralline structures appeared to be acting like a net trapping both individual spherical inclusions, Plate 4.4, and clusters of spherical inclusions, Plate 4.3.

Although not numerous, large spherical sintered agglomerates, ($7 - 10\mu\text{m}$ in diameter), Plate 4.4, and polyhedral inclusions, (1.0 to $2.0\mu\text{m}$ in diameter), Plate 4.5, were observed associated with the inclusion clusters, Plate 4.5.

Interdendritic inclusions were not observed after 12 seconds, and as the time after deoxidation progressed less isolated spherical inclusions were observed, virtually none were observed in the sample taken 43 seconds after deoxidation.

Between 20 and 100 seconds after deoxidation there was a steady decrease in the volume fraction of inclusions present, Figure 4.3. The majority of the inclusions observed were contained within clusters. Two main types of clusters were observed:

- firstly, small clusters, approximately $20\mu\text{m}$ across, containing predominantly spherical but also some polyhedral inclusions; and

- secondly, large clusters containing predominantly dendritic and spherical inclusions with a smaller number of polyhedral, coralline and sintered agglomerates, Plate 4.6. These large clusters extended up to 2mm across. In some instances the large clusters appeared to have captured small clusters in the branching dendrite arms, Plate 4.6, thereby increasing the size of the larger clusters.

During the 20 to 100 second period, large sintered aggregates, up to 20 μ m in diameter, Plate 4.7, were observed with increasing frequency. Sintered contacts between the large agglomerates and the coralline morphologies are clearly seen in Plate 4.7. The presence of these morphologies associated with degenerate dendrite forms and coralline morphologies are shown in Plates 4.8 and 4.9. Plate 4.8 clearly shows coralline inclusions exhibiting an interwoven character typical of early stage spheroidisation and formation of the sintered polycrystalline agglomerates. Plate 4.9, shows the further development of this spheroidisation process with a sintered agglomerate exhibiting a relic coralline structure.

Progressive changes in the size and morphology of inclusions within the clusters were observed with time after deoxidation, especially during the initial 200 seconds. These included, the coarsening of dendrite arms, Plate 4.10; the sintering and formation of necks between contacting polyhedral inclusions, Plate 4.11, and between contacting sintered agglomerates and coralline morphologies, Plate 4.7; the spheroidisation and amputation of dendrite branches, Plate 4.12. These changes in inclusion morphology and size are reflected in the increase in the average diameter of the inclusions and the reduction in the size range observed, Figure 4.4.

Between 100 and 200 seconds after deoxidation the volume fraction of the inclusions present decreased steadily, but, at a slower rate than previously experienced, Figure 4.3. During this period there was a change in the morphological constitution and a reduction in the size of the inclusion clusters. Spherical morphologies were virtually absent and fewer, less well developed dendrite forms were observed, Plate 4.13. The major components of the clusters were polyhedral and globular inclusions, the globular inclusions were similar in form to individual components of the coralline morphologies, Plate 4.14.

After 200 seconds, the inclusion clusters were composed exclusively of sintered polyhedral and globular inclusions, and ranged in size between 10 μ m and 20 μ m across. The average size and morphological constitution of the clusters changed little in the following 1200 seconds, Plates 4.15 and 4.16, when sampling was terminated. The disappearance of clusters containing dendritic, spherical or polycrystalline sintered agglomerate morphologies, beyond approximately 200 seconds after deoxidation, corresponded to the time at which a total oxygen content of 0.01 mass% was attained, Figure 4.2(a).

The results of energy dispersive X-ray analysis on a selection of inclusions from each of the samples taken after deoxidation are given in Tables 4.4(a) to 4.4(k). These data indicate that most of the inclusions appeared to be pure alumina within the limits of the analytical method, however, in all specimens at all times isolated inclusions were observed which contained varying amounts of calcia.

4.2.2 THE ALUMINIUM HIGH FREQUENCY FURNACE MELT

Melt AHF was melted in the high frequency furnace and deoxidised with a 0.3 mass% aluminium addition when a stable temperature of 1600°C had been achieved. The bulk composition of the steel charge prior to and after melting are given in Tables 4.1.

The total oxygen analysis data, from the samples taken before and at time intervals after the addition of the deoxidant, are given in Table 4.5 and graphically represented in Figures 4.6(a) and 4.6(b). After the addition of the deoxidant there was a rapid reduction in the total oxygen content of the melt from an initial concentration of 0.038 mass% prior to deoxidation. This rapid decrease continued until a relatively constant oxygen content was achieved approximately 100 seconds after the addition. The residual oxygen content of the melt was 0.002 mass%, which was achieved after 3 minutes and persisted to the end of the experiment at 20 minutes.

The number of inclusions measured in each sample are shown in Figure 4.7. These data show a rapid decrease in the number of inclusions measured in the initial minute after the addition of the deoxidant. The volume fraction of the inclusions measured in each sample is given in Figure 4.8. This indicates a rapid decrease in the volume fraction of the inclusions during this period. The volume fraction then declined at a slower rate.

The size distribution of the inclusions measured in each sample are given in Figures 4.9(a) to 4.9(m). Figure 4.9(a) indicates that approximately 75% of the inclusions measured in the sample taken 3 seconds after deoxidation were less than 1µm in diameter. Table 4.6 shows that the inclusions ranged in size from 0.1 to 2.7µm in diameter, with a mean diameter of 0.6µm. The

distribution of inclusion diameters in the sample taken 11 seconds after deoxidation indicates that the bulk of the inclusions were less than $2.0\mu\text{m}$ in diameter, however a small number of larger inclusions were also encountered, Figure 4.9(b). Table 4.6 reveals that whilst the mean minimum band diameter remained similar to that observed in the sample taken 3 seconds after deoxidation the mean maximum band diameter had increased to $3.2\mu\text{m}$ and consequently the mean inclusion diameter also increased to $0.92\mu\text{m}$. The size ranges of the inclusion diameters measured in the samples analysed are summarised in Figure 4.10, the mean, mean minimum band and mean maximum band diameters are plotted against the time after the addition of the deoxidant. Figure 4.11 shows the mean diameters and the 95% confidence limits for each sample.

Figures 4.10 and 4.11 indicate that there is a steady increase in the mean diameter of the inclusions in the initial 75 seconds after deoxidation, followed by a decrease. Figure 4.11 indicates that the greatest variance in inclusion size distribution is observed in the samples taken between 50 and 150 seconds after deoxidation. The spread in size distribution is further illustrated in Figures 4.9(e) to 4.9(j).

The deeply-etched sample taken prior to deoxidation showed an interdendritic distribution of spherical inclusions, the majority of which were in the size range 0.3 to $1.0\mu\text{m}$, Plate 4.17. Electron microprobe analysis indicated that these inclusions were composed of FeO, with minor quantities of MnO (8.50 mass%) and Al_2O_3 (3.50 mass%).

The sample taken 3 seconds after deoxidation contained numerous inclusion clusters both large and small. The larger clusters generally ranged in size

from 20 to 50 μm across, although clusters over 200 μm were observed. These were composed predominantly of spherical and polyhedral inclusion morphologies, Plate 4.18. The spherical inclusions were typically between 1 and 3 μm in diameter. The polyhedral inclusions exhibited two main crystal habits, octahedral bi-pyramids and fourteen sided polyhedra, with size ranging between 1 and 2 μm . The fourteen sided polyhedra appeared to be formed from the octahedra, as intermediate forms showing the truncation of the corners of the octahedra and presence of small facets at these points were also observed, Plate 4.18. These larger inclusion clusters were typified by the presence of dendritic morphologies, exhibiting stems, around 1 μm in cross-section, and under-developed branches, less than 1 μm in cross-section, Plate 4.19. Some dendrites exhibited thickening and growths between the stems and branches resulting in spear-shaped tips, Plates 4.20 and 4.21.

Small clusters present 3 seconds after deoxidation were around 10 μm across and were composed exclusively of spherical and polyhedral inclusions. These small inclusion clusters and individual inclusions were often observed contacting the arms of dendrites contained within large clusters, thereby increasing the size of the large inclusion clusters, Plates 4.19 and 4.20. Where contacts had been established, necks had formed between the adjacent inclusions, Plates 4.20 and 4.22. A small number of large sintered agglomerates, Plate 4.22, and randomly distributed individual spherical and polyhedral inclusions were also observed.

As the time after deoxidation progressed, both the relative size of the inclusion clusters and the number of primary dendritic inclusions present declined. Primary dendritic inclusions had disappeared and the number of

spherical inclusion had significantly reduced 46 seconds after deoxidation, when the total oxygen content of the melt had fallen below 0.01 mass%, Figure 4.6(a). As the relative proportion of dendritic inclusions decreased the proportion of polyhedral inclusions increased. Forty six seconds after deoxidation the inclusions present were contained in small clusters, approximately 10 μ m across. These clusters were composed of polyhedral and globular inclusions with well developed sintered contacts, Plate 4.23.

Secondary dendrites were observed in the sample taken after 139 seconds, the presence of these inclusions corresponded to a general decrease in the average inclusion diameter, Figure 4.10. The dendrite arms were typically 1 μ m in cross-section with small under-developed branches. Interestingly, the dendrite stems extended from the corners of pre-existing polyhedral inclusions, Plates 4.24 an 4.25.

The results of energy dispersive X-ray analysis on inclusions detected in a number of the samples taken after deoxidation are given in Tables 4.7(a) to 4.7(j). These data indicate that, as in the vertical tube furnace melt, the inclusions were composed predominately of Al₂O₃ and a few isolated inclusions which contained small amounts of calcia.

4.3 TITANIUM DEOXIDISED MELTS

4.3.1 The Titanium Vertical Tube Furnace Melt.

Melt TVT was melted in the vertical tube furnace and deoxidised with a 0.53 mass % titanium addition when a stable temperature of 1600°C was achieved. The bulk composition of the steel charge prior to and after melting is given in Tables 4.1.

The total oxygen analysis data, from the samples taken before and after the addition of the deoxidant are given in Table 4.8 and graphically represented in Figures 4.12(a) and 4.12(b). These data exhibit a rapid initial decrease in the oxygen content of the melt after the addition of the deoxidant from its initial oxygen level of 0.053 mass %. A stable oxygen content was achieved approximately 300 seconds after deoxidation. The residual oxygen content of the melt was 0.005 to 0.006 mass %.

The number of inclusions measured in each sample are shown in Figure 4.13. These data show an initial increase in the number of inclusions observed in the first 58 seconds after the addition of the deoxidant. This was followed by a rapid decrease to a minima at 100 seconds followed by a steady rise to the end of the experiment. The volume fraction of the inclusions measured in each sample analysed are shown in Figure 4.14. The volume fraction declined steadily throughout the experiment.

The size distribution of the inclusions measured in each sample analysed are given in Figures 4.15(a) to 4.15(i). Figure 4.15(a) indicates that there was a wide range in the size distribution of the inclusions measured in the sample taken 34 seconds after deoxidation. Table 4.9 shows that the inclusions ranged in size from 0.3 to 3.8 μm in diameter, with a mean diameter of 1.6 μm . The distribution of inclusion diameters in the sample taken 45 seconds after deoxidation indicates that a large proportion of the inclusions measured were less than 0.5 μm in diameter, however inclusions were observed up to 4.0 μm in diameter, Figure 4.15(b). Table 4.9 reveals that both the minimum and maximum inclusion diameters remained similar to those observed in the sample taken 34 seconds after deoxidation. However, the larger number of smaller inclusion diameters observed had the effect of

decreasing the mean inclusion diameter to $1.3\mu\text{m}$. The analysis of the samples taken 58 and 85 seconds after deoxidation showed a progressive increase in the mean inclusion diameter, Table 4.9. However the size distributions of the inclusions in these samples were similar to those observed in the sample taken 34 seconds after deoxidation, Figures 4.15(a)(c)(d). The samples taken at 100 seconds and beyond showed a steady decline in the mean inclusion diameter, Table 4.9, and generally a reduction in the size distribution, Figures 4.15(e) to 4.15(i). Figure 4.16 shows the mean, mean minimum and mean maximum band diameters plotted against the time after deoxidation and shows an increase in the mean diameter during the initial 85 seconds after deoxidation followed by a steady decrease, although there is a suggestion that the size increases marginally after 156 seconds.

Selected samples were prepared for microscopical examination and deeply etched so that the morphology of the inclusions could be studied using a scanning electron microscope. The sample taken prior to deoxidation contained an interdendritic distribution of spherical inclusions, Plate 4.26. Energy dispersive X-ray analysis of the interdendritic inclusions indicated that they were principally composed of FeO, with approximately 8.50 mass% MnO, and 3.50 mass% Al_2O_3 . They ranged in size from about $0.3\mu\text{m}$ to $0.9\mu\text{m}$ in diameter, and were considerably smaller than those subsequently observed. After the addition of the deoxidant several different morphological inclusion types were observed in the samples. In the sample taken 34 seconds after the addition of the deoxidant, corresponding to a total oxygen content of 0.045 mass%, globular and polyhedral inclusion morphologies were observed, together with agglomeration of the two. These agglomerations of particles ranged in size from about $5\mu\text{m}$ to over $10\mu\text{m}$.

The large agglomerating inclusions exhibited lines of surface discontinuity and the presence of smaller morphologies in the process of being adsorbed into their larger surface, Plate 4.27.

The polymorphic nature of these inclusion agglomerates is illustrated in Plate 4.28. This shows a plane polished section through the sample and clearly displays inclusions exhibiting pleochroism confirming that the agglomerates were polymorphic. The inclusions observed in plane section also exhibit porosity, Plate 4.28, this can also be observed on the surface of some inclusions in the etched state, Plate 4.27. Necks formed between adjacent agglomerating inclusions are also observed, Plate 4.28.

Plates 4.27 and 4.29 also show the presence of polyhedral inclusions, including octahedra and other more highly faceted morphologies. These were observed as both discrete particles and as complex agglomerating and spherodising clusters.

The sample taken 58 seconds after deoxidation exhibited groups of globular and polyhedral inclusions together with agglomerates forming complex clusters, Plate 4.30. The polyhedral inclusions observed in this sample were highly faceted and one such inclusion is seen exhibiting a porosity exit hole on the inclusion surface. The formation of a neck between adjacent globular inclusions was also observed. The sample taken 100 seconds after deoxidation, corresponding to a total oxygen content of the melt of 0.015 mass%, shows an inclusion cluster exhibiting highly developed sintered contacts between adjacent inclusions, Plate 4.31.

Colour optical micrographs of selected samples in plane section indicated

that the titanium bearing inclusions were composed of the phase Ti_2O_3 . The phase Ti_2O_3 exhibits chocolate brown to blue-gray pleochroism when viewed under cross-polarised light, Plate 4.28.

The energy dispersive X-ray analysis of the titanium bearing inclusions in selected samples are given in Table 4.10(a) to 4.10(j). These data indicate that the inclusions appeared to be principally composed of titanium oxide, however, in all specimens at all times isolated inclusions were observed which contained varying amounts of calcia.

4.3.2 The Titanium High Frequency Furnace Melt

Melt THF was melted in the high frequency furnace and deoxidised with a 0.53 mass% titanium addition when a stable temperature of 1600°C was achieved. The bulk composition of the steel charge prior to melting is given in Tables 4.1.

The total oxygen analysis data, from samples taken before and after the addition of the deoxidant are given in Table 4.11 and graphically depicted in Figures 4.17(a) and 4.17(b). After the addition of the deoxidant there was a rapid reduction in the total oxygen content of the melt from the pre-deoxidation concentration of 0.084 mass%, Table 4.11, Figure 4.19(a). A reasonably constant total oxygen content was achieved approximately 200 seconds after deoxidation with a residual oxygen content of approximately 0.0030 mass%, 20 minutes after deoxidation.

The number of inclusions measured in each sample are shown in Figure 4.20. These data show an initial increase in the number of inclusions observed in the first 33 seconds after the addition of the deoxidant. This was

followed by a rapid decrease to constant level 50 to 60 seconds after deoxidation. The volume fraction of the inclusions measured in each sample analysed are given in Figure 4.19. These data indicate that there was an increase in volume fraction in the first 24 seconds after deoxidation. The volume fraction then declined rapidly until approximately 50 seconds after deoxidation, thereafter, the volume fraction declined slowly.

The size distribution of the inclusions measured in each sample analysed are given in Figures 4.20(a) to 4.20(i). Figure 4.20(a) indicates that there was a wide range in the size distribution of the inclusions measured in the sample taken 3 seconds after deoxidation. Table 4.12 shows that the inclusions ranged in size from 0.1 to 5.0 μm in diameter, with a mean diameter of 0.8 μm . The distribution of inclusion diameters in the sample taken 7 seconds after deoxidation shows a similar wide range in the size distribution, and there was an increase in the proportion of the inclusions greater than 1 μm in diameter, Figure 4.20(b). Table 4.12 reveals that the mean minimum band diameter remained similar to that observed in the sample taken 3 seconds after deoxidation, but the mean maximum band diameter had decreased. However, there was larger proportion of inclusion diameters greater than 1 μm , which had the effect of increasing the mean inclusion diameter to 1.2 μm . The size distribution analysis of the samples taken 11 and 24 seconds after deoxidation showed a progressive increase in the mean and mean maximum band inclusion diameters, Table 4.12. Figures 4.20(c) and 4.20(d) indicate that there was a wide range in the size distributions of the inclusions analysed in these samples. The samples taken after 33 seconds after deoxidation exhibited a marked reduction in the mean inclusion diameter, Table 4.12. Figures 4.20(e) to 4.20(i) reveal a progressive decrease in the size distributions and a measured increase in the proportion

of inclusion diameters less than $1\mu\text{m}$. Figure 4.21 shows the mean, mean minimum and mean maximum band diameters plotted against the time after deoxidation, this clearly shows an increase in the mean diameter in the initial 24 seconds after deoxidation followed by a decrease to a comparatively constant size. Also indicated is the definite increase in the size distributions in the initial 24 seconds after deoxidation followed by a relatively uniform distribution. This is confirmed by Figure 4.22 which shows the 95% confidence limits for the mean inclusion diameters plotted against time after deoxidation. This suggests a reduction in the size range 24 seconds after deoxidation.

The deeply etched sample taken prior to deoxidation showed an interdendritic distribution of spherical inclusions similar to those shown in Plate 4.26. Energy dispersive X-ray analysis of the interdendritic inclusions indicated that they were principally composed of FeO, with approximately 8.50 mass% MnO, and 3.50 mass% Al_2O_3 . Small randomly distributed inclusions were observed in the sample taken 3 seconds after deoxidation, Plate 4.32, these were generally less than $1\mu\text{m}$ in diameter. Also observed in the sample taken 3 seconds after deoxidation were a number of other inclusion morphologies including both polyhedral and spherical morphologies forming inclusion clusters, Plate 4.33. The polyhedral inclusions examined were mainly between 1.5 and $3\mu\text{m}$ in diameter. Generally, the spherical morphologies were larger, ranging from 1.5 to over $10\mu\text{m}$ in diameter, with even the small spherical inclusions exhibiting surface porosity. Plate 4.33 also displays an inclusion which represents an intermediate stage in the formation of the large spherical morphologies. This example clearly shows that these inclusions develop from agglomerates of inclusions and exhibit the presence of a characteristic porosity vent on the inclusion surface, the

porosity is clearly visible in plane section, Plate 4.34. Fully developed large spherical morphologies, the development of sintered contacts between adjacent inclusions and various stages in the assimilation of smaller inclusions into larger spherical agglomerates are also observed, Plate 4.33. This phenomena is clearly illustrated in Plate 4.35, where a number of polyhedral and spherical inclusions are in various stages of being absorbed into a large sub-spherical agglomerate.

Colour optical micrographs obtained indicated that the titanium bearing inclusions were composed of the phase Ti_2O_3 , Plate 2.34.

The energy dispersive X-ray analysis of the titanium bearing inclusions in selected samples are given in Table 4.13(a) to 4.13(m). These data indicate that the inclusions were principally composed of Ti_2O_3 , with a few isolated inclusions containing small amounts of calcia.

4.4 SILICON DEOXIDISED MELTS

4.4.1 THE SILICON VERTICAL TUBE FURNACE MELT

Melt SVT was melted in the vertical tube furnace and deoxidised with a 0.3 mass% silicon addition when a stable temperature of 1600°C had been achieved. The bulk composition of the steel charge prior to and after melting are given in Tables 4.1.

The total oxygen analysis data, from the samples taken before and after deoxidation are given in Table 4.14 and graphically depicted in Figures 4.23(a) and 4.23(b). These data display a steady, relatively uniform decrease in the oxygen content of the melt. The residual oxygen content of the melt 20 minutes after deoxidation was approximately 0.006 mass%.

The number of inclusions measured in each sample are given in Figure 4.24. These data show a steady decrease in the number of inclusions encountered in the first 128 seconds after the addition of the deoxidant. However, the sample taken 151 seconds after deoxidation showed a marked increase in the number of inclusions observed. The subsequent samples analysed showed a slow but steady decline in the number of inclusions detected. The volume fraction of the inclusions measured in each of the samples are given in Figure 4.25. This information indicates that there was a marked decrease in the initial 150 seconds after deoxidation which was followed by a slower rate of decline. This was despite the increase in the number of inclusions observed in the sample taken 151 seconds after deoxidation.

The size distribution of the inclusions measured in each sample analysed are given in Figures 4.26(a) to 4.26(j). Figures 4.26(a) to 4.26(e) indicate that there were a wide range of size distributions in the first 82 seconds after deoxidation. Table 4.1 shows that the minimum inclusion diameters detected during this period were between 0.3 and 0.7 μm and the maximum diameters ranged between 3.7 and 6.1 μm . The mean inclusion diameters showed a slight increase during this period, peaking at 2.1 μm in the sample taken 64 seconds after deoxidation, Figure 4.27. Figures 4.26(f) to 4.26(j) show that there was an increase in the proportion of inclusions less than 1 μm , however the size range of the inclusion diameters measured remained similar to those detected previously, Figure 4.27.

Selected samples were prepared for microscopical examination and deeply etched in order that the morphology of the inclusions could be studied using a scanning electron microscope. The sample taken prior to deoxidation

contained a typical interdendritic distribution of spherical inclusions, Plate 4.36. Energy dispersive X-ray analysis of these inclusions revealed that they were composed primarily of FeO, with minor quantities of MnO (8.50 mass%) and Al₂O₃ (3.50 mass%). The inclusions ranged in size from approximately 0.3μm to 0.9μm in diameter, and were generally smaller than those subsequently observed.

After the addition of the deoxidant the dominant inclusion type observed was of a spherical morphology and was in all the samples examined. The sample taken 24 seconds after the addition of the deoxidant, containing 0.054 mass% oxygen, exhibits the spherical inclusions, Plate 4.37. These inclusions ranged in size from 0.6μm to 3μm, and were distributed throughout the sample either in isolation or forming small groups up to 10 inclusions. Also evident was the formation of necks and sintered contacts between inclusions which had collided. A similar structure is illustrated in the 53 second sample, Plate 4.38.

High magnification electron micrographs of the sample taken 128 seconds after deoxidation revealed the presence of secondary dendritic growths emanating from the surface of the spherical inclusions, Plate 4.39. The dendrite arms and branches typically having a cross section of 0.2μm.

Energy dispersive X-ray analysis of the silicon bearing inclusions in selected samples are given in Tables 4.16(a) to 4.16(k). These were all highly siliceous but exhibited significant but variable levels of FeO and MnO. The level of iron and manganese oxides detected in the inclusions was significantly less after samples 53 seconds than those earlier, Figures 4.16(d) to 4.16(k). As in previous experiments calcia was occasionally

present in isolated individual inclusions. The final sample taken 1200 seconds after deoxidation was unusual in that all inclusions examined exhibited significant calcia and alumina contents, Table 4.16(k).

4.4.2 THE SILICON HIGH FREQUENCY FURNACE MELT

Melt SHF was melted in the high frequency furnace and deoxidised with a 0.3 mass% silicon addition when a stable temperature of 1600°C had been achieved. The bulk composition of the steel charge prior to and after melting are given in Tables 4.1.

The total oxygen analysis data, from the samples taken before and after deoxidation are given in Table 4.17 and graphically depicted in Figures 4.28(a) and 4.28(b). These data indicate a rapid decrease in the total oxygen content of the melt, from a pre-deoxidation concentration of 0.0545 mass%, in the initial 22 minutes after deoxidation. Subsequently the oxygen concentration decrease at a slower rate. The residual oxygen content of the melt taken as the concentration 20 minutes after deoxidation was approximately 0.005 mass%.

The number of inclusions measured in each sample are given in Figure 4.29. These data shows a rapid decrease in the number of inclusions encountered in the first 40 - 50 seconds after the addition of the deoxidant. During the following 200 seconds a relatively constant number of inclusions were detected. The volume fraction of the inclusions measured in each of the samples are given in Figure 4.30. This information indicates that there was a marked decrease in the initial 50 seconds after deoxidation, this was followed by a slower rate of decline.

The size distribution of the inclusions measured in each sample analysed are given in Figures 4.31(a) to 4.31(j). Figure 4.31(a) indicates that there was a wide range in the size distribution of the inclusion diameters measured in the first sample taken 1 second after deoxidation. Table 4.18 shows that the mean minimum band inclusion diameter detected was $0.3\mu\text{m}$, the mean maximum band diameter $4.7\mu\text{m}$ and the mean inclusion diameter $1.5\mu\text{m}$. During the following 90 seconds there was a slight decrease in the size distributions of the inclusions measured, Figures 4.31(b) to 4.31(g). The mean minimum band and mean inclusion diameters remained constant at $0.3\text{-}0.4\mu\text{m}$ and $1.1\text{-}1.2\mu\text{m}$ respectively. However, the mean maximum band diameter ranged between 1.6 and $4.2\mu\text{m}$ during this period. Figures 4.31(h) to 4.31(j) shows that between 150 and 245 seconds after deoxidation there was a marked increase in the proportion of inclusions less than $0.5\mu\text{m}$, and a reduction in the size range of the inclusion diameters measured. The variation in the size distribution and the mean inclusion diameters for the samples analysed are summarised in Figure 4.32.

Selected samples were prepared for microscopical examination and deeply etched in order that the morphology of the inclusions could be studied using a scanning electron microscope. The sample taken prior to deoxidation contained a typical interdendritic distribution of spherical inclusions. Energy dispersive X-ray analysis of these inclusions revealed that they were composed primarily of FeO, with minor quantities of MnO (8.50 mass%) and Al_2O_3 (3.50 mass%). The sample taken 1 second after deoxidation contained spherical inclusions ranging in diameter from 0.6 to $2\mu\text{m}$, Plate 4.40. These were observed as either individual inclusions or small groups. A number of the small groups exhibited sintered contacts and the formation of necks between adjacent inclusions. The sample taken 37 seconds after

deoxidation showed a similar pattern, but a reduced number of small groups and individual inclusions. The size range of these inclusions was narrower than those previously observed, the diameters ranged from 1 to 2 μ m, Plate 4.41. Spherical inclusions exhibiting possible secondary dendritic growth were observed in a sample taken 28 seconds after deoxidation, Plate 4.42. These network growths are observed emanating from the surface of the spherical morphologies.

Energy dispersive X-ray analysis of the silicon bearing inclusions in selected samples are given in Tables 4.19(a) to 4.19(e). These data indicate that the inclusions present were composed primarily of SiO₂ with varying amounts of CaO, Al₂O₃, FeO and MnO. The results indicated that there was a progressive increase in the CaO and Al₂O₃ and decrease in the SiO₂ content of the inclusions with time after deoxidation, Figure 4.33.

4.5 CALCIUM-ALUMINIUM DEOXIDISED MELTS.

4.5.1 THE CALCIUM-ALUMINIUM VERTICAL TUBE FURNACE MELT

Melt CAVT was melted in the vertical tube furnace and deoxidised with a 0.32 mass% calcium-aluminium addition when a stable temperature of 1600°C had been achieved. The bulk compositions of the steel charge prior to and after melting are given in Tables 4.1.

The total oxygen analysis data, from the samples taken before and at time intervals after deoxidation are given in Table 4.20 and graphically represented in Figures 4.34(a) and 4.34(b). The results exhibit a rapid initial decrease in the total oxygen content of the melt, from a pre-deoxidation concentration of 0.045 mass%. A stable oxygen content was achieved approximately 200-250 seconds after deoxidation. The residual oxygen

content of the melt taken as the concentration 20 minutes after deoxidation was approximately 0.007 mass%.

4.5.2 THE CALCIUM-ALUMINIUM HIGH FREQUENCY FURNACE MELT

Melt CAHF was melted in the high frequency furnace and deoxidised with a 0.32 mass% calcium-aluminium addition when a stable temperature of 1600°C had been achieved. The bulk compositions of the steel charge prior to and after melting are given in Tables 4.1.

The total oxygen analysis data, from the samples taken before and at time intervals after deoxidation are given in Table 4.21 and graphically represented in Figures 4.35(a) and 4.35(b). The results exhibit a rapid initial decrease in the total oxygen content of the melt, from a pre-deoxidation concentration of 0.0565 mass%. A fairly constant oxygen content was achieved approximately 200 seconds after deoxidation. The residual oxygen content of the melt taken as the concentration 20 minutes after deoxidation was 0.0023 mass%.

The number of inclusions measured in each sample are shown in Figure 4.36. These data show a rapid decrease in the number of inclusions measured in the initial 50 seconds after deoxidation. The volume fractions of the inclusions measured in each sample are given Figure 4.37. This information indicates a steady decrease in the volume fraction in the first 150 seconds after deoxidation. This is then followed by a much slower rate of decline.

The size distribution of the inclusions measured in each sample are given in Figures 4.38(a) to 4.38(i). Figures 4.38(a) to 4.38(e) indicate a size range up

to 4 μm during the initial 83 seconds, with a progressive increase in the proportion of larger inclusions with time. Table 4.22 shows that during this period the inclusions measured exhibited a mean maximum band diameter of between 3.0 and 3.8 μm , a mean minimum band diameter of between 0.28 and 0.34 μm and a mean diameter of between 0.84 and 1.44 μm . The samples taken after 111 seconds after deoxidation exhibited a smaller inclusion size range, Figures 4.38(f) to 4.38(i), with the bulk of the inclusions being less than 2 μm in diameter. The size ranges of the inclusion diameter measured are summarised in Figure 4.39, with the mean, mean minimum and mean maximum band inclusion diameters being plotted against time after the addition of the deoxidant.

Selected samples were prepared for microscopical examination and deeply etched so that the morphology of the inclusions contained in the sample could be studied using a scanning electron microscope. The sample taken prior to deoxidation contained an interdendritic distribution of spherical inclusions. Energy dispersive X-ray analysis of these indicated that they were composed of FeO, with between 6 and 12 mass% MnO and 2 and 7 mass% Al₂O₃.

In general, two dominant inclusion types were observed, small (2-3 μm diameter), polyhedral inclusions and large globular inclusions, composed of numerous smaller ones, Plates 4.43 and 4.44. The polyhedral inclusions appeared to have hexagonal symmetry, Plate 4.43. Some of the polyhedral inclusions appeared as hexagonal plates which as they became accreted took on a stepped appearance before evolving into the more usual globular morphology, Plate 4.46. Some large spherical inclusions exhibited characteristic surface porosity holes, Plate 4.46. At the contact points

between individual inclusions sintered necks had developed, Plate 4.47.

Dendritic inclusions were also occasionally observed in association with the inclusion clusters.

The energy dispersive X-ray analysis of the inclusions from selected sample are given in Tables 4.23(a) to 4.23(d), which indicate that there was a range of calcia-alumina ratios present. The compositions of the inclusions analysed are superimposed on the liquidus line of the CaO-Al₂O₃ phase diagram, Figure 4.40. This indicates that whilst many inclusions were solid a large proportion of them would have been liquid at 1600°C.

Further energy dispersive X-ray analysis of inclusions in the etched state, using an analysis technique to correct for the non-planar surfaces of the inclusions are given in Plates 4.43 and 4.44. The hexagonal inclusion analysed appeared to have a relatively constant rationalised chemical composition of 10 mass% CaO and 90 mass% Al₂O₃, which is indicated by an arrow on Figure 4.40, this appears to correspond to the stoichiometric compound CaO.6Al₂O₃.

4.6 ZIRCONIUM DEOXIDISED MELTS

4.6.1 THE ZIRCONIUM VERTICAL TUBE MELT

Melt ZVT was melted in the vertical tube furnace and deoxidised with a 1.01 mass% zirconium addition when a stable temperature of 1600°C had been achieved. The bulk compositions of the steel charge prior to and after melting are given in Tables 4.1.

The total oxygen analysis data, from samples taken before and after deoxidation, are given in Table 4.24 and graphically depicted in

Figure 4.41(a) and 4.41(b). The results indicate that there was an initial rise in the oxygen content of the melt from a pre-deoxidation concentration of 0.0395 mass% to 0.0476 mass% one second after the addition of the deoxidant. There then followed a steady decrease in the total oxygen content of the melt. Samples taken 100 seconds after deoxidation indicated a slower rate of deoxidation. However the oxygen content of the melt still appeared to be decreasing 1200 seconds after the addition of the deoxidant. The final oxygen level was 0.016 mass%.

Selected samples were prepared for microscopical examination and deeply etched so that the morphology of the inclusions could be studied using a scanning electron microscope. An interdendritic network of spherical morphologies was observed in the sample taken prior to deoxidation, Plate 4.48. Energy dispersive X-ray analysis of these inclusions indicated that they were primarily composed of FeO, with minor amounts of MnO (8.5 mass%) and Al₂O₃ (3.50 mass%).

Examination of the samples taken after deoxidation indicated the presence of Dendritic morphologies with branches formed at right angles to the main dendrite arm. This suggested that the zirconium bearing inclusions had a cubic crystalline habit, Plate 4.49. Dumb-bell shaped inclusion morphologies were also observed which again appeared to have a cubic symmetry, Plate 4.50.

4.6.2 THE ZIRCONIUM HIGH FREQUENCY FURNACE MELT

Melt ZHF was melted in the high frequency furnace and deoxidised with a 1.01 mass% zirconium addition when a stable temperature of 1600°C had been achieved. The bulk compositions of the steel charge prior to and after

melting are given in Tables 4.1.

The total oxygen analysis data, from samples taken before and after deoxidation, Table 4.25 and graphically illustrated in Figure 4:42(a) and 4.42(b). The results indicate that there was an initial rise in the oxygen content of the melt from the pre-deoxidation concentration of 0.0575 mass% to 0.0635 mass% 10 seconds after the addition of the deoxidant. There then followed a rapid initial decrease in the total oxygen content of the melt, with a stable total oxygen content being obtained 300 seconds after deoxidation. The residual oxygen content of the melt taken as the concentration 20 minutes after deoxidation was between 0.004 and 0.005 mass%.

4.7 CRUCIBLE-MELT INTERACTIONS

4.7.1 THE ORIGINAL CRUCIBLE MATERIAL

Plates 4.51 and 4.52 shows scanning electron microscope images of a section through a sample of the original crucible material which had been annealed at 1600°C and slowly cooled to room temperature. Energy dispersive X-ray point (EDX) analysis of the phases in Plates 4.51 and 4.52 showed that the original crucible material consisted of periclase(MgO), point C, Plate 4.51(a) and point D, Plate 4.52(a), the silicates monticellite (CaO.MgO.SiO₂), point A, Plate 4.51(a) and points C and E, Plate 4.52(a) and merwinite (3CaO.MgO.2SiO₂), point B, Plates 4.51(a) and 4.52(a) and spinel (MgO.Al₂O₃), point D, Plate 4.51(a) and point A, Plate 4.52(a).

Energy dispersive X-ray maps showing the distribution and relative abundance of the elements magnesium, aluminium, silicon, calcium and iron are given in Plates 4.51(b) and 4.52(b). These indicate that the original crucible material was mainly composed of periclase grains in a matrix

predominantly composed of monticellite and merwinite with minor amounts of spinel.

4.7.2 THE CRUCIBLE INTERFACES IN CONTACT WITH UNDEOXIDISED STEEL

Scanning electron microscope images of sections through samples of crucible material which had been in contact with undeoxidised steel at 1600°C, indicated that similar structures were observed irrespective of the melting technique employed, Plates 4.53 to 4.56. The energy dispersive X-ray analysis showed that periclase grains (MgO), indicated by points A and B in Plates 4.53(a) and 4.54(a), point B and C, Plate 4.55(a) and point C, Plate 4.56(a) had absorbed quantities of FeO and MnO during the experiment. The concentration of these oxides was highest close to the crucible-melt interface and decreased with distance from the interface, Plates 4.53(b) to 4.56(b). The silicate phase, monticellite (CaO.MgO.SiO_2), indicated by point C in Plates 4.53(a) and 4.54(a), and observed in the areal elemental maps, Plates 4.53(b) to 4.56(b), had also absorbed some FeO and MnO diluting the MgO component of the phase. Similarly, the silicate phase, merwinite (3CaO.MgO.2SiO_2), indicated by point B in Plate 4.56(a), and Plates 4.53(b) to 4.56(b) and the spinel phase ($\text{MgO.Al}_2\text{O}_3$), indicated by point A in Plates 4.55(a) and 4.56(a), and Plates 4.53(b) to 4.56(b) had also absorbed some FeO and MnO.

4.7.3 THE CRUCIBLE INTERFACE IN CONTACT WITH THE ALUMINIUM DEOXIDISED STEEL

Scanning electron microscope images of sections through crucible material which had been in contact with aluminium deoxidised steel, at 1600°C, indicated the presence of similar structures irrespective of the melting technique used, Plates 4.57 to 4.60. EDX analysis, point A, Plate 4.57(a),

points B and E, Plate 4.58(a), points B, D and F, Plate 4.59(a) and point E Plate 4.60(a), indicated that the composition of the periclase (MgO) had not varied significantly other than a minor increase in the Al_2O_3 content and the absorption of varying quantities of FeO during the experiment. A calcium aluminate phase was observed, indicated by points C and D, Plate 4.57(a), points A, C, D and F Plate 4.58(a) and point C, plate 4.59(a), the origin of which is not immediately obvious, but may be the result of aluminium reducing the SiO_2 in the pre-existing silicate phases. The alumina, Plates 4.57(b) to 4.60(b) appears to have penetrated an estimated 1.5 mm into the crucible wall via the silicate matrix. Spinel ($\text{MgO}.\text{Al}_2\text{O}_3$), indicated by point B, Plate 4.57(a), points A and E, Plate 4.59(a) and points B, C and D, Plate 4.60(a) was also present. Spinel appeared to be more widespread, Plates 4.57(b) to 4.60(b) than previously observed in the original crucible material. Small amounts of a siliceous phase approximating to di-calcium silicate, ($2\text{CaO}.\text{SiO}_2$), but containing 11 mass% FeO was also observed, point A, Plate 5.60(a).

4.7.4 THE CRUCIBLE INTERFACE IN CONTACT WITH THE TITANIUM DEOXIDISED STEEL

Scanning electron microscope images and EDX elemental maps of sections through crucible material which had been in contact with titanium deoxidised steel, at 1600°C , are given in Plates 4.61 to 4.63. These indicated the presence of similar structures and phase compositions irrespective of the melting technique employed. The periclase phase (MgO), indicated by points C, D, E and F Plate 4.61(a) and point B, Plate 4.63(a), had absorbed quantities of titanium, aluminium and iron oxides during the experiment. The areas indicated by points A and B, Plate 4.61(a), points A and D, Plate 4.62(a) and points A and C, Plates 4.63(a), were composed of a phase

comprising of titanium oxide and lime. This was associated with the silicate phase protoenstatite ($\text{MgO} \cdot \text{SiO}_2$), indicated by point B, Plate 4.62(a) and point D, 4.63(b). A eutectic relationship between the titanium oxide and lime phase and protoenstatite was observed in Plates 4.61(a)(b) to 4.63(a)(b).

4.7.5 THE CRUCIBLE INTERFACE IN CONTACT WITH THE SILICON DEOXIDISED STEEL

Scanning electron microscope images of sections through samples of crucible material which had been in contact with silicon deoxidised steel, at 1600°C , are shown in Plates 4.64(a) to 4.66(a). EDX analysis of the periclase phase (MgO), indicated by point C, Plate 4.64(a), points D and F, Plate 4.65(a) and points C, Plate 4.66(a) showed that quantities of Al_2O_3 , FeO and MnO had been absorbed during the experiment. A magnesium silicate phase indicated by point A, Plate 4.64(a), points A, B, C and E, Plate 4.65(a) and point B, Plate 4.66(a) was composed of SiO_2 and MgO . This phase also contained minor quantities of CaO , FeO and MnO . A silicate phase approximating to monticellite was observed, point A, Plate 4.66(a), this also contained minor quantities of FeO and MnO . Also observed was a silicate phase containing MgO and Al_2O_3 , with minor quantities of CaO , FeO and MnO , point D, Plate 4.64(a). Plates 4.64(b) to 4.66(b) indicated a higher concentration of silica at the crucible-melt interface than observed in the original crucible material.

4.7.6 THE CRUCIBLE INTERFACE IN CONTACT WITH THE CALCIUM-ALUMINIUM DEOXIDISED STEEL

Scanning electron microscope images of sections through samples of crucible material which had been in contact with calcium-aluminium deoxidised steel, at 1600°C , are shown in Plate 4.67(a) and 4.68(a). These

indicated a similar structure irrespective of the melting technique used. EDX analysis of a calcium silicate phase, point B, Plate 4.67(a), the composition of which was approaching that of di-calcium silicate with other minor components. Silicate phases approximating to the compositions of monticellite and merwinite were observed at points A and B, Plate 4.68(a). A higher concentration of these silicate phases were observed compared with the original crucible material. Spinel, indicated by point A, Plate 4.67(a) and point C, Plate 4.68(a) was also observed.

4.7.7 THE CRUCIBLE INTERFACE IN CONTACT WITH THE ZIRCONIUM DEOXIDISED STEEL

Scanning electron microscope images of sections through samples of crucible material which had been in contact with zirconium deoxidised steel, at 1600°C, are shown in Plate 4.69(a) and 4.70(a). These indicated the presence of similar structure irrespective of the melting technique used. EDX analysis indicated that the periclase (MgO), point D, Plate 4.69(a) and point D, Plate 4.70(a) had absorbed small quantities of ZrO₂ and FeO during the experiment. The silicate phase derived from the pre-existing monticellite phase (CaO.MgO.SiO₂), point C, Plate 4.69(a), contained small quantities of Al₂O₃ and ZrO₂. A phase derived from spinel (MgO.Al₂O₃), point B, Plate 4.69(a), was observed which contained small quantities of ZrO₂. At the crucible-melt interface particles of a phase composed mainly of ZrO₂ with minor amounts of CaO, MgO and SiO₂ embedded in the silicate phase, point A, Plate 4.69(a) and point A, B and C, Plate 4.70(a). The distribution of the zirconium oxide particles within the silicate matrix at the crucible-melt interface is evident in Plates 4.69(b) and 4.70(b).

5.1 EXPERIMENTAL PROCEDURES

5.1.1 MELTING EQUIPMENT AND PROCEDURES

The experimental melting techniques were employed in an attempt to simulate and investigate the processes which might take place during steelmaking. However, limitations are present when endeavouring to reproduce large scale industrial melting practice in a laboratory environment. The experimental melts were considerably smaller than the tonnages regularly melted in industrial practice. Consequently, the diffusion distances and velocity rise experienced in the laboratory melts would have been substantially smaller than those in industrial furnaces. The dimensions of the crucibles used would have provided a far larger surface area to volume ratio, affording greater opportunity for reaction between the constituents of the melt and the containing crucible. In all experiments a sintered magnesia based crucible, in which the principal secondary phases were calcium-magnesium silicates, was employed. Evidence for the extent of the interaction between the crucible and the melt is provided by the presence of small variable levels of calcium oxide in the inclusions produced from non-calcium containing deoxidants. The presence of calcium oxide in these inclusions can only be derived from the low melting point calcium-magnesium silicate phases present in the refractory. The proximity of the crucible walls would have enhanced the opportunity for the capture of inclusions from the bulk melt.

The melting techniques provided essentially two types of stirring regime: a nominally quiescent melt; and an inductively stirred melt. These provided variations in the turbulence experienced by the melts, but did not reproduce the stirring regimes which would take place during large scale melting and indeed such conditions would be difficult to quantify and attain.

There were variations in the heating and cooling cycles experienced during the experiments depending on the furnace used. The platinum/platinum-rhodium thermocouples used give reproducible results. Temperature variations during deoxidation and the sampling procedures is inevitable due to the relatively small mass of molten metal. This was exacerbated in the case of the high frequency furnace melts by the need to switch off the power during sampling, although every effort was made to minimise the time taken. Whilst the fluctuations in temperature may have affected the thermodynamics and kinetics of the deoxidation processes, by adopting a consistent approach to sampling these errors were kept to a minimum.

5.1.2 METALLOGRAPHY

The samples taken from the melt were used to give an indication of the conditions prevailing in the melt at a particular point in time. However, since the samples examined had solidified they could not give a precise indication of conditions in the melt. Nevertheless, careful interpretation of these samples should give an indication of the morphology, chemical composition and distribution of the deoxidation products which existed in the melt at high temperature.

The samples represent a three dimensional arrangement of essentially irregular particles with in a steel matrix, which has implications on the analytical techniques used and the validity of the results. The analysis of the morphology and size of the inclusions was in two stages:-

1. Two-dimensional particle size analysis of a planar section through the samples. Because of the size of the inclusions was near the limit of resolution of optical microscopy, scanning electron microscopy was used. The scanning electron microscope provides accurate measurement of

size at the magnifications used, however, the statistical accuracy of measurement was limited by the low numbers and the small size of the inclusions, and practical time limitations. The nature of the planar section precluded a true interpretation of the size of complex shaped inclusions, often with gross under estimation of the size of complex shaped inclusions and inclusion agglomerates.

2. The three-dimensional deep etching technique gave a qualitative indication of the morphology of the inclusions present in the samples, however, it is difficult to quantify the particle size in three-dimensions.

5.1.3 ENERGY DISPERSIVE X-RAY ANALYSIS

The chemical composition of the deoxidation products was determined by the EDX analysis of a two-dimensional planar section through the steel sample. The analysis of very small particles using high acceleration voltages can lead to the electron beam passing through the particle, causing X-rays to be generated from the underlying and surrounding matrix. To minimise this effect a low acceleration voltage was selected and given that the inclusions were set in effectively an iron matrix, the Fe content of the analyses was only considered if manganese was present.

5.2 STEEL MELTS PRIOR TO DEOXIDATION

Interdendritic FeO-MnO-Al₂O₃ inclusions were observed in all of the samples from the undexoidised melts irrespective of the melting technique used. The morphology, distribution and composition of the interdendritic inclusions, Section 4.2, Plates 4.1, 4.17, 4.26, 4.36, and 4.48 suggested that they were liquid at 1600°C, Figure 5.1, and had become concentrated in the interdendritic liquid region of the melt during solidification. The typical size of the interdendritic inclusions was between 0.5 and 1.0µm. It is reasonable to

assume that the FeO-MnO-Al₂O₃ inclusions, being predominantly FeO, will have had a low interfacial energy similar to that of FeO melts in contact with molten iron, Table 2.2. Therefore, it is reasonable to expect that there will be little tendency for growth to occur by coalescence leading to accelerated float out from the melt in the crucible. The structure of the sample may therefore be taken to be indicative of the maximum size of the inclusions within the melt. However, it must be remembered that some of the inclusions in the samples may have been formed during solidification as a result of the increasing concentration of the oxygen, aluminium and manganese in the interdendritic regions of the melt as the temperature fell, thereby increasing the supersaturation.

5.3 ALUMINIUM DEOXIDISED MELTS

Aluminium is the most commonly used steel making deoxidant and has a powerful affinity for oxygen as demonstrated by the Gibbs Free Energy of formation of alumina (Al₂O₃), Figure 5.2. It exhibits a single valency state, namely 3⁺. The stable oxide of aluminium is α -alumina, but a number of polymorphs exist. The melting point of aluminium is 660°C and the dispersal mechanism within a steel melt at high temperature must implicitly involve a melting and dissolution mechanism assisted by convective processes in the melt.

The experimental results from the melts deoxidised with aluminium are described in Section 4.2. After deoxidation with aluminium in the vertical tube furnace and high frequency furnace melts, three co-existing, primary types of inclusion morphologies were observed; small spherical inclusions similar to the liquid FeO-MnO-Al₂O₃ inclusions concentrated in the interdendritic liquid during the solidification of samples taken prior to the deoxidation of the melts, Plate 4.2; polyhedral alumina morphologies,

Plates 4.5 and 4.18; and dendritic alumina morphologies including well developed dendrites, Plate 4.3, and coralline dendrites, Plate 4.8, and spherical sintered agglomerates, Plate 4.4.

As the deoxidant melted and dissolved the aluminium content of the melt increased by a combination of diffusion and dispersion and a new equilibrium with respect to oxygen would have been established. However, these processes would have been dependent on the solubility of the deoxidant in the liquid steel, the rate of dissolution and the degree of turbulence which would have influenced the rate of dispersion.

It has been established that mixed oxides existed in the melt prior to the addition of the deoxidant. Similar small spherical inclusions were observed in the sample taken from the vertical tube furnace melt 12 seconds after deoxidation, Plate 4.2; their presence suggests that the aluminium addition had not been fully dispersed throughout the melt. Consequently, pre-existing liquid $\text{FeO-MnO-Al}_2\text{O}_3$ inclusions, oxygen, manganese and aluminium were concentrated in the interdendritic liquid as the temperature of the melt fell during the solidification of the steel. This concentration of the solutes may have caused further precipitation of inclusions and an increase in size of any pre-existing inclusions.

The small $\text{FeO-MnO-Al}_2\text{O}_3$ spherical inclusions were not observed in the samples taken from the high frequency furnace melt, Plate 4.18, implying that the turbulence experienced had increased the rate of mixing of the aluminium. This would have the effect of producing an increased and more uniform rate of reaction between the aluminium and the oxygen in the melt. Consequently, even in the solute enriched interdendritic liquid during

solidification the supersaturation of dissolved oxygen was not sufficient for the formation of liquid mixed oxides. This suggests that the final equilibrium had been reached between the aluminium and the oxygen at a level significantly lower than that existing prior to deoxidation. And this condition occurred uniformly through out the melt.

The presence of the aluminium with a greater affinity for oxygen than either iron or manganese would have resulted in the FeO-MnO-Al₂O₃ liquid inclusions being reduced. As the aluminium content of the mixed oxides increased FeAl₂O₄ crystals would have started to precipitate forming a solid inclusion consisting of either a single or a number of crystals of hercynite. The kinetics of reduction would have proceeded relatively rapidly when the inclusions were liquid. However, as the liquidus temperature rises with increasing alumina content, Figure 5.1, the inclusions eventually solidify and the process would have slowed as continued reduction relied upon mass diffusion.

It is proposed that the spherical alumina morphologies formed from the larger mixed oxides present in the early stages of deoxidation. Given the size of these inclusions it is probable that after solidification they exhibited a polycrystalline structure, time would then have been necessary for migration of the grain boundaries and recrystallisation and grain growth before the formation of a single crystal. By the time this occurred the dissolved oxygen concentration of the melt would have decreased to a point where precipitation would have ceased and a crystalline habit would not have developed, thus any inclusions precipitate_A^d would have retained a spherical habit.

As the deoxidant was being dispersed, the supersaturation with respect to aluminium would have increased in localised regions of the melt sufficient for homogeneous or more likely heterogeneous precipitation of FeAl_2O_4 or Al_2O_3 on the surface of solid hercynite inclusions, liquid mixed oxides, or alumina particles introduced into the melt on the surface of the deoxidant. Thereby, inclusions with a hercynite core surrounded by a layer of alumina could have formed. Subsequently, the excess aluminium in solution would reduce the hercynite core, forming a solid alumina inclusion exhibiting a spherical habit, Figure 5.3. The process of reduction by aluminium was not dependent on the dissolved oxygen concentration of the melt and could continue even after it had fallen to a lower level.

Polyhedral inclusions form from 'dilute' solutions¹¹⁶ as oxide molecules are precipitated onto and incorporated into the crystal lattice at low rates. It is proposed that the polyhedral inclusions observed, Plates 4.11 and 4.18, formed in low supersaturation conditions, in regions of the melt remote from the rapidly melting and dissolving aluminium. The polyhedra grew from small solid oxide particles, these may have been liquid iron-manganese oxides which had been reduced and had aluminium bearing oxides precipitated on their surfaces until at least the composition of hercynite was reached, or were exogenous particles on which aluminium bearing oxides precipitated.

Polyhedra arise from preferred growth on certain crystallographic faces of a pre-existing crystalline phase. The majority of the polyhedra formed had essentially an octahedral habit, typical of the cubic, tetragonal and orthorhombic crystal systems. It is suggested that the phase(s) from which the polyhedra grew were either FeAl_2O_4 , $\gamma\text{-Al}_2\text{O}_3$ or $\kappa\text{-Al}_2\text{O}_3$, given that they belong to the above crystal systems, Table 5.1, and are known¹¹⁷ to form at

lower supersaturation values than $\alpha\text{-Al}_2\text{O}_3$.

Variations in the habit of the polyhedra, Plate 4.18, may have been caused by changes in interfacial energy experienced during growth due to the progressive reduction in oxygen, which is a surface active element, resulting in the non uniform growth of the crystal faces. Subsequently, the excess aluminium in solution in the melt would have reduced any remaining FeO or MnO in the inclusions, forming α - alumina inclusion exhibiting an octahedral habit.

It the vicinity of the melting and dissolving deoxidant, given the high solubility of aluminium in liquid steel, high supersaturation conditions with respect to aluminium would have prevailed. Saratovkin¹¹⁶ suggested that dendrites grow in supersaturated solutions because of the high deposition rates of the oxide molecules at the crystal surface. This type of growth occurs in order to compensate for the slow diffusion and removal by convection of solute depleted solvent from crystal faces. To achieve this, oxide molecules are preferentially deposited at the corners of the growing crystal, thereby avoiding areas of the melt already depleted in solute. This is due to the diffusion distances being less at the crystal corners than at the crystal face, Figure 2.21. Secondary alumina dendrites observed, Plates 4.24 and 4.25, which grew during a period of reoxidation confirmed that dendrite branches did grow from crystal corners.

Highly developed dendrites, Plates 4.3 and 4.6, were observed in the vertical tube furnace melt, whereas less well developed dendrites were observed in the high frequency furnace melt, Plate 4.19. This probably reflects the relative degree of turbulence experienced by the melts. Dendritic growth

occurs during periods of high supersaturation facilitated by high deoxidant concentrations. The high frequency furnace melt experienced a high degree of turbulence, whilst high concentrations of aluminium would have developed adjacent to the melting and dissolving deoxidant, the rate of dispersion of the aluminium throughout the melt would have been rapid. The vertical tube furnace melt experienced low turbulence, hence high concentrations of aluminium would have developed in the vicinity of the melting and dissolving deoxidant. Given that the rate of dispersal of the deoxidant would have been slower, these conditions would have persisted for a longer period of time. Consequently, the rate at which the new equilibrium oxygen concentration and presumably the reduction in dissolved oxygen, would have been faster in the high frequency furnace melt compared with the vertical tube furnace melt.

It is known⁸⁹ that the dissolved oxygen concentration of a melt affects the interfacial energy between the inclusion and the liquid steel, Figure 5.4. As the dissolved oxygen concentration of the melt decreased the interfacial energy between the inclusion and the melt would have increased. It is probable that the dissolved oxygen concentration in the vertical tube furnace melt decreased at a slow rate and large dendrites exhibiting a high surface to volume ratio had more time to develop. In contrast, the dissolved oxygen decreased more rapidly in the high frequency furnace melt, consequently, the dendrites did not grow as large and their morphology was determined by the increasing interfacial energy.

The majority of the dendrites in the vertical tube furnace melt exhibited secondary arms growing perpendicular to primary arms, Plate 4.5 and Figure 5.5. These represent dendrites which grew from initial crystals belonging to either the cubic, tetragonal or orthorhombic crystal systems

suggesting that they were composed of either FeAl_2O_4 , $\gamma\text{-Al}_2\text{O}_3$, or $\kappa\text{-Al}_2\text{O}_3$, Table 5.1. In comparison, some of the dendrites observed in samples from the high frequency furnace melt, exhibited six arms which had grown from a central point with a 60° angle between primary and secondary arms, Plates 4.18, Figure 5.6. This suggests that the crystal system was either hexagonal or trigonal and the initial crystalline phase was either $\theta\text{-Al}_2\text{O}_3$ or $\alpha\text{-Al}_2\text{O}_3$, Table 5.1. As supersaturation progressively increased γ -, κ -, θ - followed by α -alumina would have been precipitated. This infers that θ - or α -alumina crystalline inclusions were present in the melt at a time when dendritic growth was still taking place. This suggests that supersaturation with respect to both oxygen and aluminium was achieved more rapidly in the high frequency furnace melt. Presumably, this is due to turbulence dispersing the aluminium more rapidly resulting in the oxygen equilibrium concentration being lowered towards the new level at a faster rate.

The secondary dendrites observed, Plate 4.25, are representative of forms which would have grown from an inclusion comprising of either $\theta\text{-Al}_2\text{O}_3$ or $\alpha\text{-Al}_2\text{O}_3$.

Coralline and spheroidising dendrites and sintered agglomerates were observed mainly in the vertical tube furnace melt, Plate 4.8, and to a lesser extent in the high frequency furnace melt, Plates 4.21 and 4.22. These formed as the dissolved oxygen content of the melt decreased and the interfacial energy between the melt and dendrites increased, causing the inclusions to decrease their surface area to volume ratio, in order to minimise their surface energy. Consequently, the tips of the dendrite arms spheroidised and the more compact coralline structures were formed, Plate 4.8. Further increase in interfacial energy caused the spheroidising

dendrites to collapse and points of contact between the arms and branches of the spheroidising inclusions to form stable contacts. Stable contacts form when the liquid metal separating stems and branches of dendrites withdraws⁷⁴. This results in a decrease in surface area, causing a reduction in surface free energy which provides the driving force for mass diffusion, resulting in sintering. The progressive contact and sintering resulted in the formation of sintered agglomerates, Plate 4.9. These agglomerates were not composed exclusively of dendrites, any contacting morphologies would have grown in a similar way, Plate 4.7.

Previous worker^{77,101} proposed that some small spherical inclusions observed in aluminium deoxidised steel melts could have resulted from the spheroidisation and amputation of dendrite arms by dissolution. The contact points between primary and secondary dendrite arms were thinner than the rest of the secondary arm, Plate 4.4. This presumably occurred because the secondary arm had to grow through steel depleted in solute, before encountering melt with a higher solute concentration. The spheroidisation of the tips of dendrite arms, Plate 4.4, would have occurred as the dissolved oxygen concentration of the melt decreased. Evidence to support the existence of a possible fracture mechanism initiated at growth faults, suggested by Martin¹¹⁷, which causes the arms to shear off close to the point of contact with the primary dendrite arm was observed, Plate 4.22. Whilst dissolution may be active, these inclusions may result simply because of a weakness provided by the growth faults at the thin junction between dendrite arms. As the secondary arm shears off, spheroidisation takes place in an attempt to reduce the large surface area to volume ratio. These spherical inclusions are similar in morphology and size but must not be confused with those observed in the early stages of deoxidation, Plate 4.3, which had a

different origin.

Once the dissolved oxygen content of the melt had fallen below that necessary for the precipitation of nuclei and diffusional growth ceased, further growth and the formation of inclusion clusters became dependent on interparticle collisions. When alumina inclusions collide, stable contacts form because the contact angle, θ , between the liquid steel and the solid oxide exceeds 90° , Table 2.4. The liquid steel from the space between the inclusions at their points of contact retreats spontaneously causing a reduction in surface area and a decrease in the surface free energy. This decrease in surface free energy provides the driving force for the formation of sintered necks observed between inclusions, Plate 4.15. The higher the contact angle between the oxide and the steel melt the greater the tendency to form clusters. It can be seen from Table 2.4 that alumina has a particularly high contact angle, θ , and this accounts for large clusters of the type shown in Plate 4.3. A schematic diagram to show the formation of inclusion clusters during deoxidation with aluminium is given in Figure 5.7.

The degree of turbulence experienced by the melt would have been a major factor in the growth of inclusions and the kinetics of their removal from the melt. In agreement with other workers⁶⁸ it was noted, Figure 5.8, that the rate of removal of total oxygen from the high frequency furnace melt was more rapid than that of the vertical tube furnace melt and to a lower residual oxygen level. This faster rate reflects the high degree of turbulence experienced by the high frequency furnace melt and would have resulted in more interparticle collisions and the formation of larger clusters; more collisions occurring with the collecting surfaces, such as the crucible wall, compared with the vertical tube furnace melt. The high contact angle

between the alumina and the melt ensured that the collisions between inclusions resulted in stable contacts and the formation of large clusters.

The size of the inclusions increased in the initial 100 seconds after the addition of the aluminium deoxidant, Figure 5.9 and 5.10. This increase in size was confirmed by another study¹⁴⁹ on the samples taken from the high frequency furnace melt, Figure 5.11. It is suggested that this increase in size represents the progressive growth and sintering of inclusion clusters together with the progressive removal of the dendritic inclusions. The sections through the dendrite arms, which in flat polished section would have appeared as spherical inclusions, would have been smaller in cross section than the other inclusion morphologies and certainly not a true reflection of the dimensions of the dendrites.

The clusters appeared to have been selectively removed on the basis of their size and the morphology of the inclusions contained within them. Initially, both dendrite dominated clusters and small clusters containing polyhedra were observed in the vertical tube furnace melt. However, once the dissolved oxygen fell below 100 ppm, approximately 180 seconds after deoxidation, the clusters containing dendrites were no longer observed, Figure 5.9, this corresponded to a change in the rate of removal of total oxygen, Figure 5.9. The greater turbulence experienced by the high frequency furnace melt had the effect of reducing the amount of the time to approximately 50 seconds, for the dendrite clusters to be eliminated, Figure 5.10. The dendrites probably behaved like nets increasing the size of a cluster by capturing individual and smaller inclusion clusters by virtue of their large surface area. These larger clusters were then preferentially removed from the melt given that they had a greater probability of penetrating

the boundary layer, between melt and crucible wall and at the melt surface. The small clusters containing polyhedral inclusions persisted in the melts for a longer period of time as they had a correspondingly slower rate of removal.

5.4 TITANIUM DEOXIDISED MELT

Titanium is one of the strong deoxidisers of steel, though not as strong as aluminium, Figure 5.2. It exhibits a number of valency states, namely 2^+ , 3^+ , 4^+ . The principal deoxidation products formed in steel have been found to vary with the equilibrium concentration of titanium in the alloy. $\text{FeO}\cdot\text{Ti}_2\text{O}_3$ is found at low concentrations (less than 0.1%), Ti_3O_5 between 0.1-0.2% Ti and $\alpha\text{-Ti}_2\text{O}_3$ at greater than 0.2% Ti^{138,140}. The solubility of titanium in alpha iron reaches a maximum of about 10% at a temperature of 1300°C but decreases to 1% or less at room temperature¹⁵⁰, Figure 5.12. The melting point of titanium is 1667°C and it is reasonable to expect that the dispersal mechanism within a steel melt at high temperature must be dissolution assisted by convection.

The experimental results from the melts deoxidised with titanium are described in Section 4.3. After the addition of the deoxidant the experimental results indicated the presence of polyhedral inclusions and large spherical inclusions, Plates 4.27 and 4.33, in both the vertical tube furnace melt and the high frequency furnace melt.

Some isolated spherical inclusions were noted in the high frequency furnace melt 3 seconds after deoxidation, Plate 4.32, similar to those observed prior to deoxidation, Plate 4.26. These isolated spherical inclusions were not observed in the samples taken subsequently, nor in samples from the vertical tube furnace, although the first of these samples was only taken 34 seconds

after deoxidation. These probably reflect a low rate of dispersal of the deoxidant, slowing the rate at which the new equilibrium oxygen concentration was achieved, thus explaining the presence of liquid mixed oxide inclusions during the initial stages of the deoxidation process .

As the titanium concentration of the melt increases a new dissolved oxygen equilibrium would have been established. With a small increase in the concentration of titanium, the iron and manganese contained in any pre-existing liquid FeO-MnO-Al₂O₃ inclusions would have been reduced by the titanium. Concurrently, FeO.Ti₂O₃ and possibly Ti₂O₃ would precipitate heterogeneously on the inclusions. If the supersaturation was sufficient, FeO.Ti₂O₃ and Ti₂O₃ might nucleate homogeneously, but the presence of the more easily nucleated oxides or exogenous particles, introduced into the melt on the surface of the deoxidant would provide sites for heterogeneous nucleation which would have been thermodynamically more favourable. Progressive reduction and precipitation would have resulted in the crystallisation of FeO.Ti₂O₃ and the inclusions would have solidified. Titanium would continue to reduce the FeO present, eventually forming an inclusion composed of Ti₂O₃.

If the inclusion was relatively large when it solidified the inclusion would maintain its spherical morphology as the rates of reduction and recrystallisation would have been slower. However, this would have occurred more rapidly in smaller inclusions, allowing crystal faces to develop as the inclusions continued to grow forming polyhedra. Polyhedral growth occurs from dilute solutions, suggesting that these inclusion grew in regions of the melt which did not experience high supersaturation conditions.

Many of the polyhedra exhibited a simple octahedral habit, Plate 4.29, whilst others were more highly faceted, Plate 4.30, 4.31 and 4.32, and some exhibited a hexagonal habit, Plate 4.33. In the absence of any polymorphs of Ti_2O_3 , the octahedra would have resulted from the growth of an original $FeO.Ti_2O_3$ crystal, whereas the polyhedra exhibiting a hexagonal habit would have grown from an α -alumina type Ti_2O_3 crystal. The more highly faceted octahedral polyhedra possibly developed as the oxygen concentration decreased and thus the interfacial tension between the oxide and the melt increased, Figure 5.13. Given that simple octahedra were more numerous in the vertical tube furnace melt, which with the lower turbulence would have had a slower a rate of dissolved oxygen removal. Thus the progressive change in the composition of the liquid mixed oxides resulted in the formation, of solid inclusions which depending on size, time and spatial distribution either retained their spherical morphology or formed polyhedra. Subsequently, excess titanium in solution would have reduced the remaining FeO and MnO content of the inclusion and formed Ti_2O_3 .

It seems reasonable to assume that the large spherical morphologies were formed by the same mechanism proposed to account for the collapse and spheroidisation of the inclusions in Section 5.3. It is suggested that individual inclusions encountered each other due to the turbulent motion of the melt. Following collision, the inclusions began to agglomerate and the increase in surface free energy when stable contacts were made provided the driving force for the process of sintering and further spheroidisation. This process resulted in the formation of the sintered agglomerates, Plate 4.28. These often exhibited a characteristic metal filled cavity with an exit hole at the inclusion surface, Plates 4.30 and 4.33, resulting from the expulsion of liquid metal trapped between the individual agglomerating inclusions.

Subsequently, the solid-solid interfacial energy between individual Ti_2O_3 crystals within the inclusions provided the driving force for the process of grain boundary migration. This process resulted in large isomorphous spherical inclusions, Plate 4.28, with a smooth surface, Plate 4.33. In this way single crystal Ti_2O_3 inclusions with a spherical morphology were formed from a number of individual inclusions. It should be pointed out that under conditions of high turbulence in the high frequency furnace melt more isomorphous and fewer polymorphic inclusions were observed, Plate 4.28 and 4.34. The dissolved oxygen would have beenⁿ reduced at a faster rate, with consequent lowering of the interfacial energy. At the same time a greater number of collisions would have occurred in a short period of time, thus clustering, spheroidisation and the subsequent processes reached completion earlier. These large spherical Ti_2O_3 inclusions were comparable with the large spherical sintered agglomerates observed in the aluminium deoxidised melts, Plates 4.8 and 4.21. However, whereas the Ti_2O_3 agglomerates exhibited a tendency towards recrystallisation and grain growth. The Al_2O_3 agglomerates retained their polycrystalline structure suggesting that the oxide/oxide interfacial energy was greater for Ti_2O_3 than for Al_2O_3 .

Some small spherical inclusions may also have formed in a similar manner by the spheroidisation of small clusters of inclusions. These also exhibited the characteristic exit hole observed at the surface of the large spherical inclusions, Plate 4.33.

Subsequently, collisions occurred between the large smooth faced spherical morphologies and smaller inclusions, Plate 4.35, and further growth occurred by rapid sintering and mass diffusion. Surface nodules represent the

remnants of smaller inclusions being incorporated into the large spherical inclusions, Plate 4.35. A schematic diagram showing the distinct stages in the formation of the large spherical morphologies is given in Figure 5.14.

Compared with the aluminium deoxidised melts, the titanium deoxidised melts did not contain any dendritic inclusions. It has previously been stated that dendrites grow in supersaturated melts. Because titanium is a refractory metal melting would not occur, the dispersion of the deoxidant would have been regulated by the rate of dissolution and the degree of turbulence experienced by the melt. It is suggested that turbulence dispersed the dissolved titanium away from the bulk titanium addition before the high degrees of supersaturation necessary for dendritic growth were achieved. Consequently the morphologies present in the titanium deoxidised melts represent inclusions which grew in 'dilute' solutions.

The increase in mean size and size range of the inclusions indicates a period of growth immediately after the addition of the deoxidant, Figure 5.15 and 5.16. The growth involved the progressive collision and sintering of inclusions forming inclusion clusters, Plates 4.27 and 4.33, turbulence eventually bringing them into contact with the crucible-melt interface, where they were captured.

Growth occurred more rapidly in the inductively stirred high frequency furnace melt, with a maximum inclusion diameter occurring approximately 20 seconds after deoxidation, Figure 5.15, compared with the vertical tube furnace melt stirred by convection, with a maximum inclusion diameter occurring approximately 80 seconds after deoxidation, Figure 5.16. This is presumably because the greater turbulence experienced by the high

frequency furnace melt resulted in more collisions between inclusions. Subsequently, the size of the inclusions decreased, corresponding to a change in the rate of removal of the total oxygen. The initial oxygen removal rate was more rapid in the high frequency furnace melt compared with the vertical tube furnace melt, Figure 5.17. The changes in average size of the inclusions as deoxidation progressed were confirmed by another study¹⁴⁹ of the samples taken from the high frequency furnace melt deoxidised with titanium, Figure 5.18.

5.5 ZIRCONIUM DEOXIDISED MELTS

Zirconium is used as a deoxidant in steelmaking and has a strong chemical affinity for oxygen, Figure 5.2, comparable with both aluminium and titanium. It exhibits a single valency state, namely 4^+ . Monoclinic zirconia is the stable oxide of zirconium but higher temperature tetragonal and cubic forms exist. The solubility in iron at steelmaking temperatures, Figure 5.19, and the refractory nature of zirconium, melting point 1852°C , suggests that the dispersal mechanism in a steel melt at high temperatures will be dissolution assisted by convection similar to that of titanium.

The experimental results for the zirconium deoxidised melts are given in Section 4.6. From these it can be seen that after deoxidation with zirconium in the vertical tube furnace melt, small spherical inclusions up to $1\mu\text{m}$ in diameter, well developed dendritic morphologies, Plate 4.49, and dumb-bell shaped inclusions, Plate 4.50, were present.

The small spherical inclusions would have resulted from the reduction of pre-existing mixed oxide inclusions. These were composed predominately of FeO with minor quantities of MnO and Al_2O_3 . Zirconia exhibits very limited

solubility in FeO and no intermediate compounds are formed between FeO and ZrO₂, Figure 5.20. Thus immediately after deoxidation zirconia precipitating heterogeneously on the liquid oxide-steel melt interface and reduction of FeO and MnO by zirconium would result in an inclusion composed of liquid mangano-wustite and solid zirconia. Complete solidification of these inclusions would have occurred once all the FeO and MnO had been reduced by the zirconium. This process would have been relatively rapid as mass diffusion in liquids is faster than in solids. This compares with aluminium and titanium which both exhibit intermediate FeO.Al₂O₃ and FeO.Ti₂O₃ compounds, the solidification of these inclusions, by the processes of precipitation and reduction, would have occurred once the composition of the inclusions reached that of spinel. This would have been followed by reduction forming Al₂O₃ and Ti₂O₃ respectively. The later reduction process would have involved mass diffusion in the solid spinel phase, with this step progressing at a slower rate.

It is known¹¹⁶ that dendritic morphologies form under condition of high supersaturation, whilst the interfacial energy between the oxide and the melt remains low. The solubility in iron and the melting point of zirconium are similar to titanium, Figures 5.12 and 5.19, Table 5.4. Accordingly, relatively low supersaturation with respect to zirconium should have developed adjacent to the dissolving deoxidant and the rate of dissolution should have been similar to those experienced in the titanium deoxidised melts. However, it should be noted that the titanium addition was in the form of wire, whereas the zirconium was a thin rectangular block. Consequently, the surface area to volume ratio of the zirconium addition would have been lower, so the rate of dissolution of the zirconium would have been slower. A slower rate of dissolution would have extended the time taken for the dispersal of the

deoxidant, resulting in a slower rate of decrease in the equilibrium dissolved oxygen concentration. Hence, low interfacial energy conditions between the oxide and the melt could have persisted for a longer period of time. This effect combined with the inherently low interfacial energy known⁷⁵ to exist between zirconia and the melt, Table 2.4, could have allowed sufficient time for dendrites to develop. A subsequent increase in the interfacial energy of the melt produced by decreasing the dissolved oxygen concentration would have precluded further growth of such high surface area to volume structures typified by dendritic morphologies. This is further supported by the minimal inclusion clustering observed, Plate 4.49, compared with that observed in the aluminium and titanium deoxidised melts, Plate 4.4 and 4.27. Clustering is known to be promoted by high interfacial energies as it increases the likelihood of stable contacts forming after inclusions collide.

The dendrites exhibited a cubic symmetry, Plate 4.49, inferring that the zirconia formed was the high temperature form which had possibly been stabilised to room temperature by impurity metal oxides. As the dissolved oxygen concentration of the melts decreased there would have been a corresponding increase in the interfacial energy at the inclusion-melt interface, causing the dendrite arms to spheroidise in order to reduce their surface energy. It is suggested that the dumb-bell shaped morphologies, Plate 4.50, are the result of this spheroidisation process occurring during the growth of dendritic zirconia. The dumb-bell morphologies showed the same cubic symmetry exhibited by the well developed dendrites, inferring that these were also the high temperature form of zirconia.

Zirconia inclusions were observed, Plate 4.69 and 4.70, forming a layer between the crucible and the steel melt. This layer of zirconia inclusion was,

in places, only loosely adhered to the crucible surface. As a result, the inclusions could have been re-entrained into the melt affecting the rate of decrease in total oxygen.

Unlike the aluminium and titanium deoxidised melts, polyhedra were not observed in the melts deoxidised with zirconium. In previous sections it was suggested that such polyhedra arose from the formation of an intermediate spinel based deoxidation product. Unlike aluminium and titanium, zirconium does not form an intermediate deoxidation product between the pre-existing FeO-MnO inclusions and the final ZrO₂ particles.

It is apparent from Figure 5.21 that oxygen is removed more rapidly in the high frequency furnace melt deoxidised by zirconium which is inductively stirred compared with the vertical tube furnace melt stirred by natural convection alone. The high frequency furnace melt showed a change in the rate of total oxygen removal 200 seconds after the addition of the deoxidant, Figure 5.21, whereas the vertical tube furnace melt showed a single uniform rate of removal. The greater turbulence experienced by the high frequency furnace melt would have increased the rate of dispersion of the deoxidant. Causing the dissolved oxygen content to fall rapidly and the interfacial energy between the oxide and the melt to rise, thus improving the likelihood of coalescence following interparticle collisions.

5.6 SILICON DEOXIDISED MELTS

Silicon is a moderately powerful deoxidiser with a chemical affinity for oxygen greater than manganese and iron but less than aluminium, titanium and zirconium as demonstrated by the Gibbs Free Energy of formation of its stable oxide silica, SiO₂, Figure 5.4. It exhibits a single valency state,

namely 4⁺. Three polymorphs of SiO₂ exist, quartz, cristobalite and tridymite. The melting point of silicon is 1412°C, and no intermediate Si/Fe compounds are formed with a melting point higher than 1600°C, Figure 5.22. The dispersal mechanism within the steel melt at high temperatures would therefore, most probably have involved both melting and dissolution assisted by the convective processes in the melt, and in this respect is very similar to aluminium.

The experimental results of the melts deoxidised with silicon are given in Section 4.4. The principal inclusions observed in samples taken from both the vertical tube furnace and the high frequency furnace melts were spherical morphologies between 0.5 and 3.0µm in diameter, Plates 4.37 and 4.40. The chemical analysis of these inclusions indicated that they were composed of either silica or highly siliceous Fe-Mn silicates, Tables 4.20 and 4.24. The compositions of these inclusions indicated that they would have been solid at 1600°C, Figure 5.23.

It has been established that liquid Fe-Mn-Al oxides existed in the melt prior to deoxidation, Plate 4.36. Deoxidation would have proceeded via the progressive reduction by silicon of the liquid oxides, which undoubtedly also provided sites for the heterogeneous nucleation of silica by direct reaction with oxygen in the melt, resulting in the formation of liquid FeO-MnO silicates. As deoxidation proceeded the manganese-wustite inclusions became progressively enriched in SiO₂. When the SiO₂ content of the liquid inclusion reached approximately 50%, cristobalite would have started to precipitate eventually forming solid inclusions exhibiting a spherical morphology. The presence of a SiO₂ film on the surface of the deoxidant addition may also have provided sites for heterogeneous nucleation.

By the time the FeO-MnO silicate inclusions had become substantially solid, the concentration of dissolved oxygen in the melt would have fallen to a sufficiently low level that growth of more complex morphologies, such as dendrites and polyhedra, would not have been possible. Further reaction would have proceeded by solid state diffusion of silicon and reaction with the residual FeO-MnO, until fully SiO₂ inclusions were formed. The inclusions consequently retain their spherical morphology.

Unlike with other deoxidants, at no stage was the clustering of solid silica inclusions, to form large agglomerates, ever observed. At most only up to four inclusions were ever seen in close association. This is probably attributable to the inherently low interfacial energy between silica and the melt, Table 2.4, further lowered by moderate levels of oxygen in solution.

Although no primary dendrites were observed, secondary dendrites were noted in both melts, Plates 4.39 and 4.42. These appeared to emanate from the surface of the spherical silica inclusions, suggesting they had formed very late in the deoxidation process. It has been proposed by other workers^{134,135}, that such dendrites form during cooling and solidification of the melt as a whole. Oxygen rejected from the iron during solidification enriches the remaining metallic melt, disturbing the existing oxygen/silicon equilibrium, allowing further growth of silica in a dendritic form from pre-existing inclusions. The enhanced supersaturation of the reactants in the system and the relatively low silica/ melt interfacial energy, created by the moderately high levels of oxygen in the melt, would encourage the dendritic solidification mode.

The presence of these small delicately branched secondary silica dendrites probably accounted for the increase in the inclusion count in both the vertical tube furnace and high frequency furnace melts, 160 and 120 seconds respectively, after deoxidation. The increase in inclusions encountered did not affect the volume fraction and inclusion diameter, Figure 5.24 and 5.25.

The reduction in dissolved oxygen would be expected to be faster in the high frequency furnace melt, corresponding to a faster rate of homogenisation of the silicon deoxidant compared with the vertical tube furnace melt. The increased turbulence would also have increased the number of collisions between inclusions facilitating their coalescence to form large globules. This would account for the rapid removal of total oxygen from the high frequency furnace melt compared with the vertical tube furnace melt, Figure 5.26.

5.7 CALCIUM-ALUMINIUM DEOXIDISED MELTS

Calcium, like aluminium, has a high affinity for oxygen, the Gibbs Free Energy of formation of calcium oxide is lower than those of the other steelmaking oxides over the entire temperature range of 0-1800°C, Figure 5.2. Therefore, if equilibrium could be attained between calcium and molten steel, it would be expected that calcium would be the most effective of the steelmaking elements generally used for the purpose of deoxidation. The boiling point of calcium is 1439°C and would ordinarily be expected to be a vapour at steel making temperatures. The solubility of calcium in pure iron at 1607°C is 0.032%. However, carbon, silicon, aluminium and nickel decrease the activity of calcium in iron melts which leads to an increase in solubility¹¹⁸.

The calcium was added to the melt in the form of a calcium-aluminium alloy,

Table 3.1(d). It is doubtful that the alloy consisted of a single calcium-aluminium phase, more realistically it would have been composed of a number of phases exhibiting different melting points. The melting points of all calcium-aluminium phases are lower than 1600°C, Figure 5.27. It has been suggested that¹¹⁹ as the calcium-aluminium alloy melted and dissolved, the boundary layer of the steel melt in contact with the alloy would have become rapidly saturated in calcium. Further dissolution would have been prevented until the calcium had time to diffuse in to the bulk of the melt. Most of the calcium contained in the addition would be expected to boil-off, with only a fraction of the total calcium being retained in the steel melt. The dispersal of the aluminium component of the alloy not would have been restricted in such a way and would have been expected to have involved the processes of melting and dissolution assisted by the turbulent motion of the melt.

A number of deoxidation products may be formed when using calcium-aluminium, depending on the conditions prevailing in the melt, namely CaO, $3\text{CaO}\cdot\text{Al}_2\text{O}_3$, $12\text{CaO}\cdot 7\text{Al}_2\text{O}_3$, $\text{CaO}\cdot\text{Al}_2\text{O}_3$, $\text{CaO}\cdot 2\text{Al}_2\text{O}_3$, $\text{CaO}\cdot 6\text{Al}_2\text{O}_3$, or Al_2O_3 . The phase $3\text{CaO}\cdot\text{Al}_2\text{O}_3$ and $12\text{CaO}\cdot 7\text{Al}_2\text{O}_3$ have melting points below 1600°C, whilst the melting point of $\text{CaO}\cdot\text{Al}_2\text{O}_3$ is close to that of the melt temperature in these experiments, Figure 2.26 and Table 5.2.

The experimental results of the melts deoxidised with calcium-aluminium were described in Section 4.5. After deoxidation the following inclusion morphologies were observed; polyhedral inclusions, Plate 4.43; large spherical morphologies, Plate 4.46; large globular inclusions, Plate 4.44; and dendrites were also noted.

The majority of the inclusions observed were polyhedra suggesting that the

dominant conditions experienced by the melts were 'low' supersaturation. Pickering¹²¹, proposed that a calcium-aluminium addition may cause calcium aluminate films to form around the dissolving deoxidant. These low melting point films would then collapse allowing the calcium-aluminium to again diffuse into the steel. Thus, initially, dendrites may have formed, but the subsequent retardation in dissolution would have reduced the supersaturation in this region as turbulence dispersed the deoxidant to other regions of the melt. Consequently, predominantly low supersaturations were experienced and polyhedra were formed in preference to dendrites.

The presence of dendrites, which although not as numerous as those observed in the aluminium deoxidised melt, suggests that the conditions, presumably in the vicinity of the melting and dissolving deoxidant, were sufficient for this type of growth. High concentrations of calcium and/or aluminium would have reduced the equilibrium dissolved oxygen concentration. The initial oxygen concentrations would have created surface energy conditions conducive to dendrite formation, but as the dissolved oxygen levels fell, increasing interfacial energy would have precluded their formation.

In the case of the calcium-aluminium deoxidised melts the pre-existing liquid FeO-MnO oxides acted as a substrate for heterogeneous precipitation of the calcium-aluminium oxides. These were simultaneously reduced by the calcium and aluminium in solution until the CaO:Al₂O₃ ratio was sufficient for the precipitation of a solid phase. The hexagonal morphology of the polyhedra suggests that the phase which precipitated was CaO.6Al₂O₃, Table 5.2, and this has been confirmed by EDX analysis, Plate 4.44. These processes must have proceeded relatively rapidly, and were followed by

recrystallisation and the growth of crystal faces.

Sintered contacts were observed between the polyhedra, forming clusters. This suggests that the contact angle between the high melting point calcium aluminates and liquid steel at 1600°C was greater than 90°, and probably significantly greater than the value of 115° for silica, which exhibited virtually no tendency to form interparticulate adhesion.

The large spherical inclusions were similar in morphology to those observed in the titanium deoxidised melts and the sintered agglomerates in the aluminium deoxidised melts. Therefore, it is proposed that, as the dissolved oxygen content of the melt decreased, the interfacial energy between the oxide and the liquid steel increased causing the clusters to spheroidise. The reduction in surface area as the inclusions within the cluster contacted one another provided the driving force for the process of sintering. These large spherical inclusions exhibited a characteristic exit hole at the inclusion surface, Plate 4.46, resulting from the expulsion of liquid metal trapped between the individual agglomerating inclusions.

Existing simultaneously were inclusion clusters, Plate 4.44, which appeared to have had a liquid coating over their surface. The chemical analysis of this coating indicated that it had a CaO content 5-10% higher than the polyhedral inclusions. These compositions would have been solid at steel making temperatures, although they appear to have been liquid. It is proposed that the analysis is a combination of two or more phases, one of which exists as a surface coating and the other the core of the inclusion. Hence, a thin layer of liquid calcium aluminate covered the surface of clustering solid calcium aluminate inclusions. It is proposed that calcium in solution reacts at the

surface of the high $\text{Al}_2\text{O}_3:\text{CaO}$ ratio solid calcium aluminate, reducing the Al_2O_3 component to produce a calcium aluminate significantly enriched in CaO. It has already been shown that the polyhedra are predominantly composed of $\text{CaO}\cdot 6\text{Al}_2\text{O}_3$. Consideration of the phase diagram, Figure 4.40, clearly indicates that enrichment by calcia would significantly lower the liquidus temperature. Such a liquid film on the surface of the clusters would enhance their capabilities of further capturing and coalescing with other particles in the melt. This mechanism is illustrated in Figure 5.28 and would be expected to result in the formation of large globular inclusions which would be rapidly removed from the melt.

The turbulence experienced by the melt would have had a major influence on the rate of removal of total oxygen from the melt. As with the other deoxidants the total oxygen content of the high frequency furnace melt was removed at a faster rate than the corresponding vertical tube furnace melt. Both melts exhibited a change in the rate of oxygen removal, Figure 5.29. Examination of the size distribution of the inclusions, Figure 5.30, suggests that a peak particle size was achieved about 30 seconds after the addition of the deoxidant, with a considerable scatter in the distribution of the particle sizes. Beyond 30 seconds, the mean particle size slowly decreased, but there was a more dramatic decrease in the range of the particle sizes. Beyond 150 seconds, only a relatively narrow size range existed. This is probably a reflection of the effectiveness of the calcia enriched liquid surface film, in enhancing the capture, agglomeration and separation of particles from the melt.

5.8 GENERAL MODEL FOR DEOXIDATION.

For the successful deoxidation of a steel melt the deoxidant must be soluble in liquid steel and have an affinity for oxygen greater significantly than iron. The Gibbs standard free energy of formation (ΔG°_{1873}) at the temperature of the melt gives an indication of the spontaneity of the reaction between the deoxidant metal and oxygen, Figure 5.2. This data indicates that calcium would form the most stable oxide followed by zirconium, aluminium, titanium and silicon. This work has demonstrated, Figure 5.31 and 5.32, that a high affinity for oxygen will not ensure favourable reaction kinetics and will have little bearing on the kinetics of removal of the products of the deoxidation reaction from the melt.

Turkdogan^{29,30} has compared the effective deoxidising power of a metal in terms of the deoxidation reaction equilibria in Fe-X-O melts at 1600°C, Figure 2.2. This data shows the level of dissolved oxygen remaining in solution over a range of deoxidant concentrations. However, the data only indicates the potential for removal of dissolved oxygen, not the removal of total oxygen from the melt. For example, in this work, zirconium exhibits a higher residual total oxygen contents than aluminium, Figures 5.31 and 5.32, which is contrary to the conclusions from Turkdogan's work.

Thus, the free energies of formation and the deoxidation equilibria give little indication of the kinetics of removal of the deoxidation products from the melt.

Classical nucleation theory^{38,39} indicates that the activation energy provides the thermodynamic barrier to the formation of nuclei and that this is strongly dependent on the interfacial energy between the deoxidation product and the melt. Consequently, a deoxidation product exhibiting high interfacial energy

will be difficult to nucleate homogeneously. However, if high degrees of supersaturation of the deoxidant relative to that predicted by the deoxidation equilibrium develop in the melt, the thermodynamic barrier imposed by the high interfacial energy can be overcome, enabling homogeneous nucleation of the deoxidation product. High degrees of supersaturation may develop in the region of the melt where the deoxidant is melting and/or dissolving. Consequently, if the deoxidant exhibits a high solubility in liquid iron, homogeneous nucleation of the deoxidation product(s) may occur in this region of the melt.

However, if suitable particles are present in the melt to provide substrates, heterogeneous nucleation will preferentially take place at these. Such particles may include:-

1. liquid Fe-Mn-Al oxides which it has been established in Section 5.2 exist in the melt prior to deoxidation; and
2. exogenous oxide particles introduced into the melt on the surface of the deoxidant;

Calcium was observed in deoxidation products when the melt had not been deoxidised with calcium, the lime could only have originated from the refractory. This indicates that the crucible wall was a source of exogenous material and, therefore, must play a role in any heterogeneous deoxidation mechanism.

After deoxidation the pre-existing liquid mixed oxides are progressively reduced by the deoxidant. Dispersion of the deoxidant causes the equilibrium oxygen concentration of the melt to decrease, resulting in the precipitation of deoxidation products on the substrate provided by the liquid mixed oxides or other potential nucleation sites. The existence of an

intermediate solid $\text{FeO.M}_x\text{O}_y$ phase between FeO and M_xO_y causes the inclusions to solidify earlier, as demonstrated by aluminium and titanium which exhibit intermediate $\text{FeO.Al}_2\text{O}_3$ and $\text{FeO.Ti}_2\text{O}_3$ compounds.

Otherwise, substantial reduction of the FeO/MnO component would be required before solidification, as is the case with silicon which exhibits extensive liquid miscibility between FeO and SiO_2 , and zirconium which exhibit no intermediate phases between FeO and ZrO_2 .

The inclusions may retain a spherical morphology or with further growth form polyhedral inclusions, depending on the inclusion size and the availability of oxygen for reaction after solidification. Polyhedra require a crystalline substrate on which the characteristic crystal faces grow. Crystallisation of phases from a liquid would result in a polycrystalline inclusion.

Recrystallisation forming a single crystal is necessary before polyhedral growth occurs. The time required for this depends on the size of the inclusion and the oxide/oxide interfacial energy. Consequently, small solid spherical inclusions, composed of oxides with a high grain boundary surface energy are more likely to form polyhedral inclusions. If solidification and recrystallisation proceed slowly, and insufficient oxygen is available for further growth, the inclusions maintain a spherical morphology, as is the case with silica.

Previous workers have indicated¹¹⁶ that polyhedra crystallise from 'dilute' solutions, whereas, dendrites require supersaturated solutions before they begin to grow. High deoxidant concentrations develop adjacent to the dissolving deoxidant, providing the rate of dissolution is greater than the rate of dispersion into the bulk melt. The amount of dissolved oxygen available for reaction depends on the difference between the equilibrium oxygen

concentration of the original Fe-Mn-O melt and the new equilibrium concentration established in the melt with the deoxidant. The speed at which this is achieved depends on the rate at which the deoxidant is homogenised throughout the melt. Correspondingly, the rate of homogenisation affects the pace at which oxygen is consumed by reaction. If homogenisation is retarded, the depletion in dissolved oxygen is slower and the period of dendritic growth extended. Consequently, dendrites are more numerous in quiescent melts compared with stirred melts.

The interfacial energy between the deoxidation product and the melt is of importance, as low interfacial energies facilitate the growth of dendrites, which characteristically exhibit high surface area to volume ratios. As oxygen is removed from solution the interfacial energy increases.

Dendrites would not be expected to form in melts deoxidised with metals exhibiting melting points higher than 1600°C, e.g. titanium and zirconium. Such materials are slow to dissolve in the melt and the turbulent motion of the melt leads to its dispersal before high concentrations develop. However, if the deoxidation product displays a low interfacial energy, and more oxygen is available for reaction, dendrites may form, as demonstrated by the zirconium deoxidised melts. The lack of solid crystalline substrates prevents the growth of dendrites even if the deoxidant concentrations are high and the oxide-melt interfacial energy is low, as confirmed by the inclusions observed in the silicon deoxidised melts.

As the dissolved oxygen is removed from the melt by reaction, the interfacial energy between the deoxidation product and the melt increases, causing changes in the morphology of the growing dendrite. High interfacial energies

result in the spheroidisation of growing dendrites, as they attempt to reduce their surface area, in order to minimise the effect of surface energy. As a result coralline morphologies, Plate 4.8, and dumb-bell morphologies, Plate 4.50, grow in preference to well formed dendrites. Further spheroidisation causes the dendrites and clusters of inclusions to collapse forming sintered agglomerates and large spherical morphologies.

The nucleation and growth of the deoxidation products only brings about the removal from solution of dissolved oxygen, as immiscible particles dispersed throughout the melt. This process does not give an indication of the rate of removal of the total oxygen by the elimination of the deoxidation products from the melt.

The ability to form clusters is an important factor in the removal of deoxidation products from the melt. ^{Examples of} inclusions which form large inclusion clusters are the aluminium, titanium and calcium-aluminium deoxidation products. Large clusters form if high contact angles exist between the deoxidation product and the melt. This results in an increase in the probability of a collision between inclusions forming a stable contact. The greater the number of collisions the more clusters form and the larger they grow. Large clusters with high contact angles also have a greater probability of emerging from the melt by penetrating the boundary layer between the steel and the collecting surface. For inclusions exhibiting low contact angles, the probability of stable contacts between colliding inclusions being formed is less. As demonstrated by silica and zirconia which display limited amount of clustering.

In the case of the aluminium deoxidised melts large clusters, especially

those entrapped by dendrites, are preferentially removed from the melt when compared with smaller clusters. The rapid reduction in total oxygen corresponds with the disappearance of the large clusters, Figures 5.9 and 5.10, inferring that they contain a significant quantity of the total oxygen present in the undeoxidised melt. Smaller clusters remain in the melt for longer periods of time, implying that they are eliminated at a slower rate, Figures 5.9 and 5.10.

Rapid total oxygen removal rates occur if large clusters are formed in the melt, whilst, individual inclusions and small clusters result in a slower rate of removal. In melts which containing a range of large and small clusters, the larger ones will tend to be eliminated first.

The removal of total oxygen from steel deoxidised with the same deoxidant is affected by the amount of turbulence experience by the melt, Figures 5.31 and 5.32. Turbulent melts increase the number of collisions between inclusions, causing large clusters to grow faster and increasing the frequency at which contact is made with the collecting surfaces. Consequently, large clusters develop faster and have greater opportunity to emerge from stirred melts compared with quiescent melts.

Turbulence also increases the rate of dispersal of the deoxidant throughout the melt, causing an increase in the removal of dissolved oxygen. This leads to the increase in interfacial energy between the deoxidation products and the melt occurring more rapidly, enhancing the early formation and emergence of large clusters.

The successful elimination of deoxidation products from the melt requires

that the frequency of collisions with the collecting surfaces is as high as possible. This will increase as the turbulence increases. Once the inclusion is brought into contact with the containing vessel walls the assimilation process proceeds by the drainage of the liquid steel film followed by its rupture. Previous workers⁷⁰ have proposed that the contact angle between the oxide and the steel melt is critical to the stable position attained by the emerged fraction of the inclusion cluster, Figure 2.8. The emergence of inclusions with low contact angles may prove more difficult, as the fraction of the inclusion which can penetrate the boundary layer may be small resulting in a greater probability of re-entrainment.

This probably accounts for the two stage total oxygen removal rate observed in the high frequency furnace melts deoxidised with zirconium and silicon compared with the single uniform rate in the vertical tube furnace melt. The greater turbulence would have resulted in a 'high' contact angle being achieved earlier in the deoxidation process. A larger number of collisions would have occurred between clusters, individual inclusion and the collecting surfaces, resulting in the rapid removal of large clusters. This would be followed by the slower rate elimination of the individual inclusions and small clusters. In the vertical tube furnace melts, elimination proceeded by collision of individual and smaller clusters with the collecting surfaces. Such inclusions would have a greater probability of being re-entrained.

Based on the experimental results it is proposed that in the case of the solid deoxidation products the major criteria responsible for the rapid removal of total oxygen from a deoxidised melt are high contact angles between the deoxidation products and the melt, and high degrees of turbulence. These facilitate the rapid growth of large clusters, and increase the frequency that

they encounter the collecting surfaces and improve the probability of successful elimination from the melt. In large commercial steel making melts, where potential surfaces for capturing the inclusions are more distant, and the degree of turbulence is proportionally less than in the induction furnace melts, there may be even greater potential for the growth of inclusion clusters. The growth of such large clusters may therefore be more important in the removal of total oxygen from large volume steel melts, than is evidenced by this work.

In the case of the silicon deoxidised steel melts there is little evidence for clustering, and yet there is effective total oxygen removal from the melt. Silica is unusual in that the deoxidation products exist as liquid phase for a much greater period of time than in the cases of the other deoxidants. In the case of liquid deoxidation products collision will result in coalescence, irrespective of the interfacial energy, and result in rapid growth and elimination from the melt. The formation of a liquid deoxidation product must therefore be regarded as beneficial to the removal of total oxygen from the melt. Because silicon has a lower affinity for oxygen, it is less effective in reducing the surface energy of the system, and hence once solid silica is formed there is little inclination for clustering to occur.

Calcium-aluminium deoxidation initially resulted in the formation of an aluminium rich calcium aluminate, most probably $\text{CaO} \cdot 6\text{Al}_2\text{O}_3$. Calcium and aluminium in combination are capable of reducing the dissolved oxygen concentration to very low levels, producing a high interfacial energy system with a strong driving force for clustering. However, as deoxidation proceeded calcium rich layers formed on the surface of these particles by reduction of the alumina. The calcium ^uAl_uminate layers observed appeared to be liquid,

and this is to be expected from the phase equilibria diagram, Figure 4.40. The combination of high interfacial energy with an adhesive liquid oxide film coating the inclusions, would be expected to give the most conducive conditions for inclusion, and hence total oxygen, removal from the melt. This is clearly a desirable situation. The mechanisms by which this proceeds are complex, not fully understood, and warrant further investigation.

5.9 THE CRUCIBLE MELT INTERFACE

5.9.1 THE UNDEOXIDISED MELTS

The original annealed crucible material consisted of periclase (MgO) grains in a matrix of the silicates monticellite (CaO.MgO.SiO_2) and merwinite (3CaO.MgO.2SiO_2), Figure 5.33, with minor amounts of spinel ($\text{MgO.Al}_2\text{O}_3$), Figure 5.34. This phase constitution is consistent with the CaO:SiO₂ content of the material and the published phase equilibria. The silicates present would have given rise to a liquid phase at 1600°C, Figure 5.33.

After contact with undeoxidised steel at 1600°C, the periclase had absorbed quantities of iron and manganese oxides from the melt forming magnesio-mangano-wustite, as described in Section 4.7.2. The concentrations of Fe and Mn absorbed decreased with distance from the crucible-melt interface. Iron and manganese ions have similar ionic radii and the same charge as magnesium and will readily substitute into the periclase structure. The substitution of iron and manganese into the periclase is a solid state mass transfer process and would have been limited by the rate of diffusion, contact time and their concentration in the melt. The magnesio-mangano-wustite formed by this process would have remained solid at 1600°C, Figure 5.35.

The crucible material used in the vertical tube furnace melts had absorbed

iron and manganese to a greater depth than that used in the induction furnace melts, Plates 4.53 to 4.56. This is explained by the longer contact time between the liquid melt and the crucible material, enabling diffusion and solution to occur. The silicate phases and spinel had also absorbed some iron and manganese oxides, as described in Section 4.7.2.

5.9.2 SILICON DEOXIDISED MELTS

After deoxidation with silicon the concentration of silica at the crucible-melt interface increased. Two mechanisms are possible:-

1. direct reduction of FeO and MnO by silicon; and
2. capture and absorption of SiO₂ rich inclusions from the melt.

The FeO and MnO content of the refractory prior to deoxidation was not sufficient to justify the level of SiO₂ observed after deoxidation by a mechanism in which the oxides were reduced by silicon. Thus, the additional silica must be attributed to the capture and absorption of silica rich inclusions at the crucible-melt interface.

The silica had enriched the liquid silicate phases and had reacted with other components in the system forming a series of magnesium silicates, ranging in composition from forsterite (2MgO.SiO₂), and protoenstatite (MgO.SiO₂), Figure 5.36. The silicate fayalite (2FeO.SiO₂) was also formed. Fayalite is a relatively low melting point compound. This must be a remnant of the FeO-MnO captured from the melt prior to deoxidation, which has been partially reduced by silicon and/or captured SiO₂ from the melt.

5.9.3 CALCIUM-ALUMINIUM DEOXIDISED MELTS

The crucible material at the interface with the melt deoxidised with a calcium-aluminium addition contained a calcium silicate approaching the composition of di-calcium silicate ($2\text{CaO}\cdot\text{SiO}_2$), and the silicates monticellite ($\text{CaO}\cdot\text{MgO}\cdot\text{SiO}_2$) and merwinite ($3\text{CaO}\cdot\text{MgO}\cdot 2\text{SiO}_2$). There was considerably more merwinite present, Plate 4.67 to 4.68 compared with the annealed sample, Plate 4.51 to Plate 4.52. The lime had reacted with the monticellite at the crucible surface forming merwinite and further reaction formed di-calcium silicate, Figure 5.37. This is consistent with the effect that increasing $\text{CaO}:\text{SiO}_2$ ratio would have on the phase constitution of the system based on well established phase equilibria data. The magnesio-wustite and spinel does not appear to have been contaminated with calcium, however there was significantly more spinel compared with the annealed sample, inferring that Al_2O_3 had reacted with the MgO .

5.9.4 ALUMINIUM DEOXIDISED MELTS

Alumina reacted with the magnesia grains forming $\text{MgO}\cdot\text{Al}_2\text{O}_3$. Whilst much of this alumina would have originated from the absorption of Al_2O_3 rich inclusions from the melt, there was some evidence for reduction of FeO and MnO by aluminium. The crucible material at a depth of approximately $100\mu\text{m}$ exhibited a higher iron content compared with the crucible immediately adjacent to the crucible-melt interface, Plate 4.60. Also, iron rich globules were noted within the MgO grains, Plate 4.58, which can only have arisen from reduction of FeO by aluminium. The liquid silicate phases had absorbed high concentrations of alumina forming two phases on solidification: $\text{MgO}\cdot\text{Al}_2\text{O}_3$, Figure 5.38, and a calcium-aluminate phase, Figure 5.39.

5.9.5 TITANIUM DEOXIDISED MELTS

Ti₂O₃ had reacted with the magnesio-mangano-wustite grains forming MgO.Ti₂O₃ phase. The presence of iron rich globules, Plate 4.61, indicated that at least some of the titanium oxide had originated from the reduction of FeO and MnO. Titanium oxide had also reacted with the pre-existing liquid silicate phases, merwinite (3CaO.MgO.2SiO₂) and monticellite (CaO.MgO.SiO₂) forming a calcium-titanium oxide phase and protoenstatite (MgO.SiO₂), Plates 4.61 to 4.63.

5.8.6 ZIRCONIUM DEOXIDISED MELTS

The zirconium reacted with the FeO and MnO present in the magnesio-wustite phase, resulting in periclase contaminated with small amounts of ZrO₂. It appeared that the ZrO₂ originating from the melt had formed a layer on the surface of the crucible, Plate 4.70, with little tendency to penetrate further into the magnesia refractory. The particles of ZrO₂ in the surface layer were surrounded by a matrix of the silicate phases, monticellite and merwinite.

6. CONCLUSIONS

- ◆ Quantitative chemical and scanning electron microscopical techniques have been employed to investigate the deoxidation kinetics and oxidation product morphologies of low carbon steel melts.
- ◆ The deoxidation processes associated with five deoxidants, namely aluminium, titanium, silicon, zirconium and a calcium-aluminium alloy, have been investigated.
- ◆ The total oxygen concentrations of all melts rapidly decreased after the deoxidant addition, corresponding with a decrease in the size and number of inclusions observed, to a plateau level of total oxygen concentration and mean inclusion diameter.
- ◆ Steel samples removed prior to deoxidation exhibited only globular MnO-FeO inclusions.
- ◆ For single element deoxidants a distinct sequence of possible inclusion morphologies has been identified:
 - liquid globular;
 - solid spherical;
 - polyhedral;
 - dendritic;
 - coralline;
 - sintered agglomerates.
- ◆ The type of morphology and the terminal morphology depended on:
 - the dissolution characteristics of the deoxidant;

- the thermodynamic affinity of the deoxidant for oxygen in the melt;
 - the inclusion/melt interfacial energy characteristics;
 - the refractoriness of the oxidation products and intermediate compounds;
 - the degree of turbulence.
- ◆ Aluminium rapidly dispersed into the melt, has a high thermodynamic affinity for oxygen, producing a refractory reaction product with a high interfacial energy with the melt and exhibited all morphologies in the sequence.
 - ◆ Zirconium and titanium have high melting points and produce refractory oxides. Both formed spherical morphologies, but the higher interfacial energy between the titanium oxidation product and the melt prevented the growth of dendrites.
 - ◆ Silicon has a moderate affinity for oxygen and deoxidation proceeded by the reduction of the pre-existing inclusions leading to spherical silicates.
 - ◆ Deoxidation with the calcium-aluminium alloy involved a two stage process, in which the initial stage was dominated by the formation of aluminium rich solid oxides. Progressive reduction by calcium lead to the formation of a liquid calcium-aluminate coating, becoming increasingly rich in CaO with time.
 - ◆ The refractory crucible surface provided the most important site for the capture and removal of deoxidation products from the melt. Turbulence increased the probability of emergence at capture sites.

REFERENCES

1. **W.O. Philbrook:** International Metals Review 220, Sep. 1977, pp. 187-201.
2. **R. Kiessling and H. Nordberg:** Proc. Soviet-Swedish Symp. on Clean Steel. vol 1, Scandviken, Sweden, Mar. 1971, pp. 159-169.
3. **R. Kiessling:** Non-metallic Inclusions in Steel. Part 3, The Iron and Steel Institute, London, 1968.
4. **G.M.Faulring and S. Ramalingam:** Met. Trans. A, vol. 10, Nov. 1979, pp. 1781-1787.
5. **Metals Handbook.** 8th ed., vol 8, 304, 1973, Metals Park, Ohio, American Soc. for Metals.
6. **P.H. Lindon and J.C. Billington:** J.I.S.I., 207, 1969, pp340-347.
7. **R.J. Fruehan:** Met. Trans., 1970, vol. 1, pp. 2083-2088.
8. **R.J. Fruehan:** Met. Soc. AIME., 1969, vol. 245, pp. 1215-1219.
9. **G.K. Sigworth and J.F. Elliott:** Met. Trans., 1973, 4, pp. 105-113.
10. **G.K. Sigworth and J.F. Elliott:** Met. Sci., 1974, 8, pp. 298-310.
11. **R.J. Fruehan:** Met. Trans., 1970, vol. 1, pp. 3403-3410.
12. **D.C. Hilty and W. Crafts:** J. of Metals, 1950, 188, (2), Feb. pp. 414-423.
13. **C. Gatellier, A. Jacquemot and M. Olette:** IRSID RE 303. 1975 Electrochemical Soc. 247th Meeting, Toronto, 11-16 May 1975.
14. **T. Otanani:** Calcium Clean Steel, Materials Research and Engineering, 1981.
15. **W.J. Jackson and E.J. Ridal:** J. B.S.C.R.A., No 50, Dec 1959.
16. **D.C. Hilty and W. Crafts:** J. of Metals Trans. AIME, 1950, 188, (2), Feb., pp. 425-436.
17. **J. Andersson:** Proc. Soviet-Swedish Symp. on Clean Steel, vol. 1, Scandviken, Sweden, Mar 1971, pp. 100-110.

18. **P.E. Waudby and F.G. Wilson:** Proc. Inter. Symp. Met. Chem., Sheffield, 1971, pp. 195-197.
- 19 **H. Jager and W. Holzgruber:** *ibid.*, pp.198-201.
- 20 **W. Koch:** Stahl und Eisen., vol. 81, 1961, pp. 1592-1589.
- 21 **T. Kusakawa, Y. Watanabe and H. Okumura:** Proc. Inter. Conf. Science and Technology of Iron and Steel, Tokyo, Sep. 7-11 1970, I.S.I.J.
- 22 **A.L. Gueussier et al.:** Iron and Steel Engineer, Oct 1983, pp. 35-41.
- 23 **E.J. Dunn, D.W.P. Lynch and S.B. Gluck:** Electric Furnace Proceedings, 1976, pp. 248-253.
- 24 **J.J. deBarbadillo, F.G. Larson and S. Floreen:** *ibid.* pp. 222-229.
- 25 **BSC Technical Note.** FP/1/4/81/D.
- 26 **C. Gatellier and M. Olette:** Rev. Met., 1979, 76, pp. 377-386.
- 27 **A. Gokcen and J. Chipman:** AIME Trans., 1952, vol. 194, pp. 171-181.
- 28 **F. Patsiogiannis et al.:** EPD congress 1992, San Diego, California, pp. 885-897.
- 29 **E.T. Turkdogan:** J.I.S.I., Jan, 1972, pp. 21-36
- 30 **E.T. Turkdogan:** Arch. Eisenhüttenwes. 54, (1983), No 1, Jan, pp.1-10
- 31 **J.F. Elliott, M. Gleiser and V. Raunakuishna:** Thermochemistry for Steelmakers. vol. 2, 1963, Addison & Westly.
- 32 **E. Grethen and L. Phillippe:** Production and Application of Clean Steel, 23-26 Jun. 1970, pp. 29-34.
- 33 **J. Chipman:** Trans. Met. Soc. AIME., 1962, 224, pp. 1288-1289.
- 34 **A.M. Levin:** Izvst. VUZ Cher. Met., 1965, (12), pp. 13-21.
- 35 **C. Galellier et al.:** Rev. Met., 1969, 66, 10, pp. 673-693.
- 36 **A. F. Viskarev et al.:** Steel USSR, 1991, Oct, 20, (10), pp. 477-482.

- 37 **G. Forward and J.F. Elliott:** J. of Metals, May 1967, pp. 54-59.
- 38 **R. Becker:** Annal. Phys., 1938, (32), pp. 128-
- 39 **M. Volmer and A. Weber:** Z. Phys. Chem., 1925, (119), pp. 277-301.
- 40 **D. Turnbull and J. Fisher:** J. Chem. Phys., 1949, 17, pp. 71-73.
- 41 **M.L. Turpin and J.F. Elliott:** J.I.S.I., 1966, 204, pp. 217-225.
- 42 **B.G. Chernov:** Izvestiya Akademii Nauk SSSR Metally (Russian Metallurgy), No.6, 1987, pp. 37-39.
- 43 **E. Forster and H. Richer:** Arch Eisen., 1968, 39, (8), pp. 595-604.
- 44 **R.H. Parker:** Inclusions. Institution of Metallurgists, Monograph No.3, 1979, pp.1-12.
- 45 **L. von Bogdandy, W Meyer and I.N. Stranski:** Archiv Fur Das Eisenhüttenwesen., book 4, Apr. 1963, pp.235-241.
- 46 **H.U. Hopp:** Arch Eisenh., 1969, 40 (4), pp. 265-269.
- 47 **H. Schenck et al.:** Arch Eisen., 1970, 41, (2), pp. 131-138.
- 48 **K. Senda:** Trans. I.S.I.J., (7), 1967, pp. 136-147.
- 49 **N. Lindskog and H. Sandberg:** Scand. J. Met., 2, 1973, pp. 71-78.
- 50 **N. Lindskog:** Seminar in Process Met., Imperial College. Apr. 9, 1973.
- 51 **B. Kjellberg:** Seminar in Process Met., Imperial College. Apr. 9, 1973.
- 52 **M. Volmer:** Z. Electrochem., 1959, 35, pp. 555-
- 53 **D. Turnbull:** J. Chem. Phys., 1952, 20, pp. 411-424.
- 54 **M.G. Froberg & J. Potschke:** Freiburger Forschung 1969, B144, pp. 31-51.
- 55 **H. Straube, G. Kuhnelt and E. Plockinger:** Arch. Eisen., 1967, July, pp.509-518.
- 56 **M.V. Smoluchowski:** Physik. Z., 1916, 17, pp. 585-599.
- 57 **A. Nicholson and T. Gladman:** Iron and Steel Making, 1986, vol. 13,(2), pp. 53-69.

- 58 **U. Lindborg & K. Torssell:** Trans. AIME., 1968, (242), pp.94-102.
- 59 **G. W. Greenwood:** Acta. Met., 1956. vol.4, pp. 243-248.
- 60 **R.K. Iyengar and W.O. Philbrook:** Proc. International Conference Science and Technology of Iron and Steel. Tokyo, Sep 7-11, 1970, ISIJ.
- 61 **E.T. Turkdogan:** J.I.S.I., 1966, 204, (9), Sept. pp. 914-919.
- 62 **F.S. Ham:** J. Phys. Chem. Solids, 1958, 6, pp. 335-351.
- 63 **K. Torssell:** Proc. Soviet - Swedish Symp. on Clean Steel, vol. 1, pp. 88-99, Scandviken, Sweden, March 1971.
- 64 **R. Dvorsky:** Met. Mater. (Czech), 1988, 26, (6), pp. 383-387.
- 65 **C. Gatellier and M.Olette:** Proc. International Symp. Met. Chem Sheffield, 1971, pp. 191-194.
- 66 **Y. Miyashita, K. Nishikawa, T. Kawawa & M. Ohkubo:** 2nd Japan-USSR Symp. Phys. Chem. of Met. Processes. 1969.
- 67 **A.D.W. Hills and F.B. Pickering:** unpublished.
- 68 **J. Szekely:** Fluid Flow Phenomena in Metals Processing. Academic Press, 1979.
- 69 **K. Mukai, H. Tano, H. Sakao and K. Sano:** 2nd Japan-USSR Symp. Phys. Chem. of Met. Processes, 1969.
- 70 **P.V. Riboud and M. Olette:** Proc. 7th ICVM. 1982, Tokyo, Japan, pp. 879-889.
- 71 **P. Kozakevitch:** Surface Phenomena of Metals, SCI Monograph No. 28, 1968, pp. 223-245.
- 72 **E. Ruchenstein and R.K. Jain:** J. Chem. Soc. Faraday Trans., 2, 1974, pp. 132-147.
- 73 **P. Kozakevitch & M. Olette:** Prod. & Application of Clean Steels. 23-26 June, 1970.
- 74 **P. Kozakevitch & L.D. Lucas:** Revue de Metallurgie. Sep, 1968, 65, pp 589-598. BISI 6934.

- 75 **A. W. Cramb et al:** W Philbrook Memorial Sym. Proc. [Proc. Conf.], 1988, Apr., 17-20 Toronto, Canada, Iron and Steel Soc.pp. 259-271.
- 76 **H.A. Slowman and E.L. Evans:** J.I.S.I., May 1950, pp.81-90.
- 77 **T. Braun, J.F. Elliott and M.c. Flemings:** Met. Trans. B., vol. 10B June 1979, pp. 171-184.
- 78 **J. White:** Sintering and Related Phenomena, Proceedings of International Conference, June 1969, University of Notre Dame, Gordon and Breach, Science Publishers, 1967.
- 79 **S. Linder:** Scand. J. Met., 3, (4), 1974, pp.137-150.
- 80 **N. Lindskog and B. Kjellberg:** Scand. J. Met., 6, 1977, pp. 49-55.
- 81 **T.A. Engh and N. Lindskog:** Scand. J. Met., 4, 1975, pp. 49-58.
- 82 **N. Grevillius:** Jernkon Ann., 153, (1969), pp. 547-572.
- 83 **M. Olette and C. Galellier:** Report RE475, IRISID, Maizieres-les-Metz, France, Oct., 1977.
- 84 **A. Chojecki:** Metallurgia I ODLEWNICTWO, 1985, 11, 3, pp. 379-388.
- 85 **K. Nakanishi, E. Yokoyama and H. Ooi:** 2nd Japan-USSR Symp. Phys.-Chem. of Met. Processes, 1969, pp. 50-64.
- 86 **K. Nogi and K. Ogino:** Can. Met. Quart., 22, (1), 1983, pp. 19-28.
- 87 **K.Ogino, K. Nogi and O. Yamase:** Trans. ISIJ., March 1983, 23, (3), pp. 234-239.
- 88 **L.A. Luyckx:** Proc. Symp. on Deoxidation Practice with and without Ladle Metallurgy, Pittsburg, Apr., 1982, pp. 25-67.
- 89 **P. Coulombet and H. Gaye:** EUR 9428 FR.
- 90 **K. Suzuki, S. Banya & T. Fuwa:** Technical Note, 2nd Japan-USSR Symp. Phys-Chem of Met Processes 1969, pp. 64-65.
- 91 **S. K. Saxena:** Iron and Steelmaking, vol. 7, No. 6, 1980, pp. 281-287.
- 92 **F. Patisogiannia et al.** 76th Steelmaking Conf., Dallas, Iron and Steel Soc., 28-31 Mar., 1993, pp. 697-711.

- 93 **A. McLean:** J. of Metals, 1968, 20, No. 3, pp. 96-100.
- 94 **S. Watanabe, Y. Kaneko, A. Ohkawa & Y. Shiraishi:** International Conference on Physical Chemistry & Steelmaking, Versailles, Oct 1978, pp. 279.
- 95 **A. Adachi, N. Iwamoto & M. Ueda:** Trans ISIJ., 1966 (6), pp. 24-30.
- 96 **A.A. Vorob'ev & A.M. Levin:** Izv. VUZ Chern. Met. 1967, (12), pp.12-18.
- 97 **R. A. Rege, E. S. Szekeres & W. D. Forgeng:** Met Trans., AIMME, (1), 1970, pp. 26-52.
- 98 **S. N. Singh:** Met. Trans., 2 (1971), pp. 3248-3249.
- 99 **S. N. Singh:** Met. Trans., 5 (1974), pp. 2165-2178.
- 100 **S.W. Robinson, I.W. Martin and F.B. Pickering:** Metals Technology, May, 1979, pp. 157-169.
- 101 **K. Okohira, N. Sato & H. Mori:** Trans. ISIJ., 1974, 14, pp. 102-109.
- 102 **H. Ooi, T. Sekine & G. Kasai:** Trans ISIJ., 1975, 15, pp. 371-379.
- 103 **E. Steinmetz:** Arch. Eissenhuttenwes., 1977, 48, (11), pp.569-574. BISI Trans. 16510.
- 104 **P. E. Waudby & W. J. Salter:** JISI., 1971, 209, pp. 518-522.
- 105 **P.E. Waudby:** Inclusions. Institution of Metallurgists, Monograph No. 3, 1979, pp.13-28.
- 106 **A. Muan and E.F. Osborn:** Phase Equilibria Among Oxides in Steelmaking, Addison-Westly, 1965.
- 107 **Phase Diagrams For Ceramists:** E.M. Levin et al., The American Ceramic Society, 1964.
- 108 **E. Foster:** Arch. Eissenhuttenwes., 1969, (38), July, pp. 607-
- 109 **E. Plockinger:** I.S.I. Special Report 77, 1962, pp. 51-56.
- 110 **A. S. Venkatadri:** Trans. ISIJ., 1978, pp. 591-600.
- 111 **A. Choudhury & M. Wahlster:** Rheinstahl-Technic., 1966, 4, pp. 111-121.

- 112 **W. Tiekink et al.:** Clean Steel 4, Proc. III, Balatonsze plak, Hungrey, 1992, pp. 704-717.
- 113 **D. Elwell & H. J. Scheel:** Crystal Growth from High Temperature Solutions. Academic Press. 1975. London.
- 114 **R. F. Strickland-Constable:** Kinetics and Mechanisms of Crytallisation. Academic Press. 1968.
- 115 **H. Dormus:** Rates of Phase Transformation. Academic Press. 1985.
- 116 **D. D. Saratovkin:** Dendritic ChrySTALLISATION. Consultant Bureau Inc., New York. 1959.
- 117 **I. W. Martin:** Sheffield Polytechic. 1977. Unpublished.
- 118 **D. Sponseller & R. A. Flinn:** Trans., AIME., 1964, 230, pp. 876-888.
- 119 **D. C. Hilty & V. T. Popp:** Electr. Furnace Proc., 1969, 27, pp. 52-66.
- 120 **D. C. Hilty & W. Crafts:** Electr. Furnace Proc., 1953, 11, pp. 121-150.
- 121 **F. B. Pickering:** Inclusions and their Effect on Steel Properties, Leeds University, Sept., 1974.
- 122 **T. Ototani & Y. Kataura:** Trans. Jisi, 1972, 12, pp. 334.
- 123 **F. C. Hackett & J. McIver:** Electr. Furnace Proc., 19971, 29, pp. 117-121.
- 124 **E. J. Dunn:** Electr. Furnace Proc., 1971, 29, pp. 122.
- 125 **K. Asana & T. Nakano:** Tetsu to Hagane, 1971, pp. 1943-1952, BISI Trans., 10704.
- 126 **R. Kiessling & N. Lange:** Non Metallic Inclusions in Steel. Part I
- 127 **H. A. Slowman & E. L. Evans:** JISI, Nov., 1952, pp. 296-300.
- 128 **K. Torssell:** Jerkon Annaler. 1967, 151, pp. 890-949.
- 129 **C. A. Zapffe & C. E. Sims:** Trans AIMME. 1950, 188, pp. 425-436.
- 130 **F. B. Pickering:** Some effects of NMI on the Properties of Steel. Oct., 1989.

- 131 **F. B. Pickering:** Inclusions. Institution of Metallurgists, Monograph 3, 1979.
- 132 **F. B. Pickering:** Jerkon Annaler. 1964, 148, pp. 840-872.
- 133 **A. L. Kundu, K. M. Gupt & P. Krishna Rao:** Met Trans B, vol 20B, Oct., 1989, pp. 581-594.
- 134 **N. Aritomi & K Gunji:** Trans ISIJ, vol 19, 1979, pp. 152-161.
- 135 **N. Aritomi & K Gunji:** Trans ISIJ, vol 20, 1980, pp. 26-31.
- 136 **G. F. Comstock:** Titanium in Iron and Steel. Alloys of Iron Research Monograph Series. J Wiley. 1955.
- 137 **D. Janke & W. Fisher:** Arch. Eissenhuttenwes. 47, 1976, No 4, pp. 195-198.
- 138 **E. L. Evans & H. A. Slowman:** JISI 1953, 174, pp. 318-324.
- 139 **K. Suzuki & K. Sanbongi:** 2nd Japan-USSR Symposium on the Physical Chemistry of Met. Process. 1969, pp.23-37.
- 140 **H. Chino, Y. Nakanura, E. Tsunetome & K. Segawa:** Trans. ISIJ. vol 6, 1966, pp.167-173.
- 141 **S. Ogibayashi et al.:** Proc. 6th International Iron and Steel Congress, 1990, Nagaya, ISIJ pp. 612-617.
- 142 **F. B. Pickering:** JISI, vol 181, Oct., 1955. pp. 147-148.
- 143 **R. Kiessling & N. Lange:** Non Metallic Inclusions in Steel. Part II.
- 144 **R. A. Grange et al.:** Boron, Calcium, Columbium and Zirconium in Iron and Steel. Alloys of Iron Monograph. J Wiley and Son. 1957.
- 145 **R. J. Frueham:** Met Trans. (5), 1974, pp. 345-347.
- 146 **T.S. Harrison and S.A. Marshall:** Steel Times, Sep.,1970, pp. 629-638.
- 147 **F.B. Pickering:** The Basis of Quantitative Metallography, Institute of Metallurgical Technicians, Monograph No. 1, 1976.
- 148 **P.G. Goodhew:** Electron Microscopy and Analysis, Wykeham Science Series, 1975.

- 149 **D. P. Wilcox:** Sheffield Hallam University. 1993. (Unpublished).
- 150 **Metals reference book:** ed. C. J. Smithells, 5th ed. Butterworths, 1976.

Table 2.1 Examples of deoxidation products for liquid iron saturated with the respective oxides.

Deoxidant	Oxide	$K_{1600^{\circ}\text{C}}$	Reference
Aluminium	Al_2O_3	2.9×10^{-9}	12
	Al_2O_3	5.6×10^{-14}	11
	Al_2O_3	1.2×10^{-13}	26
Silicon	SiO_2	2.8×10^{-5}	27
Zirconium	ZrO_2	1.1×10^{-10}	13
Boron	B_2O_3	1.5×10^{-8}	7

Table 2.2 Examples of the interfacial energies for liquid iron and deoxidation products.

System	Interfacial Energy ($\text{J}\cdot\text{m}^{-2}$)
Fe-FeO	0.2-0.3
Fe- SiO_2	1.2-1.3
Fe- Al_2O_3	2.4
Fe- $\text{Al}_2\text{O}_3\cdot\text{FeO}$	1.6-1.8

Table 2.3 Supersaturation values necessary for homogeneous nucleation.

Element	Product	K_S'/K_S	Reference
Zr	ZrO_2	4.0×10^8	45
Al	Al_2O_3	10^4 - 10^7	43,46,47
Ti	TiO_2	10^3	46
Fe	FeO	1.5	37
Fe,Al	$\text{FeO}\cdot\text{Al}_2\text{O}_3$	10^7 - 10^{11}	37
Si	SiO_2	10^2 - 10^3	37

Table 2.4 Contact angles, θ , between solid oxides and liquid steel. ^{73,74,75}

Oxide	Temperature (°C)	θ
Al ₂ O ₃	1600	141
SiO ₂	1600	115
CaO	1600	132
TiO ₂	1600	84
Cr ₂ O ₃	1600	88
CaO-Al ₂ O ₃ (36/64)	1600	65
CaO-Al ₂ O ₃ (50/50)	1600	58
CaO-Al ₂ O ₃ (58/42)	1600	54
ZrO ₂	1550	122

Table 3.1(a) The refractory materials used in the experiments.

Description	Magnesia Crucibles				
Supplier	Willans Metals Ltd				
composition mass%	MgO	Al ₂ O ₃	SiO ₂	Fe ₂ O ₃	CaO
	87.80	4.00	4.00	0.12	4.00
Dimensions (mm)	length	external diameter		internal diameter	
	125	55		45	

Description	Al-Sint (Sintered Alumina Refractory Tubes)	
Supplier	Anderman & Co Ltd	
composition mass%	Al ₂ O ₃	
	99.7	
Dimensions (mm)	various	

Description	Quartz Sample Tubes	
Supplier	Algams Ltd	
composition mass%	SiO ₂	
	100.00	
Dimensions (mm)	length	internal diameter
	1000	3.0

Table 3.1 (b) Gas shroud used in the experiments.

Description	Argon gas		
Supplier	BOC		
composition	Argon	99.998 vol%	min
	Moisture	3vpm	max
	Oxygen	3vpm	max
	Hydrocarbons	1vpm	max
	Nitrogen	8vpm	max

Table 3.2 The Pyrox Vertical Tube Furnace heating schedule.

Temperature °C	Time (hours)
25	
	2
300	
	3
600	
	3
900	
	3
1200	
	5
1600	
	1.5
1600	
	8
25	

Table 3.3 The metals and alloys used as deoxidants in the experiments.

Description	Aluminium (commercially pure)
Supplier	BOC
composition mass%	Al
	99.9

Description	Zirconium (commercially pure)
Supplier	unknown
composition mass%	Zr
	99.9

Description	Titanium (commercially pure)
Supplier	IMI Kynock
composition mass%	Ti
	99.9

Description	Silicon
Supplier	London & Scandinavia Ltd
composition mass%	Si Al
	98.6 0.68

Description	Calcium-Aluminium
Supplier	Swinden Labs
composition mass%	Al Ca Si Fe Ba Zn
	87.48 10.3 0.78 1.28 <0.01 0.16

Table 3.4 The critical excitation energies of selected elements.

Element	Atomic Number	Atomic Weight	Critical Excitation Energy (kV)	
			K Series	L Series
H	1	1.01	0.0136	
He	2	4.00	0.0246	
C	6	12.01	0.283	
N	7	14.01	0.399	
O	8	16.00	0.431	
Mg	12	24.32	1.303	0.049
Al	13	26.97	1.559	0.072
Si	14	28.06	1.838	0.098
S	16	32.01	2.470	0.163
Ca	20	40.08	4.038	0.349
Ti	22	47.90	4.964	0.454
Cr	24	52.01	5.988	0.574
Mn	25	54.93	6.537	0.639
Fe	26	55.85	7.111	0.708
Ni	28	58.69	8.331	0.853
Cu	29	63.54	8.980	0.933
Zn	30	65.38	9.660	1.022
Zr	40	91.22	17.998	2.220
Mo	42	95.95	20.002	2.523
Pd	46	106.70	24.347	3.172
Te	52	127.61	31.809	4.341
La	57	138.92	38.931	5.489
Ce	58	140.13	40.449	5.729
Hf	72	178.60	65.313	9.556
Ta	73	180.83	67.400	9.876
Au	79	197.20	80.713	11.919
Pb	82	207.21	88.001	13.044

Sample	C	Mn	Si	S	P	Ni	Cr	Mo	Cu	V	Sn	Ti	Al	Mg	Zr
Base Steel	0.010	0.220	<0.015	0.001	<0.0015	0.050	0.040	0.02	0.026	0.011	<0.0015	<0.005	0.0130	0.006	<0.0010
Aluminium VT	<0.010	0.150	0.075	<0.001	<0.0015	0.050	0.040	0.02	0.030	0.012	0.0015	<0.005	0.0060	0.006	<0.0010
Aluminium HF	<0.010	0.155	0.057	<0.001	<0.0015	0.060	0.040	0.02	0.025	0.011	0.0020	<0.005	0.0200	0.008	<0.0010
Silicon VT	<0.010	0.145	0.205	0.008	0.0020	0.075	0.045	0.02	0.026	0.013	0.0015	<0.005	0.0030	0.007	0.0010
Silicon HF	<0.010	0.135	0.190	0.002	0.0015	0.020	0.030	<0.01	0.025	0.010	<0.0015	<0.005	0.0050	0.007	<0.0010
Titanium VF	0.015	0.155	0.125	0.001	<0.0015	0.060	0.045	0.02	0.030	0.013	0.0025	0.034	<0.0015	0.008	0.0015
Titanium HF	<0.010	0.140	0.035	0.003	<0.0015	0.060	0.040	0.02	0.030	0.011	0.0020	0.007	<0.0015	0.008	0.0010
Zirconium VF	<0.010	0.160	0.230	0.003	<0.0015	0.060	0.040	0.02	0.035	0.034	0.0025	<0.005	0.0110	0.010	0.0050
Zirconium HF	<0.010	0.140	0.145	0.002	0.0015	0.020	0.030	<0.01	0.025	0.010	<0.0015	<0.005	0.0015	0.008	0.0010
Ca-Al VF	<0.010	0.160	0.100	<0.001	<0.0015	0.020	0.035	<0.01	0.030	0.010	<0.0015	<0.005	0.0015	0.002	<0.0010
Ca-Al HF	<0.010	0.135	0.050	0.002	<0.0015	0.020	0.030	<0.01	0.020	0.010	<0.0015	<0.005	0.0270	0.011	<0.0010
* VF	<0.010	0.070	<0.015	0.002	<0.0015	0.020	0.020	<0.01	0.025	0.010	<0.0015	<0.005	<0.0015	0.022	<0.0010
* HF	<0.010	0.095	<0.015	0.003	0.0015	0.020	0.035	<0.01	0.025	0.010	<0.0015	<0.005	0.0030	0.005	<0.0010

Table 4.1 Chemical Composition of Steel Charge and Residual Deoxidised Melts (ARL 29500/Spark Emission Spectroscopy & Thermo-Jarrel Ash ICPA 9000).

VT = Vertical Tube Furnace

HF = High Frequency Furnace

* = Indicates composition of steel melted in the respective furnace but not deoxidised.

TABLE 4.2. Results of Oxygen Analysis for Vertical Tube Furnace Melt Deoxidised with 0.3 mass% Aluminium Addition (LECO).

Time (Seconds)	Total Oxygen Content (mass%)			Average
	Analysis			
	1	2	3	
0	.0410	.0420		.0415
12	.0410	.0410		.0410
22	.0310	.0310		.0310
34	.0270	.0420		.0345
43	.0270	.0260		.0265
55	.0200	.0110		.0195
67	.0190	.0330		.0260
96	.0270	.0160		.0215
113	.0140	.0230		.0185
156	.0170	.0150		.0160
185	.0085	.0071	.0100	.0085
240	.0064	.0074	.0068	.0068
314	.0250	.0170		.0210
453	.0054	.0051		.0053
607	.0059	.0097	.0072	.0076
946	.0046	.0061	.0050	.0052
1203	.0059	.0041	.0059	.0053

Table 4.3 Mean Diameter of Inclusions in the Vertical Tube Furnace Melt Deoxidised with 0.3 mass% Aluminium Addition, (Jeol 840 SEM/Digiscan)

Time seconds	Particle count	Mean Diameter (μm)	Minimum Size Band		Maximum Size Band	
			Range	Mean	Range	Mean
12	137	0.643	0 - 0.5	0.334	1.5 - 2.0	1.537
22	95	0.968	0 - 0.5	0.301	3.5 - 4.0	3.713
34	65	1.006	0 - 0.5	0.329	2.0 - 2.5	2.367
43	110	1.165	0 - 0.5	0.375	3.5 - 4.0	3.566
55	30	1.291	0 - 0.5	0.335	1.5 - 2.0	1.607
96	11	1.239	0.5 - 1.0	0.561	1.5 - 2.0	1.976
113	7	1.598	0 - 0.5	0.251	2.5 - 3.0	2.534
131	8	1.482	0 - 0.5	0.307	2.0 - 2.5	2.313
156	5	0.874	0 - 0.5	0.307	1.5 - 2.0	1.526
185	6	1.351	0 - 0.5	0.435	2.0 - 2.5	2.054
240	4	0.803	0 - 0.5	0.355	1.0 - 1.5	1.094

Table 4.4 (a) Chemical Composition of Selected Alumina Inclusions in the Sample taken 12 Seconds after Deoxidation in the Vertical Tube Furnace Melt, (Phillips PSEM/EDX).

Oxide Mass %			
Al ₂ O ₃	SiO ₂	MgO	CaO
96.82	0.00	0.00	3.19
100.00	0.00	0.00	0.00
100.00	0.00	0.00	0.00
99.90	0.00	0.00	0.12

Table 4.4 (b) Chemical Composition of Selected Alumina Inclusions in the Sample taken 22 Seconds after Deoxidation in the Vertical Tube Furnace Melt, (Phillips PSEM/EDX).

Oxide Mass %			
Al ₂ O ₃	SiO ₂	MgO	CaO
98.04	0.00	0.00	1.98
93.09	1.88	0.21	4.83
100.00	0.00	0.00	0.00
99.28	0.00	0.00	0.74
99.09	0.00	0.00	0.93
99.98	0.20	0.00	0.00

Table 4.4 (c) Chemical Composition of Selected Alumina Inclusions in the Sample taken 34 Seconds after Deoxidation in the Vertical Tube Furnace Melt, (Phillips PSEM/EDX).

Oxide Mass %			
Al ₂ O ₃	SiO ₂	MgO	CaO
98.57	0.00	0.00	1.45
100.00	0.00	0.00	0.00
92.93	0.00	0.00	7.08
98.54	0.00	0.00	1.48
100.00	0.00	0.00	0.00
97.43	0.00	0.00	2.40

Table 4.4 (d) Chemical Composition of Selected Alumina Inclusions in the Sample taken 43 Seconds after Deoxidation in the Vertical Tube Furnace Melt, (Phillips PSEM/EDX).

Oxide Mass %			
Al ₂ O ₃	SiO ₂	MgO	CaO
93.70	0.00	0.00	6.32
86.43	0.03	0.00	13.55
89.58	0.00	0.62	9.81
88.81	0.08	0.00	11.12
87.65	0.00	0.00	12.36
76.70	1.41	0.00	21.89

Table 4.4 (e) Chemical Composition of Selected Alumina Inclusions in the Sample taken 55 Seconds after Deoxidation in the Vertical Tube Furnace Melt, (Phillips PSEM/EDX).

Oxide Mass %			
Al ₂ O ₃	SiO ₂	MgO	CaO
96.94	0.00	0.00	3.08
99.02	0.00	0.04	0.77
96.34	0.00	0.00	3.67
97.35	0.00	0.58	2.61
96.62	0.00	0.00	3.40

Table 4.4 (f) Chemical Composition of Selected Alumina Inclusions in the Sample taken 96 Seconds after Deoxidation in the Vertical Tube Furnace Melt, (Phillips PSEM/EDX).

Oxide Mass %			
Al ₂ O ₃	SiO ₂	MgO	CaO
98.05	0.00	0.00	1.93
95.31	0.00	2.53	2.17
96.51	0.08	0.08	3.35
97.79	0.00	0.00	2.22
100.00	0.00	0.00	0.00
97.83	0.10	0.00	2.08

Table 4.4 (g) Chemical Composition of Selected Alumina Inclusions in the Sample taken 113 Seconds after Deoxidation in the Vertical Tube Furnace Melt, (Phillips PSEM/EDX).

Oxide Mass %			
Al ₂ O ₃	SiO ₂	MgO	CaO
99.14	0.00	0.00	0.88
99.43	0.00	0.00	0.59
99.07	0.00	0.00	0.95
100.00	0.00	0.00	0.00

Table 4.4 (h) Chemical Composition of Selected Alumina Inclusions in the Sample taken 131 Seconds after Deoxidation in the Vertical Tube Furnace Melt, (Phillips PSEM/EDX).

Oxide Mass %			
Al ₂ O ₃	SiO ₂	MgO	CaO
98.23	0.00	0.00	1.62
100.00	0.00	0.00	0.00
100.00	0.00	0.00	0.00
99.94	0.07	0.00	0.00

Table 4.4 (i) Chemical Composition of Selected Alumina Inclusions in the Sample taken 156 Seconds after Deoxidation in the Vertical Tube Furnace Melt, (Phillips PSEM/EDX).

Oxide Mass %			
Al ₂ O ₃	SiO ₂	MgO	CaO
100.00	0.00	0.00	0.00
99.98	0.02	0.00	0.00

Table 4.4 (j) Chemical Composition of Selected Alumina Inclusions in the Sample taken 185 Seconds after Deoxidation in the Vertical Tube Furnace Melt, (Phillips PSEM/EDX).

Oxide Mass %			
Al ₂ O ₃	SiO ₂	MgO	CaO
98.90	0.00	0.00	1.11
97.88	0.00	0.00	2.13

Table 4.4 (k) Chemical Composition of Selected Alumina Inclusions in the Sample taken 240 Seconds after Deoxidation in the Vertical Tube Furnace Melt, (Phillips PSEM/EDX).

Oxide Mass %			
Al ₂ O ₃	SiO ₂	MgO	CaO
99.95	0.00	0.00	0.07
99.60	0.04	0.39	0.00

TABLE 4.5. Results of Oxygen Analysis for High Frequency Furnace Melt Deoxidised

with 0.3 mass% Aluminium Addition (LECO).

Time (Seconds)	Total Oxygen Content (mass%)			Average
	Analysis			
	1	2	3	
0	.038	.038		
3	.030	.028		.029
21	.013	.018	.015	.0153
33	.0093	.014	.011	.0114
46	.0076	.0090	.0085	.00837
56	.0074	.015	.011	.0111
65	.0065	.0060		.00625
75	.0051	.0054		.00525
83	.0046	.0049		.00475
93	.0044	.0042		.00430
104	.0046	.0023	.0066	.00460
116	.0036	.0032		.00335
139	.0031	.0030		.00305
165	.002 ³	.0015	.0024	.00207
195	.0027	.0027		.00270
225	.0027	.0039	.0026	.00307
255	.0029	.0030		.00295
300	.0024	.0023		.00235
420	.0022	.0023		.00225
540	.0013	.0015		.00140
846	.0024	.0016	.0018	.00193
1145	.0019	.0019		.00190

Table 4.6 Mean Diameter of Inclusions in the High Frequency Furnace Melt Deoxidised with 0.3 mass% Aluminium Addition, (Jeol 840 SEM/Digiscan)

Time seconds	Particle counts	Mean Diameter (μm)	Minimum Size Band (μm)		Maximum Size Band (μm)		95% Confidence Limit
			Range	Mean	Range	Mean	
3	134	0.566	0.0 - 0.5	0.118	2.5 - 3.0	2.663	0.091
11	80	0.923	0.0 - 0.5	0.110	3.0 - 3.5	3.172	0.129
21	46	0.657	0.0 - 0.5	0.110	1.5 - 2.0	1.978	0.141
33	52	0.700	0.0 - 0.5	0.118	2.0 - 2.5	2.382	0.187
46	21	0.953	0.0 - 0.5	0.118	2.0 - 2.5	2.419	0.283
65	14	1.023	0.0 - 0.5	0.127	2.0 - 2.5	2.415	0.316
75	9	1.432	0.5 - 1.0	0.647	2.5 - 3.0	2.600	0.349
83	12	1.418	0.0 - 0.5	0.361	2.5 - 3.0	2.986	0.417
93	3	1.112	0.5 - 1.0	0.587	1.5 - 2.0	1.817	0.598
104	4	1.195	0.0 - 0.5	0.427	1.5 - 2.0	1.999	0.619
139	11	0.910	0.0 - 0.5	0.141	2.0 - 2.5	2.176	0.419
165	2	1.102	1.0 - 1.5	1.060	1.5 - 2.0	1.145	0.061
225	4	0.665	0.0 - 0.5	0.210	1.5 - 2.0	1.172	0.392
255	2	0.533	0.0 - 0.5	0.456	0.5 - 1.0	0.610	0.109

Table 4.7 (a) Chemical Composition of Selected Alumina Inclusions in the Sample taken 3 Seconds after Deoxidation in the High Frequency Furnace Melt, (Phillips PSEM/EDX).

Oxide Mass %			
Al_2O_3	SiO_2	MgO	CaO
98.05	0.00	0.24	1.73
93.81	0.00	0.58	5.62
99.44	0.00	0.57	0.01
99.69	0.00	0.33	0.00
99.60	0.00	0.42	0.00
99.85	0.00	0.16	0.00
87.93	0.09	0.16	11.83
99.58	0.00	0.44	0.00
89.72	0.16	0.13	10.00

Table 4.7 (b) Chemical Composition of Selected Alumina Inclusions in the Sample taken 11 Seconds after Deoxidation in the High Frequency Furnace Melt, (Phillips PSEM/EDX).

Oxide Mass %			
Al ₂ O ₃	SiO ₂	MgO	CaO
99.75	0.00	0.26	0.00
92.66	0.00	0.00	7.35
99.66	0.00	0.36	0.00
99.68	0.00	0.36	0.00
99.40	0.00	0.62	0.00
99.75	0.00	0.27	0.00
99.18	0.00	0.39	0.44
99.73	0.00	0.29	0.00

Table 4.7 (c) Chemical Composition of Selected Alumina Inclusions in the Sample taken 21 Seconds after Deoxidation in the High Frequency Furnace Melt, (Phillips PSEM/EDX).

Oxide Mass %			
Al ₂ O ₃	SiO ₂	MgO	CaO
89.36	0.00	0.52	10.13
99.70	0.00	0.32	0.00
95.72	0.00	0.30	3.99
98.28	0.00	0.59	1.14
98.99	0.00	1.03	0.00
99.86	0.00	0.16	0.00
91.38	0.00	1.06	7.57

Table 4.7 (d) Chemical Composition of Selected Alumina Inclusions in the Sample taken 33 Seconds after Deoxidation in the High Frequency Furnace Melt, (Phillips PSEM/EDX).

Oxide Mass %			
Al ₂ O ₃	SiO ₂	MgO	CaO
99.64	0.00	0.38	0.00
94.95	0.00	0.58	4.48
99.34	0.00	0.26	0.42
98.11	0.00	0.71	1.20
99.58	0.00	0.44	0.00
95.37	0.00	0.97	3.67
99.90	0.00	0.12	0.00

Table 4.7 (e) Chemical Composition of Selected Alumina Inclusions in the Sample taken 46 Seconds after Deoxidation in the High Frequency Furnace Melt, (Phillips PSEM/EDX).

Oxide Mass %			
Al ₂ O ₃	SiO ₂	MgO	CaO
99.25	0.00	0.76	0.00
99.69	0.00	0.11	0.21
94.04	0.00	0.52	5.44
95.49	0.00	1.07	3.46
98.95	0.00	1.05	0.00
96.21	0.00	0.47	3.33
95.22	0.00	0.09	4.71
96.29	0.00	0.91	2.81

Table 4.7 (f) Chemical Composition of Selected Alumina Inclusions in the Sample taken 56 Seconds after Deoxidation in the High Frequency Furnace Melt, (Phillips PSEM/EDX).

Oxide Mass %			
Al ₂ O ₃	SiO ₂	MgO	CaO
97.84	0.00	0.00	2.18
100.00	0.00	0.00	0.00
99.71	0.11	0.20	0.00
100.00	0.00	0.00	0.00
99.18	0.02	0.82	0.00
95.31	0.00	0.00	4.70

Table 4.7 (g) Chemical Composition of Selected Alumina Inclusions in the Sample taken 65 Seconds after Deoxidation in the High Frequency Furnace Melt, (Phillips PSEM/EDX).

Oxide Mass %			
Al ₂ O ₃	SiO ₂	MgO	CaO
99.61	0.00	0.41	0.00
98.51	0.00	0.00	1.51
100.00	0.00	0.00	0.00
99.69	0.00	0.00	0.33
95.94	0.00	0.00	4.07
99.36	0.00	0.00	0.66

Table 4.7 (h) Chemical Composition of Selected Alumina Inclusions in the Sample taken 75 Seconds after Deoxidation in the High Frequency Furnace Melt, (Phillips PSEM/EDX).

Oxide Mass %			
Al ₂ O ₃	SiO ₂	MgO	CaO
97.50	0.00	0.53	1.99
100.00	0.00	0.00	0.00
100.00	0.00	0.00	0.00
99.82	0.00	0.20	0.00
97.96	0.00	0.04	2.01
100.00	0.00	0.00	0.00

Table 4.7 (i) Chemical Composition of Selected Alumina Inclusions in the Sample taken 83 Seconds after Deoxidation in the High Frequency Furnace Melt, (Phillips PSEM/EDX).

Oxide Mass %			
Al ₂ O ₃	SiO ₂	MgO	CaO
100.00	0.00	0.00	0.00
99.79	0.00	0.23	0.00
99.81	0.00	0.21	0.00
98.69	0.00	0.00	1.32

Table 4.7 (j) Chemical Composition of Selected Alumina Inclusions in the Sample taken 93 Seconds after Deoxidation in the High Frequency Furnace Melt, (Phillips PSEM/EDX).

Oxide Mass %			
Al ₂ O ₃	SiO ₂	MgO	CaO
98.24	0.00	0.00	1.78
99.23	0.00	0.79	0.00
99.26	0.00	0.25	0.51
94.19	0.00	2.25	3.57

Table 4.8 Results of Oxygen Analysis for Vertical Tube Furnace Melt Deoxidised with 0.53 mass% Titanium Addition (LECO).

Time seconds	Total oxygen Content (mass%)			
	Analysis			Average
	1	2	3	
0	.054	.052		.05300
34	.044	.046		.04500
45	.025	.031	.027	.02770
58	.024	.023		.02350
85	.015	.015		.01500
100	.014	.016		.01500
134	.012	.013		.01250
156	.012	.013		.01250
187	.010	.011		.01050
252	.0095	.0092		.00935
307	.0087	.0110	.0084	.00855
458	.0077	.0082		.00795
606	.0072	.0073		.00725
901	.0066	.0069		.00675
1208	.0052	.0052		.00520

Table 4.9 Mean Diameter of Inclusions in the Vertical Tube Furnace Melt Deoxidised with 0.53 mass% Titanium Addition, (Jeol 840 SEM/Digiscan)

Time seconds	Particle counts	Mean Diameter (μm)	Minimum Size Band (μm)		Maximum Size Band (μm)	
			Range	Mean	Range	Mean
34	34	1.582	0.0 - 0.5	0.260	3.5 - 4.0	3.797
45	36	1.280	0.0 - 0.5	0.291	3.5 - 4.0	3.531
58	40	1.760	0.0 - 0.5	0.242	4.0 - 4.5	4.288
85	15	2.059	0.0 - 0.5	0.355	3.0 - 3.5	3.262
100	13	1.399	0.0 - 0.5	0.217	2.0 - 2.5	2.272
134	20	1.105	0.0 - 0.5	0.307	2.5 - 3.0	2.915
156	20	0.707	0.0 - 0.5	0.335	1.5 - 2.0	1.809
187	30	0.811	0.0 - 0.5	0.251	1.5 - 2.0	1.984
250	21	1.039	0.0 - 0.5	0.300	3.5 - 4.0	3.688

Table 4.10 (a) Chemical Composition of Selected Titania Inclusions in the Sample taken 34 Seconds after Deoxidation in the Vertical Tube Furnace Melt, (Phillips PSEM/EDX).

Oxide mass%				
Ti ₂ O ₃	Al ₂ O ₃	MgO	CaO	SiO ₂
97.10	0.11	0.05	2.32	0.44
99.32	0.00	0.00	0.35	0.34
98.62	0.26	0.63	0.18	0.32
99.67	0.06	0.03	0.00	0.25
97.05	0.25	0.03	2.18	0.50
98.93	0.01	0.00	0.71	0.34
99.87	0.00	0.00	0.00	0.15
99.60	0.06	0.00	0.00	0.35
96.56	0.38	0.14	2.49	0.44
94.79	0.26	0.19	4.57	0.30

Table 4.10 (b) Chemical Composition of Selected Titania Inclusions in the Sample taken 45 Seconds after Deoxidation in the Vertical Tube Furnace Melt, (Phillips PSEM/EDX).

Oxide mass%				
Ti ₂ O ₃	Al ₂ O ₃	MgO	CaO	SiO ₂
98.61	0.05	0.00	0.91	0.44
97.86	0.00	0.20	1.72	0.23
99.47	0.20	0.10	0.00	0.25
99.54	0.17	0.00	0.00	0.30
97.77	0.14	0.50	1.27	0.33
98.45	0.02	0.24	1.06	0.25

Table 4.10 (c) Chemical Composition of Selected Titania Inclusions in the Sample taken 58 Seconds after Deoxidation in the Vertical Tube Furnace Melt, (Phillips PSEM/EDX).

Oxide mass%				
Ti ₂ O ₃	Al ₂ O ₃	MgO	CaO	SiO ₂
95.84	0.13	0.00	3.67	0.37
97.68	0.02	0.23	1.76	0.32
96.96	0.19	0.06	2.50	0.31
98.13	0.11	0.00	1.40	0.37
98.18	0.18	0.18	1.09	0.40
99.38	0.13	0.16	0.00	0.35
99.46	0.12	0.08	0.00	0.35

Table 4.10 (d) Chemical Composition of Selected Titania Inclusions in the Sample taken 85 Seconds after Deoxidation in the Vertical Tube Furnace Melt, (Phillips PSEM/EDX).

Oxide mass%				
Ti ₂ O ₃	Al ₂ O ₃	MgO	CaO	SiO ₂
93.68	0.11	0.21	5.62	0.39
99.02	0.17	0.27	0.00	0.55
94.68	0.16	0.18	4.66	0.34
97.84	0.00	0.32	1.51	0.35
95.71	0.18	0.12	3.51	0.49
94.64	0.18	0.13	4.54	0.52

Table 4.10 (e) Chemical Composition of Selected Titania Inclusions in the Sample taken 100 Seconds after Deoxidation in the Vertical Tube Furnace Melt, (Phillips PSEM/EDX).

Oxide mass%				
Ti ₂ O ₃	Al ₂ O ₃	MgO	CaO	SiO ₂
99.40	0.18	0.00	0.00	0.44
95.70	0.00	0.14	3.97	0.19
96.86	0.13	0.12	2.76	0.16
97.21	0.21	0.12	2.06	0.41

Table 4.10 (f) Chemical Composition of Selected Titania Inclusions in the Sample taken 134 Seconds after Deoxidation in the Vertical Tube Furnace Melt, (Phillips PSEM/EDX).

Oxide mass%				
Ti ₂ O ₃	Al ₂ O ₃	MgO	CaO	SiO ₂
97.74	0.07	0.10	1.63	0.47
98.56	0.19	0.07	0.85	0.35

Table 4.10 (g) Chemical Composition of Selected Titania Inclusions in the Sample taken 156 Seconds after Deoxidation in the Vertical Tube Furnace Melt, (Phillips PSEM/EDX).

Oxide mass%				
Ti ₂ O ₃	Al ₂ O ₃	MgO	CaO	SiO ₂
95.95	0.03	0.08	3.67	0.28
99.54	0.12	0.12	0.00	0.28
95.85	0.31	0.17	3.31	0.37
92.20	0.30	0.00	7.13	0.37

Table 4.10 (h) Chemical Composition of Selected Titania Inclusions in the Sample taken 181 Seconds after Deoxidation in the Vertical Tube Furnace Melt, (Phillips PSEM/EDX).

Oxide mass%				
Ti ₂ O ₃	Al ₂ O ₃	MgO	CaO	SiO ₂
99.45	0.27	0.12	0.00	0.18
96.83	0.15	0.04	2.59	0.41

Table 4.10 (i) Chemical Composition of Selected Titania Inclusions in the Sample taken 252 Seconds after Deoxidation in the Vertical Tube Furnace Melt, (Phillips PSEM/EDX).

Oxide mass%				
Ti ₂ O ₃	Al ₂ O ₃	MgO	CaO	SiO ₂
96.87	0.53	0.34	1.88	0.40
99.27	0.28	0.26	0.00	0.20
95.41	0.18	0.14	3.93	0.35
93.80	0.20	0.00	5.62	0.39

Table 4.10 (j) Chemical Composition of Selected Titania Inclusions in the Sample taken 307 Seconds after Deoxidation in the Vertical Tube Furnace Melt, (Phillips PSEM/EDX).

Oxide mass%				
Ti ₂ O ₃	Al ₂ O ₃	MgO	CaO	SiO ₂
97.63	0.12	0.00	1.99	0.28
99.43	0.31	0.00	0.00	0.27

Table 4.11 Results of Oxygen Analysis for the High Frequency Furnace Melt Deoxidised with 0.53 mass% Titanium Addition (LECO).

Time seconds	Total oxygen Content (mass%)			
	Analysis			Average
	1	2	3	
0	.084	.084		.0840
3	.028	.035	.030	.0310
7	.020	.019		.0195
11	.016	.016		.0160
24	.014	.014		.0140
33	.012	.011		.0115
44	.010	.010		.0100
55	.010	.010		.0100
67	.0086	.0088		.0087
86	.0073	.0073		.0073
108	.0066	.0068		.0067
120	.0066	.0068		.0067
141	.0057	.0055		.0056
155	.0059	.0059		.0059
176	.0050	.0051		.00505
225	.0045	.0044		.00445
270	.0040	.0039		.00395
300	.0037	.0038		.00375
420	.0032	.0044	.0026	.00340
540	.0027	.0023	.0023	.00243
900	.0030	.0030		.00300
1140	.0065	.0064		.00645

Table 4.12 Mean Diameter of Inclusions in the High Frequency Furnace Melt Deoxidised with 0.53 mass% Titanium Addition, (Jeol 840 SEM/Digiscan)

Time seconds	Particle counts	Mean Diameter (µm)	Minimum Size Band (µm)		Maximum Size Band (µm)		95% Confidence Limit
			Range	Mean	Range	Mean	
3	51	0.841	0.0 - 0.5	0.118	4.5 - 5.0	4.984	0.256
7	25	1.174	0.0 - 0.5	0.141	4.0 - 4.5	4.052	0.413
11	50	1.325	0.0 - 0.5	0.110	5.0 - 5.5	5.288	0.315
24	56	1.395	0.0 - 0.5	0.173	7.0 - 7.5	7.195	0.351
33	63	0.555	0.0 - 0.5	0.110	3.0 - 3.5	3.100	0.121
44	31	0.735	0.0 - 0.5	0.110	2.0 - 2.5	2.030	0.174
55	26	0.681	0.0 - 0.5	0.148	2.0 - 2.5	2.040	0.195
67	36	0.950	0.0 - 0.5	0.127	2.0 - 2.5	2.458	0.166
120	26	0.589	0.0 - 0.5	0.110	2.0 - 2.5	2.194	0.184
141	20	0.651	0.0 - 0.5	0.150	2.5 - 3.0	2.632	-
176	24	0.403	0.0 - 0.5	0.182	1.5 - 2.0	1.506	-
225	7	0.367	0.0 - 0.5	0.189	0.5 - 1.0	0.615	-
270	4	0.676	0.0 - 0.5	0.177	0.5 - 1.0	0.972	-

Table 4.13 (a) Chemical Composition of Selected Titania Inclusions in the Sample taken 3 Seconds after Deoxidation in the Vertical Tube Furnace Melt, (Phillips PSEM/EDX).

Oxide mass%				
Ti ₂ O ₃	Al ₂ O ₃	MgO	CaO	SiO ₂
99.49	0.12	0.00	0.00	0.40
96.07	0.24	0.08	3.22	0.40
98.91	0.13	0.00	0.83	0.14
99.65	0.05	0.00	0.00	0.32
96.65	0.05	0.00	2.92	0.39
97.73	0.08	0.05	1.83	0.32
99.60	0.00	0.00	0.00	0.41
97.85	0.12	0.11	1.58	0.36

Table 4.13 (b) Chemical Composition of Selected Titania Inclusions in the Sample taken 7 Seconds after Deoxidation in the Vertical Tube Furnace Melt, (Phillips PSEM/EDX).

Oxide mass%				
Ti ₂ O ₃	Al ₂ O ₃	MgO	CaO	SiO ₂
99.40	0.09	0.18	0.00	0.34
99.16	0.32	0.16	0.00	0.37
95.17	0.12	0.04	4.46	0.23
96.76	0.02	0.11	2.51	0.60
99.60	0.13	0.00	0.00	0.30
99.54	0.01	0.00	0.00	0.47
99.40	0.13	0.00	0.00	0.49
99.43	0.10	0.00	0.05	0.44

Table 4.13 (c) Chemical Composition of Selected Titania Inclusions in the Sample taken 11 Seconds after Deoxidation in the Vertical Tube Furnace Melt, (Phillips PSEM/EDX).

Oxide mass%				
Ti ₂ O ₃	Al ₂ O ₃	MgO	CaO	SiO ₂
96.02	0.20	0.00	3.39	0.40
99.31	0.22	0.12	0.00	0.36
99.13	0.31	0.16	0.00	0.41
99.15	0.30	0.07	0.00	0.49
95.30	0.16	0.00	3.84	0.71
99.45	0.10	0.19	0.00	0.28
99.38	0.19	0.03	0.00	0.41
95.76	0.19	0.00	3.56	0.50

Table 4.13 (d) Chemical Composition of Selected Titania Inclusions in the Sample taken 24 Seconds after Deoxidation in the Vertical Tube Furnace Melt, (Phillips PSEM/EDX).

Oxide mass%				
Ti ₂ O ₃	Al ₂ O ₃	MgO	CaO	SiO ₂
99.47	0.05	0.07	0.00	0.43
98.27	0.08	0.08	1.24	0.34
95.17	0.06	0.15	4.24	0.39
98.07	0.16	0.00	1.30	0.48
99.22	0.29	0.00	0.00	0.51
99.05	0.19	0.09	0.28	0.40
98.74	0.11	0.00	0.66	0.50
98.62	0.08	0.00	0.88	0.44

Table 4.13 (e) Chemical Composition of Selected Titania Inclusions in the Sample taken 33 Seconds after Deoxidation in the Vertical Tube Furnace Melt, (Phillips PSEM/EDX).

Oxide mass%				
Ti ₂ O ₃	Al ₂ O ₃	MgO	CaO	SiO ₂
97.05	0.17	0.29	2.15	0.36
99.58	0.18	0.01	0.00	0.31
95.35	0.15	0.19	4.01	0.32
96.11	0.15	0.00	3.31	0.44
98.56	0.22	0.32	0.47	0.45
99.66	0.07	0.01	0.00	0.28
99.73	0.00	0.00	0.00	0.29
96.30	0.22	0.00	3.07	0.43

Table 4.13 (f) Chemical Composition of Selected Titania Inclusions in the Sample taken 44 Seconds after Deoxidation in the Vertical Tube Furnace Melt, (Phillips PSEM/EDX).

Oxide mass%				
Ti ₂ O ₃	Al ₂ O ₃	MgO	CaO	SiO ₂
93.67	0.29	0.10	5.42	0.53
99.34	0.08	0.27	0.00	0.32
99.45	0.19	0.00	0.00	0.38
92.69	0.10	0.00	6.77	0.46
99.12	0.31	0.15	0.00	0.44
98.95	0.34	0.26	0.00	0.47

Table 4.13 (g) Chemical Composition of Selected Titania Inclusions in the Sample taken 55 Seconds after Deoxidation in the Vertical Tube Furnace Melt, (Phillips PSEM/EDX).

Oxide mass%				
Ti ₂ O ₃	Al ₂ O ₃	MgO	CaO	SiO ₂
99.19	0.21	0.19	0.00	0.42
99.20	0.19	0.20	0.00	0.42
96.06	0.15	0.10	3.24	0.47
99.36	0.03	0.19	0.00	0.44
99.24	0.19	0.11	0.00	0.47
96.60	0.29	0.16	2.48	0.48

Table 4.13 (h) Chemical Composition of Selected Titania Inclusions in the Sample taken 67 Seconds after Deoxidation in the Vertical Tube Furnace Melt, (Phillips PSEM/EDX).

Oxide mass%				
Ti ₂ O ₃	Al ₂ O ₃	MgO	CaO	SiO ₂
99.36	0.23	0.00	0.00	0.42
96.47	0.18	0.08	2.93	0.35
97.88	0.33	0.00	1.39	0.40
99.21	0.31	0.03	0.00	0.46
99.22	0.28	0.11	0.00	0.41
99.11	0.22	0.23	0.00	0.45

Table 4.13 (i) Chemical Composition of Selected Titania Inclusions in the Sample taken 86 Seconds after Deoxidation in the Vertical Tube Furnace Melt, (Phillips PSEM/EDX).

Oxide mass%				
Ti ₂ O ₃	Al ₂ O ₃	MgO	CaO	SiO ₂
96.85	0.13	0.15	2.50	0.39
95.75	0.34	0.22	3.34	0.37
97.76	0.17	0.21	1.26	0.40
99.01	0.22	0.44	0.00	0.35
99.11	0.30	0.09	0.00	0.51
99.18	0.36	0.00	0.00	0.47

Table 4.13 (j) Chemical Composition of Selected Titania Inclusions in the Sample taken 120 Seconds after Deoxidation in the Vertical Tube Furnace Melt, (Phillips PSEM/EDX).

Oxide mass%				
Ti ₂ O ₃	Al ₂ O ₃	MgO	CaO	SiO ₂
96.64	0.55	0.27	2.16	0.40
96.20	0.49	0.32	2.61	0.39
99.08	0.35	0.17	0.00	0.42
94.82	0.54	0.97	3.22	0.46
94.13	0.39	0.22	4.74	0.53
97.78	0.54	0.51	0.79	0.39

Table 4.13 (k) Chemical Composition of Selected Titania Inclusions in the Sample taken 155 Seconds after Deoxidation in the Vertical Tube Furnace Melt, (Phillips PSEM/EDX).

Oxide mass%				
Ti ₂ O ₃	Al ₂ O ₃	MgO	CaO	SiO ₂
95.97	0.57	1.22	1.75	0.50
95.64	0.54	0.99	2.37	0.48
96.17	0.53	1.30	1.56	0.45
97.57	0.82	1.33	0.00	0.29

Table 4.13 (l) Chemical Composition of Selected Titania Inclusions in the Sample taken 225 Seconds after Deoxidation in the Vertical Tube Furnace Melt, (Phillips PSEM/EDX).

Oxide mass%				
Ti ₂ O ₃	Al ₂ O ₃	MgO	CaO	SiO ₂
98.05	0.61	1.02	0.00	0.34
97.56	0.78	1.27	0.00	0.41
97.89	0.59	1.33	0.00	0.20
97.73	0.73	1.30	0.00	0.25

Table 4.13 (m) Chemical Composition of Selected Titania Inclusions in the Sample taken 270 Seconds after Deoxidation in the Vertical Tube Furnace Melt, (Phillips PSEM/EDX).

Oxide mass%				
Ti ₂ O ₃	Al ₂ O ₃	MgO	CaO	SiO ₂
95.09	0.59	1.20	2.88	0.28
97.95	0.66	1.16	0.00	0.24
97.67	0.44	1.02	0.76	0.12
95.47	0.49	0.59	3.23	0.24

Table 4.14 Results of Oxygen Analysis for Vertical Tube Furnace Melt Deoxidised with 0.3 mass% Silicon Addition (LECO).

Time Seconds	Total Oxygen Content (mass%)		
	Analysis		Average
	1	2	
0	.057	.057	.057
24	.054	.054	.054
37	.052	.053	.0525
53	.051	.051	.0510
64	.050	.049	.0495
82	.047	.047	.0470
110	.044	.045	.0445
128	.043	.044	.0435
151	.041	.042	.0415
184	.038	.039	.0385
244	.034	.033	.0335
307	.032	.032	.0320
461	.027	.027	.0270
621	.019	.019	.0190
916	.0095	.0091	.0093
1200	.0064	.0064	.0064

Table 4.15 Mean Diameter of Inclusions in the Vertical Tube Furnace Melt Deoxidised with 0.3 mass% Silicon Addition, (Jeol 840 SEM/Digiscan)

Time seconds	Particle counts	Mean Diameter (μm)	Minimum Size Band (μm)		Maximum Size Band (μm)	
			Range	Mean	Range	Mean
24	65	1.737	0.0 - 0.5	0.303	3.5 - 4.0	3.797
37	60	1.456	0.0 - 0.5	0.413	3.5 - 4.0	3.654
53	51	1.933	0.0 - 0.5	0.413	5.0 - 5.5	5.251
64	39	2.104	0.5 - 1.0	0.692	6.0 - 6.5	6.095
82	32	1.433	0.0 - 0.5	0.320	4.0 - 4.5	4.273
110	30	1.347	0.0 - 0.5	0.277	3.0 - 3.5	3.063
128	32	1.497	0.0 - 0.5	0.221	4.5 - 5.0	4.517
151	66	1.093	0.0 - 0.5	0.224	5.5 - 6.0	5.583
184	62	1.081	0.0 - 0.5	0.288	3.0 - 3.5	3.134
244	43	0.804	0.0 - 0.5	0.251	2.5 - 3.0	2.644

Table 4.16 (a) Chemical Composition of Selected Silicate Inclusions in the Sample taken 24 Seconds after Deoxidation in the Vertical Tube Furnace Melt, (Phillips PSEM/EDX).

Oxide mass%					
FeO	SiO ₂	CaO	MgO	MnO	Al ₂ O ₃
1.73	68.01	23.50	0.00	1.38	5.39
1.77	83.30	9.23	0.00	1.29	4.40
1.71	97.57	0.29	0.00	0.14	0.29
1.28	98.51	0.00	0.01	0.19	0.00
1.36	98.08	0.00	0.00	0.57	0.00

Table 4.16 (b) Chemical Composition of Selected Silicate Inclusions in the Sample taken 37 Seconds after Deoxidation in the Vertical Tube Furnace Melt, (Phillips PSEM/EDX).

Oxide mass%					
FeO	SiO ₂	CaO	MgO	MnO	Al ₂ O ₃
1.37	97.98	0.00	0.14	0.19	0.32
1.52	97.26	0.00	0.02	1.02	0.17
1.32	98.58	0.00	0.00	0.09	0.00
2.65	92.70	1.56	0.08	0.98	2.03
1.93	83.41	0.78	0.00	3.77	10.11
2.50	95.29	0.00	0.00	0.74	1.47
12.31	60.71	0.00	0.26	25.63	1.09
17.20	59.73	0.00	0.00	21.69	1.39

Table 4.16 (c) Chemical Composition of Selected Silicate Inclusions in the Sample taken 53 Seconds after Deoxidation in the Vertical Tube Furnace Melt, (Phillips PSEM/EDX).

Oxide mass%					
FeO	SiO ₂	CaO	MgO	MnO	Al ₂ O ₃
1.84	95.65	0.00	0.08	1.49	0.93
1.26	98.70	0.00	0.00	0.04	0.00
1.74	93.79	0.00	0.15	1.14	3.18
0.90	98.91	0.00	0.01	0.06	0.12
2.49	95.18	0.00	0.00	0.57	1.76
1.57	93.85	1.77	0.00	0.76	2.05
8.27	72.81	3.07	0.05	14.33	1.48
13.17	56.59	6.94	0.00	19.43	3.86

Table 4.16 (d) Chemical Composition of Selected Silicate Inclusions in the Sample taken 64 Seconds after Deoxidation in the Vertical Tube Furnace Melt, (Phillips PSEM/EDX).

Oxide mass%					
FeO	SiO ₂	CaO	MgO	MnO	Al ₂ O ₃
1.55	90.60	3.79	0.00	1.00	3.07
1.17	98.75	0.00	0.00	0.08	0.00
1.41	78.67	15.42	0.00	1.05	3.46
2.06	91.23	3.70	0.15	1.06	1.80
1.48	73.57	19.09	0.00	1.18	4.68
2.46	87.37	7.54	0.00	0.74	1.90
2.37	90.71	1.22	0.24	2.42	3.04
1.53	96.30	0.00	0.00	0.62	1.56

Table 4.16 (e) Chemical Composition of Selected Silicate Inclusions in the Sample taken 82 Seconds after Deoxidation in the Vertical Tube Furnace Melt, (Phillips PSEM/EDX).

Oxide mass%					
FeO	SiO ₂	CaO	MgO	MnO	Al ₂ O ₃
1.45	97.16	0.07	0.00	0.63	0.75
2.16	91.46	4.12	0.00	0.71	1.55
1.32	94.64	2.09	0.00	0.56	1.39
1.34	97.00	0.00	0.01	0.54	1.10
1.36	92.09	3.27	0.00	0.88	2.40
1.92	96.87	0.00	0.03	0.64	0.54
1.94	91.80	3.16	0.10	0.71	2.28

Table 4.16 (f) Chemical Composition of Selected Silicate Inclusions in the Sample taken 110 Seconds after Deoxidation in the Vertical Tube Furnace Melt, (Phillips PSEM/EDX).

Oxide mass%					
FeO	SiO ₂	CaO	MgO	MnO	Al ₂ O ₃
1.17	98.52	0.00	0.08	0.18	0.04
3.53	93.55	0.00	0.00	0.97	1.95
0.98	94.87	2.11	0.03	0.53	1.48
1.55	97.64	0.00	0.05	0.22	0.53
1.50	95.00	0.92	0.00	1.03	2.55
1.52	96.16	0.00	0.00	0.65	1.66

Table 4.16 (g) Chemical Composition of Selected Silicate Inclusions in the Sample taken 128 Seconds after Deoxidation in the Vertical Tube Furnace Melt, (Phillips PSEM/EDX).

Oxide mass%					
FeO	SiO ₂	CaO	MgO	MnO	Al ₂ O ₃
1.33	98.05	0.21	0.00	0.24	0.17
2.66	88.37	5.74	0.08	0.96	2.19
1.64	96.47	0.94	0.00	0.30	0.66
1.33	94.35	1.26	0.00	0.90	2.16
1.68	84.47	9.77	0.04	1.00	3.04
1.36	95.35	0.41	0.00	0.71	2.17

Table 4.16 (h) Chemical Composition of Selected Silicate Inclusions in the Sample taken 184 Seconds after Deoxidation in the Vertical Tube Furnace Melt, (Phillips PSEM/EDX).

Oxide mass%					
FeO	SiO ₂	CaO	MgO	MnO	Al ₂ O ₃
1.78	92.67	1.21	0.00	1.69	2.65
5.53	82.25	8.60	0.04	1.12	2.46
1.41	95.00	1.31	0.00	0.71	1.57
1.21	97.35	0.00	0.00	0.41	1.02

Table 4.16 (i) Chemical Composition of Selected Silicate Inclusions in the Sample taken 307 Seconds after Deoxidation in the Vertical Tube Furnace Melt, (Phillips PSEM/EDX).

Oxide mass%					
FeO	SiO ₂	CaO	MgO	MnO	Al ₂ O ₃
1.18	93.67	2.41	0.10	0.79	1.84
1.18	94.90	0.05	0.18	0.92	2.31
1.39	93.05	1.98	0.00	0.90	2.68
1.30	95.15	0.22	0.00	0.94	2.40
1.37	94.62	1.54	0.00	0.82	1.66
6.30	90.23	0.00	0.00	1.41	2.06

Table 4.16 (j) Chemical Composition of Selected Silicate Inclusions in the Sample taken 620 Seconds after Deoxidation in the Vertical Tube Furnace Melt, (Phillips PSEM/EDX).

Oxide mass%					
FeO	SiO ₂	CaO	MgO	MnO	Al ₂ O ₃
1.44	93.37	2.37	0.00	0.79	1.84
1.22	94.27	1.74	0.00	0.92	2.31
1.42	94.55	0.82	0.00	0.90	2.68
0.02	99.90	0.04	0.00	0.94	2.40
1.34	95.52	0.07	0.13	0.82	1.66
1.53	94.10	1.61	0.00	1.41	2.06

Table 4.16 (k) Chemical Composition of Selected Silicate Inclusions in the Sample taken 1200 Seconds after Deoxidation in the Vertical Tube Furnace Melt, (Phillips PSEM/EDX).

Oxide mass%					
FeO	SiO ₂	CaO	MgO	MnO	Al ₂ O ₃
1.29	58.61	22.45	0.38	5.13	12.13
4.70	60.35	22.47	0.37	3.86	8.24
9.39	53.06	21.54	0.19	4.77	11.07
2.88	63.61	19.16	0.00	4.66	9.69

Table 4.17 Results of Oxygen Analysis for High Frequency Furnace Melt Deoxidised with 0.3 mass% Silicon Addition (LECO).

Time Seconds	Total Oxygen Content (mass%)		
	Analysis		
	1	2	Average
0	0.054	0.055	0.0545
1	0.052	0.052	0.0520
20	0.043	0.043	0.0430
28	0.039	0.039	0.0390
37	0.032	0.032	0.0320
51	0.027	0.026	0.0265
68	0.021	0.021	0.0210
90	0.017	0.017	0.0170
105	0.015	0.014	0.0145
120	0.013	0.013	0.0130
150	0.010	0.011	0.0105
180	0.0098	0.0099	0.00985
245	0.0080	0.0084	0.00820
300	0.0078	0.0078	0.00780
450	0.0052	0.0054	0.00530
600	0.0044	0.0042	0.00430
905	0.0043	0.0047	0.00450
1200	0.0053	0.0055	0.00540

Table 4.18 Mean Diameter of Inclusions in the High Frequency Furnace Melt Deoxidised with 0.3 mass% Silicon Addition, (Jeol 840 SEM/Digiscan)

Time seconds	Particle counts	Mean Diameter (μm)	Minimum Size Band (μm)		Maximum Size Band (μm)	
			Range	Mean	Range	Mean
1	106	1.528	0.0 - 0.5	0.337	4.5 - 5.0	4.700
20	101	1.129	0.0 - 0.5	0.310	3.0 - 3.5	3.376
28	76	1.125	0.0 - 0.5	0.388	2.5 - 3.0	2.817
37	63	1.137	0.0 - 0.5	0.385	4.0 - 4.5	4.236
51	62	1.060	0.0 - 0.5	0.364	2.0 - 2.5	2.244
68	49	1.191	0.0 - 0.5	0.449	1.5 - 2.0	1.567
90	64	1.031	0.0 - 0.5	0.331	2.5 - 3.0	2.600
150	80	0.570	0.0 - 0.5	0.278	1.0 - 1.5	1.087
180	63	0.615	0.0 - 0.5	0.317	1.0 - 1.5	1.397
245	67	0.455	0.0 - 0.5	0.299	1.5 - 2.0	1.567

Table 4.19 (a) Chemical Composition of Selected Silicate Inclusions in the Sample taken 20 Seconds after Deoxidation in the High Frequency Furnace Melt, (Phillips PSEM/EDX).

Oxide mass%					
FeO	SiO ₂	CaO	MgO	MnO	Al ₂ O ₃
1.71	83.79	8.17	0.00	1.93	4.40
2.49	86.22	4.64	0.14	2.23	4.28
1.92	85.24	7.23	0.00	1.78	3.83
1.87	88.57	3.58	0.00	2.11	3.86
1.88	88.58	3.56	0.00	2.11	3.87

Table 4.19 (b) Chemical Composition of Selected Silicate Inclusions in the Sample taken 28 Seconds after Deoxidation in the High Frequency Furnace Melt, (Phillips PSEM/EDX).

Oxide mass%					
FeO	SiO ₂	CaO	MgO	MnO	Al ₂ O ₃
1.91	87.64	3.61	0.00	2.30	4.54
2.03	79.93	8.06	0.00	3.24	6.75
1.89	70.36	21.14	0.13	1.79	4.72
4.03	71.39	13.44	0.00	4.04	7.10
2.17	91.17	0.94	0.00	1.76	3.96
2.73	85.74	4.56	0.00	2.26	4.70

Table 4.19 (c) Chemical Composition of Selected Silicate Inclusions in the Sample taken 37 Seconds after Deoxidation in the High Frequency Furnace Melt, (Phillips PSEM/EDX).

Oxide mass%					
FeO	SiO ₂	CaO	MgO	MnO	Al ₂ O ₃
2.60	79.96	4.42	0.12	4.36	8.54
3.56	78.78	6.14	0.00	3.62	7.91
1.05	98.79	0.00	0.13	0.02	0.00
6.18	74.53	10.82	0.00	2.83	5.65
2.97	74.20	10.65	0.00	3.80	8.38

Table 4.19 (d) Chemical Composition of Selected Silicate Inclusions in the Sample taken 57 Seconds after Deoxidation in the High Frequency Furnace Melt, (Phillips PSEM/EDX).

Oxide mass%					
FeO	SiO ₂	CaO	MgO	MnO	Al ₂ O ₃
2.71	70.50	12.25	0.01	4.66	9.87
1.27	63.39	18.37	0.17	4.48	12.32
1.04	58.05	23.43	0.00	4.59	12.88
1.45	64.17	14.75	0.00	5.10	14.52

Table 4.19 (e) Chemical Composition of Selected Silicate Inclusions in the Sample taken 68 Seconds after Deoxidation in the High Frequency Furnace Melt, (Phillips PSEM/EDX).

Oxide mass%					
FeO	SiO ₂	CaO	MgO	MnO	Al ₂ O ₃
1.69	54.46	26.47	0.27	4.66	12.45
8.32	71.20	18.25	0.11	0.81	1.31
2.05	51.63	29.54	0.18	4.73	11.87
1.48	49.86	32.83	0.00	3.94	11.90

Table 4.20 Results of Oxygen Analysis for Vertical Tube Furnace Melt Deoxidised with 0.32 mass% Calcium-Aluminium Addition (LECO).

Time Seconds	Total Oxygen Content (mass%)			
	1	2	3	Average
0	.045	.045		.045
15	.020	.016	.033	.023
28	.033	.036		.0345
37	.035	.016	.031	.0273
56	.029	.015	.031	.0250
74	.024	.027		.0255
87	.026	.011	.025	.0207
105	.0088	.024	.020	.0176
124	.0073	.017	.015	.0131
149	.0170	.020	.017	.0180
178	.0150	.015		.0150
272	.0190	.011	.011	.0137
317	.0077	.0067	.012	.0088
441	.0150	.0081	.0083	.0105
526	.0100	.0110	.0130	.0113
619	.0054	.0072	.0080	.00687
932	.0052	.0096	.0079	.00747
1087	.0078	.0061	.0089	.00760
1219	.0066	.0046	.0066	.00593

Table 4.21 Results of Oxygen Analysis for High Frequency Furnace Melt Deoxidised with 0.32 mass% Calcium-Aluminium Addition (LECO).

Time Seconds	Total Oxygen Content (mass%)			
	1	2	3	Average
0	.056	.057		.0565
14	.046	.022	.033	.0337
19	.017	.013	.018	.0267
30	.015	.013	.025	.0177
38	.028	.031	.015	.0247
48	.029	.013	.015	.0223
60	.014	.016	.014	.0147
83	.012	.017		.0145
98	.015	.013		.0140
111	.014	.015		.0145
130	.021	.0088	.0060	.0119
155	.017	.0044	.0190	.0135
184	.0040	.0037		.00385
235	.0087	.0033	.0043	.00543
297	.0032	.0029		.00305
605	.0022	.0021		.00215
900	.0021	.0020		.00205
1185	.0023	.0023		.00230

Table 4.22 Mean Diameter of Inclusions in the High Frequency Furnace Melt Deoxidised with 1.01 mass% Calcium-Aluminium Addition, (Jeol 840 SEM/Digiscan)

Time seconds	Particle counts	Mean Diameter (μm)	Minimum Size Band (μm)		Maximum Size Band (μm)	
			Range	Mean	Range	Mean
14	212	0.836	0.0 - 0.5	0.307	3.0 - 3.5	3.413
19	77	1.124	0.0 - 0.5	0.340	3.5 - 4.0	3.501
30	56	1.193	0.0 - 0.5	0.282	3.0 - 3.5	3.047
48	47	1.061	0.0 - 0.5	0.293	3.5 - 4.0	3.805
83	55	1.441	0.0 - 0.5	0.312	3.5 - 4.0	3.671
111	17	0.800	0.0 - 0.5	0.413	1.5 - 2.0	1.683
130	10	1.032	0.0 - 0.5	0.420	2.0 - 2.5	2.244
184	8	0.588	0.0 - 0.5	0.324	0.5 - 1.0	0.701
297	12	0.760	0.0 - 0.5	0.355	1.0 - 1.5	1.080

Table 4.23 (a) Chemical Composition of Selected Calcium-Aluminium Inclusions in the Sample taken 14 Seconds after Deoxidation in the High Frequency Furnace Melt, (Phillips PSEM/EDX).

Oxide Mass%	
Al_2O_3	CaO
38.31	61.69
100.00	00.00
61.73	38.27
84.93	15.07
97.15	2.85
60.86	39.14

Table 4.23 (b) Chemical Composition of Selected Calcium-Aluminium Inclusions in the Sample taken 19 Seconds after Deoxidation in the High Frequency Furnace Melt, (Phillips PSEM/EDX).

Oxide Mass%	
Al_2O_3	CaO
96.58	3.42
45.76	54.24
98.48	1.52
37.38	62.62
49.58	50.42

Table 4.23 (c) Chemical Composition of Selected Calcium-Aluminium Inclusions in the Sample taken 30 Seconds after Deoxidation in the High Frequency Furnace Melt, (Phillips PSEM/EDX).

Oxide Mass%	
Al ₂ O ₃	CaO
60.75	39.25
37.76	62.24
93.53	6.47
42.00	58.00
40.15	59.85
41.90	58.10

Table 4.23 (d) Chemical Composition of Selected Calcium-Aluminium Inclusions in the Sample taken 38 Seconds after Deoxidation in the High Frequency Furnace Melt, (Phillips PSEM/EDX).

Oxide Mass%	
Al ₂ O ₃	CaO
40.90	59.10
49.27	50.73

Table 4.24 Results of Oxygen Analysis for Vertical Tube Furnace Melt Deoxidised with 1.01 mass% Zirconium Addition (LECO).

Time Seconds	Total Oxygen Content (mass%)			
	1	2	3	Average
0	.039	.041		.0395
1	.051	.043	.049	.0476
15	.042	.044		.0430
26	.044	.045		.0445
37	.037	.045	.042	.0413
63	.042	.040		.0410
79	.050	.038	.035	.0410
113	.039	.036		.0375
140	.039	.038		.0385
198	.034	.038		.0355
307	.033	.034		.0335
462	.074	.060		.0670
605	.037	.033		.0350
904	.023	.020		.0215
1213	.016	.016		.0160

Table 4.25 Results of Oxygen Analysis for High Frequency Furnace Melt Deoxidised with 1.01 mass% Zirconium Addition (LECO).

Time Seconds	Total Oxygen Content (mass%)			
	1	2	3	Average
0	.059	.056		.0575
10	.064	.063		.0635
17	.057	.039	.046	.0473
75	.040	.044		.0420
106	.014	.015		.0145
119	.013	.013		.0130
140	.011	.010		.0105
172	.0081	.0078		.00795
221	.0067	.0060		.00635
275	.0049	.0051		.00500
339	.0046	.0048		.00470
450	.0048	.0048		.00475
609	.0046	.0045		.00465
900	.0037	.0038		.00375
1197	.0042	.0040		.00410

Table 5.1 Crystal systems of the various aluminium deoxidation products⁹⁵.

Phase	Crystal System
Hercynite	Cubic
γ -Alumina	Cubic, Tetragonal, Orthorhombic
κ -Alumina	Orthorhombic
θ -Alumina	Hexagonal
α -Alumina	Hexagonal, Trigonal

Table 5.2 Contact angles and melting points of Alumina, Lime and Calcium -aluminates^{75,143,150}.

Phase	Melting point (°C)	Contact angle at 1600°C	Crystal system
CaO	2570	132	cubic
CaO.Al ₂ O ₃ (58/42)	1605	54	unknown
CaO.2Al ₂ O ₃	~1750		mono/tetrag
CaO.6Al ₂ O ₃	~1850		hexagonal
12CaO.7Al ₂ O ₃ (50/50)	1455	58	cubic
3CaO.Al ₂ O ₃ (36/64)	1535	65	cubic
Al ₂ O ₃	2050	144	hex/trigonal

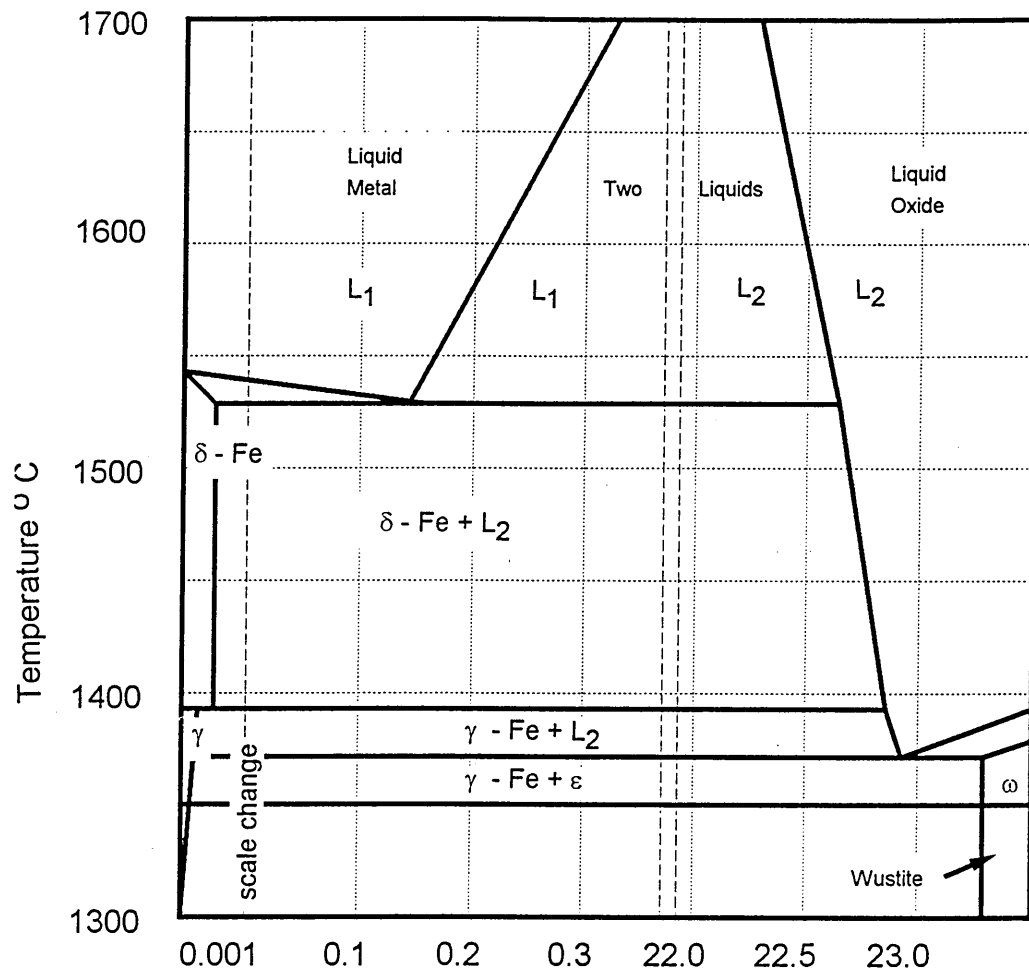


Figure 2.1 Portion of iron-oxygen phase diagram⁵.

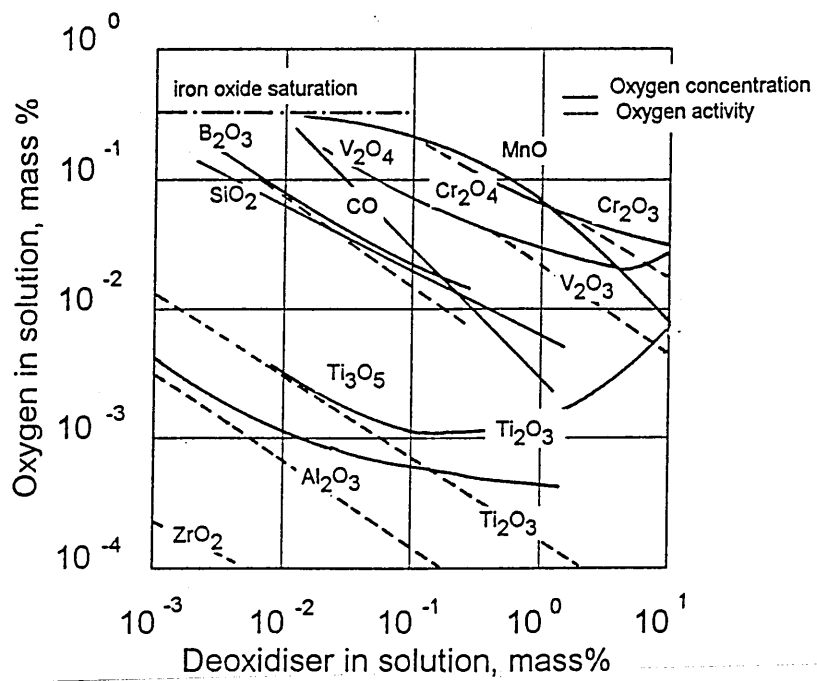


Figure 2.2 Deoxidation equilibria in liquid iron alloys at 1600 °C.

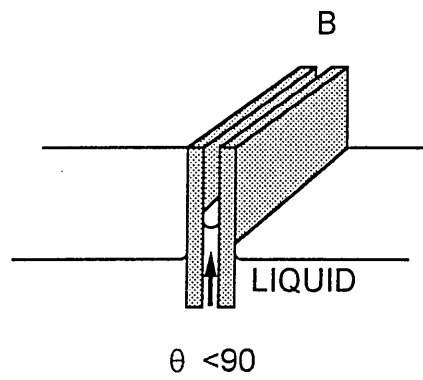
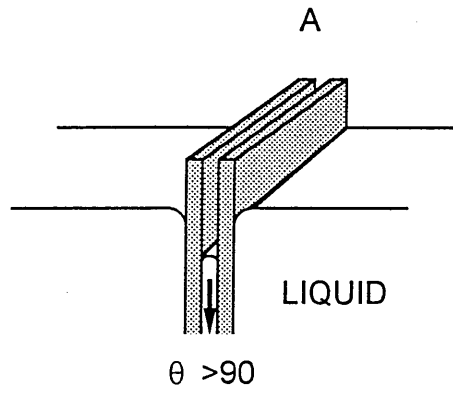


Figure 2.3 The part played by the contact angle in establishing contact between two partly submerged lamellae. 74

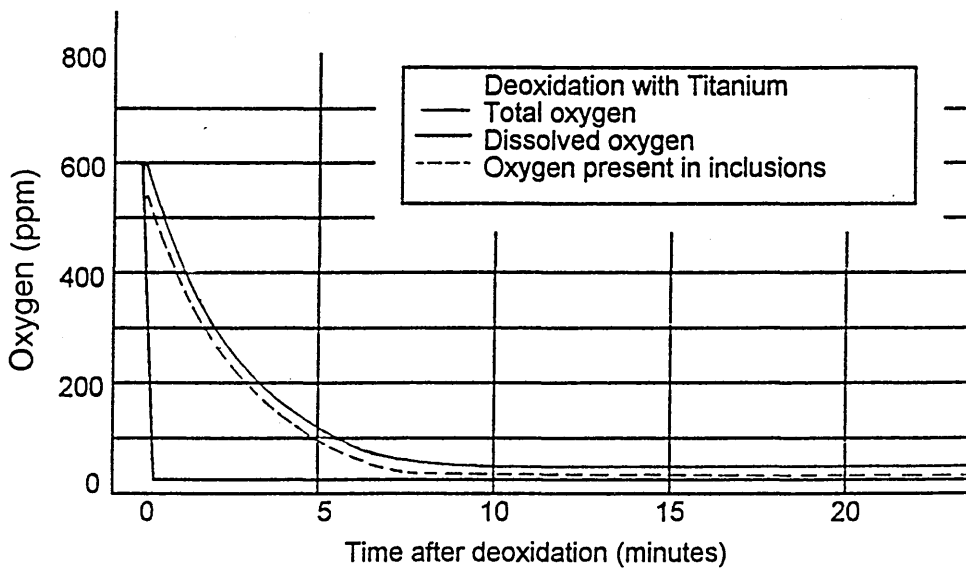
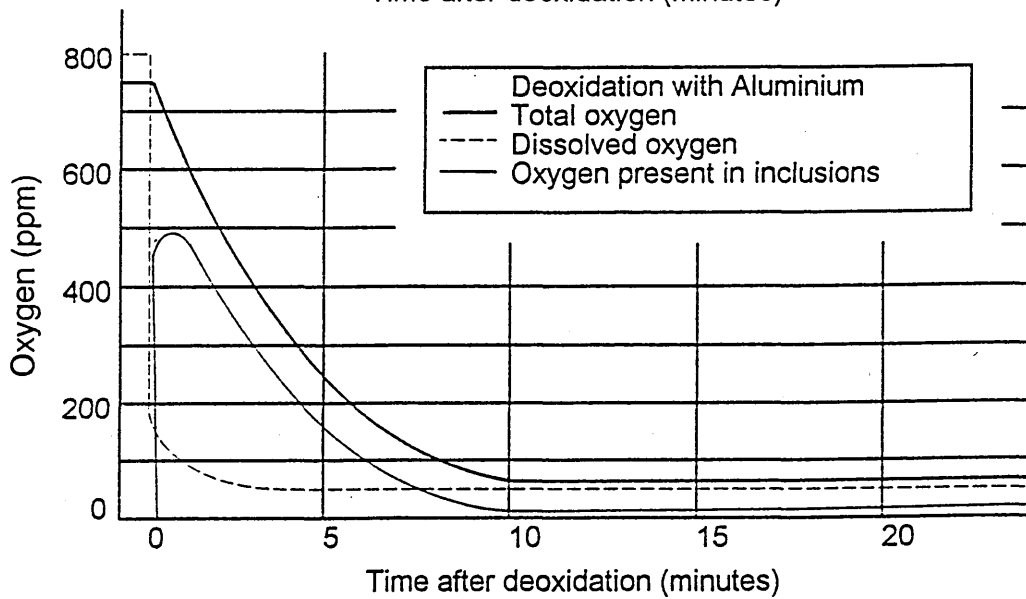
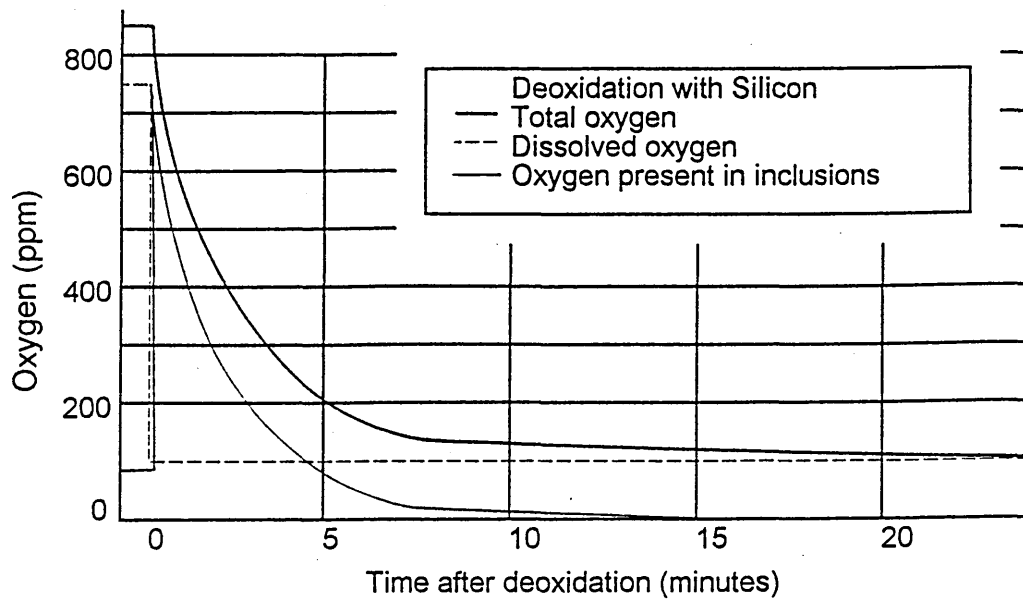


Figure 2.4 Deoxidation of pure iron with, silicon, aluminium and titanium ⁶³

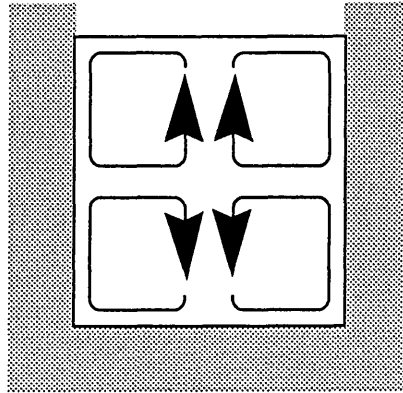


Figure 2.5 Flow pattern of liquid iron in a high frequency induction furnace⁸⁵.

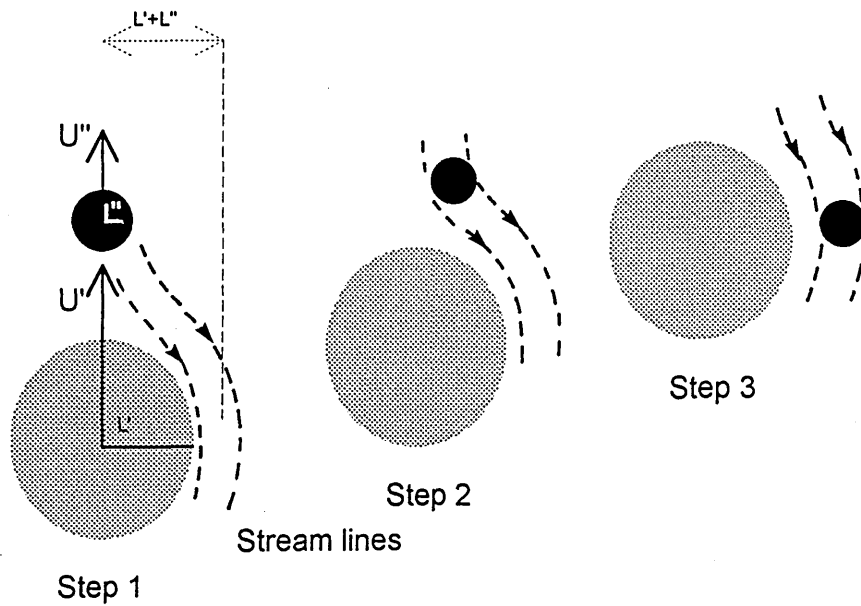


Figure 2.6 Illustration of the approach of a large particle to a smaller particle⁷⁹.

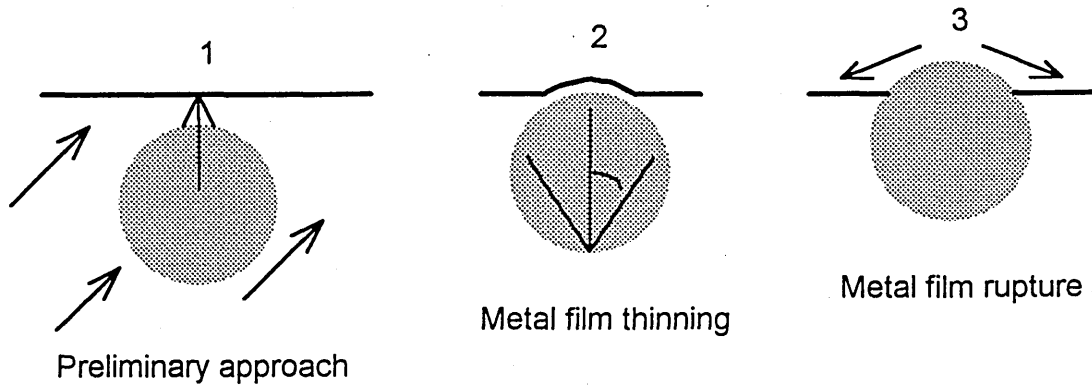


Figure 2.7 Steps in the emergence of inclusions⁷⁰.

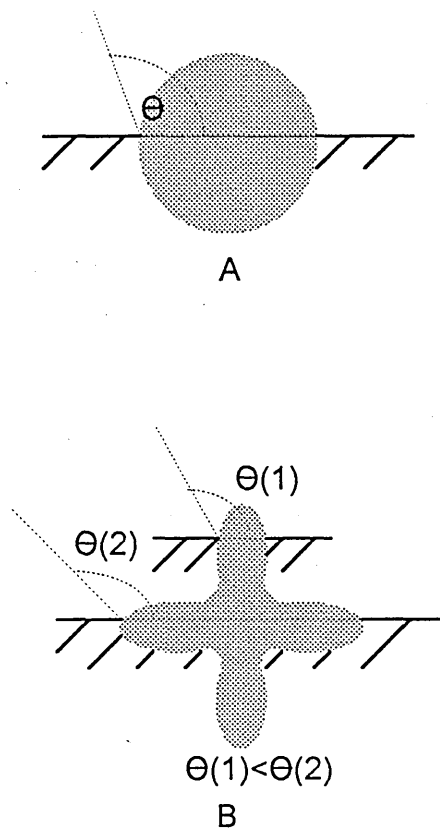


Figure 2.8 Stable position of emergence for solid inclusions:- Influence of contact angle (θ) on different shapes⁷⁰.

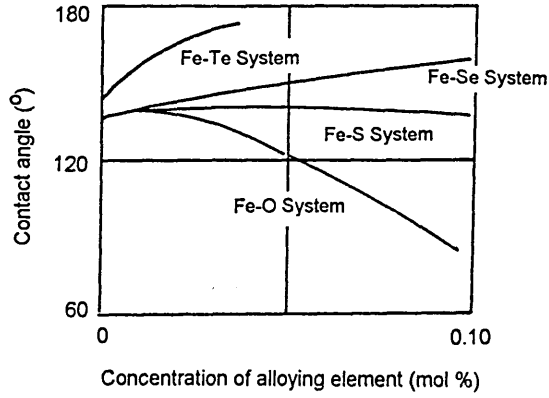


Figure 2.9 Effect of alloying element on the contact angle between molten iron and an alumina plate at 1600°C⁸⁶.

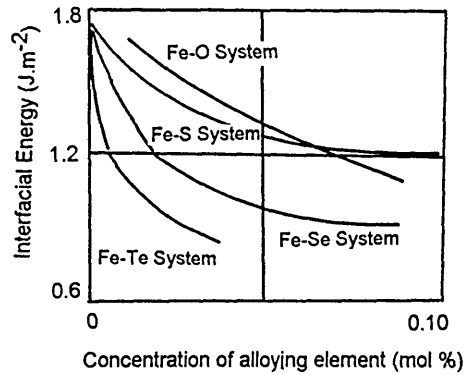


Figure 2.10 Effect of alloying element on the interfacial tension of molten iron at 1600°C⁸⁶.

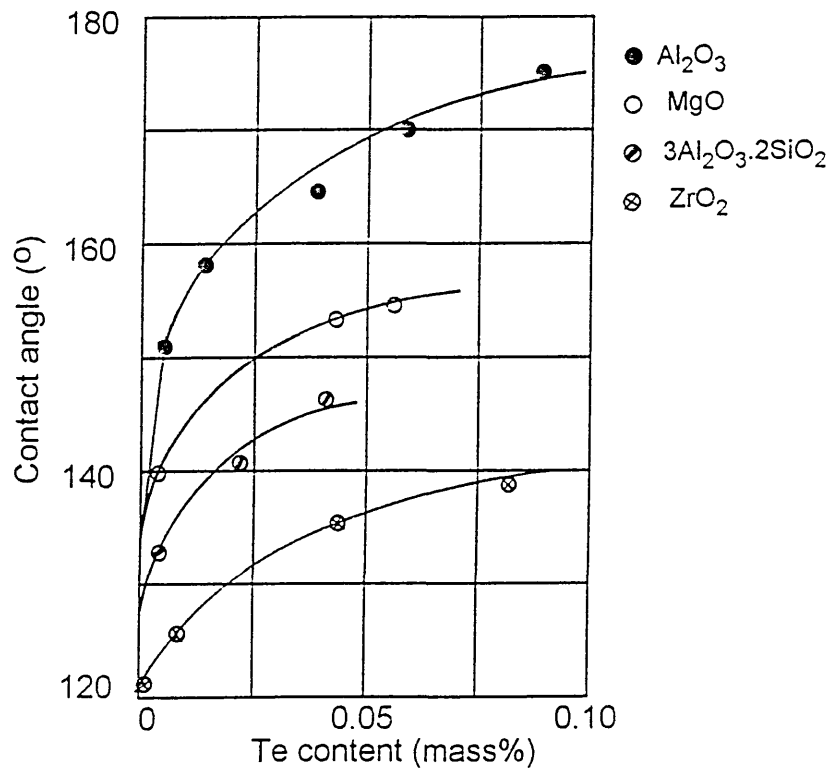


Figure 2.11 The effect of tellurium on the contact angle between molten iron and solid oxide at 1600°C⁸⁶.

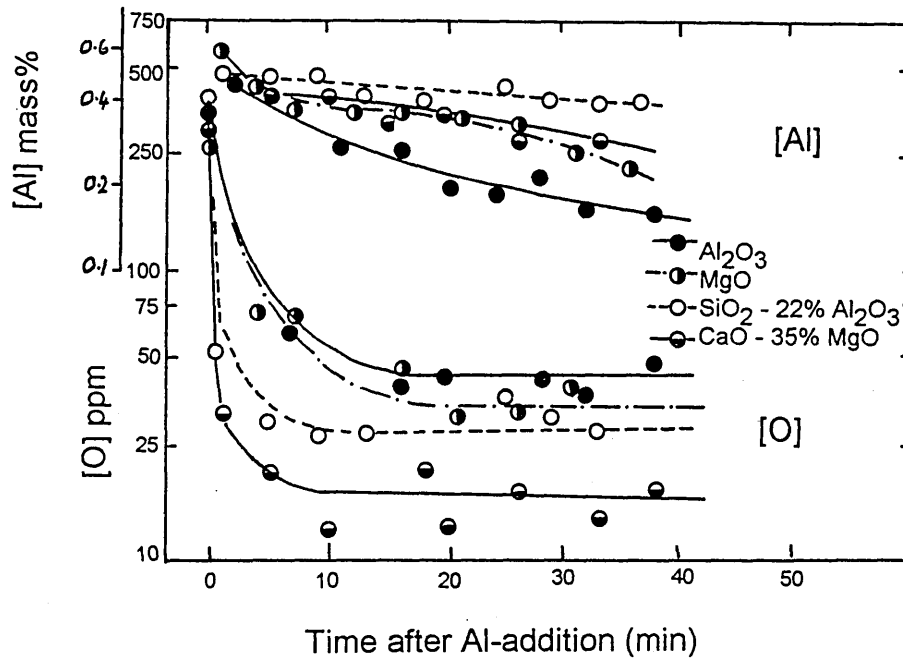


Figure 2.12 Changes in oxygen and aluminium contents of liquid iron in various crucibles after a 0.5 mass% aluminium addition at 1600°C⁸⁵.

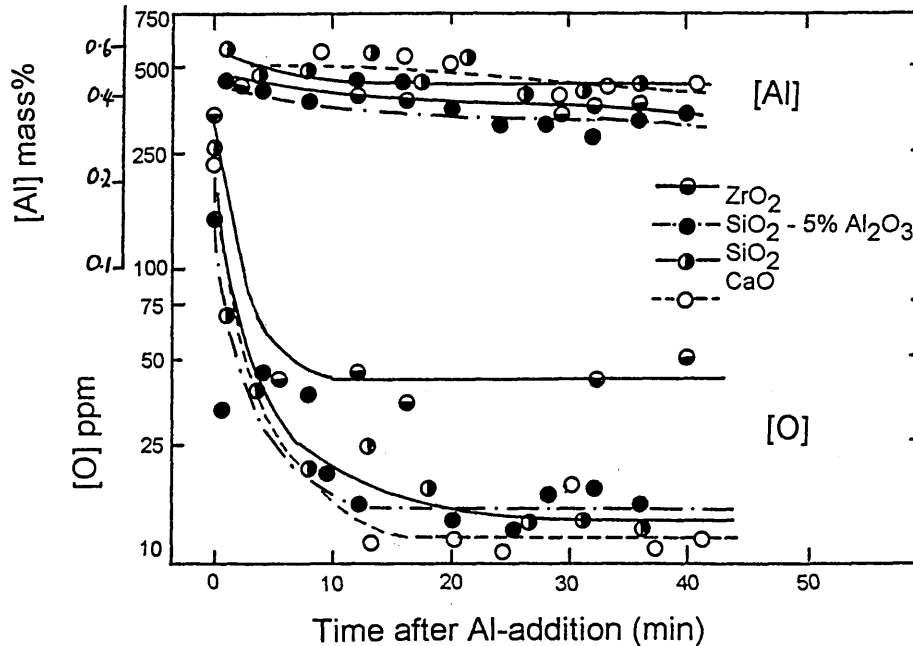


Figure 2.13 Changes in oxygen and aluminium contents of liquid iron in various crucibles after a 0.5 mass% aluminium addition at 1600°C⁸⁵.

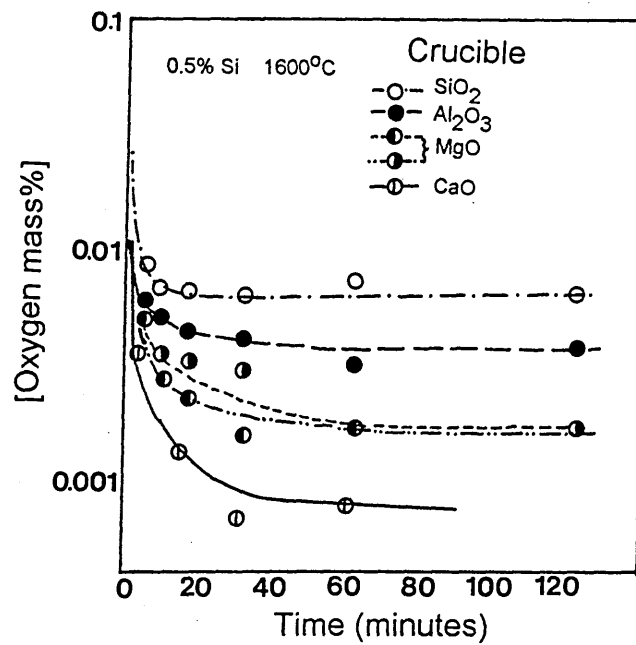


Figure 2.14 Deoxidation curves with silicon in silica, magnesia, alumina and lime crucibles at 1600°C⁹⁰.

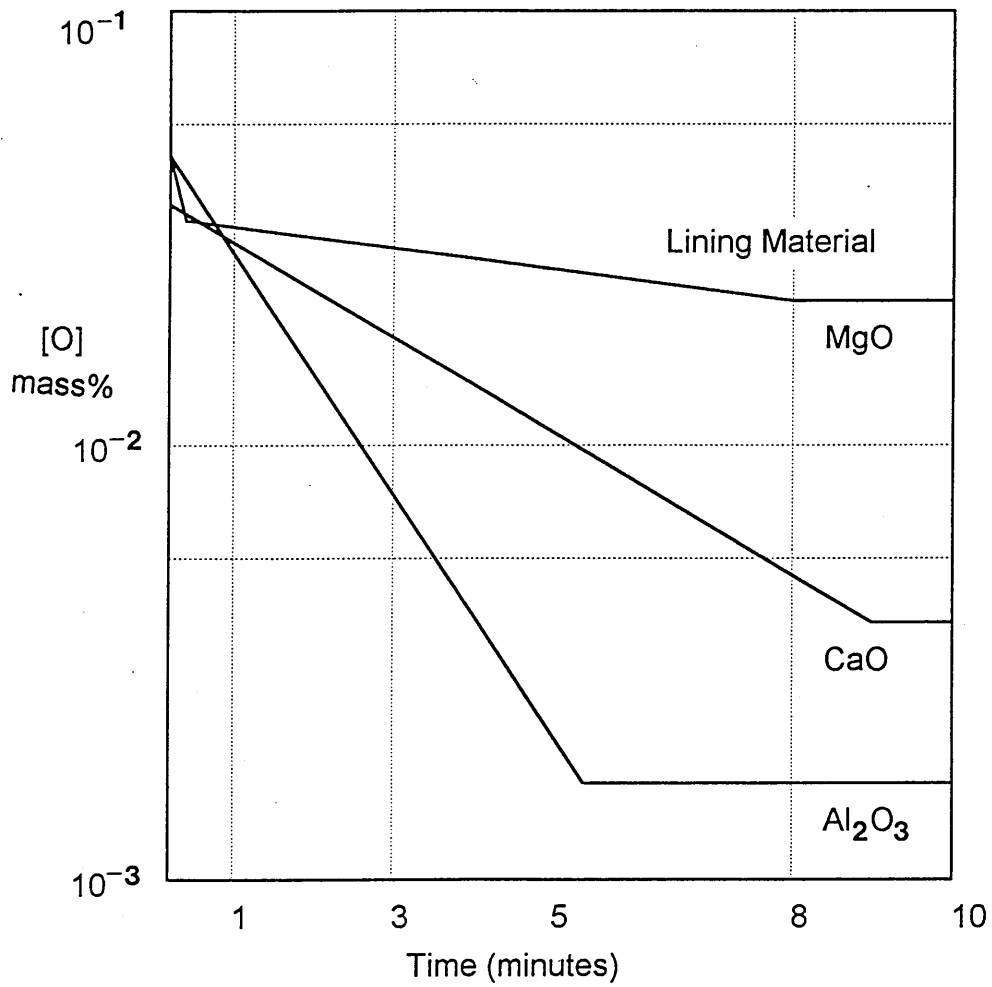


Figure 2.15 Influence of the ladle lining material on the change of [O] in iron melts after a 0.5 mass% Ca addition. ¹⁴

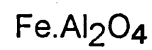
Electron of Iron Species leans
around Aluminium Species



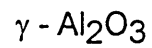
Nucleation of oxide



Formation of Hercynite



Reaction of Hercynite with
Aluminium



Iron Species in Hercynite
go out to molten Iron

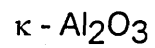


Figure 2.16 Mechanisms of formation of aluminous oxides⁹⁴.

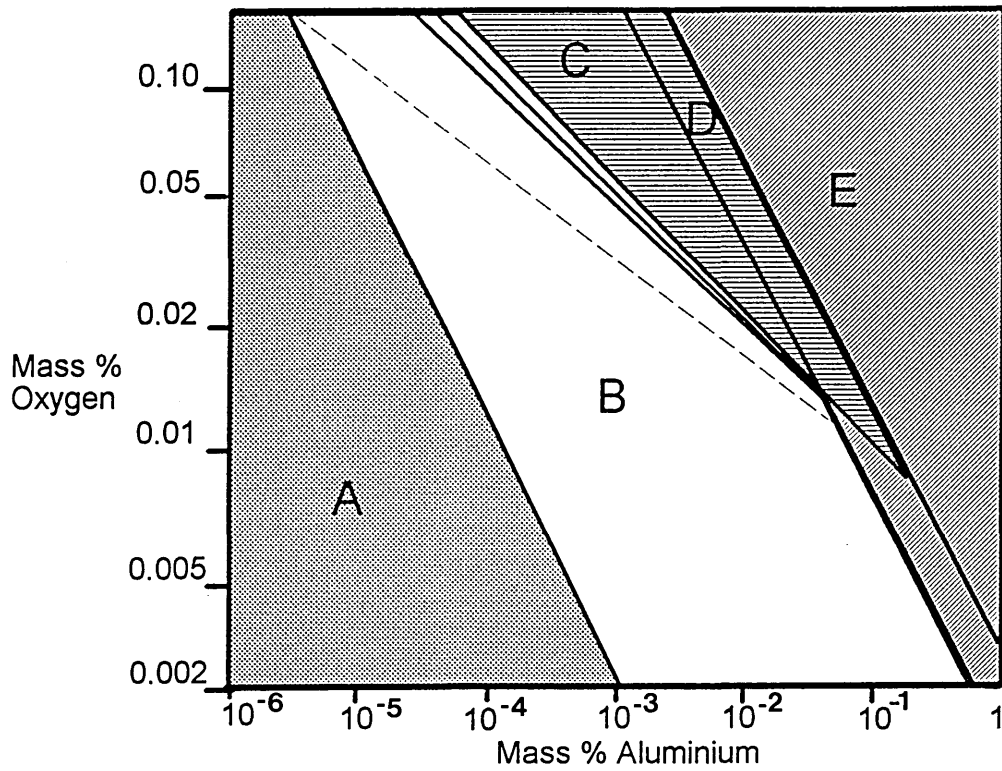


Figure 2.17 Diagram showing the conditions for the formation of nuclei in Fe-O-Al melts⁹⁶.

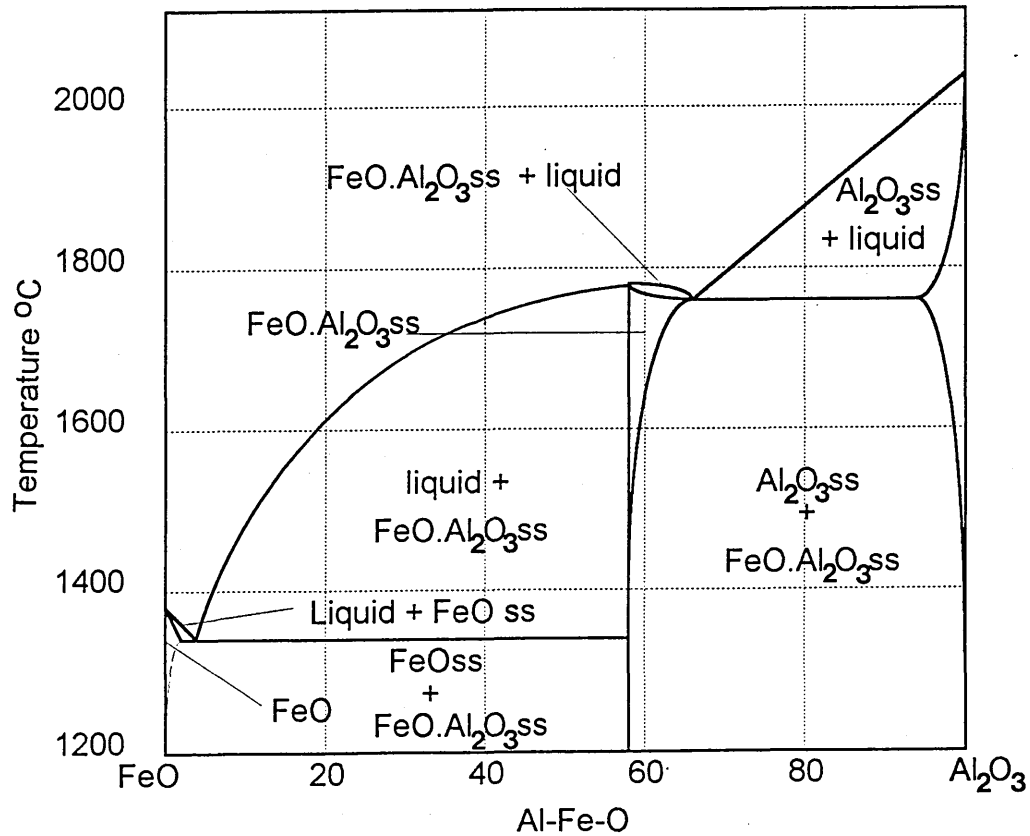


Figure 2.18 The Al-Fe-O phase diagram ¹⁰⁶

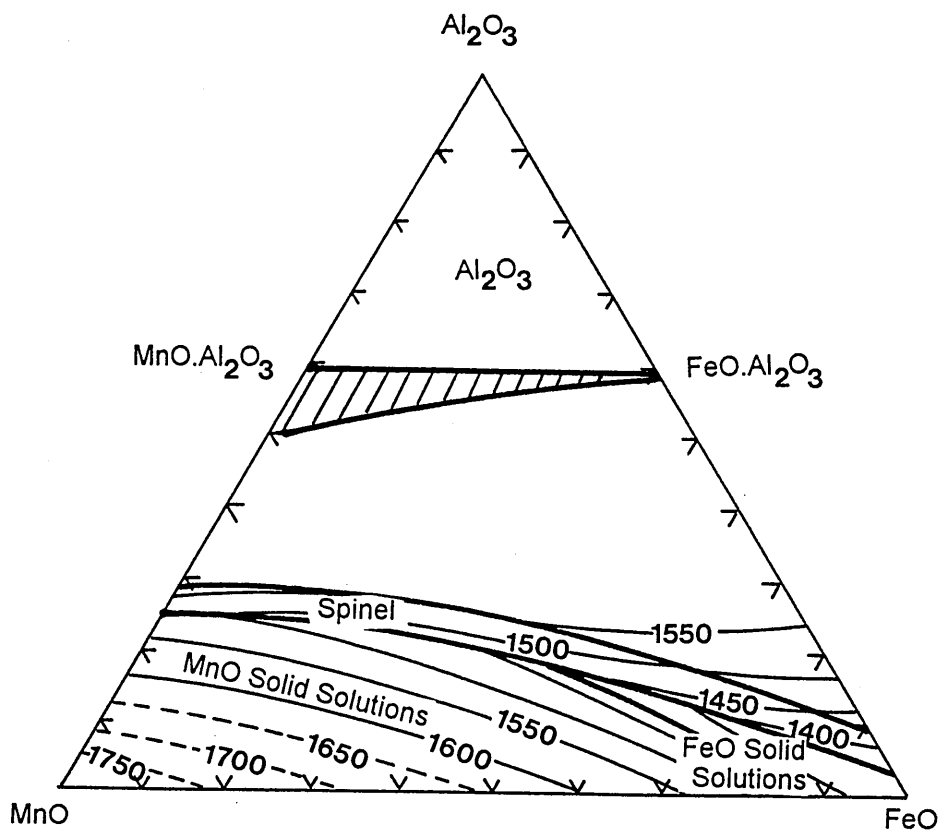


Figure 2.19 Phase diagram for the Al₂O₃-FeO-MnO system.¹⁰⁷

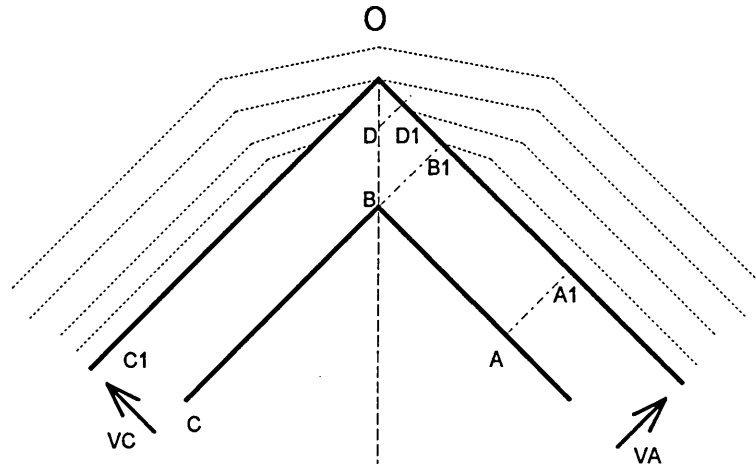


Figure 2.20 Displacement of impurities by two adjacent faces of a growing crystal.¹¹⁶

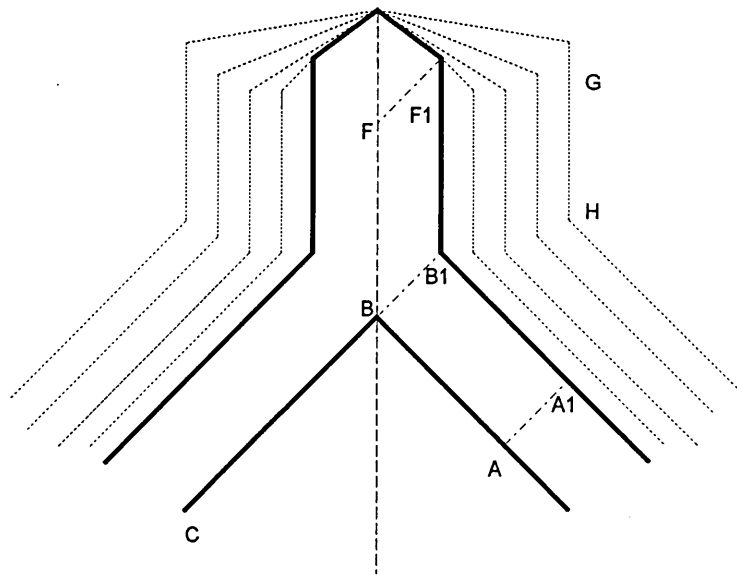


Figure 2.21 Formation of a primary stem or branch on an edge.¹¹⁶

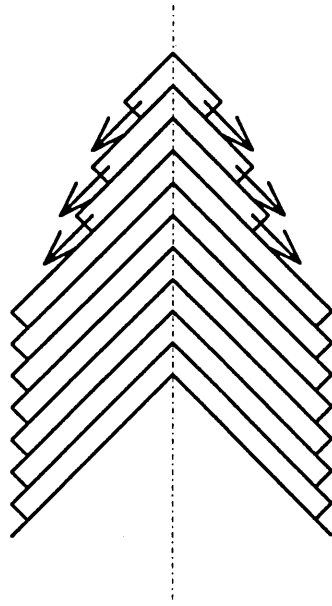


Figure 2.22 Formation of steps on a dendrite stem by layer deposition¹¹⁶.

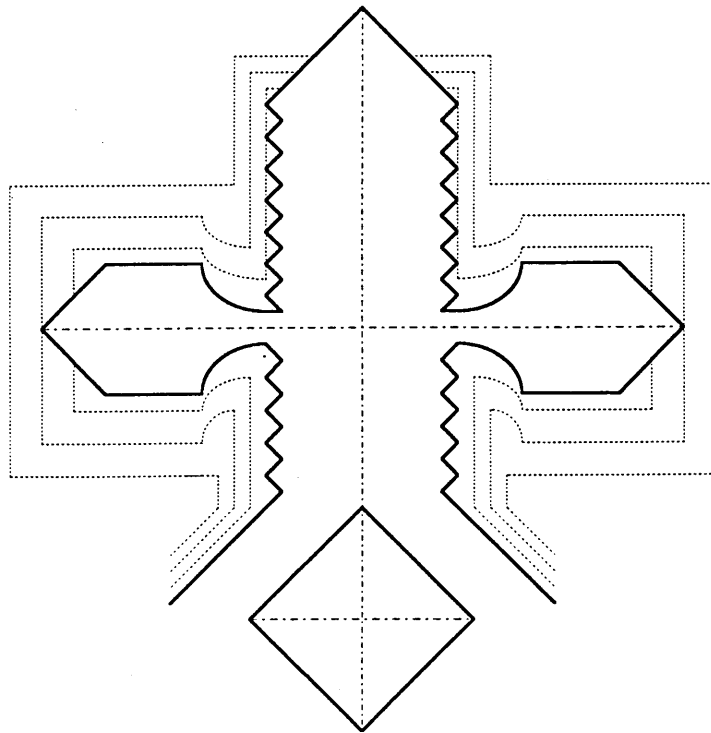


Figure 2.23 Formation of a secondary stem, with thin bridge at the root¹¹⁶.

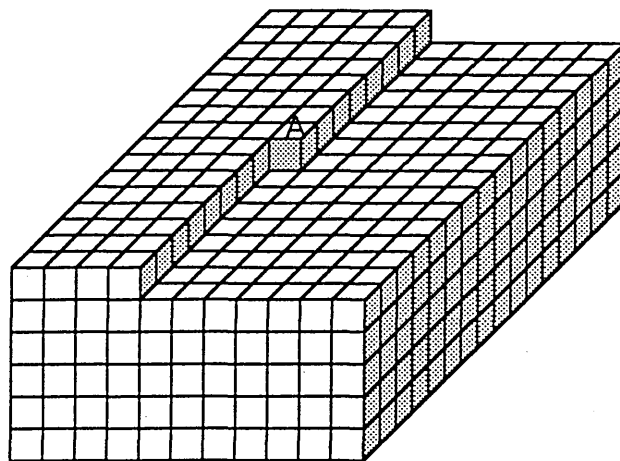


Figure 2.24 Schematic diagram showing the growth of crystal lattices by the addition of molecules, the repeatable growth step mechanism¹¹⁴.

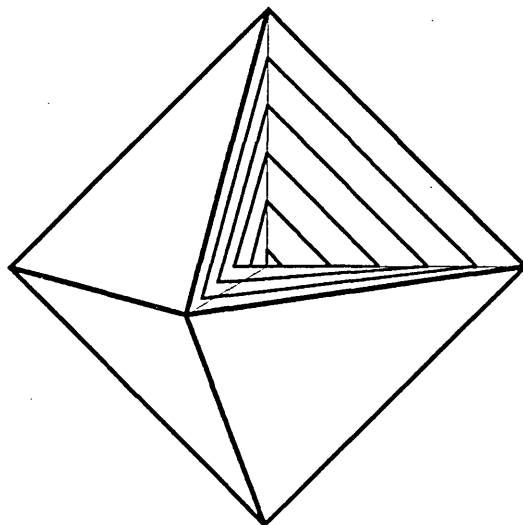


Figure 2.25 Polyhedral growth by growth pyramids of its faces resulting from the layers of adsorbed molecules¹¹⁶.

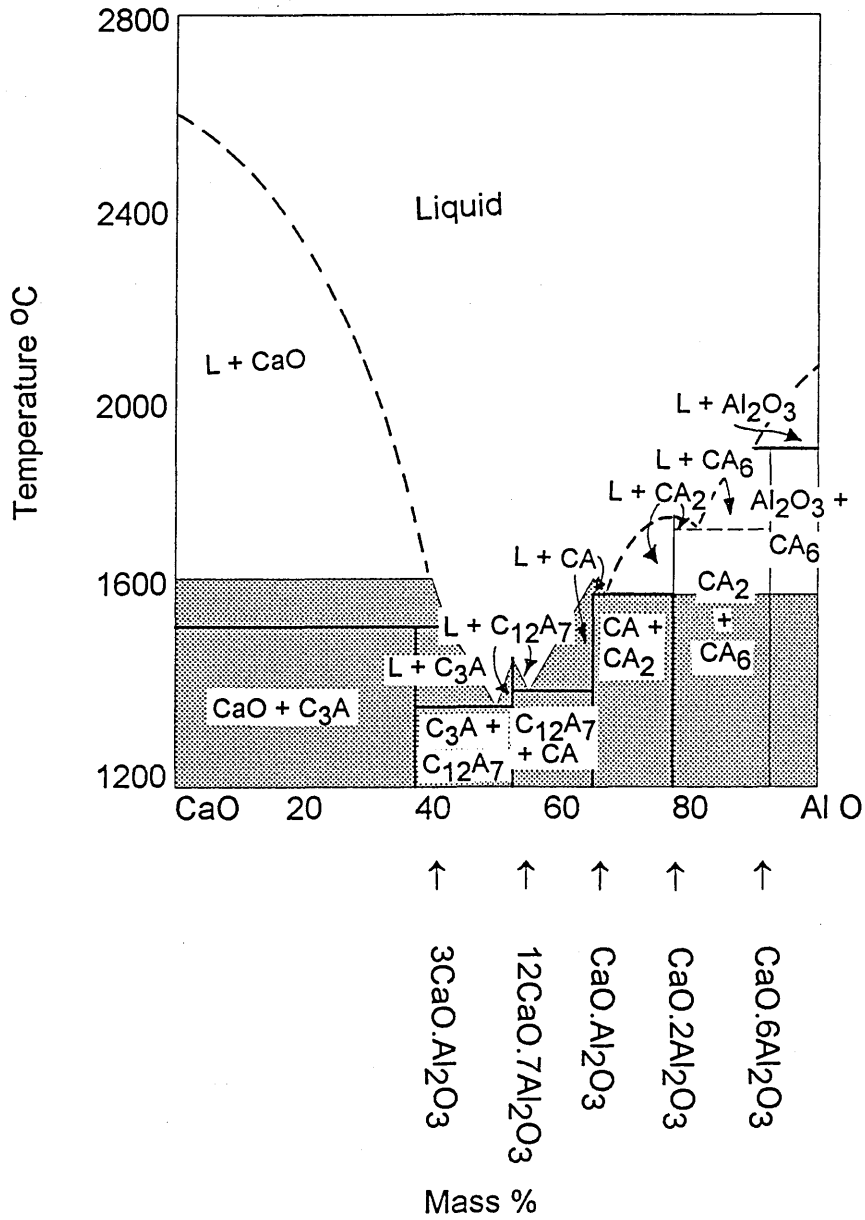


Figure 2.26 The CaO-Al₂O₃ equilibrium diagram.¹⁰⁶

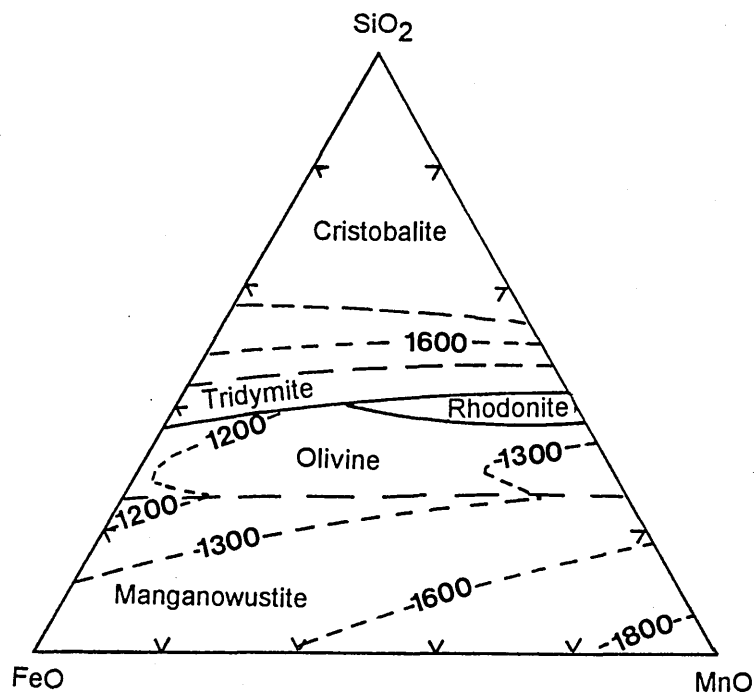


Figure 2.27 Phase diagram for the SiO₂-FeO-MnO system.¹³¹

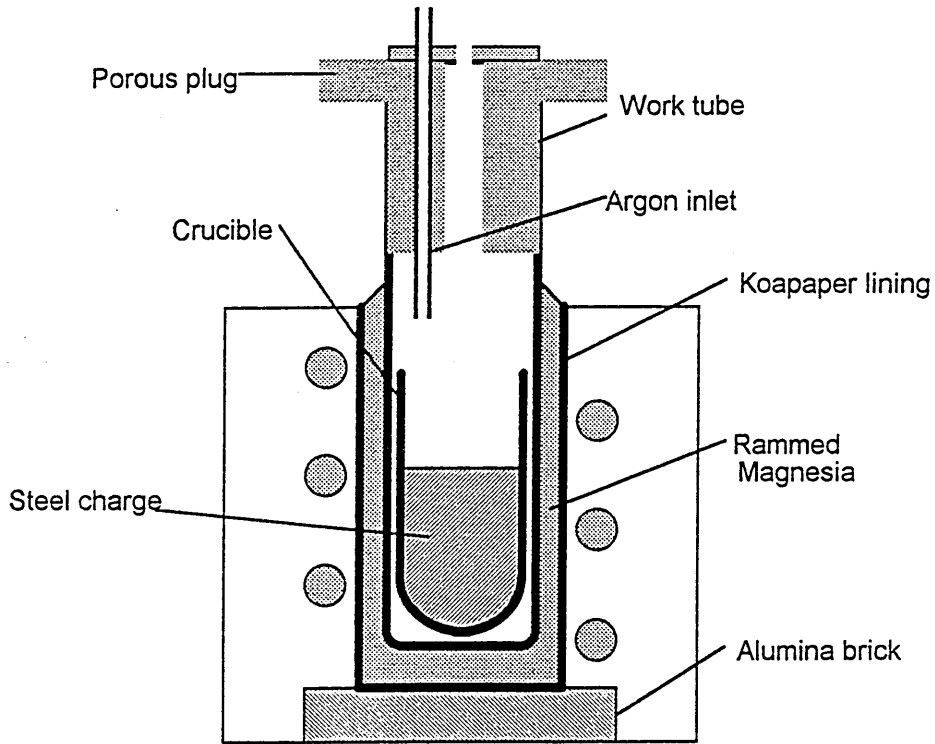


Figure 3.1 High frequency furnace arrangement.

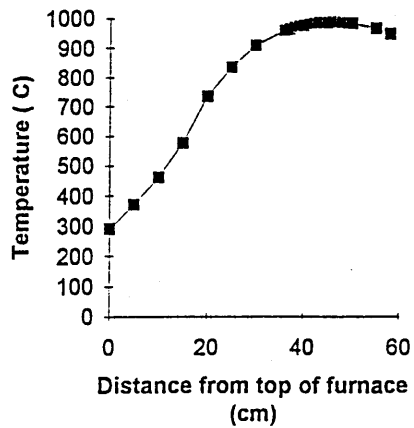


Figure 3.2 Temperature profile of the Carbolite pyrox vertical tube furnace, with the furnace set at 1000°C.

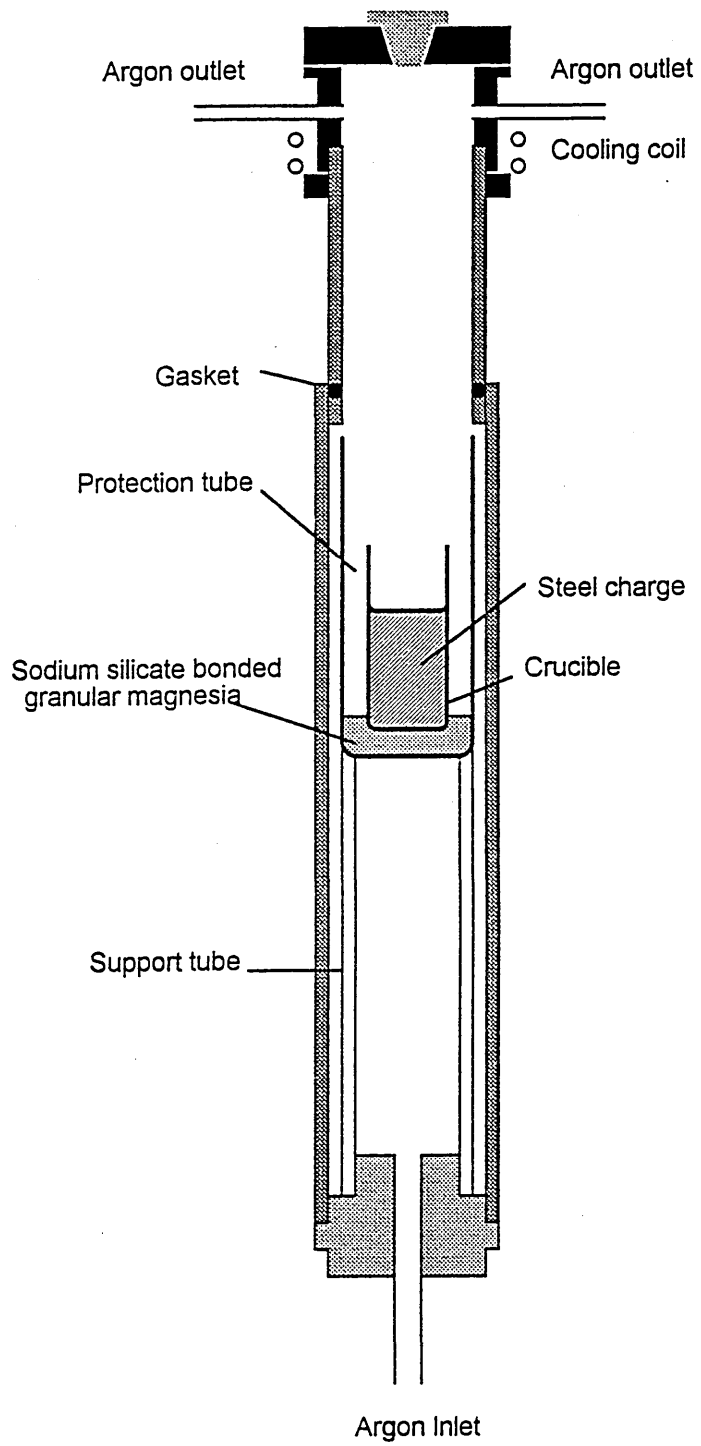


Figure 3.3 Vertical tube furnace experimental equipment

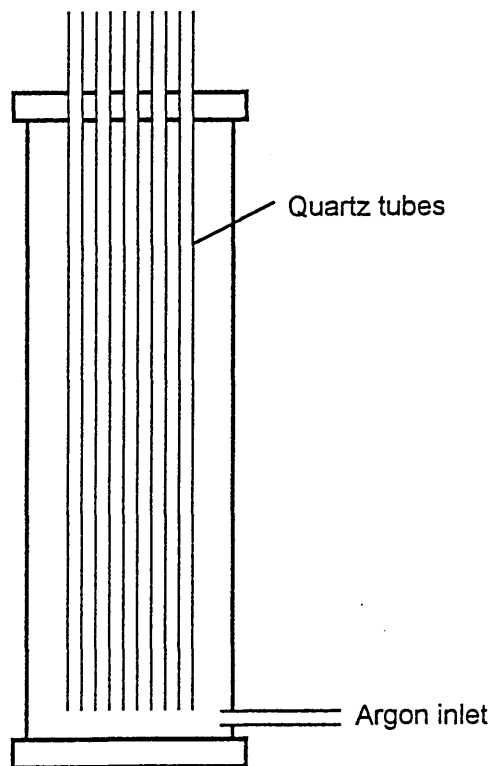


Figure 3.4 Equipment used to flush the quartz tubes with argon gas.

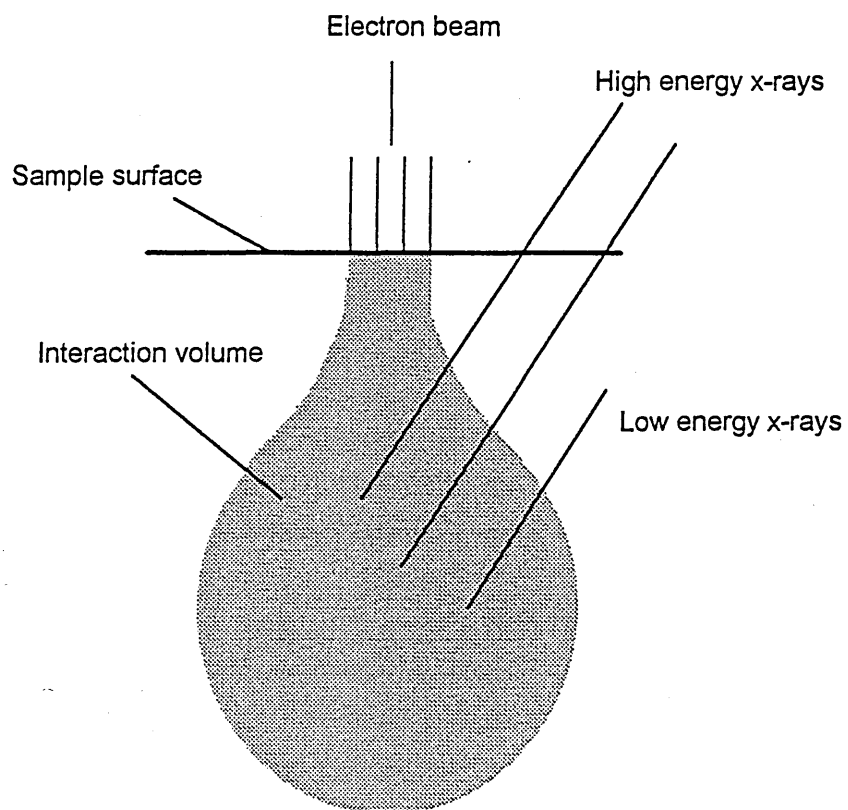


Figure 3.5 The interaction volume within a solid specimen from which x-rays are emitted.

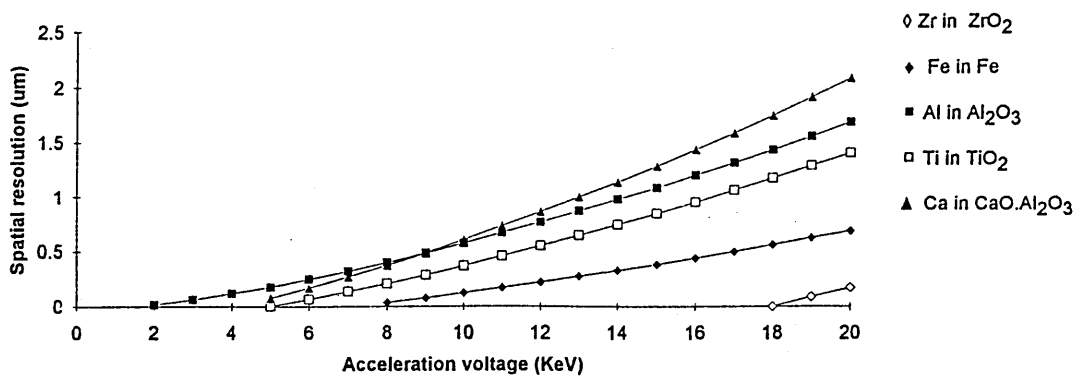


Figure 3.6 Spatial resolutions of selected elements in specific oxides.

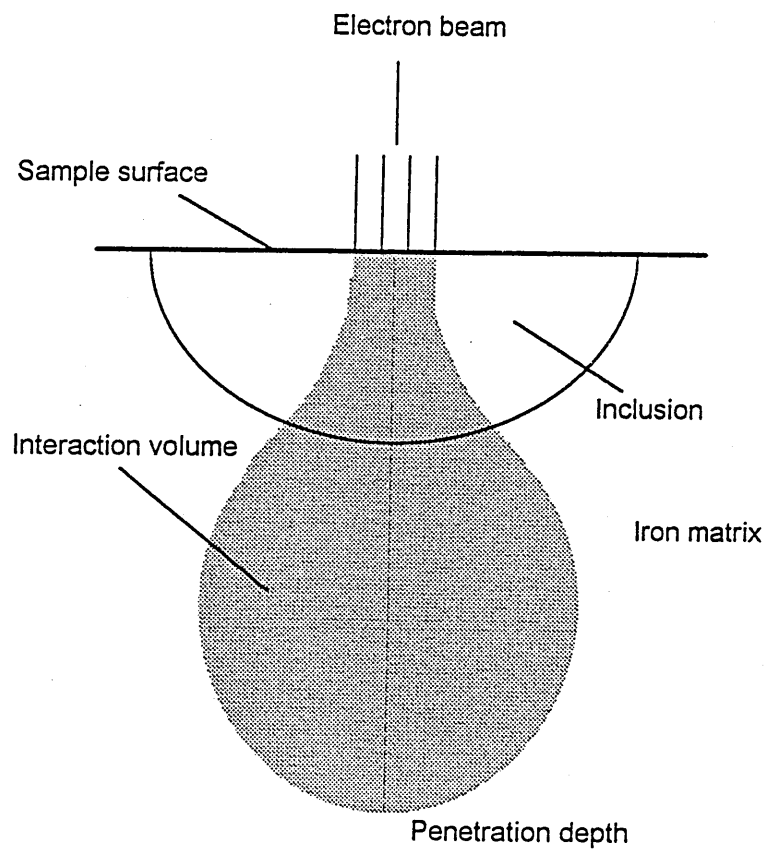


Figure 3.7 The interaction volume formed when using high acceleration voltages.

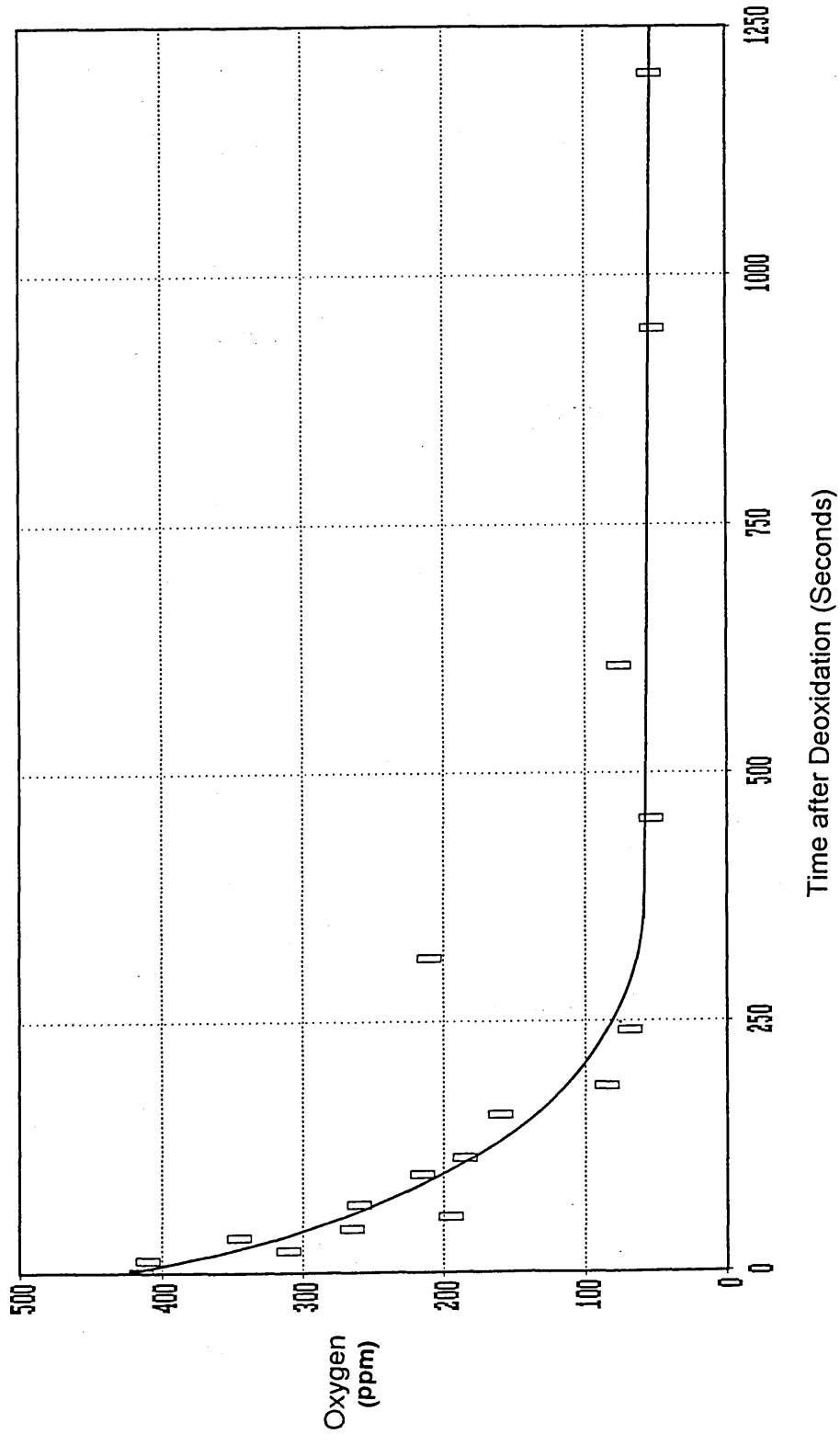


Figure 4.1(a) Total Oxygen Analysis Versus Time after Deoxidation with 0.3 mass% Aluminium Addition in the Vertical Tube Furnace Melt (LECO).

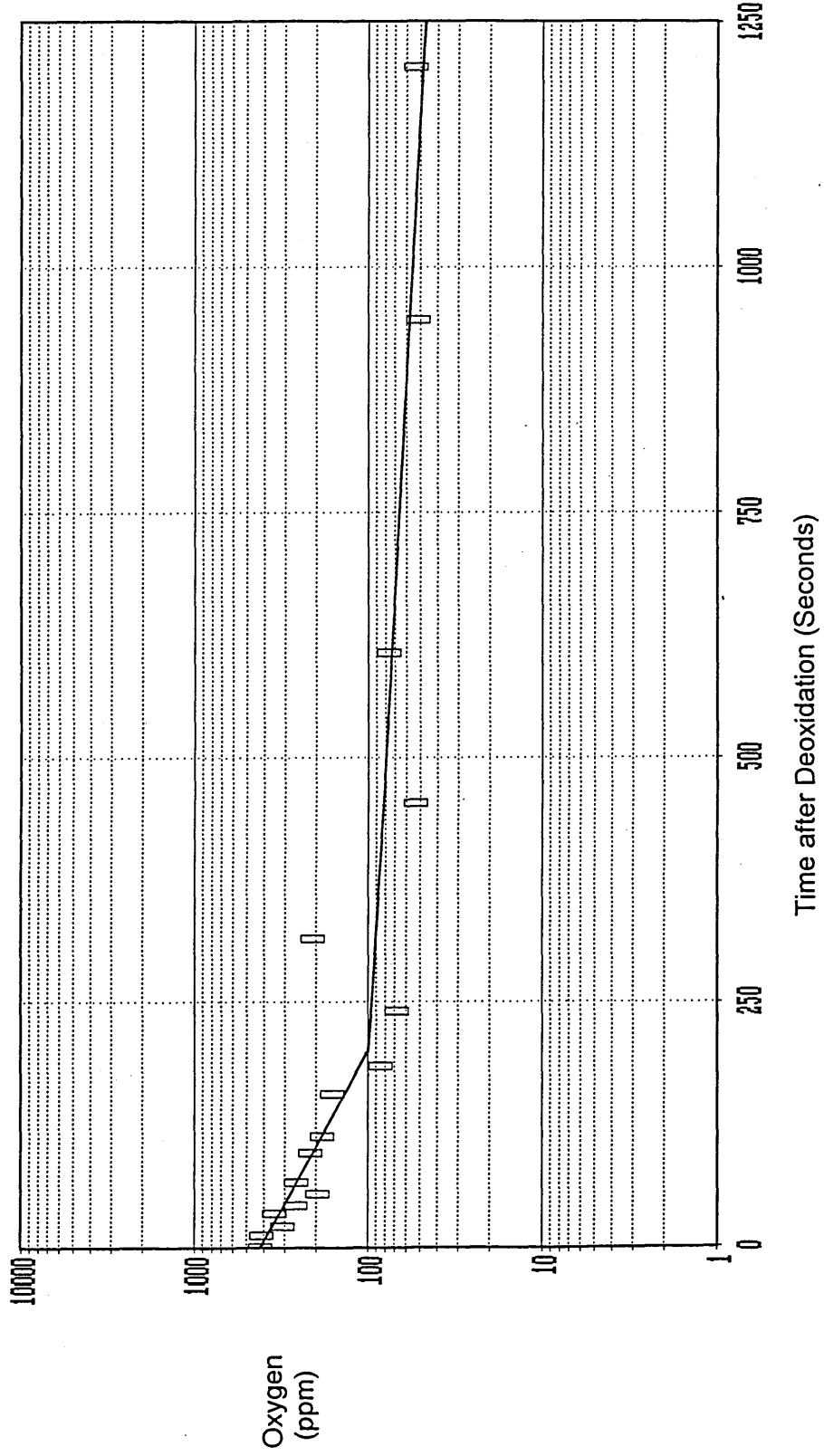


Figure 4.1(b) Total Oxygen Analysis Versus Time after Deoxidation with 0.3 mass% Aluminium Addition in the Vertical Tube Furnace Melt (LECO).

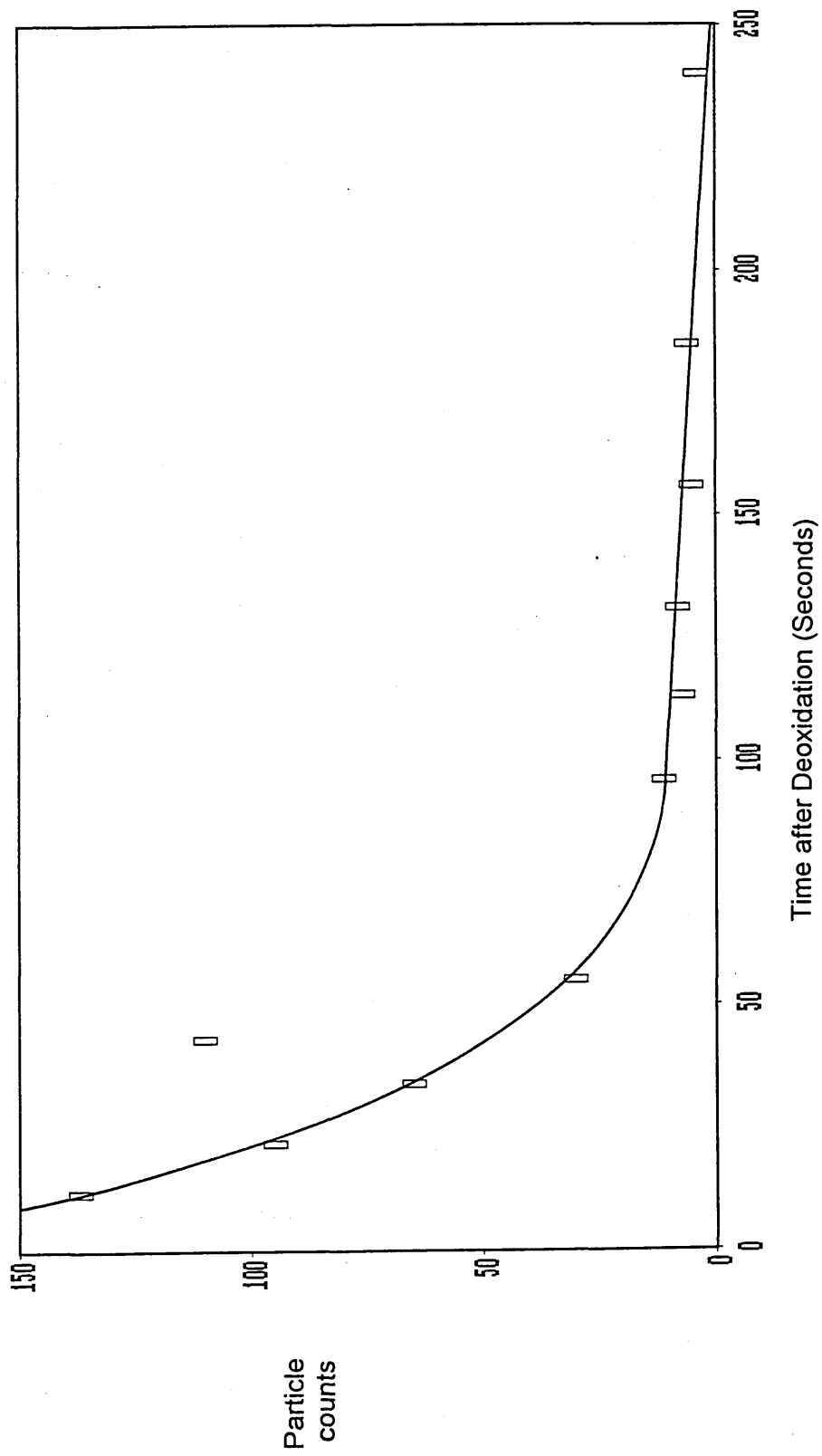


Figure 4.2 Number of Alumina Inclusions Counted Versus Time after Deoxidation in the Vertical Tube Furnace Melt (JEOL 840 SEM/Digiscan).

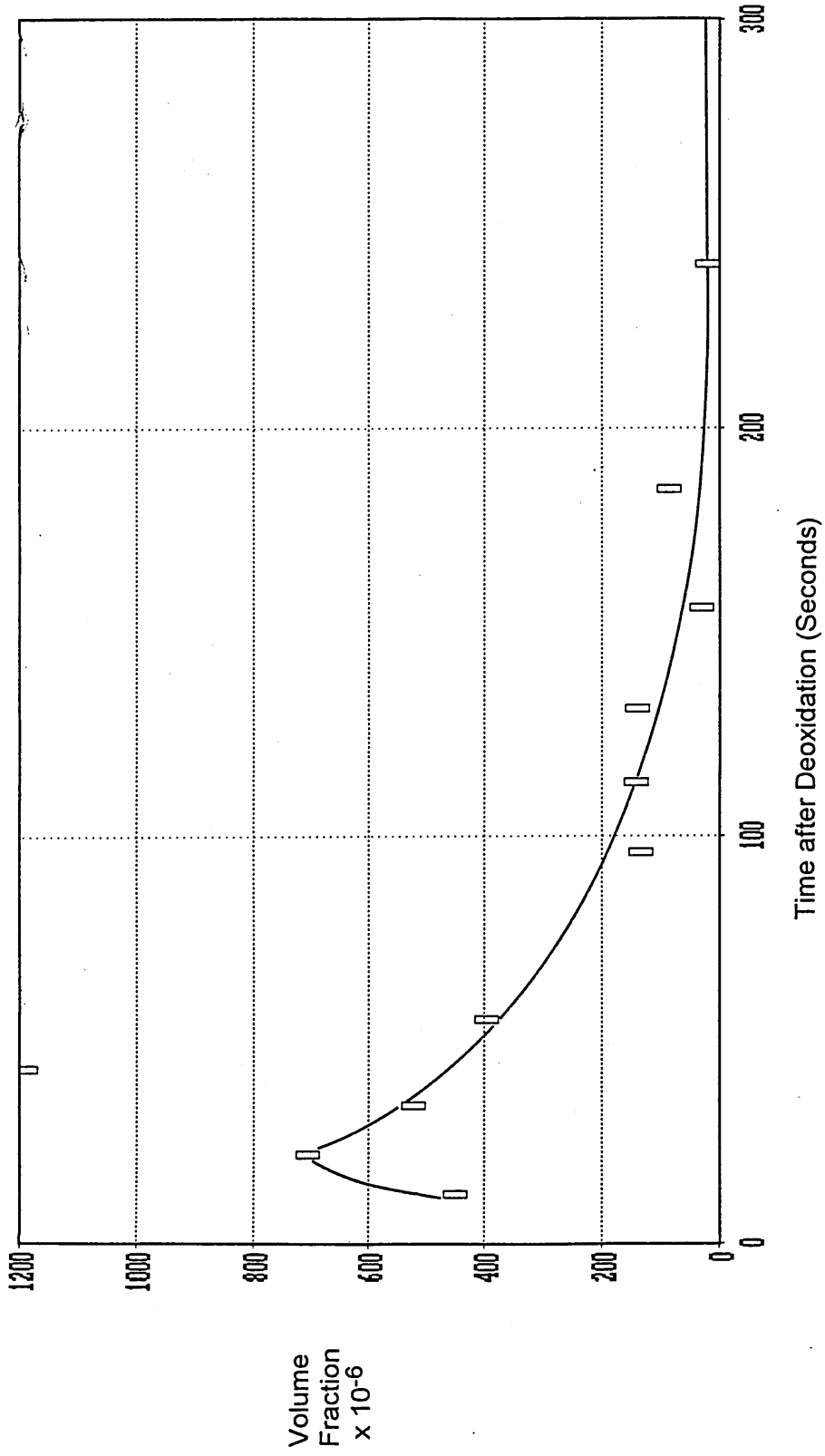


Figure 4.3 Volume Fraction of Alumina Inclusions Versus Time after Deoxidation in the Vertical Tube Furnace Melt (JEOL 840 SEM/Digiscan) .

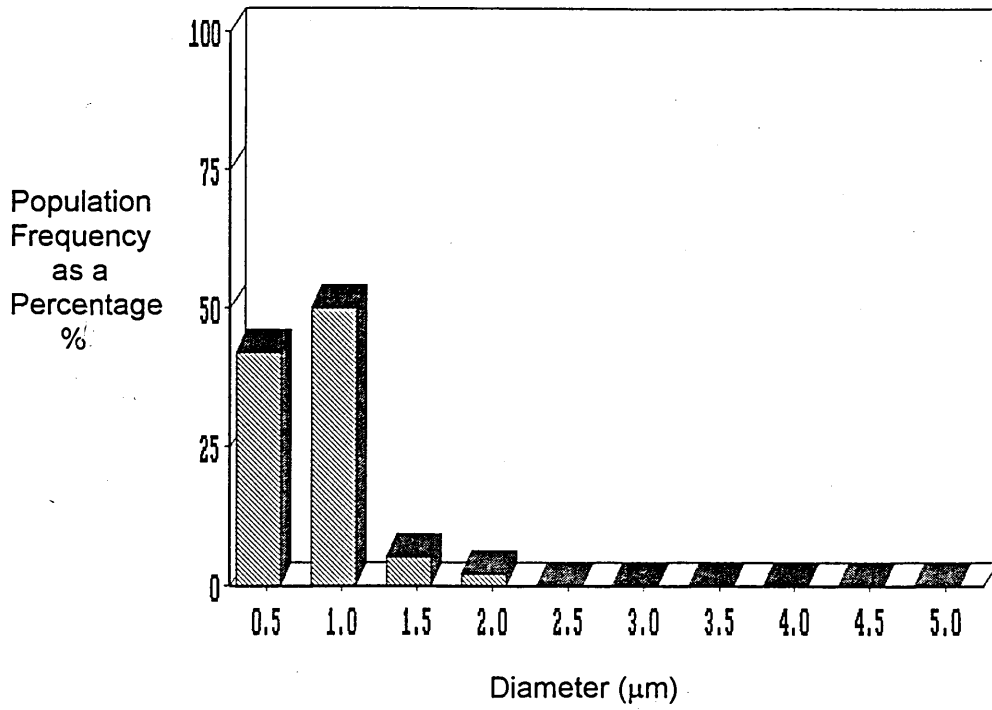


Figure 4.4 (a) Size Distribution of Alumina Inclusions in the Sample taken 12 Seconds after Deoxidation in the Vertical Tube Furnace Melt (Jeol 840 SEM/Digiscan).

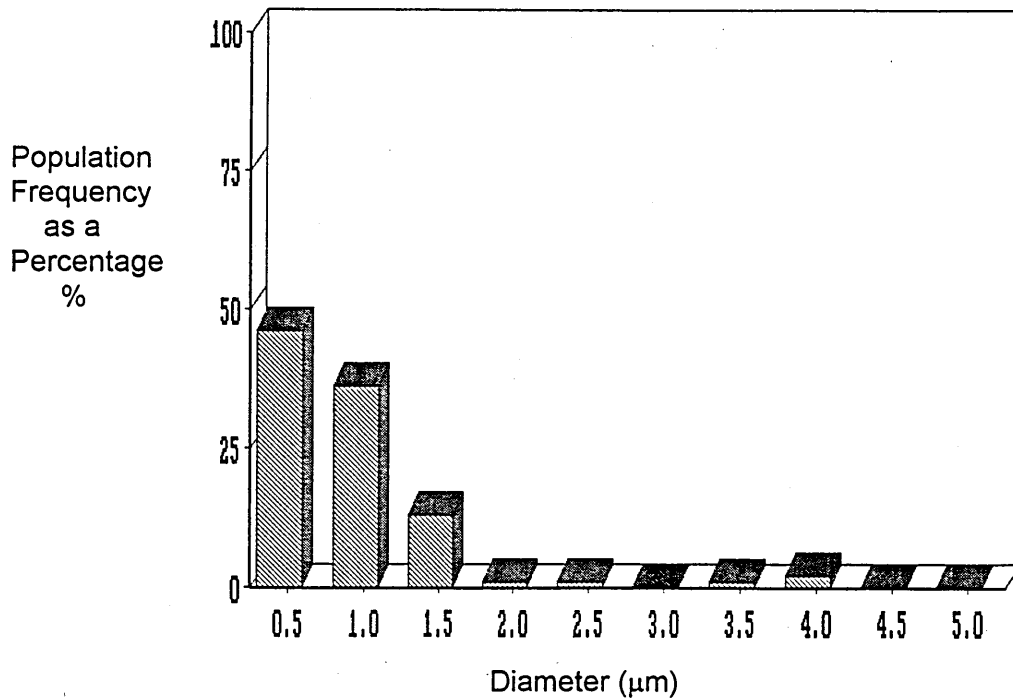


Figure 4.4 (b) Size Distribution of Alumina Inclusions in the Sample taken 22 Seconds after Deoxidation in the Vertical Tube Furnace Melt (Jeol 840 SEM/Digiscan).

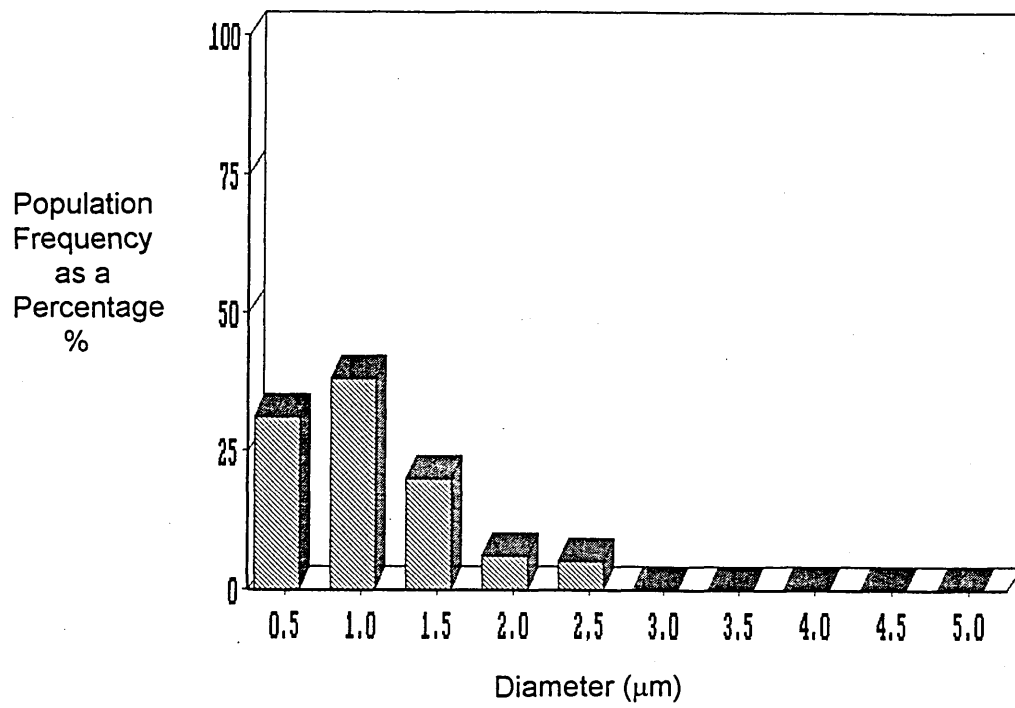


Figure 4.4 (c) Size Distribution of Alumina Inclusions in the Sample taken 34 Seconds after Deoxidation in the Vertical Tube Furnace Melt (Jeol 840 SEM/Digiscan).

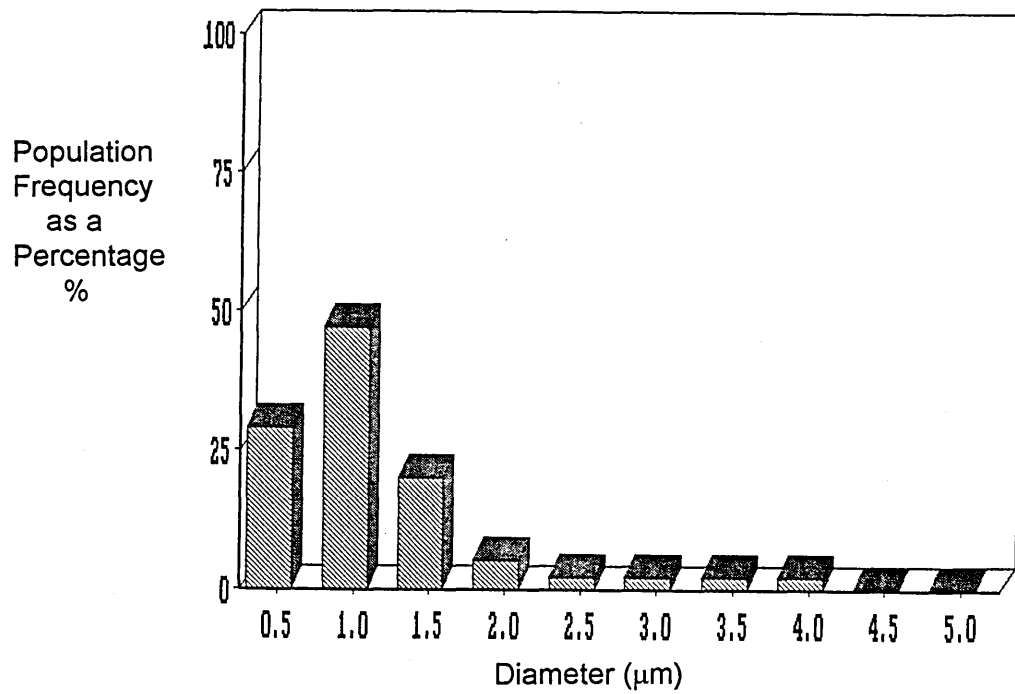


Figure 4.4 (d) Size Distribution of Alumina Inclusions in the Sample taken 43 Seconds after Deoxidation in the Vertical Tube Furnace Melt (Jeol 840 SEM/Digiscan).

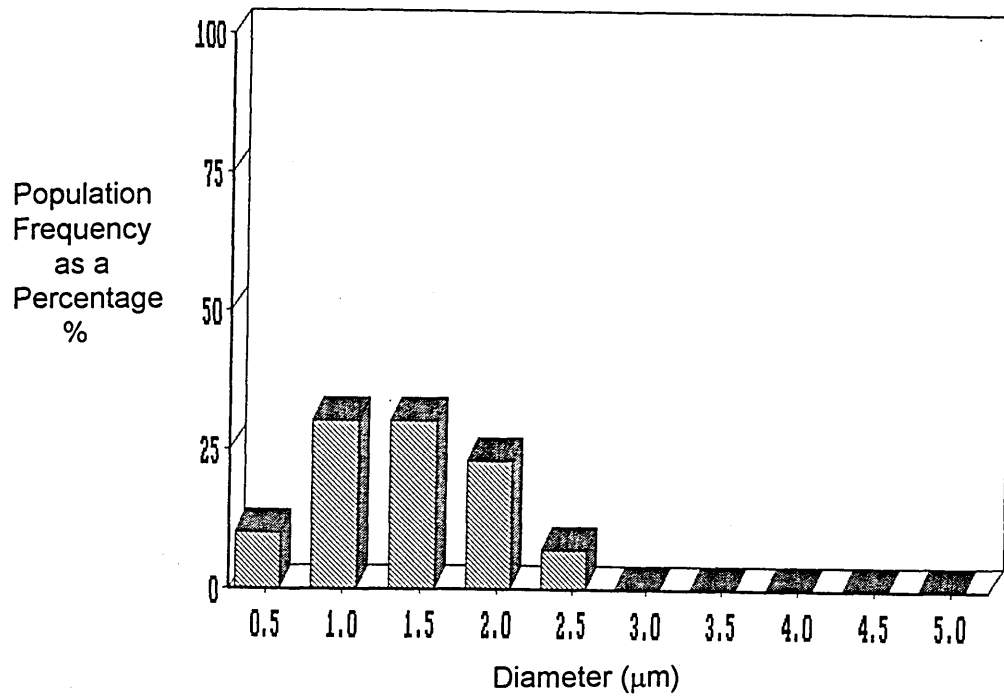


Figure 4.4 (e) Size Distribution of Alumina Inclusions in the Sample taken 55 Seconds after Deoxidation in the Vertical Tube Furnace Melt (Jeol 840 SEM/Digiscan).

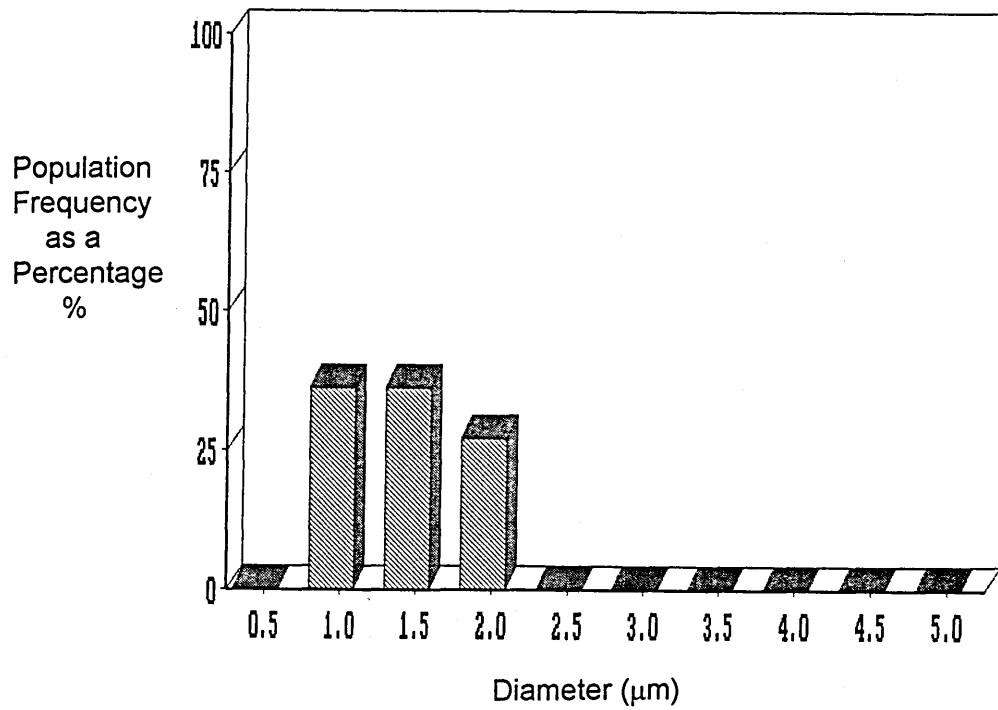


Figure 4.4 (f) Size Distribution of Alumina Inclusions in the Sample taken 96 Seconds after Deoxidation in the Vertical Tube Furnace Melt (Jeol 840 SEM/Digiscan).

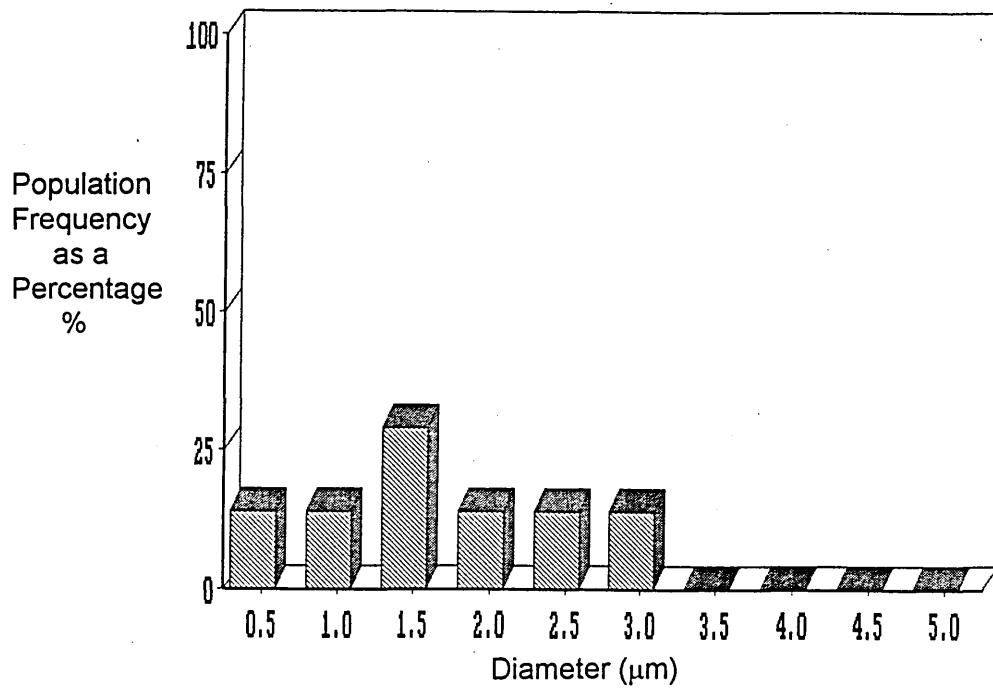


Figure 4.4 (g) Size Distribution of Alumina Inclusions in the Sample taken 113 Seconds after Deoxidation in the Vertical Tube Furnace Melt (Jeol 840 SEM/Digiscan).

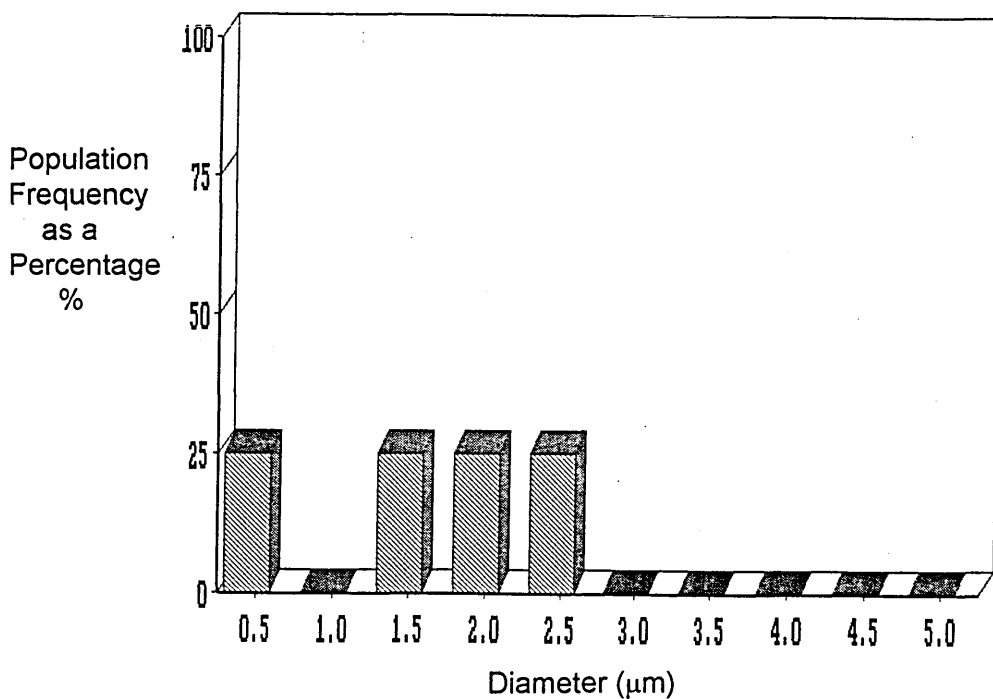


Figure 4.4 (h) Size Distribution of Alumina Inclusions in the Sample taken 131 Seconds after Deoxidation in the Vertical Tube Furnace Melt (Jeol 840 SEM/Digiscan).

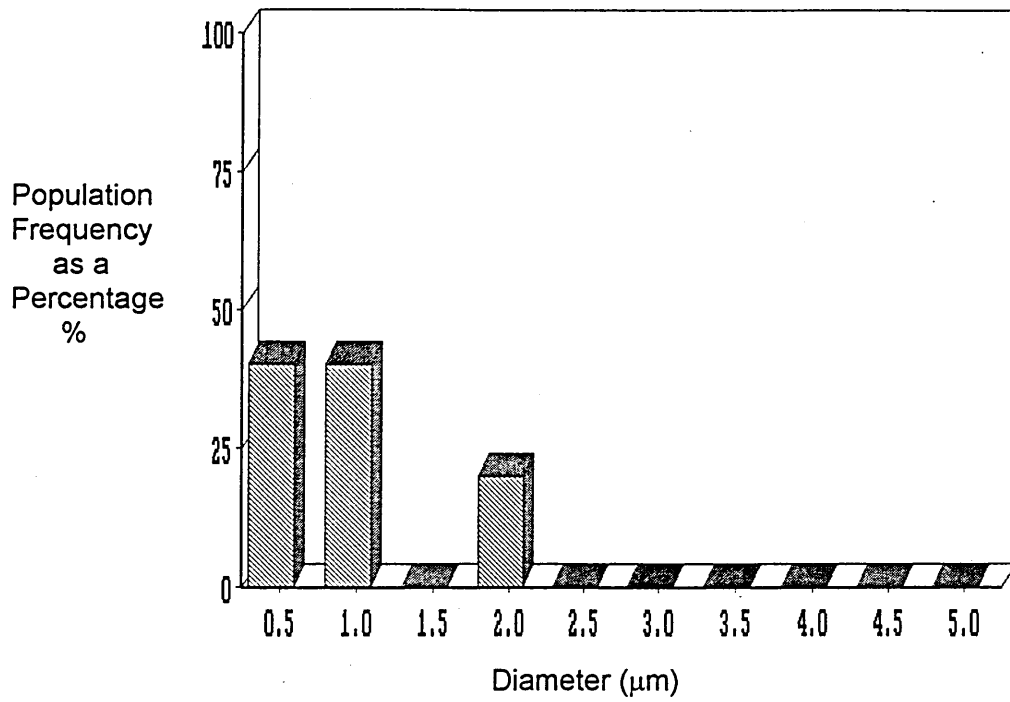


Figure 4.4 (i) Size Distribution of Alumina Inclusions in the Sample taken 156 Seconds after Deoxidation in the Vertical Tube Furnace Melt (Jeol 840 SEM/Digiscan).

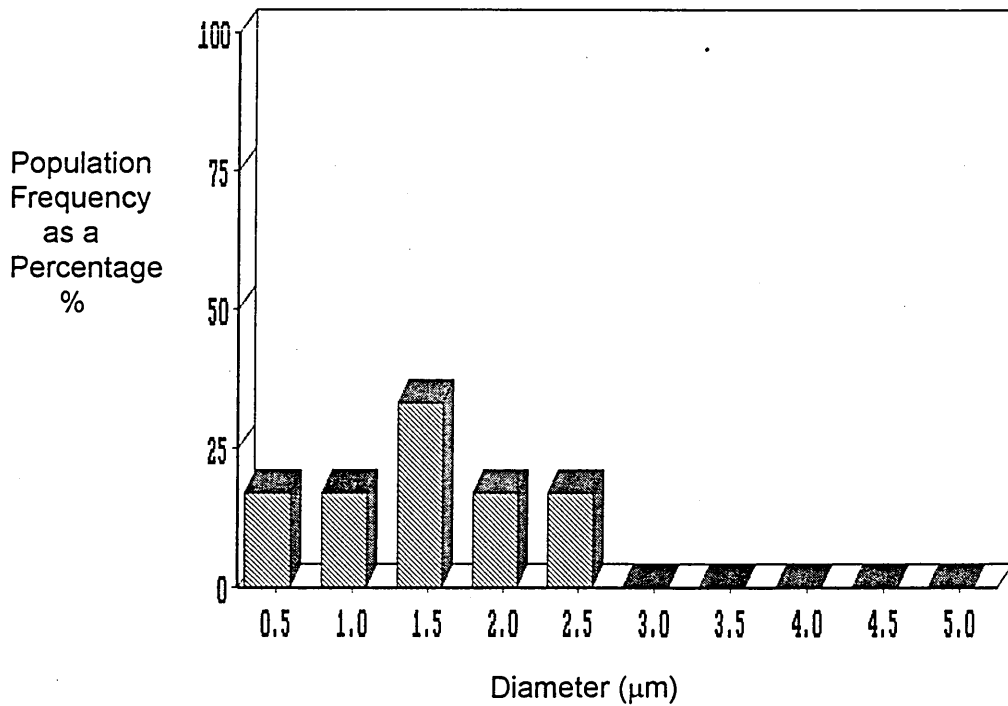


Figure 4.4 (j) Size Distribution of Alumina Inclusions in the Sample taken 185 Seconds after Deoxidation in the Vertical Tube Furnace Melt (Jeol 840 SEM/Digiscan).

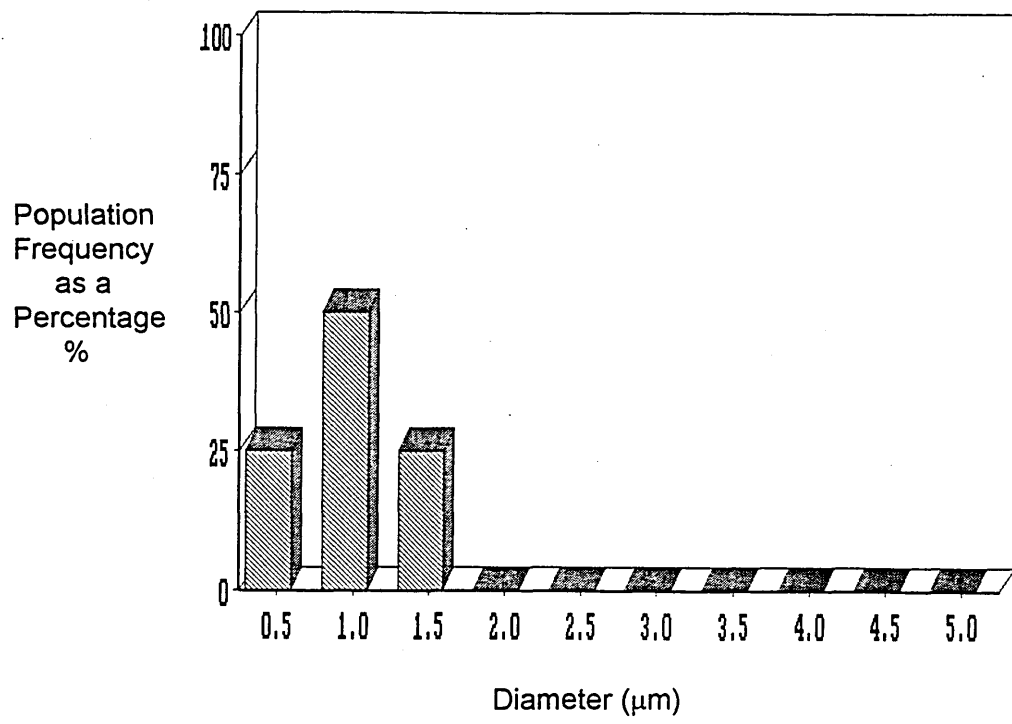


Figure 4.4 (k) Size Distribution of Alumina Inclusions in the Sample taken 240 Seconds after Deoxidation in the Vertical Tube Furnace Melt (Jeol 840 SEM/Digiscan).

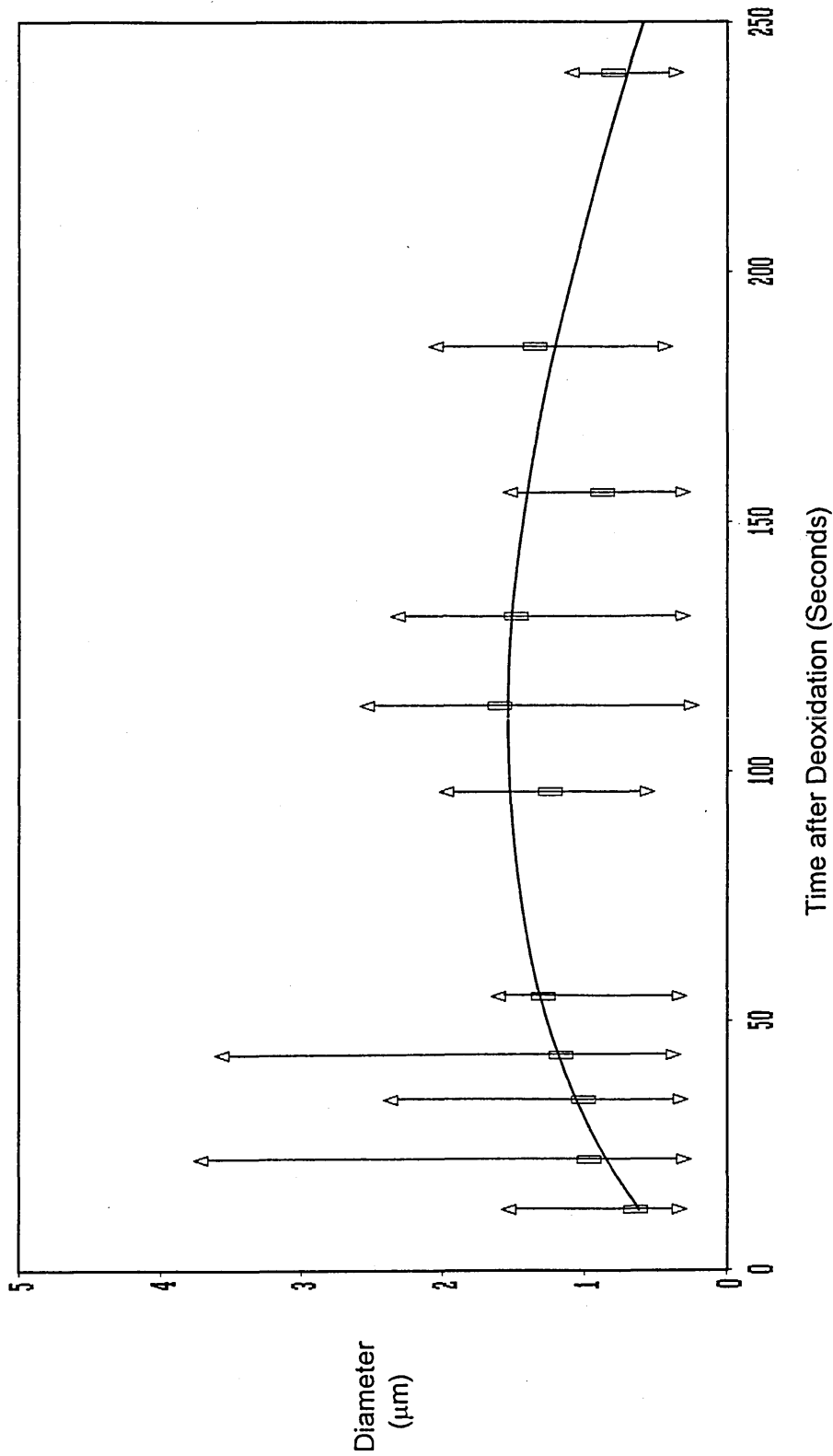


Figure 4.5 Mean Alumina Inclusions Diameter Versus Time after Deoxidation in the Vertical Tube Furnace Melt (JEOL 840 SEM/Digiscan).

△ - Mean from Maximum Size Band ▽ - Mean from Minimum Size Band □ - Mean Diameter

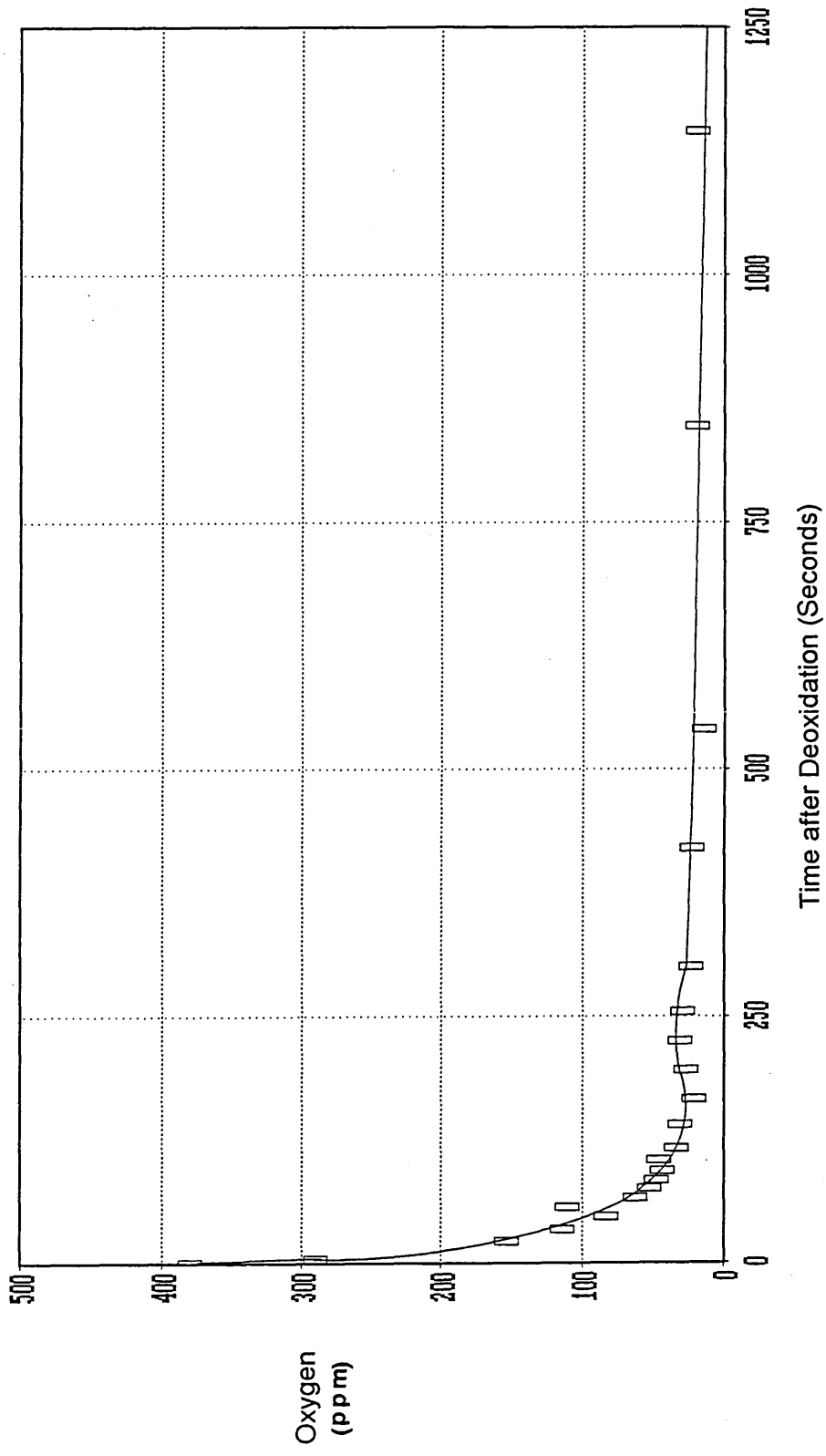


Figure 4.6(a) Total Oxygen Analysis Versus Time after Deoxidation with 0.3 mass% Aluminium Addition in the High Frequency Furnace Melt (LECO).

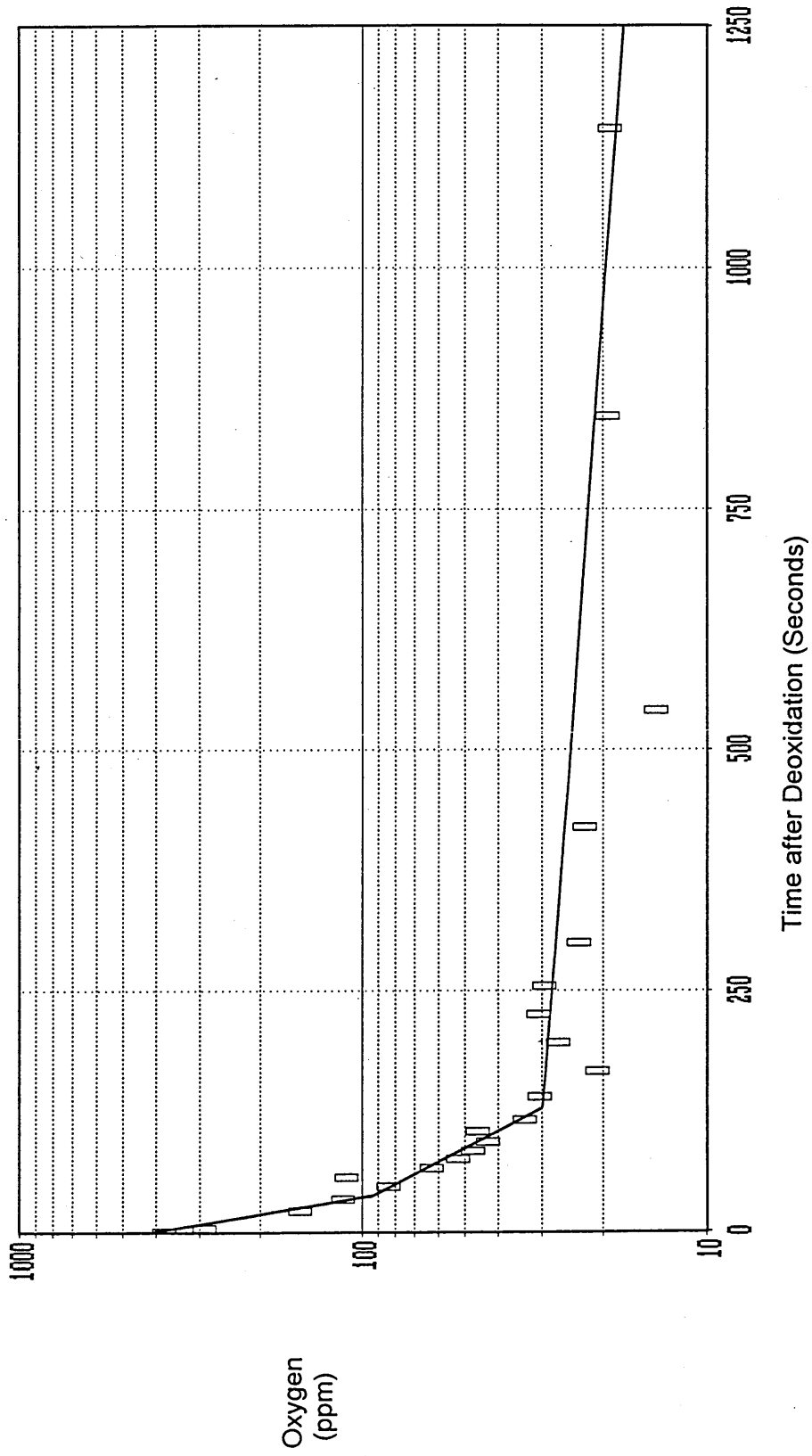


Figure 4.6(b) Total Oxygen Analysis Versus Time after Deoxidation with 0.3 mass% Aluminium Addition in the High Frequency Furnace Melt (LECO).

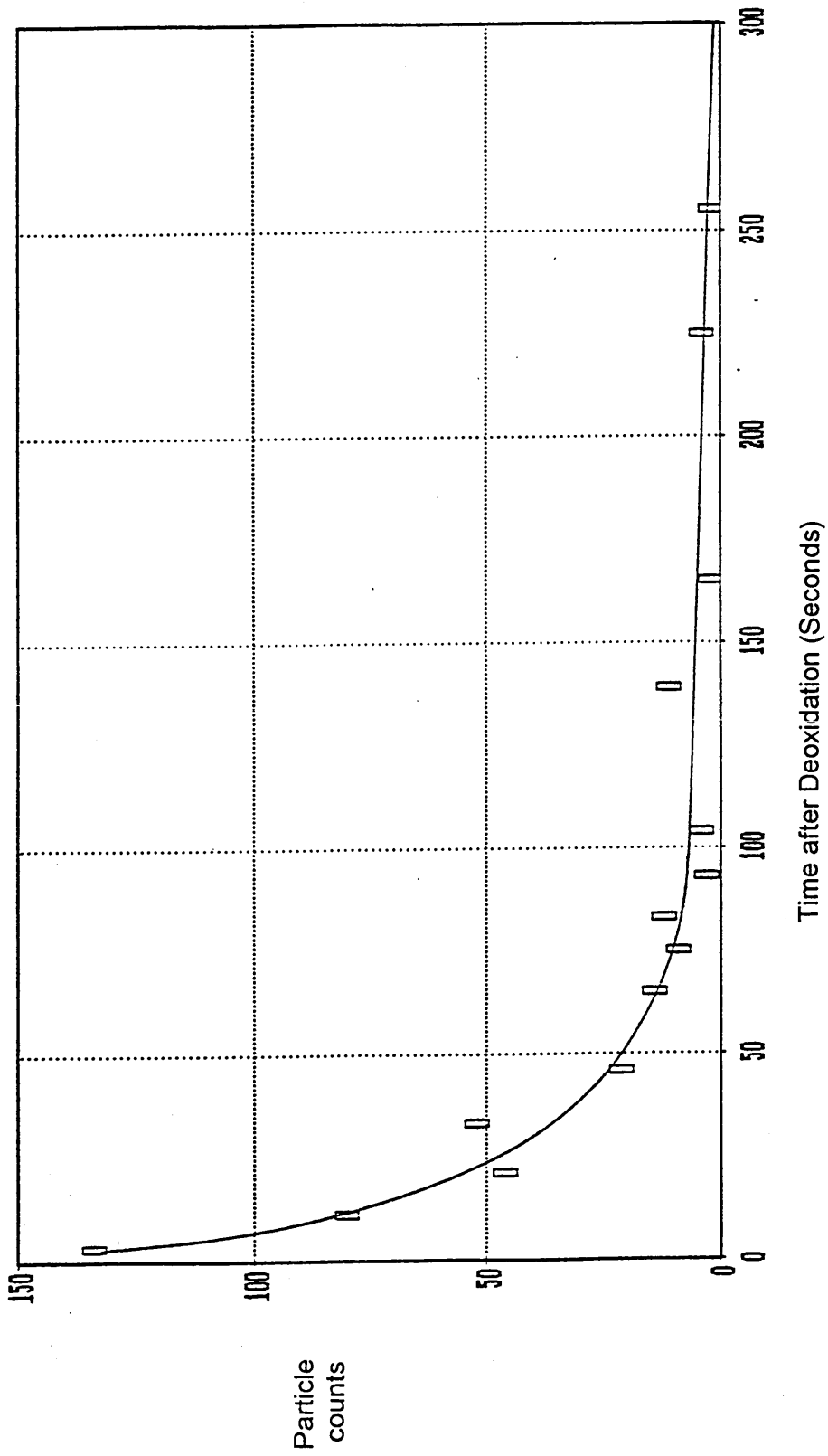


Figure 4.7 Number of Alumina Inclusions Counted Versus Time after Deoxidation in the High Frequency Furnace Melt (JEOL 840 SEM/Digiscan) .

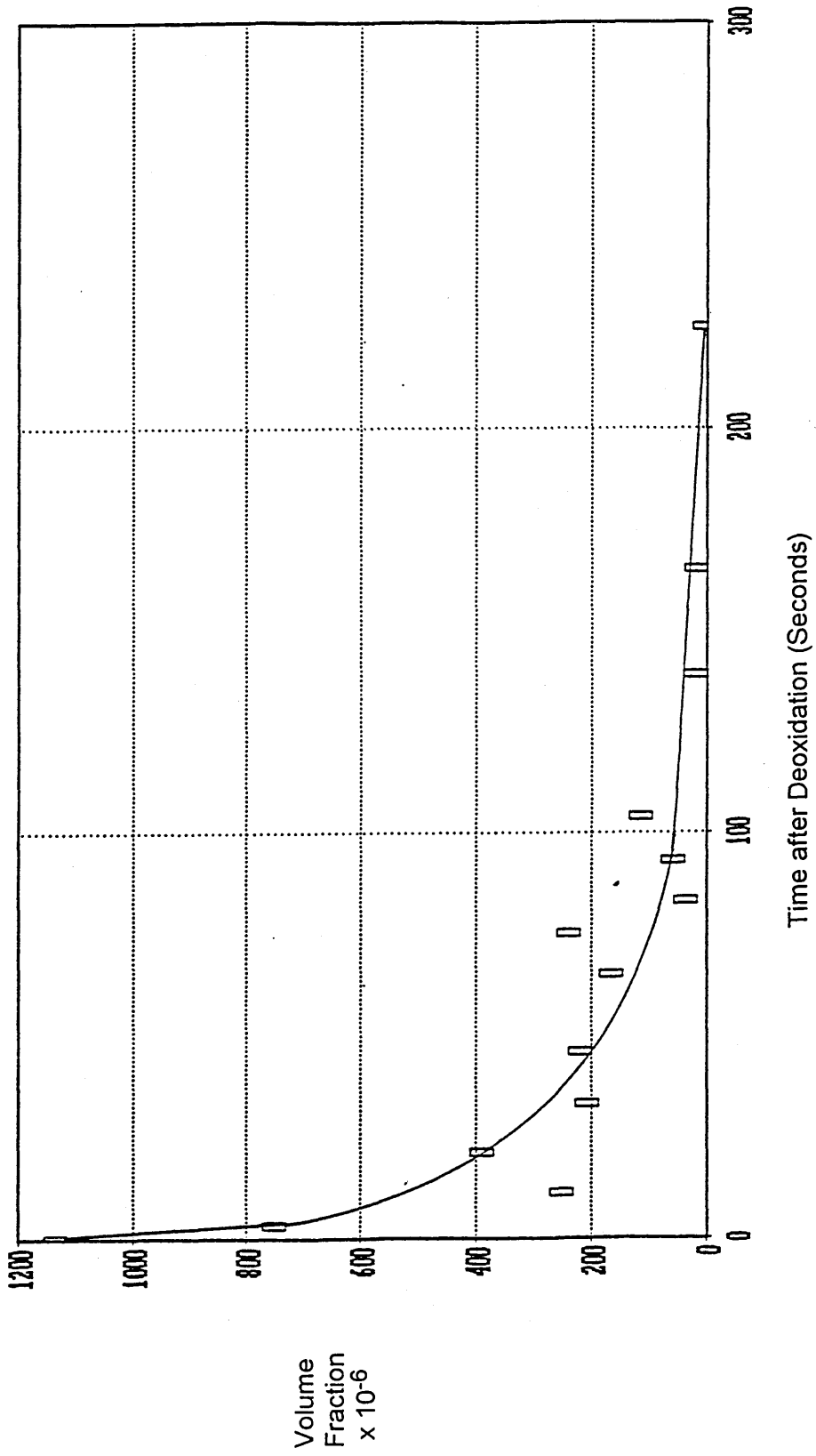


Figure 4.8 Volume Fraction of Alumina Inclusions Versus Time after Deoxidation in the High Frequency Furnace Melt (JEOL 840 SEM/Digiscan) .

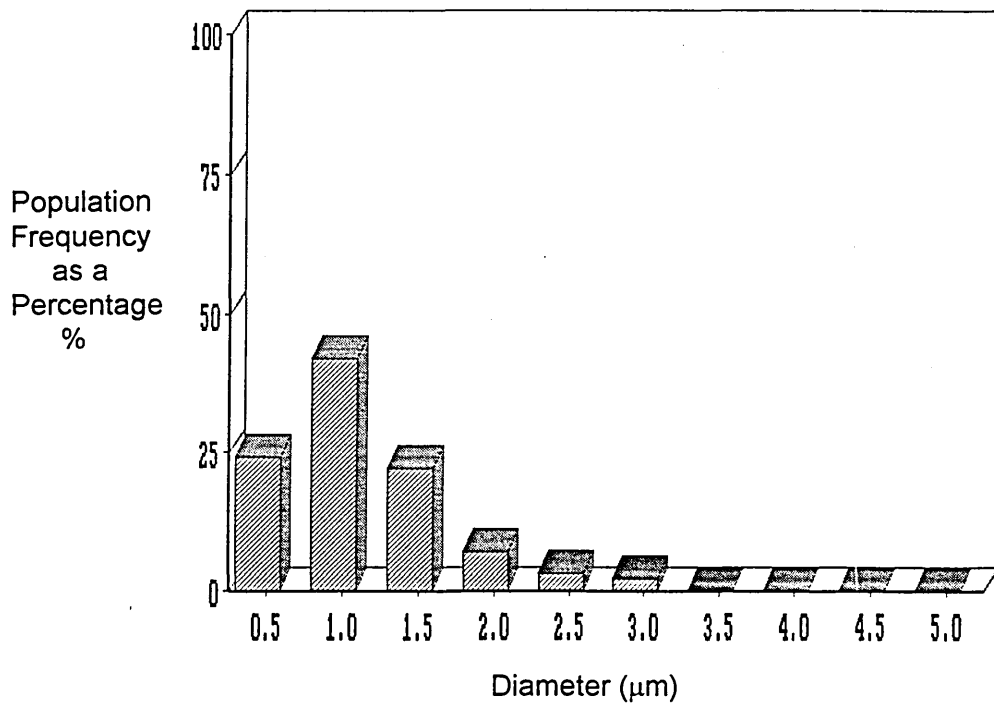


Figure 4.9 (a) Size Distribution of Alumina Inclusions in the Sample taken 3 Seconds after Deoxidation in the High Frequency Furnace Melt (Jeol 840 SEM/Digiscan).

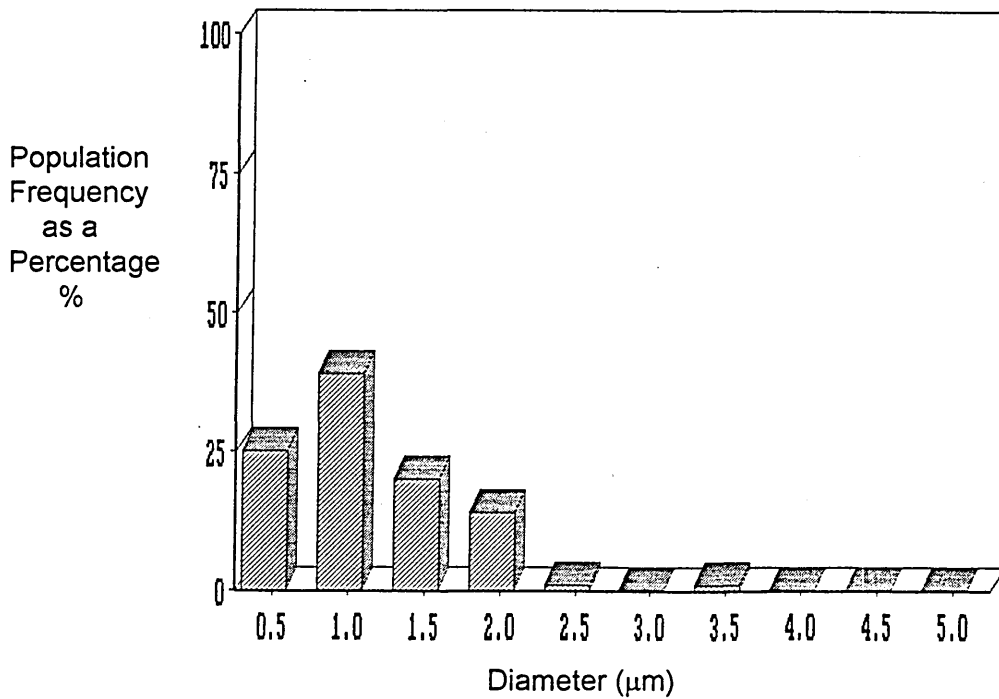


Figure 4.9 (b) Size Distribution of Alumina Inclusions in the Sample taken 11 Seconds after Deoxidation in the High Frequency Furnace Melt (Jeol 840 SEM/Digiscan).

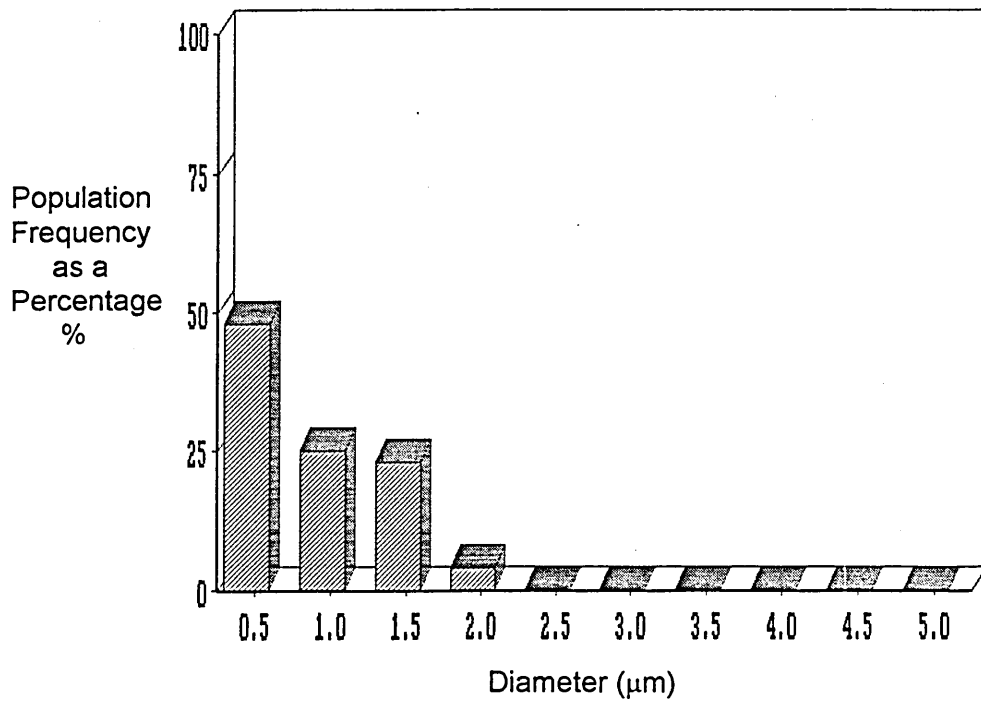


Figure 4.9 (c) Size Distribution of Alumina Inclusions in the Sample taken 21 Seconds after Deoxidation in the High Frequency Furnace Melt (Jeol 840 SEM/Digiscan).

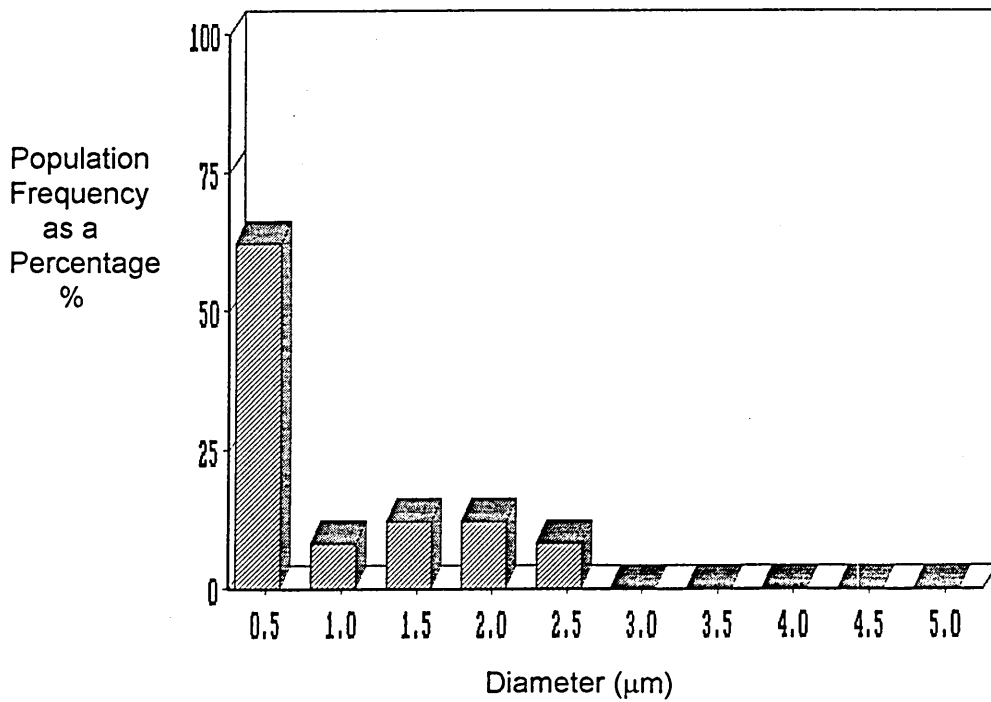


Figure 4.9 (d) Size Distribution of Alumina Inclusions in the Sample taken 33 Seconds after Deoxidation in the High Frequency Furnace Melt (Jeol 840 SEM/Digiscan).

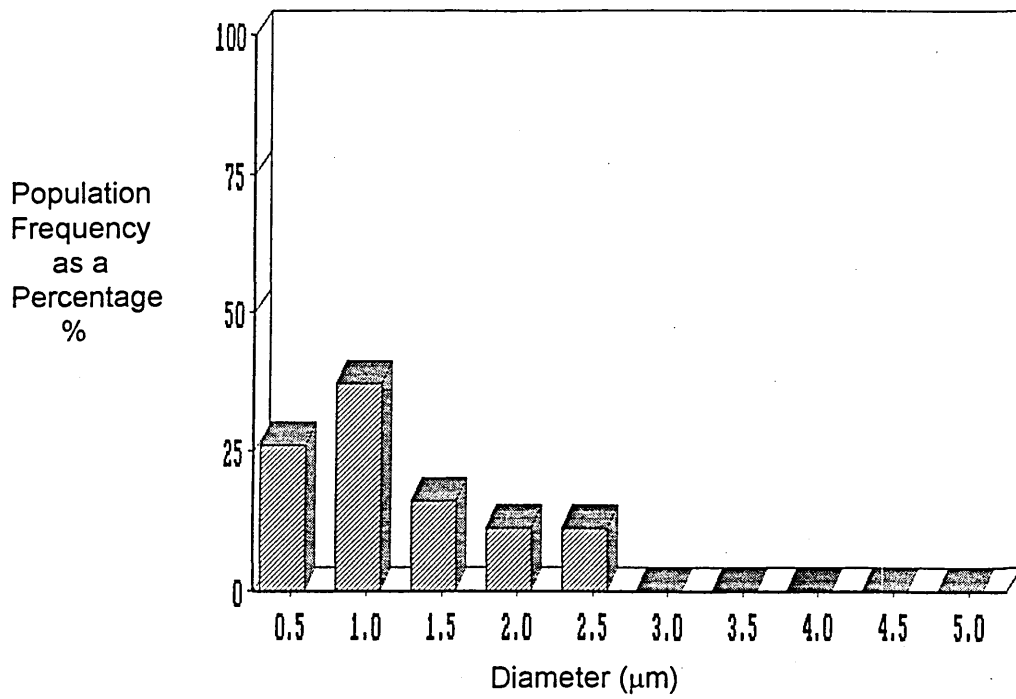


Figure 4.9 (e) Size Distribution of Alumina Inclusions in the Sample taken 46 Seconds after Deoxidation in the High Frequency Furnace Melt (Jeol 840 SEM/Digiscan).

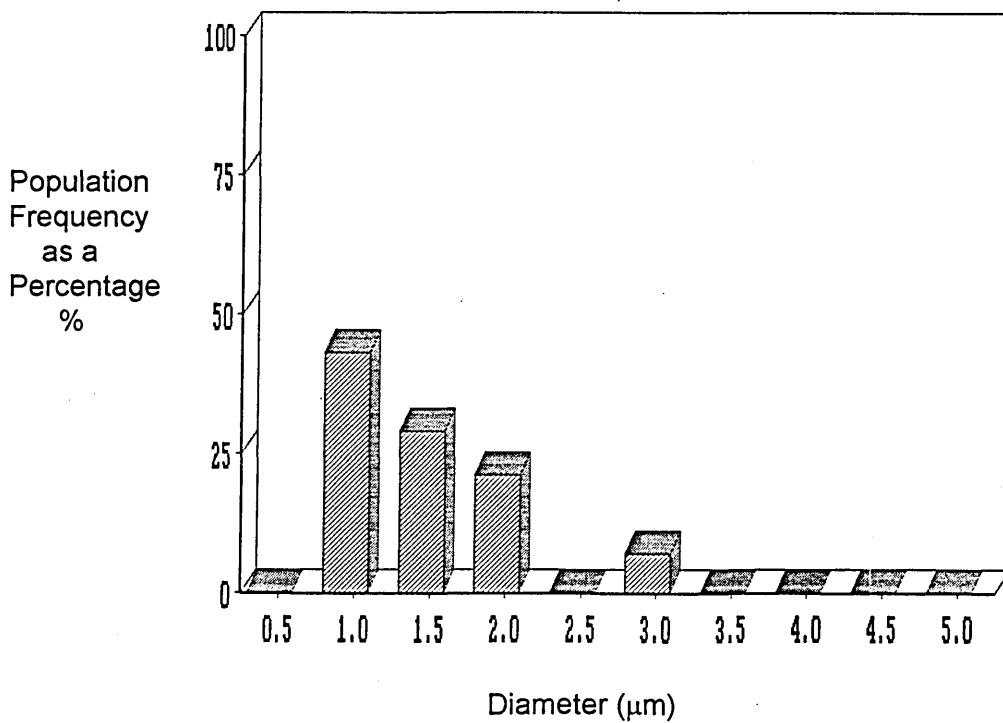


Figure 4.9 (f) Size Distribution of Alumina Inclusions in the Sample taken 65 Seconds after Deoxidation in the High Frequency Furnace Melt (Jeol 840 SEM/Digiscan).

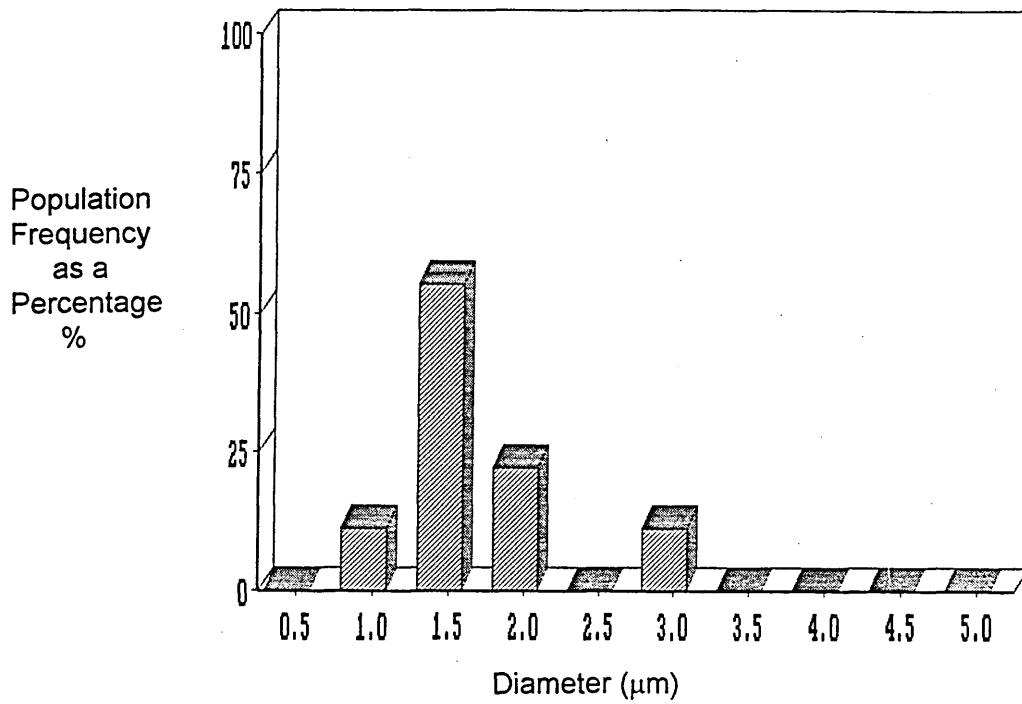


Figure 4.9 (g) Size Distribution of Alumina Inclusions in the Sample taken 75 Seconds after Deoxidation in the High Frequency Furnace Melt (Jeol 840 SEM/Digiscan).

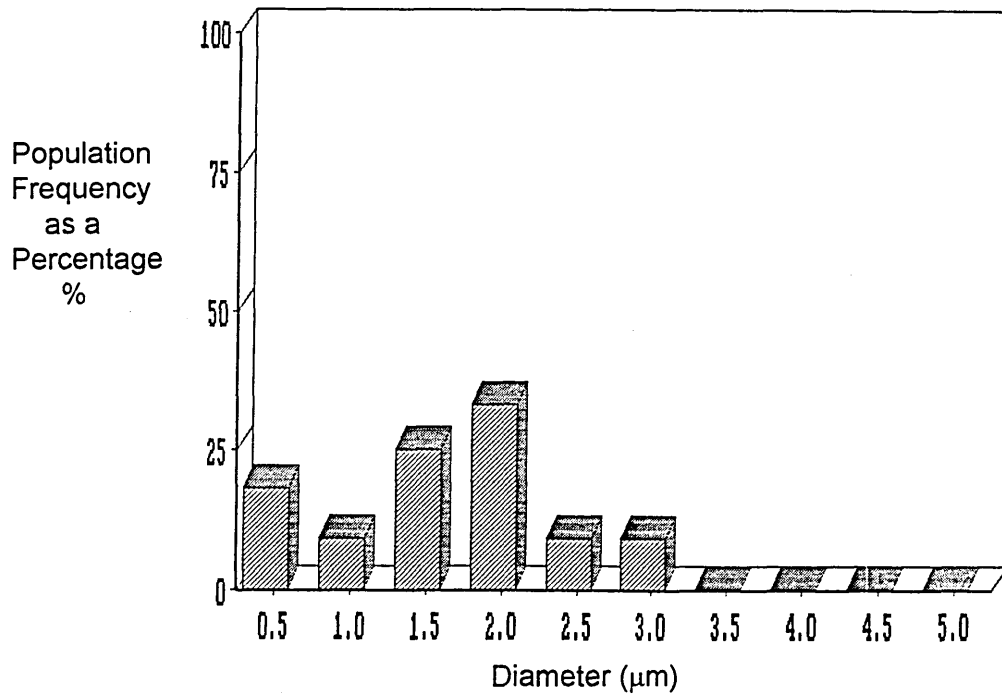


Figure 4.9 (h) Size Distribution of Alumina Inclusions in the Sample taken 83 Seconds after Deoxidation in the High Frequency Furnace Melt (Jeol 840 SEM/Digiscan).

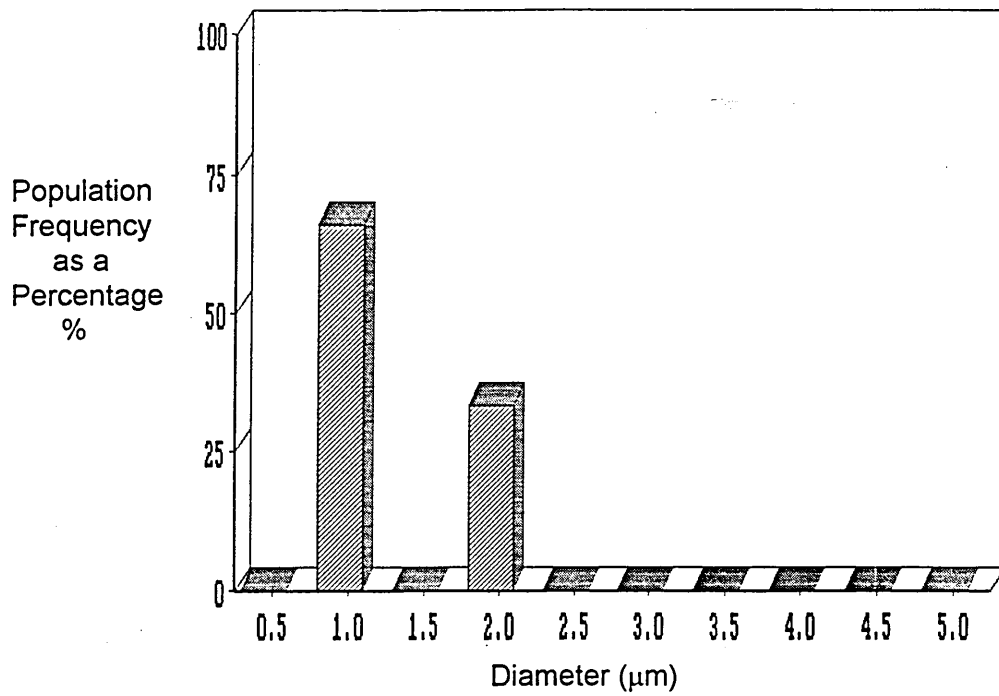


Figure 4.9 (i) Size Distribution of Alumina Inclusions in the Sample taken 93 Seconds after Deoxidation in the High Frequency Furnace Melt (Jeol 840 SEM/Digiscan).

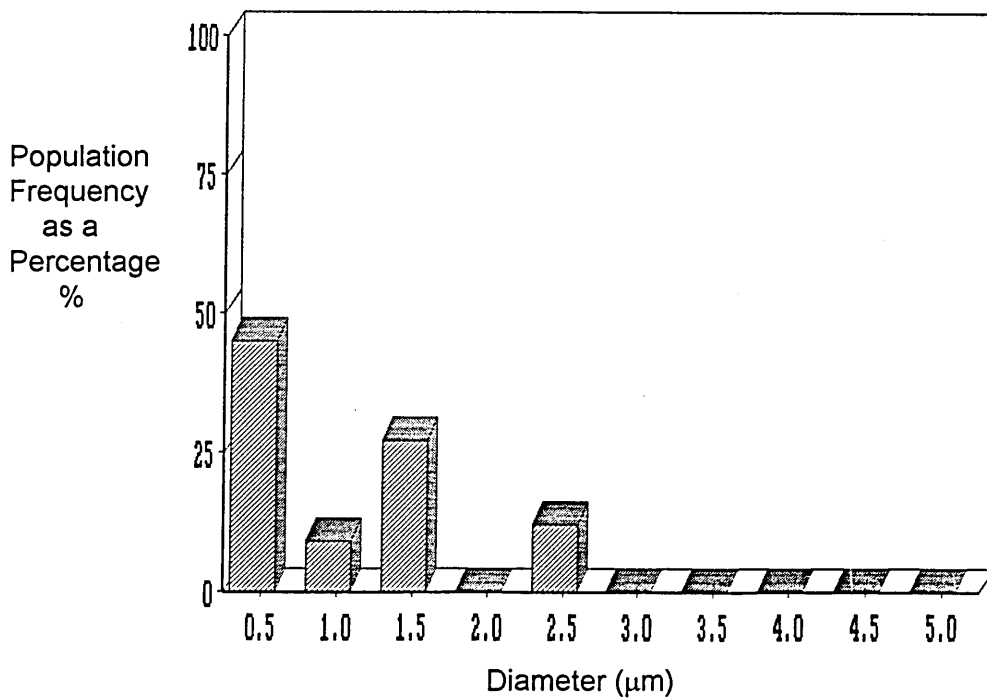


Figure 4.9 (j) Size Distribution of Alumina Inclusions in the Sample taken 139 Seconds after Deoxidation in the High Frequency Furnace Melt (Jeol 840 SEM/Digiscan).

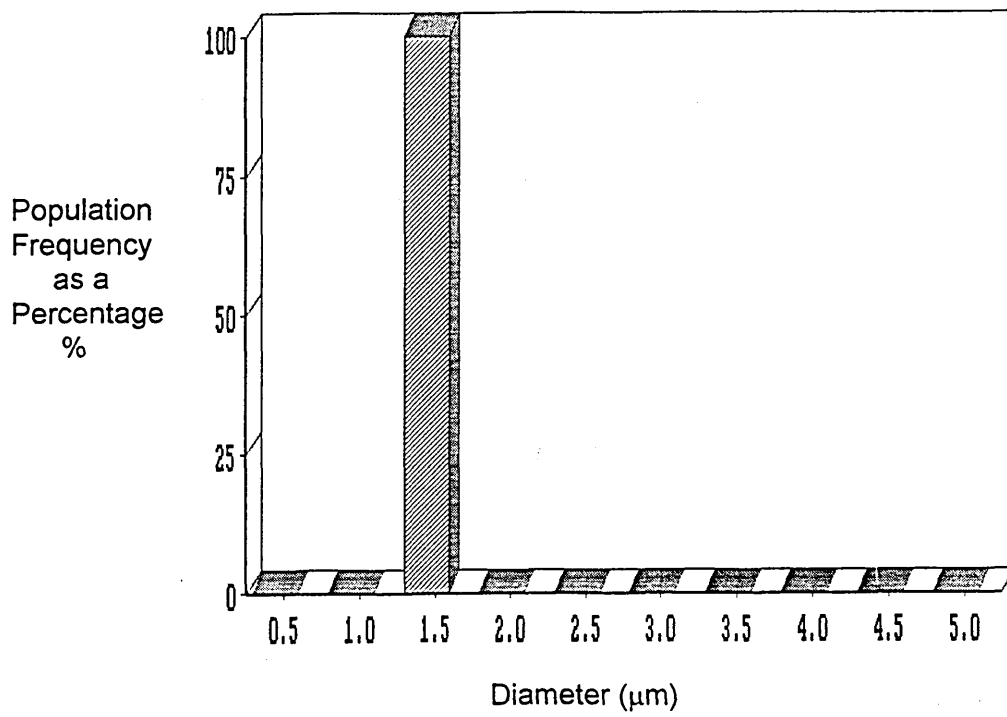


Figure 4.9 (k) Size Distribution of Alumina Inclusions in the Sample taken 165 Seconds after Deoxidation in the High Frequency Furnace Melt (Jeol 840 SEM/Digiscan).

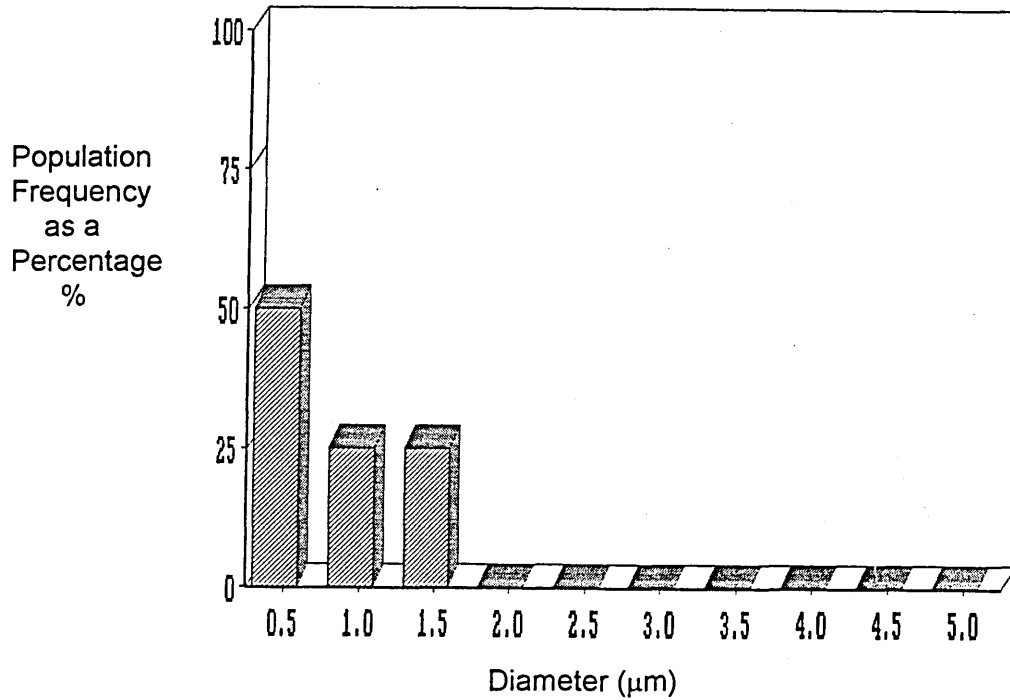


Figure 4.9 (l) Size Distribution of Alumina Inclusions in the Sample taken 225 Seconds after Deoxidation in the High Frequency Furnace Melt (Jeol 840 SEM/Digiscan).

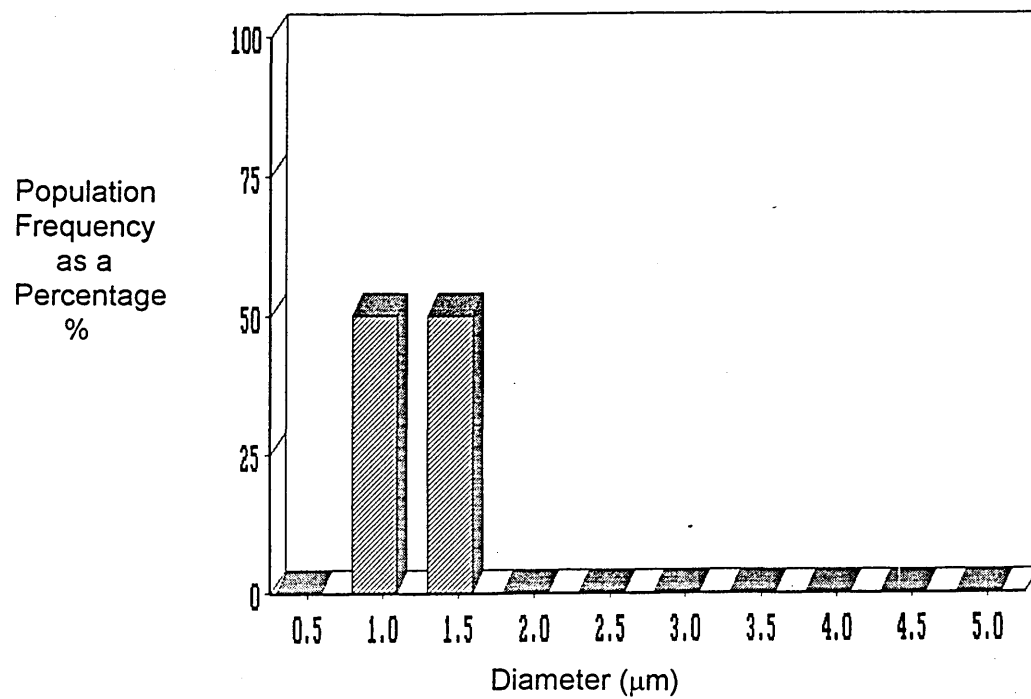


Figure 4.9 (m) Size Distribution of Alumina Inclusions in the Sample taken 255 Seconds after Deoxidation in the High Frequency Furnace Melt (Jeol 840 SEM/Digiscan).

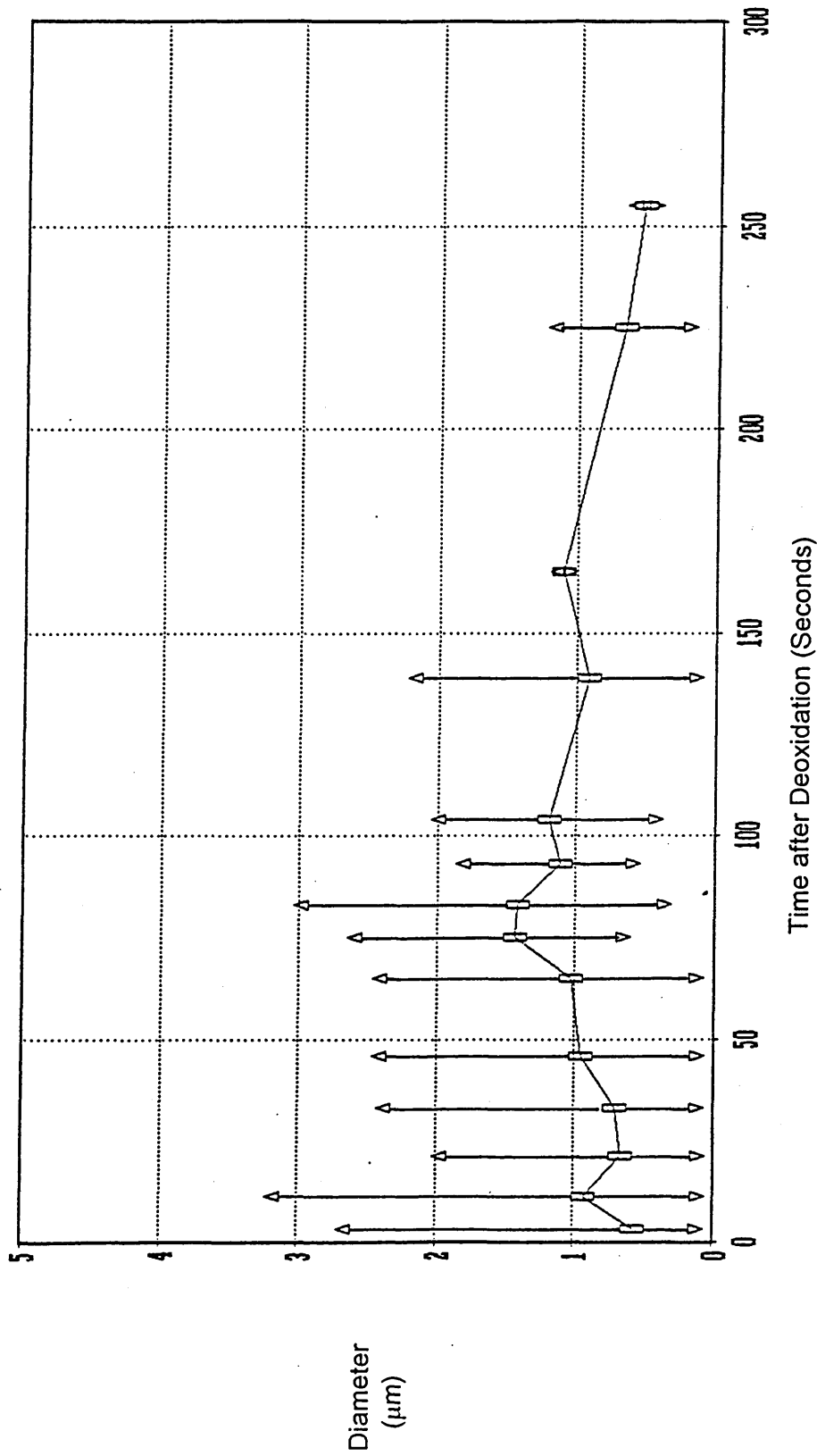


Figure 4.10 Mean Alumina Inclusions Diameter Versus Time after Deoxidation in the High Frequency Furnace Melt (JEOL 840 SEM/Digiscan).

△ - Mean from Maximum Size Band ▽ - Mean from Minimum Size Band □ - Mean Diameter

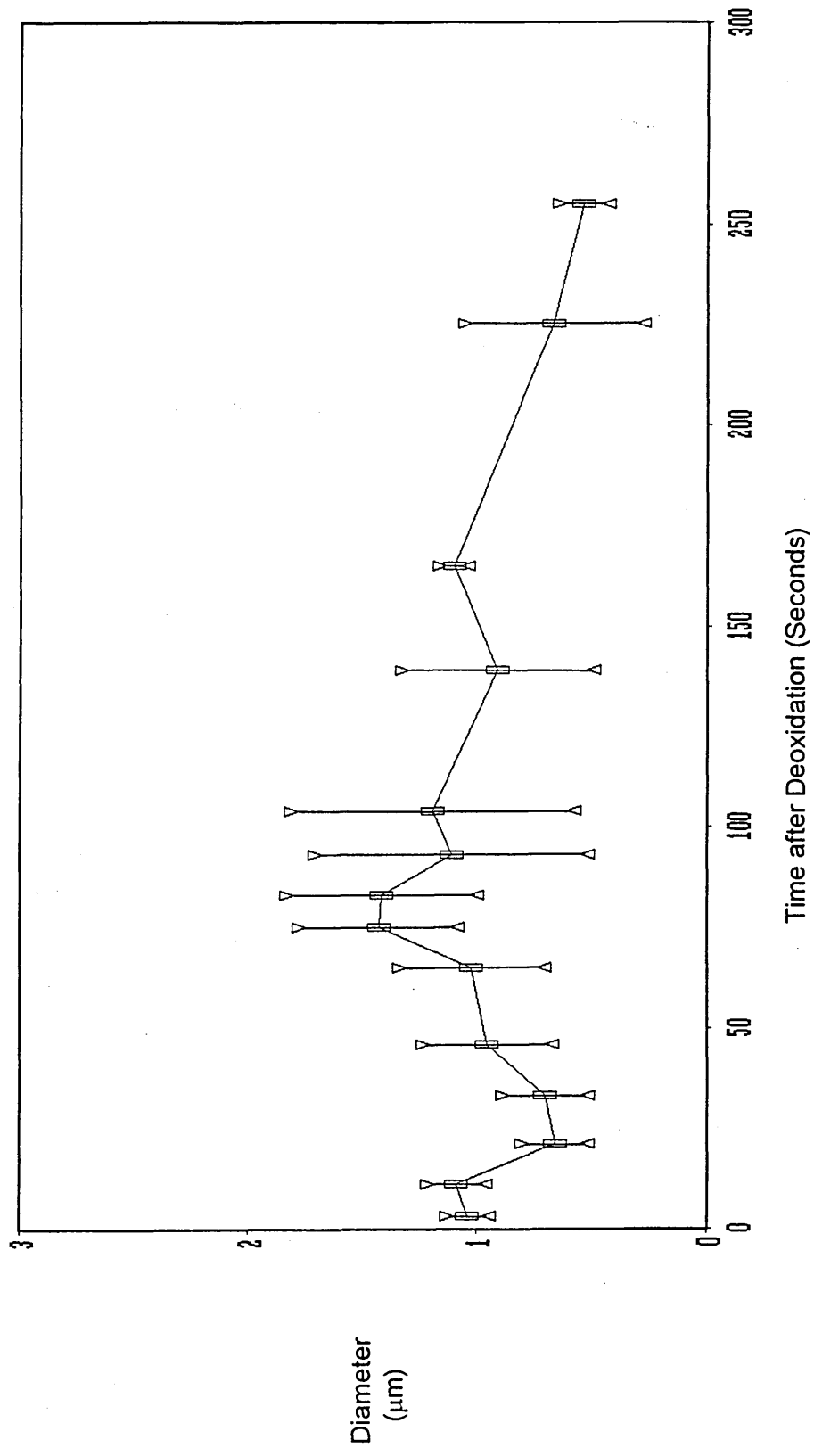


Figure 4.11 Mean Alumina Inclusions Diameter Versus Time after Deoxidation in the High Frequency Furnace Melt (JEOL 840 SEM/Digiscan).

▽ - Upper 95% Confidence Limit △ - Lower 95% Confidence Limit □ - Mean Diameter

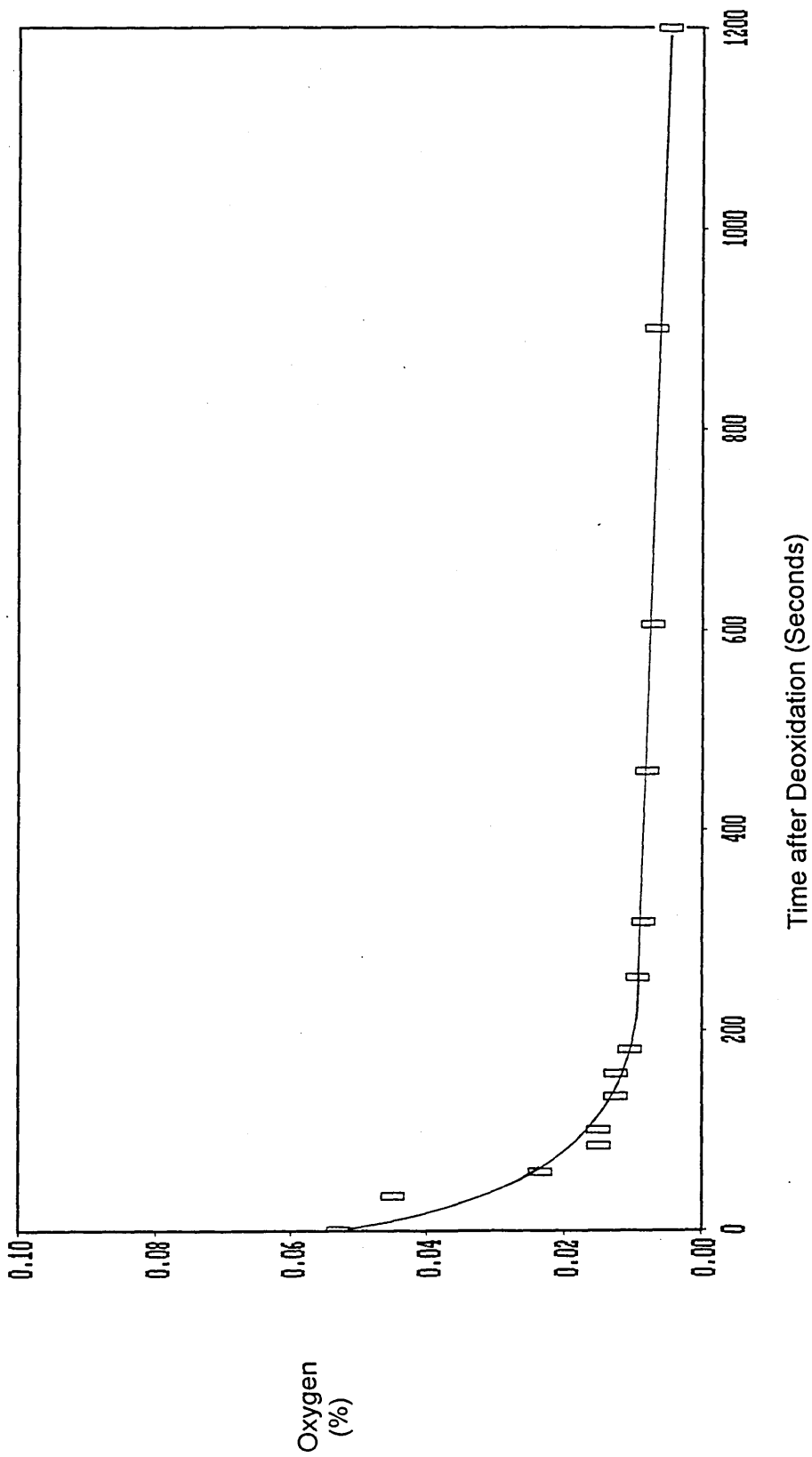
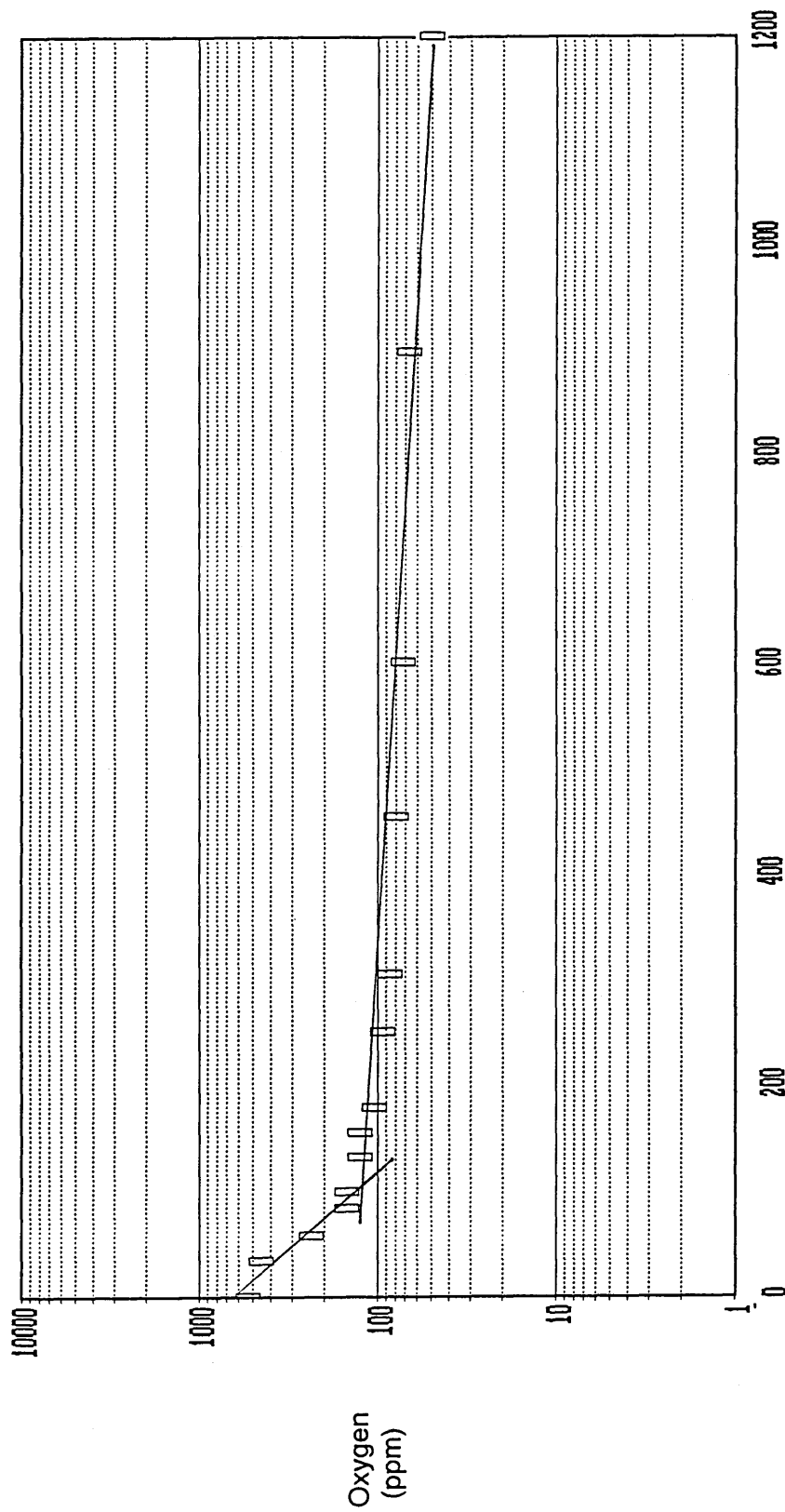


Figure 4.12(a) Total Oxygen Analysis Versus Time after Deoxidation with 0.53 mass% Titanium Addition in the Vertical Tube Furnace Melt (LECO).



Time after Deoxidation (Seconds)

Figure 4.12(b) Total Oxygen Analysis Versus Time after Deoxidation with 0.53 mass% Titanium Addition in the Vertical Tube Furnace Melt (LECO).

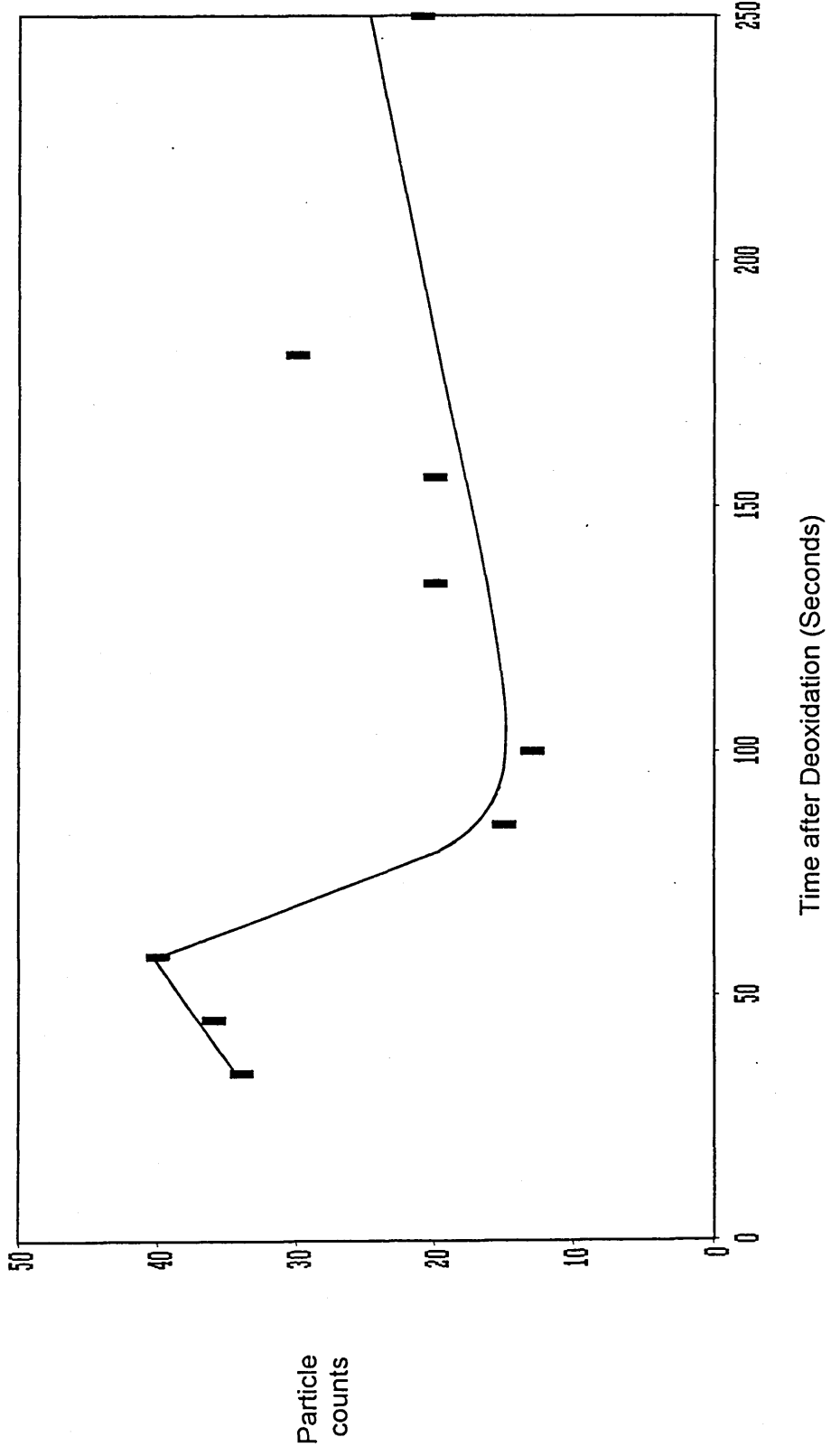


Figure 4.13 Number of Titania Inclusions Counted Versus Time after Deoxidation in the Vertical Tube Furnace Melt (JEOL 840 SEM/Digiscan).

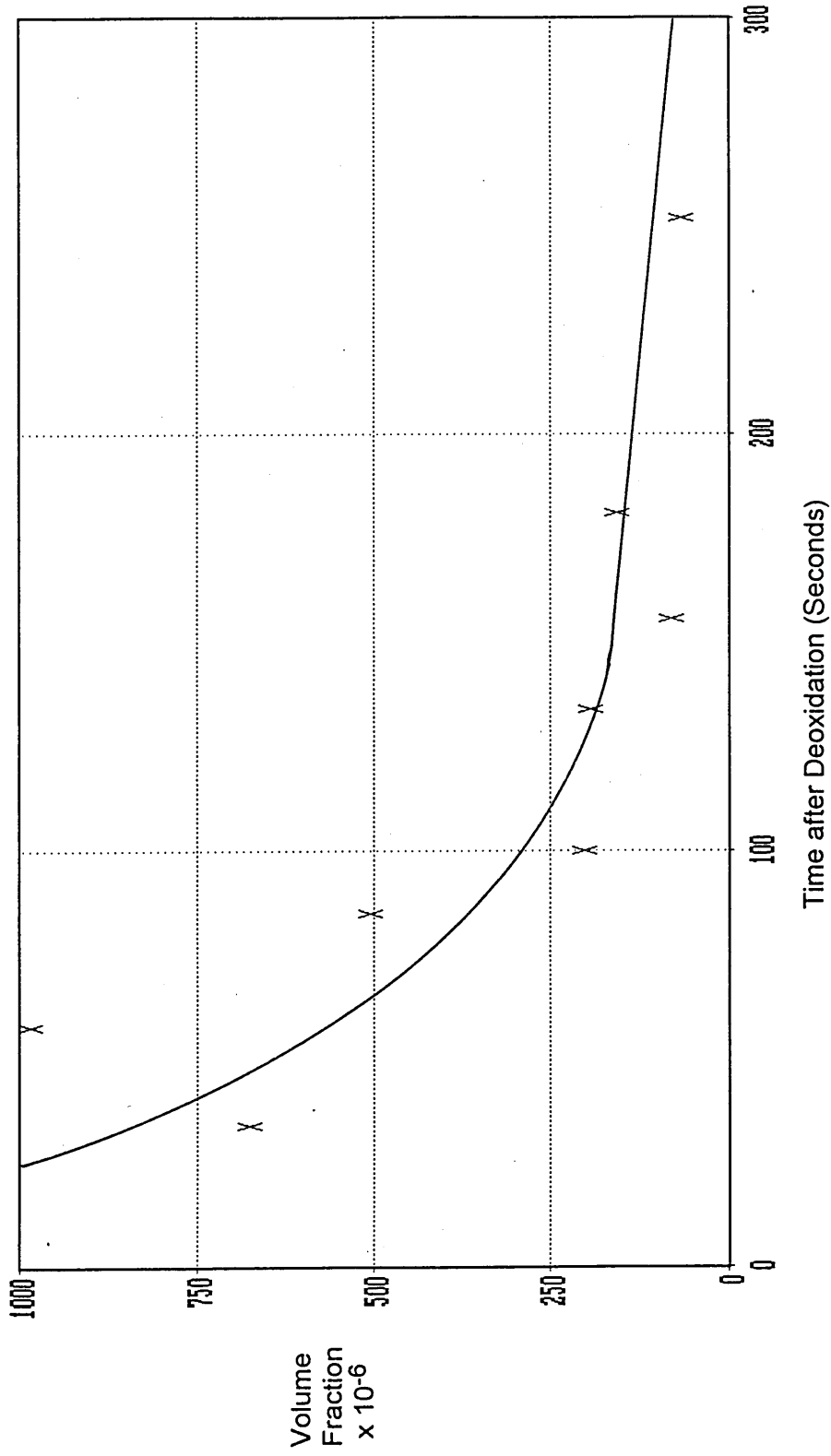


Figure 4.14 Volume Fraction of Titania Inclusions Versus Time after Deoxidation in the Vertical Tube Furnace Melt (JEOL 840 SEM/Digiscan) .

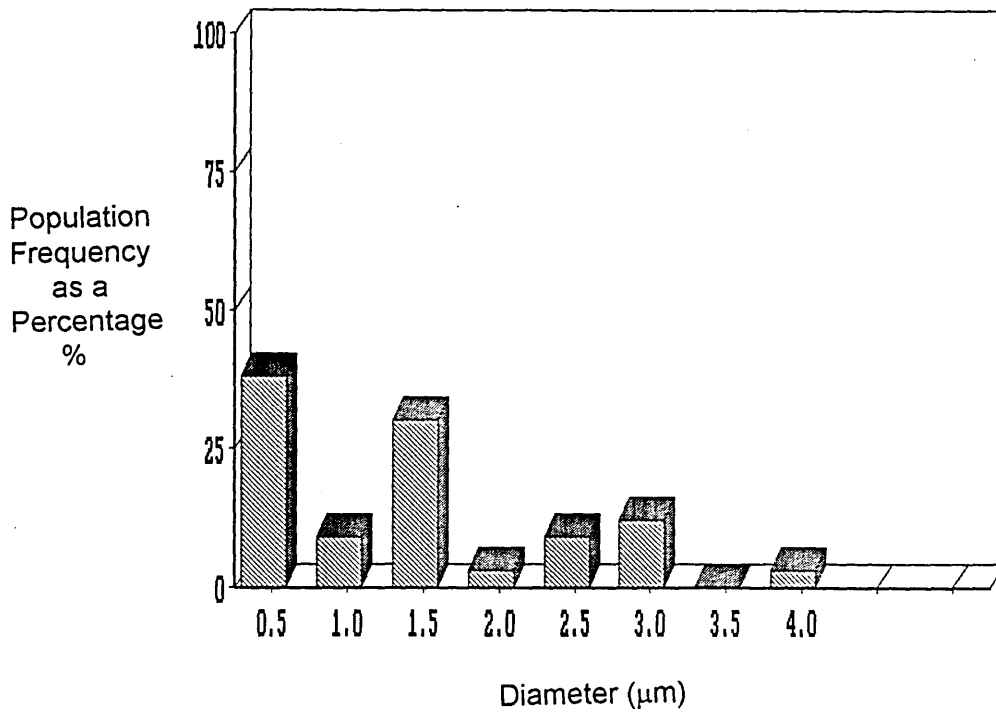


Figure 4.15 (a) Size Distribution of Titania Inclusions in the Sample taken 34 Seconds after Deoxidation in the Vertical Tube Furnace Melt (Jeol 840 SEM/Digiscan).

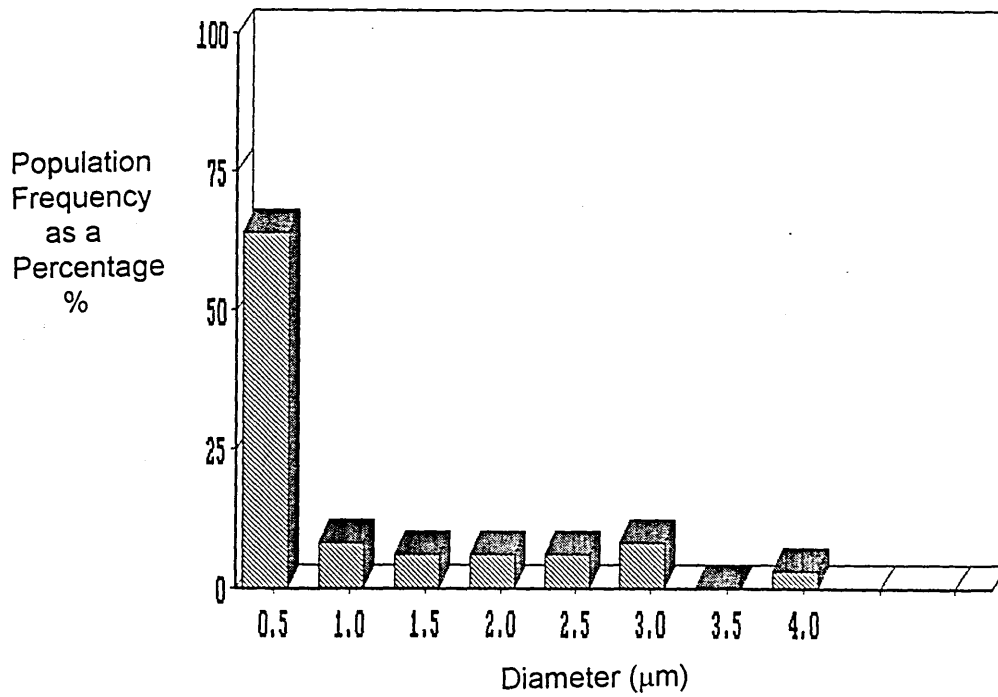


Figure 4.15 (b) Size Distribution of Titania Inclusions in the Sample taken 45 Seconds after Deoxidation in the Vertical Tube Furnace Melt (Jeol 840 SEM/Digiscan).

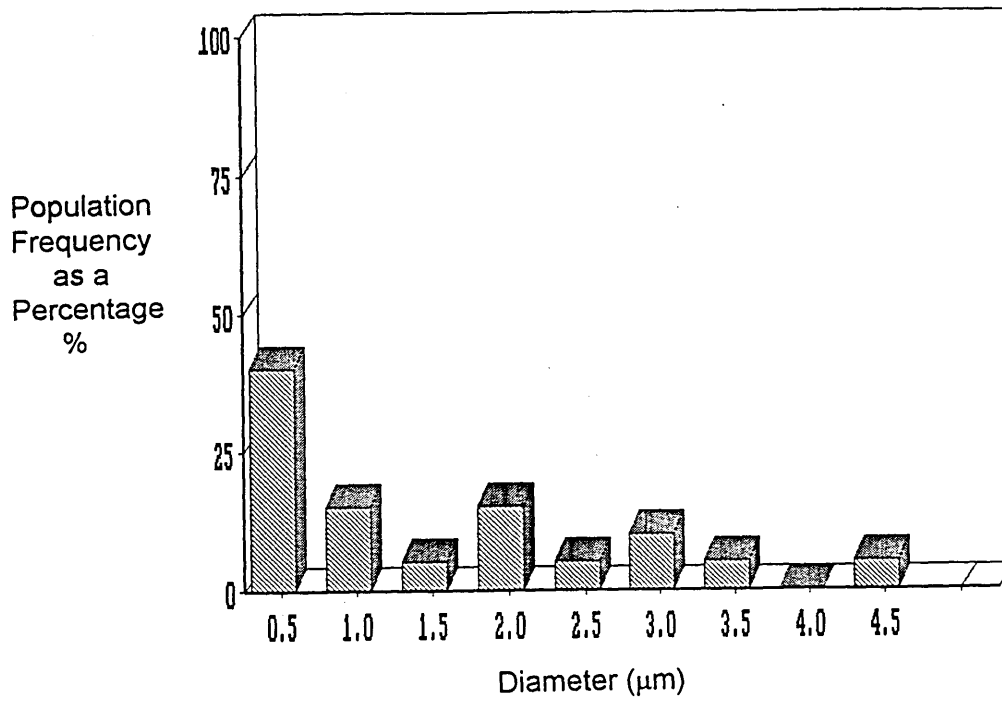


Figure 4.15 (c) Size Distribution of Titania Inclusions in the Sample taken 58 Seconds after Deoxidation in the Vertical Tube Furnace Melt (Jeol 840 SEM/Digiscan).

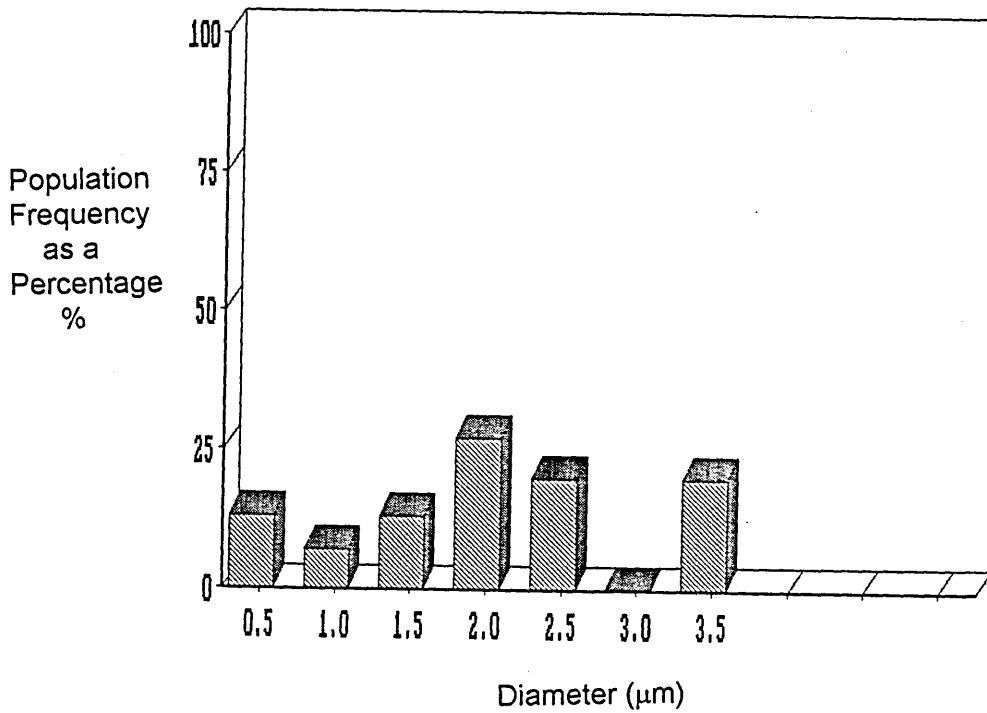


Figure 4.15 (d) Size Distribution of Titania Inclusions in the Sample taken 85 Seconds after Deoxidation in the Vertical Tube Furnace Melt (Jeol 840 SEM/Digiscan).

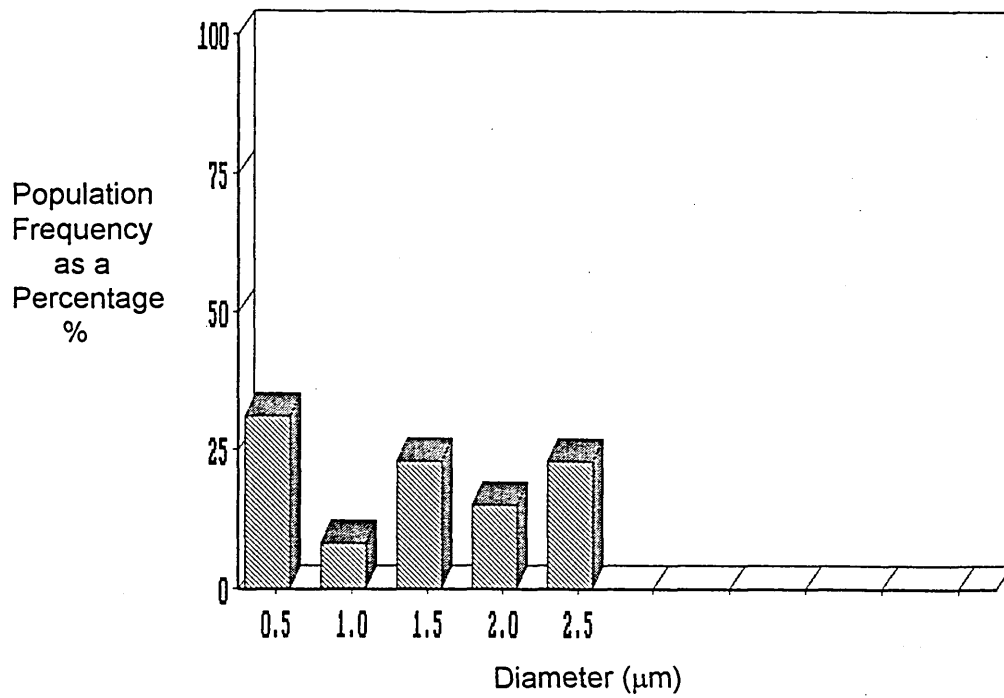


Figure 4.15 (e) Size Distribution of Titania Inclusions in the Sample taken 100 Seconds after Deoxidation in the Vertical Tube Furnace Melt (Jeol 840 SEM/Digiscan).

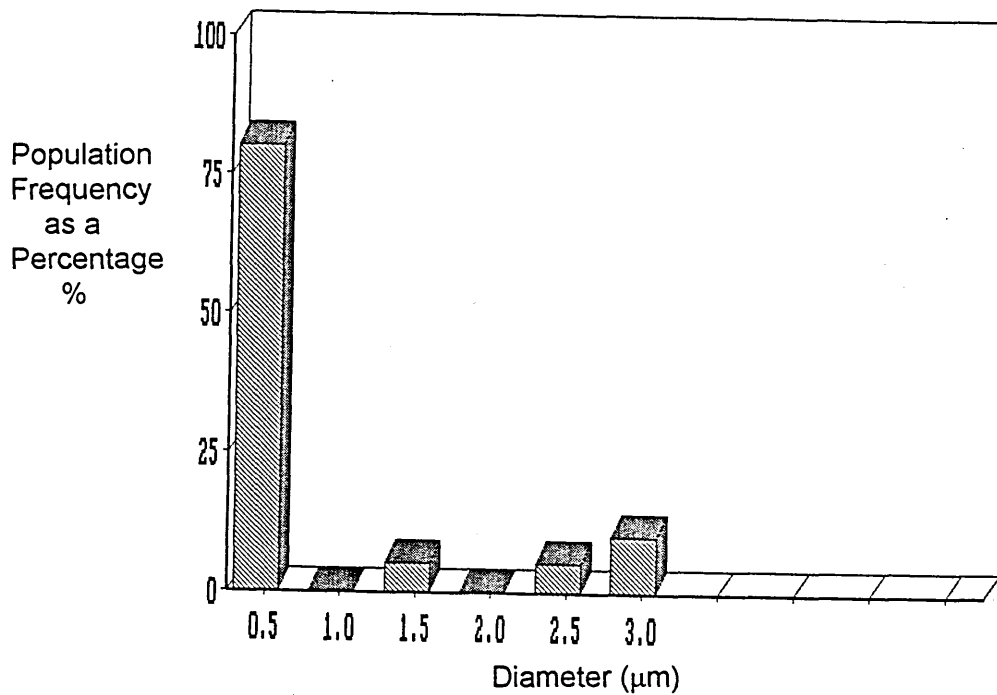


Figure 4.15 (f) Size Distribution of Titania Inclusions in the Sample taken 134 Seconds after Deoxidation in the Vertical Tube Furnace Melt (Jeol 840 SEM/Digiscan).

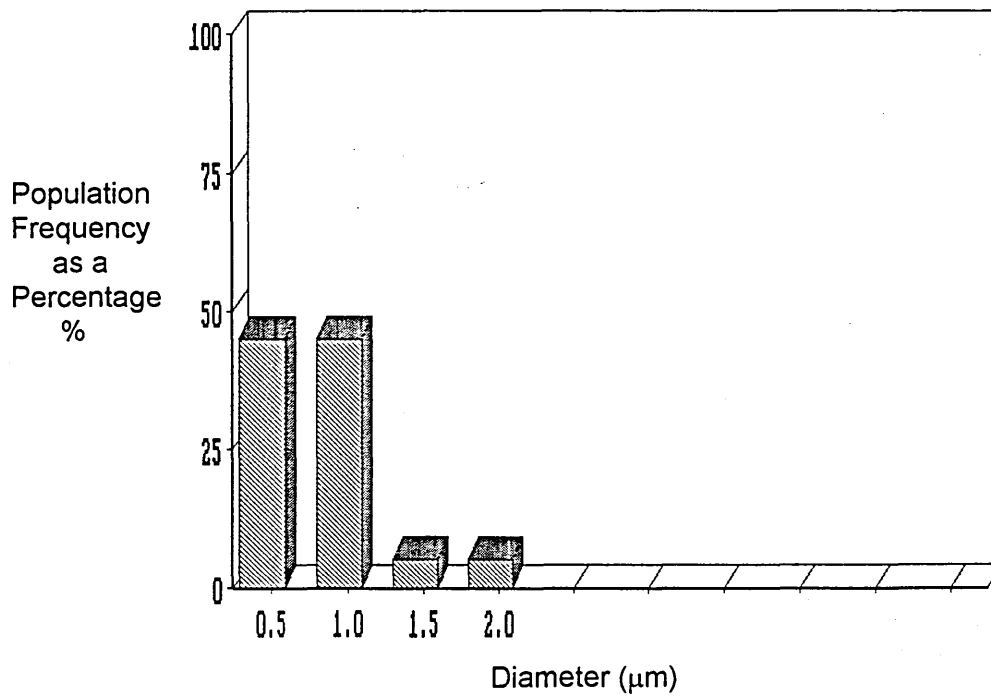


Figure 4.15 (g) Size Distribution of Titania Inclusions in the Sample taken 156 Seconds after Deoxidation in the Vertical Tube Furnace Melt (Jeol 840 SEM/Digiscan).

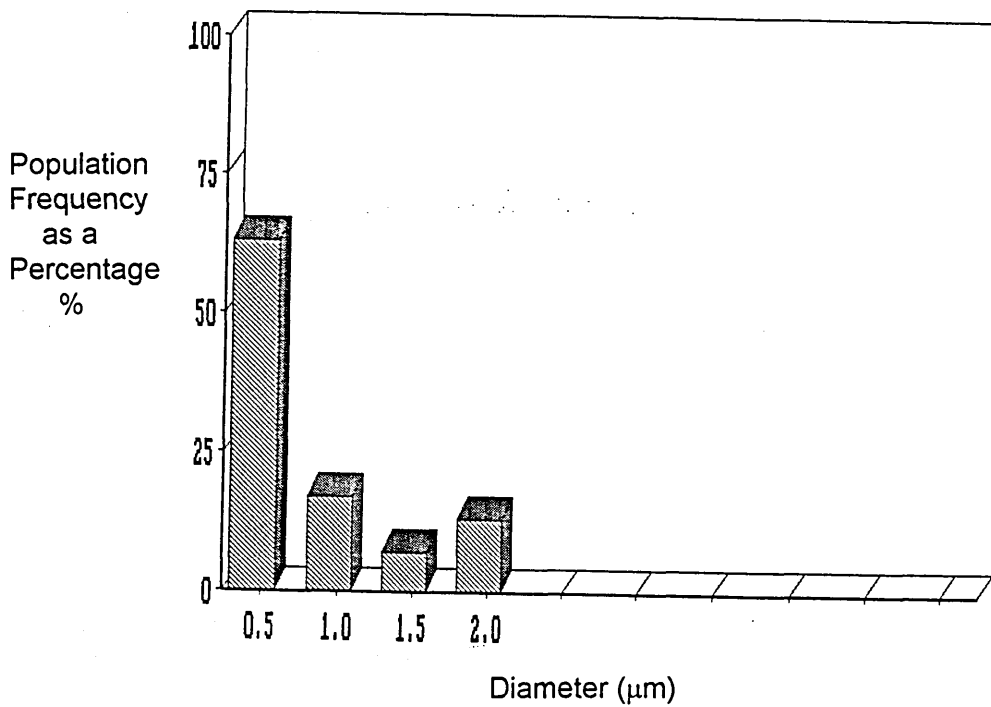


Figure 4.15 (h) Size Distribution of Titania Inclusions in the Sample taken 181 Seconds after Deoxidation in the Vertical Tube Furnace Melt (Jeol 840 SEM/Digiscan).

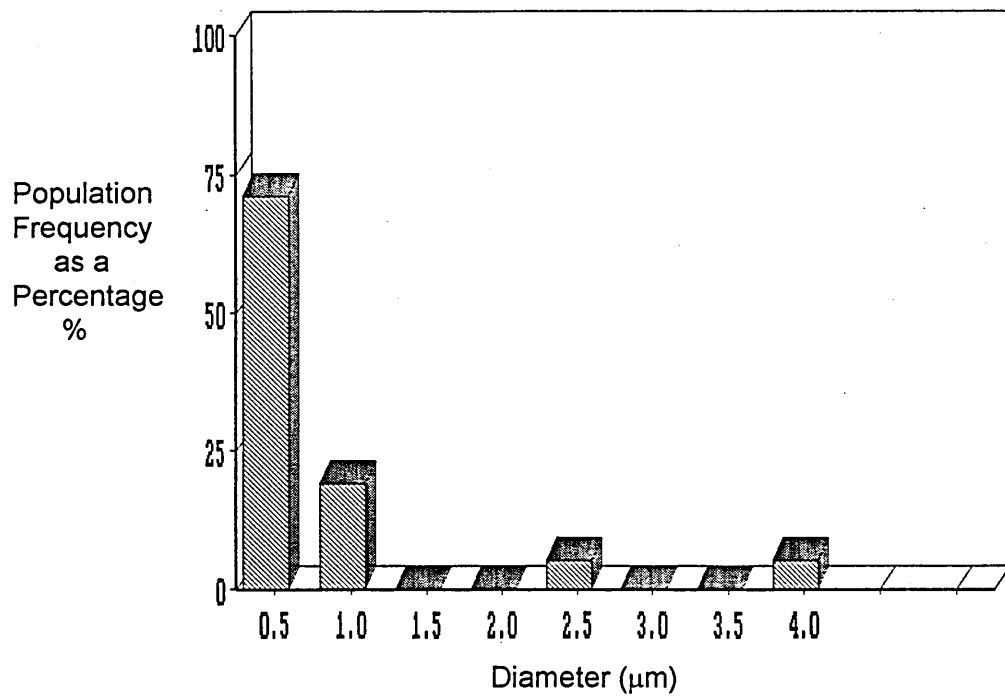


Figure 4.15 (i) Size Distribution of Titania Inclusions in the Sample taken 252 Seconds after Deoxidation in the Vertical Tube Furnace Melt (Jeol 840 SEM/Digiscan).

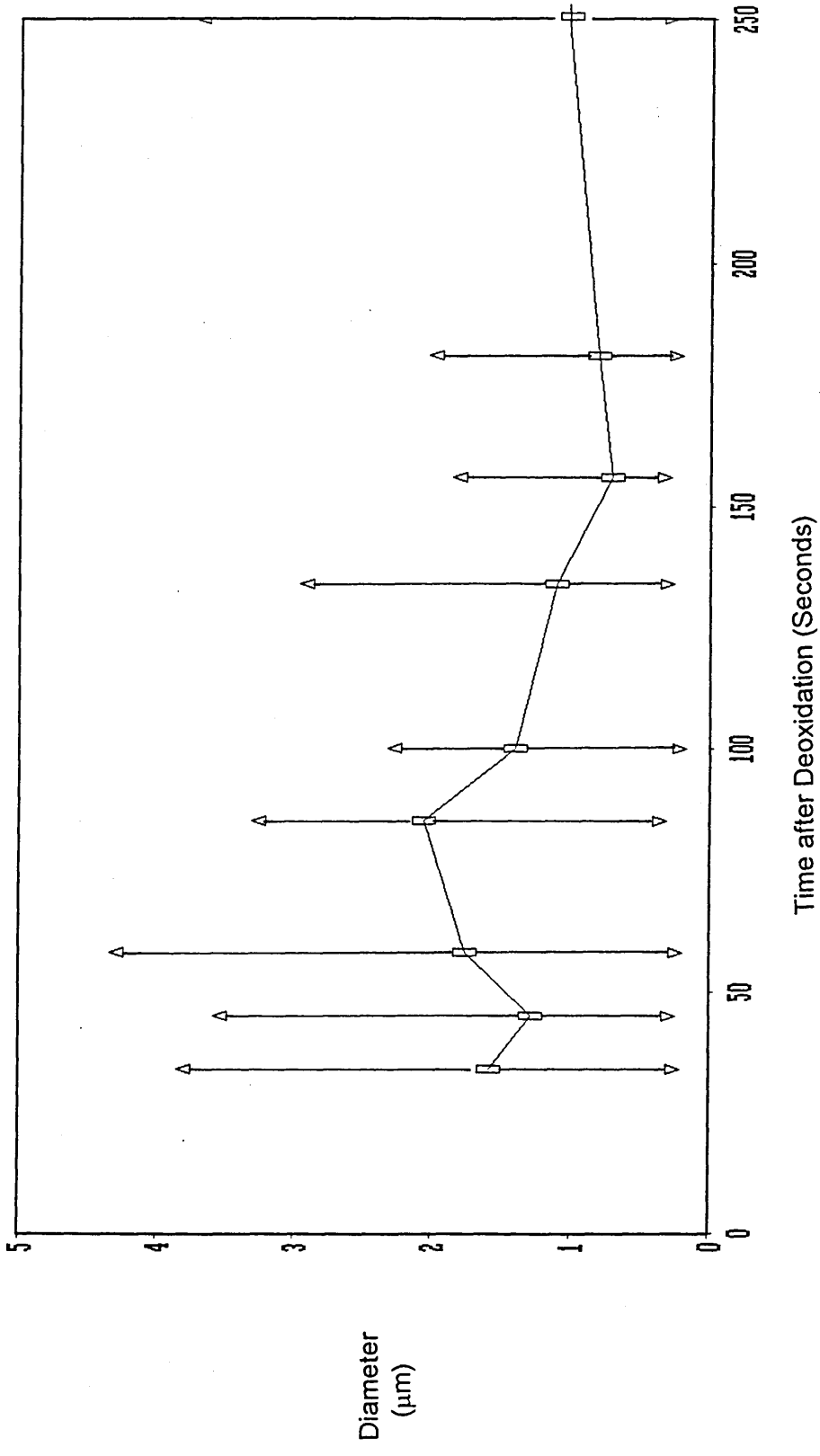


Figure 4.16 Mean Titania Inclusions Diameter Versus Time after Deoxidation in the Vertical Tube Furnace Melt (JEOL 840 SEM/Digiscan).

△ - Mean from Maximum Size Band ▽ - Mean from Minimum Size Band □ - Mean Diameter

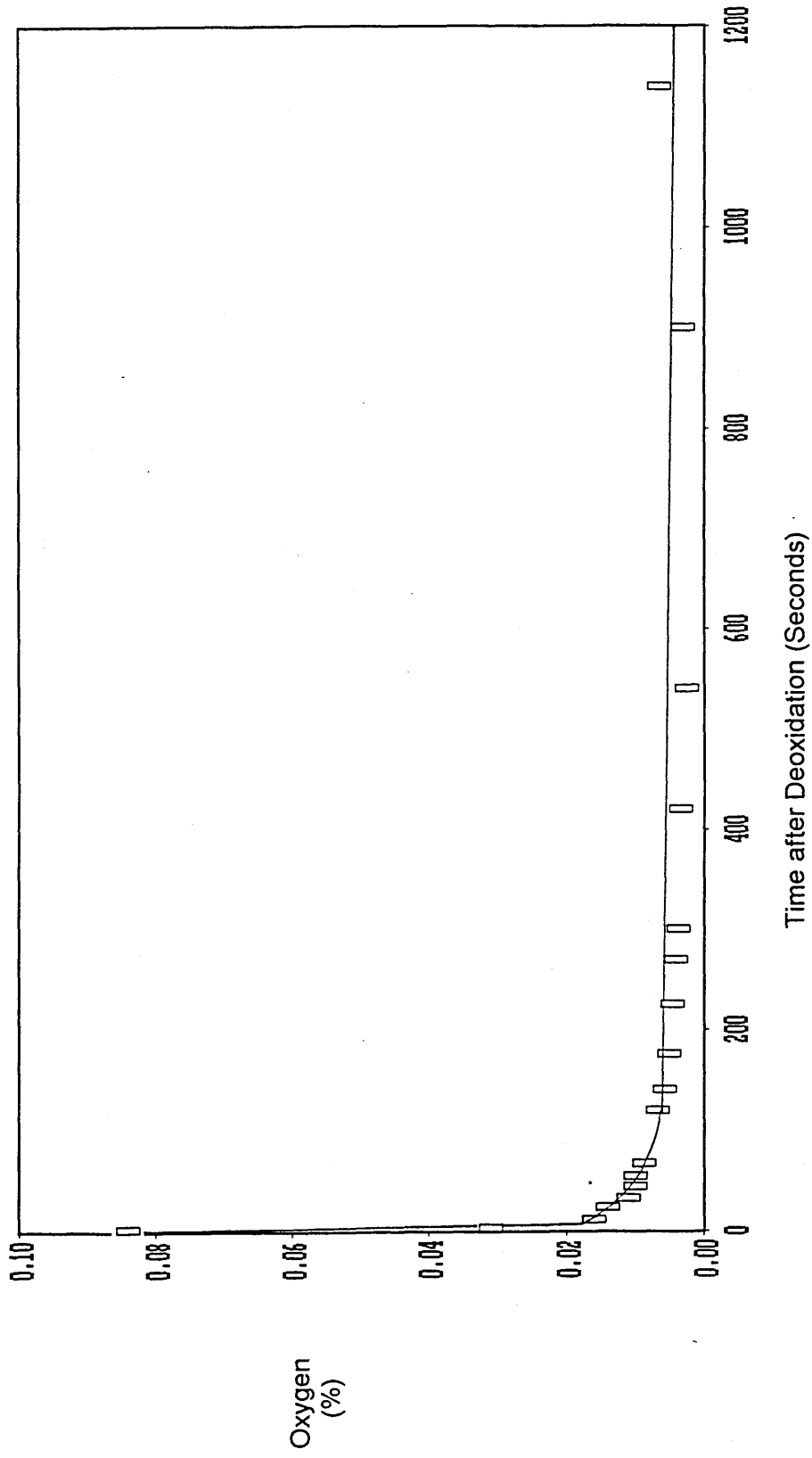


Figure 4.17(a) Total Oxygen Analysis Versus Time after Deoxidation with 0.53 mass% Titanium Addition in the High Frequency Furnace Melt (LECO).

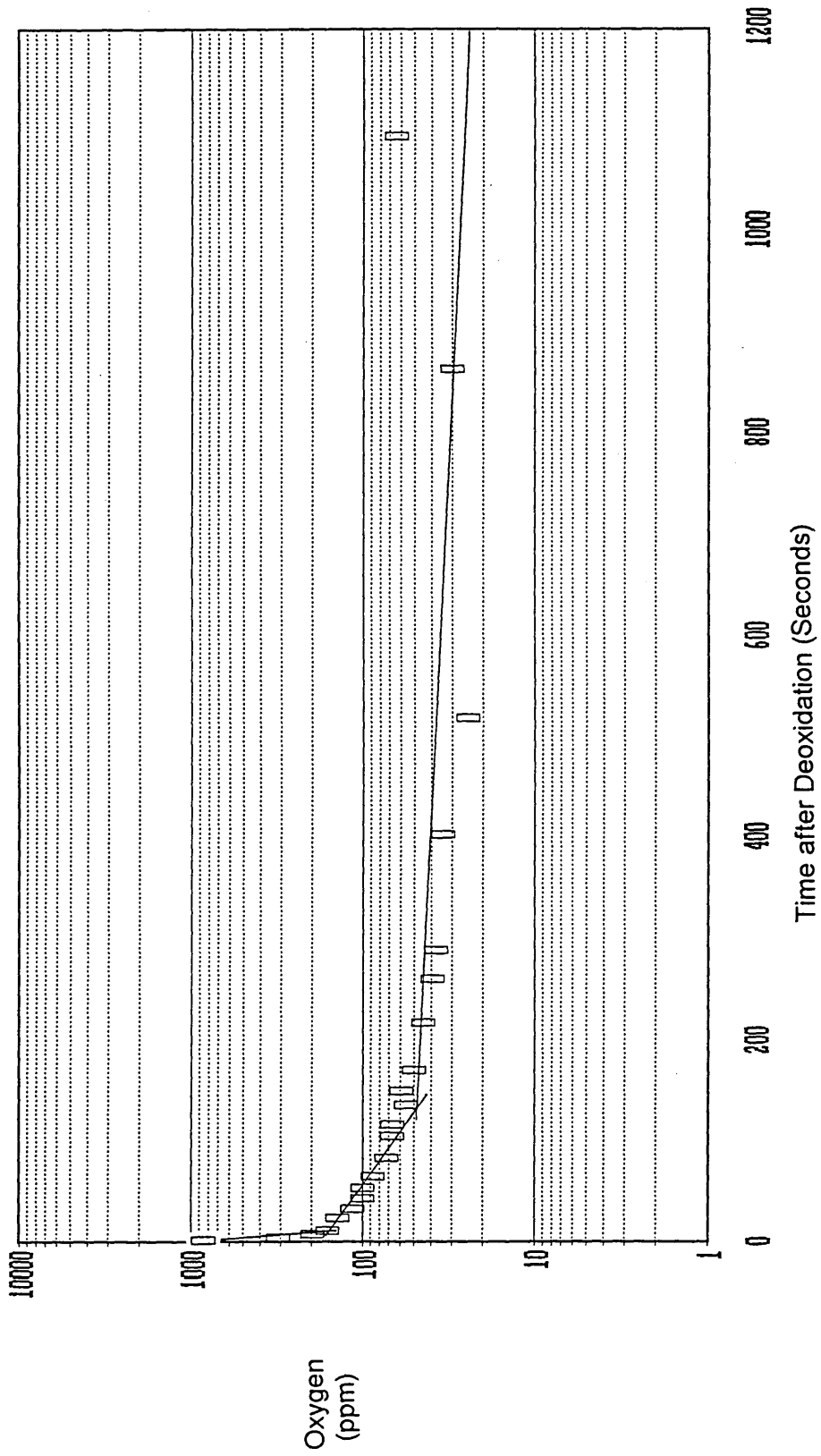


Figure 4.17(b) Total Oxygen Analysis Versus Time after Deoxidation with 0.53 mass% Titanium Addition in the High Frequency Furnace Melt (LECO).

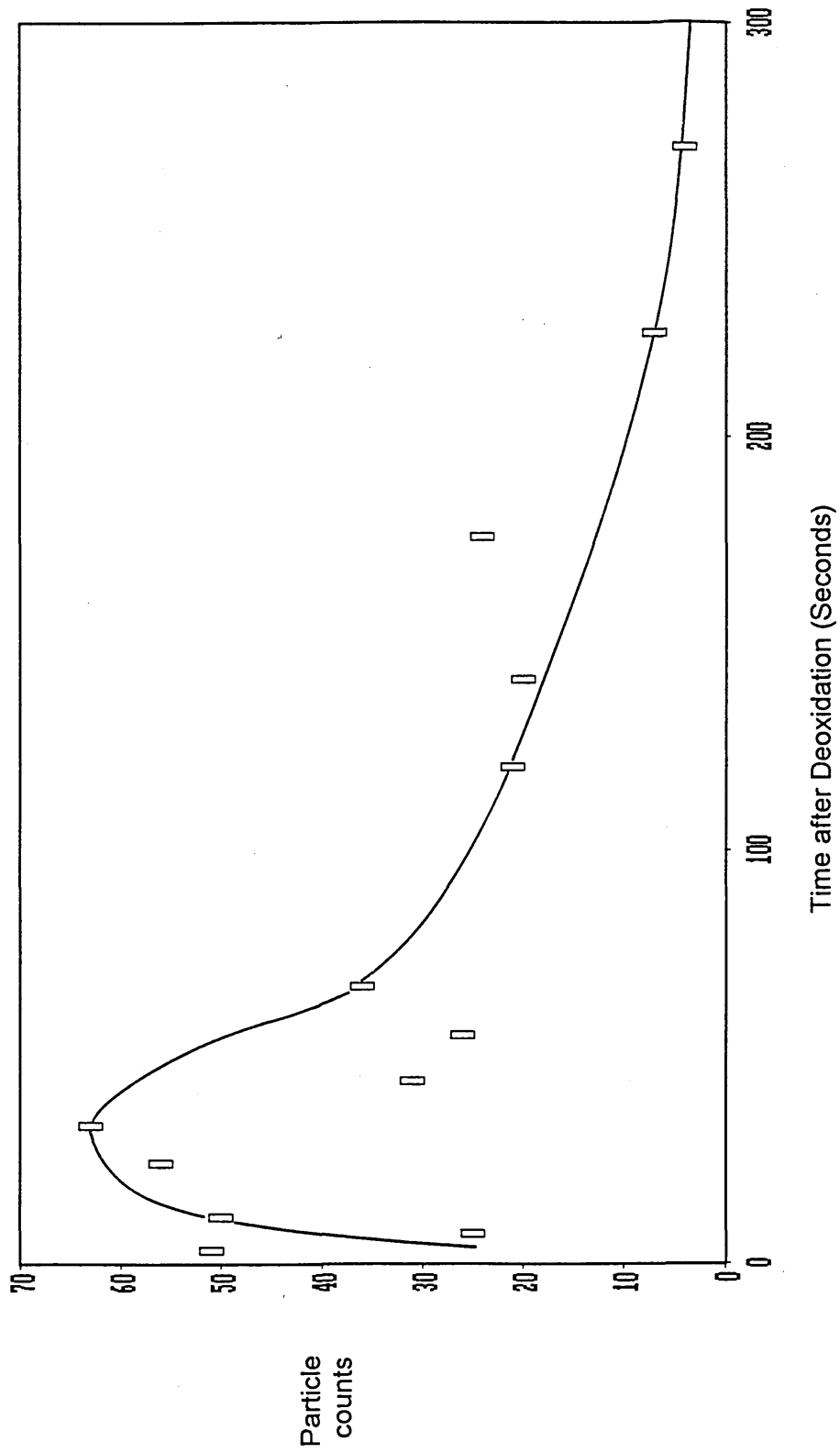


Figure 4.18 Number of Titania Inclusions Counted Versus Time after Deoxidation in the High Frequency Furnace Melt (JEOL 840 SEM/Digiscan).

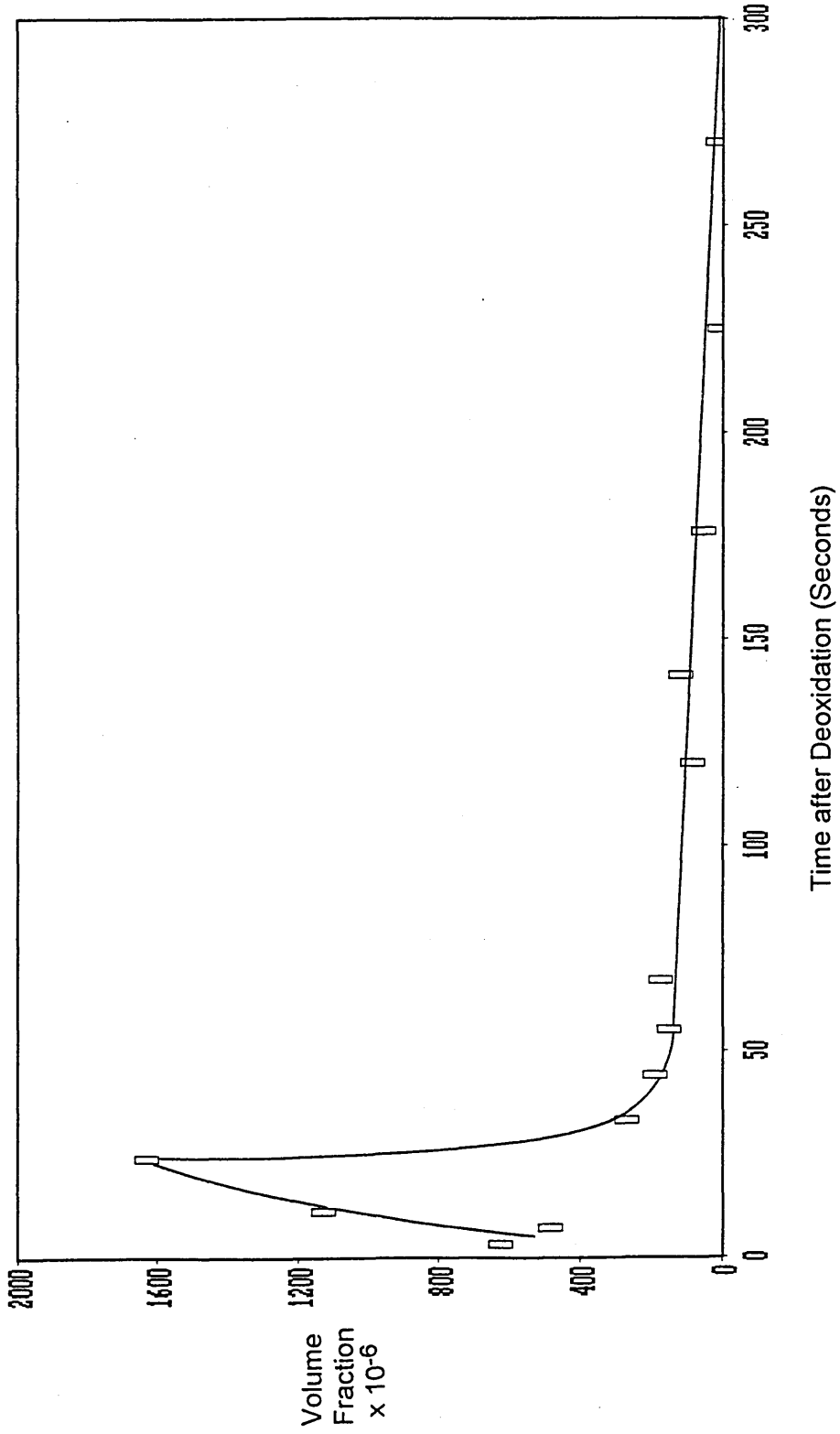


Figure 4.19 Volume Fraction of Titania Inclusions Versus Time after Deoxidation in the High Frequency Furnace Melt (JEOL 840 SEM/Digiscan).

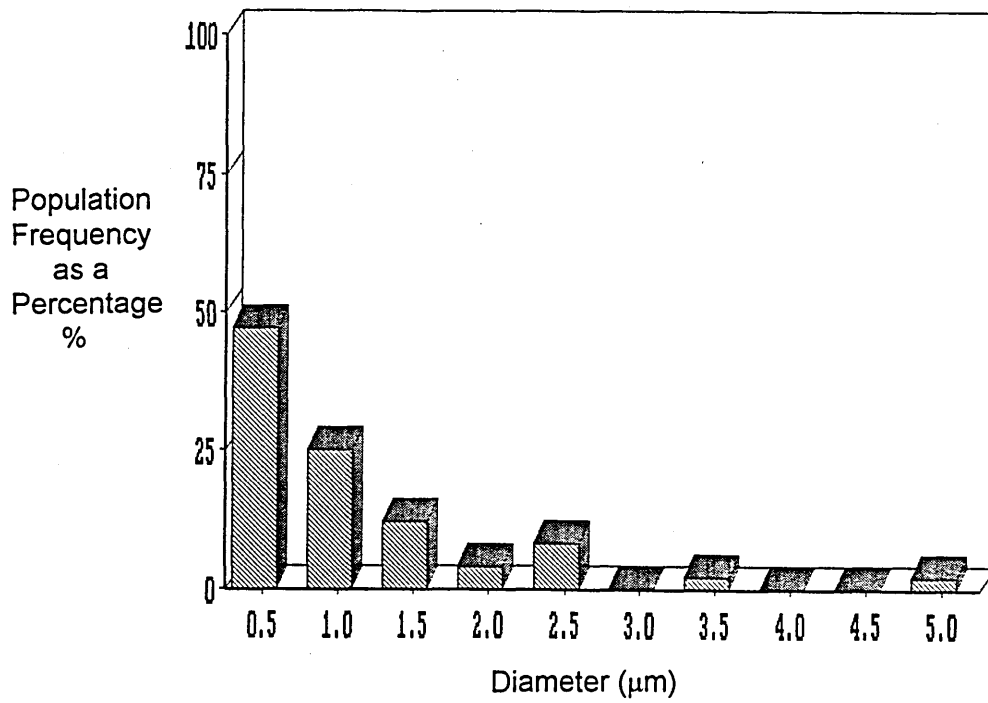


Figure 4.20 (a) Size Distribution of Titania Inclusions in the Sample taken 3 Seconds after Deoxidation in the High Frequency Furnace Melt (Jeol 840 SEM/Digiscan).

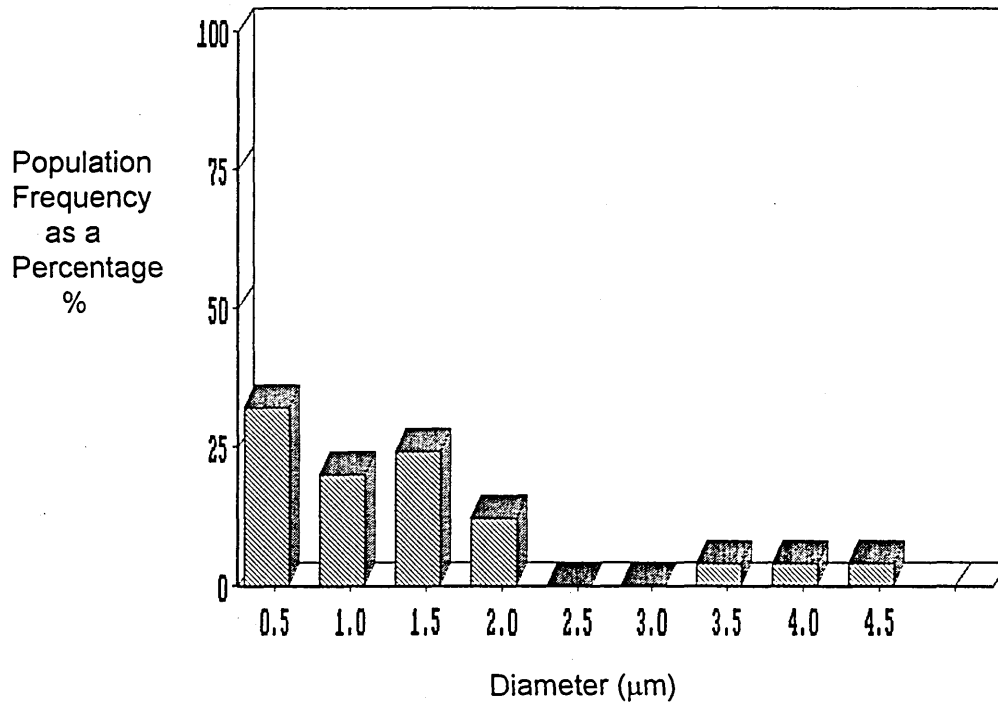


Figure 4.20 (b) Size Distribution of Titania Inclusions in the Sample taken 7 Seconds after Deoxidation in the High Frequency Furnace Melt (Jeol 840 SEM/Digiscan).

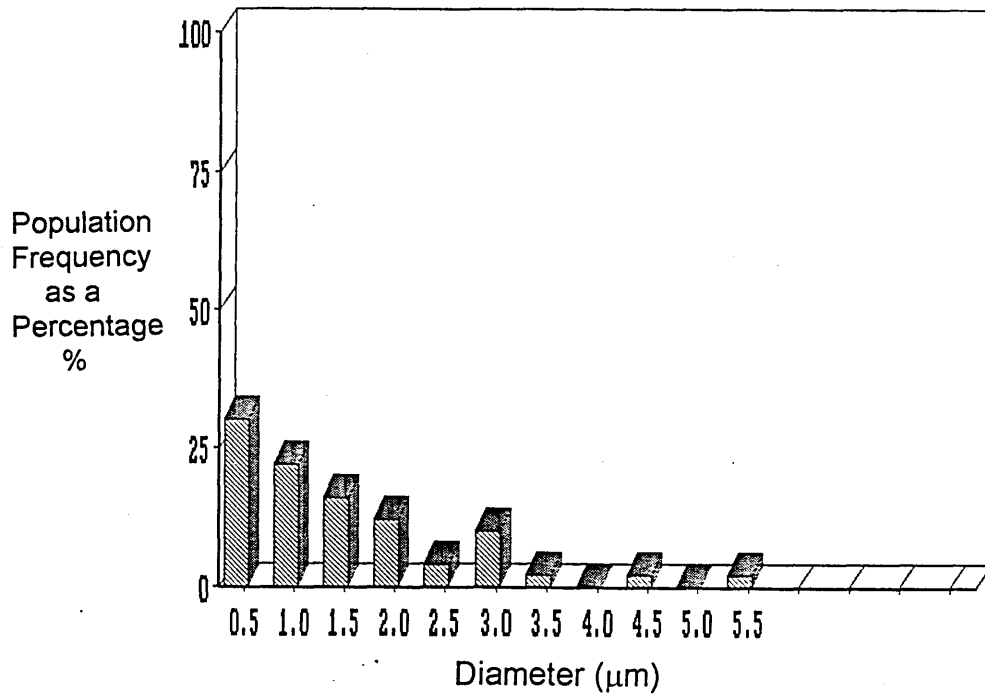


Figure 4.20 (c) Size Distribution of Titania Inclusions in the Sample taken 11 Seconds after Deoxidation in the High Frequency Furnace Melt (Jeol 840 SEM/Digiscan).

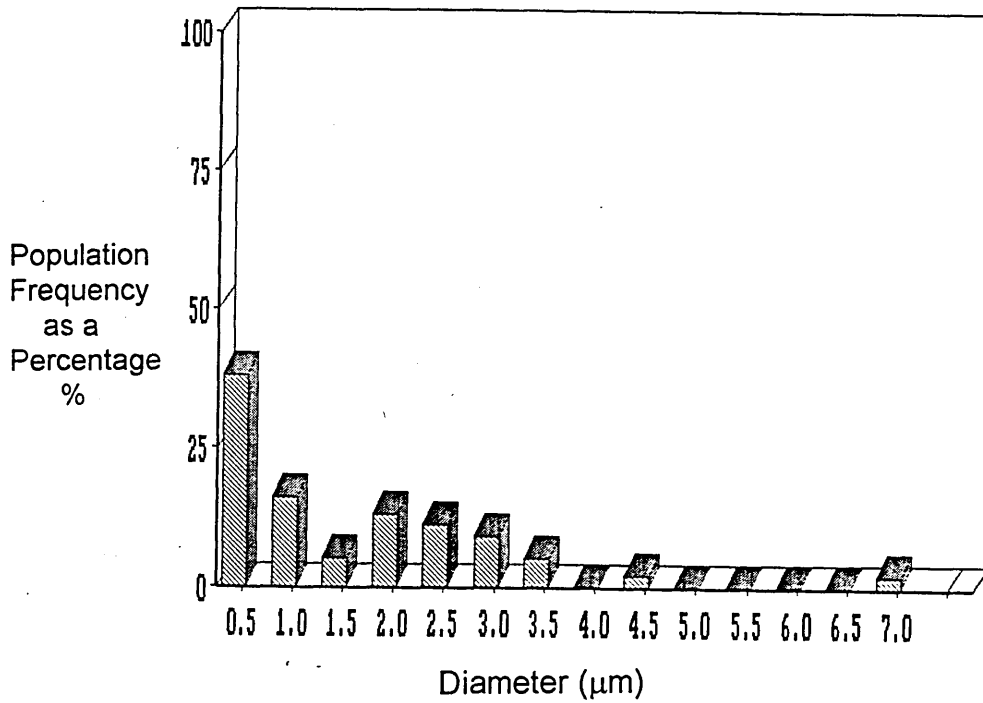


Figure 4.20 (d) Size Distribution of Titania Inclusions in the Sample taken 24 Seconds after Deoxidation in the High Frequency Furnace Melt (Jeol 840 SEM/Digiscan).

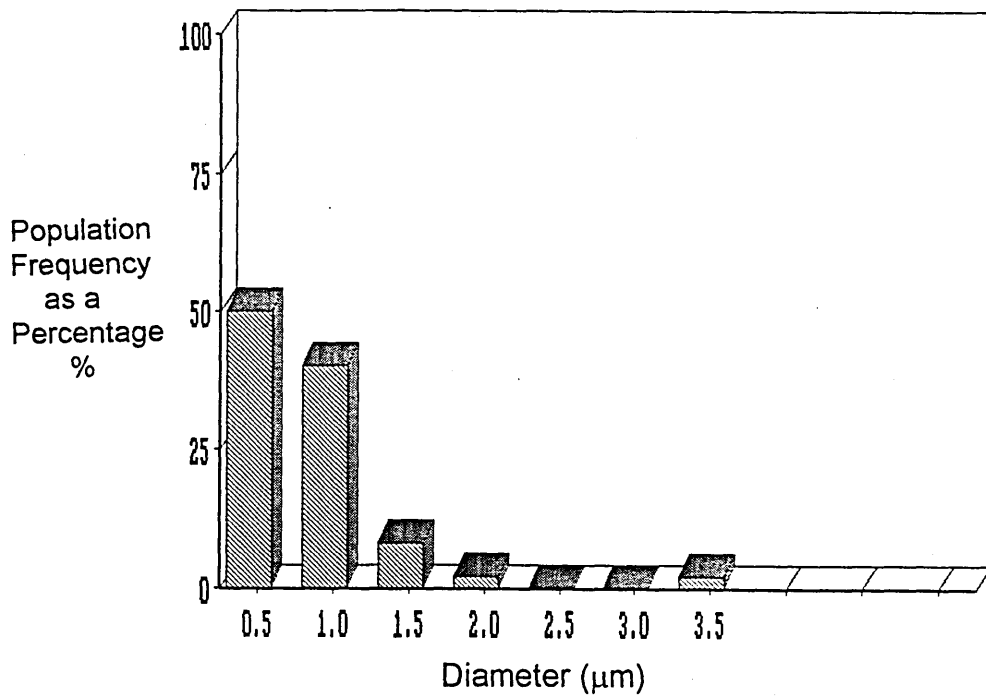


Figure 4.20 (e) Size Distribution of Titania Inclusions in the Sample taken 33 Seconds after Deoxidation in the High Frequency Furnace Melt (Jeol 840 SEM/Digiscan).

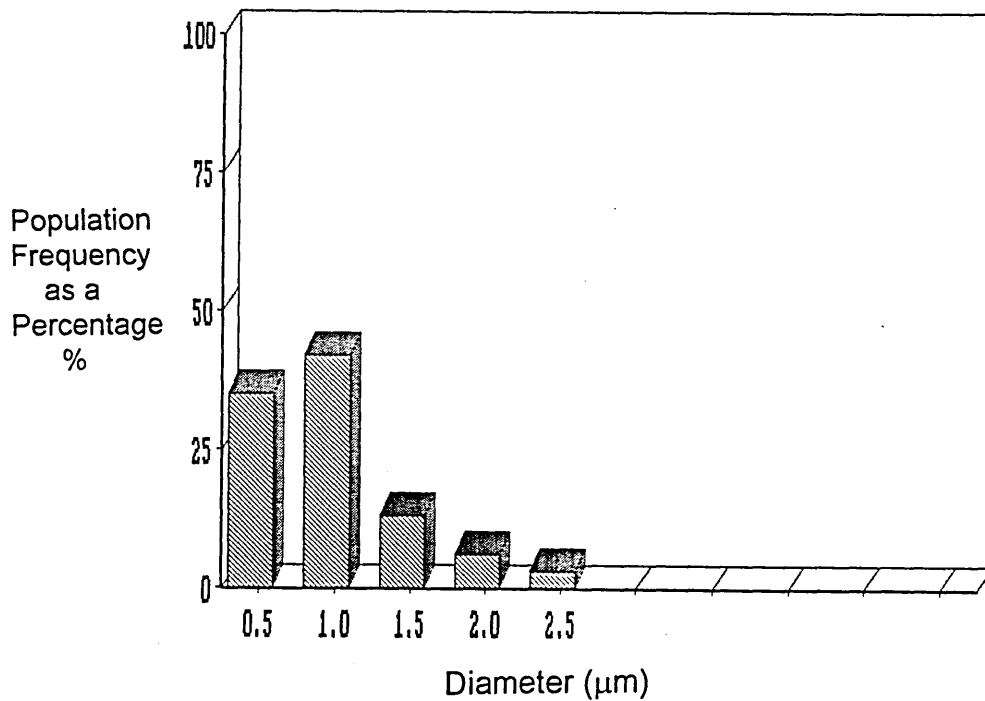


Figure 4.20 (f) Size Distribution of Titania Inclusions in the Sample taken 44 Seconds after Deoxidation in the High Frequency Furnace Melt (Jeol 840 SEM/Digiscan).

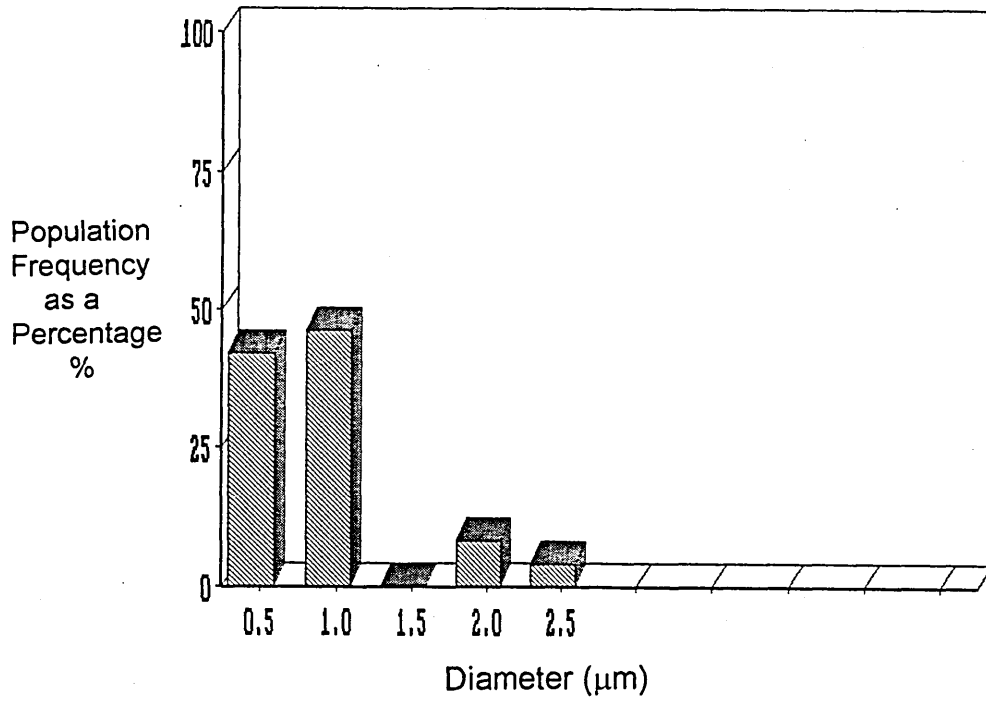


Figure 4.20(g) Size Distribution of Titania Inclusions in the Sample taken 55 Seconds after Deoxidation in the High Frequency Furnace Melt (Jeol 840 SEM/Digiscan).

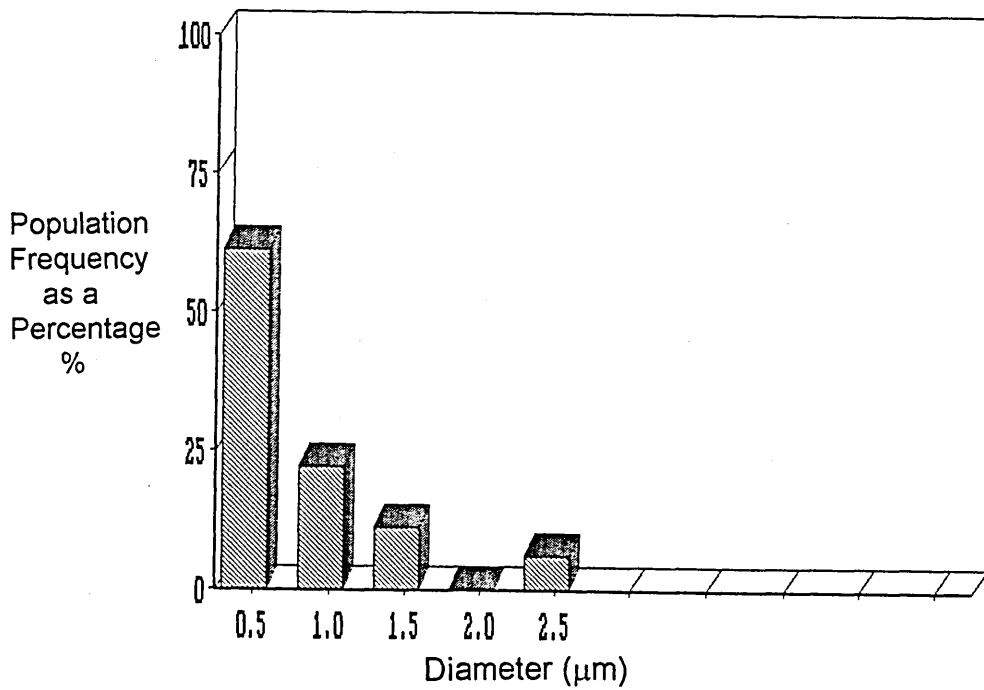


Figure 4.20(h) Size Distribution of Titania Inclusions in the Sample taken 67 Seconds after Deoxidation in the High Frequency Furnace Melt (Jeol 840 SEM/Digiscan).

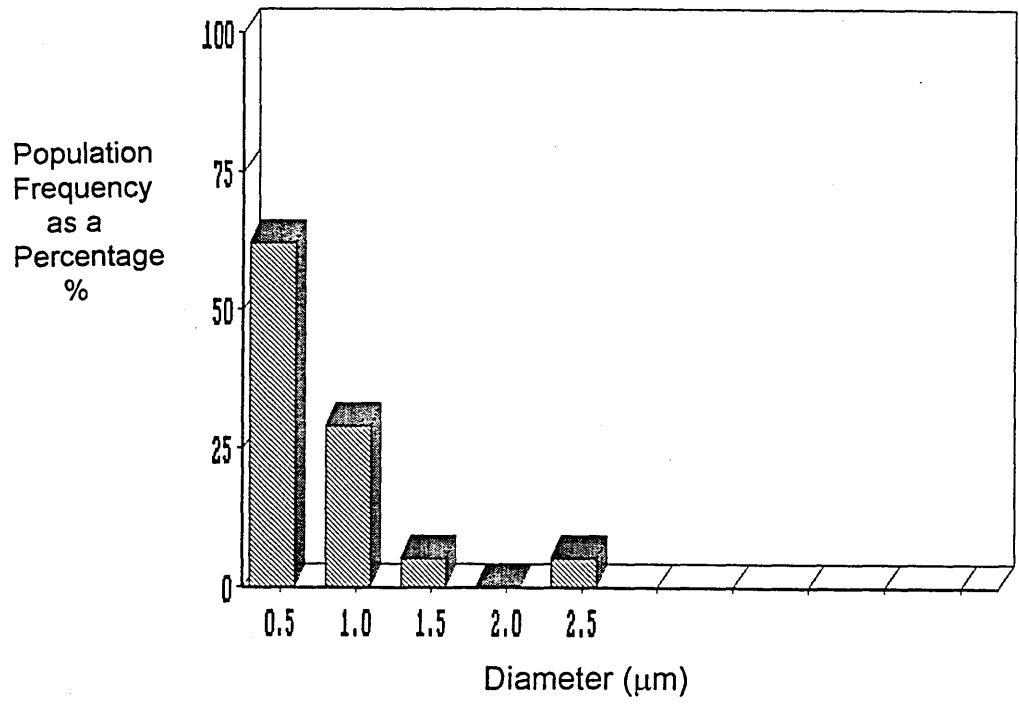


Figure 4.20(i) Size Distribution of Titania Inclusions in the Sample taken 120 Seconds after Deoxidation in the High Frequency Furnace Melt (Jeol 840 SEM/Digiscan).

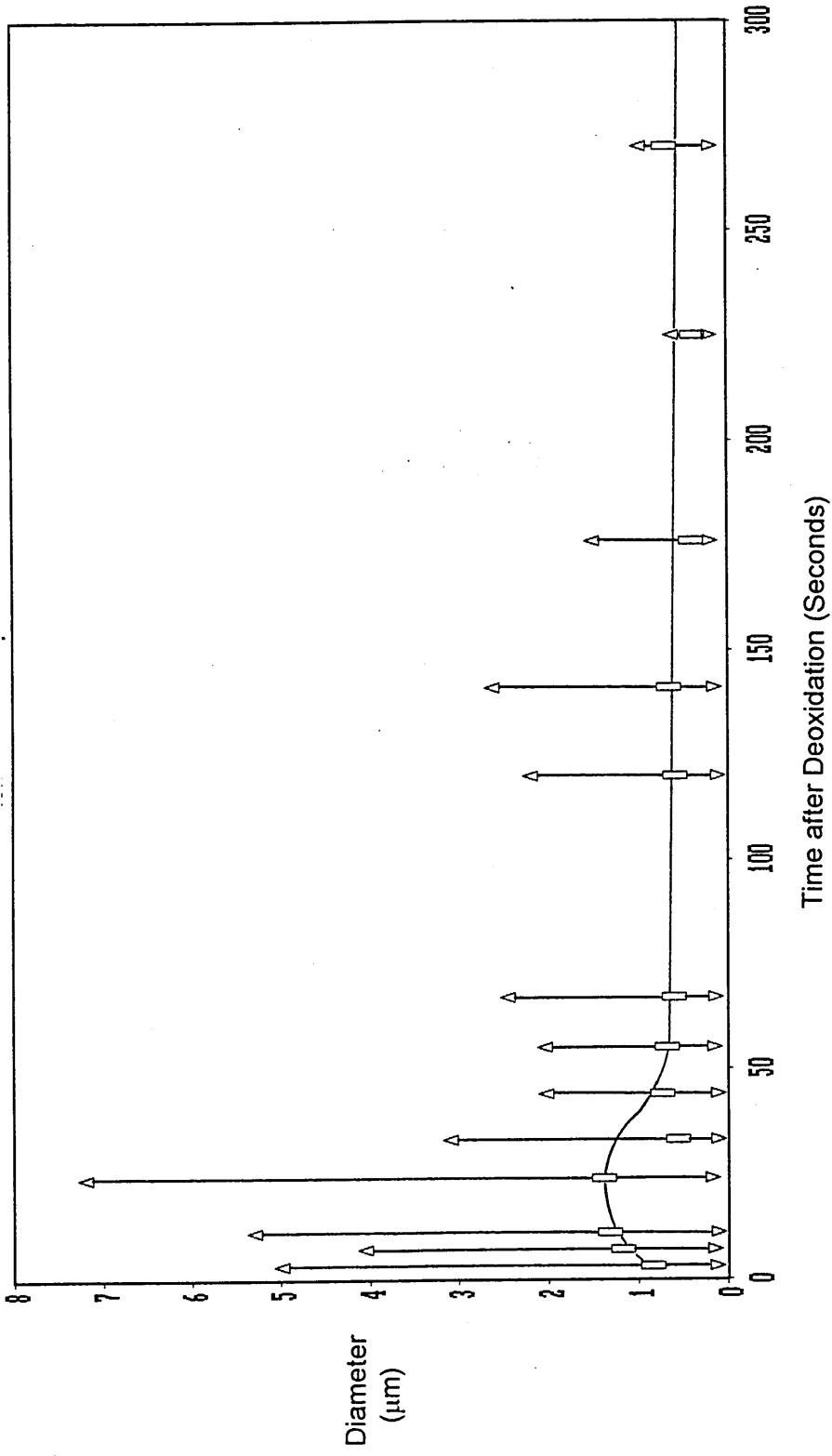


Figure 4.21 Mean Titania Inclusions Diameter Versus Time after Deoxidation in the High Frequency Furnace Melt (JEOL 840 SEM/Digiscan).

Δ - Mean from Maximum Size Band ▽ - Mean from Minimum Size Band □ - Mean Diameter

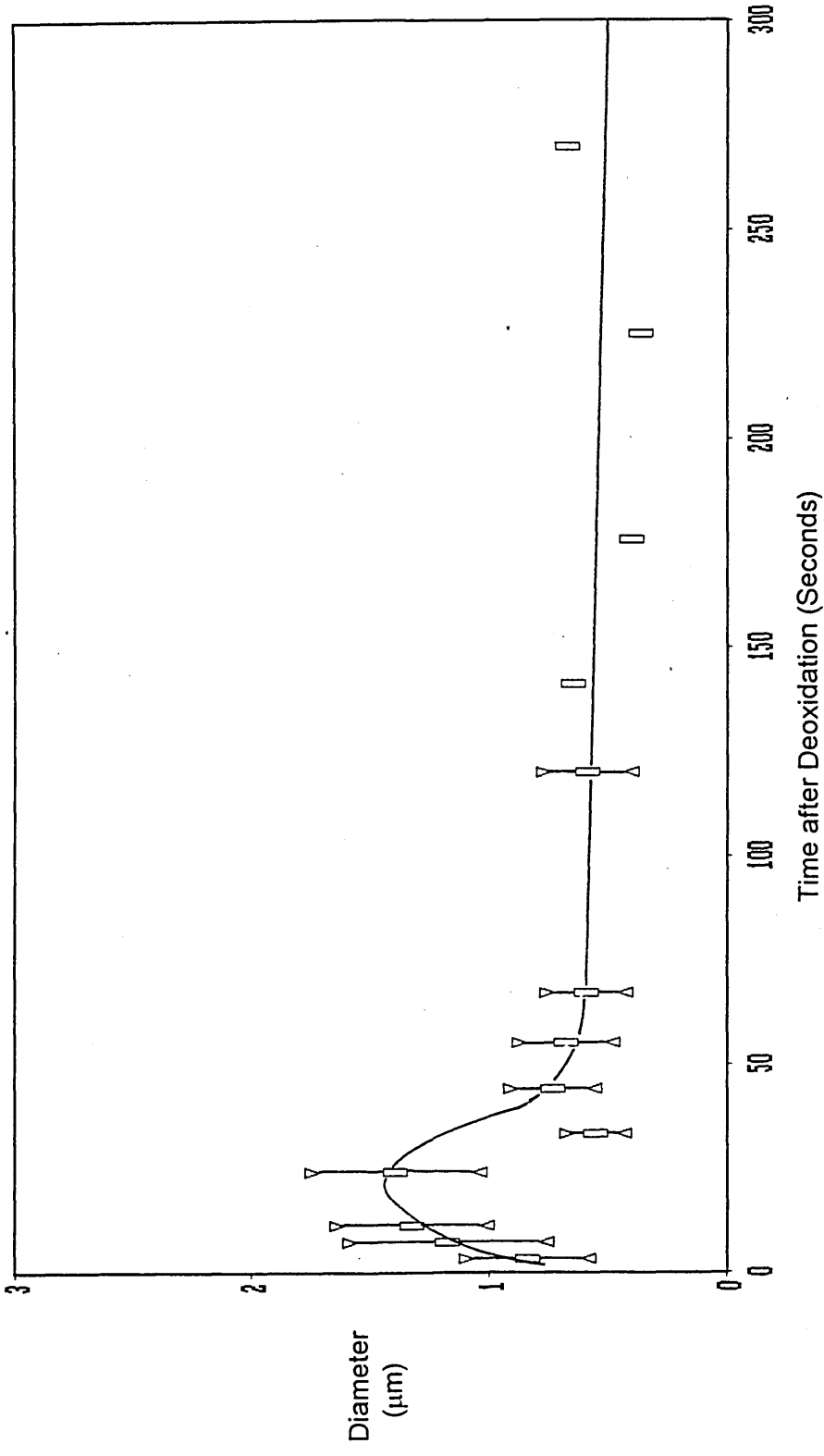


Figure 4.22 Mean Titania Inclusions Diameter Versus Time after Deoxidation in the High Frequency Furnace Melt (JEOL 840 SEM/Digiscan).

▽ - Upper 95% Confidence Limit △ - Lower 95% Confidence Limit □ - Mean Diameter

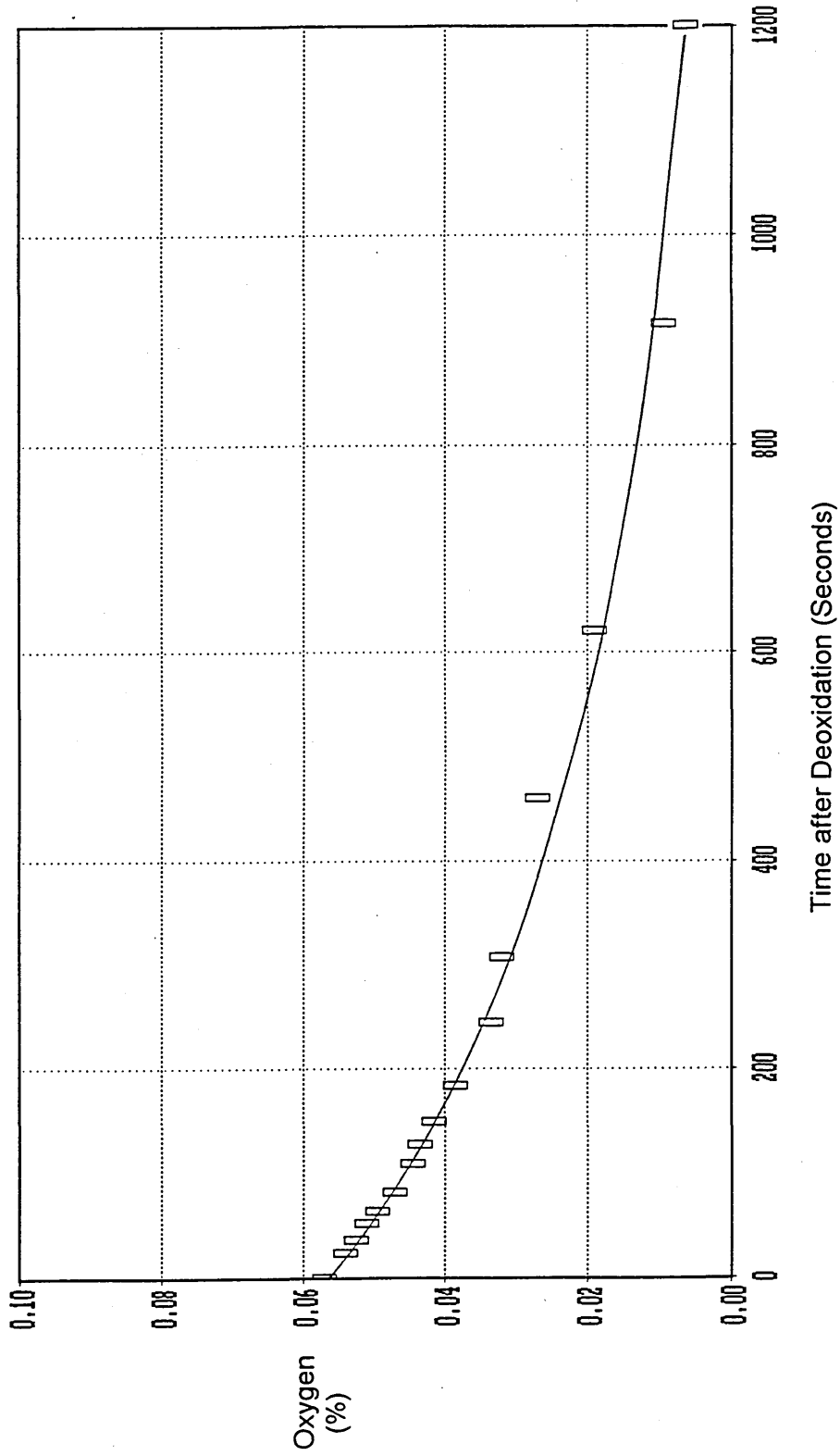


Figure 4.23(a) Total Oxygen Analysis Versus Time after Deoxidation with 0.3 mass% Silicon Addition in the Vertical Tube Furnace Melt (LECO).

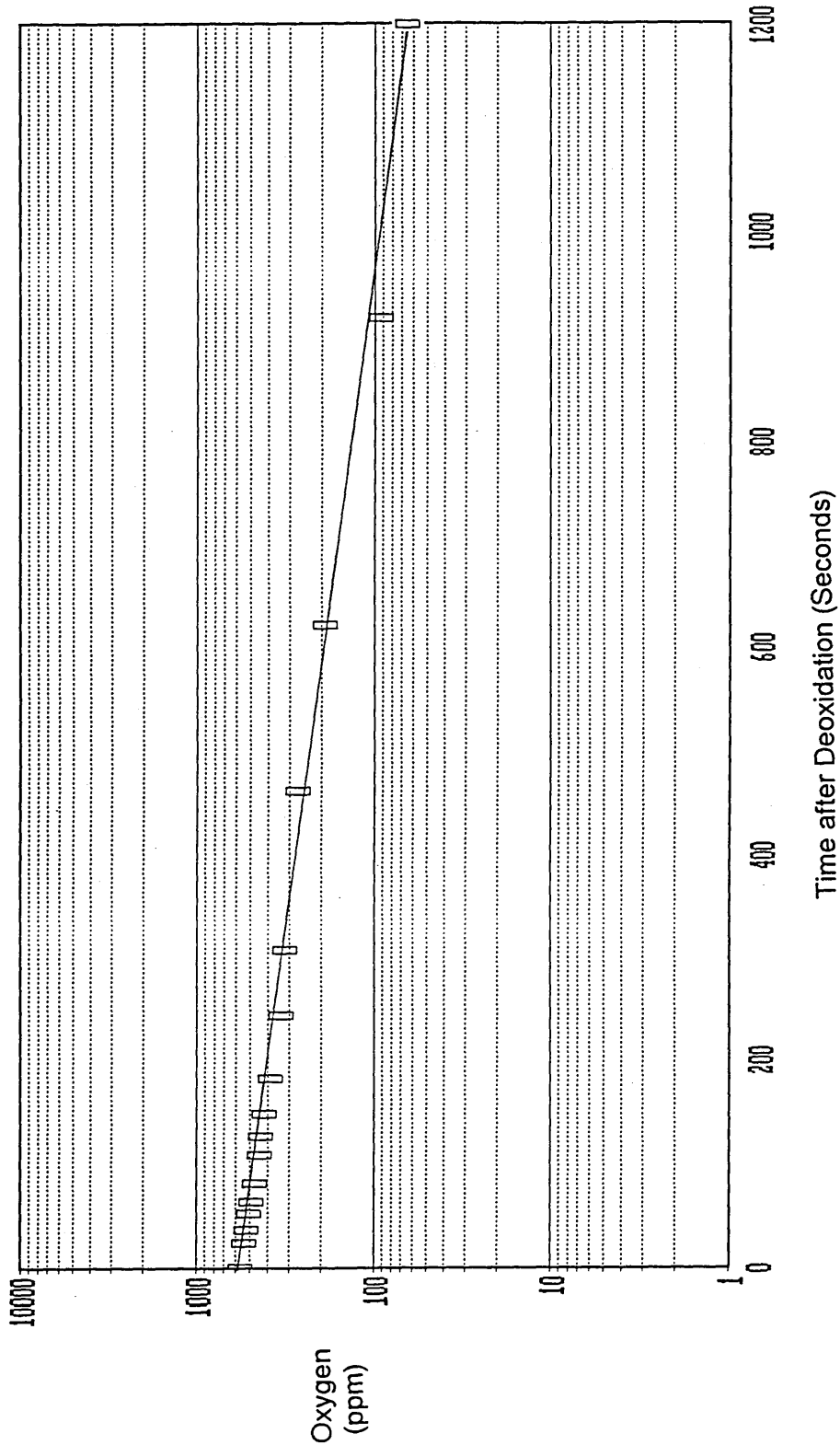


Figure 4.23(b) Total Oxygen Analysis Versus Time after Deoxidation with 0.3 mass% Silicon Addition in the Vertical Tube Furnace Melt (LECO).

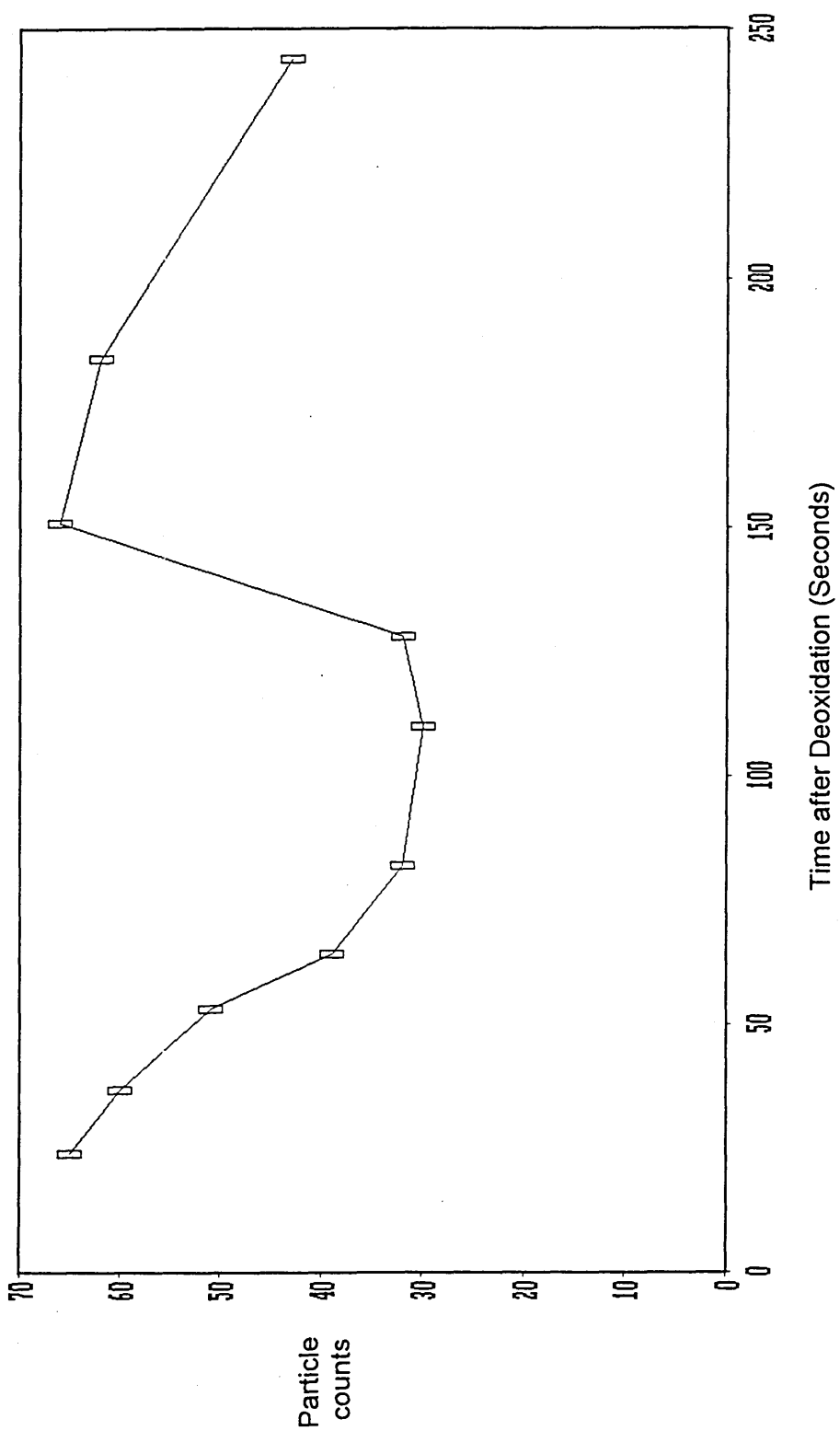


Figure 4.24 Number of Silica Inclusions Counted Versus Time after Deoxidation in the Vertical Tube Furnace Melt (JEOL 840 SEM/Digiscan).

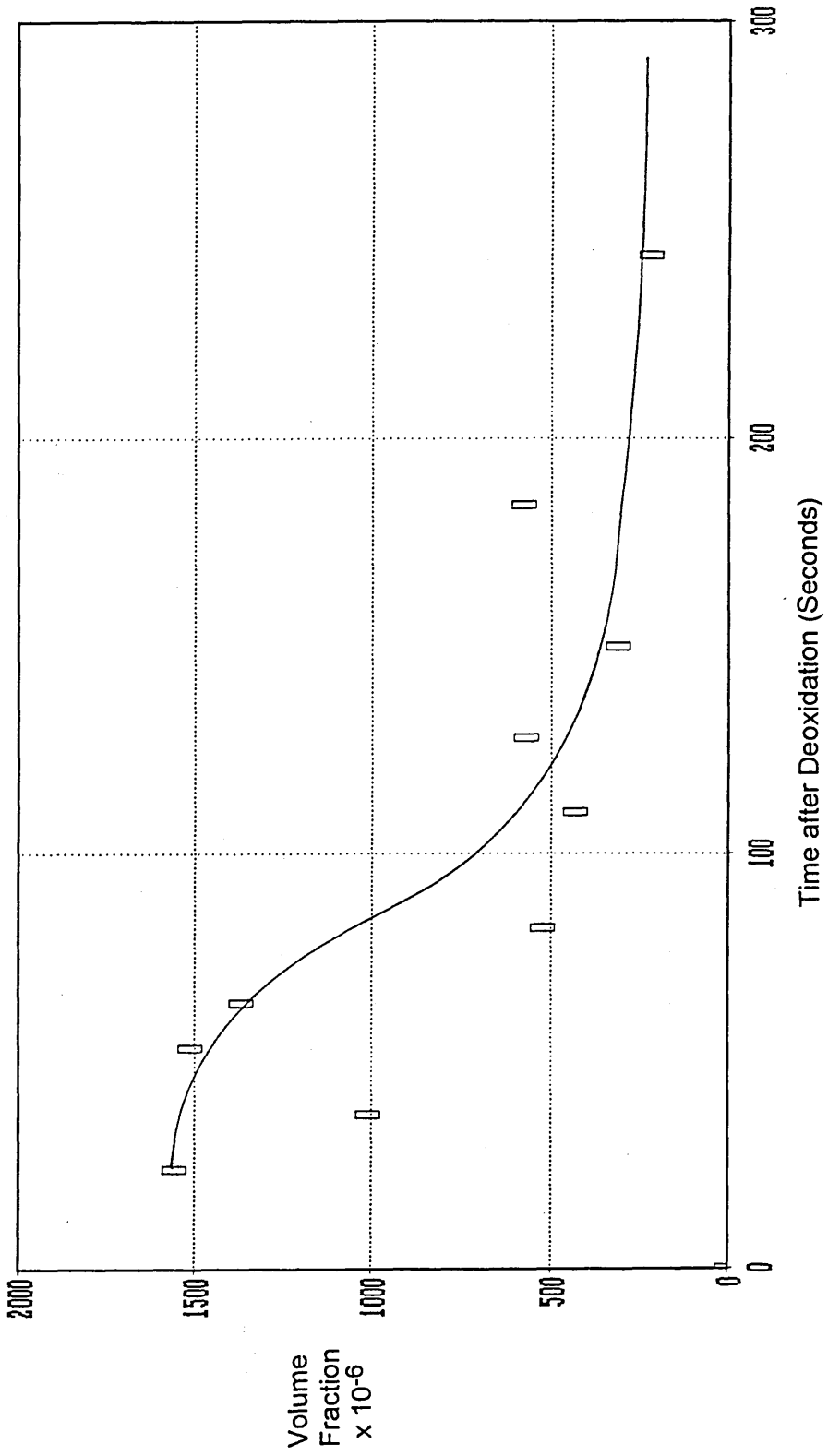


Figure 4.25 Volume Fraction of Silica Inclusions Versus Time after Deoxidation in the Vertical Tube Furnace Melt (JEOL 840 SEM/Digiscan).

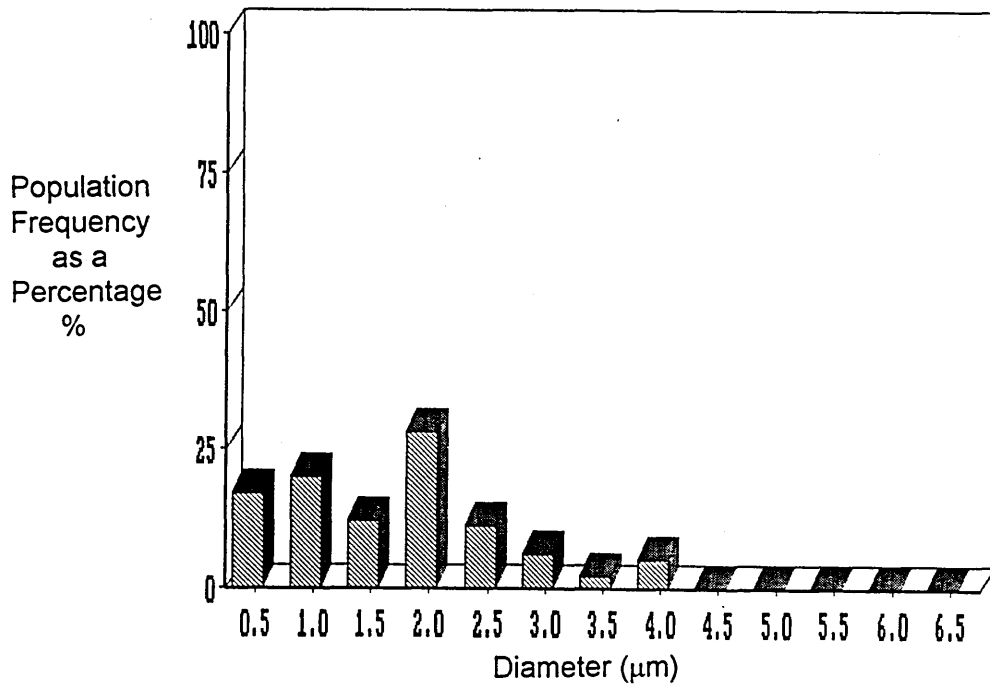


Figure 4.26 (a) Size Distribution of Silica Inclusions in the Sample taken 24 Seconds after Deoxidation in the Vertical Tube Furnace Melt (Jeol 840 SEM/Digiscan).

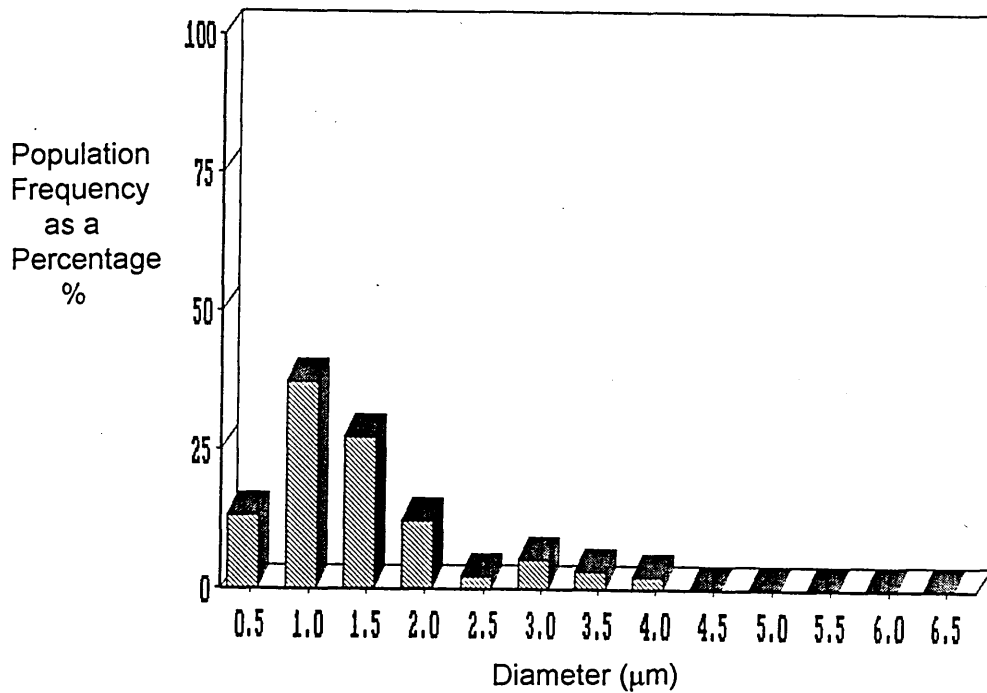


Figure 4.26 (b) Size Distribution of Silica Inclusions in the Sample taken 37 Seconds after Deoxidation in the Vertical Tube Furnace Melt (Jeol 840 SEM/Digiscan).

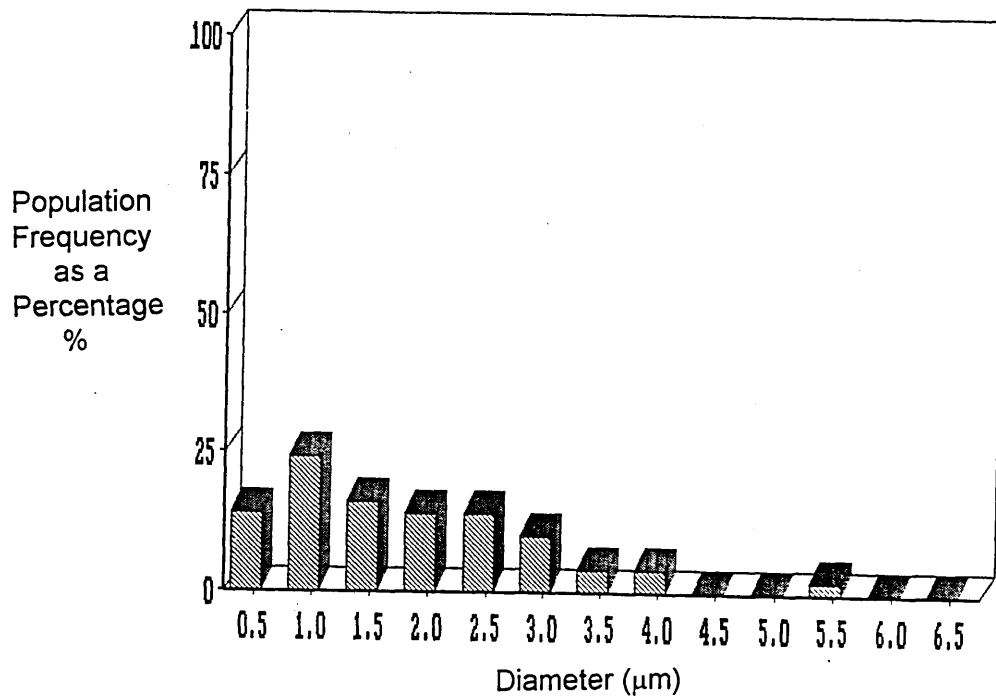


Figure 4.26 (c) Size Distribution of Silica Inclusions in the Sample taken 53 Seconds after Deoxidation in the Vertical Tube Furnace Melt (Jeol 840 SEM/Digiscan).

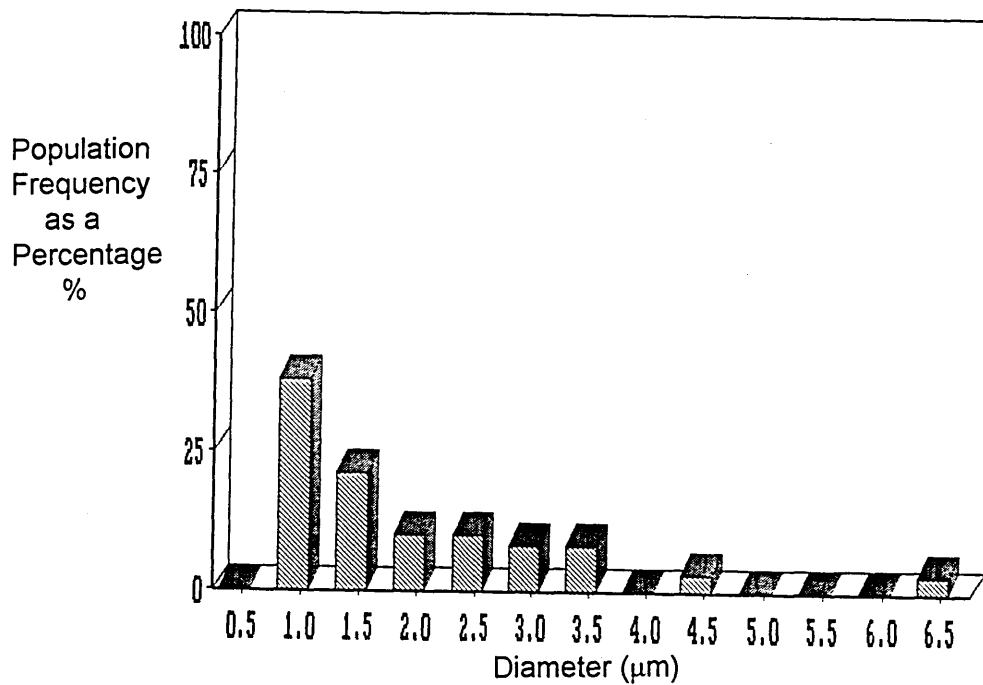


Figure 4.26 (d) Size Distribution of Silica Inclusions in the Sample taken 64 Seconds after Deoxidation in the Vertical Tube Furnace Melt (Jeol 840 SEM/Digiscan).

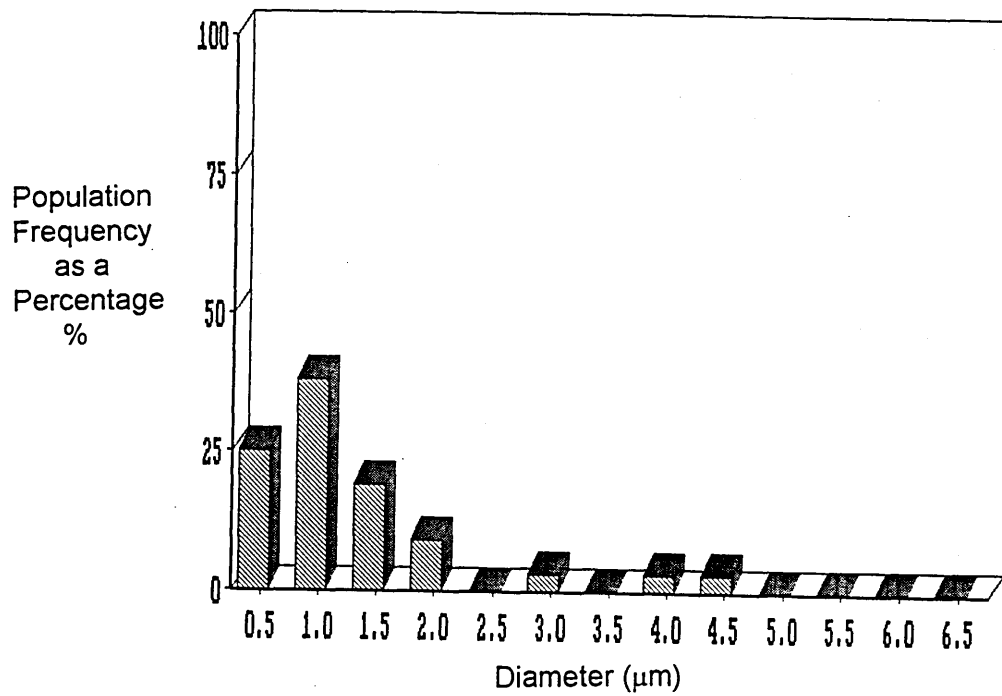


Figure 4.26 (e) Size Distribution of Silica Inclusions in the Sample taken 82 Seconds after Deoxidation in the Vertical Tube Furnace Melt (Jeol 840 SEM/Digiscan).

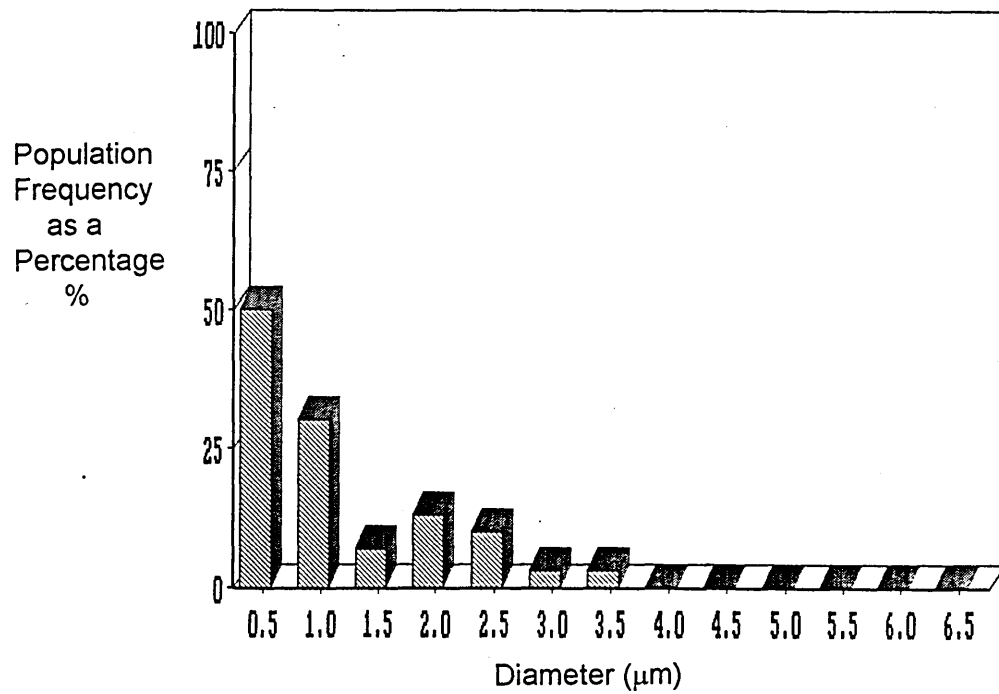


Figure 4.26 (f) Size Distribution of Silica Inclusions in the Sample taken 110 Seconds after Deoxidation in the Vertical Tube Furnace Melt (Jeol 840 SEM/Digiscan).

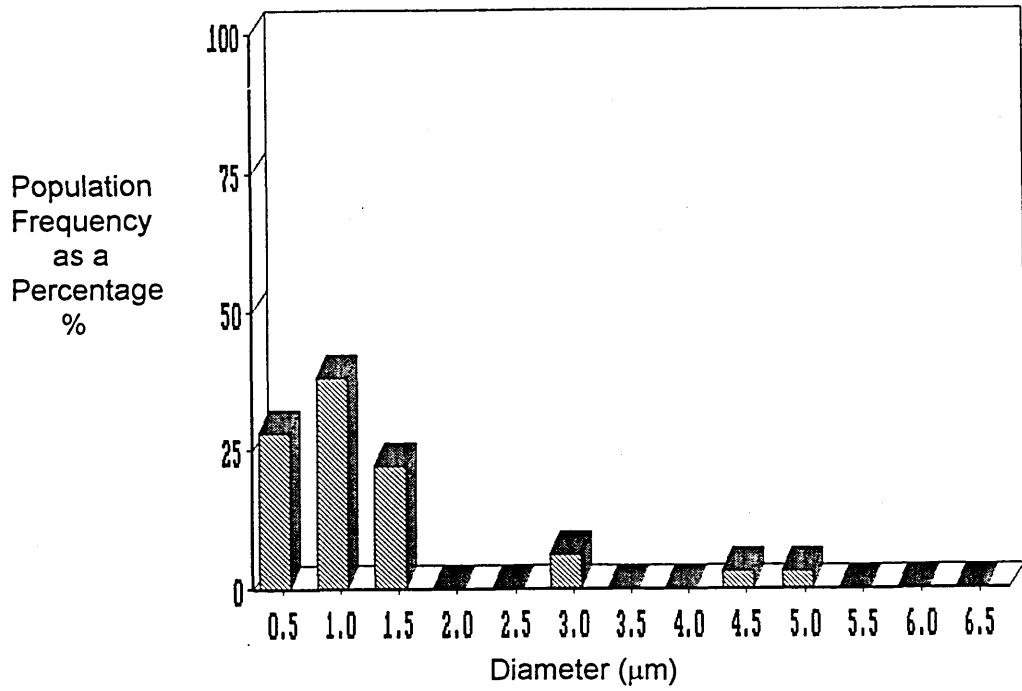


Figure 4.26 (g) Size Distribution of Silica Inclusions in the Sample taken 128 Seconds after Deoxidation in the Vertical Tube Furnace Melt (Jeol 840 SEM/Digiscan).

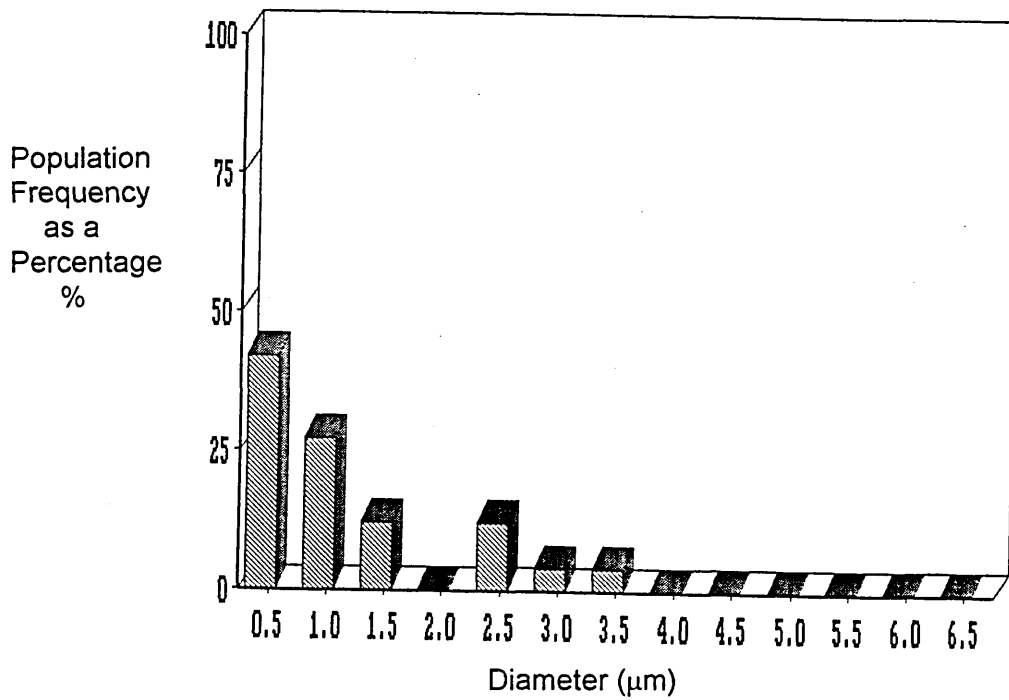


Figure 4.26 (h) Size Distribution of Silica Inclusions in the Sample taken 151 Seconds after Deoxidation in the Vertical Tube Furnace Melt (Jeol 840 SEM/Digiscan).

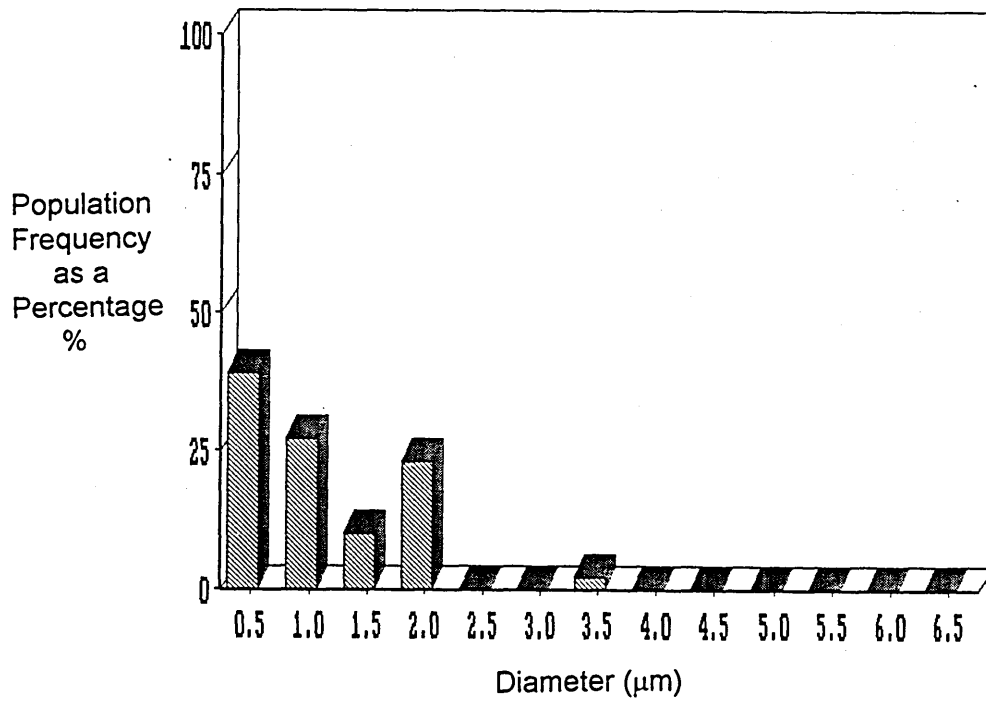


Figure 4.26 (i) Size Distribution of Silica Inclusions in the Sample taken 184 Seconds after Deoxidation in the Vertical Tube Furnace Melt (Jeol 840 SEM/Digiscan).

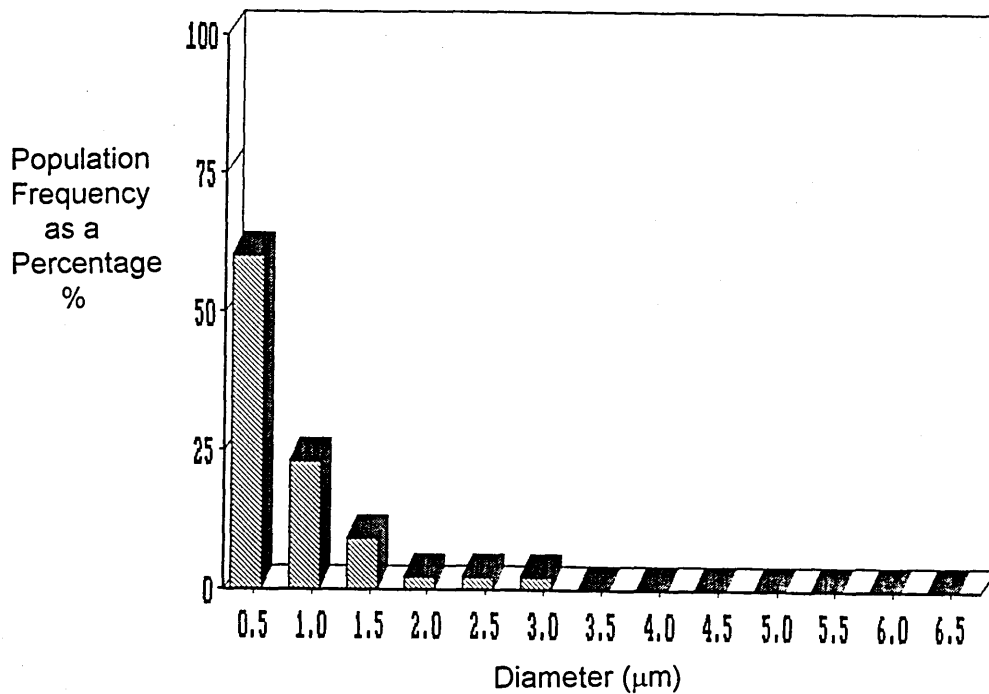


Figure 4.26 (j) Size Distribution of Silica Inclusions in the Sample taken 244 Seconds after Deoxidation in the Vertical Tube Furnace Melt (Jeol 840 SEM/Digiscan).

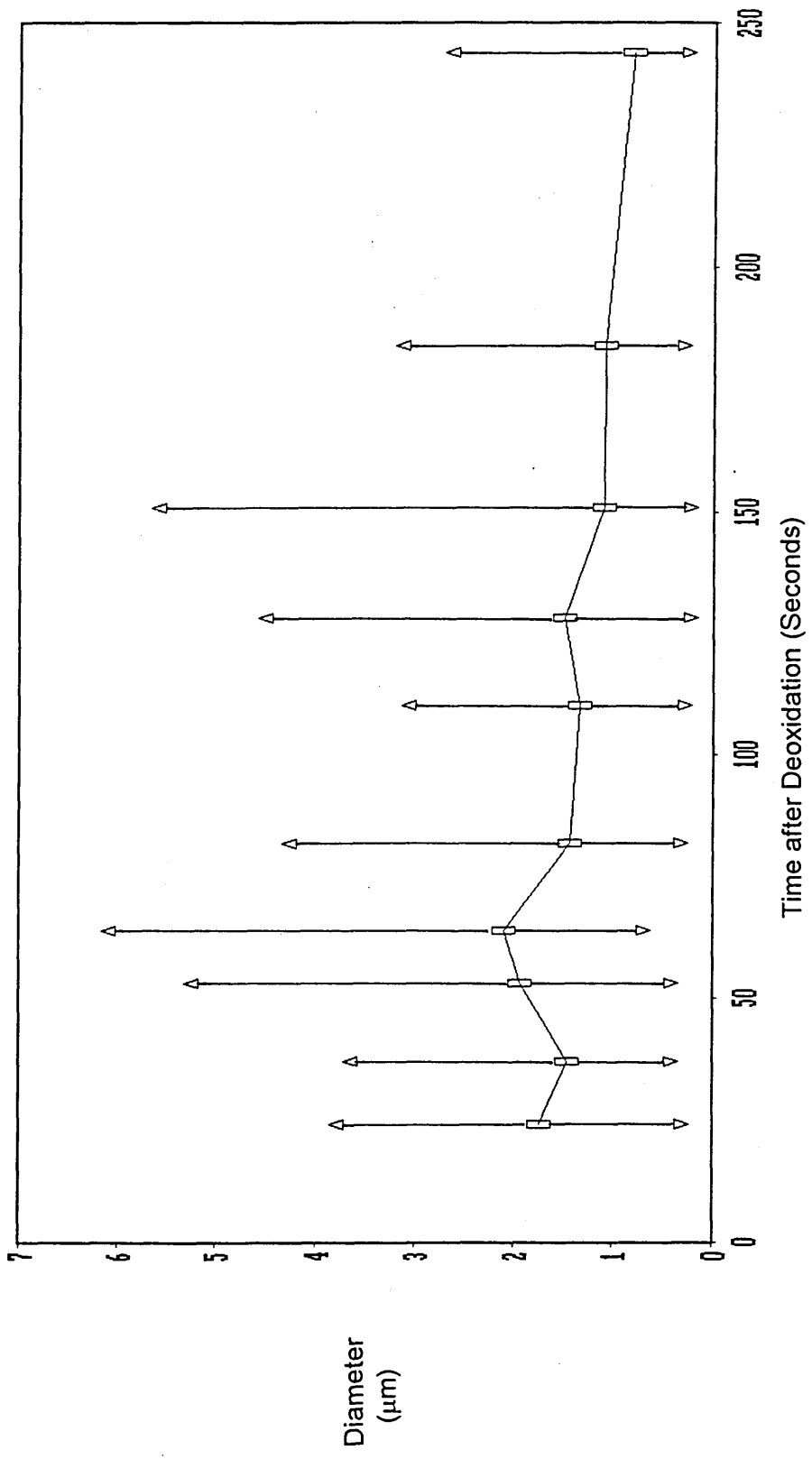


Figure 4.27 Mean Silica Inclusions Diameter Versus Time after Deoxidation in the Vertical Tube Furnace Melt (JEOL 840 SEM/Digiscan) .

△ - Mean from Maximum Size Band ▽ - Mean from Minimum Size Band □ - Mean Diameter

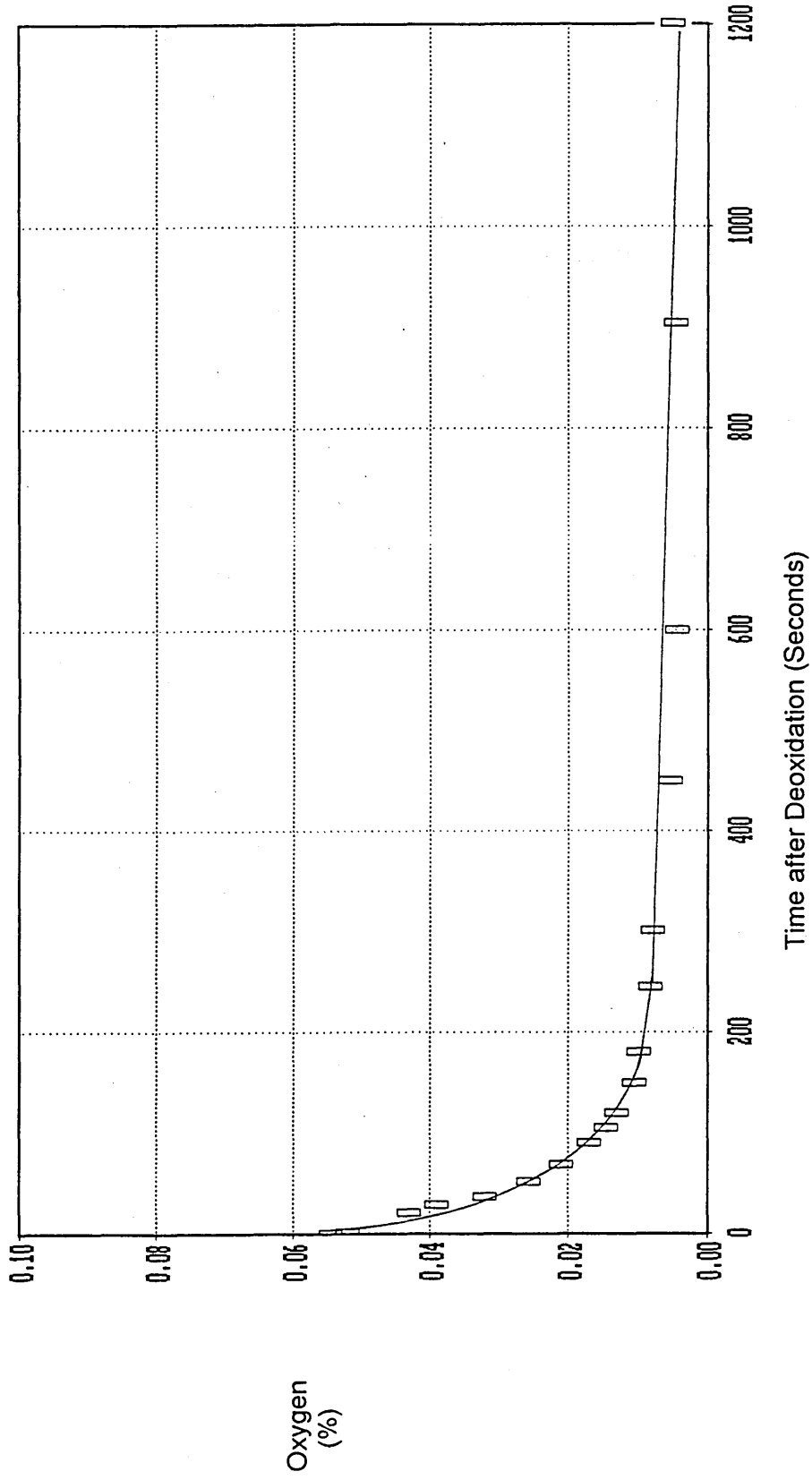


Figure 4.28(a) Total Oxygen Analysis Versus Time after Deoxidation with 0.3 mass% Silicon Addition in the High Frequency Furnace Melt (LECO).

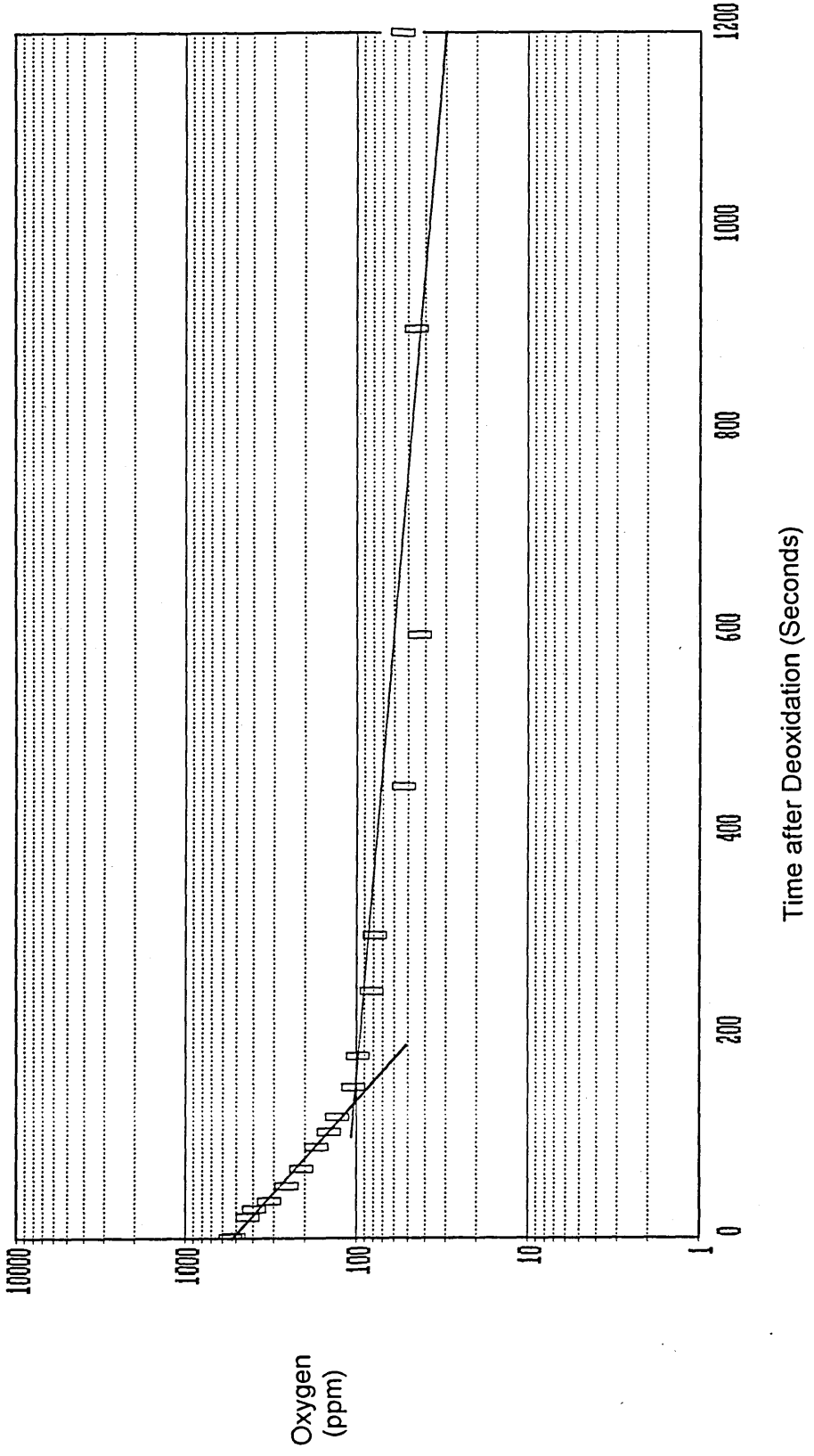


Figure 4.28(b) Total Oxygen Analysis Versus Time after Deoxidation with 0.3 mass% Silicon Addition in the High Frequency Furnace Melt (LECO).

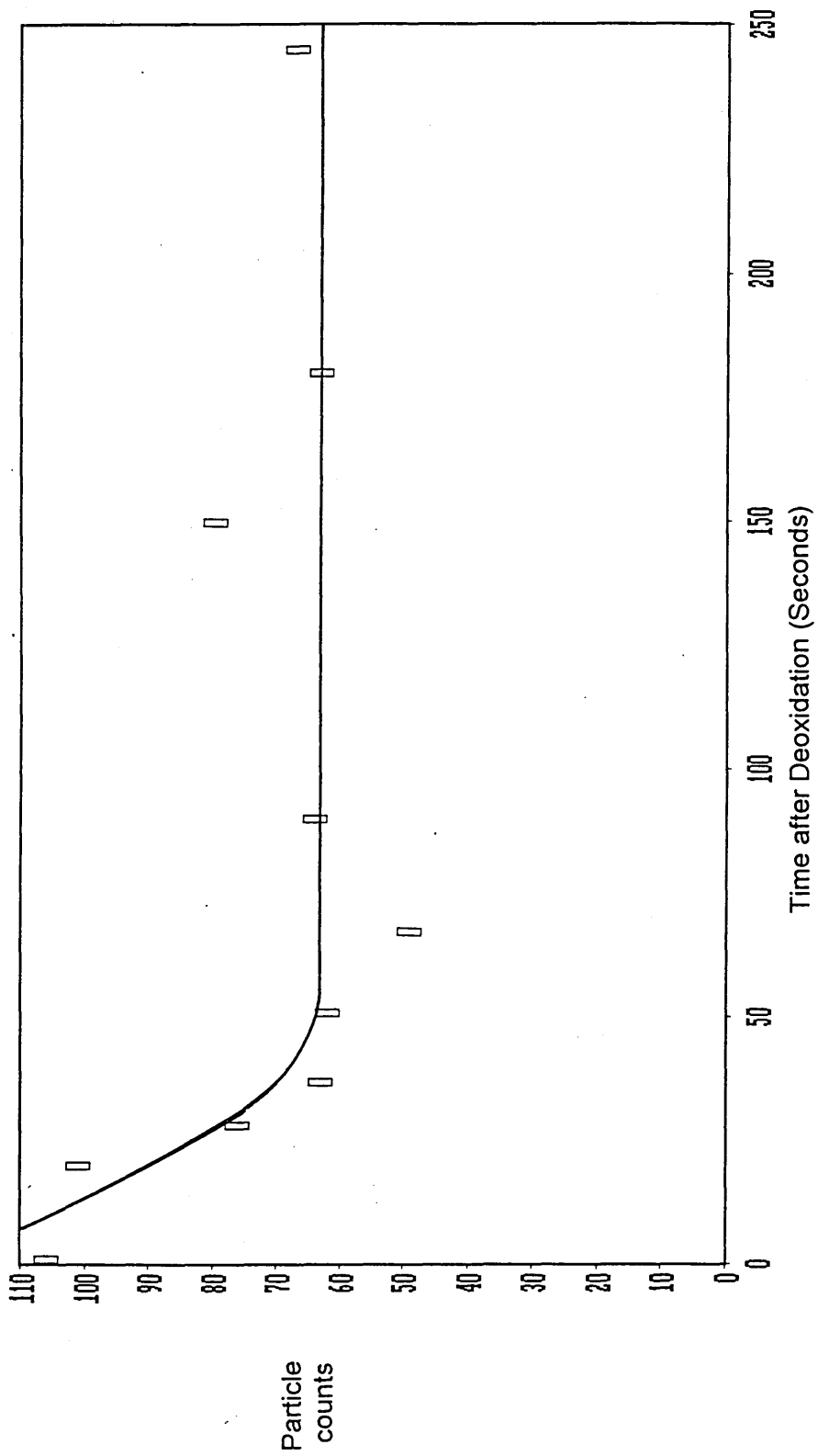


Figure 4.29 Number of Silica Inclusions Counted Versus Time after Deoxidation in the High Frequency Furnace Melt (JEOL 840 SEM/Digiscan).

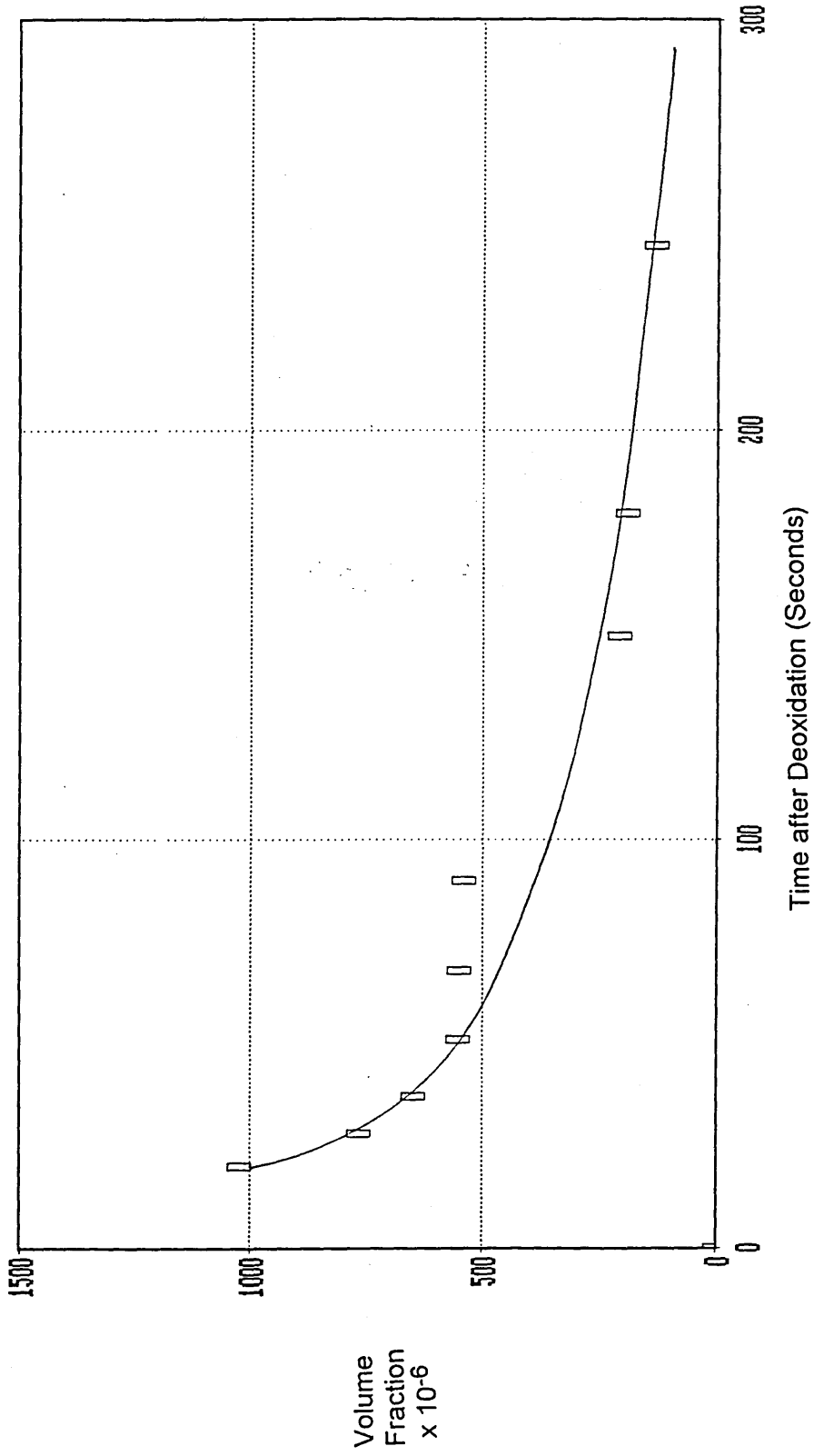


Figure 4.30 Volume Fraction of Silica Inclusions Versus Time after Deoxidation in the High Frequency Furnace Melt (JEOL 840 SEM/Digiscan) .

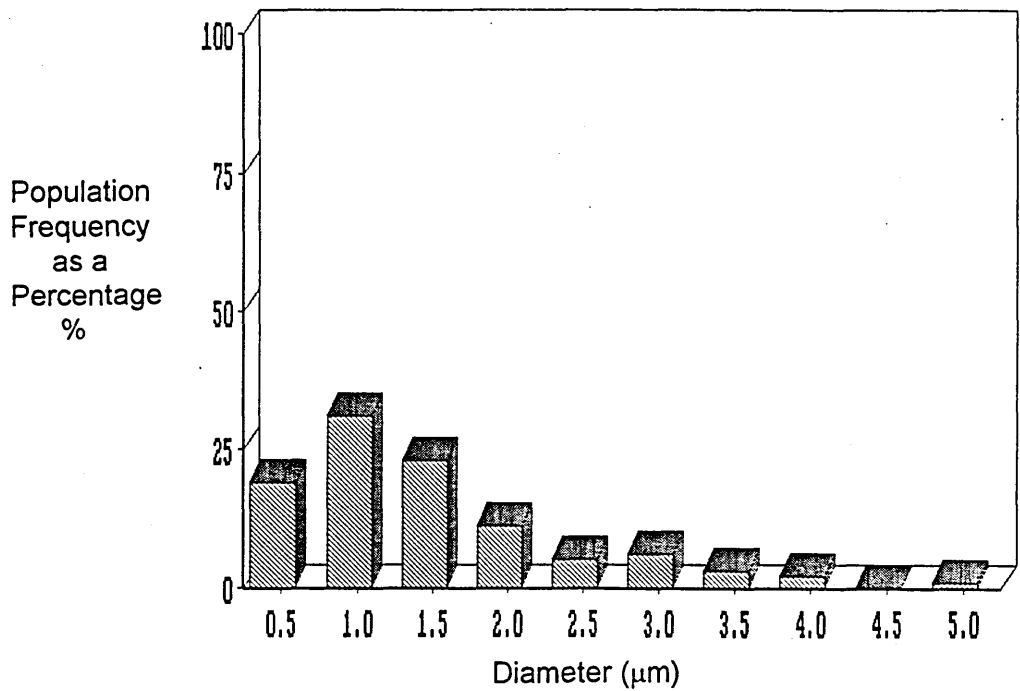


Figure 4.31 (a) Size Distribution of Silica Inclusions in the Sample taken 1 Seconds after Deoxidation in the High Frequency Furnace Melt (Jeol 840 SEM/Digiscan).

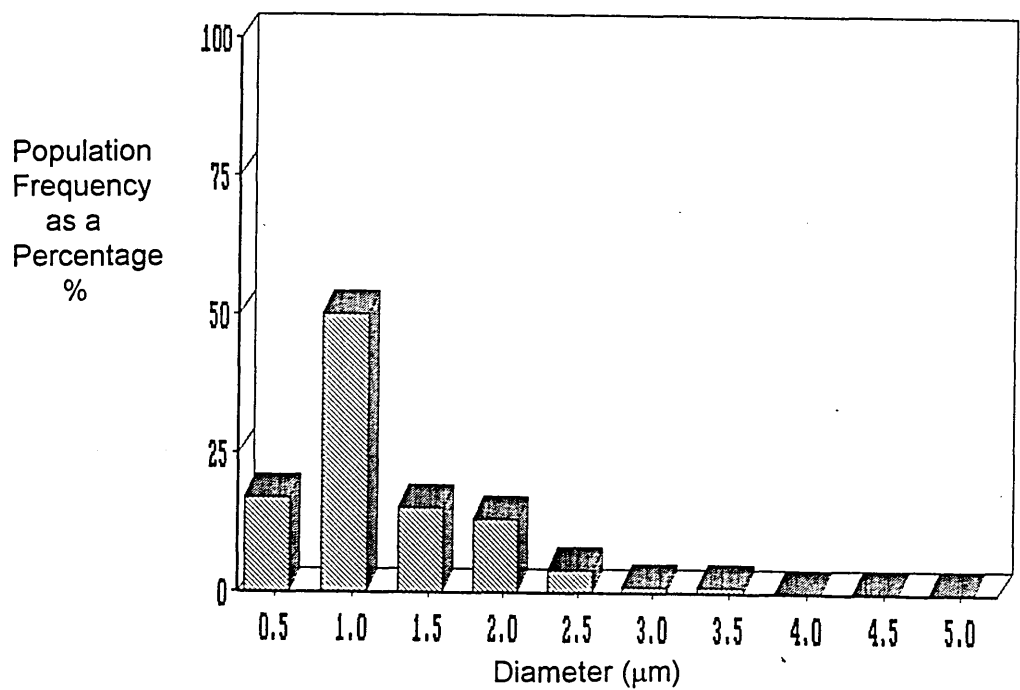


Figure 4.31 (b) Size Distribution of Silica Inclusions in the Sample taken 20 Seconds after Deoxidation in the High Frequency Furnace Melt (Jeol 840 SEM/Digiscan).

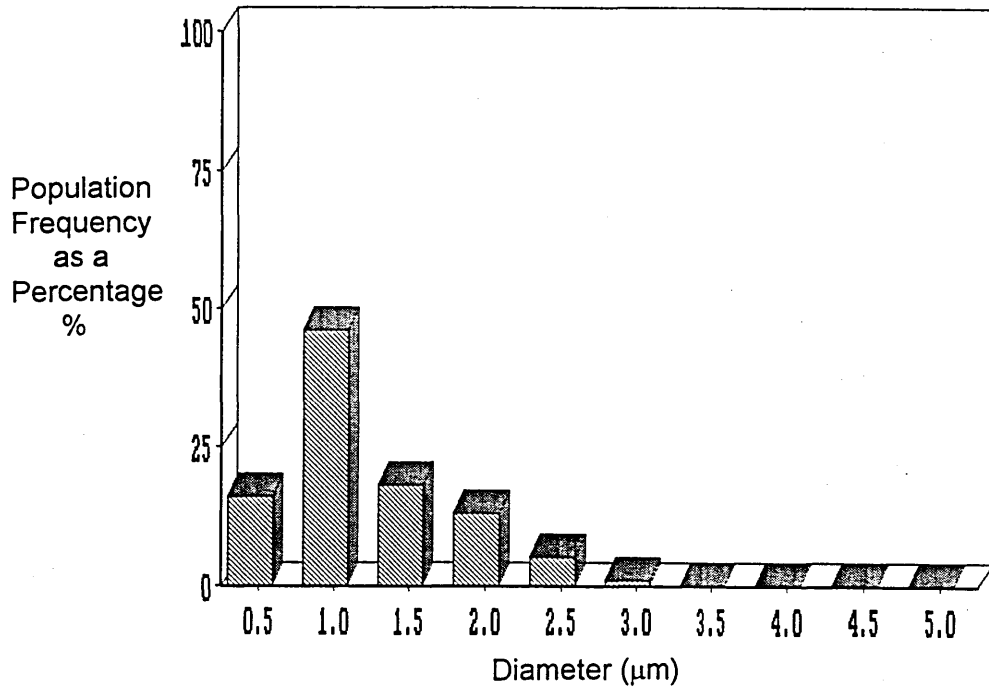


Figure 4.31 (c) Size Distribution of Silica Inclusions in the Sample taken 28 Seconds after Deoxidation in the High Frequency Furnace Melt (Jeol 840 SEM/Digiscan).

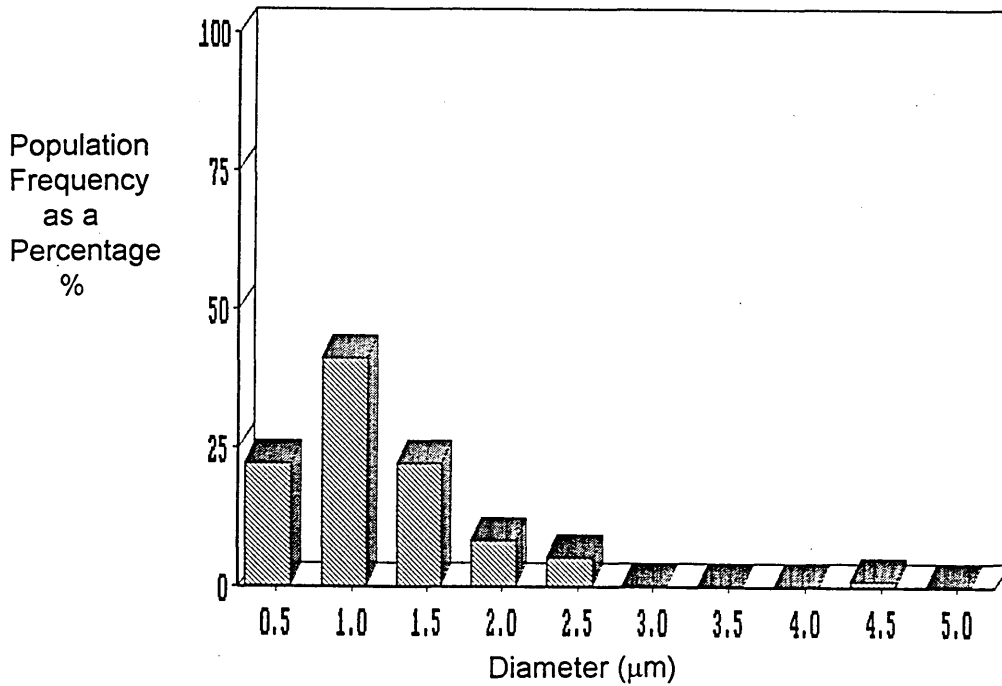


Figure 4.31 (d) Size Distribution of Silica Inclusions in the Sample taken 37 Seconds after Deoxidation in the High Frequency Furnace Melt (Jeol 840 SEM/Digiscan).

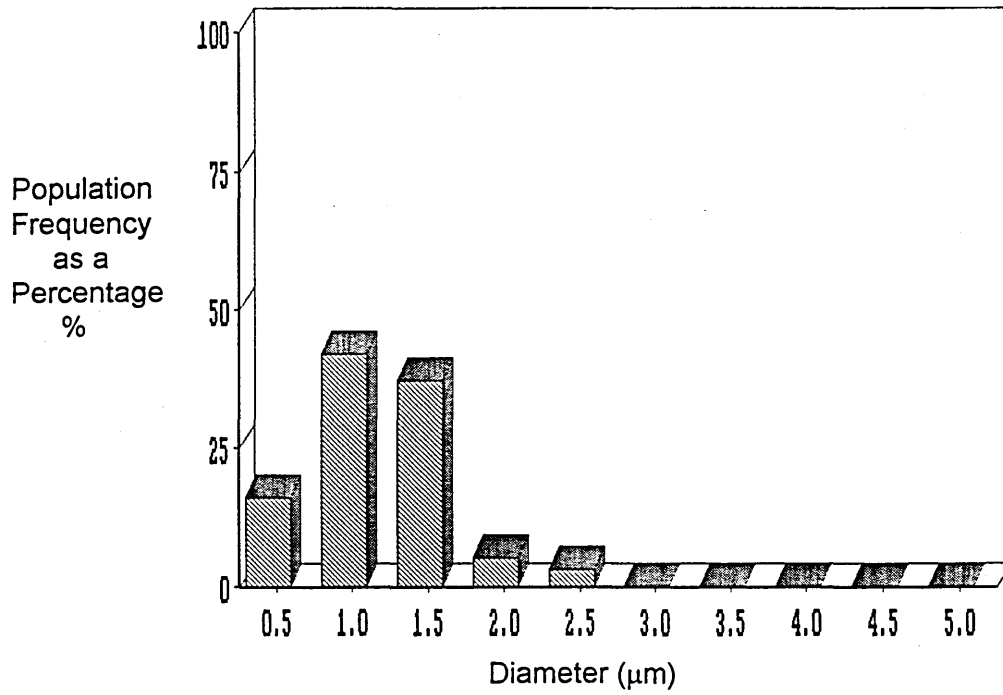


Figure 4.31 (e) Size Distribution of Silica Inclusions in the Sample taken 51 Seconds after Deoxidation in the High Frequency Furnace Melt (Jeol 840 SEM/Digiscan).

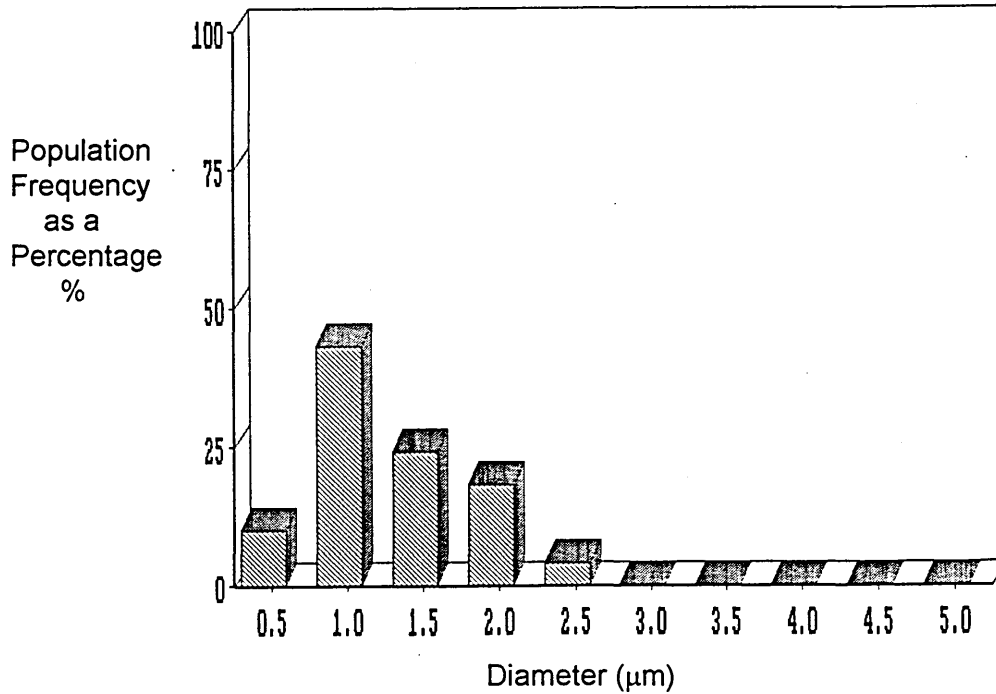


Figure 4.31 (f) Size Distribution of Silica Inclusions in the Sample taken 68 Seconds after Deoxidation in the High Frequency Furnace Melt (Jeol 840 SEM/Digiscan).

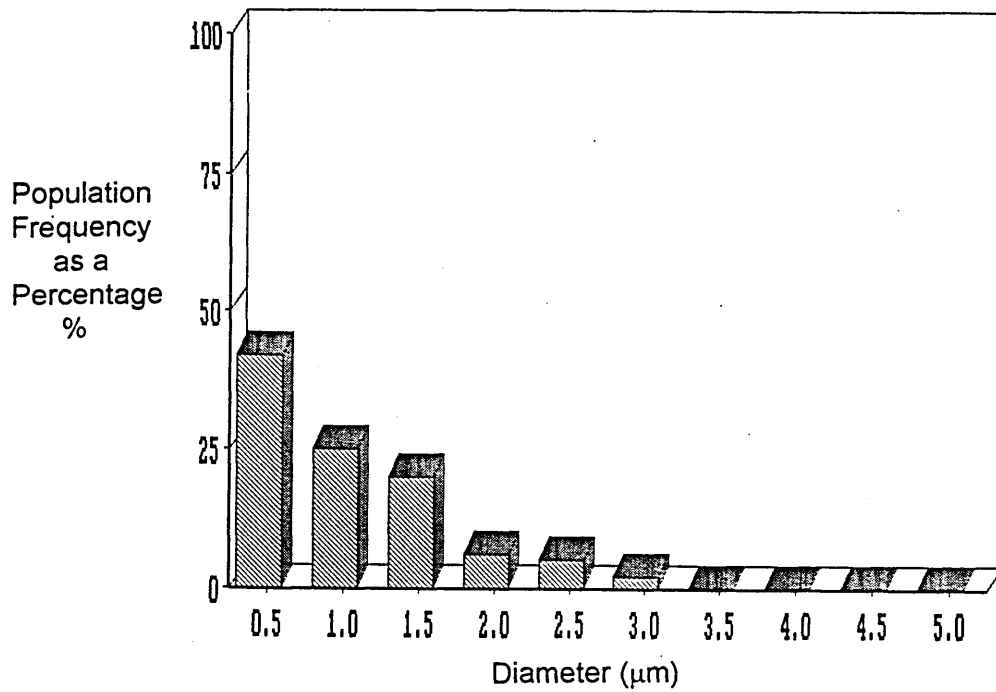


Figure 4.31 (g) Size Distribution of Silica Inclusions in the Sample taken 90 Seconds after Deoxidation in the High Frequency Furnace Melt (Jeol 840 SEM/Digiscan).

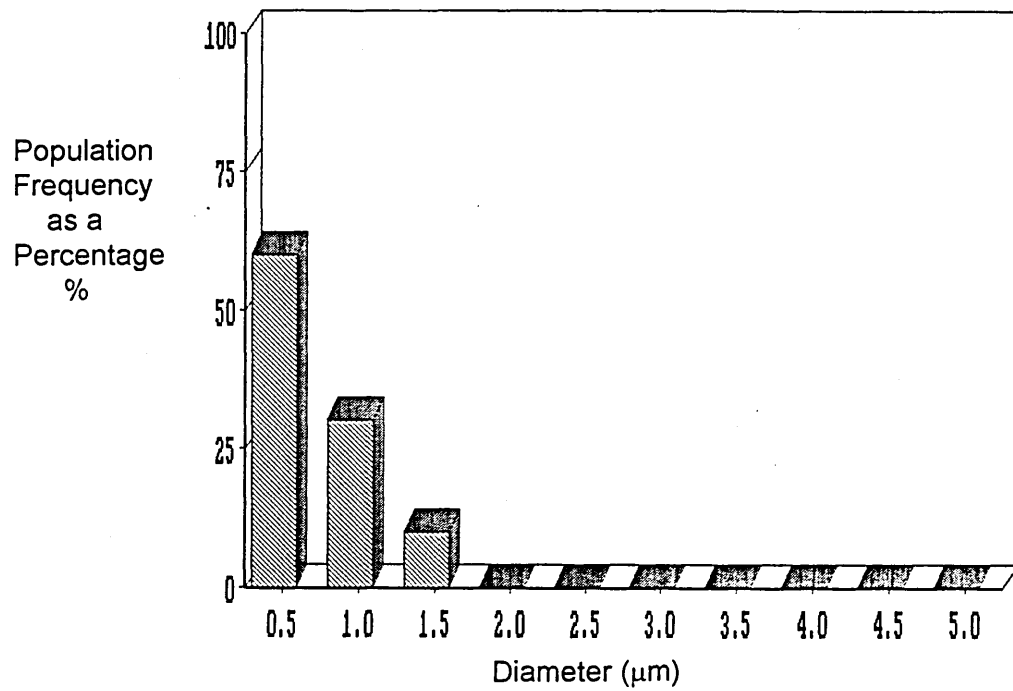


Figure 4.31 (h) Size Distribution of Silica Inclusions in the Sample taken 150 Seconds after Deoxidation in the High Frequency Furnace Melt (Jeol 840 SEM/Digiscan).

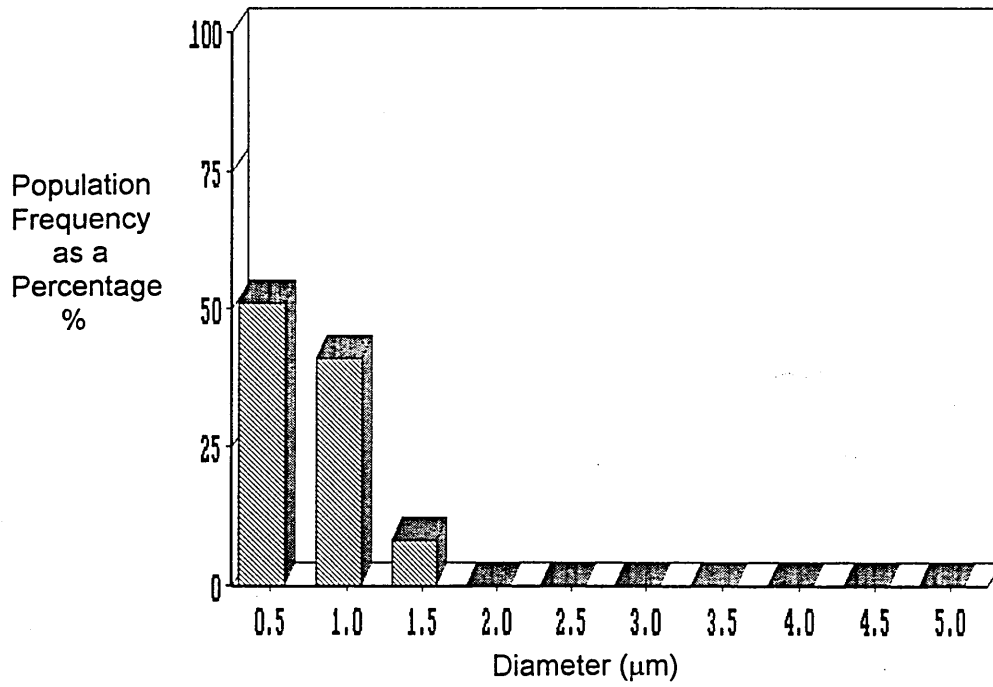


Figure 4.31 (i) Size Distribution of Silica Inclusions in the Sample taken 180 Seconds after Deoxidation in the High Frequency Furnace Melt (Jeol 840 SEM/Digiscan).

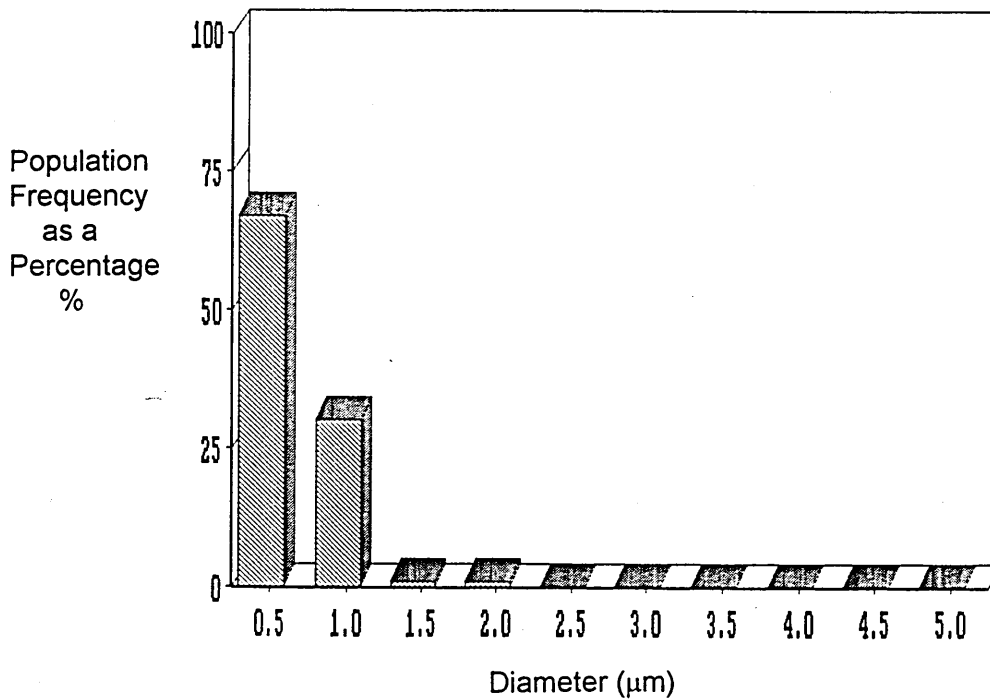


Figure 4.31 (j) Size Distribution of Silica Inclusions in the Sample taken 245 Seconds after Deoxidation in the High Frequency Furnace Melt (Jeol 840 SEM/Digiscan).

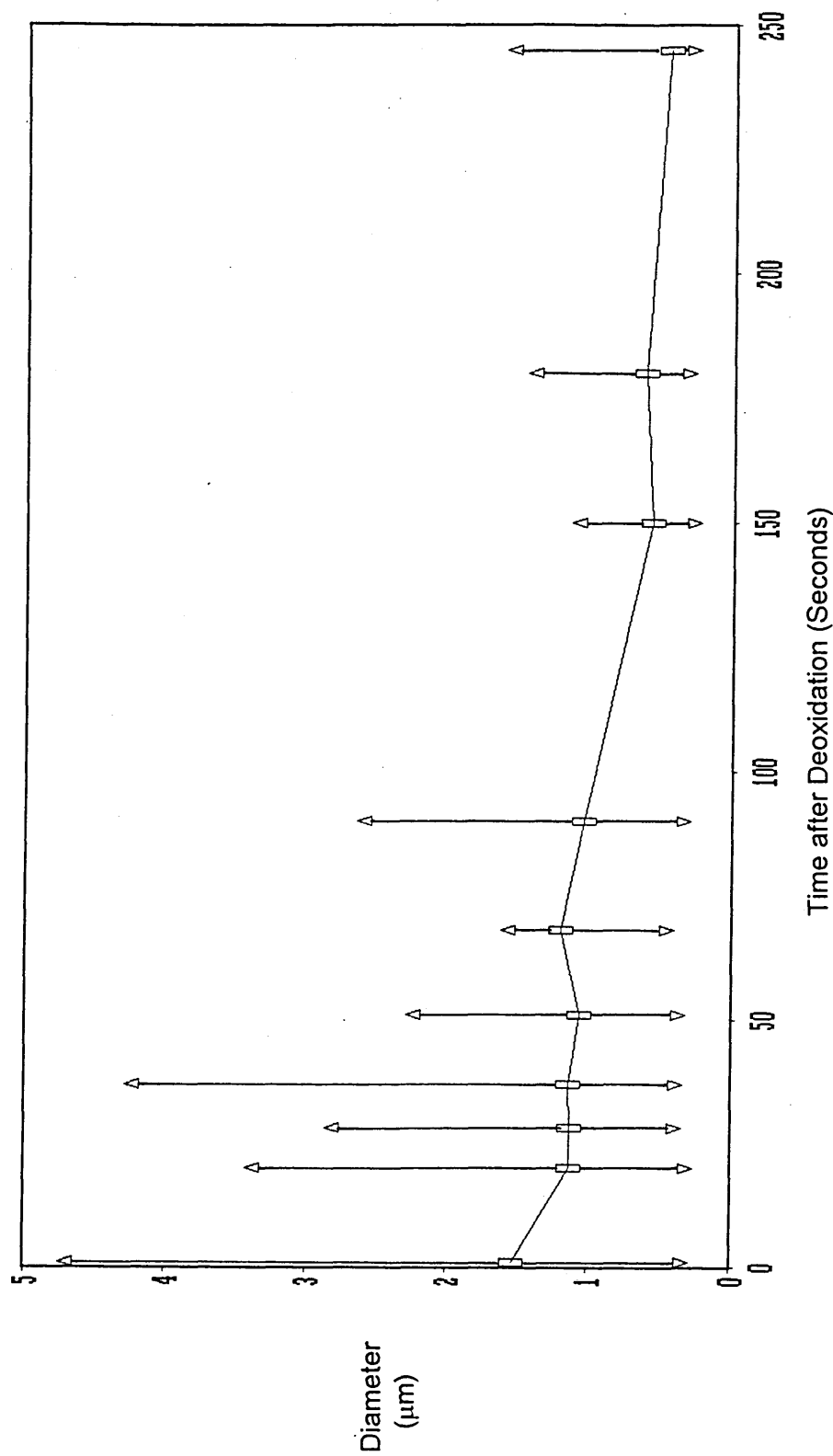


Figure 4.32 Mean Silica Inclusions Diameter Versus Time after Deoxidation in the High Frequency Furnace Melt (JEOL 840 SEM/Digiscan).

△ - Mean from Maximum Size Band ▽ - Mean from Minimum Size Band □ - Mean Diameter

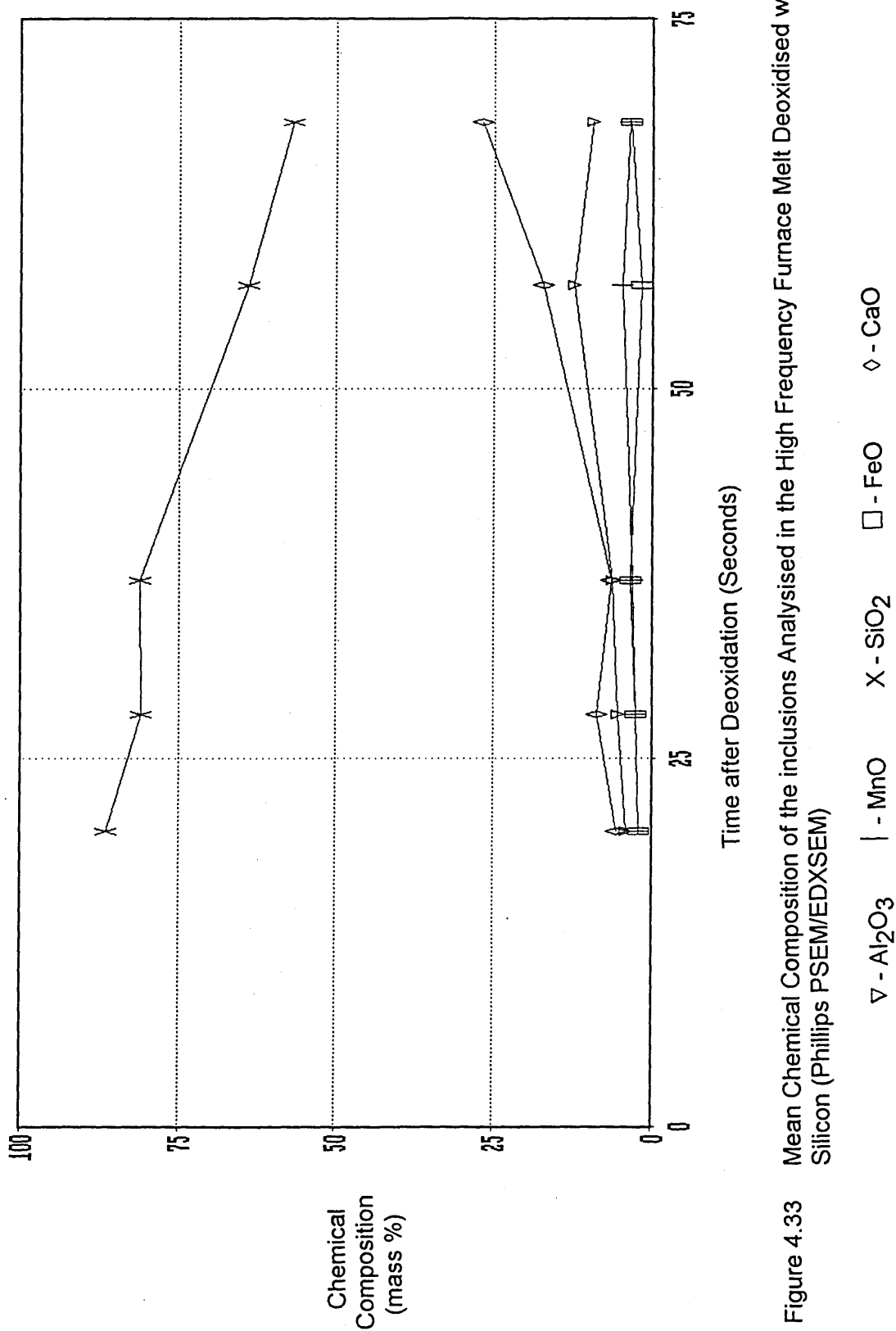


Figure 4.33 Mean Chemical Composition of the inclusions Analysed in the High Frequency Furnace Melt Deoxidised with 0.3 mass% Silicon (Phillips PSEM/EDXSEM)

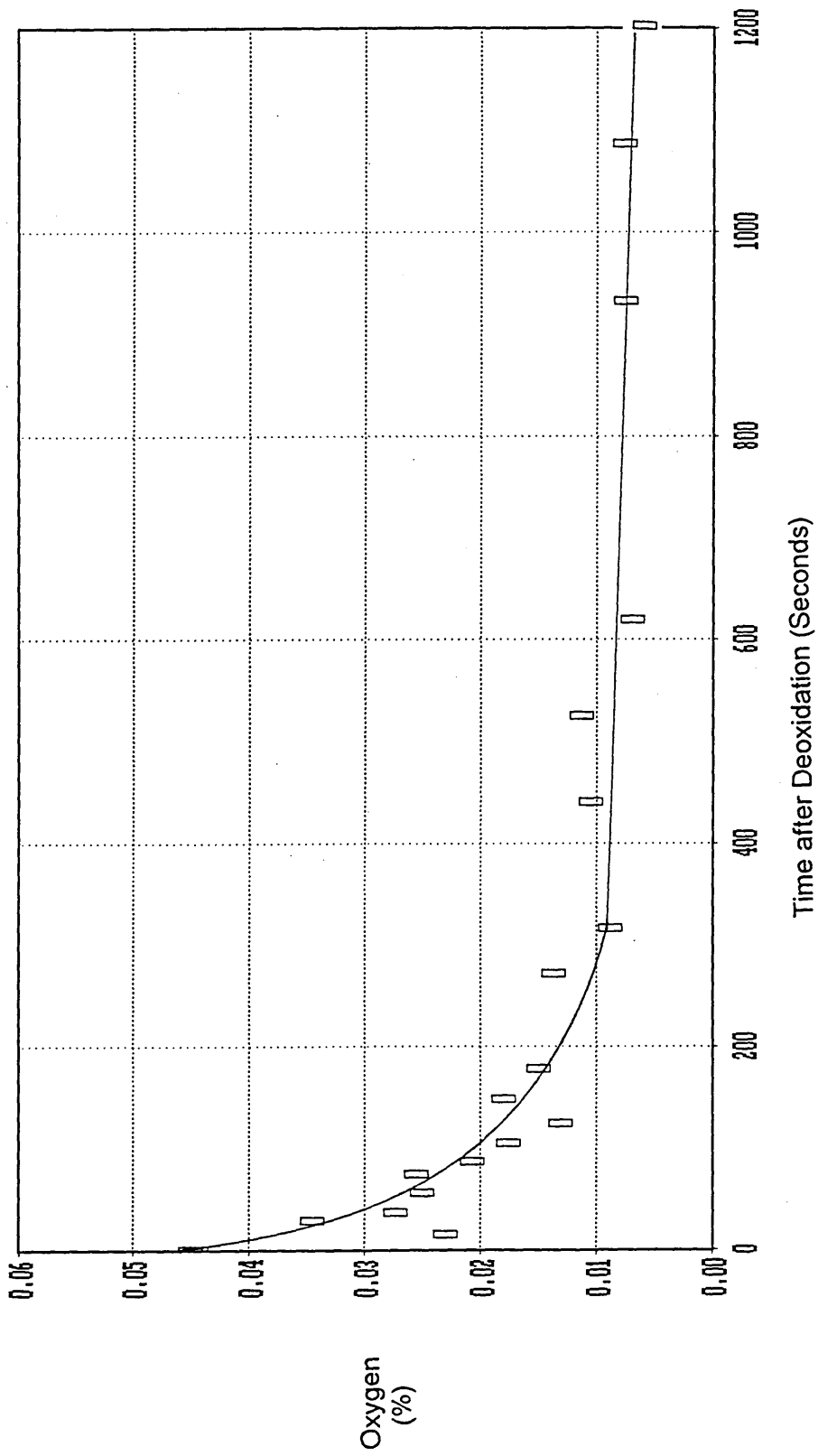


Figure 4.34(a) Total Oxygen Analysis Versus Time after Deoxidation with 0.32 mass% Calcium-Aluminum Addition in the Vertical Tube Furnace Melt (LECO).

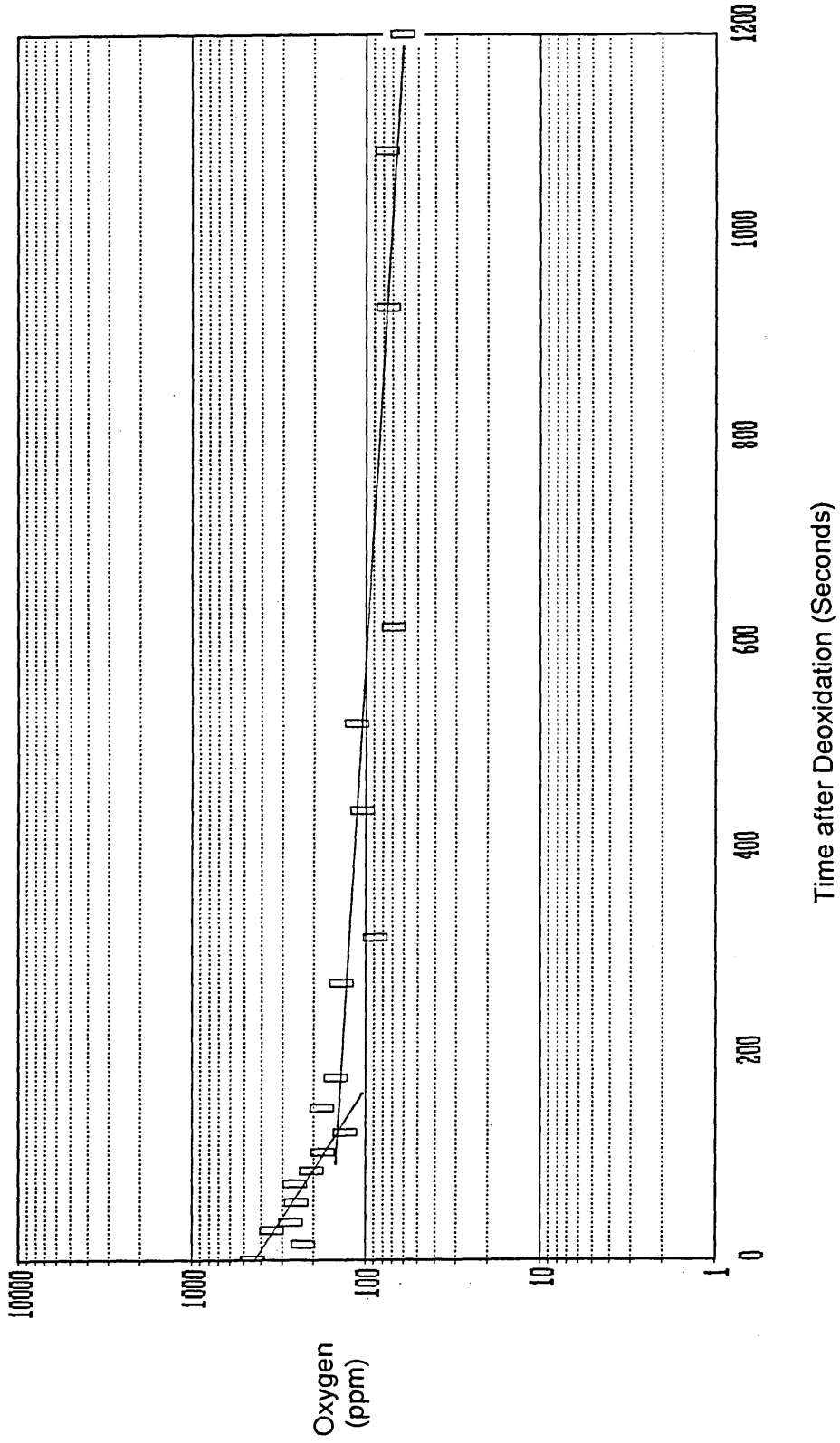


Figure 4.34(b) Total Oxygen Analysis Versus Time after Deoxidation with 0.32 mass% Calcium-Aluminium Addition in the Vertical Tube Furnace Melt (LECO).

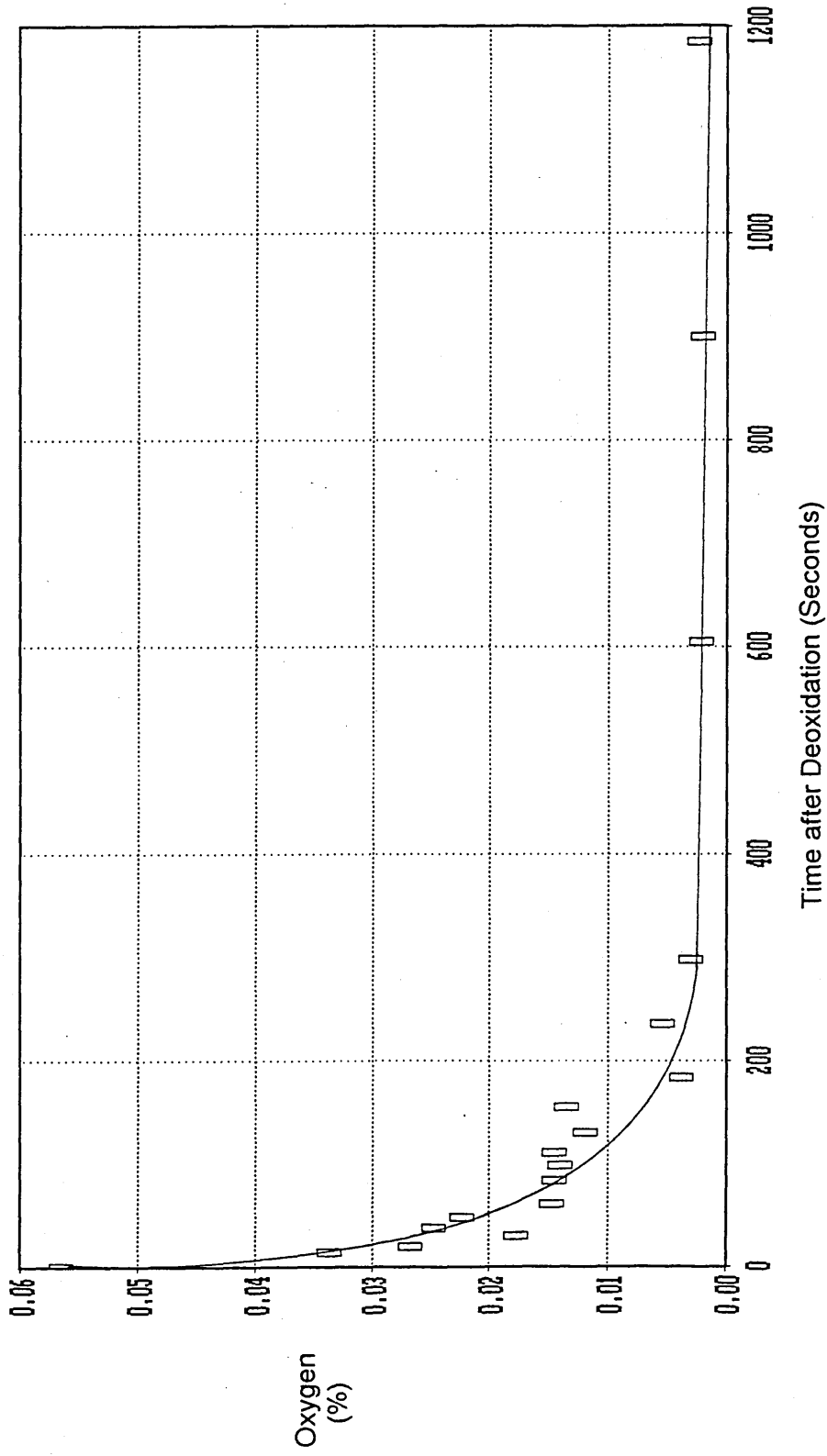


Figure 4.35(a) Total Oxygen Analysis Versus Time after Deoxidation with 0.32 mass% Calcium-Aluminium Addition in the High Frequency Furnace Melt (LECO).

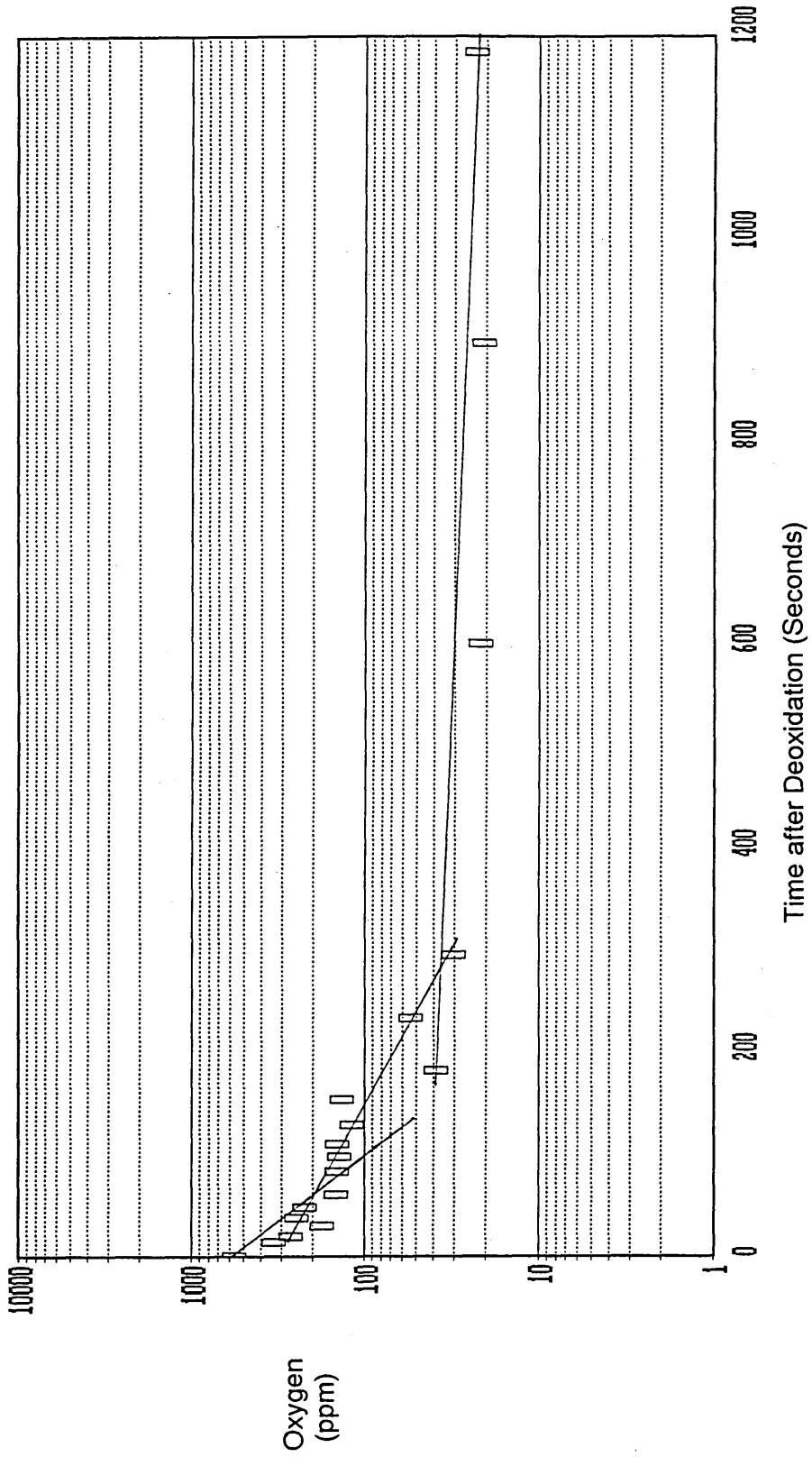


Figure 4.35(b) Total Oxygen Analysis Versus Time after Deoxidation with 0.32 mass% Calcium-Aluminium Addition in the High Frequency Furnace Melt (LECO).

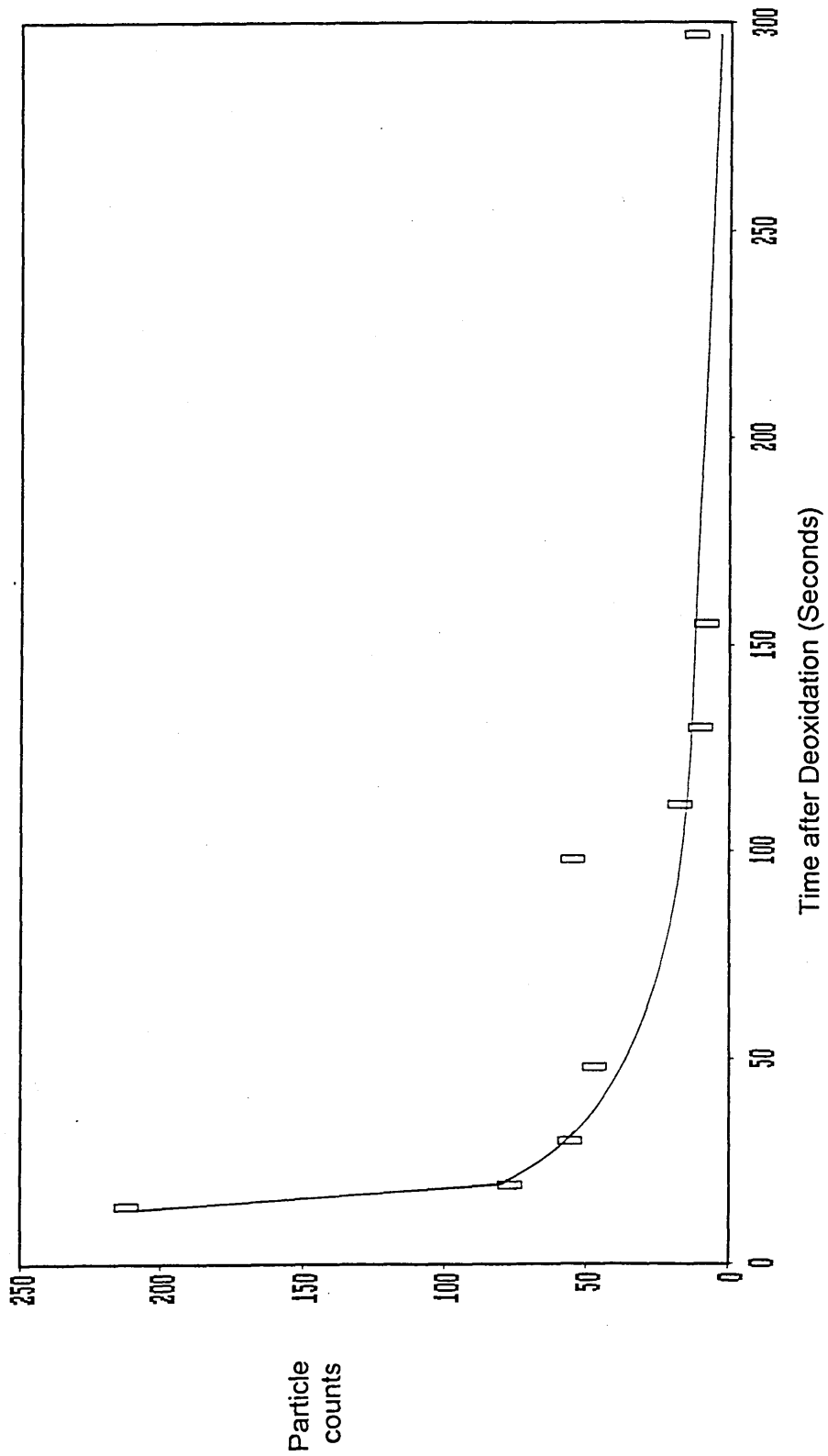


Figure 4.36 Number of Calcium-Aluminium Inclusions Counted Versus Time after Deoxidation in the High Frequency Furnace Melt (JEOL 840 SEM/Digiscan).

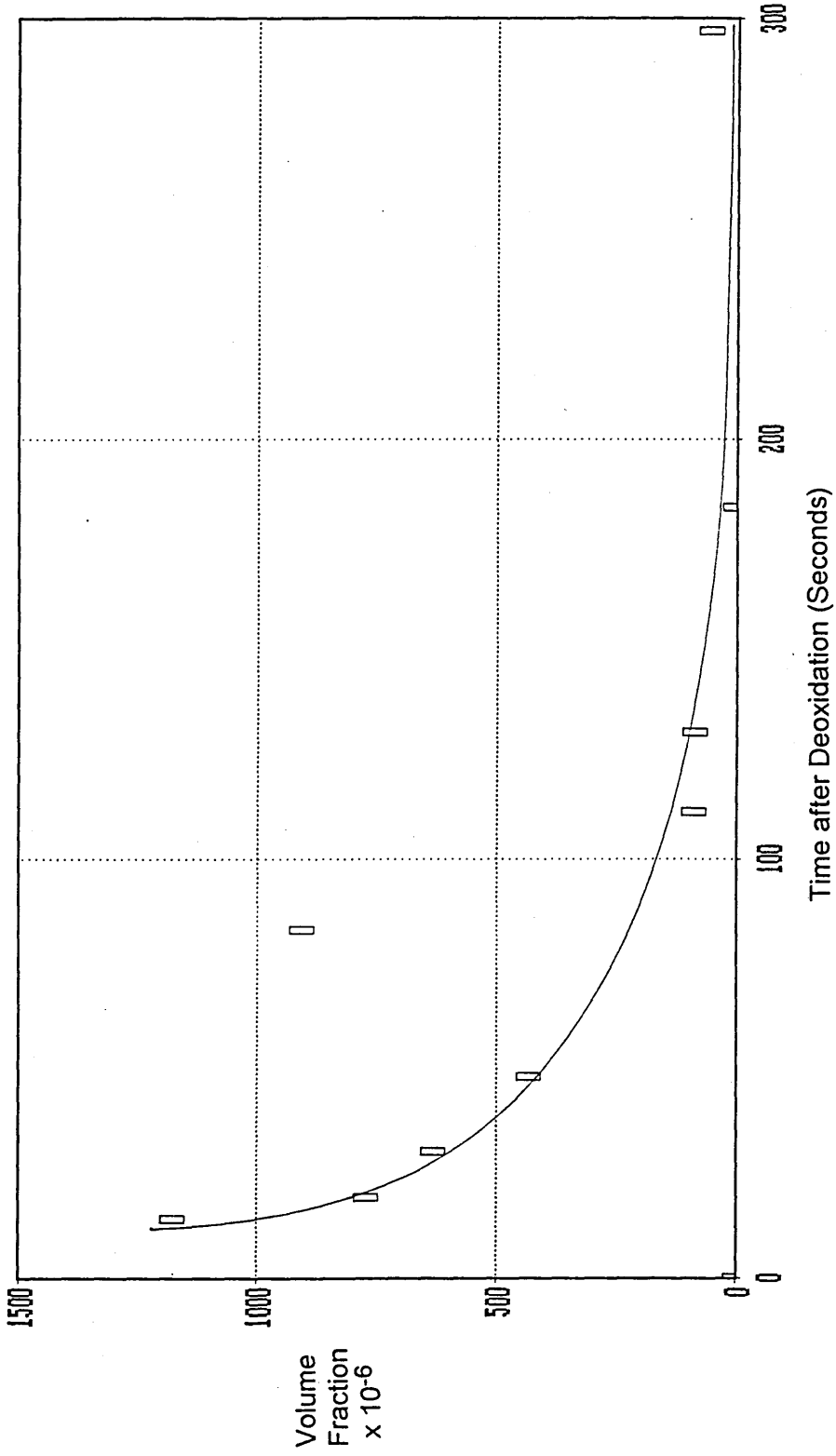


Figure 4.37 Volume Fraction of Calcium-Aluminium Inclusions Versus Time after Deoxidation in the High Frequency Furnace Melt (JEOL 840 SEM/Digiscan) .

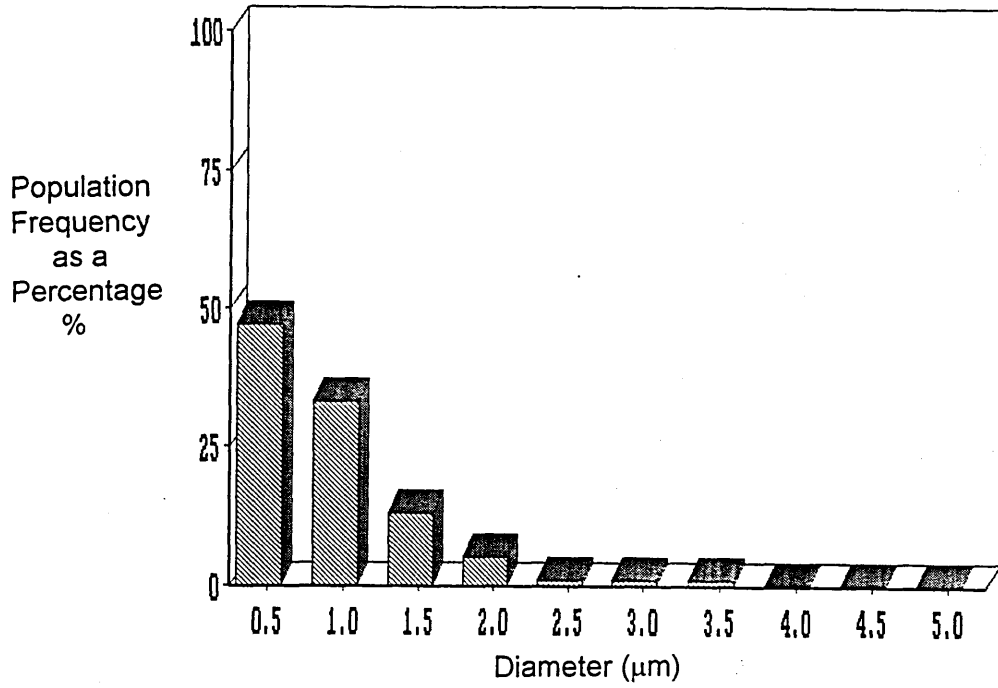


Figure 4.38 (a) Size Distribution of Calcium-Aluminium Inclusions in the Sample taken 14 Seconds after Deoxidation in the High Frequency Furnace Melt (Jeol 840 SEM/Digiscan).

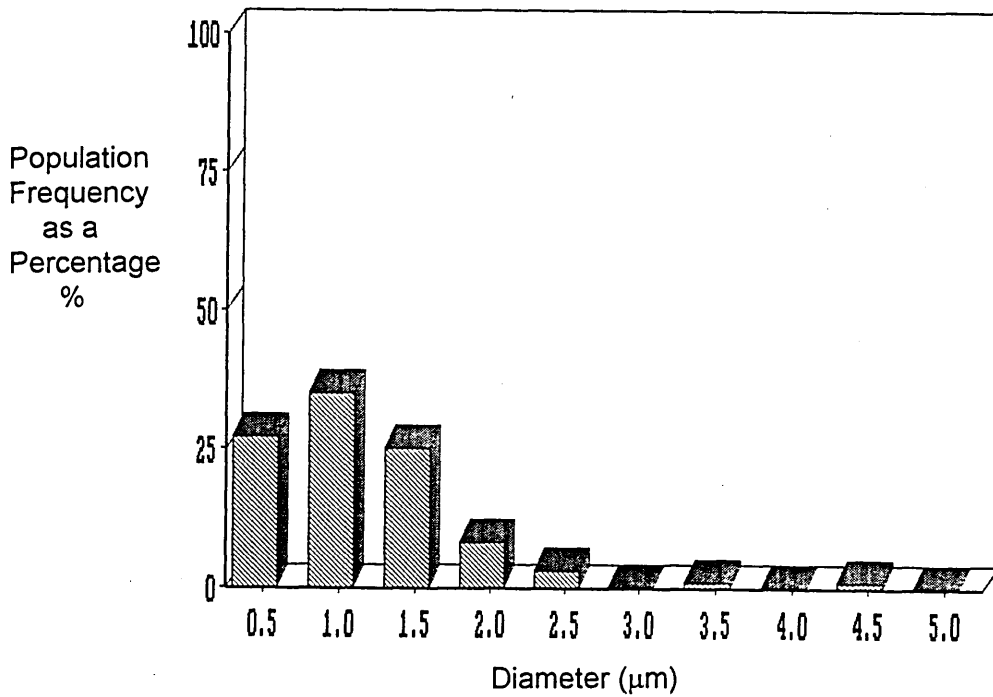


Figure 4.38 (b) Size Distribution of Calcium-Aluminium Inclusions in the Sample taken 19 Seconds after Deoxidation in the High Frequency Furnace Melt (Jeol 840 SEM/Digiscan).

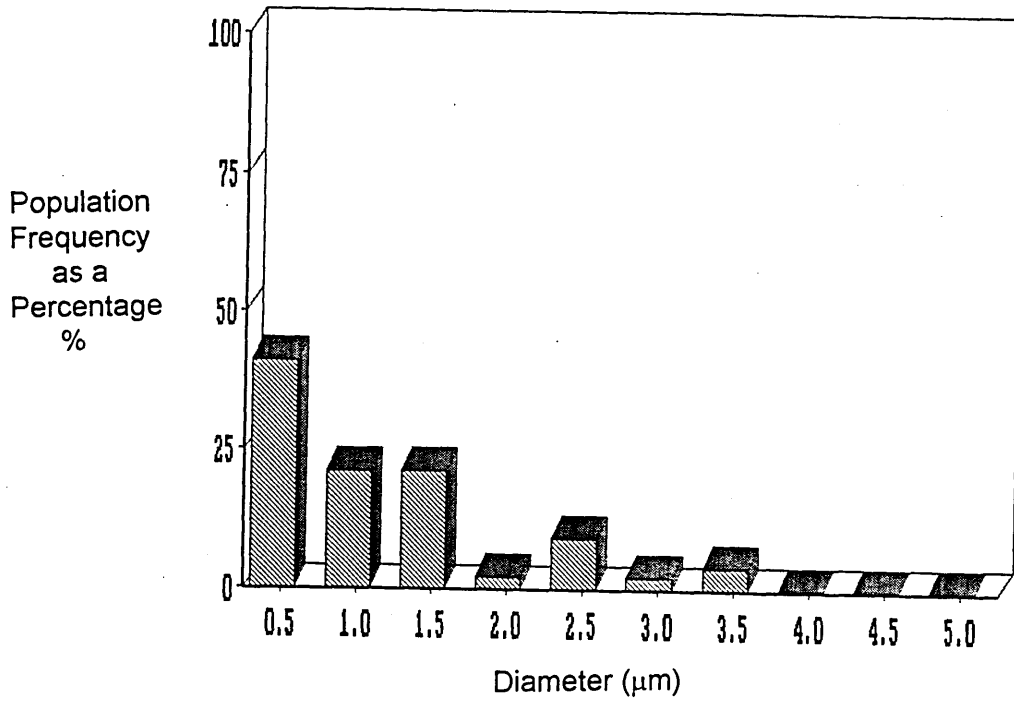


Figure 4.38 (c) Size Distribution of Calcium-Aluminium Inclusions in the Sample taken 30 Seconds after Deoxidation in the High Frequency Furnace Melt (Jeol 840 SEM/Digiscan).

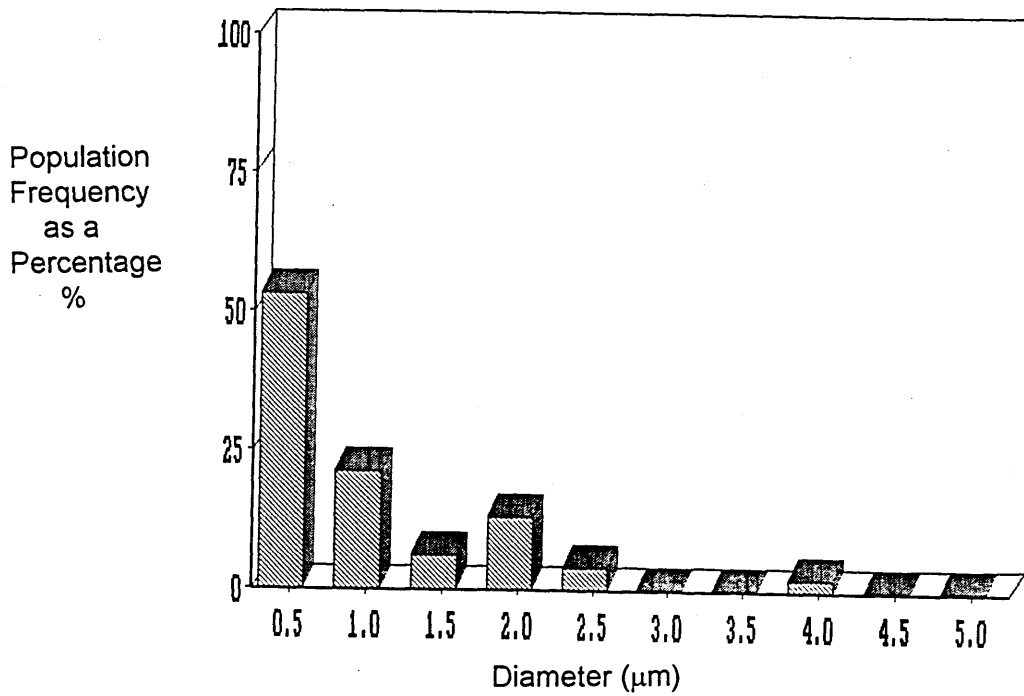


Figure 4.38 (d) Size Distribution of Calcium-Aluminium Inclusions in the Sample taken 48 Seconds after Deoxidation in the High Frequency Furnace Melt (Jeol 840 SEM/Digiscan).

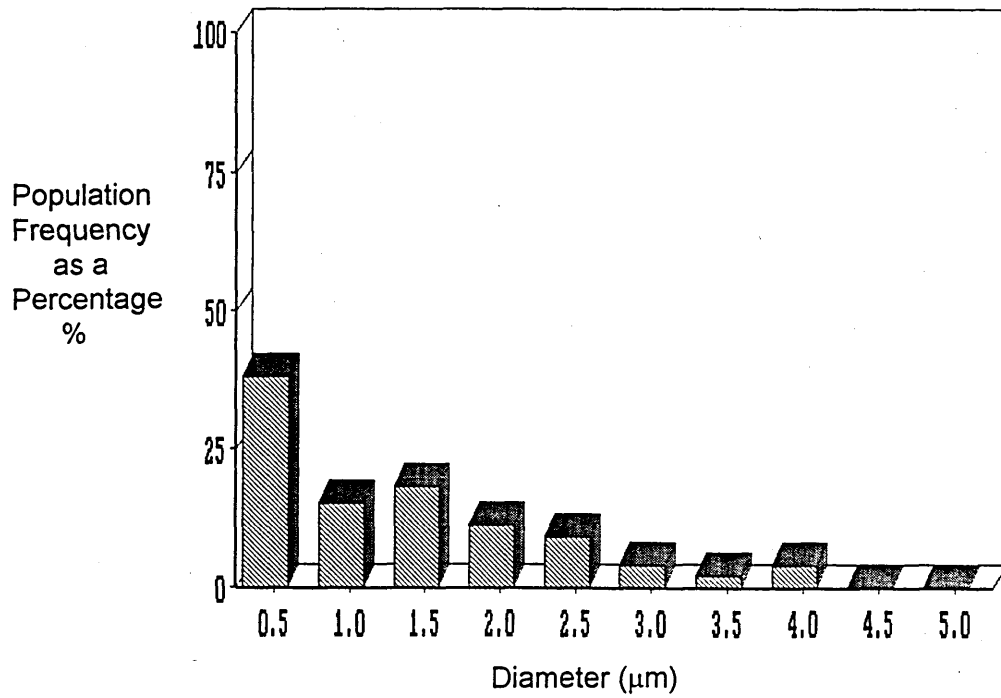


Figure 4.38 (e) Size Distribution of Calcium-Aluminium Inclusions in the Sample taken 83 Seconds after Deoxidation in the High Frequency Furnace Melt (Jeol 840 SEM/Digiscan).

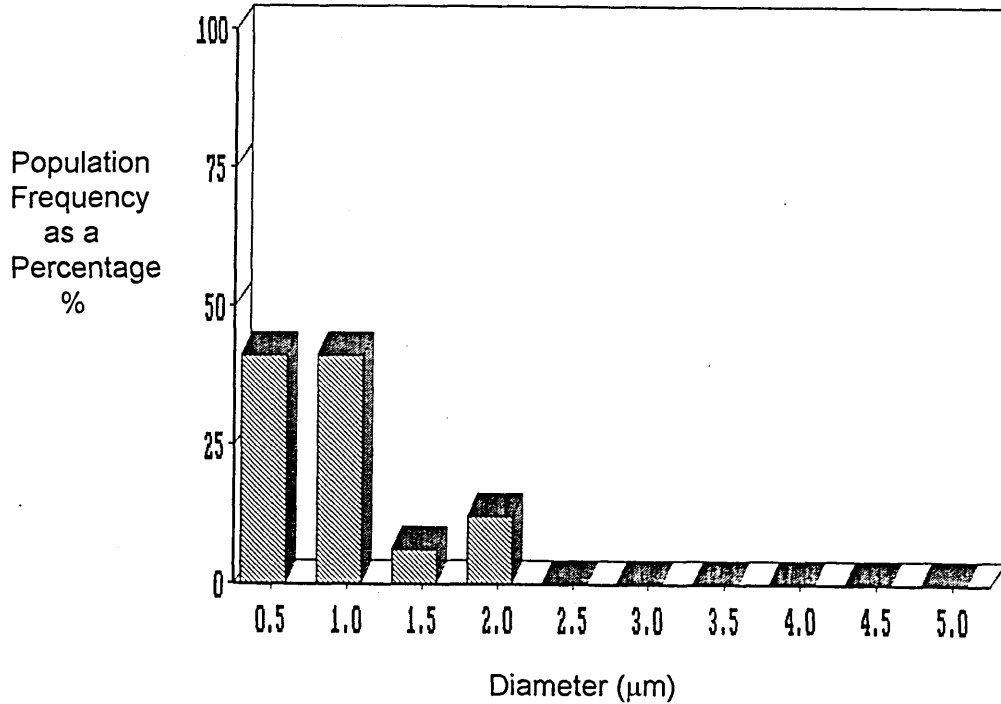


Figure 4.38 (f) Size Distribution of Calcium-Aluminium Inclusions in the Sample taken 111 Seconds after Deoxidation in the High Frequency Furnace Melt (Jeol 840 SEM/Digiscan).

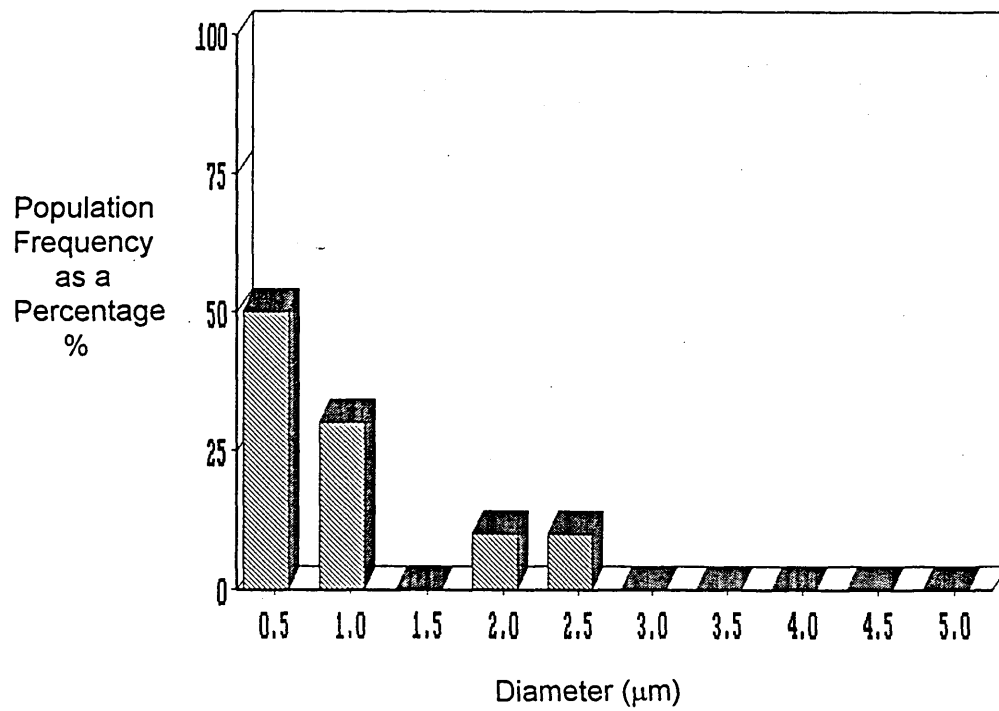


Figure 4.38 (g) Size Distribution of Calcium-Aluminium Inclusions in the Sample taken 130 Seconds after Deoxidation in the High Frequency Furnace Melt (Jeol 840 SEM/Digiscan).

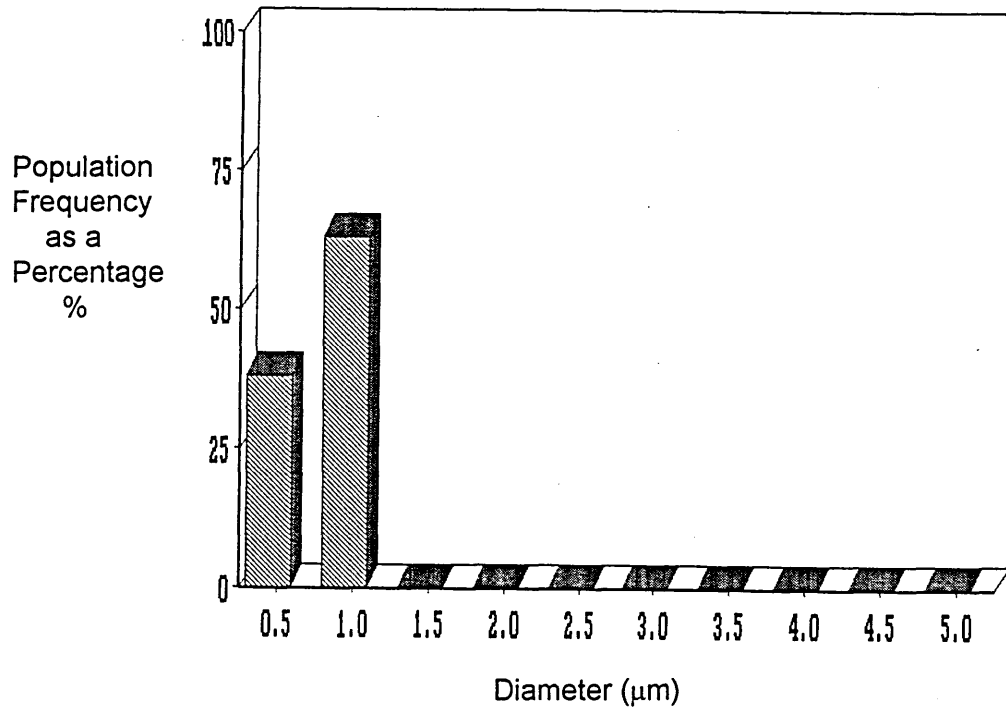


Figure 4.38 (h) Size Distribution of Calcium-Aluminium Inclusions in the Sample taken 184 Seconds after Deoxidation in the High Frequency Furnace Melt (Jeol 840 SEM/Digiscan).

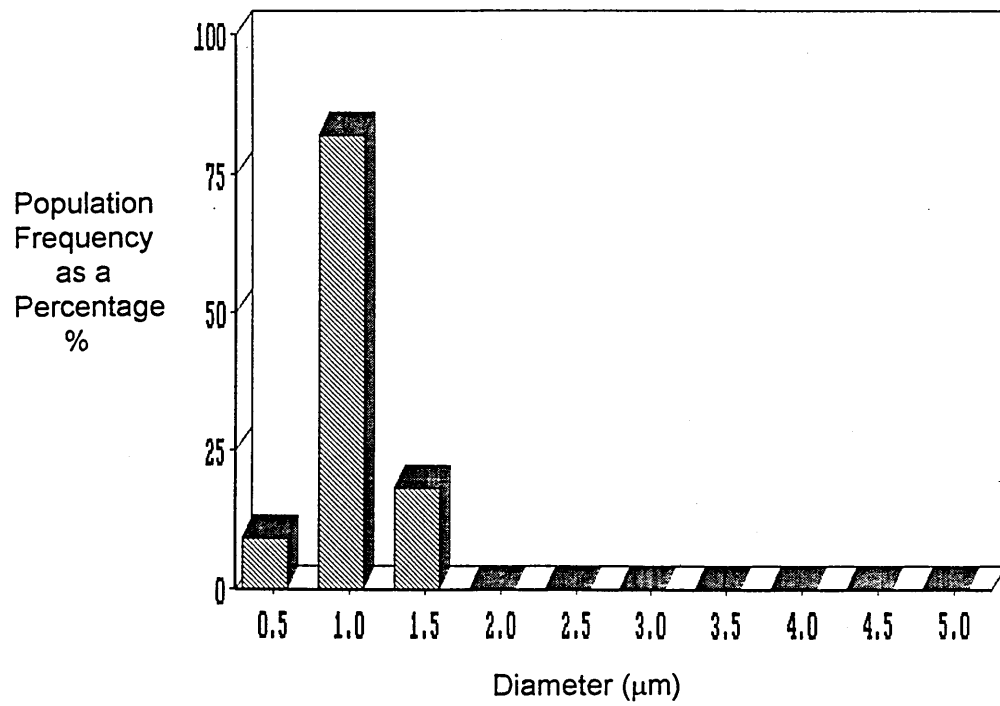


Figure 4.38 (i) Size Distribution of Calcium-Aluminium Inclusions in the Sample taken 297 Seconds after Deoxidation in the High Frequency Furnace Melt (Jeol 840 SEM/Digiscan).

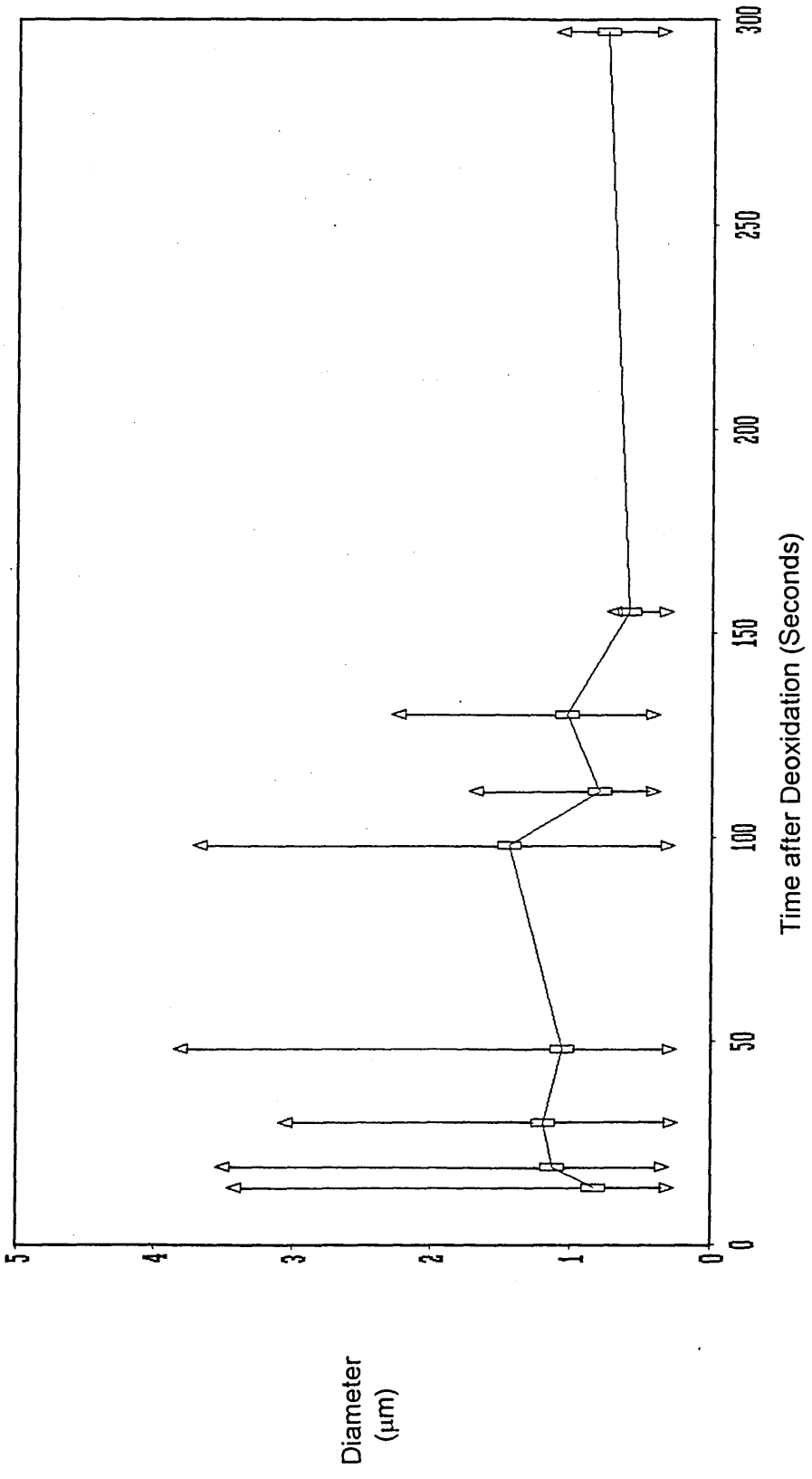


Figure 4.39 Mean Calcium-Aluminum Inclusions Diameter Versus Time after Deoxidation in the High Frequency Furnace Melt (JEOL 840 SEM/Digiscan).

△ - Mean from Maximum Size Band ▽ - Mean from Minimum Size Band □ - Mean Diameter

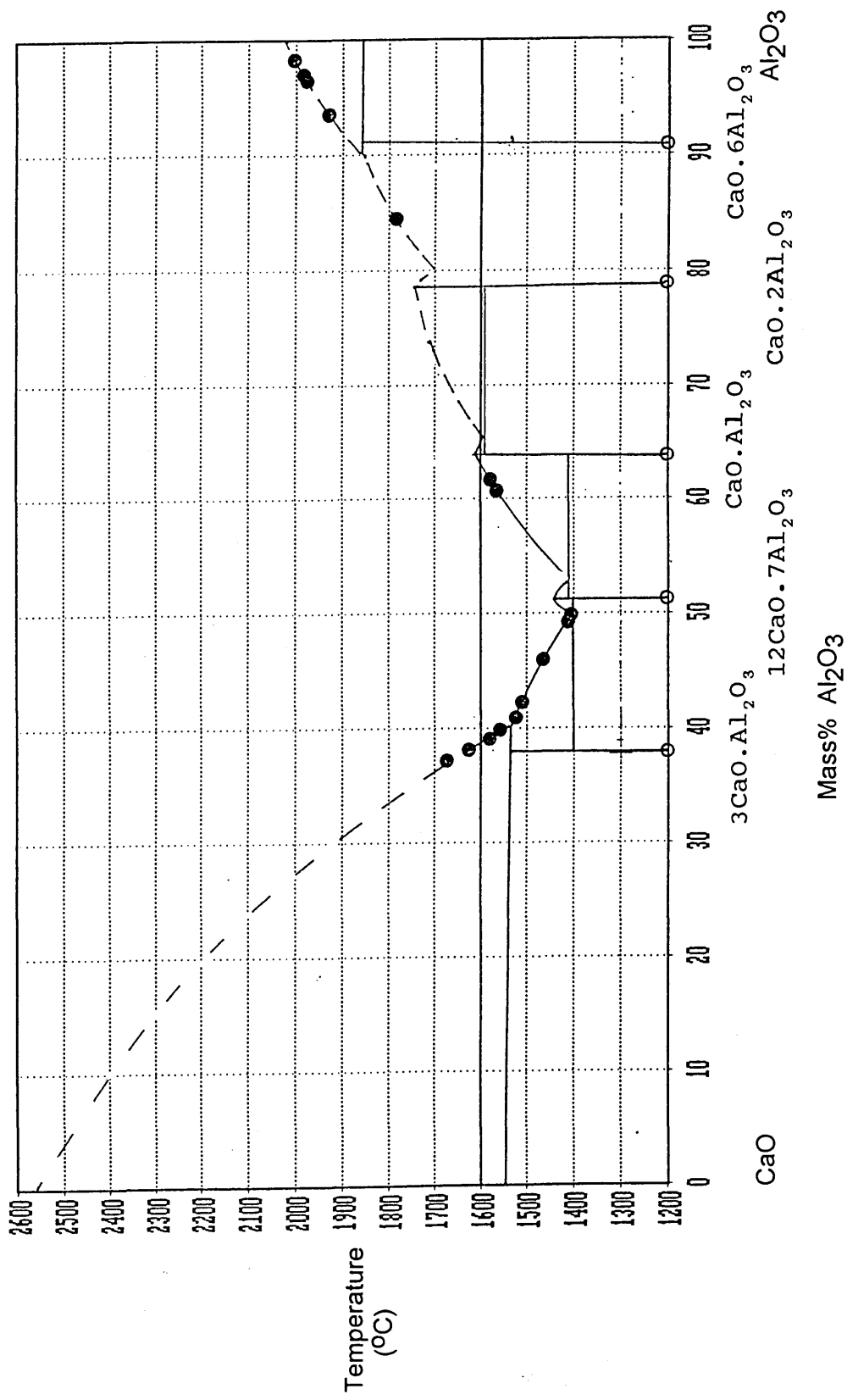


Figure 4.40 Phase Diagram for the System CaO-Al₂O₃, the Composition of the Inclusions in the Samples taken from the Melt Deoxidised with 0.32 mass% Calcium-Aluminium are plotted on the Liquidus Line (Phillips PSEM/EDX).

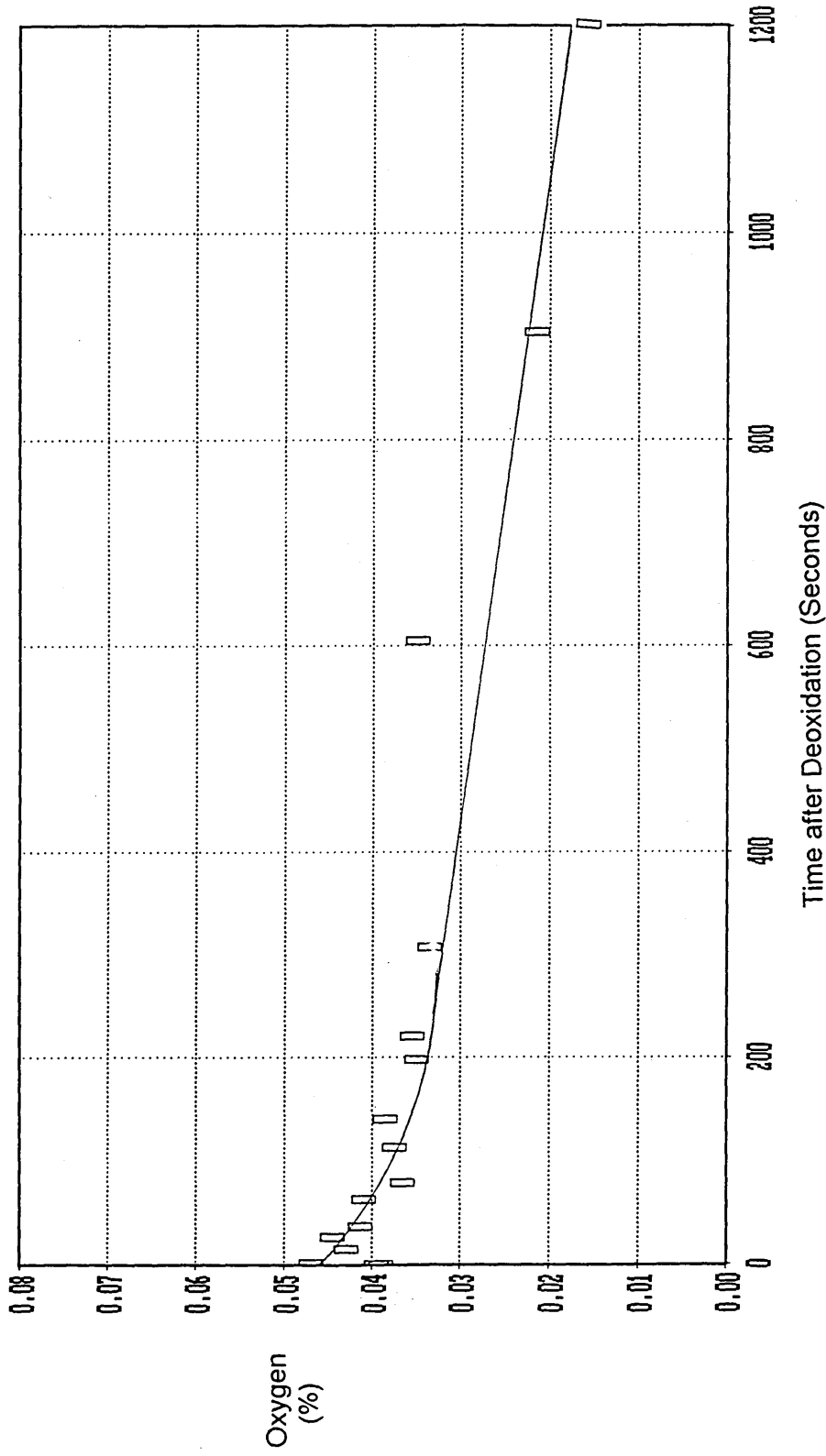


Figure 4.41(a) Total Oxygen Analysis Versus Time after Deoxidation with 1.01 mass% Zirconium Addition in the Vertical Tube Furnace Melt (LECO).

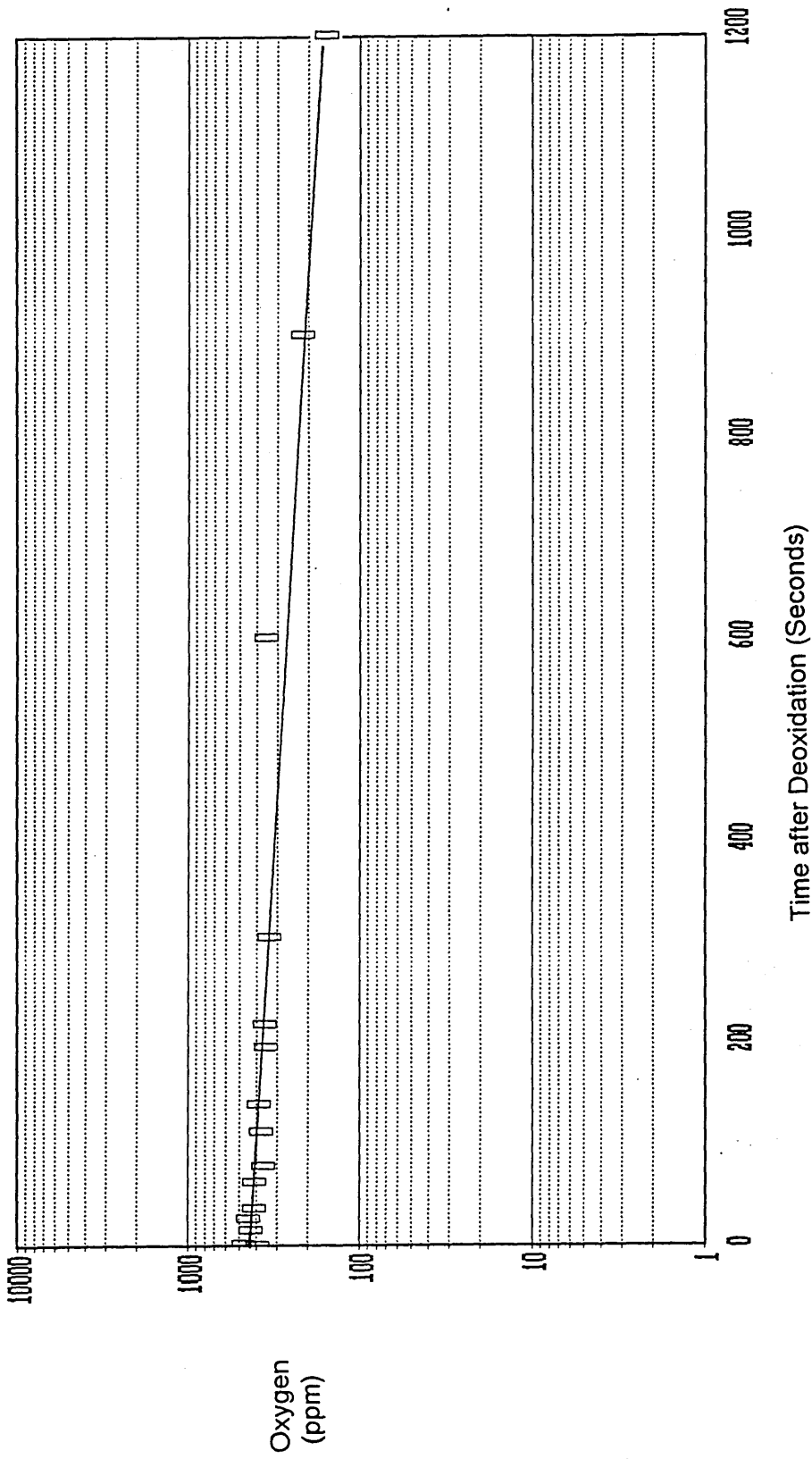


Figure 4.41(b) Total Oxygen Analysis Versus Time after Deoxidation with 1.01 mass% Zirconium Addition in the Vertical Tube Furnace Melt (LECO).

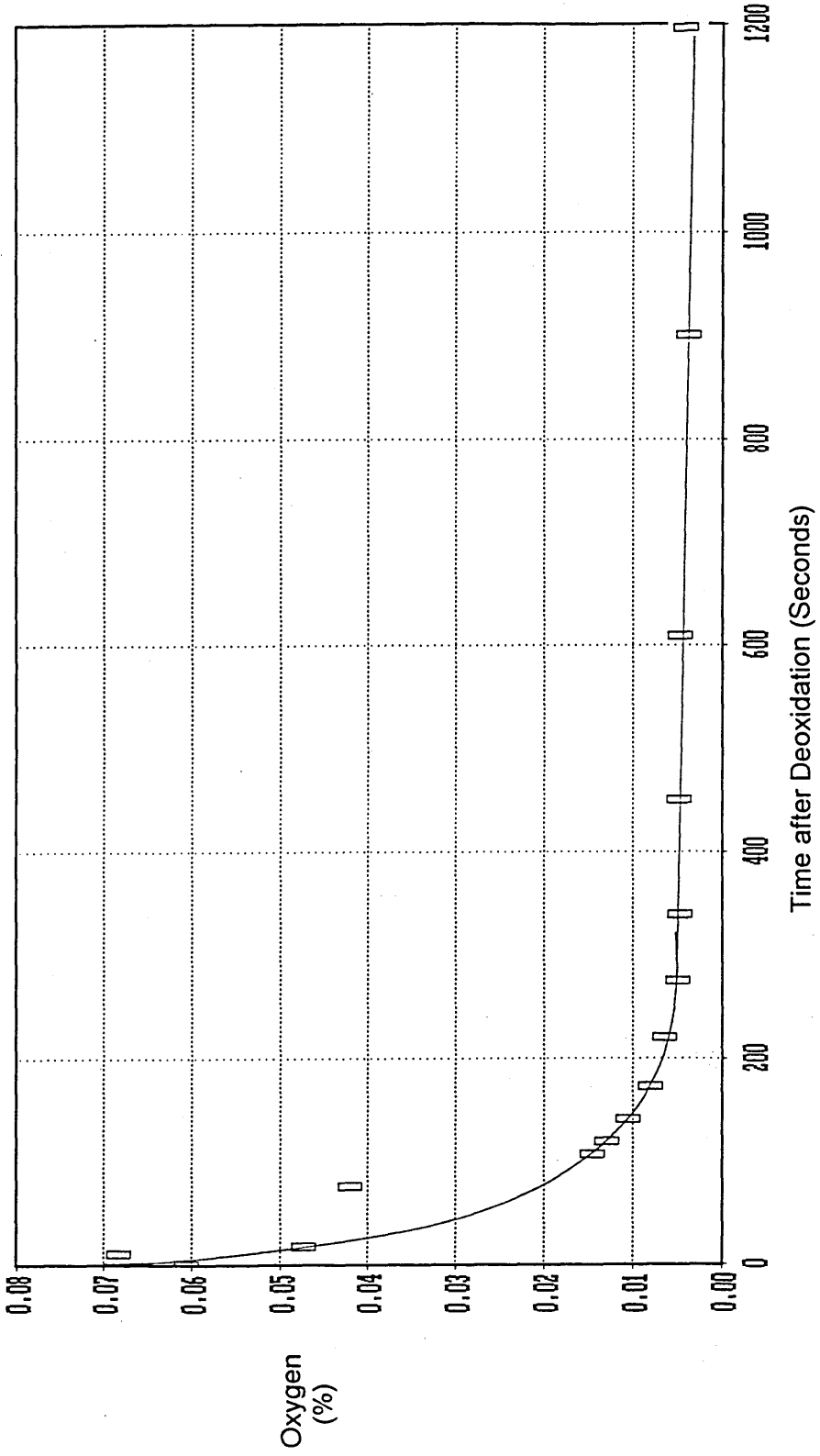


Figure 4.42(a) Total Oxygen Analysis Versus Time after Deoxidation with 1.01 mass% Zirconium Addition in the High Frequency Furnace Melt (LECO).

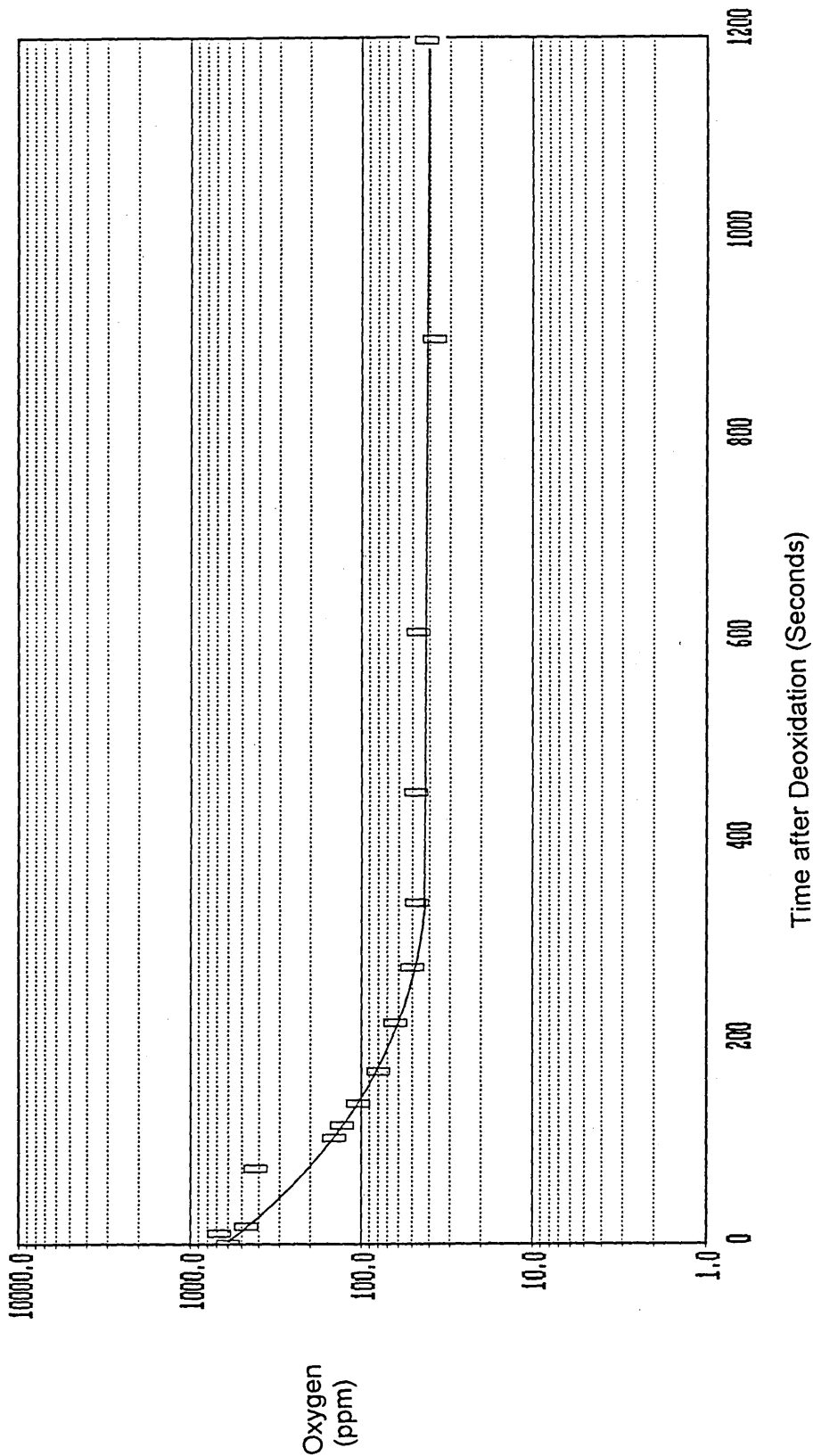


Figure 4.42(b) Total Oxygen Analysis Versus Time after Deoxidation with 0.32 mass% Zirconium Addition in the High Frequency Furnace Melt (LECO).

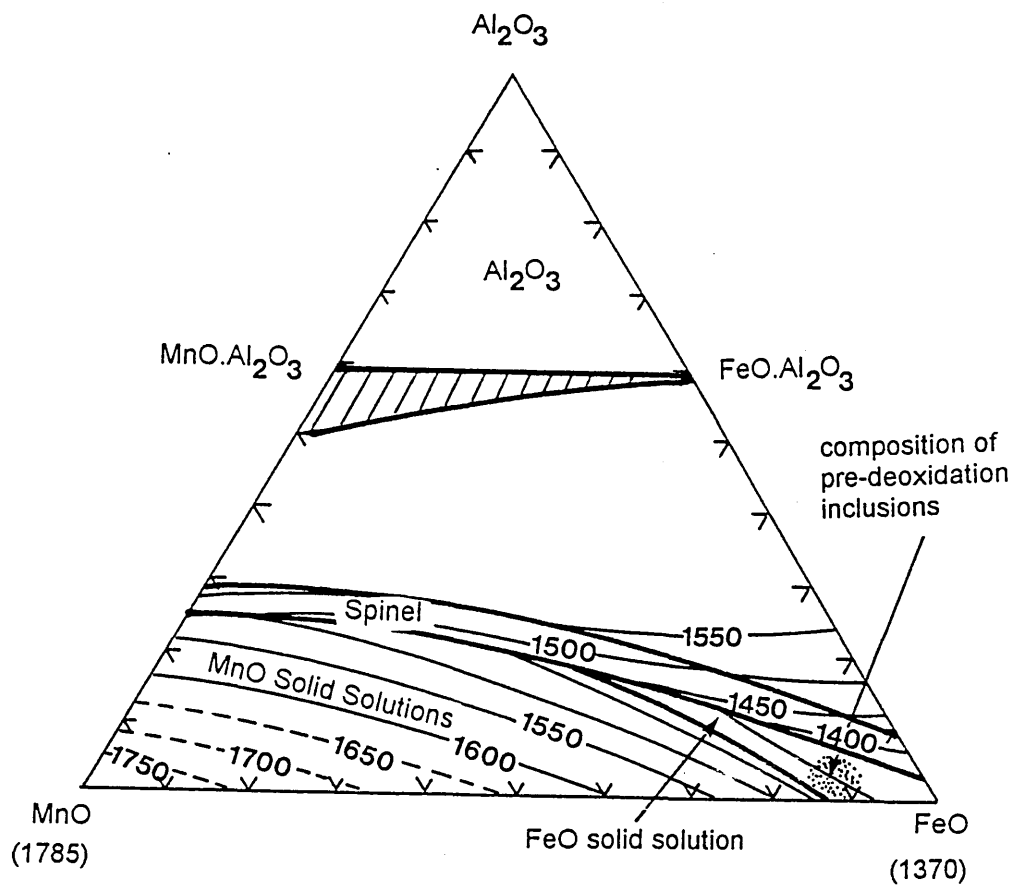


Figure 5.1 FeO-MnO-Al₂O₃ phase diagram showing the composition of the pre-deoxidation inclusions.

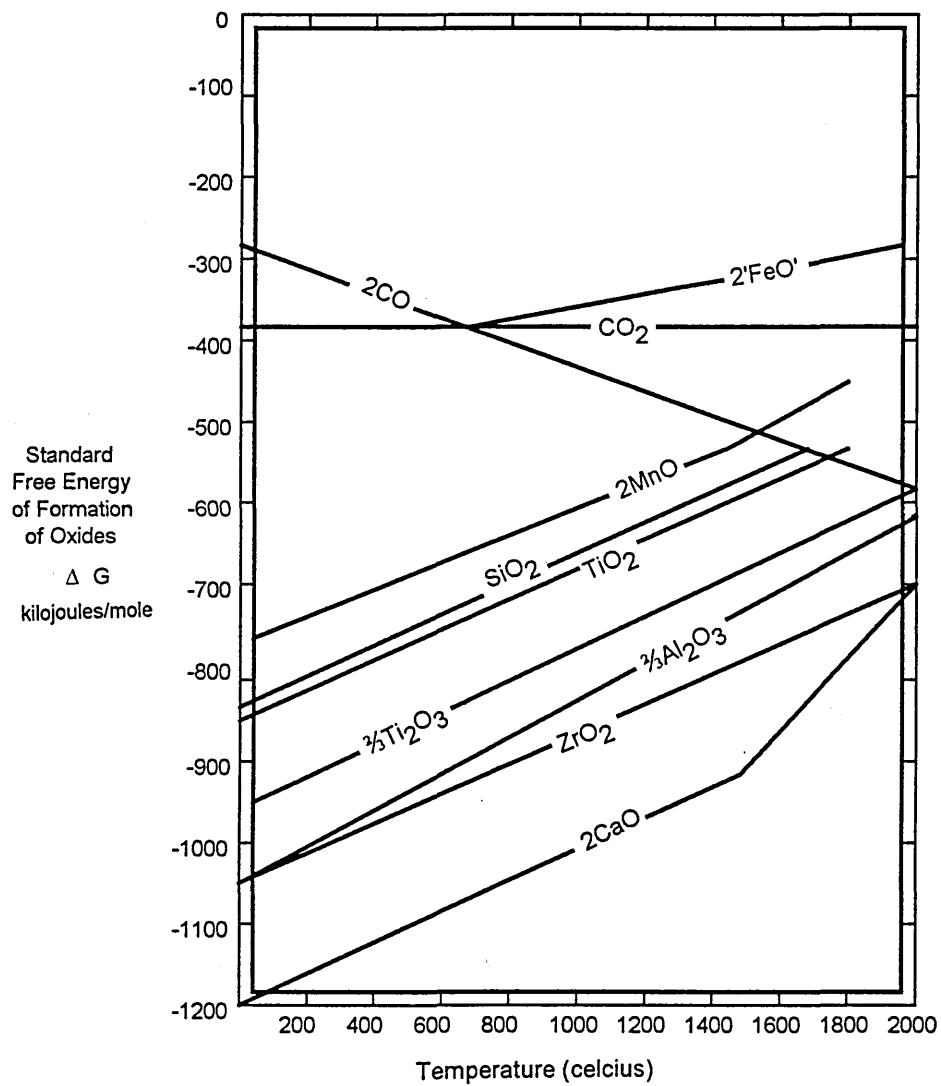


Figure 5.2 The standard free energies of formation of various oxides, at one atmosphere pressure.

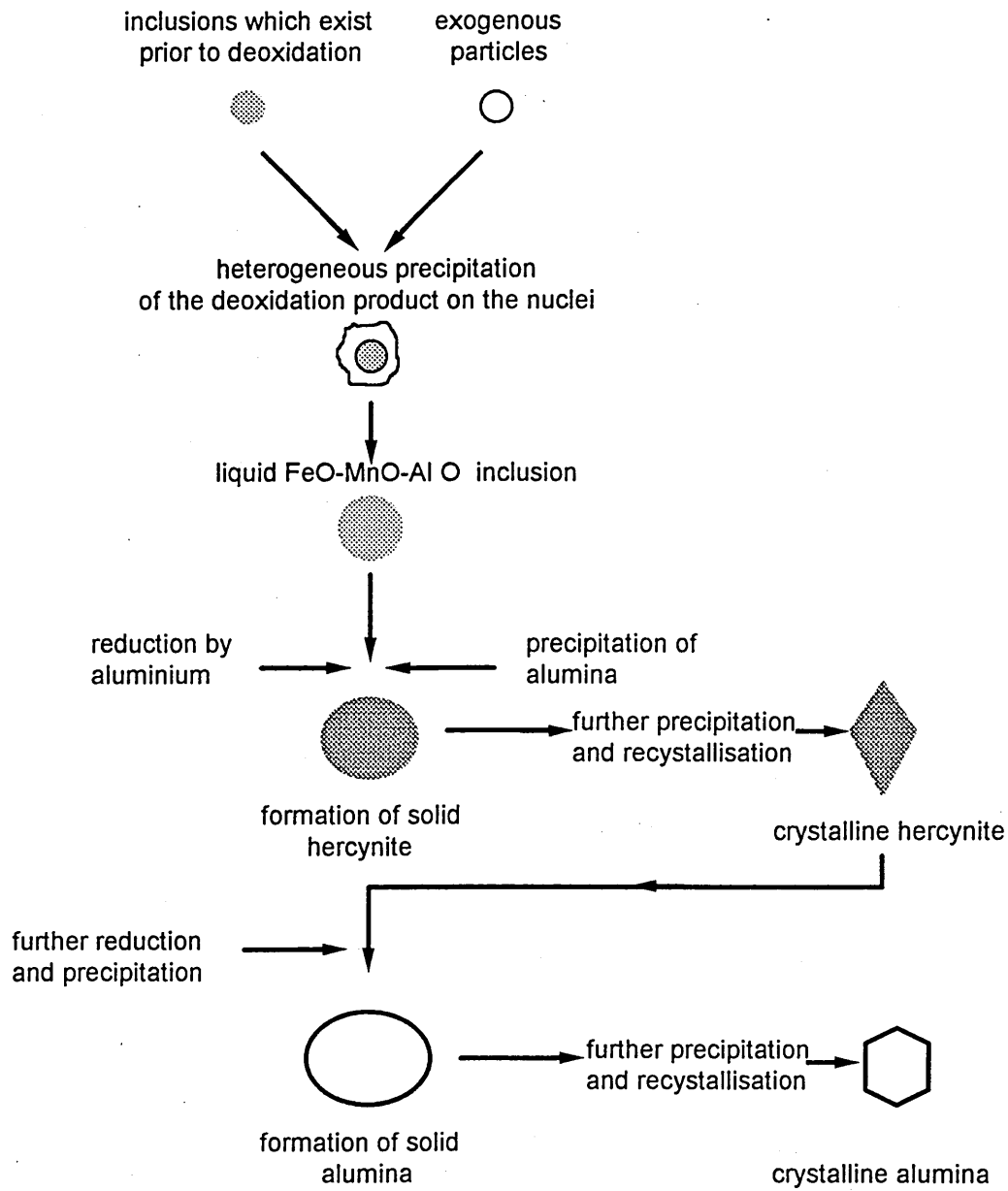


Figure 5.3 Formation of spherical alumina morphologies and polyhedra.

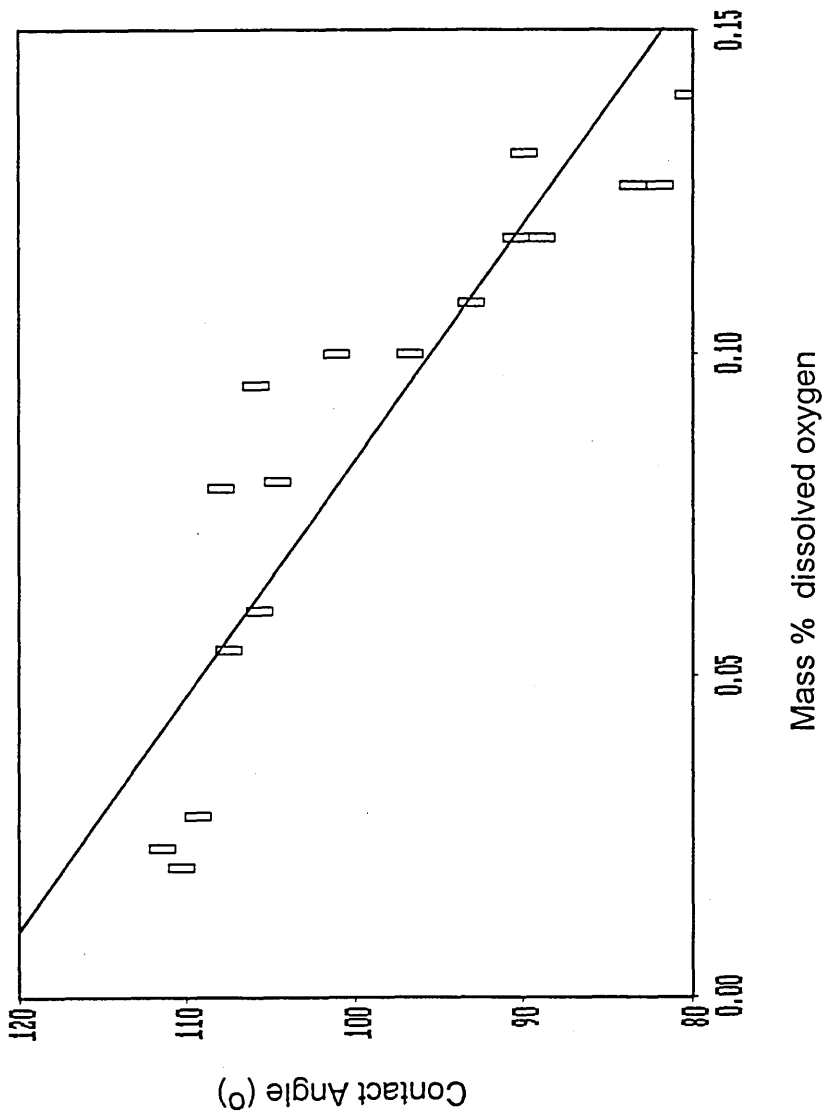


Figure 5.4 The measured values of the contact angles between Fe-O drops and an alumina substrate at $1600 \pm 10^\circ\text{C}$.

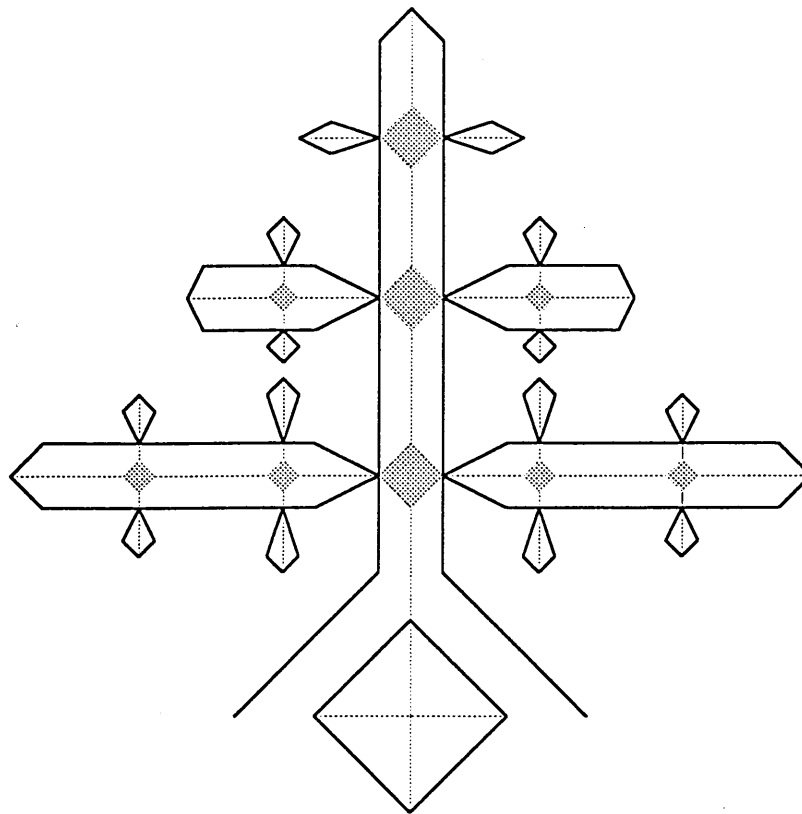


Figure 5.5 The morphology of dendrites, with secondary arms growing perpendicular to primary branches.

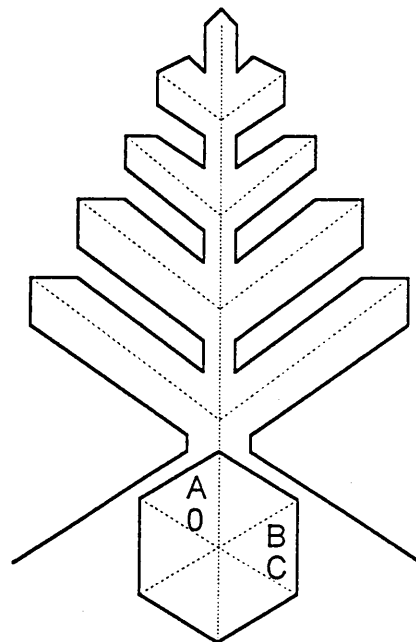


Figure 5.6 Morphology of dendrites growing from a hexagonal crystal.

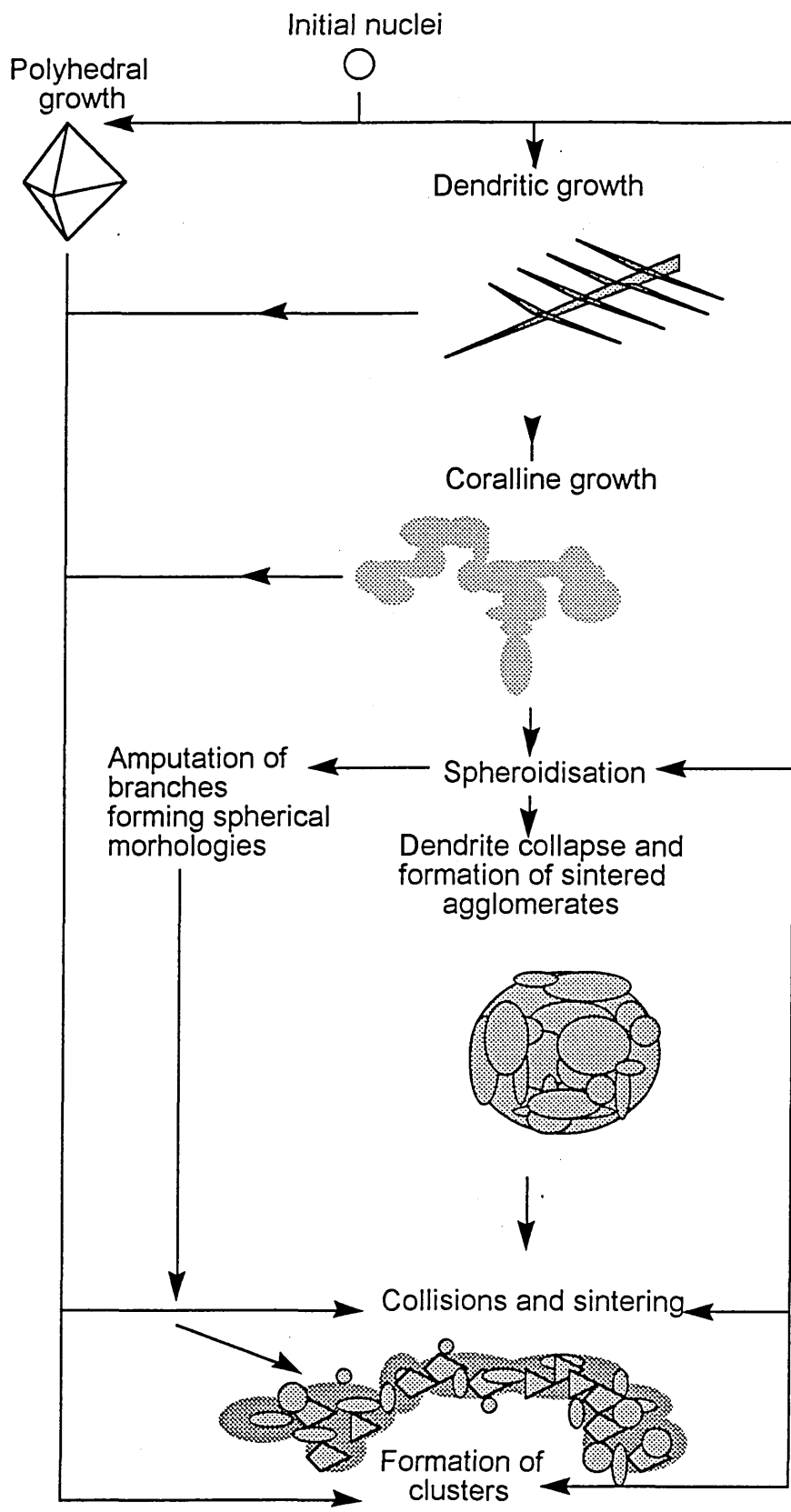


Figure 5.7 The formation of inclusion clusters during deoxidation with aluminium.

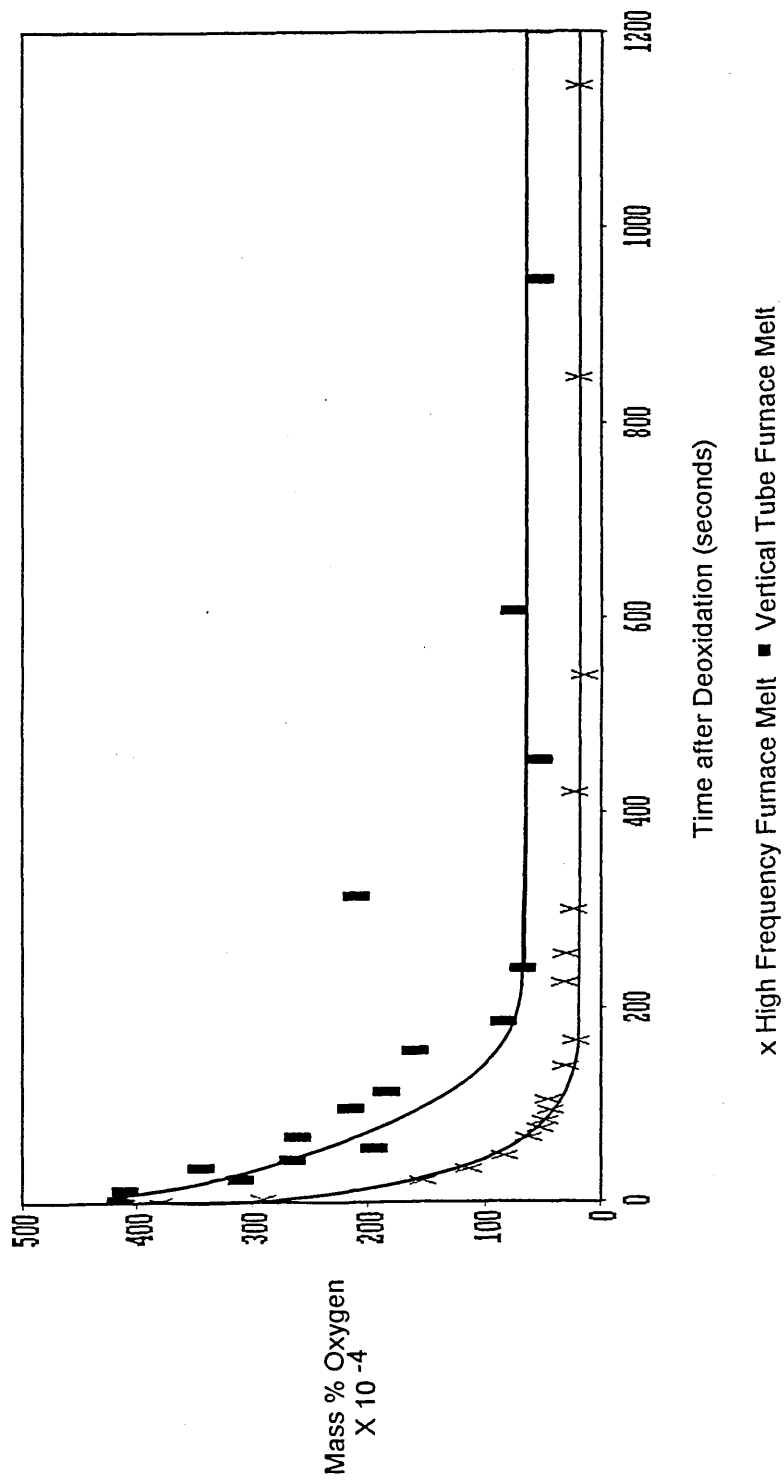
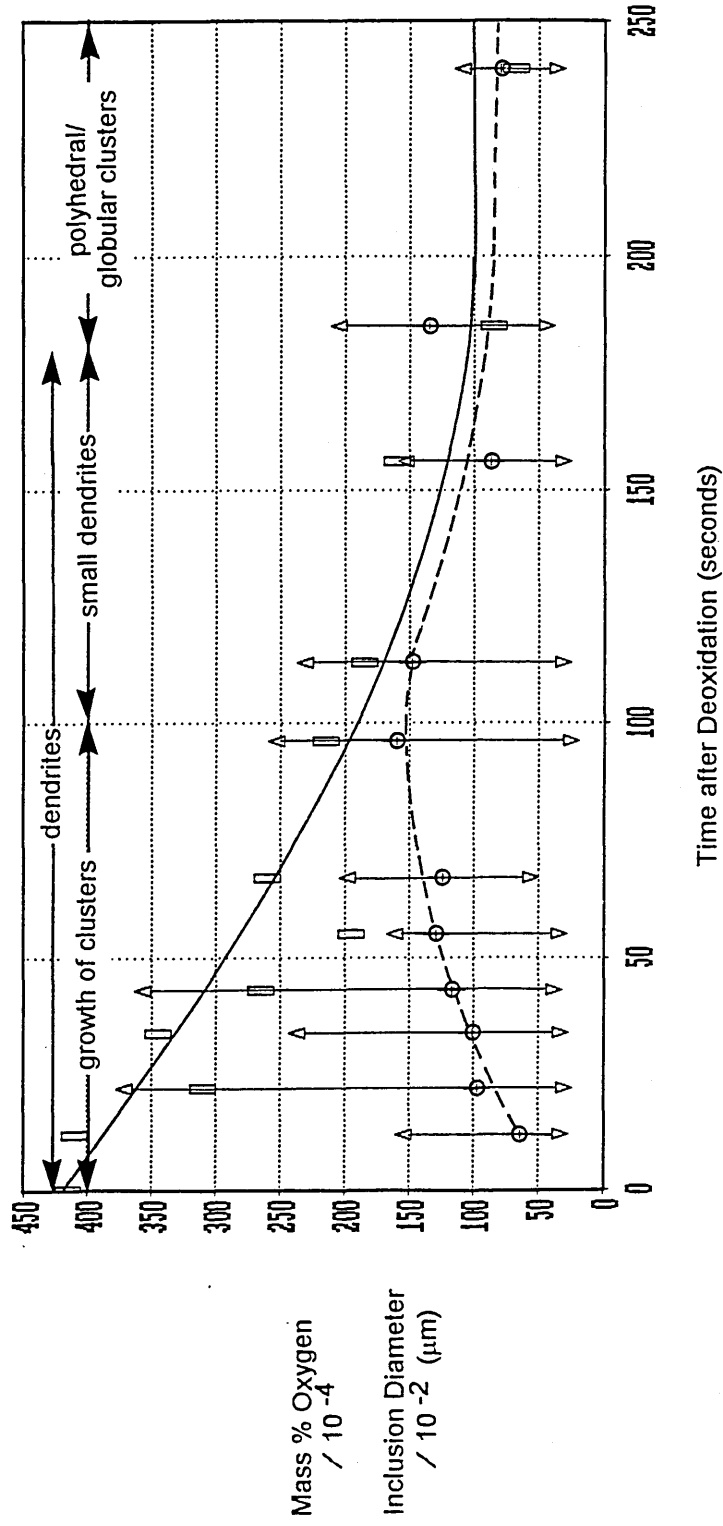
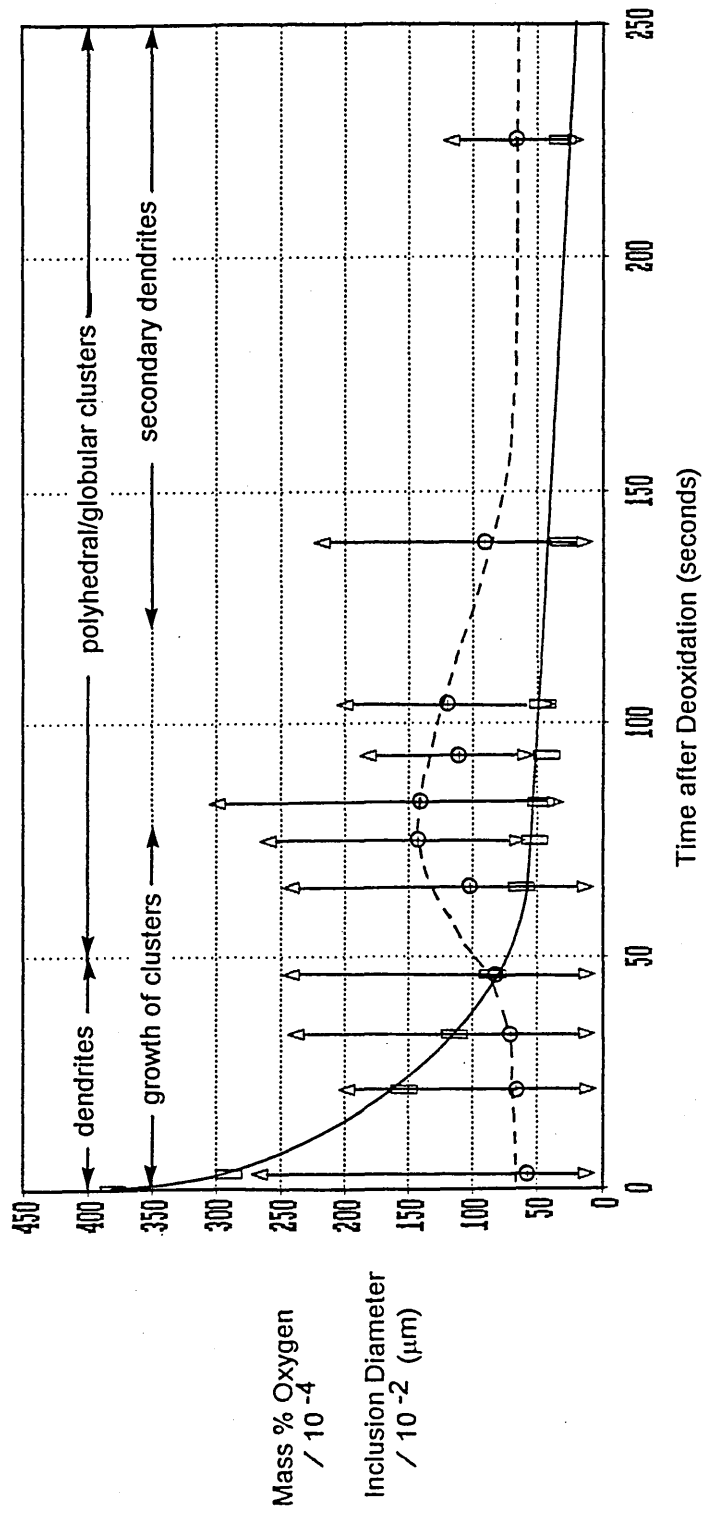


Figure 5.8 Removal of oxygen from the Aluminium deoxidised melts.



▽ mean from minimum size band ⊕ mean diameter △ mean from maximum size band □ oxygen

Figure 5.9 Removal of oxygen and change in the average diameter of the inclusions in the Aluminium deoxidised Vertical Tube Furnace Melt.



▽ mean from minimum size band ⊕ — mean diameter Δ mean from maximum size band □ — oxygen

Figure 5.10 Removal of oxygen and change in the average diameter of the inclusions in the Aluminium deoxidised High Frequency Furnace Melt.

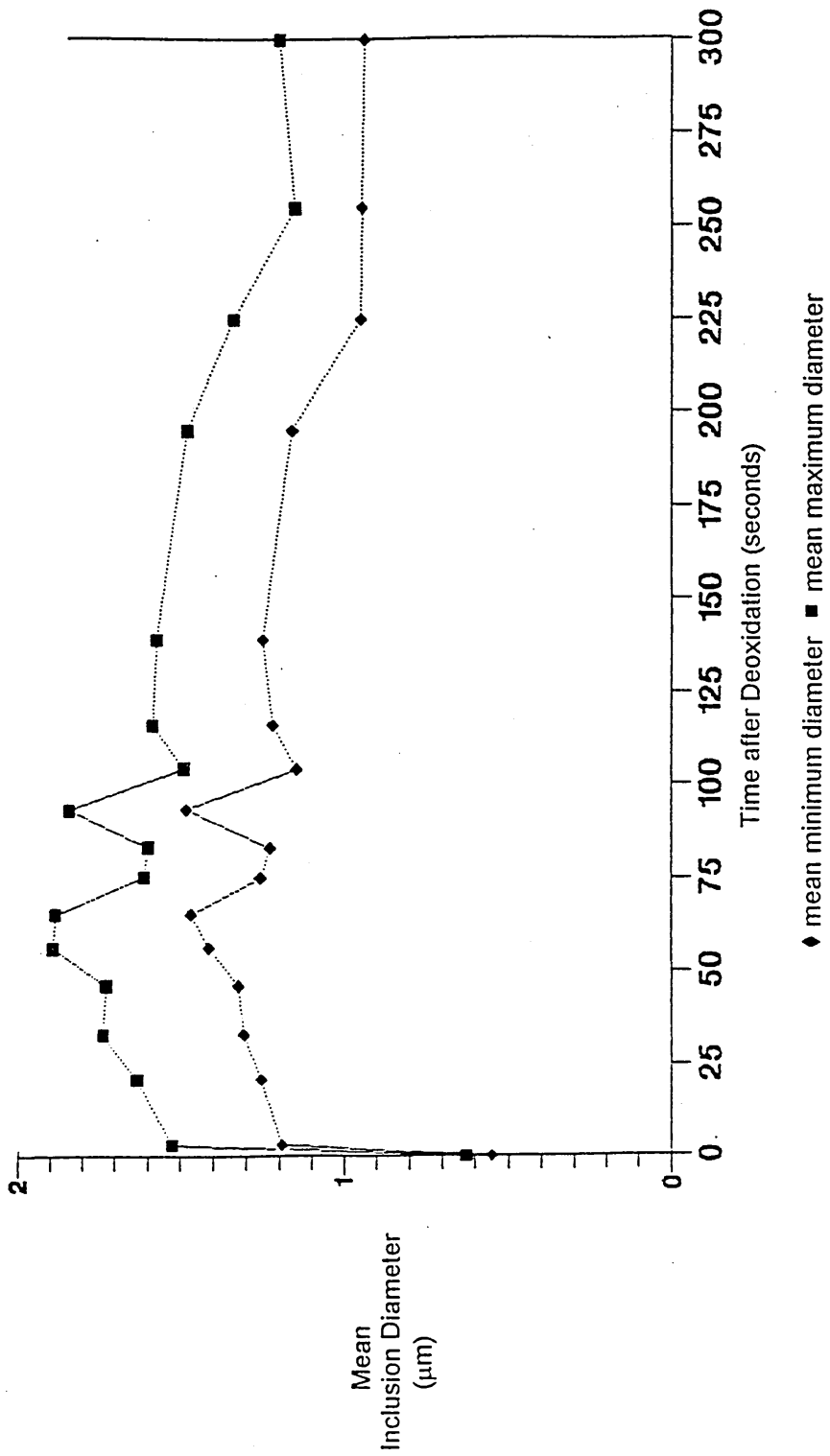


Figure 5.11 Change in the mean minimum and maximum diameter of the inclusions in the Aluminium deoxidised High Frequency Furnace Melt, determined using an IBAS2 Image Analysis system 149

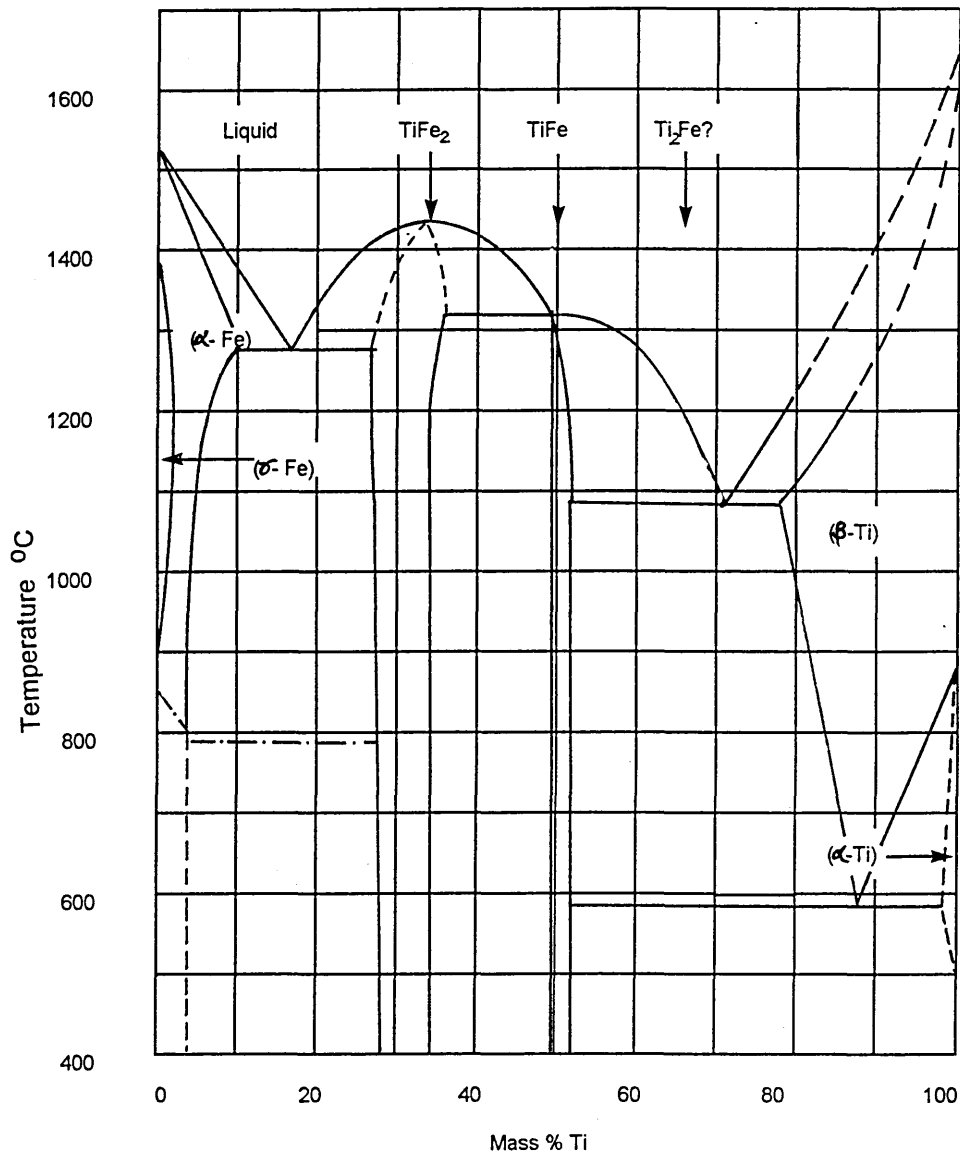
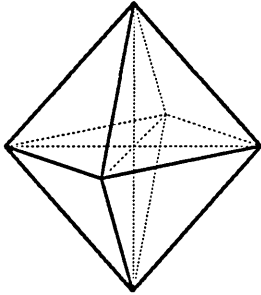
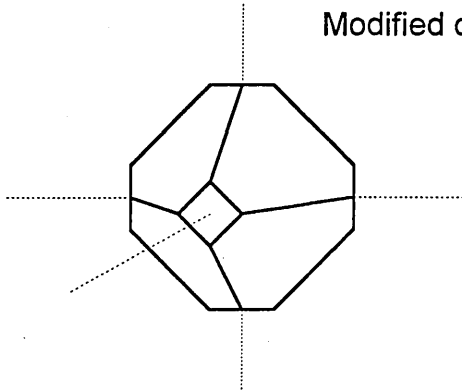


Figure 5.12 The binary phase diagram for the Fe-Ti System¹⁵⁰

Simple octahedron



Modified octahedron



Fourteen sided polyhedron

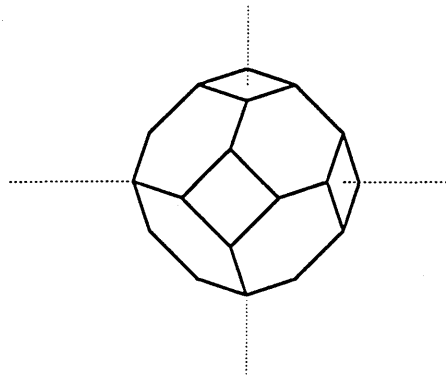
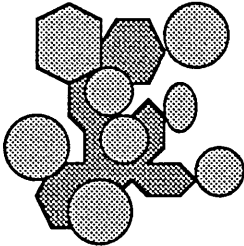
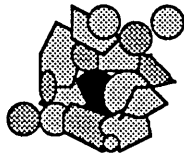


Figure 5.13 The modification of octahedra as the interfacial tension between the melt and the oxide phase increases.

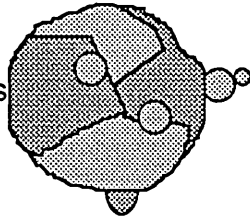
Initial agglomeration
of spherical & polyhedral
inclusion morphologies



Spherodisation & formation
of a polymorphic inclusion



Diffusion of grain boundaries



Spherodisation with
collisions resulting
in further growth

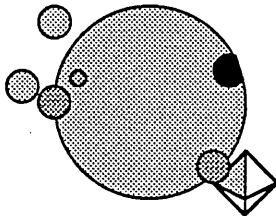
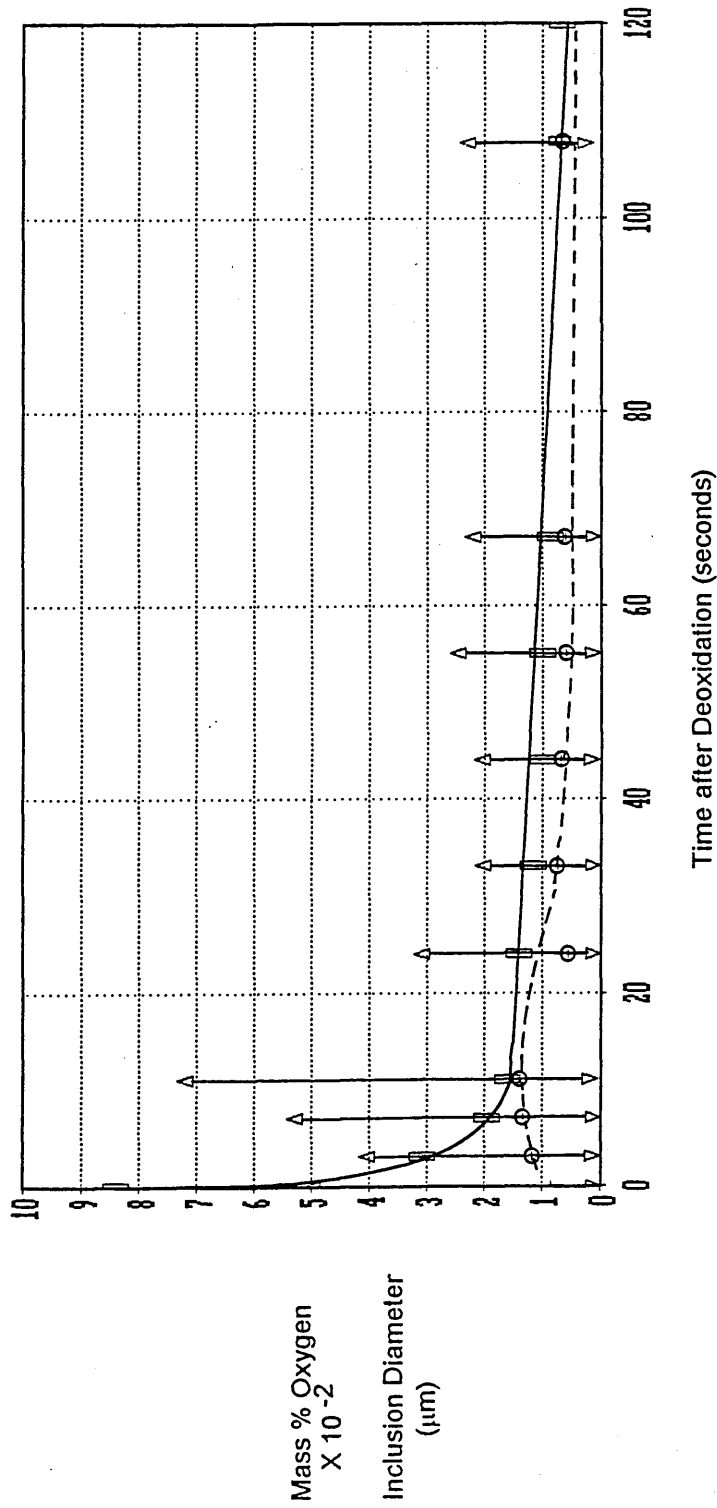


Figure 5.14 Schematic diagram to show the stages in the formation & spherodisation of titania inclusions.



▽ mean from minimum size band ⊕ mean diameter Δ mean from maximum size band □ oxygen

Figure 5.15 Removal of oxygen and change in the average diameter of the inclusions in the Titanium deoxidised High Frequency Furnace Melt.

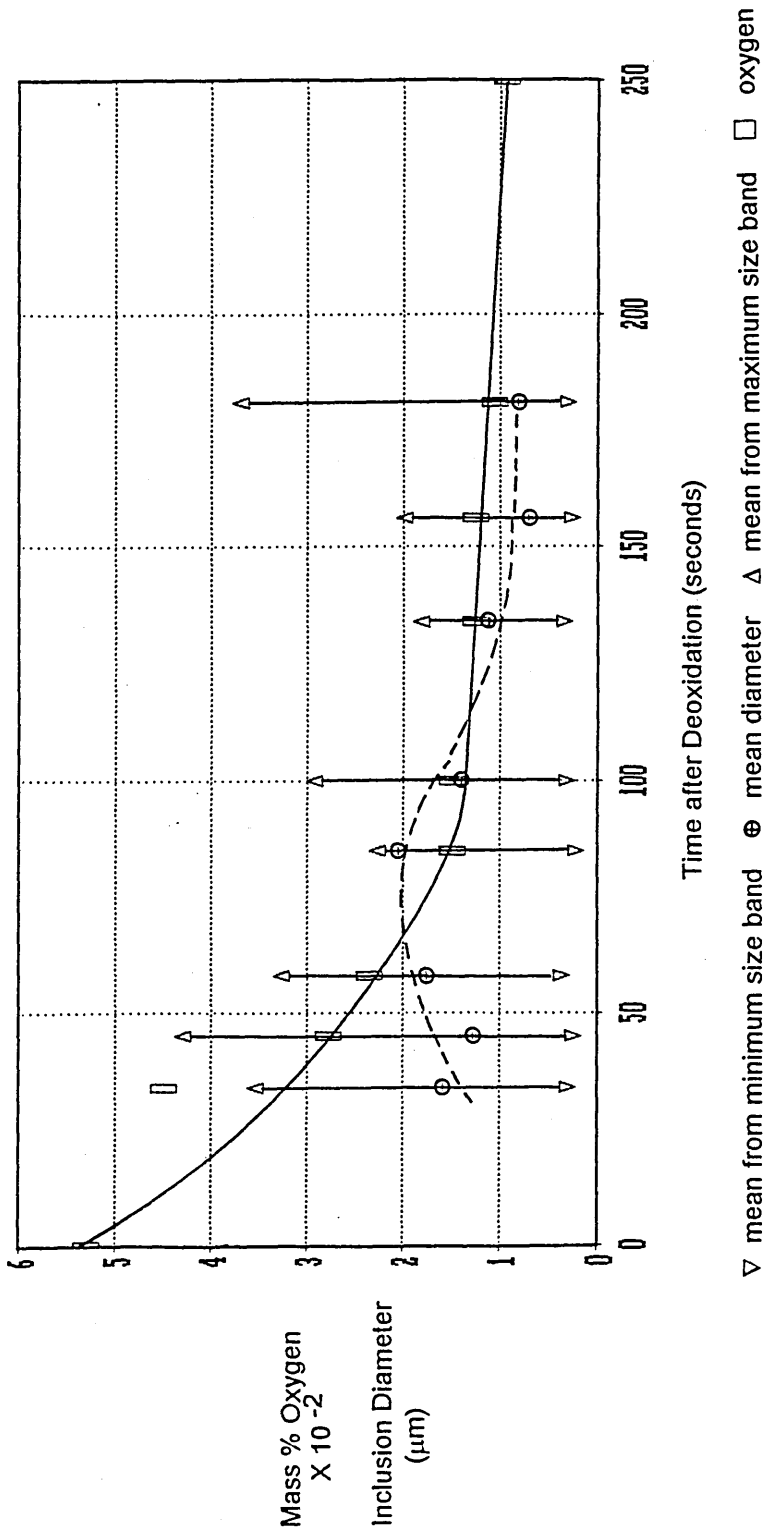
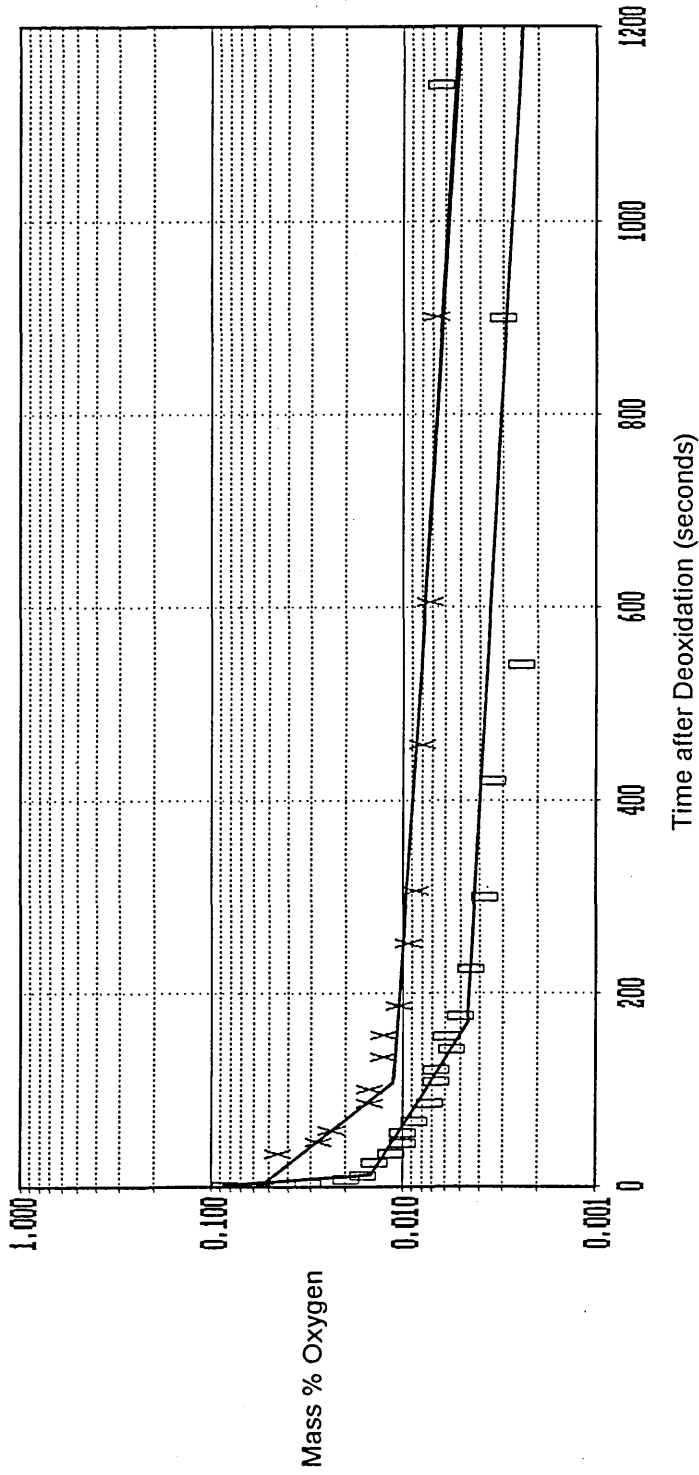


Figure 5.16 Removal of oxygen and change in the average diameter of the inclusions in the Titanium deoxidised Vertical Tube Furnace Melt.



□ High Frequency Furnace Melt X Vertical Tube Furnace Melt
 Figure 5.17 Removal of oxygen from the Titanium deoxidised melts.

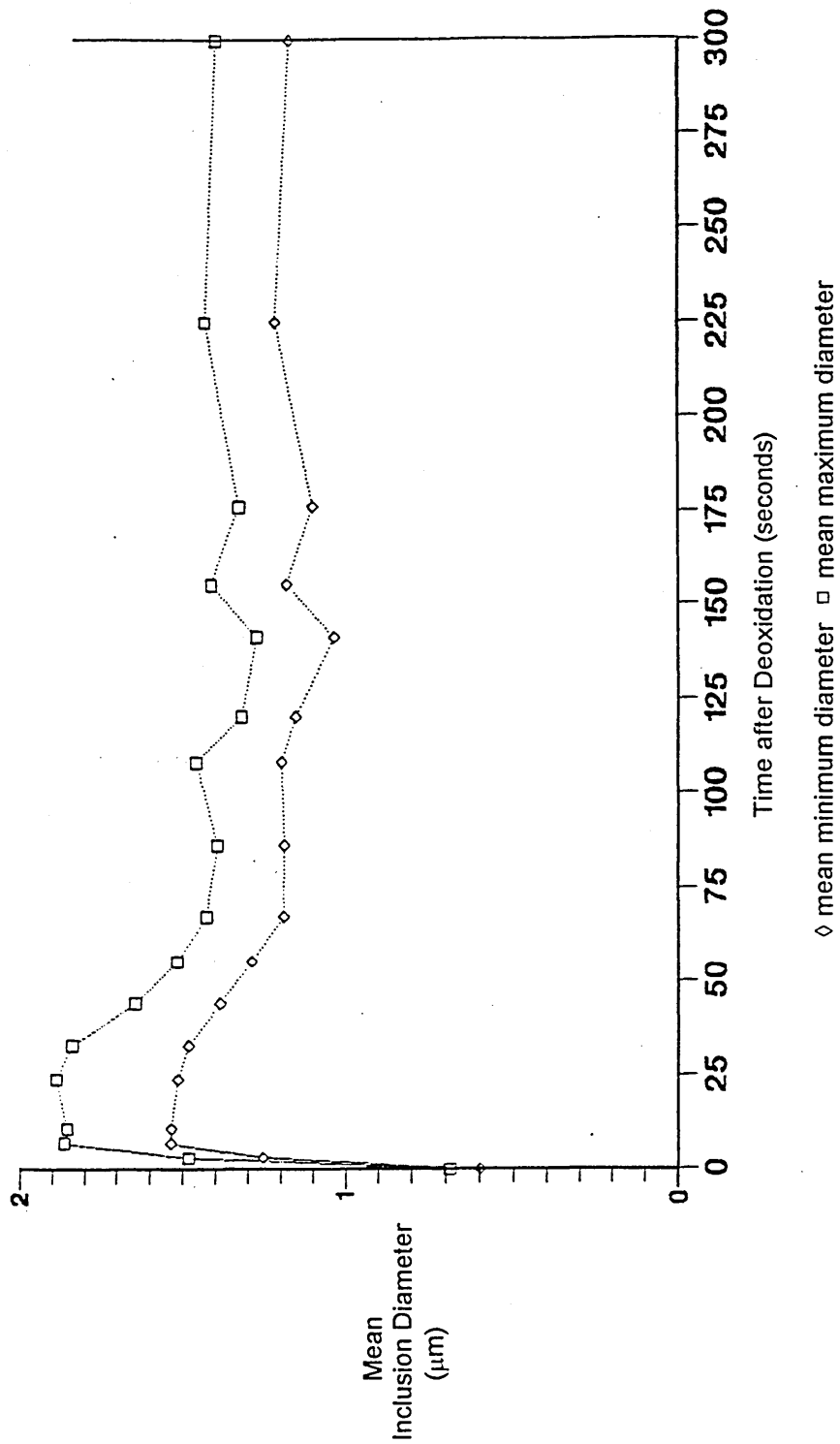


Figure 5.18 Change in the mean minimum and maximum diameter of the inclusions in the Titanium deoxidised High Frequency Furnace Melt, determined using an IBAS2 Image Analysis system 149

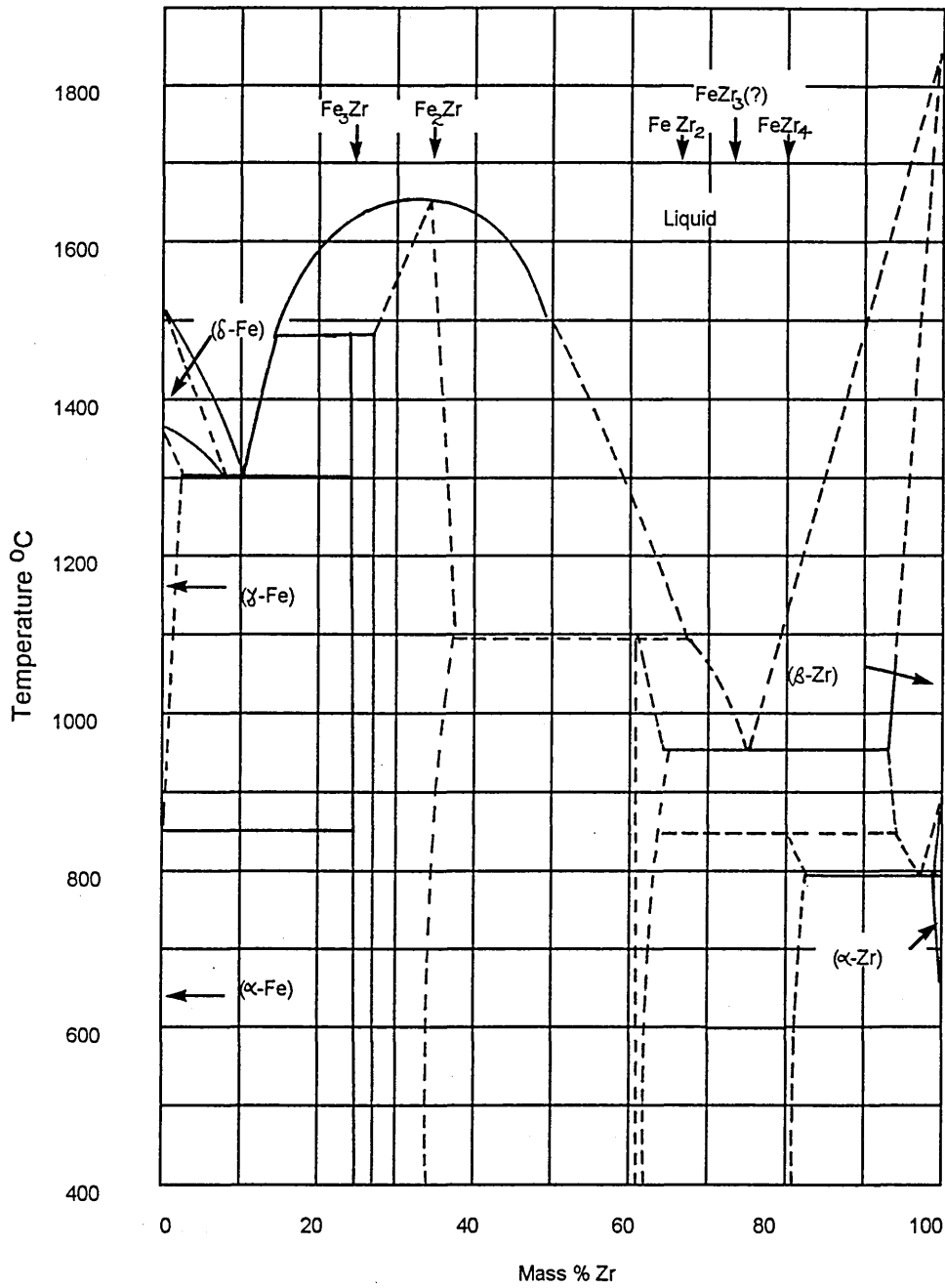


Figure 5.19 The binary phase diagram for the Fe-Zr system¹⁵⁰

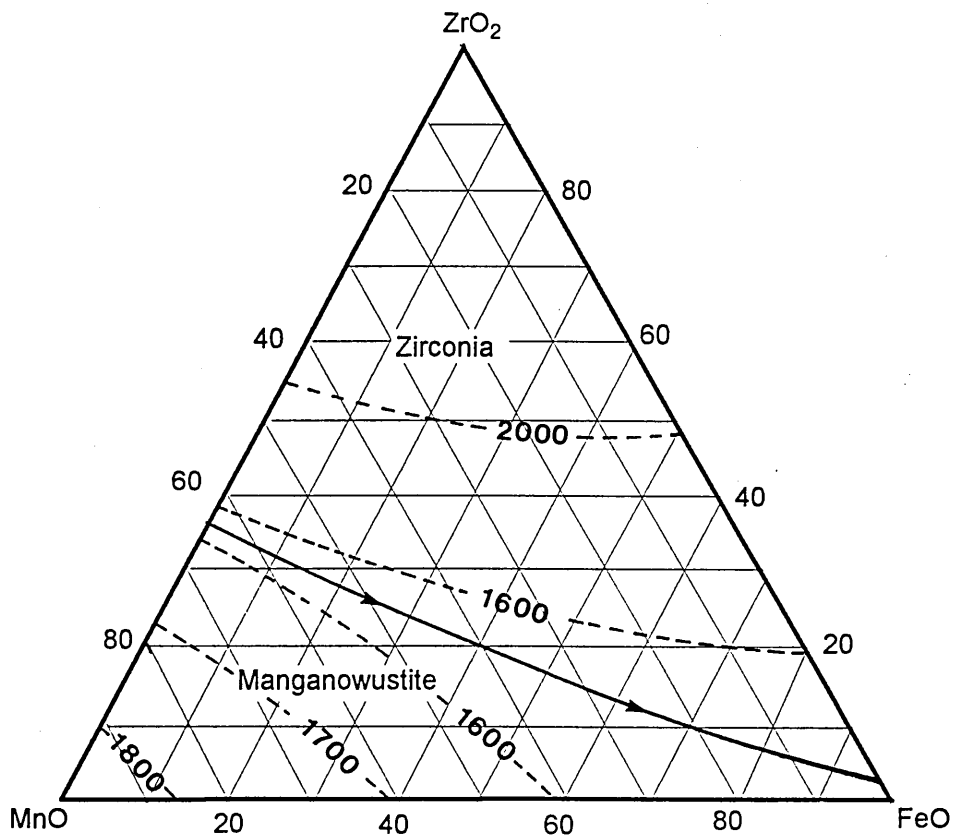
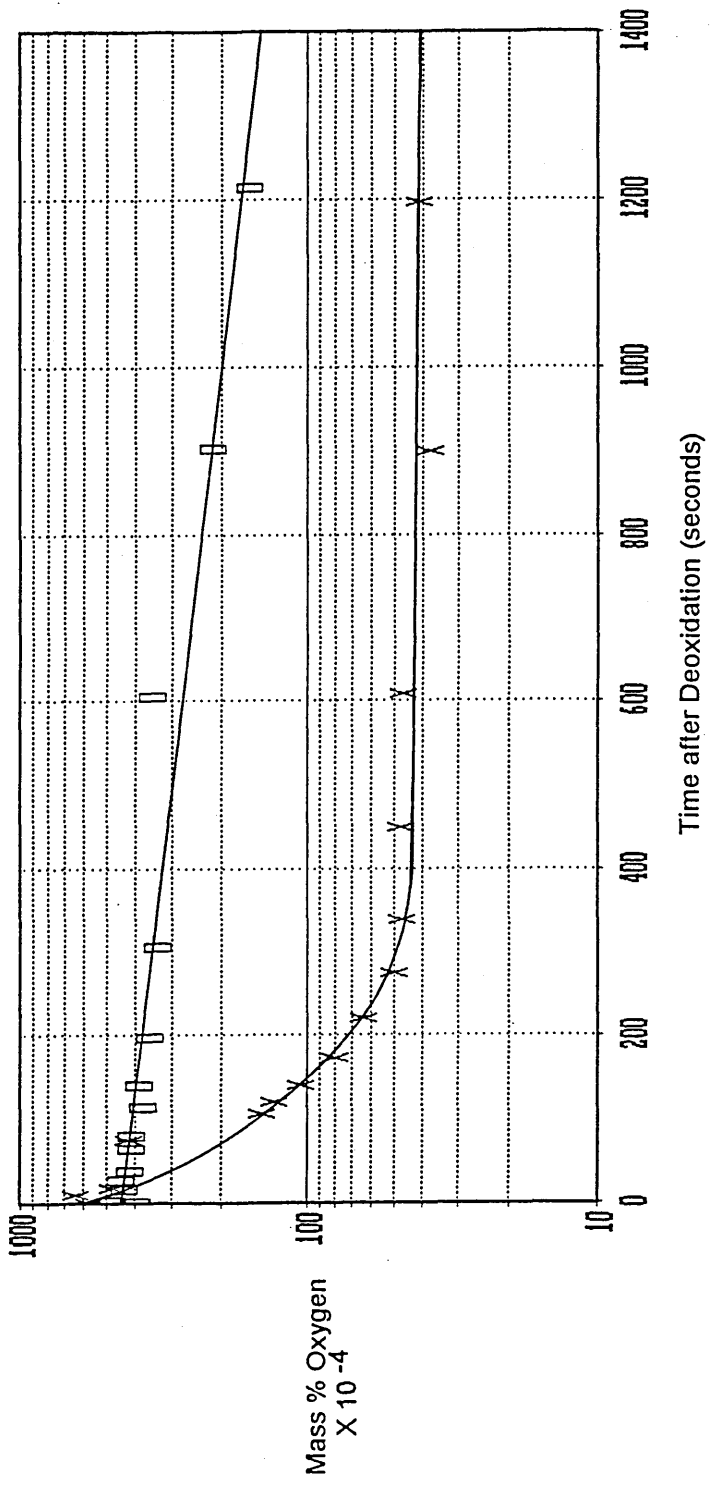


Figure 5.20 Ternary phase diagram for the system FeO-MnO-ZrO₂ ¹⁰⁷ .



x High Frequency Furnace Melt □ Vertical Tube Furnace Melt

Figure 5.21 Removal of oxygen from the Zirconium deoxidised melts.

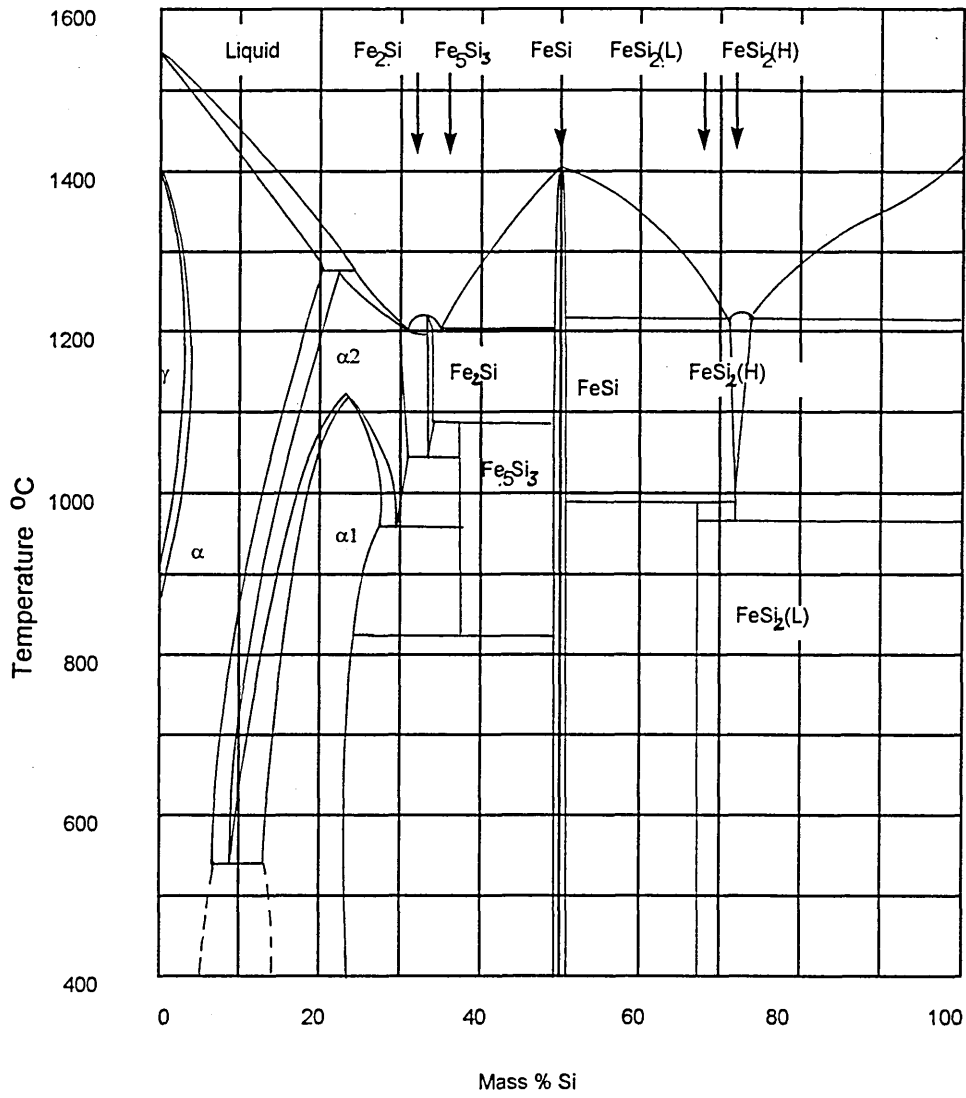


Figure 5.22 The binary phase diagram for the Fe-Si System.¹⁵⁰

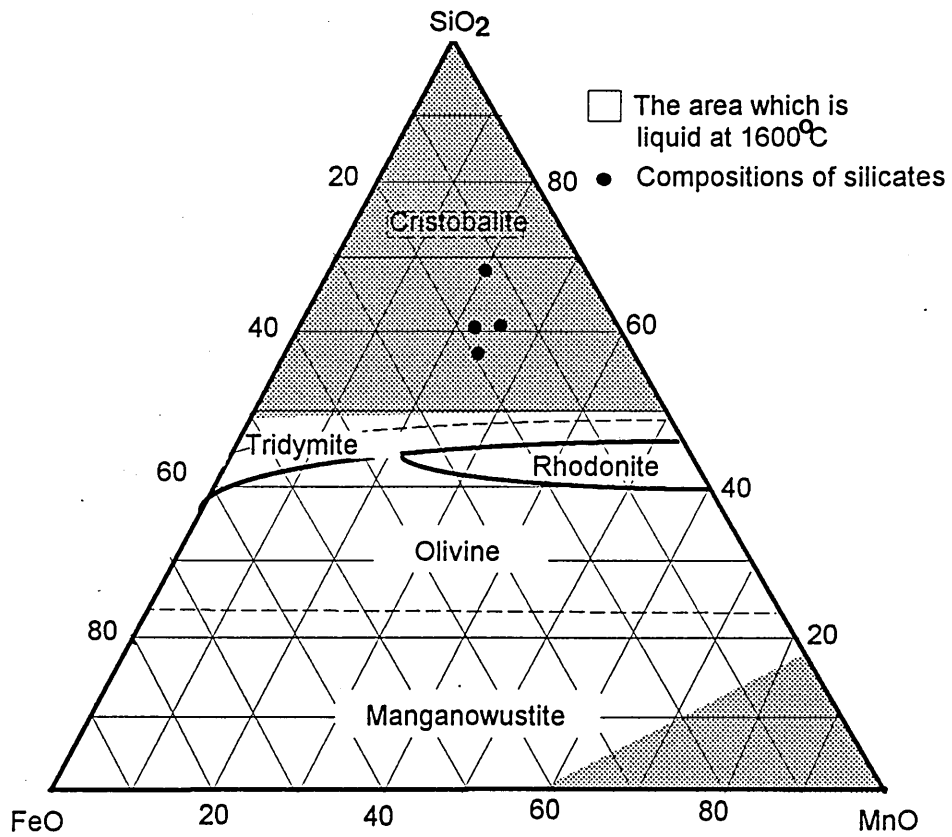


Figure 5.23 Phase diagram for the SiO₂-FeO-MnO system¹⁰⁷.

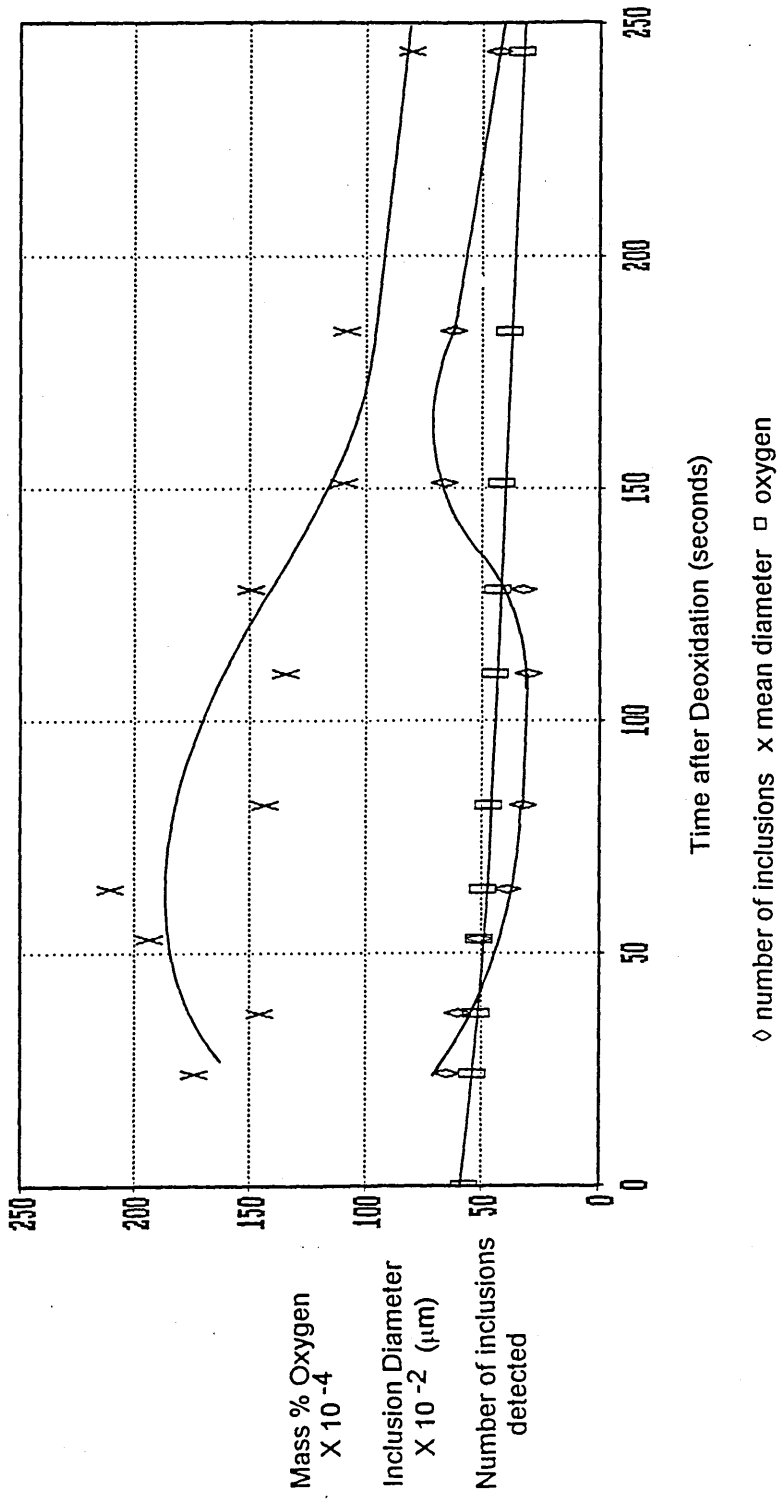


Figure 5.24 Removal of oxygen, change in the average diameter and number of inclusions counted in the Silicon deoxidised Vertical Tube Furnace Melt.

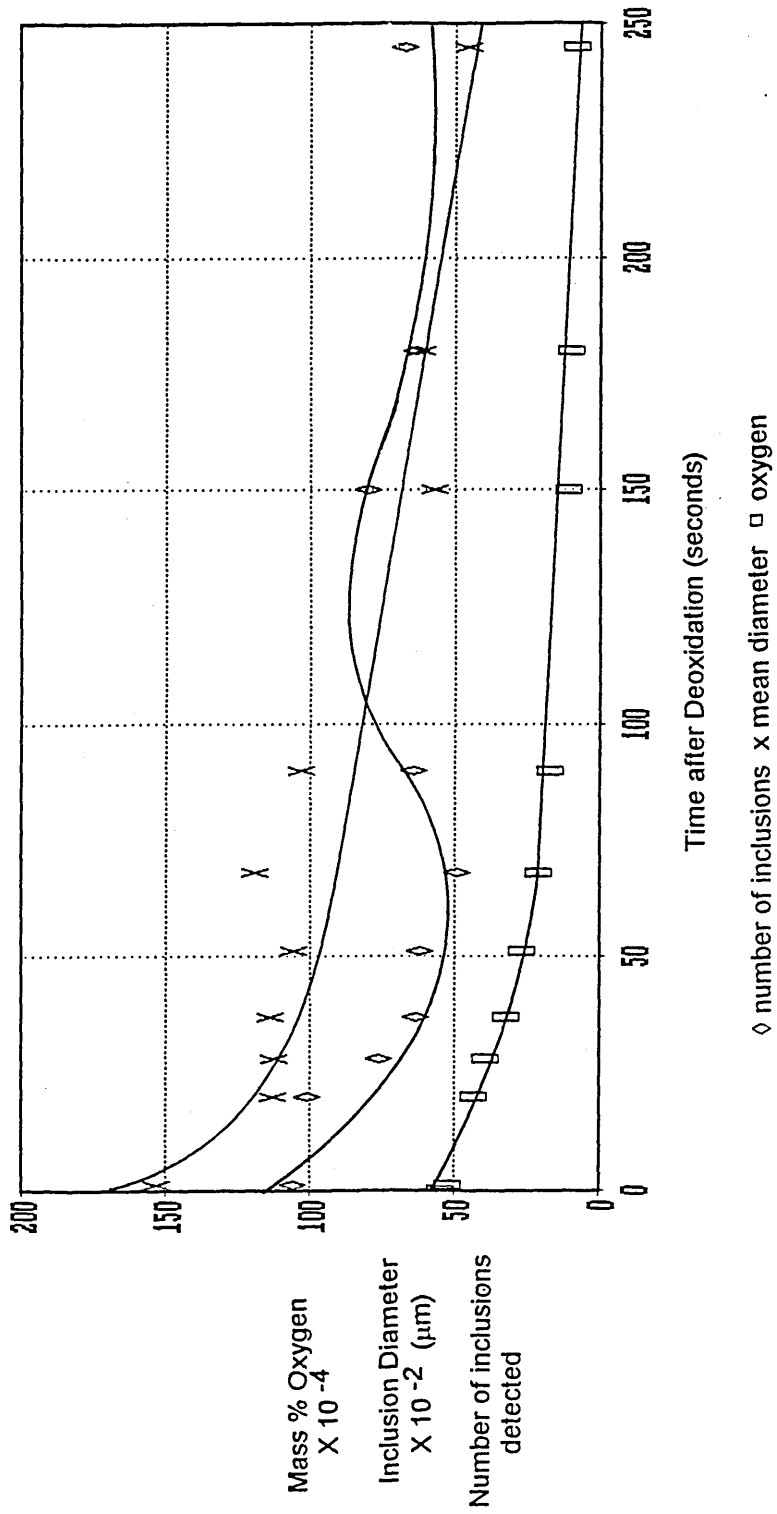
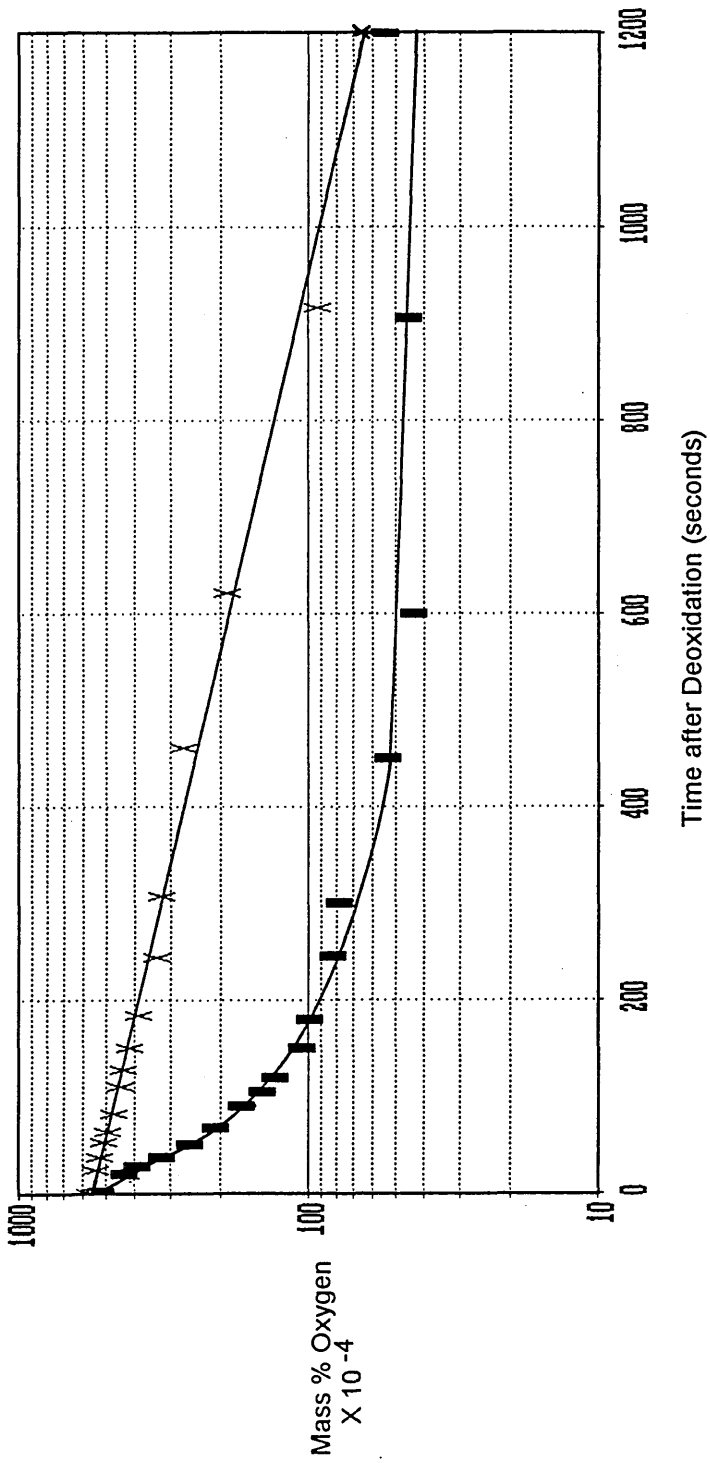


Figure 5. 25 Removal of oxygen, change in the average diameter and number of inclusions counted in the Silicon deoxidised High Frequency Furnace Melt.



■ High Frequency Furnace Melt x Vertical Tube Furnace Melt

Figure 5.26 Removal of oxygen from the silicon deoxidised melts.

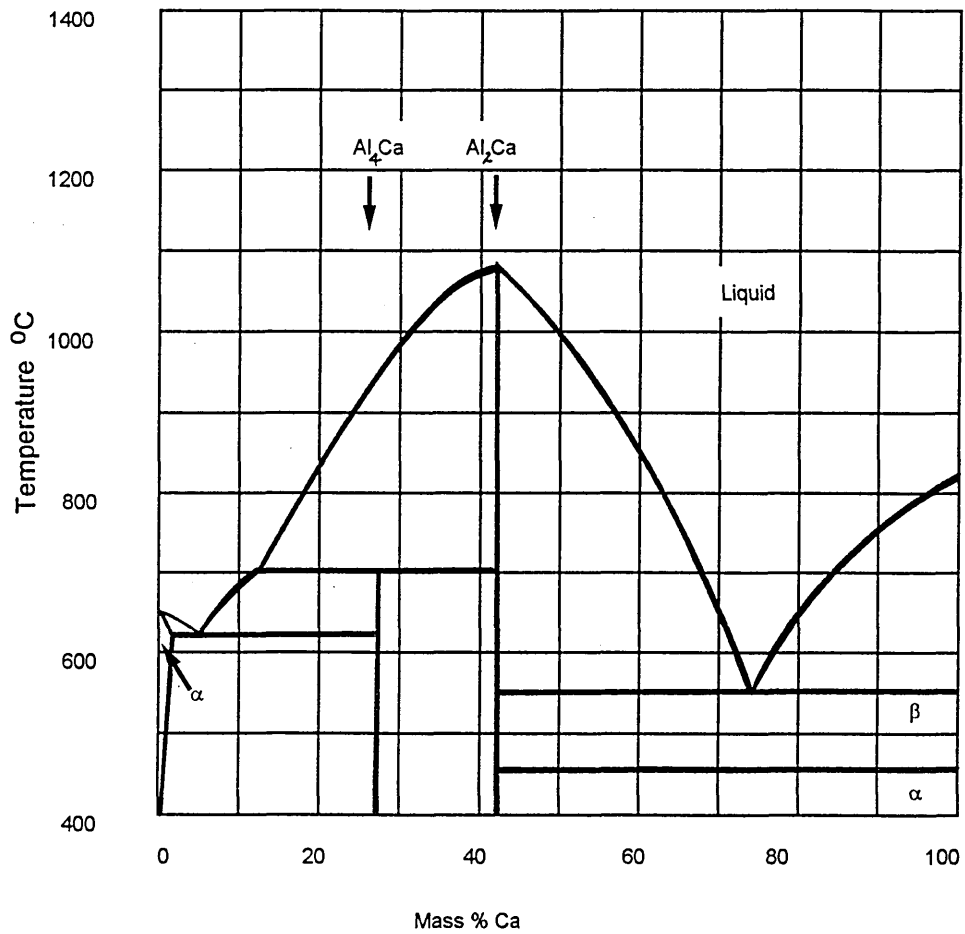


Figure 5.27 The binary phase diagram for the Al-Ca System.¹⁵⁰

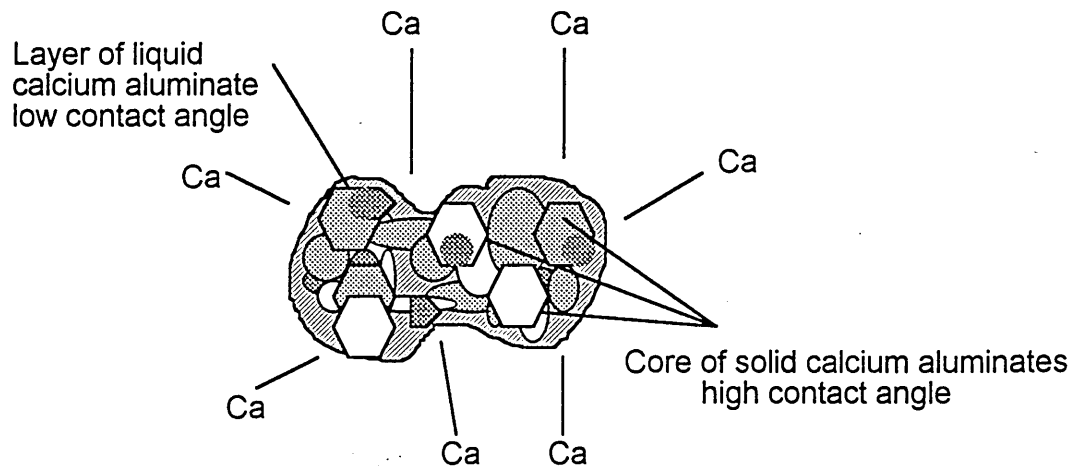


Figure 5.28 Formation of a calcium aluminate inclusion cluster with a liquid surface.

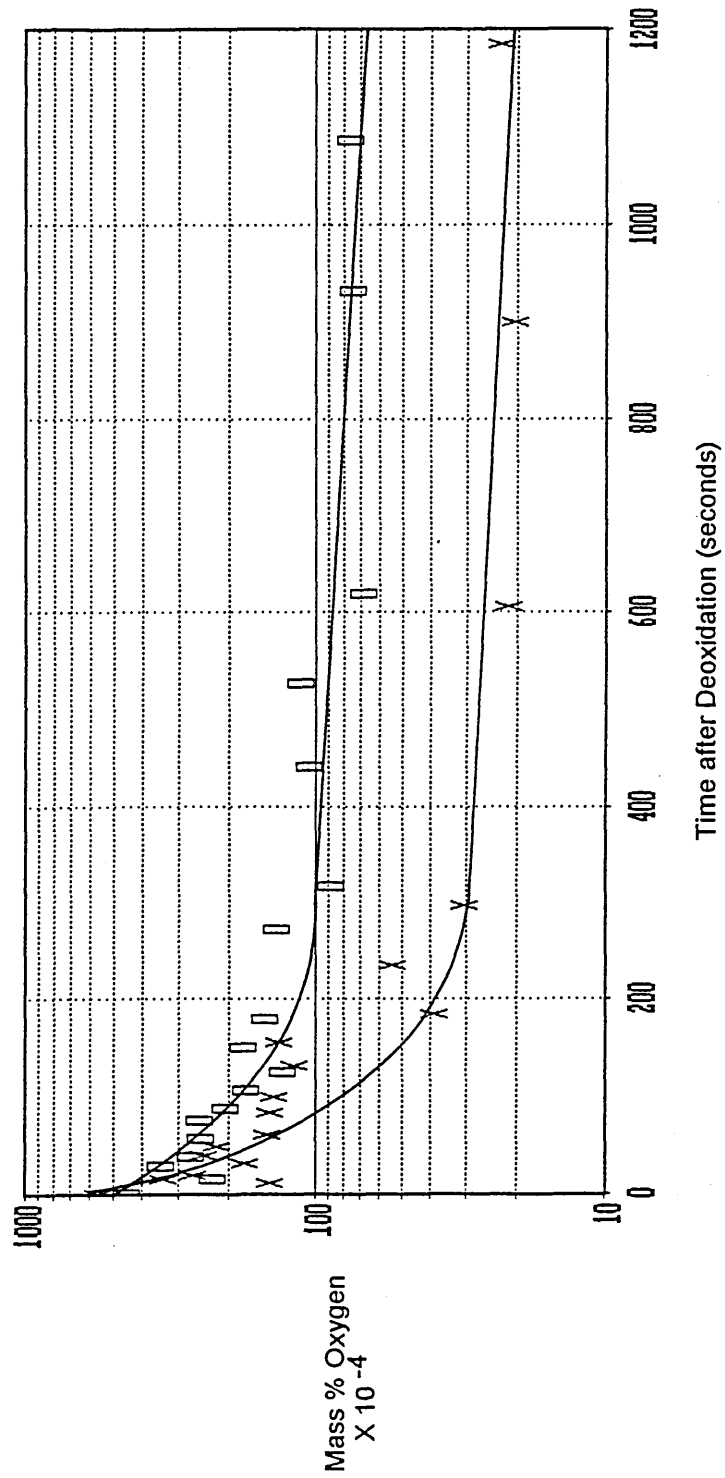


Figure 5. 29 Removal of oxygen from the Calcium-aluminium deoxidised melts.

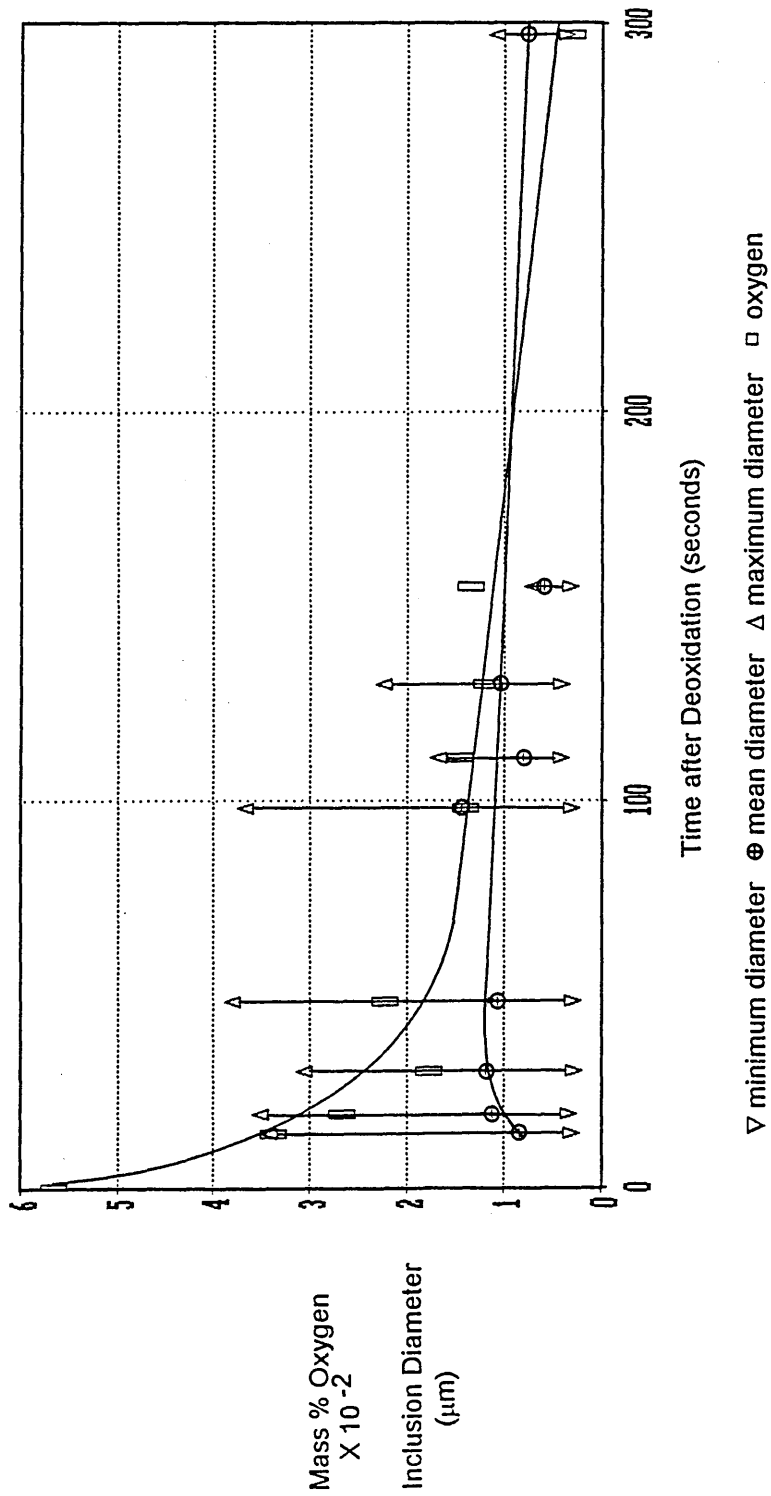
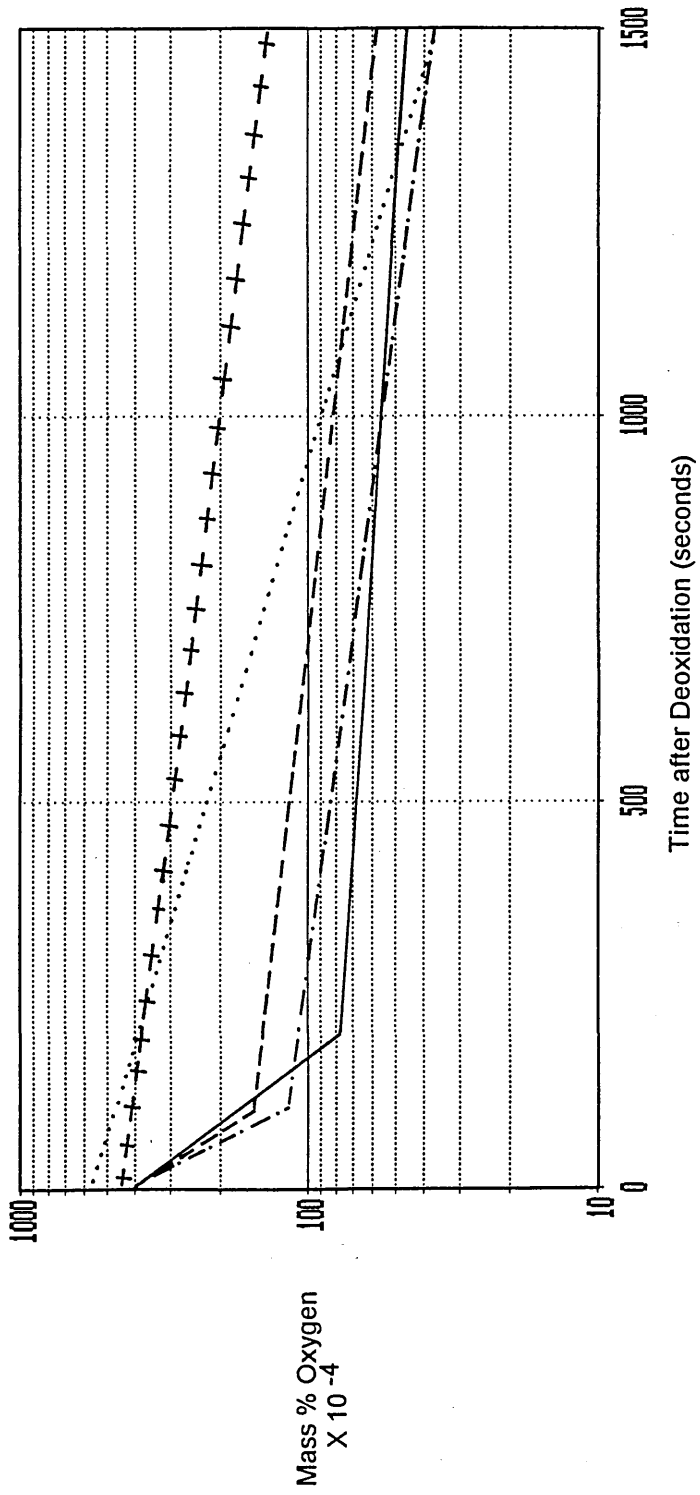


Figure 5.30 Removal of oxygen, change in the average diameter and number of inclusions counted in the Calcium - aluminium deoxidised High Frequency Furnace Melt.



--- Titanium Deoxidised Melt — Aluminium Deoxidised Melt ... Silicon Deoxidised Melt
 -- Calcium-aluminium Deoxidised Melt + Zirconium Deoxidised Melt

Figure 5.31 Removal of oxygen from the Vertical Tube Furnace Melts.

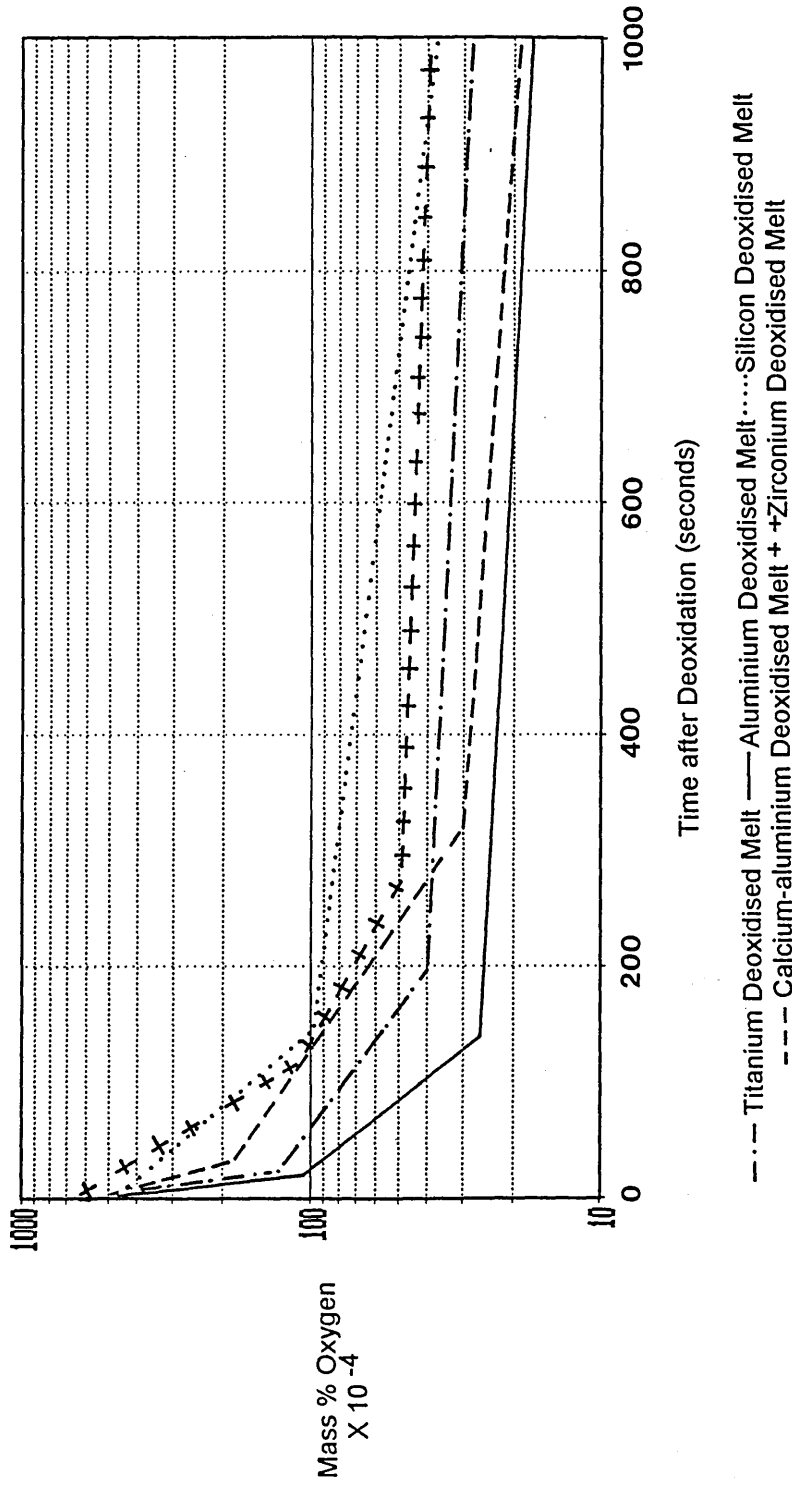


Figure 5.32 Removal of oxygen from the High Frequency Furnace Melts.

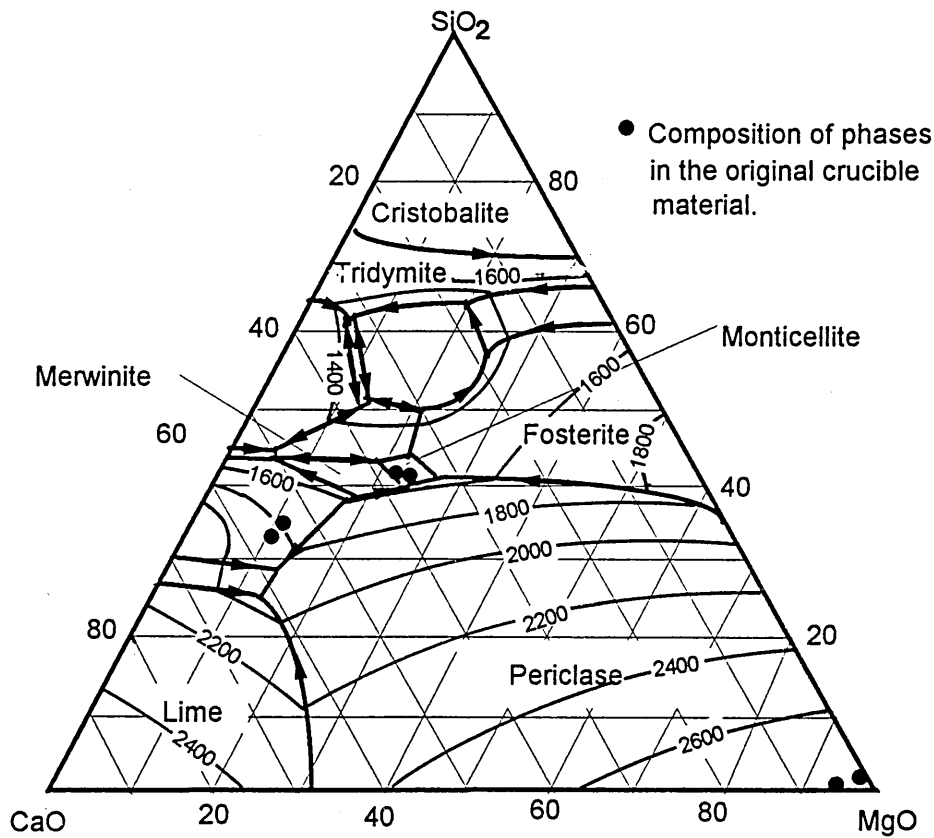


Figure 5.33 Phase diagram for the SiO₂-CaO-MgO system¹⁰⁶, indicating the composition of the silicates in the annealed crucible.

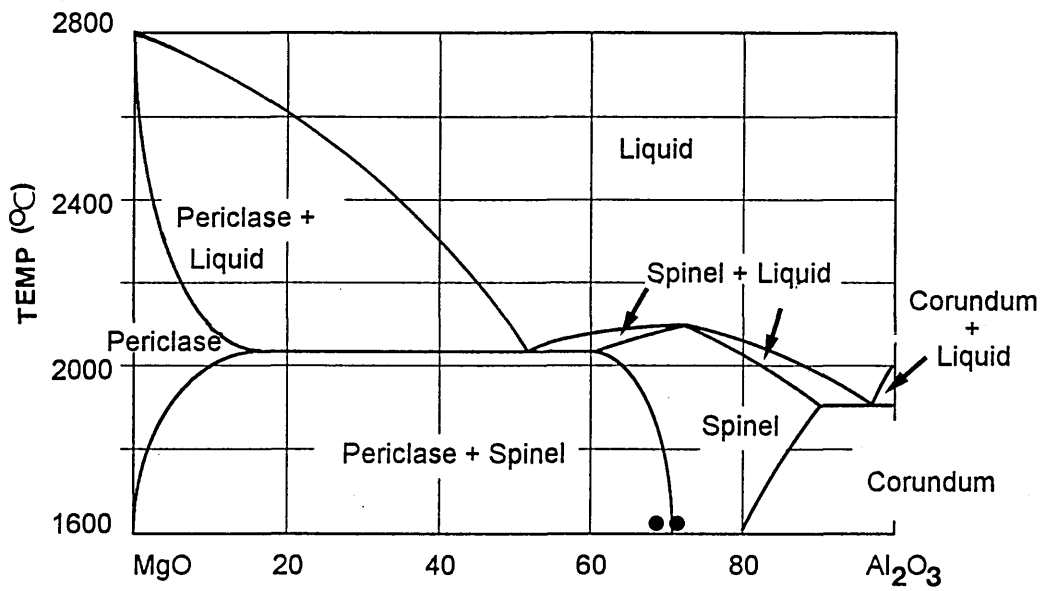


Figure 5.34 Phase diagram for the MgO-Al₂O₃ system¹⁰⁶, showing the composition of the spinel phase in the annealed crucible material (●●).

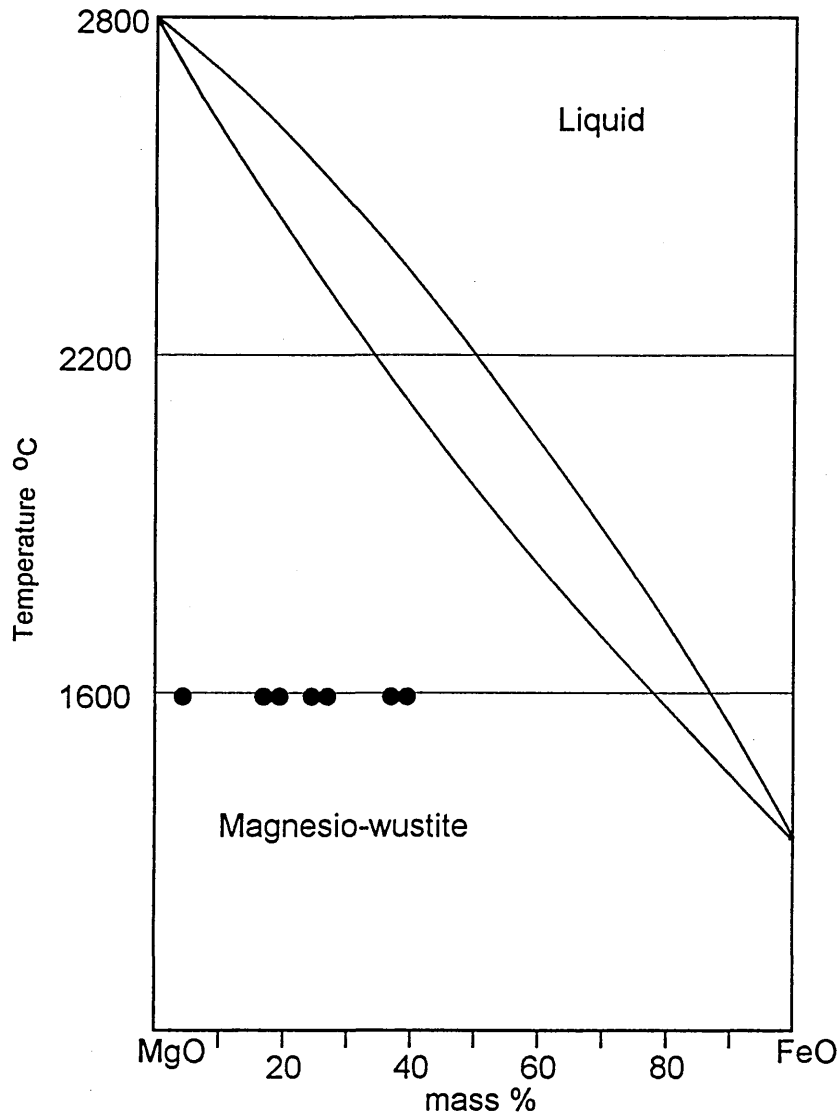


Figure 5.35 Phase diagram for the MgO-FeO system in contact with metallic iron¹⁰⁶, showing the composition of the magnesio-wustite phase at the crucible-melt interface after contact with the undeoxidised melt (●●)

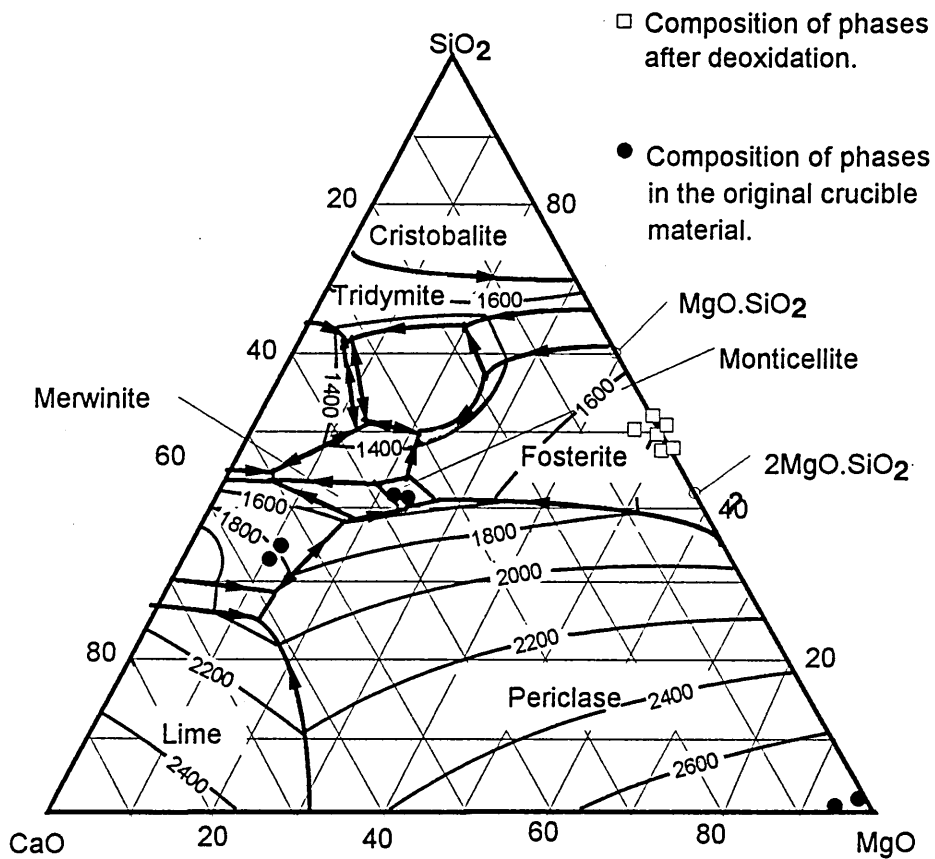


Figure 5.36 Phase diagram for the SiO₂-CaO-MgO system, indicating the composition of the silicates in the annealed crucible, and the composition of the phases after deoxidation with silicon.

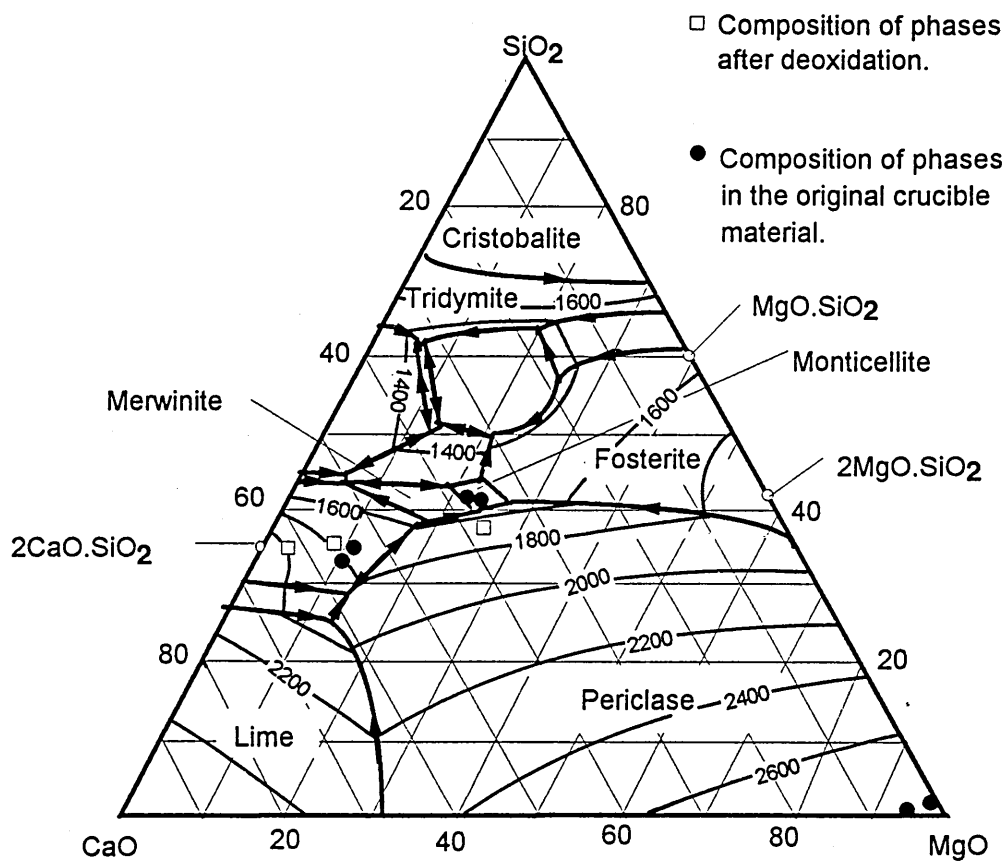


Figure 5.37 . Phase diagram for the SiO₂-CaO-MgO system, indicating the composition of the silicates in the annealed crucible, and the composition of the phases after deoxidation with calcium-aluminium.

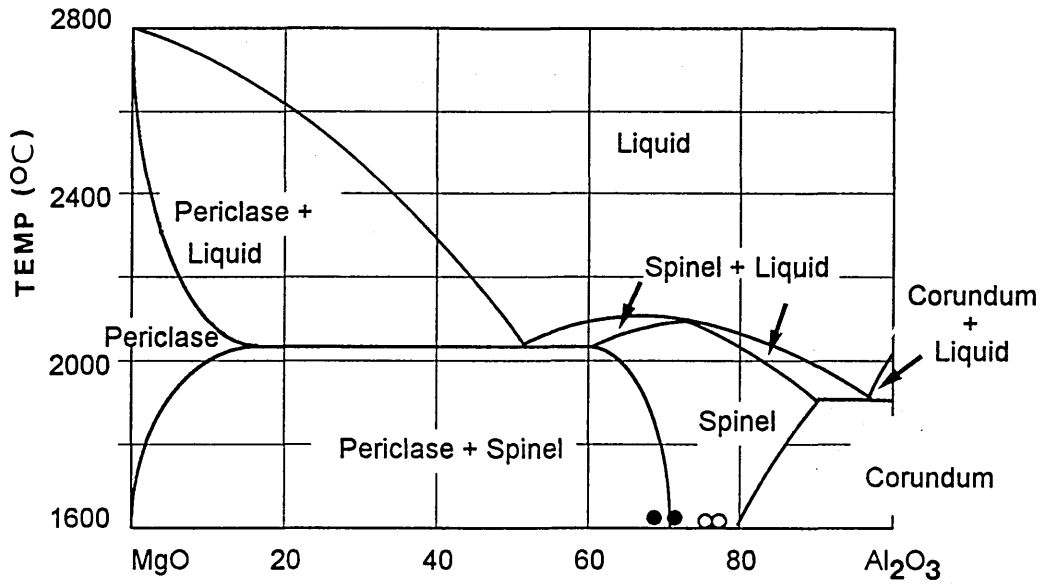


Figure 5.38 Phase diagram for the MgO-Al₂O₃ system¹⁰⁶, showing the composition of the spinel phase in the annealed crucible material (●●), and the composition after crucible had been in contact with the aluminium deoxidised melt (○○).

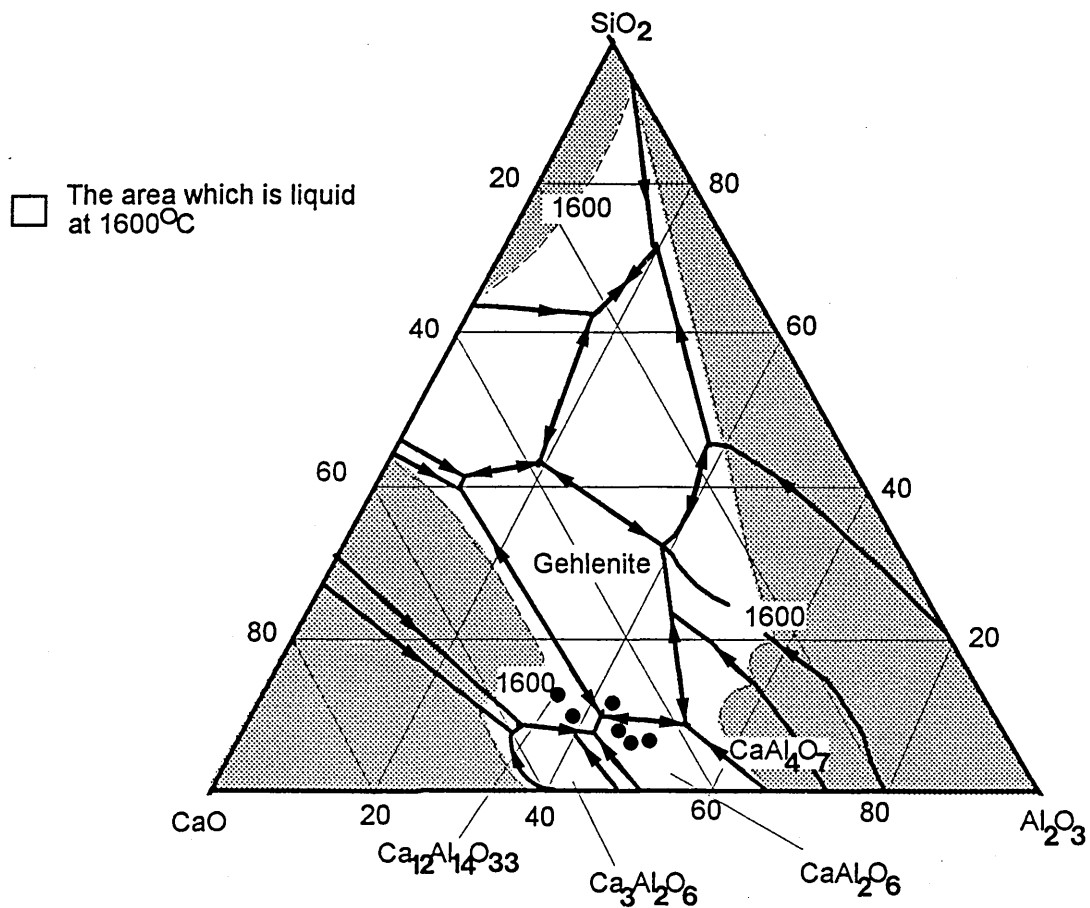


Figure 5.39 Phase diagram for the SiO₂-CaO-Al₂O₃ system, showing the composition of the CaO-Al₂O₃ phases in the crucible material after contact with the aluminium deoxidised melts (●●).

Plate 4.1

Sample AVT 1. Suction sample taken before deoxidation of melt with 0.3 mass% aluminium addition in the vertical tube furnace.

Total oxygen content of the sample 415 ppm.

SEM Micrograph

Magnification 1,100 X

Showing an interdendritic network of Fe-Mn-Al oxide inclusions.

Plate 4.2

Sample AVT 2. Suction sample taken 12 seconds after deoxidation of melt with 0.3 mass% aluminium addition in the vertical tube furnace.

Total oxygen content of the sample 410 ppm.

SEM Micrograph

Magnification 2,300 X

Showing randomly distributed spherical inclusions 1.0 - 1.5 μm in diameter.

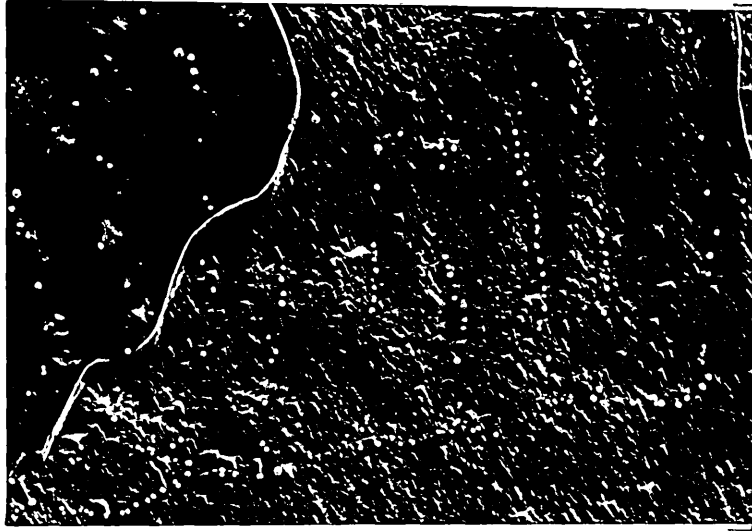


Plate 4.3

Sample AVT 2. Suction sample taken 12 seconds after deoxidation of melt with 0.3 mass% aluminium addition in the vertical tube furnace.

Total oxygen content of the sample 410 ppm.

SEM Micrograph

Magnification 2,300 X

Showing randomly distributed spherical inclusions 1.0 - 4.0 μm in diameter and well developed dendrites exhibiting both stems and primary, secondary and tertiary branching.



Plate 4.4

Sample AVT 2. Suction sample taken 12 seconds after deoxidation of melt with 0.3 mass% aluminium addition in the vertical tube furnace.

Total oxygen content of the sample 410 ppm.

SEM Micrograph

Magnification 3,200 X

Showing underdeveloped dendrites with stems and spheroidising primary branches (1); globular coralline morphologies originating from the dendrite stems (2); and large spherical sintered agglomerates(3).

Plate 4.5

Sample AVT 2. Suction sample taken 12 seconds after deoxidation of melt with 0.3 mass% aluminium addition in the vertical tube furnace.

Total oxygen content of the sample 400 ppm.

SEM Micrograph

Magnification 5,500 X

Showing polyhedral inclusion morphologies (1) associated with a small inclusion cluster.

Plate 4.6

Sample AVT 6. Suction sample taken 55 seconds after deoxidation of melt with 0.3 mass% aluminium addition in the vertical tube furnace.

Total oxygen content of the sample 195 ppm.

SEM Micrograph

Magnification 3,200 X

Showing small inclusion clusters and individual inclusions being collected on the arms and branches of large dendrites.

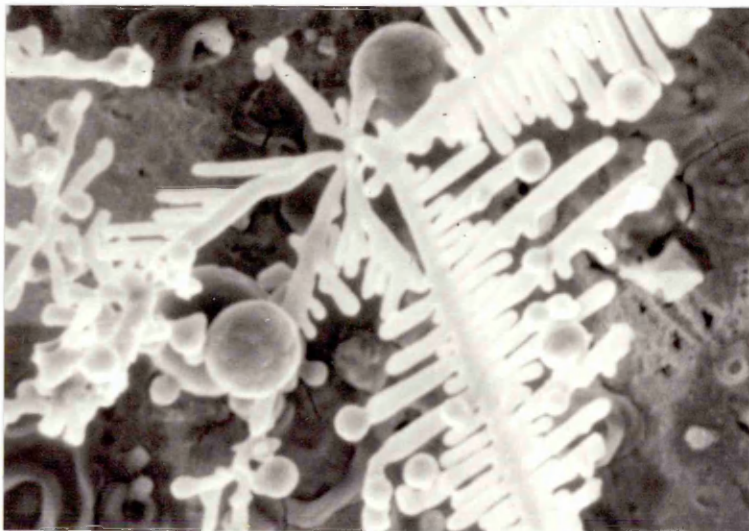
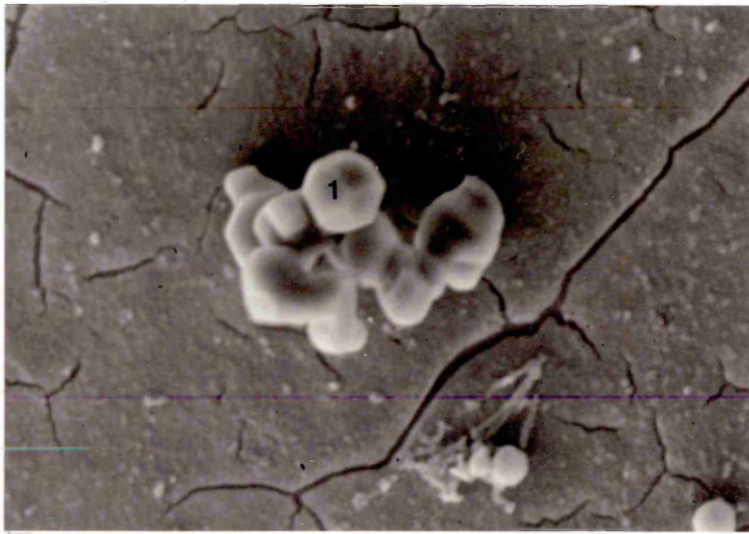
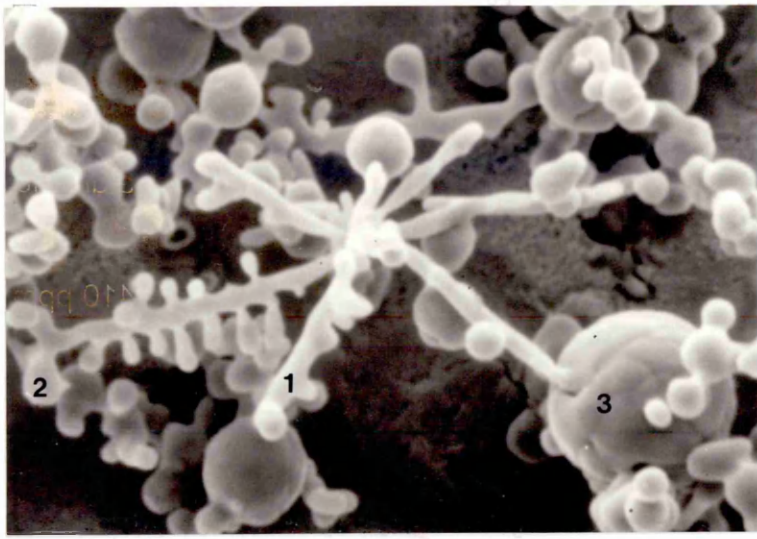


Plate 4.7

Sample AVT 5. Suction sample taken 43 seconds after deoxidation of melt with 0.3 mass% aluminium addition in the vertical tube furnace.

Total oxygen content of the sample 265 ppm.

SEM Micrograph

Magnification 2,000 X

Showing a large sintered agglomerate, 22 μ m in diameter, with sintered contacts developing between the sintered agglomerate and smaller coralline morphologies.

Plate 4.8

Sample AVT 9. Suction sample taken 96 seconds after deoxidation of melt with 0.3 mass% aluminium addition in the vertical tube furnace.

Total oxygen content of the sample 215 ppm.

SEM Micrograph

Magnification 4,500 X

Showing large sintered agglomerates and coralline morphologies. The coralline morphologies exhibit an interwoven character typical of spherodisation which results in the formation of sintered agglomerates.

Plate 4.9

Sample AVT 9. Suction sample taken 96 seconds after deoxidation of melt with 0.3 mass% aluminium addition in the vertical tube furnace.

Total oxygen content of the sample 215 ppm.

SEM Micrograph

Magnification 7,000 X

Showing a large sintered agglomerate, clearly exhibiting the relic form of a coralline type morphology.

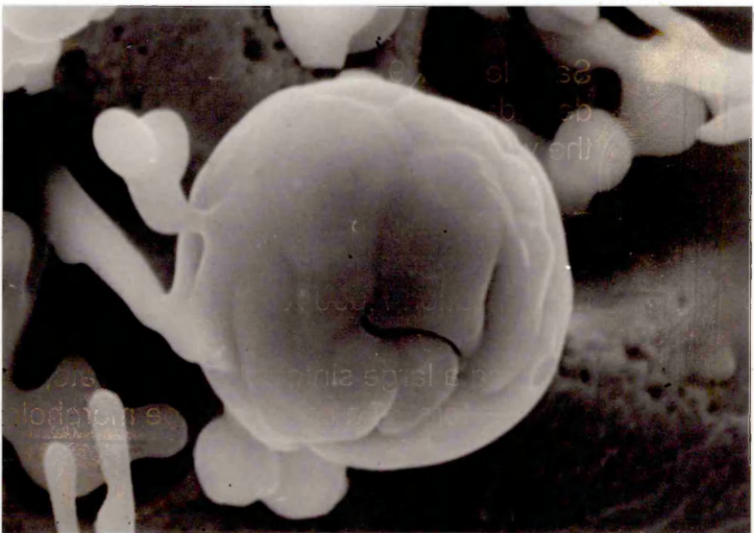
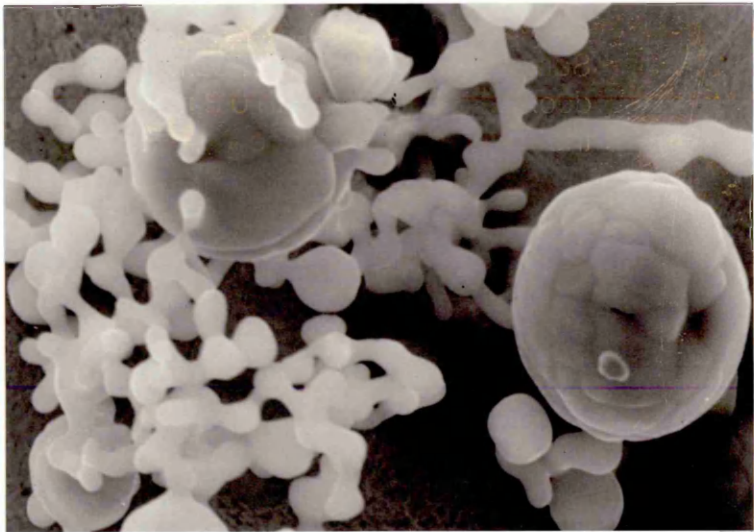
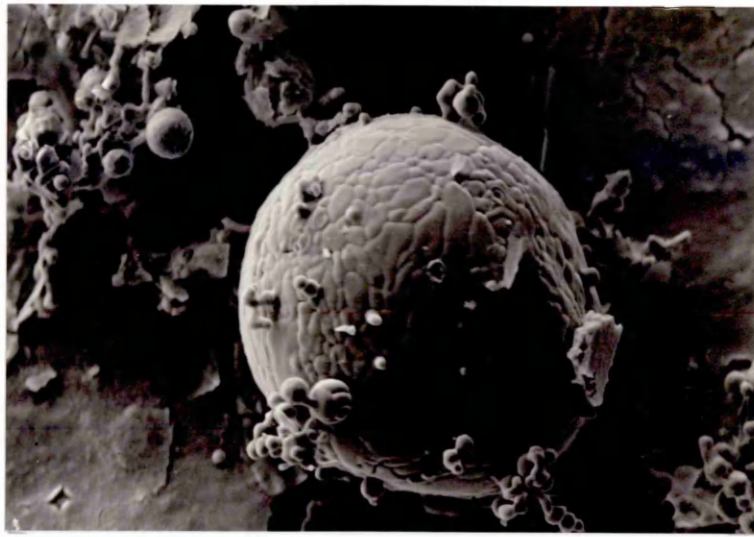


Plate 4.10

Sample AVT 5. Suction sample taken 43 seconds after deoxidation of melt with 0.3 mass% aluminium addition in the vertical tube furnace.

Total oxygen content of the sample 265 ppm.
SEM Micrograph
Magnification 2,600 X

Showing a dendrite morphology exhibiting coarsening of the dendrite arms.

Plate 4.11

Sample AVT 9. Suction sample taken 96 seconds after deoxidation of melt with 0.3 mass% aluminium addition in the vertical tube furnace.

Total oxygen content of the sample 215 ppm.
SEM Micrograph
Magnification 5,000 X

Showing the sintering and formation of necks between contacting polyhedral inclusions.

Plate 4.12

Sample AVT 5. Suction sample taken 43 seconds after deoxidation of melt with 0.3 mass% aluminium addition in the vertical tube furnace.

Total oxygen content of the sample 265 ppm.
SEM Micrograph
Magnification 2,350 X

Showing the spherodisation and amputation of dendrite branches.

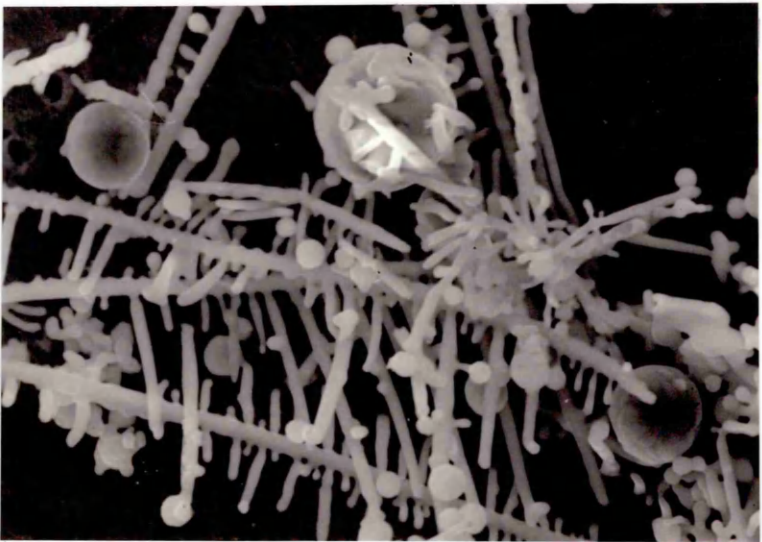
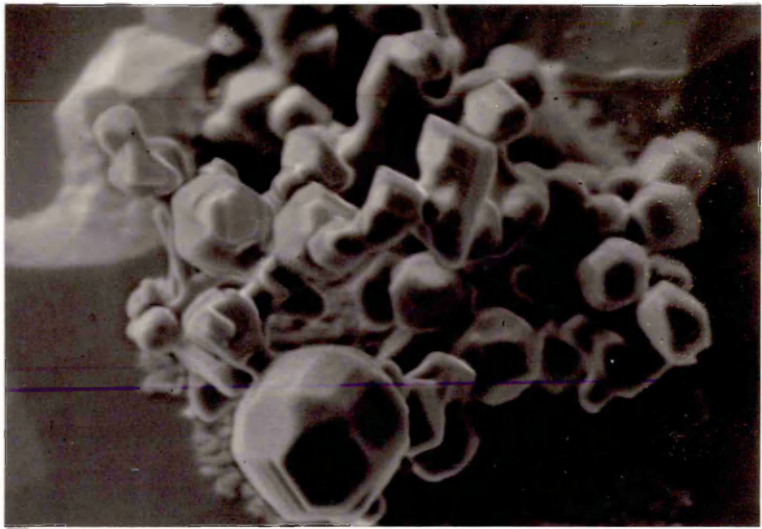


Plate 4.16

Sample AVT 19. Suction sample taken 1203 seconds after deoxidation of melt with 0.3 mass% aluminium addition in the vertical tube furnace.

Total oxygen content of the sample 53 ppm.

SEM Micrograph

Magnification 6,500 X

Showing a small cluster comprising of polyhedral inclusions, exhibiting highly sintered contacts.

Plate 4.17

Sample AHF 1. Suction sample taken before deoxidation of melt with 0.3 mass% aluminium addition in the high frequency furnace.

Total oxygen content of the sample 380 ppm.

SEM Micrograph

Magnification 1,200 X

Showing an interdendritic network of Fe-Mn-Al oxide inclusions.

Plate 4.18

Sample AHF 2. Suction sample taken 3 seconds after deoxidation of melt with 0.3 mass% aluminium addition in the high frequency furnace.

Total oxygen content of the sample 290 ppm.

SEM Micrograph

Magnification 3,400 X

Showing a large cluster of inclusions, containing dendritic, spherical and polyhedral inclusion morphologies. The following polyhedral forms are observed (1) octahedra; (2) modified octahedra; and (3) octahedra exhibiting truncated corners.

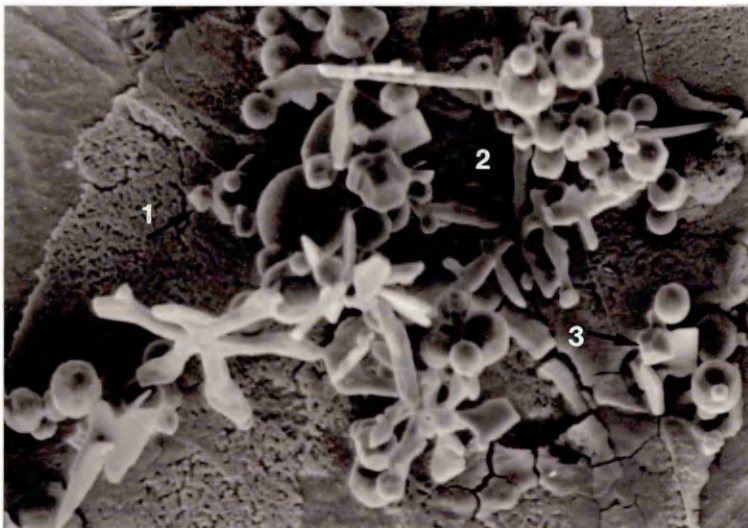
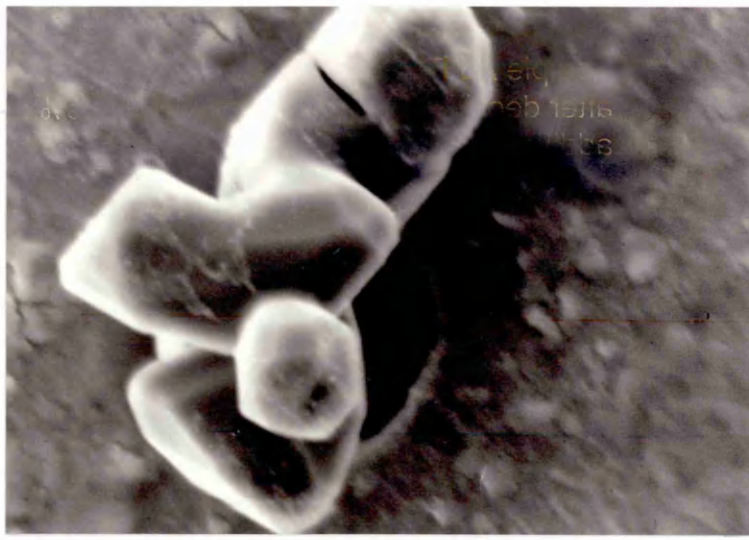


Plate 4.19

Sample AHF 2. Suction sample taken 3 seconds after deoxidation of melt with 0.3 mass% aluminium addition in the high frequency furnace.

Total oxygen content of the sample 290 ppm.

SEM Micrograph

Magnification 1,700 X

Showing a large cluster of inclusions, containing dendritic, spherical and polyhedral inclusion morphologies. The dendritic inclusions exhibit stems and a system of under-developed branches.

Plate 4.20

Sample AHF 2. Suction sample taken 3 seconds after deoxidation of melt with 0.3 mass% aluminium addition in the high frequency furnace.

Total oxygen content of the sample 290 ppm.

SEM Micrograph

Magnification 2,600 X

Showing a large cluster of inclusions, containing dendritic, spherical and polyhedral inclusion morphologies. The dendritic inclusions exhibit thickening and growths between stems and branches resulting in spear shaped tips. Small clusters containing polyhedral and spherical inclusions are observed contacting the larger clusters.

Plate 4.21

Sample AHF 4. Suction sample taken 21 seconds after deoxidation of melt with 0.3 mass% aluminium addition in the high frequency furnace.

Total oxygen content of the sample 153 ppm.

SEM Micrograph

Magnification 7,000 X

Dendritic inclusions exhibiting growth faults and fracturing of the dendrite arms.

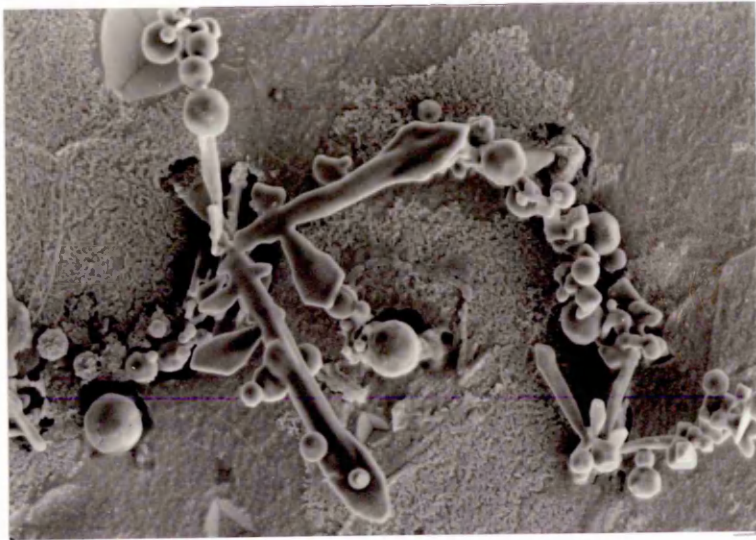
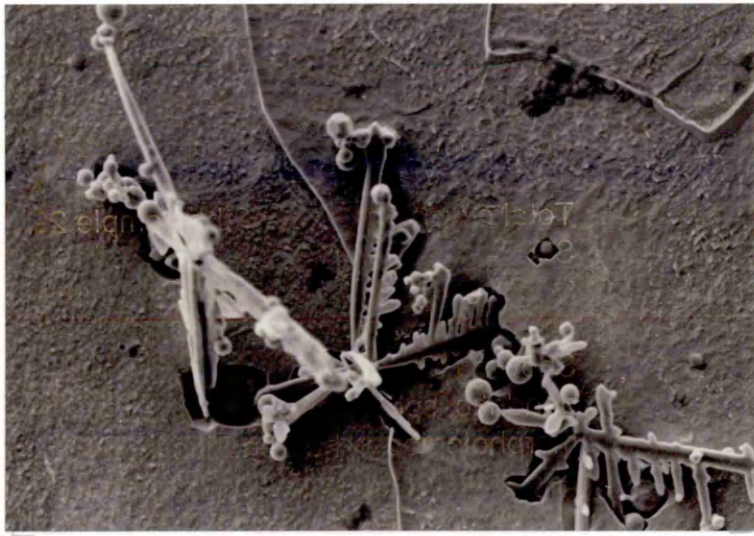


Plate 4.22

Sample AHF 2. Suction sample taken 3 seconds after deoxidation of melt with 0.3 mass% aluminium addition in the high frequency furnace.

Total oxygen content of the sample 290 ppm.
SEM Micrograph
Magnification 3,400 X

Showing a small cluster of inclusions, containing spherical and polyhedral inclusion morphologies contacting a larger cluster containing dendritic inclusions. Polycrystalline sintered agglomerates are also observed

Plate 4.23

Sample AHF 17. Suction sample taken 225 seconds after deoxidation of melt with 0.3 mass% aluminium addition in the high frequency furnace.

Total oxygen content of the sample 31 ppm.
SEM Micrograph
Magnification 12,500 X

Small inclusion cluster composed of polyhedral and sub-angular inclusions, exhibiting well developed sintered contacts.

Plate 4.24

Sample AHF 14. Suction sample taken 139 seconds after deoxidation of melt with 0.3 mass% aluminium addition in the high frequency furnace.

Total oxygen content of the sample 31 ppm.
SEM Micrograph
Magnification 5,000 X

A group of secondary dendrites associated with small clusters of polyhedral and sub-angular inclusions. The dendrite stems can be observed emanating from the corners of pre-existing polyhedral inclusions.

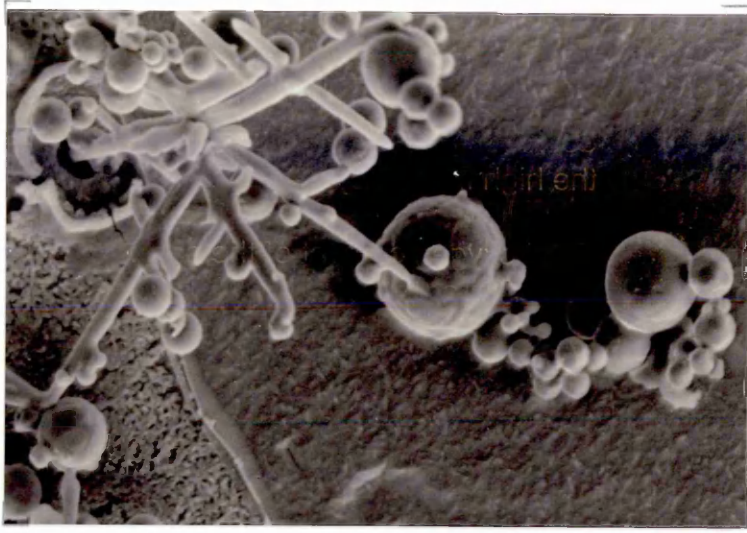


Plate 4.25

Sample AHF 16. Suction sample taken 195 seconds after deoxidation of melt with 0.3 mass% aluminium addition in the high frequency furnace.

Total oxygen content of the sample 27 ppm.

SEM Micrograph

Magnification 10,000 X

A secondary dendrite with the dendrite stems emanating from each corner of a hexagonal plate-like inclusion.

Plate 4.26

Sample TVT 1. Suction sample taken before deoxidation of melt with 0.53 mass% titanium addition in the vertical tube furnace.

Total oxygen content of the sample 530 ppm.

SEM Micrograph

Magnification 2,600 X

Showing an interdendritic network of Fe-Mn-Al oxide inclusions.

Plate 4.27

Sample TVT 4. Suction sample taken 34 seconds after deoxidation of melt with 0.53 mass% titanium addition in the vertical tube furnace.

Total oxygen content of the sample 450 ppm.

SEM Micrograph

Magnification 2,600 X

Showing a cluster of spherical and polyhedral inclusion morphologies. Microanalysis results indicated that the inclusions with in this sample were mainly composed of Ti_2O_3 .

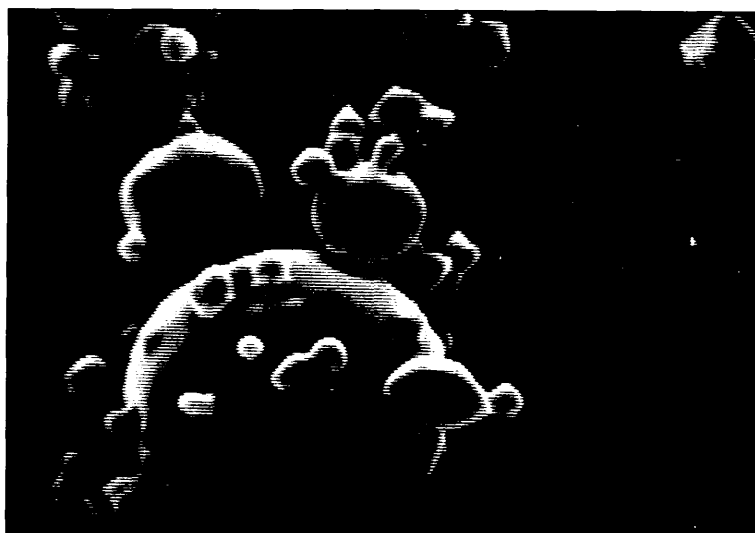
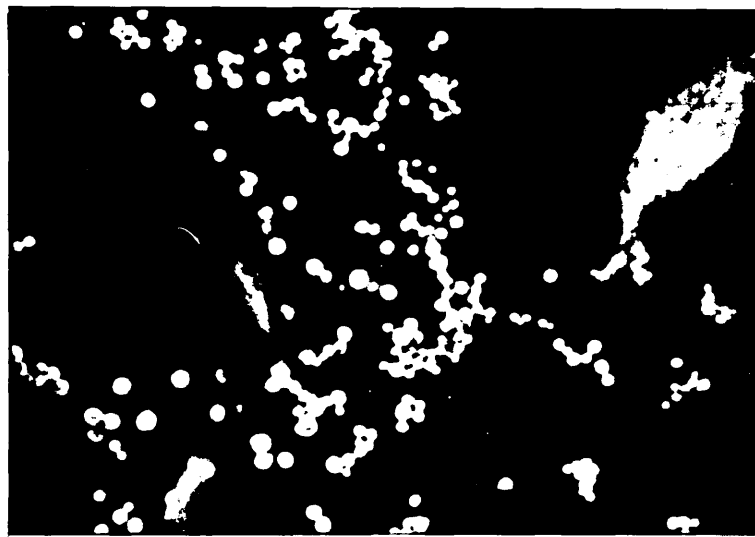


Plate 4.28

Sample TVT 6. Suction sample taken 58 seconds after deoxidation of melt with 0.53 mass% titanium addition in the vertical tube furnace.

Total oxygen content of the sample 240 ppm.
Optical Micrograph
Magnification 1,000 X

Showing a cluster of inclusions in plane section under polarised light. The inclusions exhibit pleochroism which indicates that the inclusions are polymorphic. Some inclusions also exhibit porosity.

Plate 4.29

Sample TVT 4. Suction sample taken 34 seconds after deoxidation of melt with 0.53 mass% titanium addition in the vertical tube furnace.

Total oxygen content of the sample 450ppm.
SEM Micrograph
Magnification 3,200 X

Showing a cluster of globular, polyhedral and octahedral inclusion morphologies.

Plate 4.30

Sample TVT 6. Suction sample taken 58 seconds after deoxidation of the melt with 0.53 mass% titanium addition in the vertical tube furnace.

Total oxygen content of the sample 240 ppm.
SEM Micrograph
Magnification 3,200 X

Showing a cluster of globular and polyhedral inclusion morphologies. A highly faceted polyhedral inclusion can be seen exhibiting a porosity 'exit hole'. Necks are also observed between adjacent inclusions.

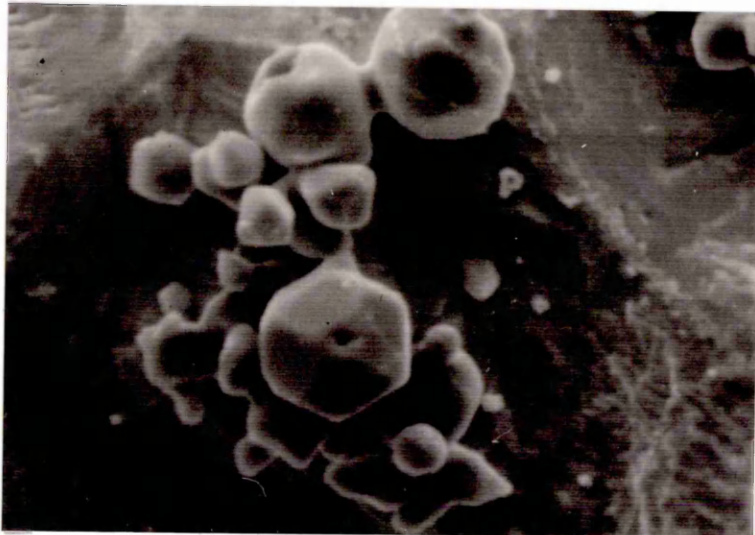
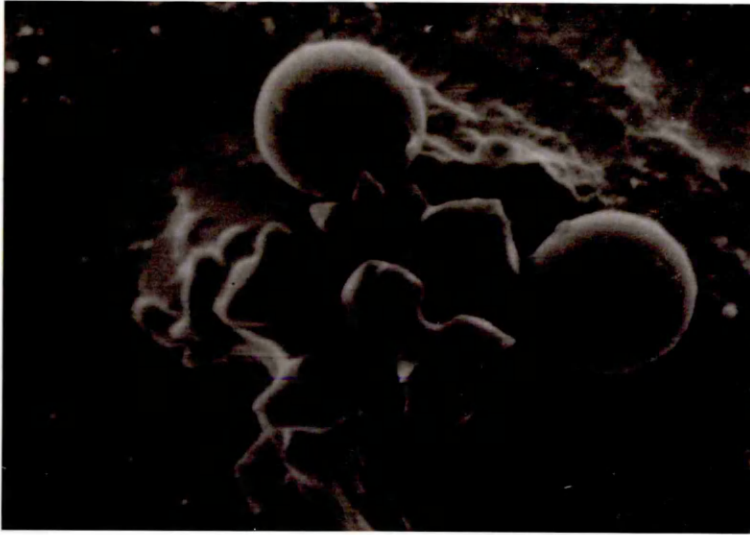
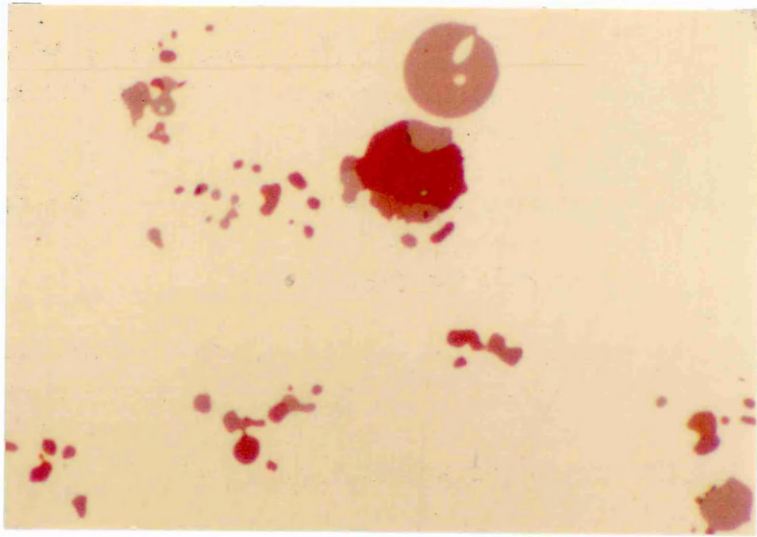


Plate 4.31

Sample TVT 9. Suction sample taken 100 seconds after deoxidation of melt with 0.53 mass% titanium in the vertical tube furnace.

Total oxygen content of the sample 150 ppm.
SEM Micrograph
Magnification 6,400 X

Showing an inclusion cluster exhibiting highly developed sintered contacts (necks) between adjacent inclusions.

Plate 4.32

Sample THF 2. Suction sample taken 3 seconds after deoxidation of melt with 0.53 mass% titanium in the high frequency furnace.

Total oxygen content of the sample 310 ppm.
SEM Micrograph
Magnification 1,800 X

Showing an inclusion cluster containing globular and polyhedral inclusion morphologies. Also observed are numerous small random/spherical inclusions.

Plate 4.33

Sample THF 2. Suction sample taken 3 seconds after deoxidation of melt with 0.53 mass% titanium in the high frequency furnace.

Total oxygen content of the sample 310 ppm.
SEM Micrograph
Magnification 2,900 X

Showing an inclusion cluster containing large spherical and polyhedral inclusion morphologies. The stages in the development of large spherical inclusion morphologies are observed.

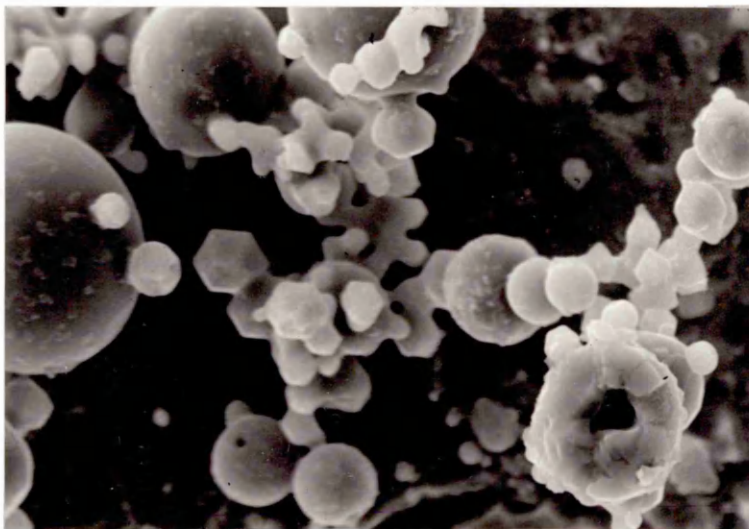
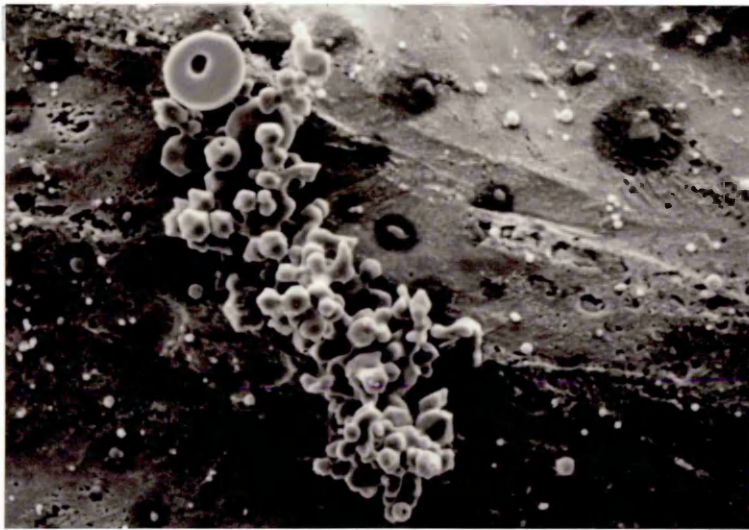
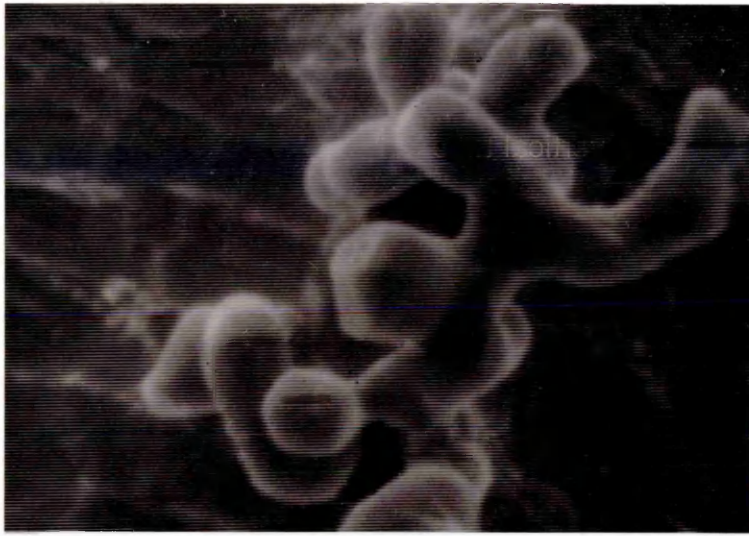


Plate 4.34

Sample THF 2. Suction sample taken 3 seconds after deoxidation of melt with 0.53 mass% titanium in the high frequency furnace.

Total oxygen content of the sample 310 ppm.
Optical Micrograph
Magnification 1,000 X

Showing a cluster of inclusions in plane section under polarised light. The inclusions exhibit a colour change when rotated in polarised light indicating they are composed of Ti_2O_3 . Some inclusions also exhibit porosity.

Plate 4.35

Sample THF 2. Suction sample taken 3 seconds after deoxidation of melt with 0.53 mass% titanium in the high frequency furnace.

Total oxygen content of the sample 310 ppm.
SEM Micrograph
Magnification 3,900 X

Showing small spherical and polyhedral inclusions diffusing into a large sub-spherical agglomerate.

Plate 4.36

Sample SVT 2. Suction sample taken prior to deoxidation of melt with 0.3mass% silicon in the vertical tube furnace.

Total oxygen content of the sample 570 ppm.
SEM Micrograph
Magnification 3,200 X

Showing a typical interdendritic distribution of spherical Fe-Mn-Al oxide particles.

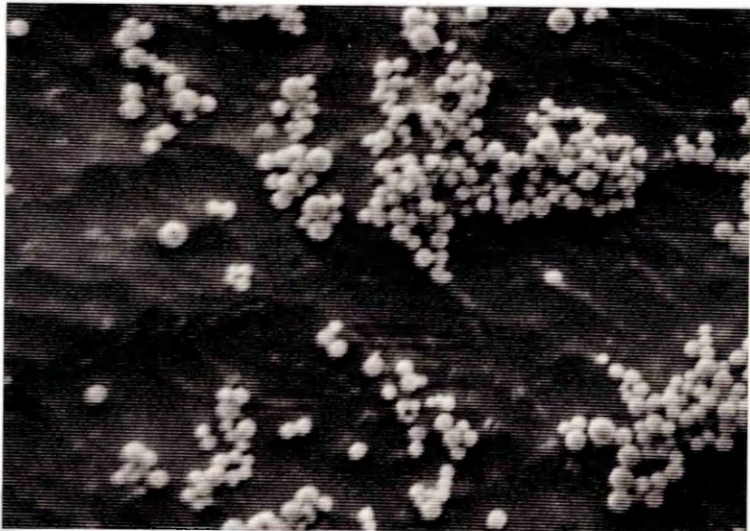
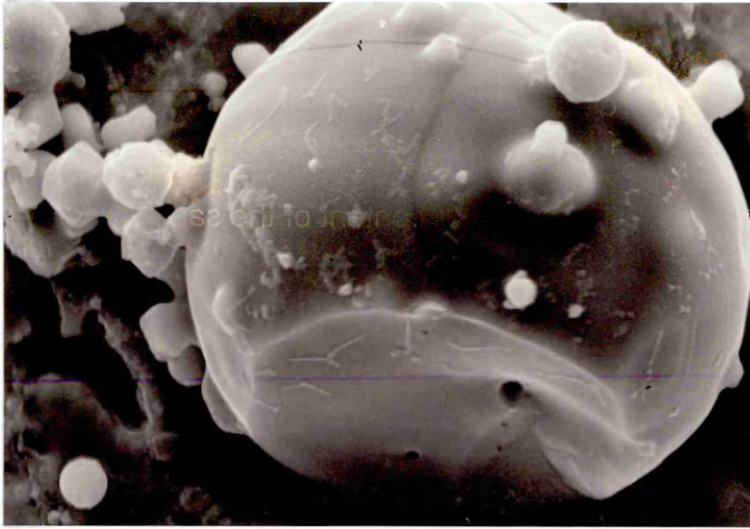
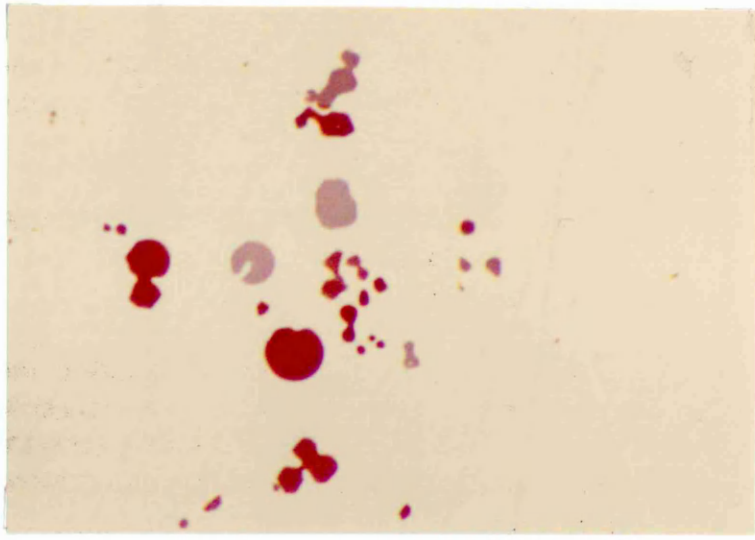


Figure 1

Plate 4.37

Sample SVT 4. Suction sample taken 24 seconds after deoxidation of melt with 0.3 mass% silicon in the vertical tube furnace.

Total oxygen content of the sample 540 ppm.
SEM Micrograph
Magnification 6,400 X

Showing a typical small group of spherical silica inclusions. Sintered contacts and the formation of necks between adjacent inclusions are observed.

Plate 4.38

Sample SVT 6. Suction sample taken 53 seconds after deoxidation of melt with 0.3 mass% silicon in the vertical tube furnace.

Total oxygen content of the sample 510 ppm.
SEM Micrograph
Magnification 3,200 X

Showing a small group of spherical silica inclusions, some inclusions exhibit well developed sintered contacts.

Plate 4.39

Sample SVT 10. Suction sample taken 128 seconds after deoxidation of melt with 0.3 mass% silicon in the vertical tube furnace.

Total oxygen content of the sample 435 ppm.
SEM Micrograph
Magnification 15,000 X

Showing well developed dendritic type growths emanating from the surface of the spherical silica inclusions.

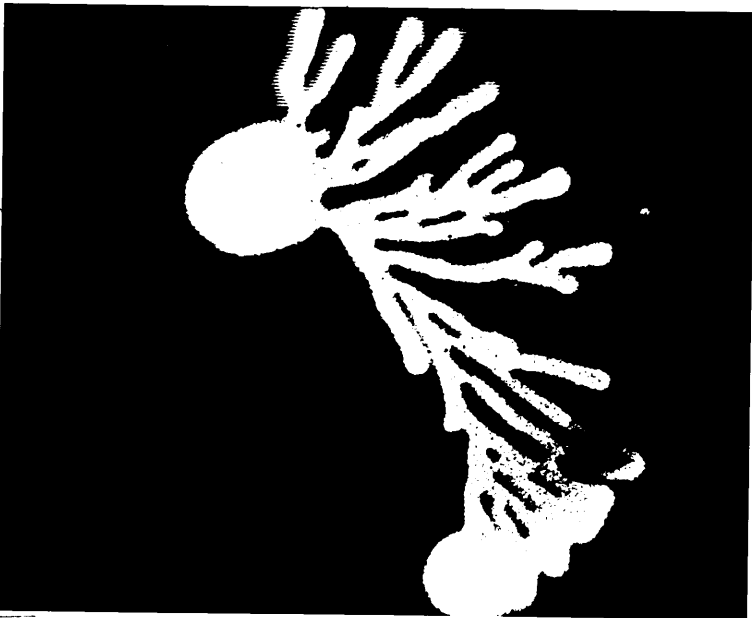
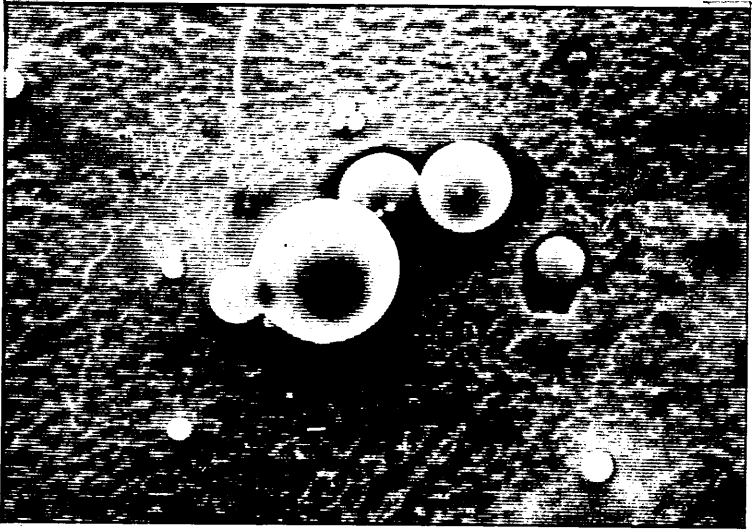
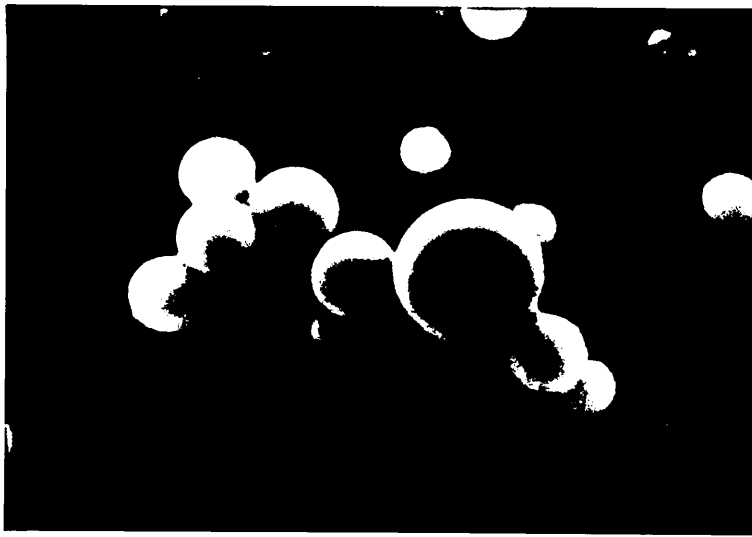


Plate 4.40

Sample SHF 2. Suction sample taken one seconds after deoxidation of melt with 0.3 mass% silicon in the high frequency furnace.

Total oxygen content of the sample 520 ppm.
SEM Micrograph
Magnification 3,200 X

Showing randomly distributed and small groups of silica inclusions some of which exhibit sintered contacts and the formation of necks.

Plate 4.41

Sample SHF 6. Suction sample taken 37 seconds after deoxidation of melt with 0.3 mass% silicon in the high frequency furnace.

Total oxygen content of the sample 320 ppm.
SEM Micrograph
Magnification 3,200 X

Showing randomly distributed and small groups of silica inclusions some of which exhibit the formation of necks between adjacent inclusions.

Plate 4.42

Sample SHF 5. Suction sample taken 28 seconds after deoxidation of melt with 0.3 mass% silicon in the high frequency furnace.

Total oxygen content of the sample 390 ppm.
SEM Micrograph
Magnification 6,400 X

Showing poorly developed dendritic type growths emanating from the surface of a number of spherical silica inclusions.

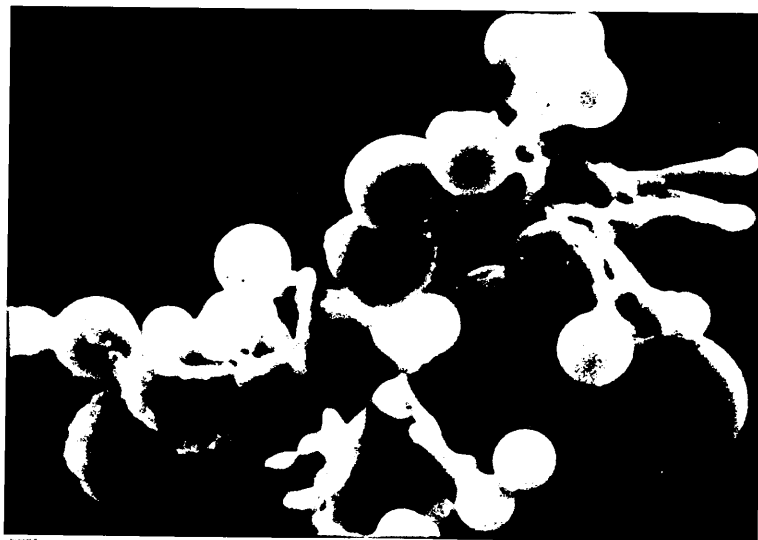
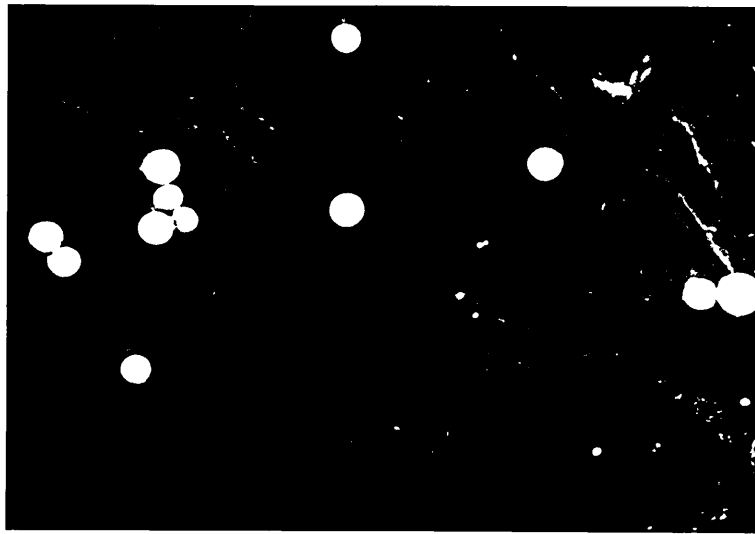
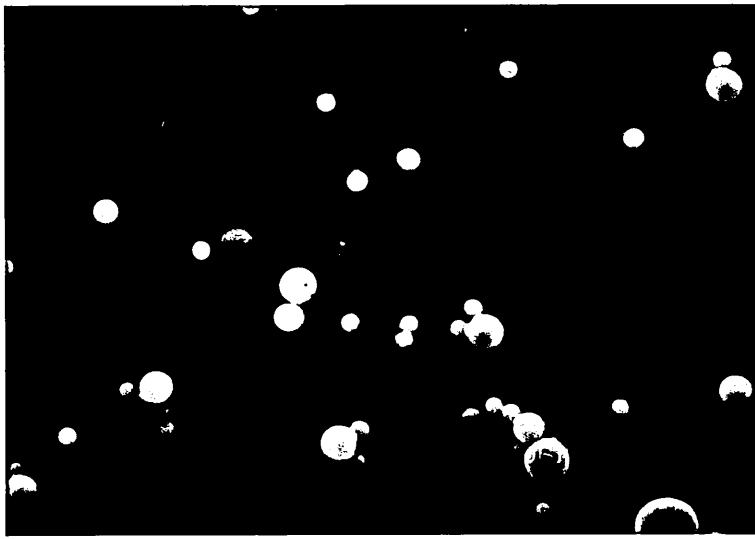


Plate 4.43

Sample CAHF 5. Suction sample taken 30 seconds after deoxidation of melt with 0.32 mass% calcium-aluminium in the high frequency furnace.

Total oxygen content of the sample 177 ppm.
SEM Micrograph
Magnification 3,000 X

Showing polyhedral and hexagonal morphologies forming a large inclusion cluster.

Chemical composition of specific inclusions

Oxide mass%			
	Al ₂ O ₃	CaO	FeO
A	87	10	3
B	87	10	3
C	87	10	3

Plate 4.44

Sample CAHF 5. Suction sample taken 30 seconds after deoxidation of melt with 0.32 mass% calcium-aluminium in the high frequency furnace.

Total oxygen content of the sample 177 ppm.
SEM Micrograph
Magnification 3,000 X

Showing polymorphic, hexagonal and large globular morphologies forming a large inclusion cluster.

Chemical composition of specific inclusions

Oxide mass%			
	Al ₂ O ₃	CaO	FeO
D	82	17	2
E	91	4	5
F	84	13	3

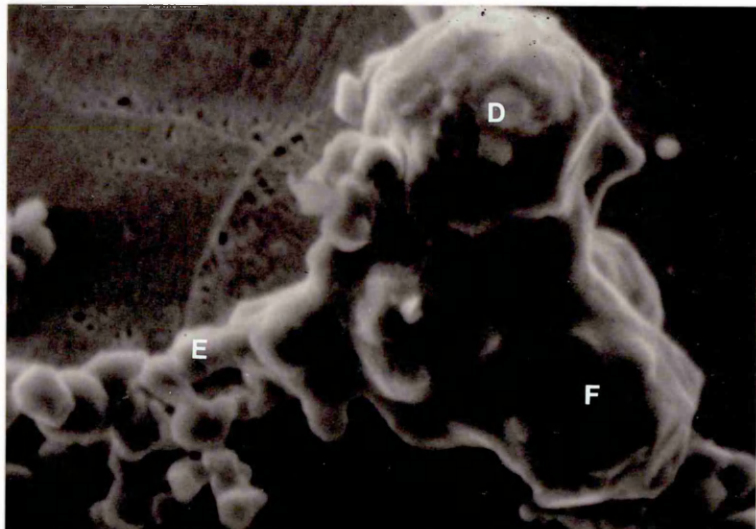
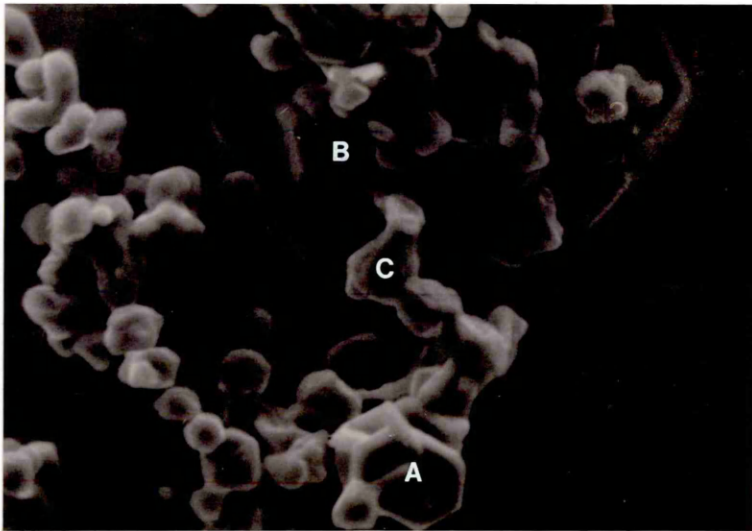


Plate 4.45

Sample CAHF 5. Suction sample taken 30 seconds after deoxidation of melt with 0.32 mass% calcium-aluminium in the high frequency furnace.

Total oxygen content of the sample 177 ppm.

SEM Micrograph

Magnification 5,000 X

Showing a large number of hexagonal morphologies, together with small globular and polymorphic inclusions.

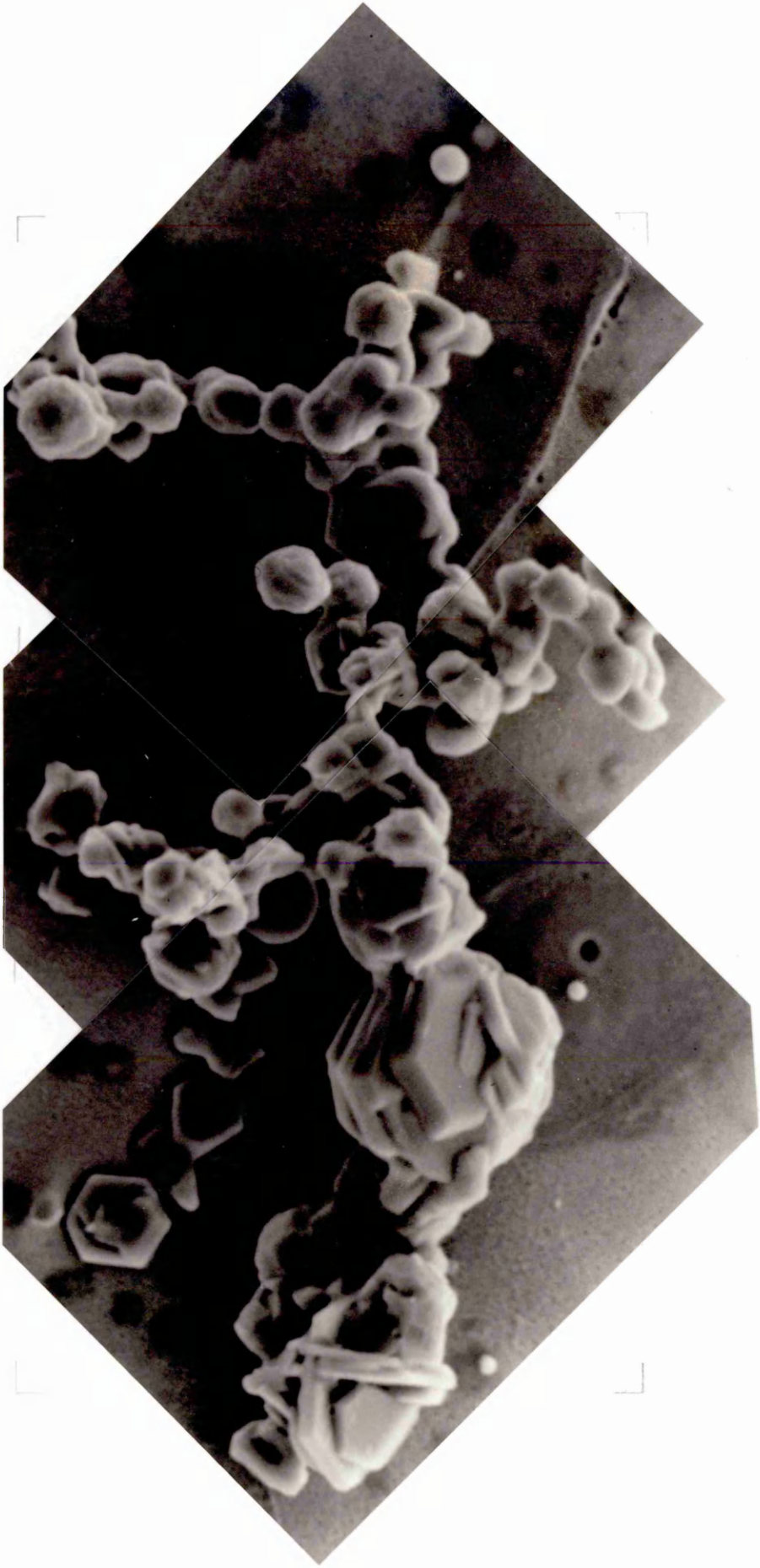


Plate 4.46

Sample CAHF 4. Suction sample taken 19 seconds after deoxidation of melt with 0.32 mass% calcium-aluminium in the high frequency furnace.

Total oxygen content of the sample 267 ppm.
SEM Micrograph
Magnification 5,500 X

Showing a large spherical morphology with a porosity hole at the surface associated with small spherical and hexagonal inclusions.

Plate 4.47

Sample CAHF 5. Suction sample taken 30 seconds after deoxidation of melt with 0.32 mass% calcium-aluminium in the high frequency furnace.

Total oxygen content of the sample 177 ppm.
SEM Micrograph
Magnification 3,000 X

Showing a large number of hexagonal morphologies, together with small globular and polymorphic inclusions.

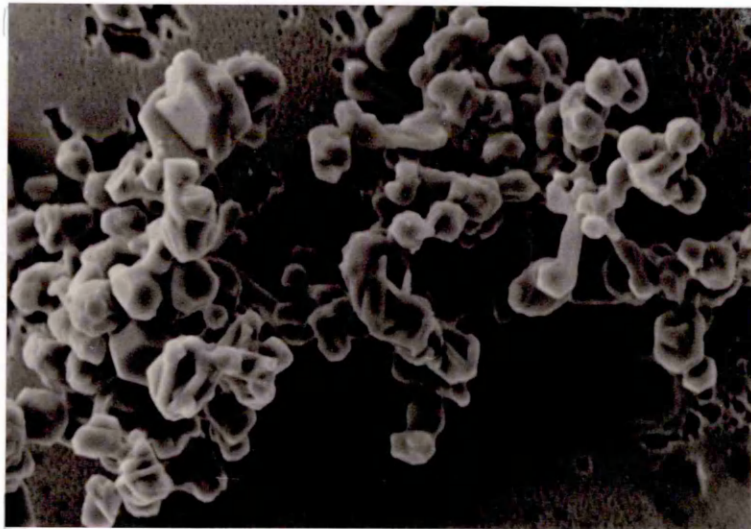
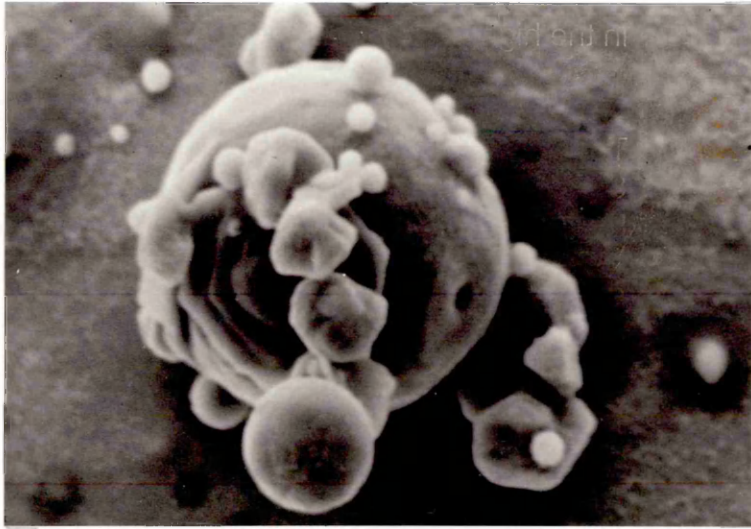


Plate 4.48

Sample ZVT 1. Suction sample taken prior to deoxidation of melt with 1.01 mass% zirconium in the vertical tube furnace.

Total oxygen content of the sample 390 ppm.
SEM Micrograph
Magnification 1,000 X

Showing a typical interdendritic distribution of spherical Fe-Mn-Al oxide particles.

Plate 4.49

Sample ZVT 6. Suction sample taken 37 seconds after deoxidation of melt with 1.01 mass% zirconium in the vertical tube furnace.

Total oxygen content of the sample 413 ppm.
SEM Micrograph
Magnification 2,500 X

Showing well developed dendritic type morphology with branches formed at right angles to the main dendrite arms.

Plate 4.50

Sample ZVT 6. Suction sample taken 37 seconds after deoxidation of melt with 1.01 mass% zirconium in the vertical tube furnace.

Total oxygen content of the sample 413 ppm.
SEM Micrograph
Magnification 7,000 X

Showing a dumb-bell type structure consisting of a series of globules growing at right angles from a central body.

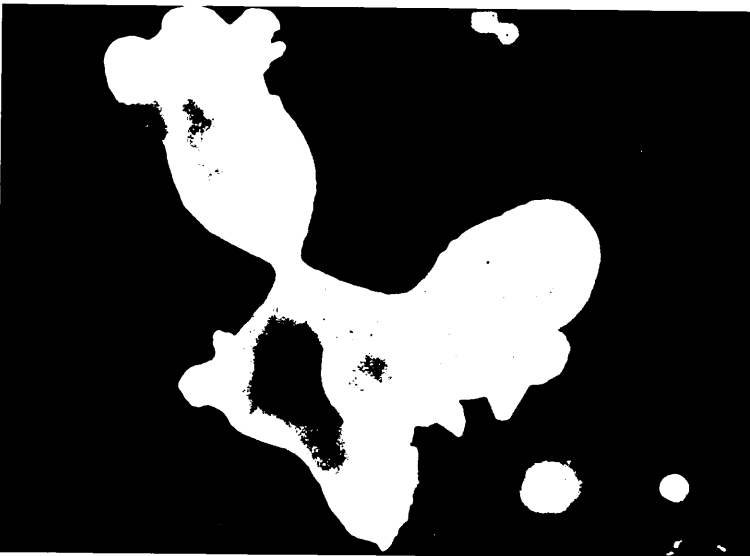
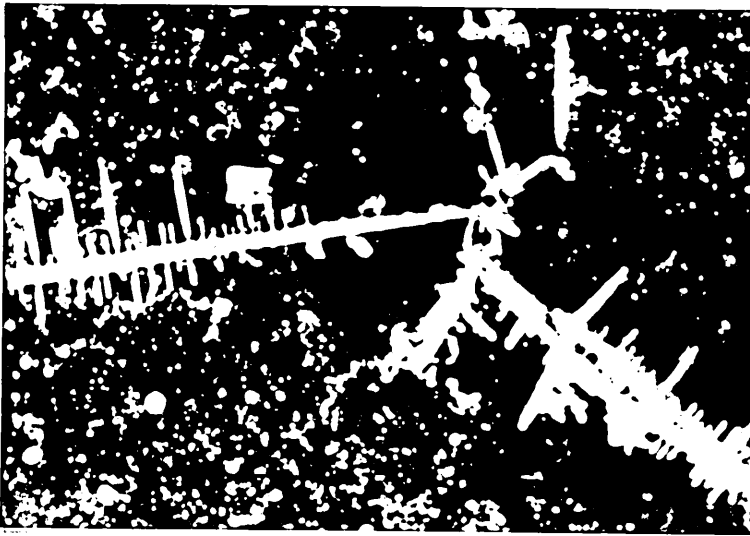
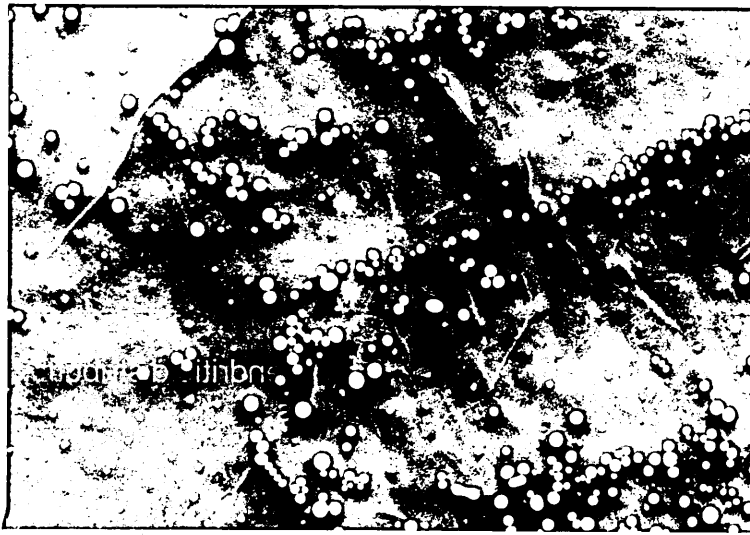


Plate 4.51(a)

Original crucible material.

The energy dispersive X-ray analysis of the points indicated on the micrograph. (JEOL 840 SEM/EDX)

Oxide mass%				
	CaO	Al ₂ O ₃	SiO ₂	MgO
A	36.0		37.0	27.0
B	53.0		35.0	12.0
C				100.0
D		70.0		30.0

SEM Micrograph.

Magnification 200 X

Plate 4.51(b)

Energy dispersive X-ray elemental maps of Plate 4.51(a) for magnesium, aluminium, silicon, calcium and iron. (JEOL 840 SEM/DIGIMAP)

Magnification of each map 100 X

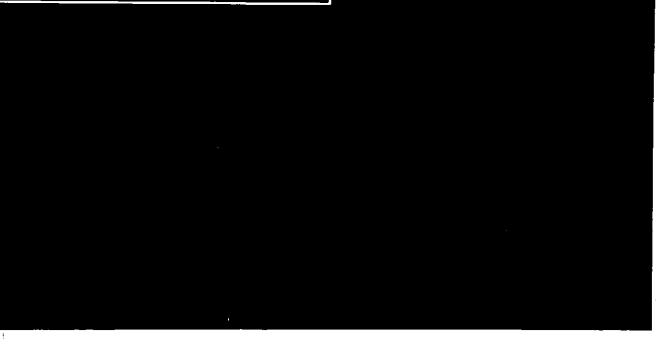
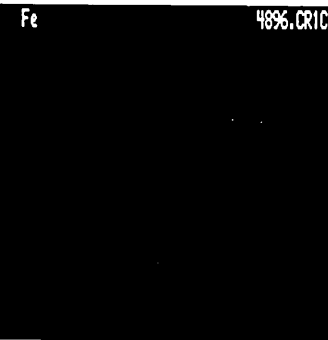
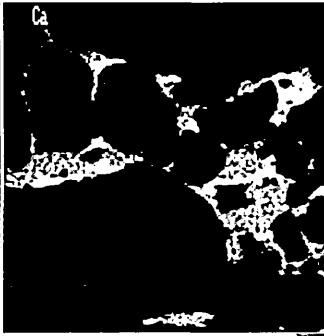
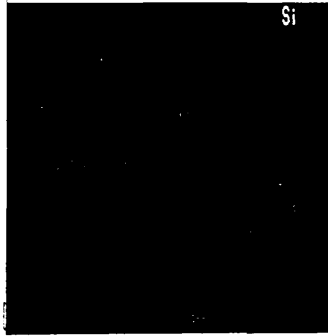
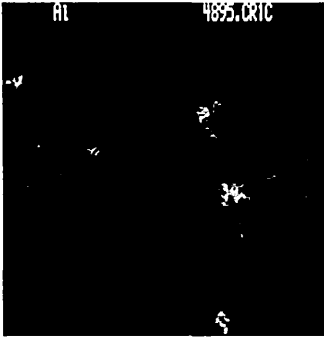
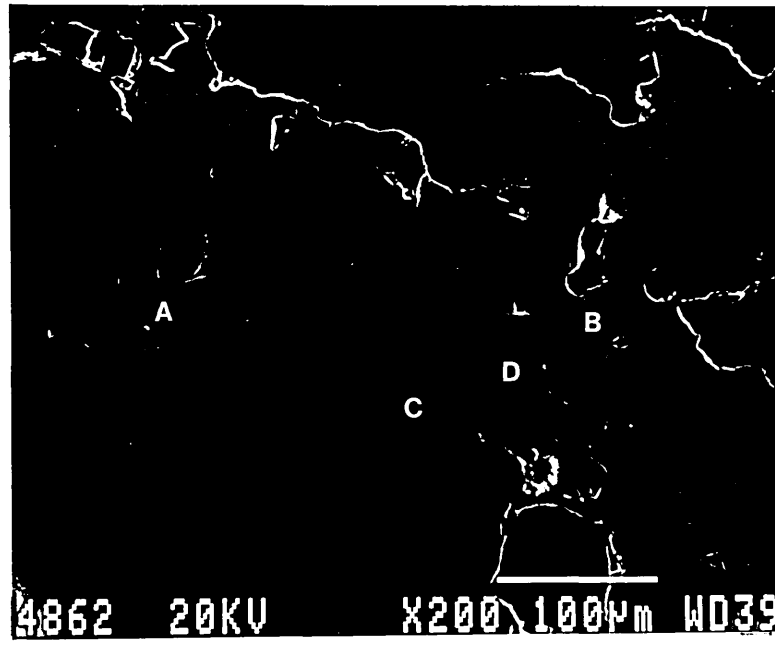


Plate 4.52(a)

Original crucible material.

The energy dispersive X-ray analysis of the points indicated on the micrograph. (JEOL 840 SEM/EDX)

Oxide mass%				
	CaO	Al ₂ O ₃	SiO ₂	MgO
A		69.0		30.0
B	56.0		34.0	10.0
C	36.0		37.0	27.0
D				99.0
E	37.0		37.0	24.0

SEM Micrograph.

Magnification 330 X

Plate 4.52(b)

Energy dispersive X-ray elemental maps of Plate 4.52(a) for magnesium, aluminium, silicon, calcium and iron. (JEOL 840 SEM/DIGIMAP)

Magnification of each map 165 X

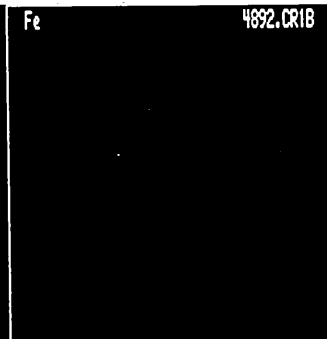
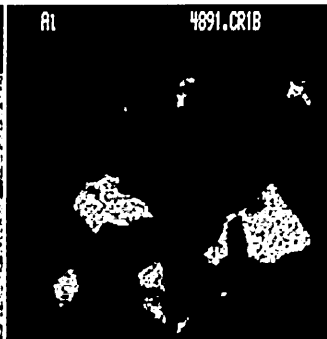
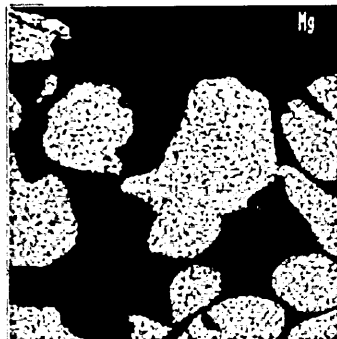
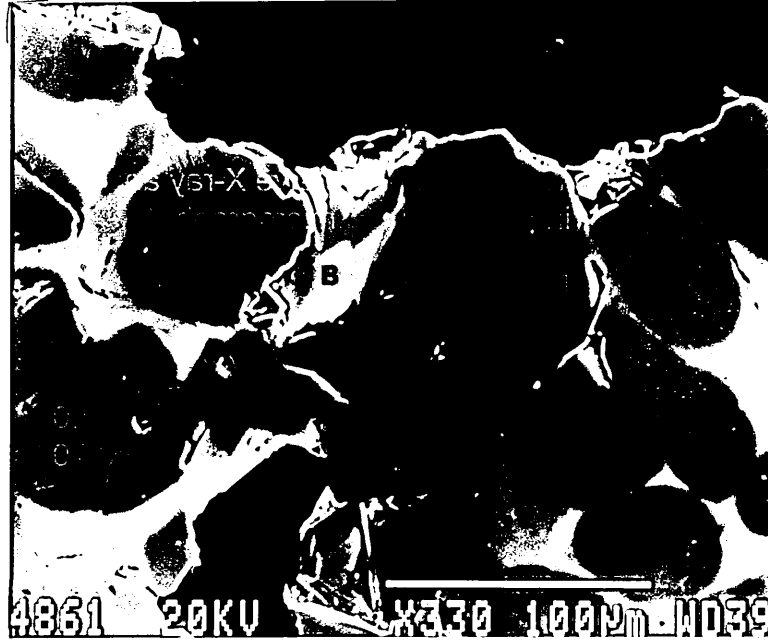


Plate 4.53(a)

Crucible interface which was in contact with an undeoxidised steel melt, in the high frequency furnace.

The energy dispersive X-ray analysis of the points indicated on the micrograph. (JEOL 840 SEM/EDX)

Oxide mass%						
	CaO	Al ₂ O ₃	SiO ₂	MgO	FeO	MnO
A				75.0	19.0	5.0
B				85.0	3.0	2.0
C	37.0		36.0	22.0	11.0	3.0

SEM Micrograph.

Magnification 50 X

Plate 4.53(b)

Energy dispersive X-ray elemental maps of Plate 4.53(a) for magnesium, aluminium, silicon, calcium and iron. (JEOL 840 SEM/DIGIMAP)

Magnification of each map 25 X

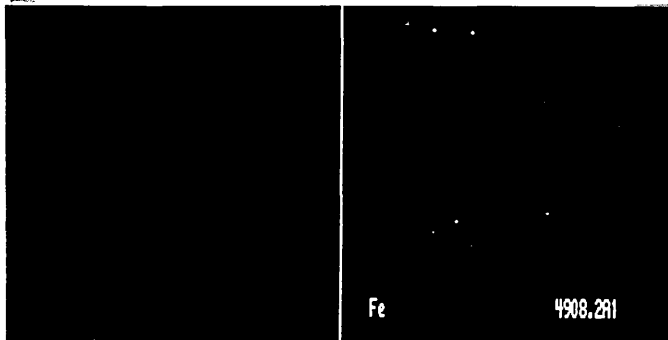
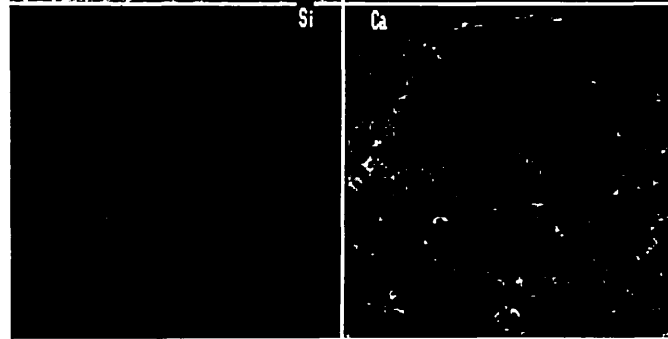
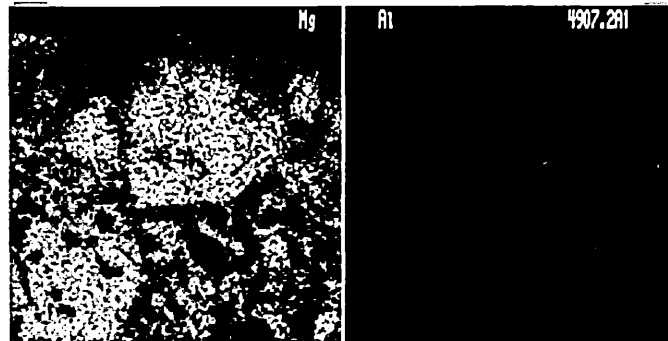


Plate 4.54(a)

Crucible interface which was in contact with an undeoxidised steel melt, in the high frequency furnace.

The energy dispersive X-ray analysis of the points indicated on the micrograph. (JEOL 840 SEM/EDX)

Oxide mass%						
	CaO	Al ₂ O ₃	SiO ₂	MgO	FeO	MnO
A				60.0	32.0	7.0
B		3.0		80.0	13.0	3.0
C	36.0		35.0	20.0	4.0	3.0

SEM Micrograph.

Magnification 330 X

Plate 4.54(b)

Energy dispersive X-ray elemental map of Plate 4.54(a) for iron, indicating that the FeO concentration decreased with distance from the crucible surface. (JEOL 840 SEM/DIGIMAP)

Magnification of each map 165 X

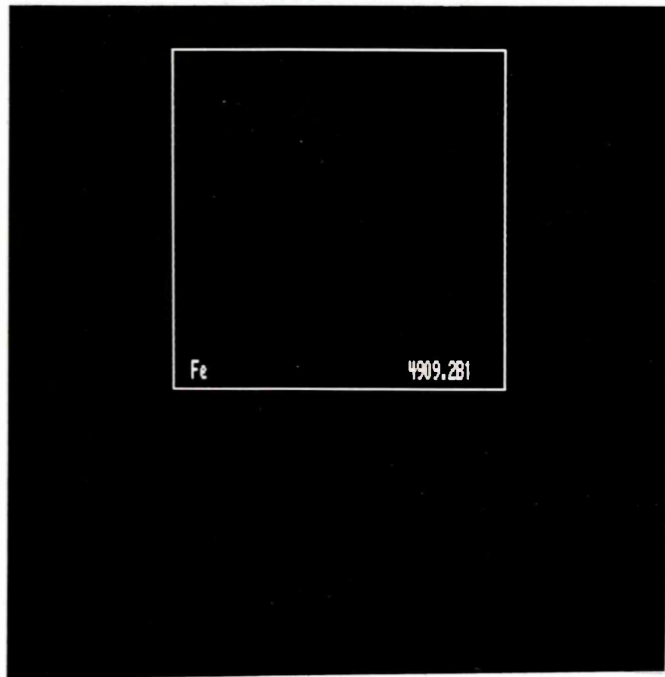
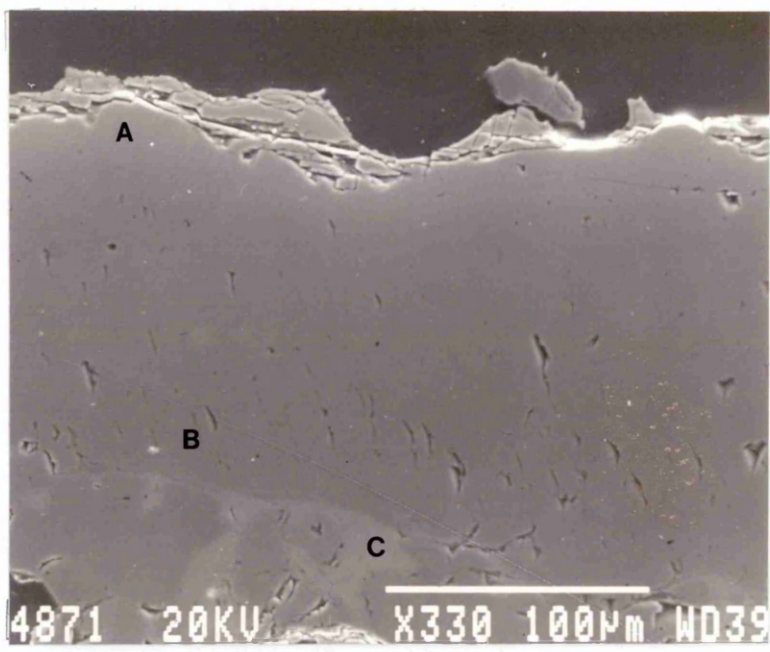


Plate 4.55(a)

Crucible interface which was in contact with an undeoxidised steel melt, in the vertical tube furnace.

The energy dispersive X-ray analysis of the points indicated on the micrograph. (JEOL 840 SEM/EDX)

Oxide mass%						
	CaO	Al ₂ O ₃	SiO ₂	MgO	FeO	MnO
A		14.0		58.0	21.0	6.0
B				73.0	20.0	6.0
C				98.0	2.0	

SEM Micrograph.

Magnification 50 X

Plate 4.55(b)

Energy dispersive X-ray elemental maps of Plate 4.55(a) for magnesium, aluminium, silicon, calcium and iron. (JEOL 840 SEM/DIGIMAP)

Magnification of each map 25 X

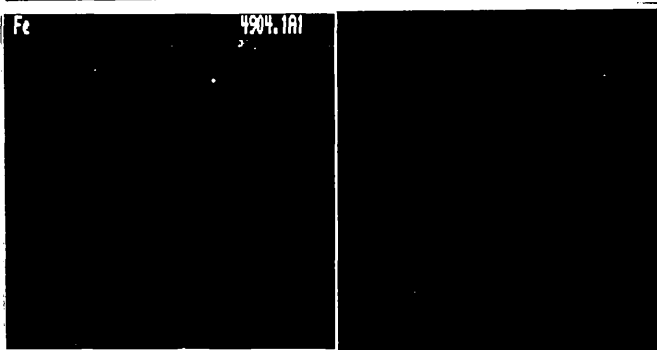
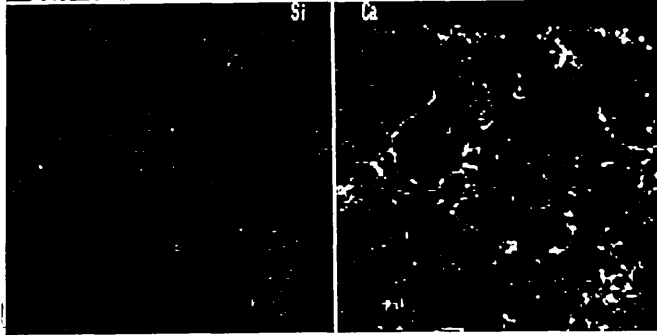
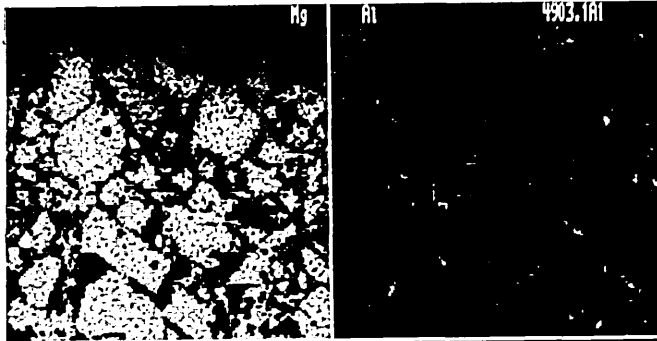
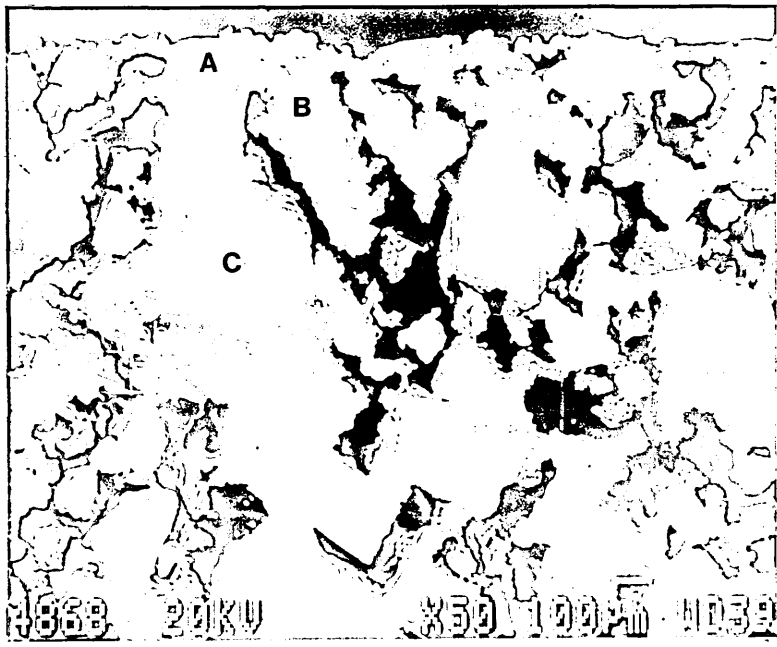


Plate 4.56(a)

Crucible interface which was in contact with an undeoxidised steel melt, in the vertical tube furnace.

The energy dispersive X-ray analysis of the points indicated on the micrograph. (JEOL 840 SEM/EDX)

Oxide mass%						
	CaO	Al ₂ O ₃	SiO ₂	MgO	FeO	MnO
A		62.0		26.0	5.0	2.0
B	53.0		34.0	10.0	2.0	1.0
C				63.0	29.0	7.0

SEM Micrograph.

Magnification 330 X

Plate 4.56(b)

Energy dispersive X-ray elemental maps of Plate 4.56(a) for magnesium, aluminium, silicon, calcium and iron. (JEOL 840 SEM/DIGIMAP)

Magnification of each map 165 X

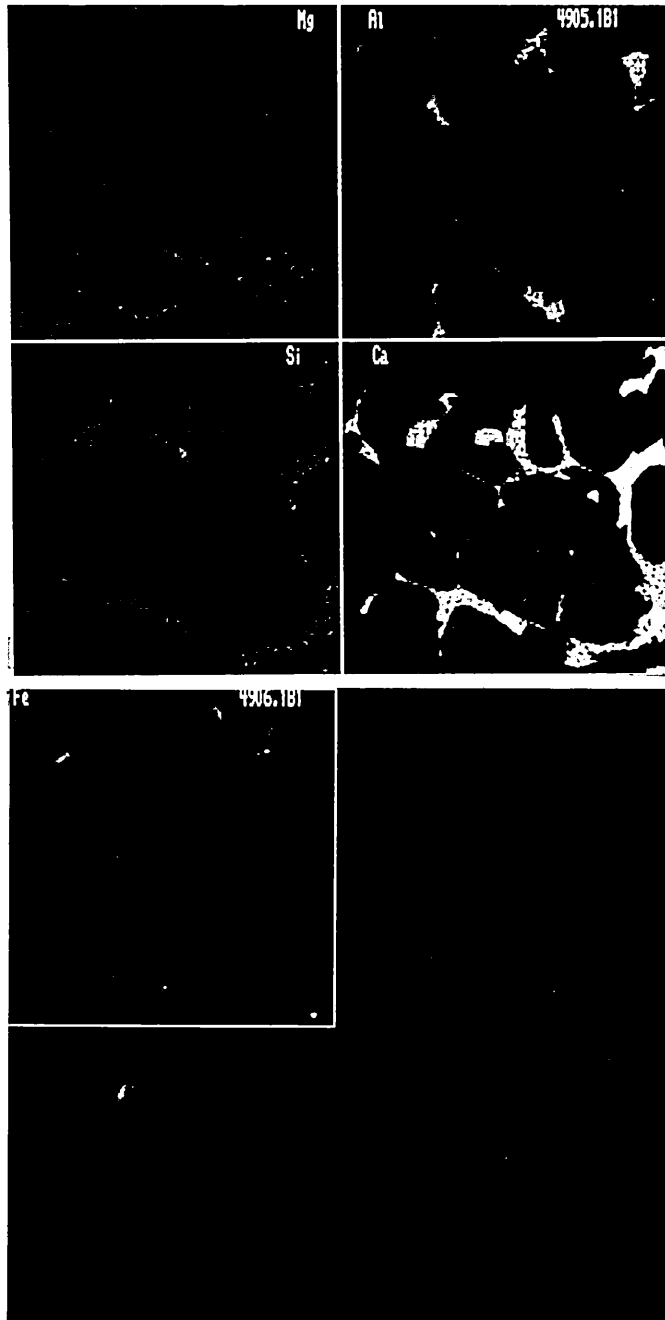
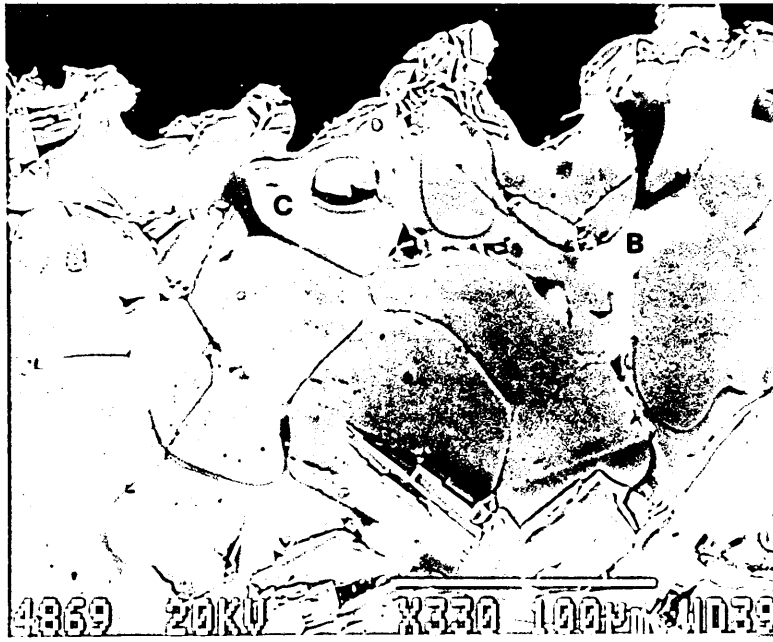


Plate 4.57(a)

Crucible interface which was in contact with the aluminium deoxidised steel melted in the high frequency furnace.

The energy dispersive X-ray analysis of the points indicated on the micrograph. (JEOL 840 SEM/EDX)

Oxide mass%					
	CaO	Al ₂ O ₃	SiO ₂	MgO	FeO
A		2.0		89.0	7.0
B		76.0		24.0	
C	46.0	47.0	3.0	3.0	
D	51.0	40.0	7.0	3.0	

SEM Micrograph.

Magnification 50 X

Plate 4.57(b)

Energy dispersive X-ray elemental maps of Plate 4.57(a) for magnesium, aluminium, silicon, calcium and iron. (JEOL 840 SEM/DIGIMAP)

Magnification of each map 25 X

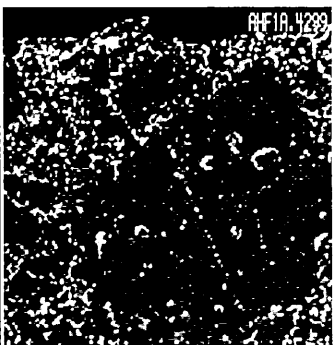
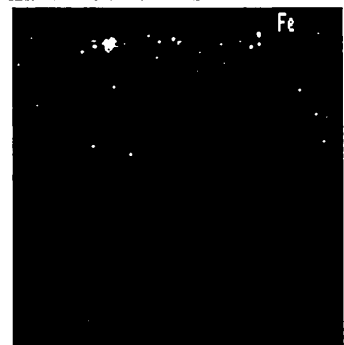
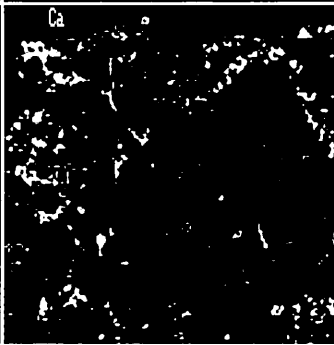
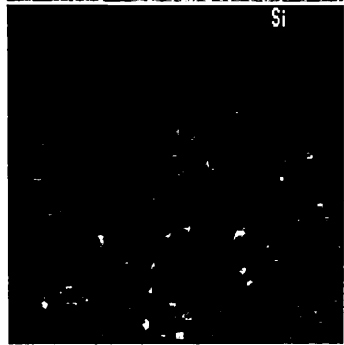
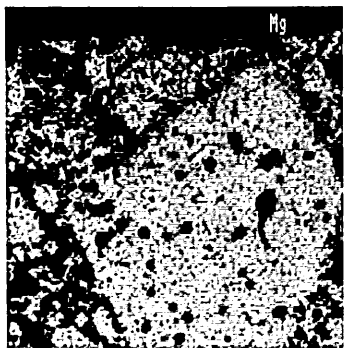
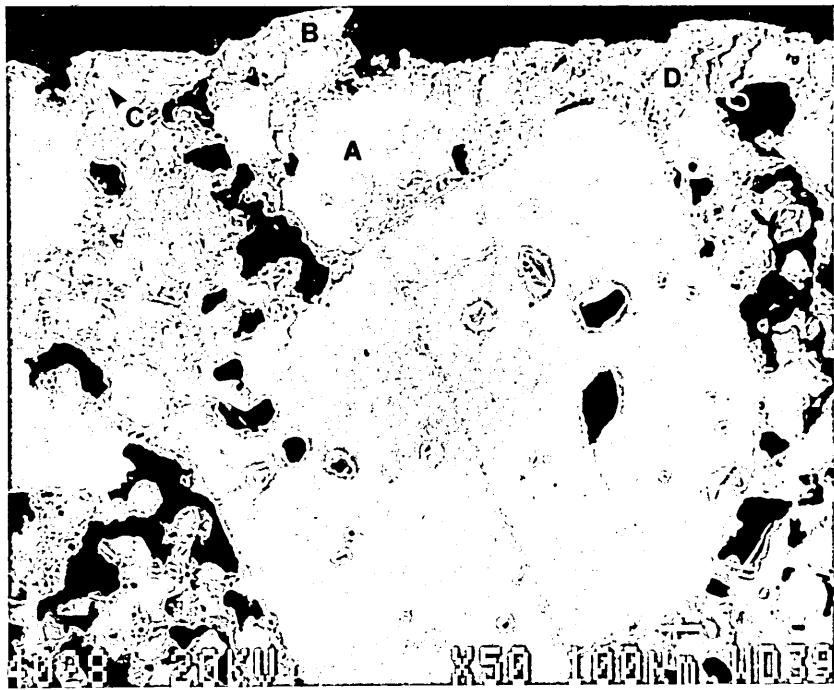


Plate 4.58(a)

Crucible interface which was in contact with the aluminium deoxidised steel melted in the high frequency furnace.

The energy dispersive X-ray analysis of the points indicated on the micrograph.(JEOL 840 SEM/EDX)

	Oxide mass%			
	CaO	Al ₂ O ₃	SiO ₂	MgO
A	44.0	49.0	4.0	4.0
B				100.0
C	47.0	42.0	7.0	3.0
D	46.0	45.0	5.0	3.0
E		2.0		98.0
F	49.0	35.0	10.0	5.0

SEM Micrograph.

Magnification 330 X

Plate 4.58(b)

Energy dispersive X-ray elemental maps of Plate 4.58(a) for magnesium, aluminium, silicon, calcium and iron. (JEOL 840 SEM/DIGIMAP)

Magnification of each map 165 X

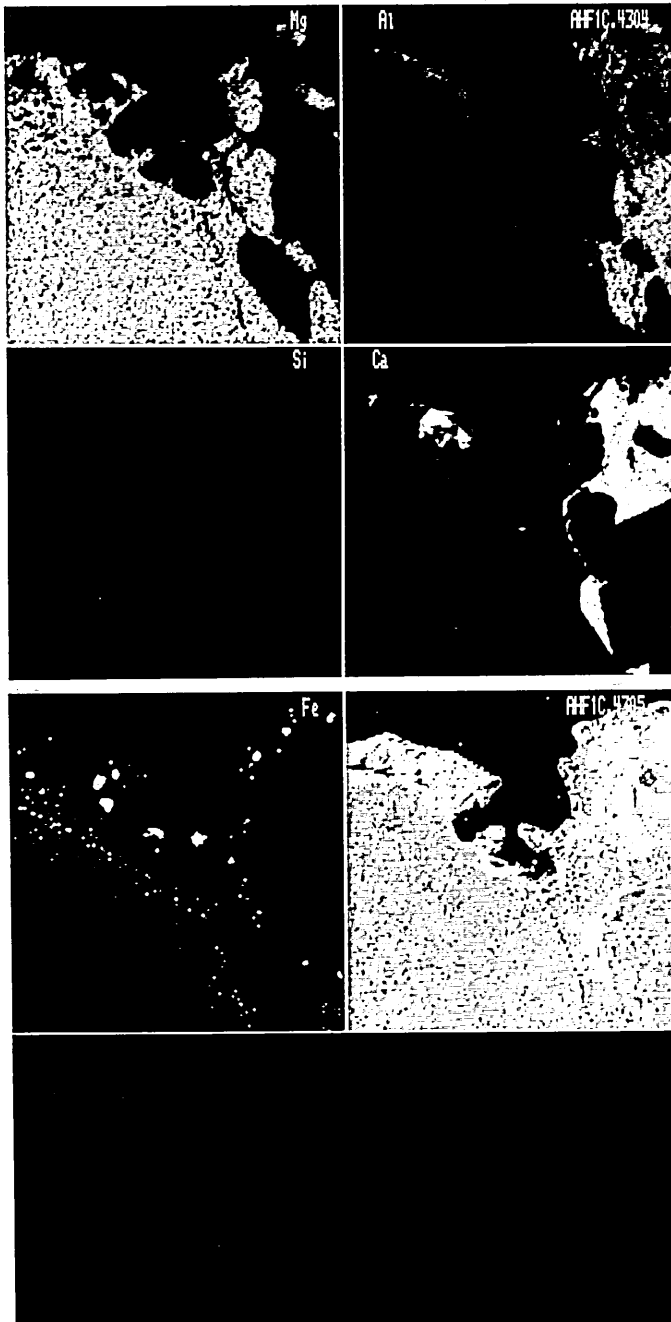
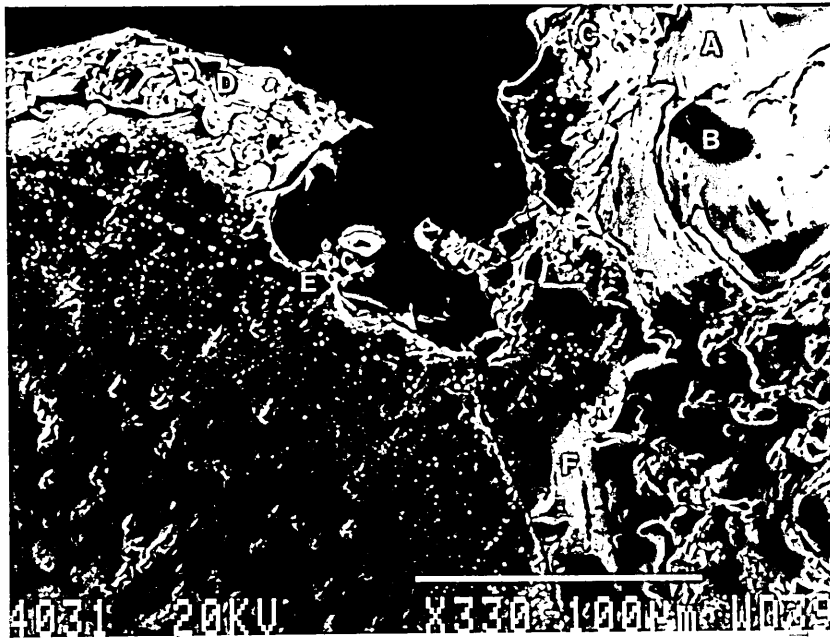


Plate 4.59(a)

Crucible interface which was in contact with the aluminium deoxidised steel melted in the vertical tube furnace.

The energy dispersive X-ray analysis of the points indicated on the micrograph. (JEOL 840 SEM/EDX)

Oxide mass%					
	CaO	Al ₂ O ₃	SiO ₂	MgO	FeO
A		75.0		24.0	
B				94.0	5.0
C	47.0	34.0	7.0	2.0	10.0
D		2.0		78.0	17.0
E		76.0		24.0	
F				72.0	26.0

SEM Micrograph.

Magnification 50 X

Plate 4.59(b)

Energy dispersive X-ray elemental maps of Plate 4.59(a) for magnesium, aluminium, silicon, calcium and iron. (JEOL 840 SEM/DIGIMAP)

Magnification of each map 25 X

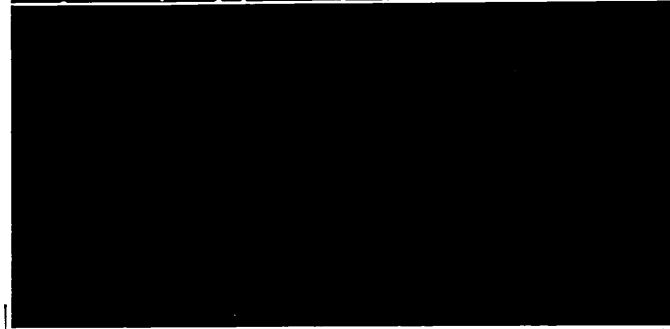
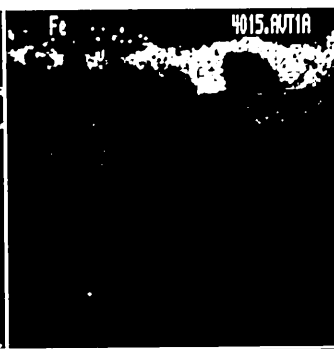
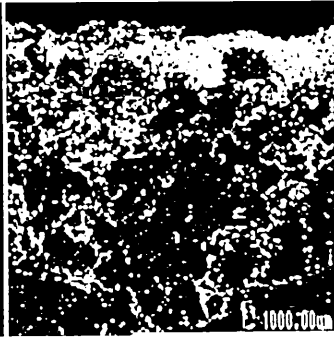
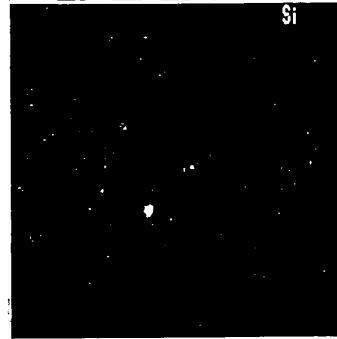
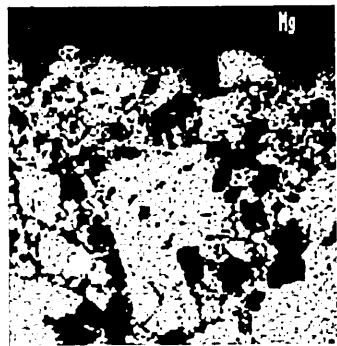
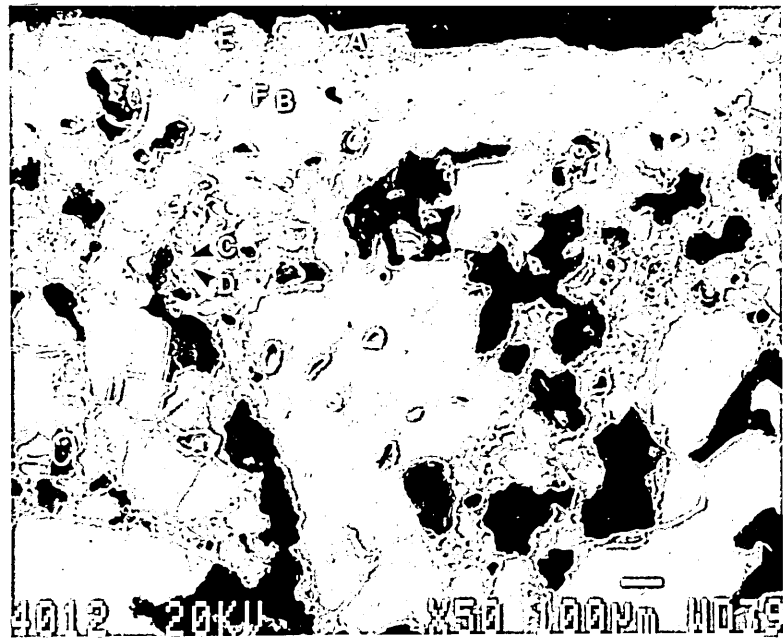


Plate 4.60(a)

Crucible interface which was in contact with the aluminium deoxidised steel melted in the vertical tube furnace.

The energy dispersive X-ray analysis of the points indicated on the micrograph. (JEOL 840 SEM/EDX)

Oxide mass%					
	CaO	Al ₂ O ₃	SiO ₂	MgO	FeO
A	65.0		33.0		1.0
B		75.0		24.0	
C		75.0		24.0	
D		75.0		24.0	
E				33.0	67.0

SEM Micrograph.

Magnification 200 X

Plate 4.60(b)

Energy dispersive X-ray elemental maps of Plate 4.60(a) for magnesium, aluminium, silicon, calcium and iron. (JEOL 840 SEM/DIGIMAP)

Magnification of each map 100 X

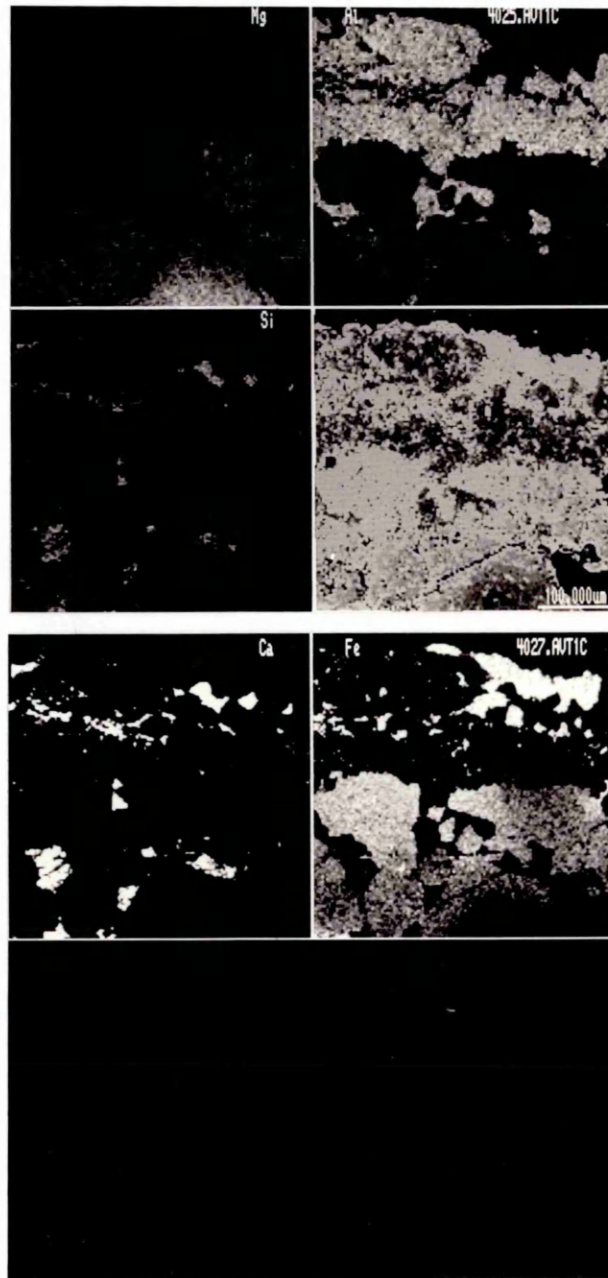
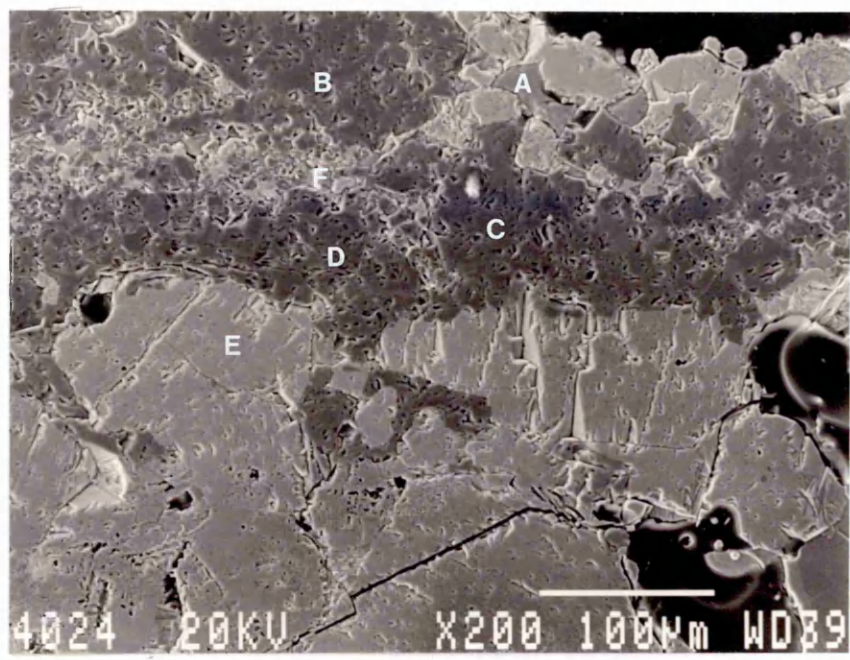


Plate 4.62(a)

Crucible interface which was in contact with the titanium deoxidised steel melted in the vertical tube furnace.

The energy dispersive X-ray analysis of the points indicated on the micrograph. (JEOL 840 SEM/EDX)

Oxide mass%						
	Ti ₂ O ₃ *	CaO	Al ₂ O ₃	SiO ₂	MgO	FeO
A	57.0	41.0				
B	1.0	4.0		48.0	41.0	5.0
C						99.0
D	53.0	36.0		4.0	3.0	2.0

SEM Micrograph.

Magnification 330 X

* assuming that titanium bearing phase is the same as that observed in the inclusions.

Plate 4.62(b)

Energy dispersive X-ray elemental maps of Plate 4.62(a) for magnesium, aluminium, silicon, calcium, titanium, manganese and iron. (JEOL 840 SEM/DIGIMAP)

Magnification of each map 165 X

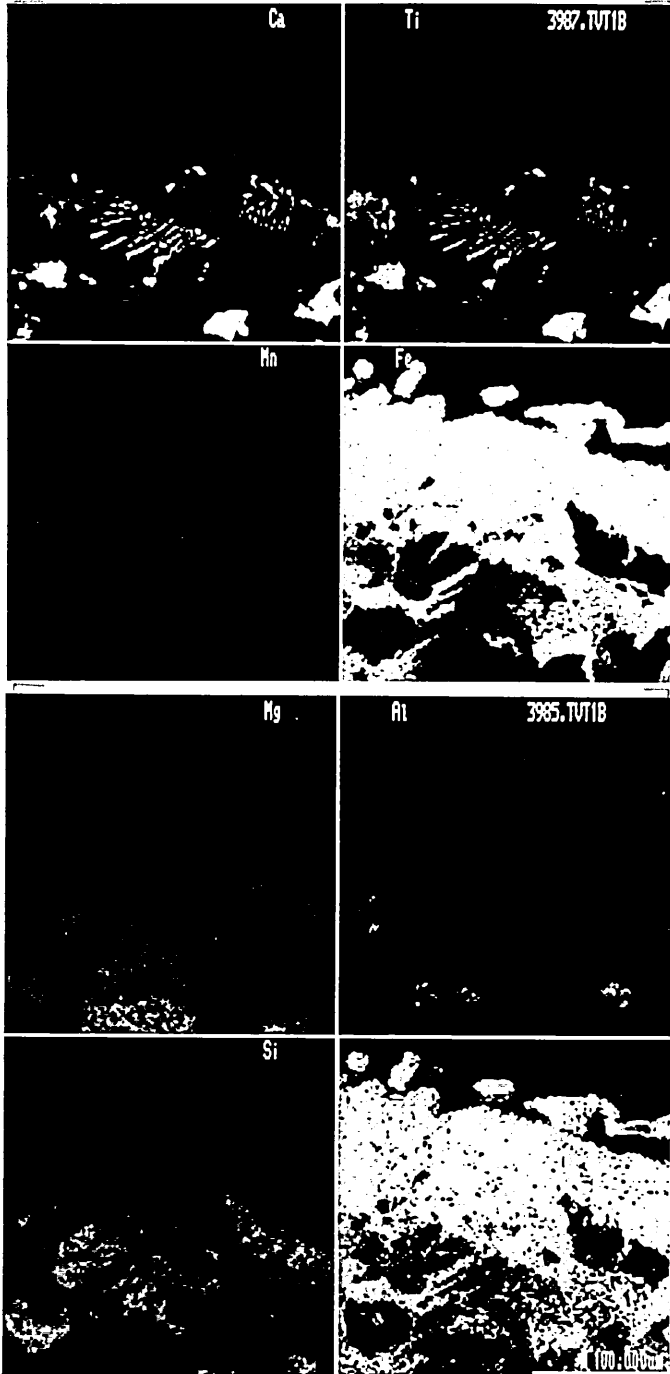
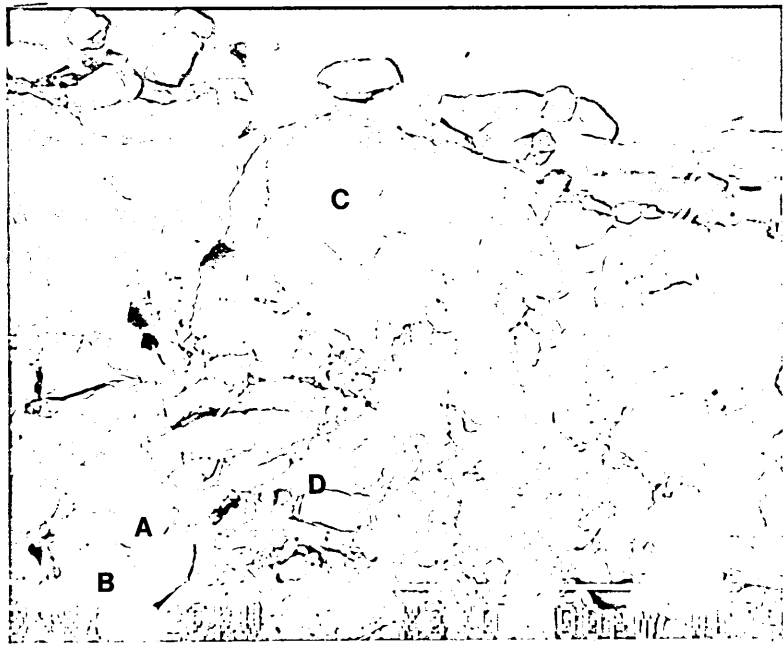


Plate 4.63(a)

Crucible interface which was in contact with the titanium deoxidised steel melted in the vertical tube furnace.

The energy dispersive X-ray analysis of the points indicated on the micrograph. (JEOL 840 SEM/EDX)

Oxide mass%						
	Ti ₂ O ₃ *	CaO	Al ₂ O ₃	SiO ₂	MgO	FeO
A	54.0	38.0		4.0	4.0	
B	2.0				90.0	8.0
C	57.0	41.0				
D	1.0	5.0		49.0	41.0	1.0

SEM Micrograph.

Magnification 450 X

* assuming that titanium bearing phase is the same as that observed in the inclusions.

Plate 4.63(b)

Energy dispersive X-ray elemental maps of Plate 4.63(a) for magnesium, aluminium, silicon, calcium, titanium, manganese and iron. (JEOL 840 SEM/DIGIMAP)

Magnification of each map 225 X

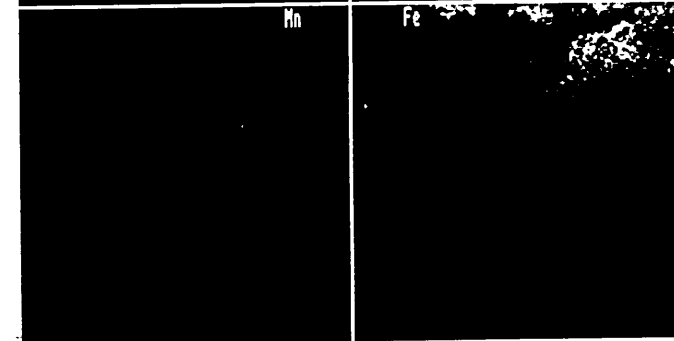
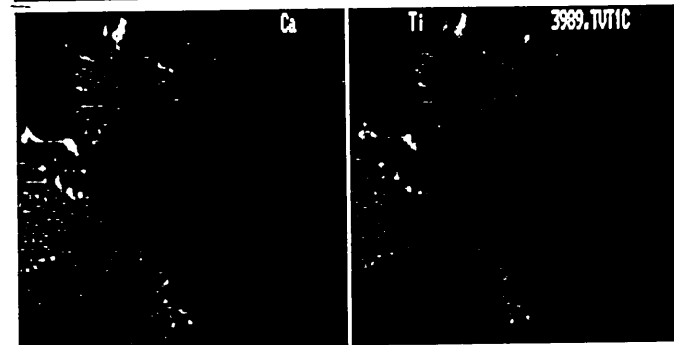
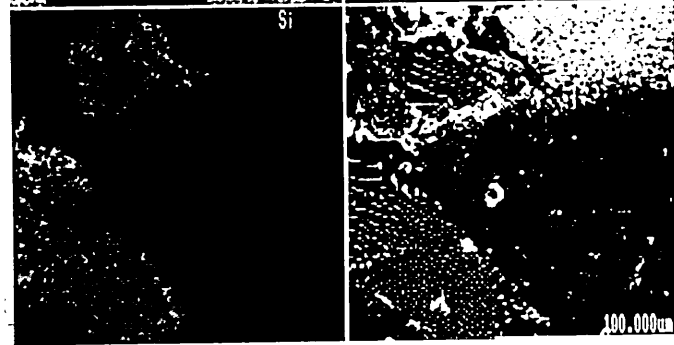
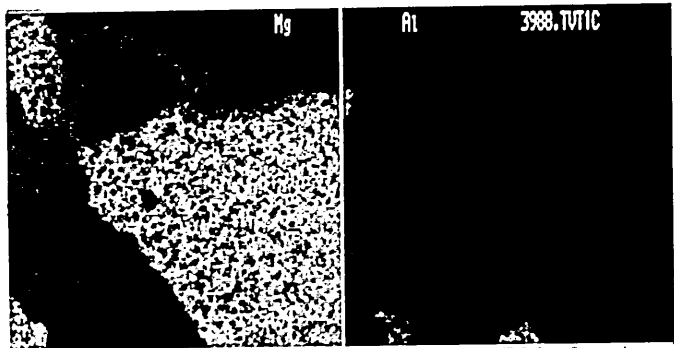
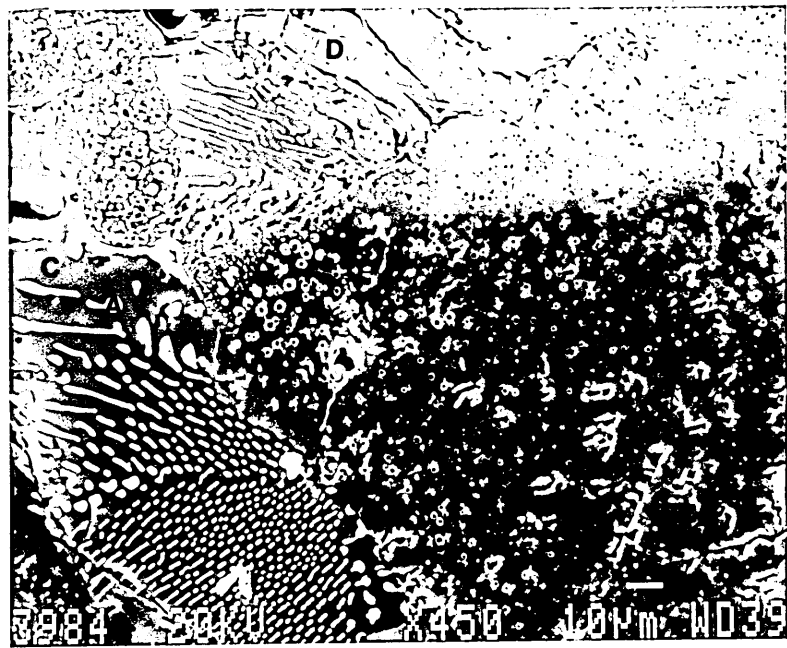


Plate 4.64(a)

Crucible interface which was in contact with the silicon deoxidised steel melted in the high frequency furnace.

The energy dispersive X-ray analysis of the points indicated on the micrograph. (JEOL 840 SEM/EDX)

Oxide mass%						
	CaO	Al ₂ O ₃	SiO ₂	MgO	FeO	MnO
A	2.0		50.0	46.0	2.0	1.0
B	2.0		29.0	4.0	60.0	5.0
C		3.0		85.0	10.0	2.0
D	4.0	16.0	30.0	43.0	5.0	2.0

SEM Micrograph.

Magnification 200 X

Plate 4.64(b)

Energy dispersive X-ray elemental maps of Plate 4.64(a) for magnesium, aluminium, silicon, calcium, manganese and iron. (JEOL 840 SEM/DIGIMAP)

Magnification of each map 100 X

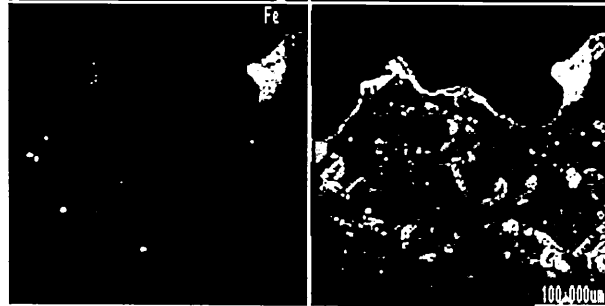
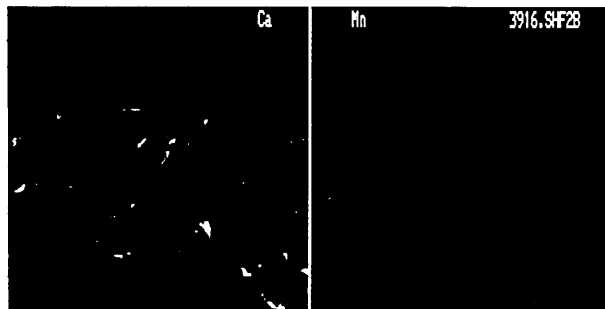
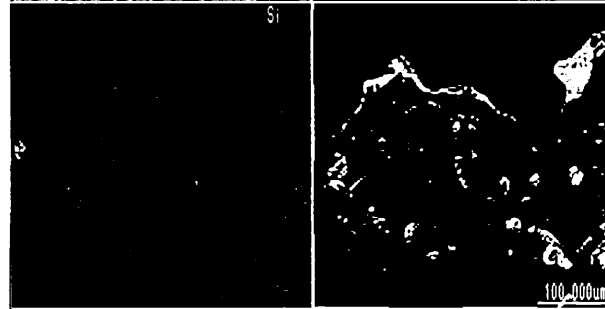
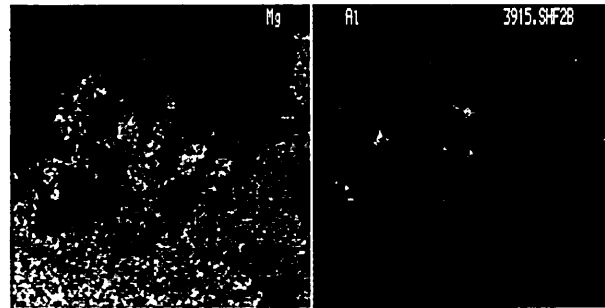
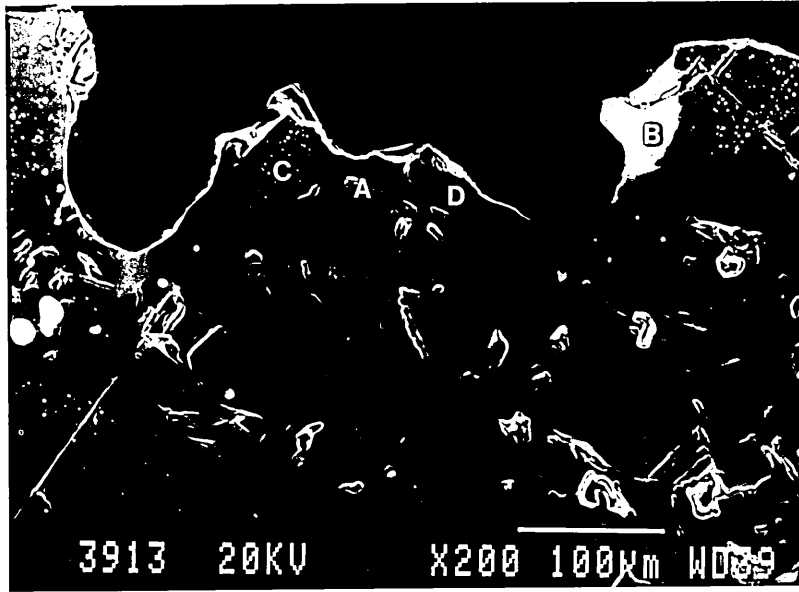


Plate 4.65(a)

Crucible interface which was in contact with the silicon deoxidised steel melted in the high frequency furnace.

The energy dispersive X-ray analysis of the points indicated on the micrograph. (JEOL 840 SEM/EDX)

	Oxide mass%					
	CaO	Al ₂ O ₃	SiO ₂	MgO	FeO	MnO
A			50.0	44.0	4.0	2.0
B		1.0	52.0	33.0	8.0	5.0
C	2.0	2.0	54.0	31.0	7.0	5.0
D		2.0		98.0		
E			49.0	43.0	6.0	2.0
F				58.0	34.0	6.0

SEM Micrograph.

Magnification 50 X

Plate 4.65(b)

Energy dispersive X-ray elemental maps of Plate 4.65(a) for magnesium, aluminium, calcium, silicon, manganese and iron. (JEOL 840 SEM/DIGIMAP)

Magnification of each map 25 X

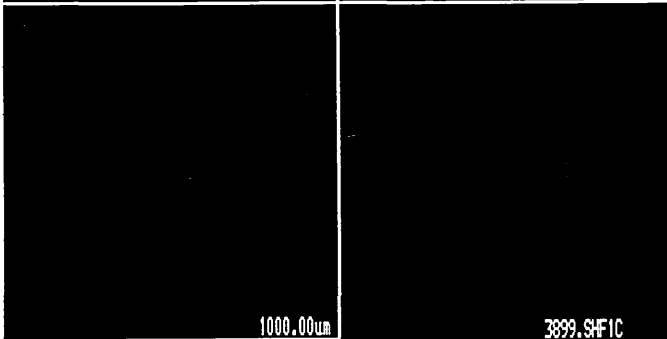
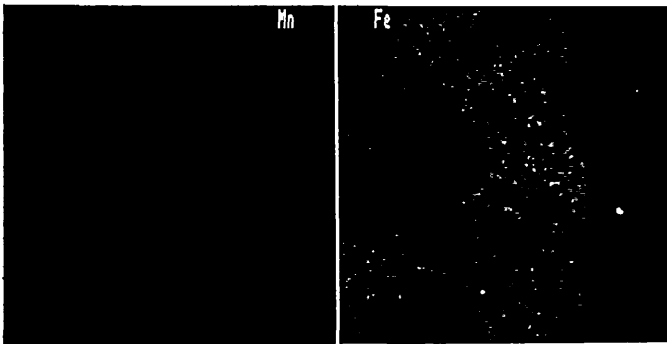
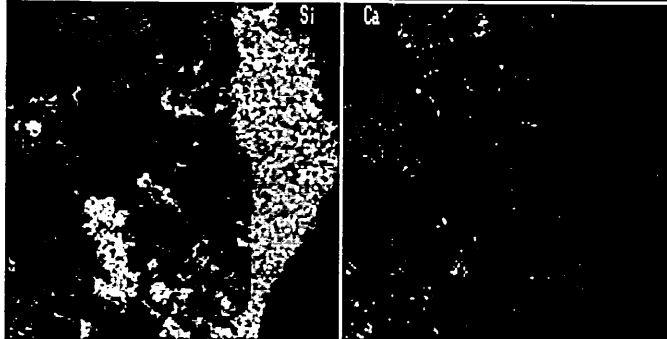
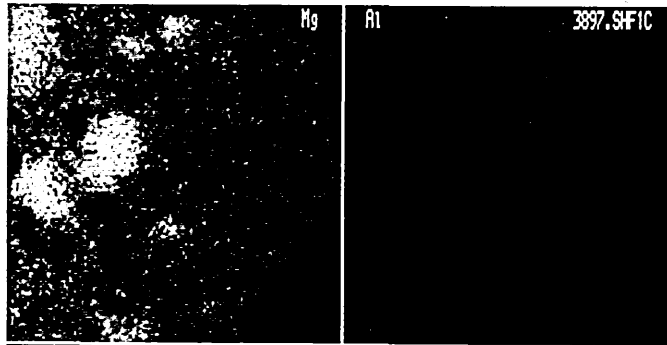


Plate 4.66(a)

Crucible interface which was in contact with the silicon deoxidised steel melted in the vertical tube furnace.

The energy dispersive X-ray analysis of the points indicated on the micrograph. (JEOL 840 SEM/EDX)

Oxide mass%						
	CaO	Al ₂ O ₃	SiO ₂	MgO	FeO	MnO
A	36.0		41.0	19.0	2.0	2.0
B	5.0		50.0	40.0	2.0	2.0
C		1.0		93.0	4.0	2.0

SEM Micrograph.

Magnification 200 X

Plate 4.66(b)

Energy dispersive X-ray elemental maps of Plate 4.66(a) for magnesium, aluminium, calcium and silicon. (JEOL 840 SEM/DIGIMAP)

Magnification of each map 100 X

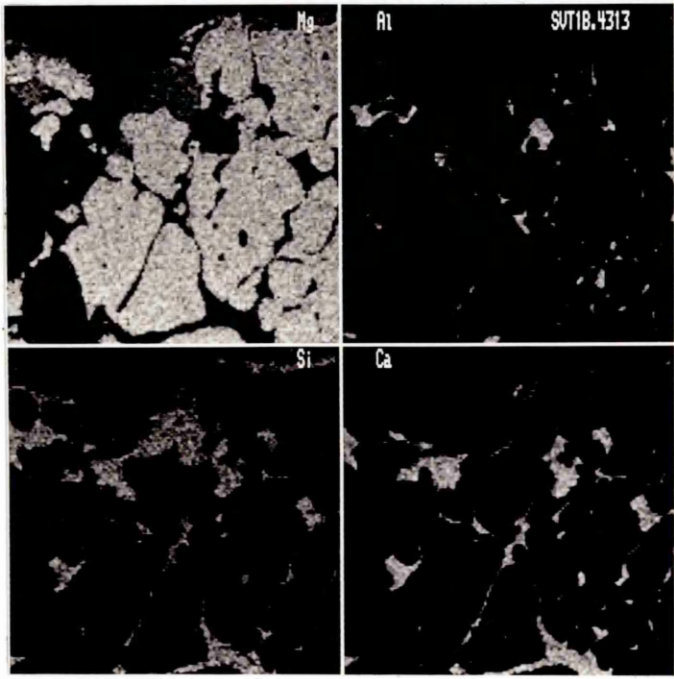
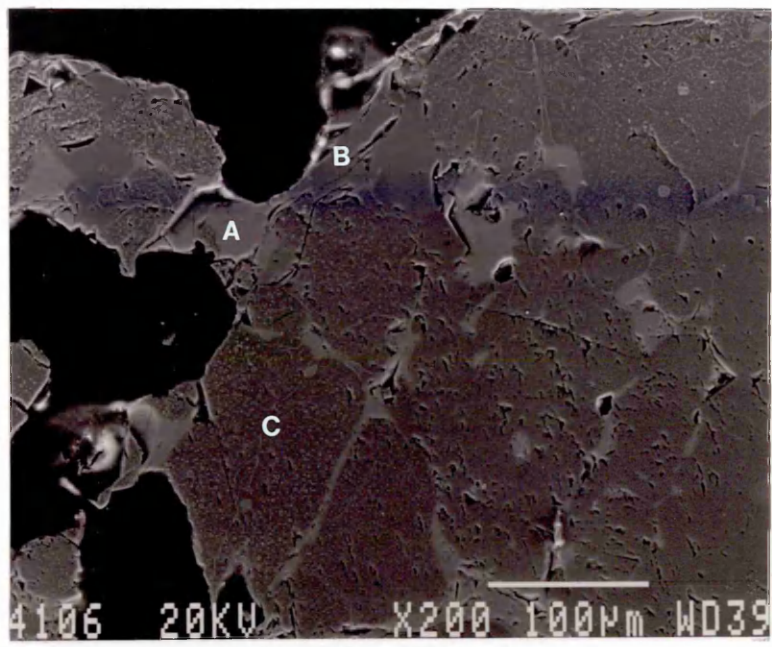


Plate 4.67(a)

Crucible interface which was in contact with the calcium-aluminium deoxidised steel melted in the high frequency furnace.

The energy dispersive X-ray analysis of the points indicated on the micrograph. (JEOL 840 SEM/EDX)

Oxide mass%					
	CaO	Al ₂ O ₃	SiO ₂	MgO	FeO
A		52.0		45.0	2.0
B	58.0	6.0	32.0	3.0	

SEM Micrograph.

Magnification 330 X

Plate 4.67(b)

Energy dispersive X-ray elemental maps of Plate 4.67(a) for magnesium, aluminium, calcium, silicon, and iron. (JEOL 840 SEM/DIGIMAP)

Magnification of each map 165 X

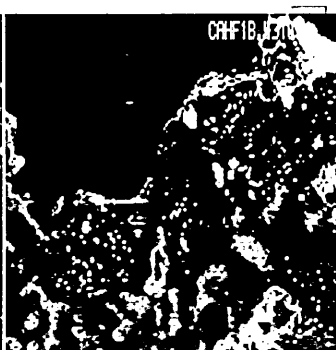
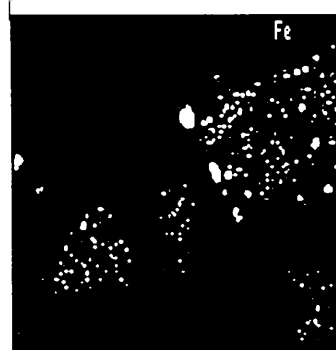
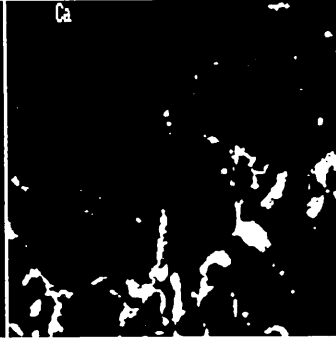
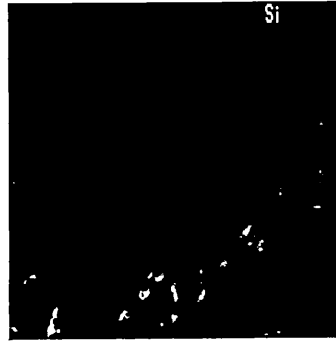
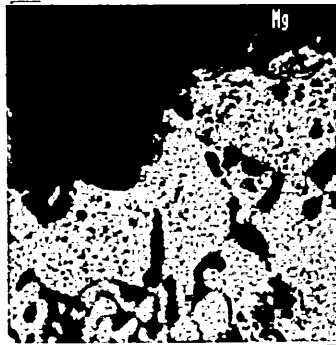


Plate 4.68(a)

Crucible interface which was in contact with the calcium-aluminium deoxidised steel melted in the vertical tube furnace.

The energy dispersive X-ray analysis of the points indicated on the micrograph. (JEOL 840 SEM/EDX)

Oxide mass%				
	CaO	Al ₂ O ₃	SiO ₂	MgO
A	55.0		35.0	11.0
B	39.0		37.0	23.0
C		70.0		30.0

SEM Micrograph.

Magnification 330 X

Plate 4.68(b)

Energy dispersive X-ray elemental maps of Plate 4.68(a) for magnesium, aluminium, calcium, silicon, and iron. (JEOL 840 SEM/DIGIMAP)

Magnification of each map 165 X

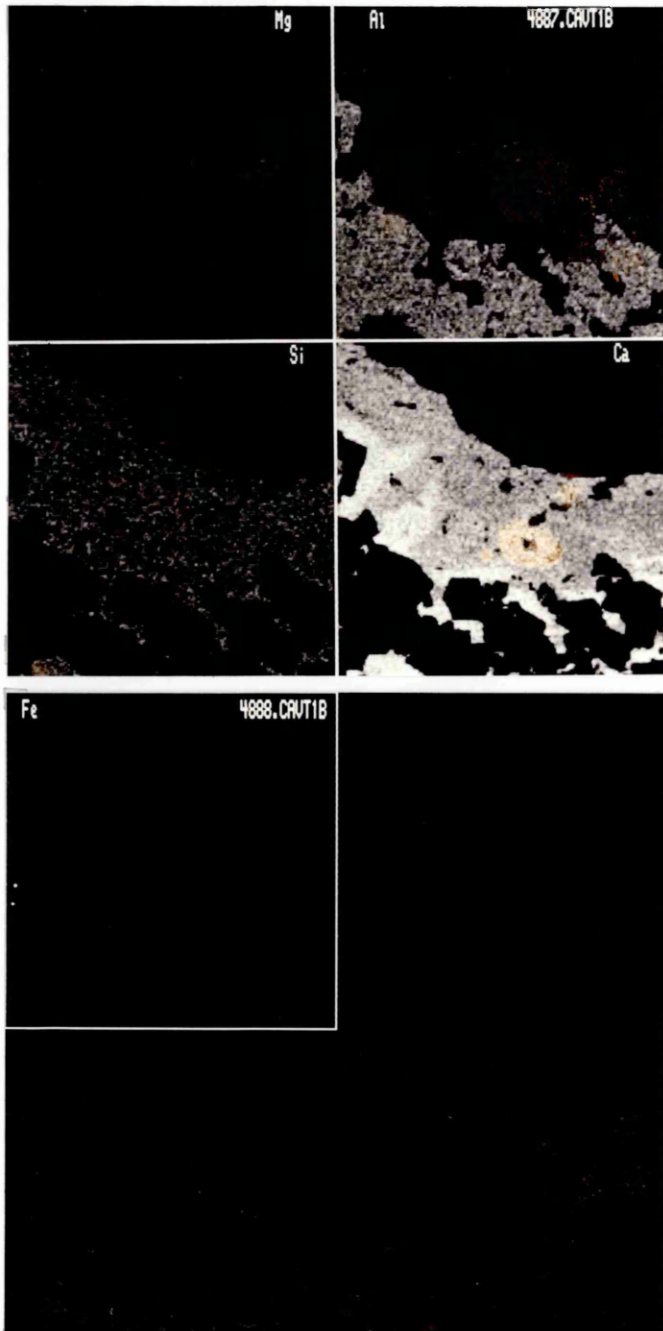
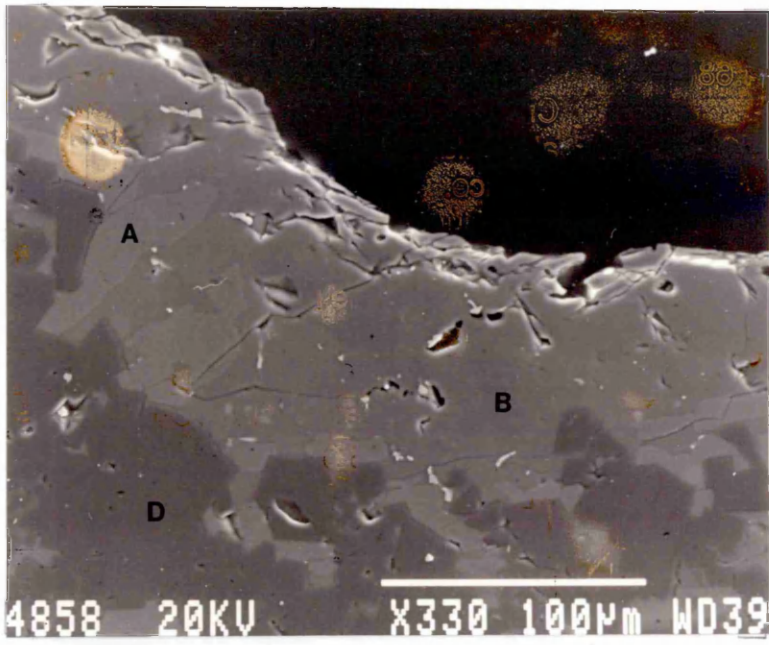


Plate 4.69(a)

Crucible interface which was in contact with the zirconium deoxidised steel melted in the vertical tube furnace.

The energy dispersive X-ray analysis of the points indicated on the micrograph. (JEOL 840 SEM/EDX)

Oxide mass%						
	ZrO ₂	CaO	Al ₂ O ₃	SiO ₂	MgO	FeO
A	87.0	7.0		3.0	2.0	<1.0
B	6.0		64.0		29.0	<1.0
C	7.0	34.0	4.0	35.0	20.0	<1.0
D	4.0				95.0	<1.0

SEM Micrograph

Magnification 330 X

Plate 4.69(b)

Energy dispersive X-ray elemental maps of Plate 4.69(a) for magnesium, aluminium, silicon, zirconium, calcium and iron. (JEOL 840 SEM/DIGIMAP)

Magnification of each map 165 X

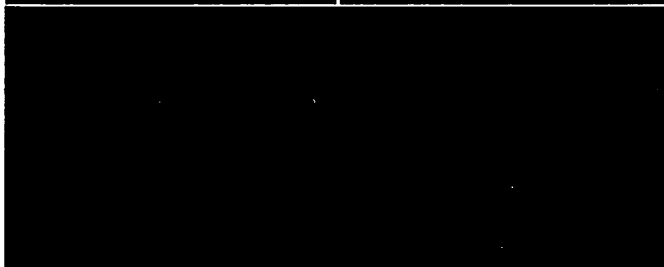
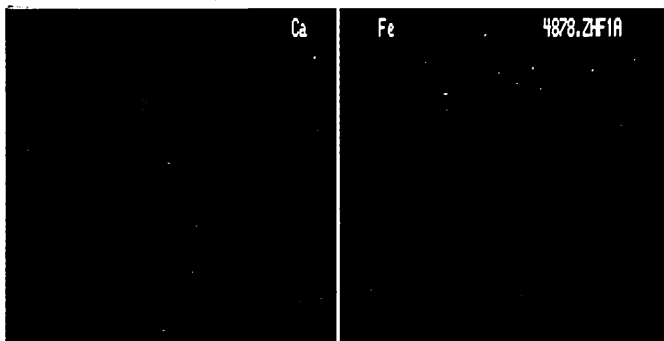
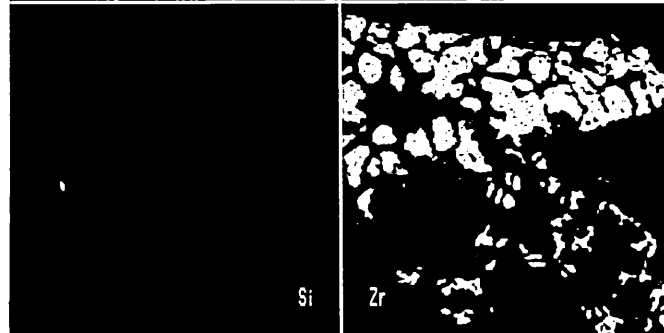
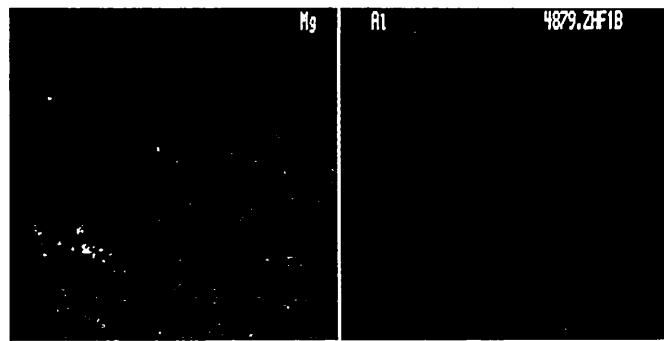
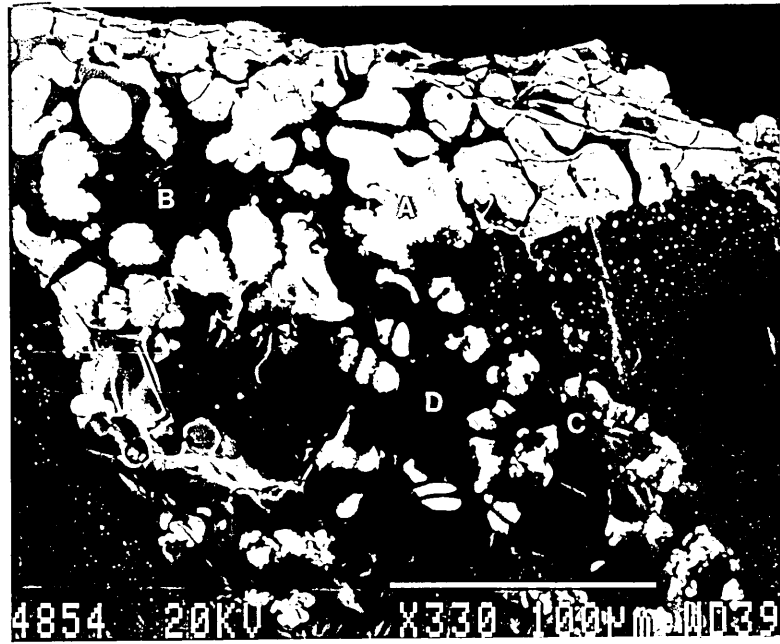


Plate 4.70(a)

Crucible interface which was in contact with the zirconium deoxidised steel melted in the high frequency furnace.

The energy dispersive X-ray analysis of the points indicated on the micrograph. (JEOL 840 SEM/EDX)

	Oxide mass%					
	ZrO ₂	CaO	Al ₂ O ₃	SiO ₂	MgO	FeO
A	74.0	26.0				
B	87.0	11.0		2.0		
C	73.0				27.0	
D					91.0	9.0

SEM Micrograph

Magnification 200 X

Plate 4.70(b)

Energy dispersive X-ray elemental maps of Plate 4.70(a) for magnesium, aluminium, silicon, zirconium, calcium and iron. (JEOL 840 SEM/DIGIMAP)

Magnification of each map 100 X

